

Remote Sensing and Digital Image Processing

Claudia Kuenzer  
Stefan Dech *Editors*

# Thermal Infrared Remote Sensing

Sensors, Methods, Applications



# Thermal Infrared Remote Sensing

# Remote Sensing and Digital Image Processing

---

VOLUME 17

---

**Series Editor:**

Freek D. van der Meer  
*Department of Earth Systems Analysis  
International Institute for  
Geo-Information Science and  
Earth Observation (ITC)  
Enchede, The Netherlands  
&  
Department of Physical Geography  
Faculty of Geosciences  
Utrecht University  
The Netherlands*

**EARSel Series Editor:**

André Marçal  
*Department of Mathematics  
Faculty of Sciences  
University of Porto  
Porto, Portugal*

**Editorial Advisory Board:**

Michael Abrams  
*NASA Jet Propulsion Laboratory  
Pasadena, CA, U.S.A.*

Paul Curran  
*University of Bournemouth, U.K.  
Finland*

Arnold Dekker  
*CSIRO, Land and Water Division  
Canberra, Australia*

Steven M. de Jong  
*Department of Physical Geography  
Faculty of Geosciences  
Utrecht University, The Netherlands*

Michael Schaepman  
*Department of Geography  
University of Zurich, Switzerland*

**EARSel Editorial Advisory Board:**

Mario A. Gomarasca  
*CNR - IREA Milan, Italy*

Martti Hallikainen  
*Helsinki University of Technology  
Finland*

Håkan Olsson  
*University of Zurich, Switzerland  
Swedish University  
of Agricultural Sciences  
Sweden*

Eberhard Parlow  
*University of Basel  
Switzerland*

Rainer Reuter  
*University of Oldenburg  
Germany*

For further volumes:  
<http://www.springer.com/series/6477>

Claudia Kuenzer • Stefan Dech  
Editors

# Thermal Infrared Remote Sensing

Sensors, Methods, Applications



Springer

*Editors*

Claudia Kuenzer  
German Remote Sensing  
Data Center (DFD)  
Earth Observation Center (EOC)  
German Aerospace Center (DLR)  
Oberpfaffenhofen, Germany

Stefan Dech  
German Remote Sensing  
Data Center (DFD)  
Earth Observation Center (EOC)  
German Aerospace Center (DLR)  
Oberpfaffenhofen, Germany

ISSN 1567-3200

ISBN 978-94-007-6638-9

ISBN 978-94-007-6639-6 (eBook)

DOI 10.1007/978-94-007-6639-6

Springer Dordrecht Heidelberg New York London

Library of Congress Control Number: 2013941729

For Chapters 5, 6, 9, 18: © Springer (outside the USA)

© Springer Science+Business Media Dordrecht 2013

This work is subject to copyright. All rights are reserved by the Publisher, whether the whole or part of the material is concerned, specifically the rights of translation, reprinting, reuse of illustrations, recitation, broadcasting, reproduction on microfilms or in any other physical way, and transmission or information storage and retrieval, electronic adaptation, computer software, or by similar or dissimilar methodology now known or hereafter developed. Exempted from this legal reservation are brief excerpts in connection with reviews or scholarly analysis or material supplied specifically for the purpose of being entered and executed on a computer system, for exclusive use by the purchaser of the work. Duplication of this publication or parts thereof is permitted only under the provisions of the Copyright Law of the Publisher's location, in its current version, and permission for use must always be obtained from Springer. Permissions for use may be obtained through RightsLink at the Copyright Clearance Center. Violations are liable to prosecution under the respective Copyright Law.

The use of general descriptive names, registered names, trademarks, service marks, etc. in this publication does not imply, even in the absence of a specific statement, that such names are exempt from the relevant protective laws and regulations and therefore free for general use.

While the advice and information in this book are believed to be true and accurate at the date of publication, neither the authors nor the editors nor the publisher can accept any legal responsibility for any errors or omissions that may be made. The publisher makes no warranty, express or implied, with respect to the material contained herein.

*Cover illustration:* Airborne thermal scanner image of Munich city centre, Germany. Kindly provided by Prof. Dr. Peter Reinartz, DLR. Visualization: Nils Sparwasser, DLR.

Printed on acid-free paper

Springer is part of Springer Science+Business Media ([www.springer.com](http://www.springer.com))

# Foreword



Temperature is one of the most important physical environmental variables monitored by Earth observing remote sensing systems. Be it land surface temperature, sea surface temperature, or air temperature, temperature ranges define the boundaries of habitats on our planet. Already thousands of years ago, temperature defined where we humans can settle and survive. Which plant resources are available? What wildlife is present? Which crops can be grown? Which diseases are prevalent? Which water surfaces will freeze, which will remain ice-free? Where do frequent wildfires occur? Temperature boundaries contribute largely to the answers to all these questions.

Nowadays, in an era of technological progress but also concern about climate change, the above questions still remain important. But new ones have arisen as well. On the local scale, we are interested in a variety of phenomena, such as urban microclimate dynamics, urban heat island effects, industry-related thermal water pollution, and burning oil and gas wells, to give only some examples. On the regional scale, we need reliable information on where forest fires flare up, where geothermal fields hold the potential for energy generation, or where coal is wastefully consumed by underground coal fires. On the global scale, our interest lies in global dynamics and the consequences of global warming and climate change. We need to understand ocean current temperature changes, need to know if the freeze-and-thaw behaviour of coastal waters, rivers, and lakes is changing, and how altered evaporation patterns impact our water resources.

Temperature information with good spatial and temporal coverage is a key to addressing most of these challenges. Consequently, thermal infrared Earth observation data and derived products are a crucial source of valuable information. Sensors for thermal infrared observations can be ground-based, airborne, or space-borne. Ground-based remote observation performed with novel handheld thermal camera systems enables the detection of energy leaks in buildings,

performance monitoring of machines in industry, and a survey of local geothermal phenomena. Airborne thermal infrared surveys support city planning, precision agriculture, and mineral mapping. With space-borne Earth observation technology we can monitor phenomena at all scales. For this task a variety of thermal infrared sensors are flown on an international fleet of Earth observing satellites.

The famous NOAA-AVHRR sensor family has been enabling thermal mapping at 1 km spatial resolution since 1979. At the same resolution, the MODIS sensor has also mapped the temperature state of Earth in 16 thermal bands since the year 2000. At the higher resolution of 120–60 m, all the well-known Landsat sensors (MSS-3 onwards, TM, ETM+) monitored our planet in the thermal domain – allowing a view into our past from their launch up until 1978. The new Landsat Data Continuity Mission, LCDM, launched in 2013, also includes a thermal band.

The German Aerospace Center, DLR, designed and operated the BIRD (2001–2004) and TET-1 missions (launched in 2012), which contributed and still contributes to thermal observations of the Earth's surface. This is only an incomplete snapshot of available resources, and numerous future sensor missions are planned.

The thermal infrared community is growing day by day. Many international scientists active in thermal infrared remote sensing have contributed to this book, providing an introduction to this important domain and describing selected sensors, analysis methods, and applications. I am convinced that it will be a milestone on the pathway of thermal infrared remote sensing and will trigger scientific discussion about advances and remaining gaps and also spark the excitement of scientists new to this field.

I hope that I have awakened your interest in thermal infrared remote sensing as one important tool to assess the state of our environment.  
May you enjoy your reading!



Prof. Dr.-Ing. Johann-Dietrich Wörner  
Chairman of the Executive Board  
German Aerospace Center DLR  
Cologne, Germany

# Acknowledgements

We would like to thank the European Association of Remote Sensing Laboratories (EARSeL) for supporting this book project via long-term backing of the Special Interest Group on Thermal Remote Sensing, SIG-TRS, as well as promotional activities. Special thanks go to Rudi Goossens, former Chairman of EARSeL, for his encouragement to establish SIG-TRS, as well as to Gesine Boettcher, Ioannis Manakos, and André Marçal.

The chapters presented in this book were contributed by renowned scientists in the field of thermal infrared remote sensing from around the world. This work would not have been possible without each author's voluntary and enthusiastic commitment to this book project. We thank all authors for the very smooth process of chapter compilation.

We are extremely grateful to the following experts who have volunteered to peer-review the chapters of this book. Investing their time and knowledge, the reviewers significantly helped to shape the final chapters with their critical comments and suggestions.

Alphabetically, we express our sincere thanks to:

Michael Abrams (National Aeronautics and Space Administration, NASA, Jet Propulsion Laboratory, JPL, California Institute of Technology, Pasadena, CA, USA); Stefania Amici (Istituto Nazionale di Geofisica e Vulcanologia, INGV Rome, Italy); Clement Atzberger (University of Natural Resources and Life Sciences, BOKU, Vienna, Austria); Fabrizia Buongiorno (Istituto Nazionale di Geofisica e Vulcanologia, INGV, Rome, Italy); Stefan Dech (German Remote Sensing Data Center, DFD, Earth Observation Center, EOC, German Aerospace Center, DLR, Oberpfaffenhofen, Germany); Brean Duncan (Innovative Health Applications, Kennedy Space Center, FL, USA); Corinne Frey (University of Wuerzburg, Wuerzburg, Germany); Susan Giegerich (Berlin, Germany); Roland Goetze (Rigorous Systems Research Group, RSRG – University of Bonn, Bonn, Germany); Huadong Guo (Center of Earth Observation and Digital Earth, CEODE, Beijing, China); Christian Haselwimmer (Geophysical Institute, University of Alaska Fairbanks, Fairbanks, AK, USA); Wieke Heldens (German Aerospace Center, DLR, German Remote Sensing Data Center, DFD, Earth

Observation Center, EOC, German Aerospace Center, DLR, Oberpfaffenhofen, Germany); Andreas Hirner (European Commission – Joint Research Centre, JRC, IPSC – GlobeSec – Critech, Ispra, Italy); Topher Hughes (National Aeronautics and Space Administration, NASA, Jet Propulsion Laboratory, Pasadena, CA, USA); Juliane Huth (German Remote Sensing Data Center, DFD, Earth Observation Center, EOC, German Aerospace Center, DLR, Oberpfaffenhofen, Germany); Doris Klein (German Aerospace Center, DLR, German Remote Sensing Data Center, DFD, Earth Observation Center, EOC, German Aerospace Center, DLR, Oberpfaffenhofen, Germany); Simone Kotthaus (King’s College London, London, UK); Claudia Kuenzer (German Remote Sensing Data Center, DFD, Earth Observation Center, EOC, German Aerospace Center, DLR, Oberpfaffenhofen, Germany); Rachel Lee (University of Pittsburgh, Pittsburgh, PA, USA); Christopher Merchant (School of GeoSciences, The University of Edinburgh, Edinburgh, UK); Florian Moder (Ministry of Science and Technology Southern Representative Office, MOST-SRO, Ho Chi Minh City, Vietnam); Jan-Peter Mund (Eberswalde University for Sustainable Development, Eberswalde, Germany); Vahid Naeimi (University of Wuerzburg, Wuerzburg, Germany); Markus Neteler (Fondazione Edmund Mach, FEM, Research and Innovation Centre, CRI, S. Michele all’Adige, Italy); Markus Niklaus (German Remote Sensing Data Center, DFD, Earth Observation Center, EOC, German Aerospace Center, DLR, Oberpfaffenhofen, Germany); Marco Ottinger (University of Wuerzburg, Wuerzburg, Germany); Eberhard Parlow (University of Basel, Basel, Switzerland); Jay Parrish (Pennsylvania State University, University Park, PA, USA); Dale Quattrochi (National Aeronautics and Space Administration, NASA, Marshall Space Flight Center, MSFC, Huntsville, AL, USA); Rolf Richter (German Remote Sensing Data Center, DFD, Earth Observation Center, EOC, German Aerospace Center, DLR, Oberpfaffenhofen, Germany); Gilles Rock (University of Trier, Trier, Germany); Christian Schweitzer (Helmholz-Centre for Environmental Research, UFZ, Leipzig, Germany); José Sobrino (Global Change Unit, Image Processing Laboratory, IPL University of Valencia, Valencia, Spain); Nils Sparwasser (German Aerospace Center, DLR, Earth Observation Center, EOC, German Remote Sensing Data Center, DFD, Oberpfaffenhofen, Germany); Kerstin Stelzer (Brockmann Consult, Geesthacht, Germany); Ping Tang (Institute of Remote Sensing Applications, IRS, Beijing, China); Anke Tetzlaff (European Academy of Bozen/Bolzano, EURAC, Bolzano, Italy); Vo Quoc Tuan (Can Tho University, CTU, Can Tho, Vietnam); Margarete Vasterling (Federal Institute for Geosciences and Natural Resources, BGR, Central Seismological Observatory, Nuclear Test Ban, Hannover, Germany); James Voogt (University of Western Ontario, Ontario, Canada); Wolfgang Wagner (Vienna University of Technology, Vienna, Austria); Torsten Welle (United Nations University – Institute for Environment and Human Security, UNU-EHS, Bonn, Germany); Li Zaho-Liang (Image Sciences, Computer Sciences and Remote Sensing Laboratory, LSIIT, French National Center for Scientific Research, CNRS, University of Strasbourg, Illkirch, France); Jianzhong Zhang (Beijing ESKY Technology Ltd., China).

Special thanks go to Susan Giegerich for her support in proofreading and language editing selected chapters, as well as to Nils Sparwasser (Science Visualization and Geoinformation, DLR, EOC, DFD) for designing the title page.

We are especially grateful to Philipp Koch for his excellent cooperation and outstanding editorial support during the preparation of this book.



# Contents

<b>1 Theoretical Background of Thermal Infrared Remote Sensing . . . . .</b>	<b>1</b>
Claudia Kuenzer and Stefan Dech	
<b>2 Geometric Calibration of Thermographic Cameras . . . . .</b>	<b>27</b>
Thomas Luhmann, Johannes Piechel, and Thorsten Roelfs	
<b>3 Thermal Infrared Spectroscopy in the Laboratory and Field in Support of Land Surface Remote Sensing . . . . .</b>	<b>43</b>
Christoph A. Hecker, Thomas E.L. Smith, Beatriz Ribeiro da Luz, and Martin J. Wooster	
<b>4 Challenges and Opportunities for UAV-Borne Thermal Imaging . . . . .</b>	<b>69</b>
Margarete Vasterling and Uwe Meyer	
<b>5 NASA's Hyperspectral Thermal Emission Spectrometer (HyTES) . . . . .</b>	<b>93</b>
Simon J. Hook, William R. Johnson, and Michael J. Abrams	
<b>6 NASA's Hyperspectral Infrared Imager (HyspIRI) . . . . .</b>	<b>117</b>
Michael J. Abrams and Simon J. Hook	
<b>7 Spaceborne Thermal Infrared Observation – An Overview of Most Frequently Used Sensors for Applied Research . . . . .</b>	<b>131</b>
Claudia Kuenzer, Huadong Guo, Marco Ottinger, Jianzhong Zhang, and Stefan Dech	
<b>8 Thermal Remote Sensing with Small Satellites: BIRD, TET and the Next Generation BIROS . . . . .</b>	<b>149</b>
Eckehard Lorenz	
<b>9 Landsat and Thermal Infrared Imaging . . . . .</b>	<b>177</b>
Terry Arvidson, Julia Barsi, Murzy Jhabvala, and Dennis Reuter	

<b>10</b>	<b>Review of High Resolution Thermal Infrared Applications and Requirements: The Fuegosal Synthesis Study . . . . .</b>	197
	José A. Sobrino, Fabio Del Frate, Matthias Drusch, Juan C. Jiménez-Muñoz, and Paolo Manunta	
<b>11</b>	<b>Cross-Comparison of Daily Land Surface Temperature Products from NOAA-AVHRR and MODIS . . . . .</b>	215
	Corinne Myrtha Frey, Claudia Kuenzer, and Stefan Dech	
<b>12</b>	<b>Comparison of the Thermal Sensors of SEVIRI and MODIS for LST Mapping . . . . .</b>	233
	Caixia Gao, Xiaoguang Jiang, Zhao-Liang Li, and Françoise Nerry	
<b>13</b>	<b>A Water Vapor Scaling (WVS) Method for Improving Atmospheric Correction of Thermal Infrared (TIR) Data . . . . .</b>	253
	Glynn Hulley	
<b>14</b>	<b>Time Series Corrections and Analyses in Thermal Remote Sensing . . . . .</b>	267
	José A. Sobrino and Yves Julien	
<b>15</b>	<b>Thermal Remote Sensing of Sea Surface Temperature . . . . .</b>	287
	Christopher J. Merchant	
<b>16</b>	<b>Soil Moisture from Thermal Infrared Satellite Data: Synergies with Microwave Data . . . . .</b>	315
	Claudia Kuenzer, Ursula Gessner, and Wolfgang Wagner	
<b>17</b>	<b>Application of the Apparent Thermal Inertia Concept for Soil Moisture Estimation in Agricultural Areas . . . . .</b>	331
	Claudia Notarnicola, Katarzyna Ewa Lewińska, Marouane Temimi, and Marc Zebisch	
<b>18</b>	<b>Thermal Remote Sensing of Active Vegetation Fires and Biomass Burning Events . . . . .</b>	347
	Martin J. Wooster, Gareth Roberts, Alistair M.S. Smith, Joshua Johnston, Patrick Freeborn, Stefania Amici, and Andrew T. Hudak	
<b>19</b>	<b>Analysis of Lava Flow Effusion Rate Using High Spatial Resolution Infrared Data . . . . .</b>	391
	Valerio Lombardo and Maria Fabrizia Buongiorno	
<b>20</b>	<b>Thermal Analysis of Volcanoes Based on 10 Years of ASTER Data on Mt. Etna . . . . .</b>	409
	Maria Fabrizia Buongiorno, David Pieri, and Malvina Silvestri	

Contents	xiii
<b>21 Thermal Infrared Remote Sensing of Surface and Underground Coal Fires . . . . .</b>	429
Claudia Kuenzer, Jianzhong Zhang, Li Jing, Guo Huadong, and Stefan Dech	
<b>22 Thermal Infrared Remote Sensing of Geothermal Systems . . . . .</b>	453
Christian Haselwimmer and Anupma Prakash	
<b>23 Analysis of Surface Thermal Patterns in Relation to Urban Structure Types: A Case Study for the City of Munich . . . . .</b>	475
Wieke Heldens, Hannes Taubenböck, Thomas Esch, Uta Heiden, and Michael Wurm	
<b>24 Mineral Mapping with Airborne Hyperspectral Thermal Infrared Remote Sensing at Cuprite, Nevada, USA . . . . .</b>	495
Dean N. Riley and Christoph A. Hecker	
<b>25 Validation of Thermal Infrared (TIR) Emissivity Spectra Using Pseudo-invariant Sand Dune Sites . . . . .</b>	515
Glynn Hulley and Alice Baldridge	
<b>Index . . . . .</b>	529



# Contributors

**Michael J. Abrams** Jet Propulsion Laboratory, California Institute of Technology, National Aeronautics and Space Administration (NASA), Pasadena, CA, USA

**Stefania Amici** Istituto Nazionale di Geofisica e Vulcanologia (INGV), Rome, Italy

**Terry Arvidson** Information Systems and Global Solutions, Lockheed Martin, Greenbelt, MD, USA

**Alice Baldridge** Planetary Science Institute, Tucson, AZ, USA

**Julia Barsi** Science Systems and Applications Inc. (SSAI), Lanham, MD, USA

**Maria Fabrizia Buongiorno** Istituto Nazionale di Geofisica e Vulcanologia (INGV), Rome, Italy

**Stefan Dech** German Remote Sensing Data Center (DFD), Earth Observation Center (EOC), German Aerospace Center (DLR), Oberpfaffenhofen, Germany

**Fabio Del Frate** GEO-K, Tor Vergata University, Rome, Italy

**Matthias Drusch** European Space Research and Technology Centre (ESTEC), European Space Agency (ESA), Noordwijk, The Netherlands

**Thomas Esch** German Remote Sensing Data Center (DFD), Earth Observation Center (EOC), German Aerospace Center (DLR), Oberpfaffenhofen, Germany

**Patrick Freeborn** Department of Geography, King's College London (KCL), London, UK

**Corinne Myrtha Frey** Department of Remote Sensing in cooperation with the German Aerospace Center (DLR)

Department of Geography and Geology, University of Würzburg, Würzburg, Germany

**Caixia Gao** College of Resources and Environment, Graduate University of Chinese Academy of Sciences, Beijing, China

Image Sciences, Computer Sciences and Remote Sensing Laboratory (LSIIT), UdS, CNRS, Illkirch, France

**Ursula Gessner** German Remote Sensing Data Center (DFD), Earth Observation Center (EOC), German Aerospace Center (DLR), Oberpfaffenhofen, Germany

**Guo Huadong** Center for Earth Observation and Digital Earth (CEOED), Beijing, China

**Christian Haselwimmer** Geophysical Institute, University of Alaska Fairbanks, Fairbanks, AK, USA

**Christoph A. Hecker** Faculty of Geo-Information Science and Earth Observation (ITC), University of Twente, Enschede, The Netherlands

**Uta Heiden** German Remote Sensing Data Center (DFD), Earth Observation Center (EOC), German Aerospace Center (DLR), Oberpfaffenhofen, Germany

**Wieke Heldens** German Remote Sensing Data Center (DFD), Earth Observation Center (EOC), German Aerospace Center (DLR), Oberpfaffenhofen, Germany

**Simon J. Hook** Jet Propulsion Laboratory, California Institute of Technology, National Aeronautics and Space Administration (NASA), Pasadena, CA, USA

**Andrew T. Hudak** US Forest Service Rocky Mountain Research Station, Moscow Forestry Sciences Laboratory, Moscow, ID, USA

**Glynn Hulley** Jet Propulsion Laboratory, California Institute of Technology, National Aeronautics and Space Administration (NASA), Pasadena, CA, USA

**Murzy Jhabvala** Goddard Space Flight Center (GSFC), National Aeronautics and Space Administration (NASA), Greenbelt, MD, USA

**Xiaoguang Jiang** College of Resources and Environment, Graduate University of Chinese Academy of Sciences, Beijing, China

**Juan C. Jiménez-Muñoz** Global Change Unit, Image Processing Laboratory (IPL), University of Valencia, Valencia, Spain

**Li Jing** College of Resources Science and Technology, Beijing Normal University, Beijing, China

**William R. Johnson** Jet Propulsion Laboratory, California Institute of Technology, National Aeronautics and Space Administration (NASA), Pasadena, CA, USA

**Joshua Johnston** Department of Geography, King's College London (KCL), London, UK

Canadian Forest Service, Natural Resources Canada, Great Lakes Forestry Centre, Sault Ste. Marie, ON, Canada

**Yves Julien** Global Change Unit, Image Processing Laboratory (IPL), University of Valencia, Valencia, Spain

**Claudia Kuenzer** German Remote Sensing Data Center (DFD), Earth Observation Center (EOC), German Aerospace Center (DLR), Oberpfaffenhofen, Germany

**Katarzyna Ewa Lewińska** European Academy of Bozen/Bolzano (EURAC), Bolzano, Italy

**Zhao-Liang Li** Engineering, Computing and Imaging Laboratory (ICube), Uds, CNRS, Illkirch, France

Key Laboratory of Resources and Environment Information System, Institute of Geographic Science and Natural Resources Research, CAS, Beijing, China

**Valerio Lombardo** Istituto Nazionale di Geofisica e Vulcanologia (INGV), Rome, Italy

**Eckehard Lorenz** Optical Information Systems, DLR, Berlin, Germany

**Thomas Luhmann** Institute for Applied Photogrammetry and Geoinformatics (IAPG), Jade University of Applied Sciences, Oldenburg, Germany

**Paolo Manunta** PLANETEK Italia, Bari, Italy

**Christopher J. Merchant** Department of Meteorology, University of Reading, Reading, UK

**Uwe Meyer** Sub-Department B2.1 – Geophysical Exploration – Technical Mineralogy, Federal Institute for Geosciences and Natural Resources (BGR), Hannover, Germany

**Françoise Nerry** Engineering, Computing and Imaging Laboratory (ICube), Uds, CNRS, Illkirch, France

**Claudia Notarnicola** European Academy of Bozen/Bolzano (EURAC), Bolzano, Italy

**Marco Ottlinger** German Remote Sensing Data Center (DFD), Earth Observation Center (EOC), German Aerospace Center (DLR), Oberpfaffenhofen, Germany

**Johannes Piechel** Institute for Applied Photogrammetry and Geoinformatics (IAPG), Jade University of Applied Sciences, Oldenburg, Germany

**David Pieri** Jet Propulsion Laboratory, California Institute of Technology, Pasadena, CA, USA

**Anupma Prakash** Geophysical Institute, University of Alaska Fairbanks, Fairbanks, AK, USA

**Dennis Reuter** Goddard Space Flight Center (GSFC), National Aeronautics and Space Administration (NASA), Greenbelt, MD, USA

**Beatriz Ribeiro da Luz** University of Sao Paulo, Sao Paulo, Brazil

**Dean N. Riley** The Aerospace Corporation, Chantilly, VA, USA

SpecTIR, LLC, Fairfax, VA, USA

**Gareth Roberts** Geography and Environment, University of Southampton, Southampton, UK

**Thorsten Roelfs** Institute for Applied Photogrammetry and Geoinformatics (IAPG), Jade University of Applied Sciences, Oldenburg, Germany

**Malvina Silvestri** Istituto Nazionale di Geofisica e Vulcanologia (INGV), Rome, Italy

**Alistair M.S. Smith** Department of Forest Resources, College of Natural Resources, University of Idaho, Moscow, ID, USA

**Thomas E.L. Smith** Department of Geography, King's College London (KCL), London, UK

**José A. Sobrino** Global Change Unit, Image Processing Laboratory (IPL), University of Valencia, Valencia, Spain

**Hannes Taubenböck** German Remote Sensing Data Center (DFD), Earth Observation Center (EOC), German Aerospace Center (DLR), Oberpfaffenhofen, Germany

**Marouane Temimi** NOAA-CREST, The City College, The City University of New York, New York, NY, USA

**Margarete Vasterling** Sub-Department B4.3 – Central Seismological Observatory, Nuclear Test Ban, Federal Institute for Geosciences and Natural Resources (BGR), Hannover, Germany

**Wolfgang Wagner** Department of Geodesy and Geoinformation, Vienna University of Technology, Vienna, Austria

**Martin J. Wooster** Department of Geography, King's College London (KCL), London, UK

**Michael Wurm** German Remote Sensing Data Center (DFD), Earth Observation Center (EOC), German Aerospace Center (DLR), Oberpfaffenhofen, Germany

**Marc Zebisch** European Academy of Bozen/Bolzano (EURAC), Bolzano, Italy

**Jianzhong Zhang** Beijing ESKY Technology Ltd., Beijing, China

# Chapter 1

## Theoretical Background of Thermal Infrared Remote Sensing

Claudia Kuenzer and Stefan Dech

**Abstract** Thermal infrared (TIR) data is acquired by a multitude of ground-based, airborne, and spaceborne remote sensing instruments. A broad variety of fields apply thermal infrared remote sensing, for example to assess general land- or sea-surface temperature dynamics, detect forest, coal and peat fires, map urban heat islands or thermal water pollution, differentiate geologic surfaces, analyze soil moisture, or even to test materials, to name only a few applications. As thermal infrared data has to be analyzed slightly differently than reflective data, this chapter contains the relevant theoretical background. The thermal domain of the electromagnetic spectrum, the laws of Planck, Stefan-Boltzmann, Wien, and Kirchhoff, as well as important parameters such as kinetic and radiance temperature, emissivity, and thermal inertia are briefly explained. The chapter thus provides readers with a common understanding before proceeding to subsequent chapters.

### 1.1 Introduction

All objects with a temperature above absolute zero (0 K, which equals  $-273^{\circ}\text{C}$ ) emit electromagnetic radiation. Our earth has an average temperature of about 300 K and its peak of electromagnetic emittance is located in the thermal infrared, TIR, domain at about 9.7  $\mu\text{m}$  (Tipler 2000; Sabins 1996). The earth absorbs a large part of the incoming solar radiation and a corresponding amount is emitted at longer wavelengths.

Remote sensing sensors responsive in the thermal domain have the ability to record this TIR radiation. Radiation – as opposed to conduction or convection, where heat is transferred through matter – is an energy transfer process, which also works in/through a vacuum (Sabins 1996). TIR sensors thus enable the derivation of

---

C. Kuenzer (✉) • S. Dech  
German Remote Sensing Data Center (DFD), Earth Observation Center (EOC),  
German Aerospace Center (DLR), Oberpfaffenhofen, Germany  
e-mail: [Claudia.Kuenzer@dlr.de](mailto:Claudia.Kuenzer@dlr.de)

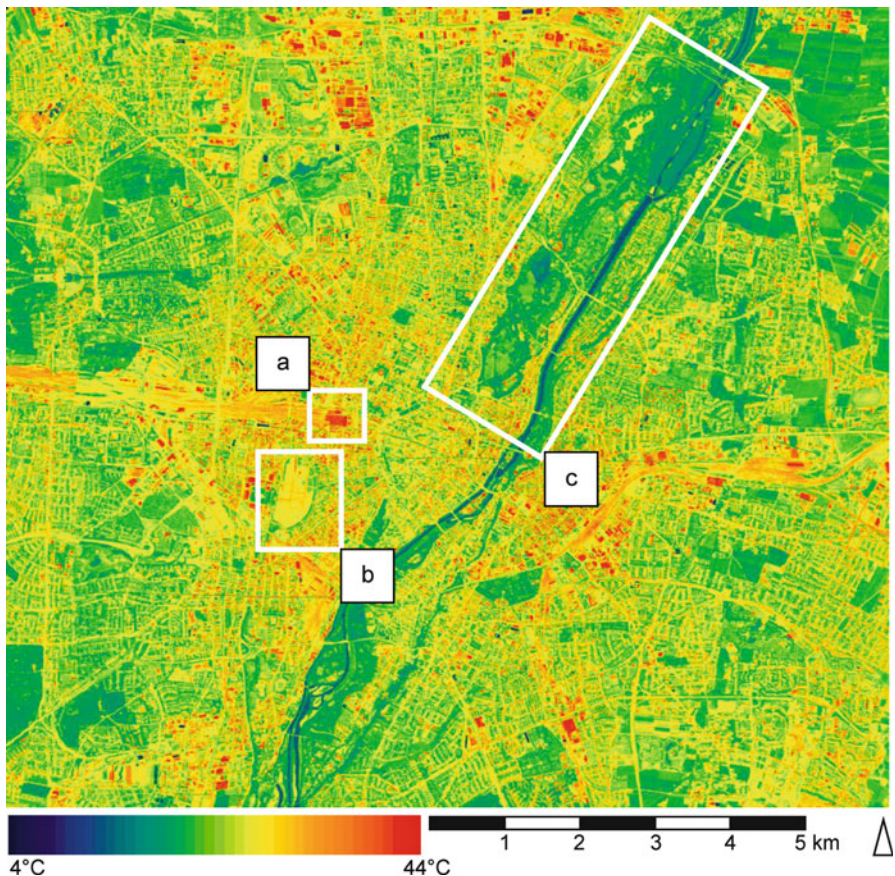


**Fig. 1.1** Thermal daytime land surface temperature image of Munich, 1982, based on data acquired with an airborne Bendix Scanner. Areas marked include the Munich central train station (a), the location – a large meadow – of the annual Oktoberfest (b) and the southern part of the English Garden, Munich's largest inner-city park (c) (Imagery courtesy of DLR)

thermal radiance images of objects on the earth's surface. Such imagery can display the kinetic temperature of objects at the resolution of the respective sensor. The necessary correction steps for certain object-inherent as well as geometric and atmospheric effects will be addressed later in this chapter.

The most commonly known products derived from TIR imagery are land surface temperature, LST, (see Fig. 1.1) and sea surface temperature, SST (Dech et al. 1998). However, thermal data have a much larger potential than just the derivation of these standard products. These data enable the assessment of thermal anomalies (forest fires, coal fires, thermal pollution, energy leaks in buildings, inflamed areas in thermal medical imagery), the analysis of moisture conditions, or even the monitoring of machine performance in industrial applications, and – depending on sensor and resolution – the assessment of thermal dynamics at different scales (see Figs. 1.2 and 1.3).

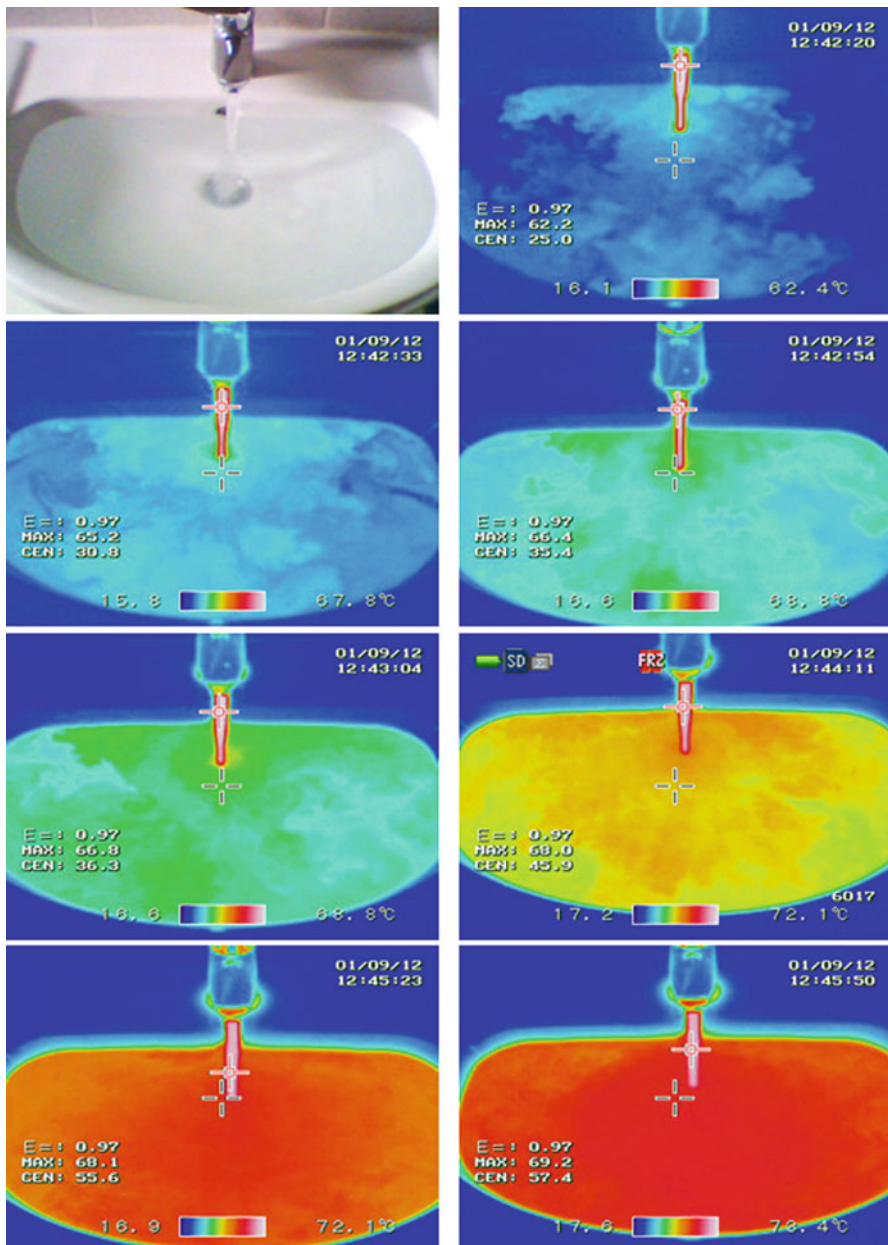


**Fig. 1.2** Thermal dynamics. Hot water runs into a sink filled with colder water of 22 °C. The hot water has a temperature between 62.2 and 69.2 °C (during the course of 1 min the hot water coming from the tap increases in temperature). The mixing of the hotter into the colder water is clearly evident in the image sequence. Emissivity is set to 0.97 as water in Munich, Germany, is extremely hard at over >2.5 mmol/l CaCO<sub>3</sub> (Photographs: C. Kuenzer)

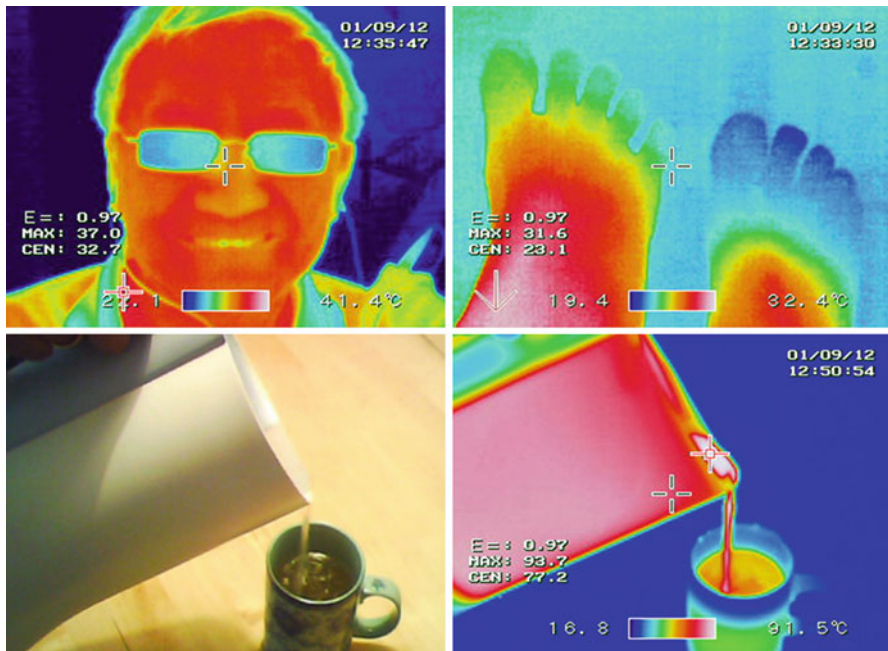


**Fig. 1.3** Thermal camera images. *Upper left:* person wearing glasses. The background as well as the glasses are colder than the human skin, which has a temperature between 36 and 37 °C. *Upper right:* a male foot (*left*) and a female foot (*right*). Since blood circulation towards the toes in the female foot is less accentuated than in the male foot, the female foot appears overall colder. *Lower left:* optical image of hot water poured from an electric water kettle into a tea mug. *Lower right:* The hottest parts of this image are at the spout and in the stream of water flowing into the mug. Note the temperature increase of the mug (*green*) caused by heat conduction (Photographs: C. Kuenzer)

A broad overview of the fleet of currently available TIR sensors and the large spectrum of TIR remote sensing applications can be found in the following chapters of this book. This chapter presents the theoretical background of thermal infrared remote sensing, which must be understood to correctly analyze and interpret TIR data.

## 1.2 Theoretical Background

### 1.2.1 *The Thermal Infrared Domain and Atmospheric Windows*

There is no strict or physical definition of the thermal infrared domain. According to Sabins (1996) the thermal infrared wavelength domain extends from about 3 to 14  $\mu\text{m}$ . In this range thermal mapping of the earth's surface is possible due

to atmospheric windows in the 3–5  $\mu\text{m}$  range, as well as in the 8–14  $\mu\text{m}$  range (see also Fig. 1.4 below). Within the 8–14  $\mu\text{m}$  range only a narrow absorption band of ozone,  $\text{O}_3$ , exists, which is omitted by most sensors. Within the 3–5  $\mu\text{m}$  range reflected sunlight can still slightly contaminate the (emitted) thermal signal, which has to be taken into account when analyzing daytime 3–5  $\mu\text{m}$  TIR imagery.

However, different authors define the TIR domain slightly differently. According to Löffler (1994) as well as Lillesand and Kiefer (1994) the TIR domain ranges from 3 to 1,000  $\mu\text{m}$ . The main characteristic common to all definitions is the fact that TIR remote sensing records emitted radiation, whereas multispectral remote sensing in the visible, VIS, and near infrared, NIR, domain records reflected radiation. Only within the shorter wavelength part of the TIR spectrum ( $<5 \mu\text{m}$ ) can the thermal signal still be slightly disturbed by reflected radiation.

### 1.2.2 Planck's Law

Planck's blackbody radiation law, Planck's law for short, describes the electromagnetic radiation emitted by a blackbody at a given wavelength  $M_\lambda$  as a function of the blackbody's absolute temperature (Planck 1900). A blackbody is defined as an (hypothetical, nonexisting) ideal radiator that totally absorbs and re-emits all energy incident upon it. Simply by specifying a certain wavelength in Eq. 1.1 below,  $M_\lambda$  can be calculated from the body's temperature (see also Fig. 1.5).

$$M_\lambda = \frac{2\pi hc^2}{\lambda^5(e^{hc/\lambda kT} - 1)} \quad (1.1)$$

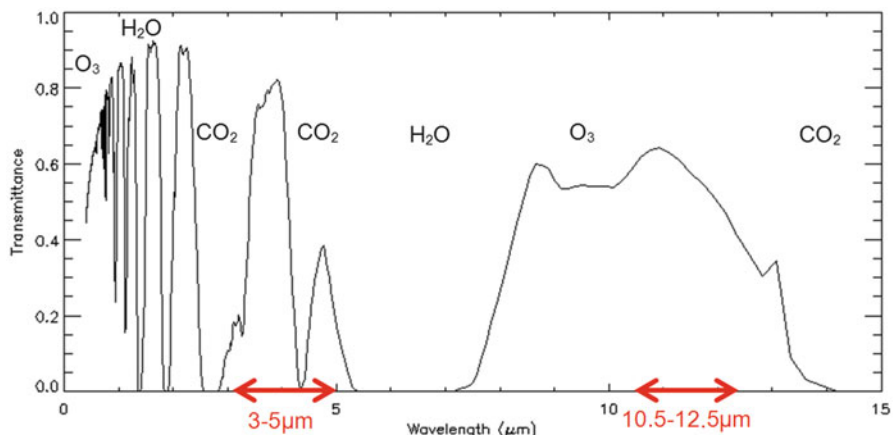


**Fig. 1.4** The thermal infrared wavelength domain, typical absorption bands induced by gasses and water, and atmospheric transmittance (atmospheric windows) (Figure courtesy of Rudolf Richter)

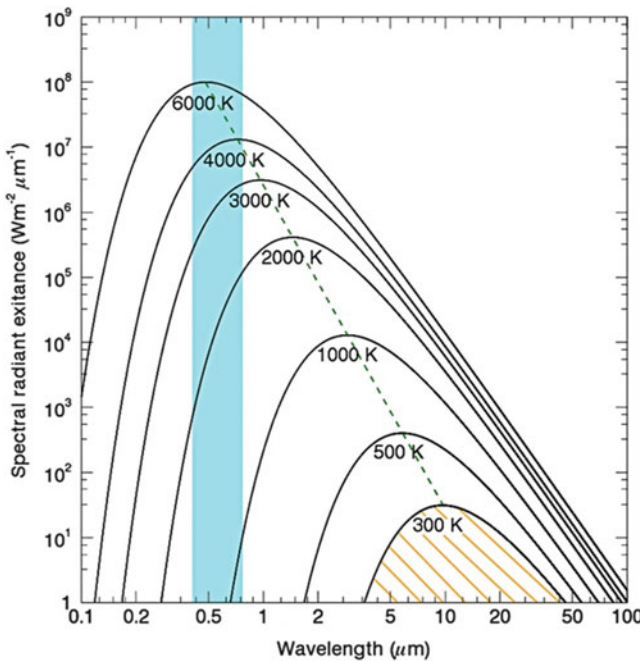


**Fig. 1.5** Blackbody radiation curves at different selected temperatures, as derived from Eq. 1.1. The laws of Planck, Stefan-Boltzmann (marked area under the 300 K curve) and Wien (green dotted line) are depicted in this figure. The blue bar indicates the VIS region

with:

$$M_\lambda = \text{spectral radiant exitance } [\text{W m}^{-2} \mu\text{m}^{-1}]$$

$$h = \text{Planck's constant } [6.626 \times 10^{-34} \text{ J s}]$$

$$c = \text{speed of light } [2.9979246 \times 10^8 \text{ m s}^{-1}]$$

$$k = \text{Boltzmann constant } [1.3806 \times 10^{-23} \text{ J K}^{-1}]$$

$$T = \text{absolute temperature } [\text{K}]$$

$$\lambda = \text{wavelength } [\mu\text{m}]$$

The total energy a blackbody radiates and the wavelength of maximum emittance depend on the temperature of the blackbody and can be described by Stefan-Boltzmann's law and Wien's law (Walker 2008; Tipler 2000).

### 1.2.3 Stefan-Boltzmann Law

The Stefan-Boltzmann law (Eq. 1.2) describes the total electromagnetic radiation emitted by a blackbody as a function of the absolute temperature of that blackbody (Walker 2008; Tipler 2000; Sabins 1996). The emitted radiation corresponds to the area under the radiation curve (integral) as depicted in Fig. 1.5.

$$T_{RadBB} = \sigma T_{kin}^4 \quad (1.2)$$

$T_{RadBB}$  = radiant flux of a blackbody [ $\text{W/m}^2$ ],

$T$  = absolute kinetic temperature [K]

$\sigma$  = Stefan-Boltzmann constant [ $5.6697 \times 10^{-8} \text{ W m}^{-2} \text{ K}^{-4}$ ]

This equation shows that the higher the temperature of the radiating object the greater the total amount of radiation (energy) it emits. The relation is not linear; irradiance is proportional to the fourth power of the black body's temperature.

#### 1.2.4 Wien's Displacement Law

Wien's law (Heal 2003; Walker 2008; Tipler 2000) describes the wavelength at which maximum spectral radiant exitance occurs:

$$\lambda_{\max} = \frac{A}{T} \quad (1.3)$$

$\lambda_{\max}$  = wavelength of maximum spectral radiant exitance [ $\mu\text{m}$ ]

$A$  = Wien's constant [ $2897.8 \mu\text{m K}$ ]

$T$  = absolute kinetic temperature [K]

With increasing temperature of an object, its maximum exitance  $\lambda_{\max}$  shifts to shorter wavelengths. This can be seen in Fig. 1.5. With an average temperature of 5,778 K (5,505 °C), the sun has its peak emission in the VIS domain of the spectrum (roughly at green: 0.55  $\mu\text{m}$ ), while a much colder object such as the earth has its peak of emission in the TIR.

Wien's dependency of temperature and peak emission can also be observed in multispectral remote sensing data, such as depicted in Fig. 1.6 below. In the optical true color image (upper left) it can be seen that lava from Kilauea volcano is flowing to the ocean. The lava appears black, as surface crusts have already built on the lava streams, hiding the orange glowing lava under the crust. However, some parts of the lava are still incredibly hot, as can be seen in the thermal band 6 (10.4–12.5  $\mu\text{m}$ ) Landsat data shown in the lower right image. The white areas here represent hot areas which are much warmer than the background. Clouds clearly visible as white structures in the upper left and upper right figure appear dark in band 6 due to their low temperature. On the grey scale image of band 7 (2.09–2.35  $\mu\text{m}$ ) clouds appear white as reflection still plays a large role in this wavelength domain. At the same time the hottest areas of the lava appear as white structures in the central lower part of the image. These white areas are much smaller in extent than the very bright areas in band 6 and therefore depict only the very hottest regions within the lava stream, which must have temperatures well above 90 °C to stand out here (see also Table 1.2 later in this chapter).

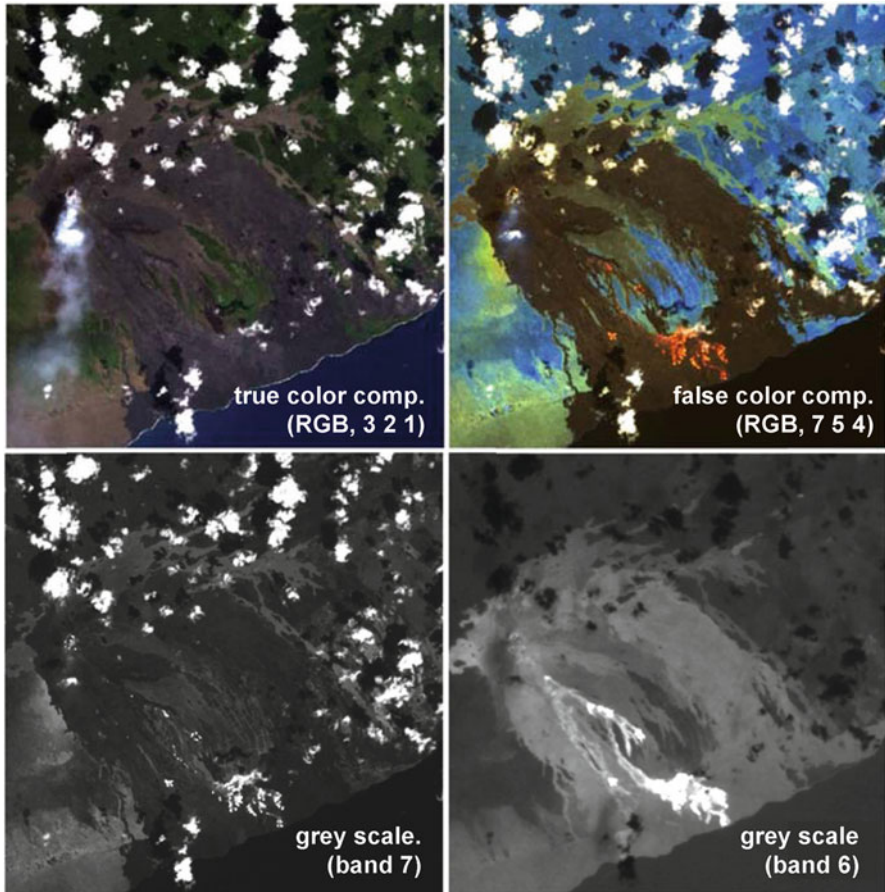


**Fig. 1.6** Landsat 7 ETM+ data of Kilauea Volcano, Hawaii, USA, February 14th, 2000, *Upper left*: true color composite with the red, green and blue bands displayed in RGB; *upper right*: false color composite with the two SWIR (shortwave infrared) bands 7 and 5 and NIR band 4 displayed in RGB; *lower left*: grey scale image of shortwave infrared band 7 (2.09–2.35  $\mu\text{m}$ ); *lower right*: grey scale image of the thermal infrared, TIR, band 6 (10.40–12.50  $\mu\text{m}$ )

### 1.2.5 Kirchhoff's Law and the Relevance of Emissivity

Planck's law defines the radiation released by a blackbody. Very few terrestrial surfaces act as perfect black bodies following Planck's law. Most objects emit less than predicted from their kinetic temperature. This fact is taken into account by the emissivity coefficient ( $\epsilon_{(\lambda)}$ ).  $\epsilon$  is the radiant flux of an object at a given temperature over the radiant flux of a blackbody at the same temperature. For a blackbody, all absorbed radiation is emitted again ('good absorbers are good emitters') and

Kirchhoff's law (1860) applies, stating that the emittance at a given wavelength is equal to its absorbance at the same wavelength:

$$\varepsilon_{(\lambda)} = \alpha_{(\lambda)} \quad (1.4)$$

Taking into account energy conservation, where the sum of absorption ( $\alpha$ ), reflection ( $\rho$ ), and transmission ( $\tau$ ) equals 1, and Eq. 1.4:

$$\varepsilon_{(\lambda)} + \rho_{(\lambda)} + \tau_{(\lambda)} = 1 \quad (1.5)$$

As most objects are opaque and do not transmit radiation, Eq. 1.5 can be re-formulated as:

$$\varepsilon_{(\lambda)} + \rho_{(\lambda)} = 1 \quad (1.6)$$

Hence, the spectral emittance of an object can be calculated from its reflectance (for a blackbody), and vice versa. While materials with a high  $\varepsilon$  absorb large amounts of incident energy and radiate large quantities of energy, materials with low  $\varepsilon$  absorb and radiate lower amounts of energy (Kirchhoff 1860; Sabins 1996).

Emissivity varies depending on surface type and wavelength but is not temperature dependent (Flynn et al. 2001). Table 1.1 presents emissivities of common surfaces averaged for the wavelength range of 8–14  $\mu\text{m}$ .

Based on Eq. 1.2 and the definition of emissivity, the conversion of radiance temperature to kinetic temperature is according to:

$$T_{(\text{rad})} = \varepsilon^{(1/4)*} T_{(\text{kin})} \quad (1.7)$$

Due to emissivities below 1 for real materials, the radiance temperature,  $T_{(\text{rad})}$ , measured by a sensor is always lower than the real kinetic (surface) temperature,  $T_{(\text{kin})}$ , of an object.

This is a crucial fact for thermal data analysis, as it means that objects with exactly the same kinetic temperature can differ significantly in their radiant temperature. Depending on the variability of land cover surfaces (varying geologic surfaces, moisture conditions, amounts of vegetation cover, etc.) an image has to be corrected for the emissivity effect when aiming to retrieve kinetic pixel (object) temperatures. Emissivity related radiometric divergences are especially accentuated in urban areas. As emissivities of metals (e.g., aluminium, tin or copper roofs) are extremely low, the sensed temperatures will appear much lower than the sensed temperatures of surrounding objects of the same kinetic temperature (see Figs. 1.7 and 1.8). On the other hand, water surfaces and vegetation with emissivities close to one permit a quite exact assessment of their kinetic temperature (Table 1.1).

**Table 1.1** Emissivity of different surfaces in the 8–14 μm wavelength range as compiled from different sources

Surface	Emissivity at 8–14 μm
Carbon powder	0.98–0.99
Water	0.98
Ice	0.97–0.98
Plant leaves, healthy	0.96–0.99
Plant leaves, dry	0.88–0.94
Asphalt	0.96
Sand	0.93
Basalt	0.92
White paper	0.90
Wood	0.87
Granite	0.83–0.87
Polished metals, averaged	0.02–0.21
Aluminium foil	0.036

Own measurements, Lillesand et al. (2008), Sabins (1996)

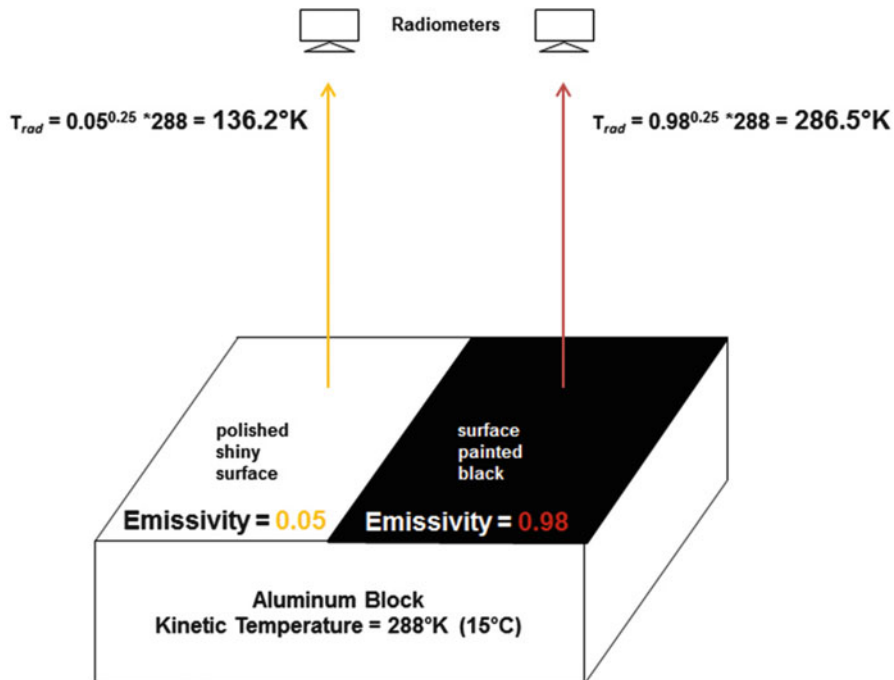


**Fig. 1.7** Impact of emissivity on radiance temperature recorded at the sensor. A block of aluminium with constant kinetic temperature and very low emissivity is partially covered with a carbon-rich dark paint. Note the different temperature readings due to varying emissivities. Although the object is 15 °C, it appears as  $-136.8^{\circ}\text{C}$  on the uncovered side, and as  $13.5^{\circ}\text{C}$  on the painted side (calculation based on Eqs. 1.2 and 1.7) (Modified after Sabins 1996)

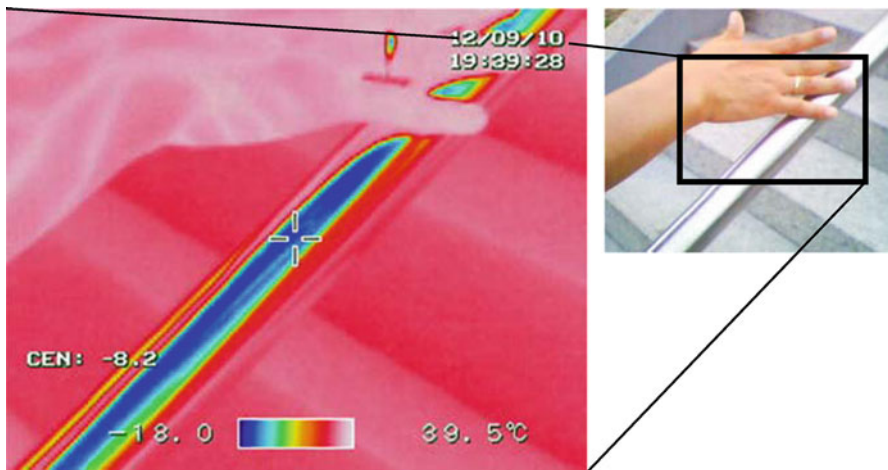


**Fig. 1.8** Impact of emissivity differences on radiance temperature recorded at the sensor of a hand-held thermal camera. The picture was taken on September 10th, 2012. It shows a polished metal handrail bordering a concrete stair. Ambient air temperature at picture acquisition was around 22 °C. The human hand shows temperature values up to 37 °C. Note that even the veins within the hand can be seen as *white* (hottest) *lines*. The handrail appears at a radiance temperature of  $-8^{\circ}\text{C}$  (cross at image center). Of course the rail is not minus  $8^{\circ}\text{C}$  cold. However, as this picture was taken with a standard emissivity value of 1 (without emissivity correction) the handrail appears to be very cold. The same applies to the gold ring on the person's finger

### 1.3 Thermal Remote Sensing Data Acquisition

For thermal imaging the TIR energy radiated from an object is transferred via a scan mirror onto a detector. These detectors are usually cooled with liquid nitrogen to minimize detector-inherent noise. At the same time thermal scanners often contain controlled radiant temperature sources for calibration purposes. Details on TIR detectors can be found in Norwood and Lansing (1983). TIR detectors can be ground-based or flown on aircraft or satellites.

#### 1.3.1 *Sensitivity of Thermal Infrared Sensors*

Thermal infrared sensors will be discussed in much more detail in the following chapters of this book. Here, only one example is given, based on the very commonly used spaceborne Landsat-7 Enhanced Thematic Mapper (short ETM+) sensor. All Landsat bands are acquired in either a low- or a high-gain mode spanning slightly different dynamic ranges. Gain selection is defined in the gain strategy of the Long Term Acquisition Plan (LTAP), depending on acquisition time and the dominating surface types in a scene (percentages of land, desert, ice/snow, water, sea ice, etc.).

**Table 1.2** Temperature of saturation in the low- and high-gain bands of Landsat-7 ETM+

Spectral band	μm regions	Minimum temperature [°C]	Maximum temperature [°C]
1 (blue)	0.45–0.51	1,051 (1,075)	1,483 (1,526)
2 (green)	0.52–0.60	900 (922)	1,301 (1,340)
3 (red)	0.63–0.69	755 (775)	1,119 (1,156)
4 (NIR)	0.75–0.90	595 (613)	926 (961)
5 (MIR)	1.55–1.75	206 (217)	417 (440)
6 (TIR)	10.40–12.50	–33 (–134)	51 (77)
7 (MIR)	2.09–2.35	92 (101)	258 (276)
8 (pan)	0.52–0.90	702 (721)	1,056 (1,092)

Source: Flynn et al. (2001), modified, as in Kuenzer (2005)

These are known a priori as Landsat cover fixed frames, defined by path and row. Except for very specific requests the user has no influence on the gain setting in the reflective modes. Nevertheless, ETM+ band 6 will always be recorded and delivered in the low- and high-gain modes, extending the dynamic range of the data.

Detector saturation can occur if a surface has extremely high temperatures. Similarly, a surface will not be detected thermally if its temperature decreases below a certain threshold. Table 1.2 lists the minimum and maximum temperatures in the low-gain and high-gain (in brackets) setting, indicating the lowest or highest pixel-integrated temperature which can be detected in a certain wavelength region. It should be noted that band 6 ranges from 10.4 to 12.5 μm only, to avoid the effects of ozone adsorption. Its broad band width of 2 μm combined with only 60 m ground resolution enables a sufficient thermal energy yield. It can be seen that mid-infrared band 5 can be used to detect thermal anomalies of very high temperatures leading to saturation in band 6 (see also Fig. 1.6). Even near-infrared channel 4 offers options for the detection of extremely high temperatures. Compared to former Landsat TM (Thematic Mapper), the low- and high-gain options of ETM+ offer a higher dynamic range. Nevertheless, the thermal bands of ETM+ have proven less suitable for high temperature studies. They saturate at 51 and 77 °C respectively, while TM band 6 saturated at around 90 °C. It is also often stated that ETM+ still suffers from an antiquated 8-bit dynamic range, limiting radiance steps to 256 instead of, e.g., 4096 if a 12-bit system was used (Flynn et al. 2001).

### 1.3.2 Daytime and Nighttime Data Acquisition

One very big advantage of TIR remote sensing is the fact that data can be acquired independent of the sun as an illumination source. So thermal data can also be acquired during the night, when remote sensing in the VIS and NIR is not possible. Several sensors can be specifically tasked to collect thermal data during the night (e.g., Aster (Advanced Spaceborne Thermal Emission and Reflection Radiometer), Landsat TM, ETM+), and some are constantly mapping the earth in the TIR range, such as MODIS (Moderate Resolution Imaging Spectroradiometer) (see Fig. 1.9), NOAA-AVHRR

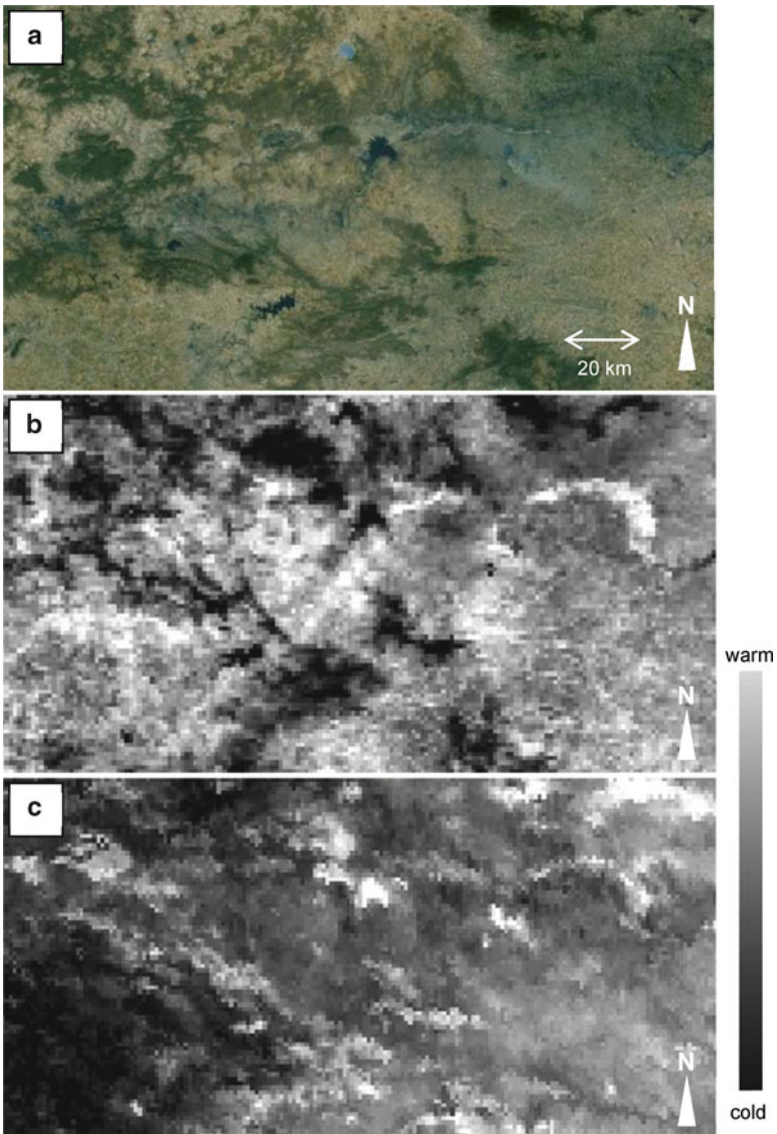


**Fig. 1.9** Optical Landsat imagery (a), and daytime (morning, b) and nighttime (pre-dawn, c) thermal data acquired by MODIS in 2005 over a coal mining area in northeast India. Forested areas appear cool (bright) during the day, and warm at night; the same applies to lakes. One outstanding feature is the Jharia coal field in the *upper right part* of the image (crescent-shaped structure), which appears hot during daytime due to the low albedo and low thermal inertia of coal, and which also appears hot in pre-dawn data due to underground coal fires. The area presented covers about 230 km × 90 km. *UL* 24°02'51N, 84°59'24E, *LR* 23°06'58N, 86°34'30E

(National Oceanic and Atmospheric Administration – Advanced Very High Resolution Radiometer) or MSG SEVIRI (Meteosat Second Generation – Spinning Enhanced Visible and Infrared Imager), to name only a few.

Nighttime data is especially suitable for detecting thermal anomalies, such as hot anomalies induced by forest fires, and especially weak thermal anomalies induced by subsurface coal fires (Zhang and Kuenzer 2007; Zhang et al. 2007), peat fires, industry-related thermal water pollution, or geothermal phenomena.

Other communities, such as scientists or practitioners working in the field of model assimilation and validation, need not only one or two nighttime data sets per day, but rather nighttime as well as daytime data at dense temporal intervals covering a complete day.

During daytime uneven solar heating of the background (due to varying sun-sensor-object geometry, topography, thermal inertia) often hampers the extraction of thermally anomalous pixels, while in nighttime data – especially pre-dawn data – the solar component is much less accentuated and thermal emission of natural surfaces such as rocks, vegetation, etc. is at a minimum. Therefore, it is easier to extract anomalous pixels whose temperature is elevated independent of solar radiation. As the MODIS sensor – for example – is flown on two platforms, TERRA and AQUA, it is possible to acquire up to four thermal images of the same area within 1 day (see Fig. 1.9). Usually, data is available for the morning, afternoon, early night, and pre-dawn. This holds a large potential for multi-diurnal thermal mapping, such as presented in Kuenzer et al. (2008).

## 1.4 Pre-processing of Thermal Remote Sensing Data

Thermal infrared remote sensing data has to be corrected for systematic and nonsystematic geometric distortions, just like data from bands of reflective wavelengths. Usually the data is corrected simultaneously together with the reflective bands when an image stack of data is adjusted based on a data set with higher geometric accuracy, e.g., via ground control points. Details on geometric correction of image data can be found in Richards (1986).

To radiometrically correct thermal bands the physical principles of thermal absorption and emission apply. Not the reflectance in per cent has to be calculated for each pixel, but the temperature of a surface in °C or K. In a first step, sensor calibration functions are used to calculate the energy retrieved at the sensor (in  $\text{W}/\text{m}^2/\text{sr}/\mu\text{m}$ ) from the recorded digital number, DN. The calibration functions are linear equations defined via two calibration coefficients,  $c_0$  (offset) and  $c_1$  (gain). The coefficients are usually frequently updated by the data providers and distributed with the raw data. Following this first step, the emitted radiance at ground level is derived. The necessary atmospheric correction takes advantage of the fact that in the thermal spectral region of 8–14  $\mu\text{m}$  water vapor is the dominating disturbing parameter, while aerosols play

only a negligible role. The radiance equation in the thermal region can be expressed as:

$$L_{\text{Sat}} = L_p + \tau_v \times \varepsilon \times L_{\text{Surf}}(T) + \tau_v(1 - \varepsilon) \times F_{\text{th}}/\pi \quad (1.8)$$

With (all wavelength dependent):

$L_{\text{Sat}}$ : at-sensor radiance

$L_p$ : thermal path radiance

$\tau_v$ : ground to sensor atmospheric transmittance

$\varepsilon$ : surface emissivity

$T$ : surface temperature

$L_{\text{Surf}}$ : blackbody radiance at the ground surface

$F_{\text{th}}$ : thermal downwelling flux on the ground

The first term in Eq. 1.8 gives the thermal path radiance. This is thermal radiation from the atmosphere reaching the sensor having never interacted with the surface. The last term in Eq. 1.8 is the downwelling thermal radiation reflected (by the surface) back to space. The central term, finally, gives the radiation emitted by the surface of temperature ( $T$ ) and transmitted to the sensor.

The equation can be resolved for  $T$  from the measured  $L_{\text{Sat}}$ ,  $L_p$ ,  $\tau_v$  and  $F_{\text{th}}$  can be derived from atmospheric measurements or pre-calculated databases (e.g., often pre-calculated based on MODTRAN (Moderate resolution atmospheric Transmission) radiative transfer code).

Emissivity effects can be corrected approximately by classifying the optical channels of an image into different surface types and assigning an emissivity value to each land cover class. This approach is integrated in several atmospheric correction codes, such as ATCOR-3 (Atmospheric and Topographic Correction for Satellite Imagery), pre-classifying the image into three classes (water, vegetation, bare ground). Using this approach, the emissivity problem is at least approximated.

Richter (2003) and Vidal (1991) state that as a rule of thumb a 0.01 emissivity error leads to a temperature error of 0.5–1 K. Actually, the emissivity-induced error depends on the object temperature and the emissivity of the object, as demonstrated by calculations presented in Table 1.3 below. With lower emissivities temperature errors of over 10 K can be reached. For typical land cover types a 0.01 change leads to a temperature error of 0.7–1 °C. However, absolute temperature errors can be up to 25 °C, and for metal surfaces even above 100 °C (see also Figs. 1.7 and 1.8).

Therefore, detailed emissivity correction is recommended when aiming to retrieve exact surface temperatures (Becker 1987). Even if a priori classification knowledge exists, this is difficult though, since the emissivity of a pixel depends on the composition of surfaces. In case of a mixed pixel, mixed emissivities would have to be calculated. Approaches to derive the emissivity of surfaces were, amongst others, developed and applied by Becker (1987), Nerry et al. (1990), Hook et al. (1992) and Kealy and Hook (1993).

**Table 1.3** Emissivity-induced temperature errors for an object of 288 K (15 °C)

Emissivity	Trad (K)	Trad (°C)	Error (from T <sub>kin</sub> in K)	Error (for emissivity change of 0.01 in K)
0.03	119.86	-153.14	-168.14	8.94
0.04	128.80	-144.20	-159.20	7.39
0.05	136.19	-136.81	-151.81	6.35
0.06	142.54	-130.46	-145.46	5.60
0.07	148.14	-124.86	-139.86	5.03
0.08	153.17	-119.83	-134.83	4.58
0.09	157.74	-115.26	-130.26	4.21
...	...	...	...	...
0.3	213.14	-59.86	-74.86	1.75
0.31	214.90	-58.10	-73.10	1.71
...	...	...	...	...
0.7	263.43	-9.57	-24.57	0.94
0.71	264.37	-8.63	-23.63	0.93
0.72	265.29	-7.71	-22.71	0.92
...	...	...	...	...
0.97	285.82	12.82	-2.18	0.73
0.98	286.55	13.55	-1.45	0.73

## 1.5 Analysis of Thermal Infrared Data

There are numerous methods and approaches which are especially suitable for the analysis of TIR data; many of them being presented in the later chapters of this book. Many authors focus exclusively on the derivation of LST and SST (Baroncini et al. 2008; Eastwood et al. 2011; Freitas et al. 2010; Gleason et al. 2002; Hulley et al. 2011; Iwasaki et al. 2008; Li et al. 2004; Sobrino et al. 1994), others on sensor performance comparisons (e.g., Frey et al. 2012; Batra et al. 2006), or thermal pattern development over time (e.g., Kant et al. 2009), as well as thermal anomaly extraction (Panda et al. 2007; Kuenzer et al. 2007). A large community uses TIR data for model validation and assimilation (weather and climate models) (Jang et al. 2010; McNider et al. 1994; Pipunic et al. 2008). Furthermore, many authors utilize TIR data as additional information in multispectral data classification. Huth et al. (2012), Klein et al. (2012) and Kuenzer (2005) all have demonstrated the value of TIR data as a discriminator for certain surfaces which might not differ substantially in the VIS and NIR domain. Kuenzer (2005) for example showed that very dark coal surfaces in mining regions cannot be distinguished from fully shadowed areas in the VIS and NIR domain as both have nearly zero reflectance in all bands. However, the two can be differentiated in the TIR, as shadow areas are usually much cooler than coal surfaces, which heat up very fast during the day. However, some less known methods apart from the above exist as well, and will be introduced in the following.

### 1.5.1 Considering Diurnal Temperature Dynamics: Thermal Inertia and Apparent Thermal Inertia

Objects of the land surface and even water of the oceans all have diurnal thermal characteristics and distinct diurnal temperature curves. An object's diurnal temperature curve represents its temperature behavior over the course of a 24 h cycle. It illustrates how much and how fast an object heats up and cools down during the day. The diurnal temperature curve depends on the object's material properties (in particular its thermal inertia), season (sun-object geometry defining strength of illumination), atmospheric disturbances, and – complicating the matter for land surfaces – its exposure (aspect, slope).

Figure 1.10 illustrates the contrasting diurnal temperature variation of water and dry soil/rock. Differences mainly result from different material properties (Tipler 2000), amongst other physical parameters expressed by the thermal inertia. The thermal inertia,  $I$  ( $\text{J}/\text{m}^2/\text{K}/\text{s}^{-5}$ ), is defined as the resistance of a material to heating. The thermal inertia is the product of three factors: the energy needed to raise the temperature of a material by  $1^\circ\text{C}$  (heat capacity  $c$ ) per mass unit of the substance, the density of a material,  $p$ , and the thermal conductivity,  $k$ , of the object (see also Table 1.4).

$$I = \sqrt{c \times p \times k} \quad (1.9)$$

Variations in  $I$  result in changes to  $\Delta T$  (Kahle et al. 1976).  $\Delta T$  is the difference between the maximum and minimum temperature occurring during a diurnal solar cycle. Low thermal inertias indicate low resistance to temperature change, resulting in a high  $\Delta T$  (e.g., rocks). The opposite applies to surfaces with high thermal inertia (e.g., water).

While remote sensing does not allow for the direct derivation of thermal inertia ( $c$ ,  $p$  and  $k$  can only be measured in situ), the concept still allows the impact of object characteristics (e.g., moisture of soils or vegetation) on  $T$  and  $\Delta T$  to be exploited. Maximum and minimum radiant temperatures can be measured from thermal daytime and nighttime remote sensing images.

$\Delta T$  is calculated by subtracting the nighttime from the daytime temperature for corresponding ground resolution cells. Already Idso et al. (1975) investigated the potential of  $\Delta T$  for soil moisture retrieval and found the data helpful for deriving soil moisture in the 0–4 cm horizon.

Later, the relationship of low  $\Delta T$  for materials with a high  $I$ , and vice versa, was extended to calculate the so-called Apparent Thermal Inertia, ATI. The ATI is defined as:

$$\text{ATI} = (1 - A)/\Delta T \quad (1.10)$$

where  $A$  is the albedo of the pixel in the visible band. The albedo is included to compensate for the effect that dark materials absorb more sunlight than do light

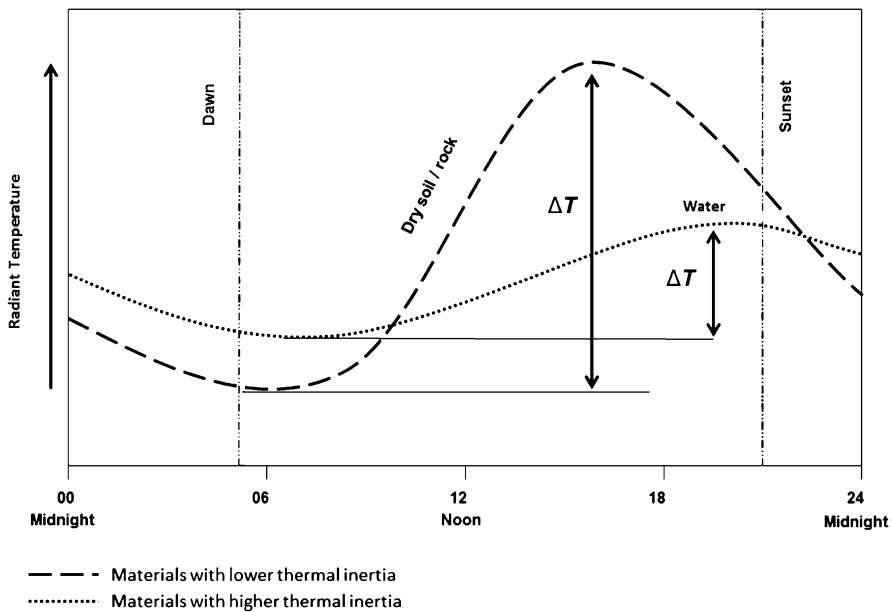


**Fig. 1.10** Diurnal temperature variation of water and dry soil/rock. Each object shows a distinct diurnal temperature cycle determined by the thermal inertia of the object and the history of the incoming solar radiation (Modified from Lillesand et al. 2008)

**Table 1.4** Thermal properties of geologic materials

Material	Thermal conductivity, k [W/m/K]	Thermal capacity, c [J/kg/K]	Thermal inertia, I [J/m <sup>2</sup> /K/s <sup>5</sup> ]
Clay soil	0.0030	0.35	0.042
Sandstone	0.0120	0.19	0.074
Limestone	0.0048	0.17	0.045
Shale	0.0042	0.17	0.041
Sandy soil	0.0014	0.24	0.024

Source: Sabins (1996)

materials. Hence, by including the term 1-A the effect that a dark material typically has a higher  $\Delta T$  than an otherwise identical light material is somewhat compensated.

An example of ATI image utilization is shown in this book in the chapter by Notarnicola et al. (2013), who employed ATI data to qualitatively differentiate different stages of soil moisture conditions. Unlike thermal inertia, which is a fixed object-inherent value, ATI must be interpreted carefully as neither the albedo in the VIS (Bidirectional reflectance distribution function, BRDF, effects, etc.), nor  $\Delta T$  are fixed. ATI, for example, cannot compensate for relief induced variations in  $\Delta T$ . In an area of uniform material shadowed areas have a lower radiant temperature during the day and hence a lower  $\Delta T$  than the exact same material exposed on a

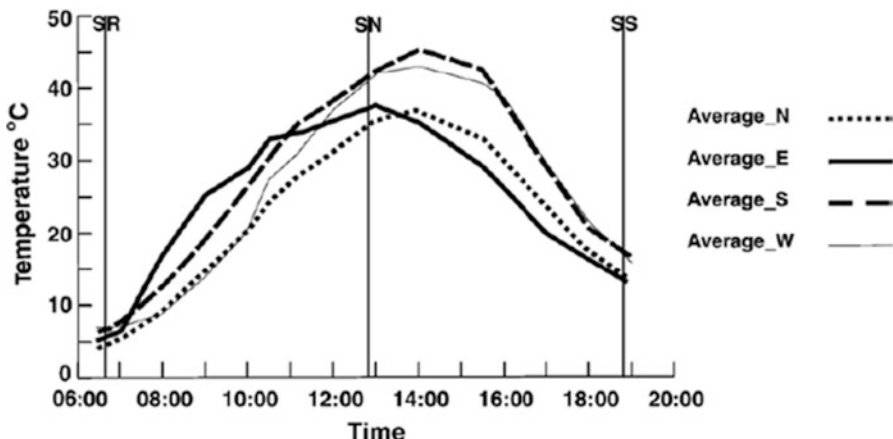


**Fig. 1.11** Diurnal temperature variation of desert sand depending on different aspects (exposure to the east, south, west and north) (Source: Zhang and Kuenzer 2007)

sunlit slope. Here, topographic data and solar elevation and azimuth information have to be employed to overcome the relief-induced variation of  $\Delta T$ .

Figure 1.11 depicts this increase of complexity of a diurnal temperature curve if one and the same material occurs at different aspects (thermal anisotropy). The temperatures of a small sand dune (2 m high) in the Gobi desert, China, were measured in situ at numerous points on four slopes with north, east, south and west exposition. Temperature measurements for each aspect were averaged. Measurements were recorded with a handheld radiometer at 10 min intervals and started at six AM and ended at eight PM. Figure 1.11 demonstrates the following:

- Quartz-rich desert sand reaches temperature differences of above 40 °C during a time span from 6:00 in the morning until the temperature peak is reached slightly after solar noon (SN).
- East-exposed surfaces heat faster in the morning than the other aspect directions (they are illuminated earlier)
- South- and west-exposed slopes heat up the most and stay warmer longer in the late afternoon/evening
- While peak temperature reaches only about 35 °C on east- and north-exposed slopes, temperatures of over 45 °C are reached on south and west slopes
- At e.g., a Landsat local overpass time of 10:30, temperatures of the same object/surface can differ by up to 10 °C.

To account for such effects in thermal data over land TIR imagery has to be corrected for differing solar illumination times due to varying sun-sensor-object geometries, varying sensor overpass times, and topographic (aspect, slope) effects – especially when aiming at thermal change detection or time series analysis. These corrections have to be applied in addition to several other pre-processing and correction steps: (1) sensor calibration with constantly updated calibration

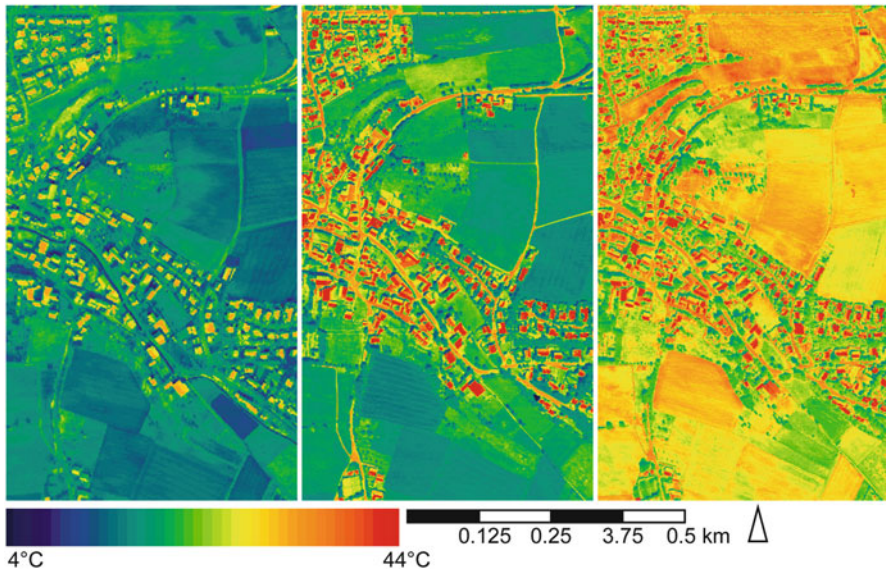


**Fig. 1.12** Thermal mapping of Dahl, near Paderborn, Germany in winter (*left*), spring (*middle*), and summer (*right*), based on airborne data acquired with the DAEDALUS scanner at 300 m flight altitude. Pixel spacing is 80 cm by 80 cm (Imagery courtesy of DLR)

coefficients, (2) atmospheric corrections to retrieve object radiance, (3) emissivity corrections to receive kinetic temperature (all explained in previous sections).

### 1.5.2 Considering Intra-Annual Temperature Development: Implications for TIR Change Detection and Time Series Analysis

The temperature behavior of objects is not only characterized by their diurnal temperature variation within a 24 h cycle, but also by an annual temperature curve.  $\Delta T$  of the 24 h cycle varies with season, and just like an average  $\Delta T$  for a diurnal cycle exists, an average  $\Delta T$  over the course of one year (for a specified solar time) also exists. This annual  $\Delta T$  is not a  $\Delta T$  derived from daytime and nighttime data, but the temperature difference of an object between an acquisition, e.g., in winter and in summer during an identical acquisition time (see Fig. 1.12).

This annual variability of temperature has to be taken into account, when time series of daytime TIR data are analyzed. Many studies investigate, e.g., so-called urban heat island effects (Schwarz et al. 2011; Streutker 2003; Tiangco et al. 2008) and some of these studies focus on the comparison of only two or a few scenes.

If one wants to derive clear indications whether a city is ‘getting hotter’ over time (usually due to increased surface sealing) one has to ensure that the data

utilized is representative (same day of year, same acquisition time, same sensor, same correction methods), also with respect to temporal coverage. The comparison of just two data sets is therefore not suitable. Instead, a time series of many scenes acquired during the same date and time should be analyzed to derive a real trend. In climate- or SST-related TIR analyses, long term time series of TIR data (e.g., 30+ years based on AVHRR data) are employed to ensure the exclusion of outlier effects and to derive solid quantitative statements.

The analysis of annual temperature variability is important for many applications such as the assessment of conditions for crop growth, the assessment of soil temperature for construction, the analysis of temperature variability impacts on building materials, or – when looking at ocean temperature – the consequences of temperature variability for nutrient loads, biodiversity, navigability, or tourism.

As a general comment, it should be noted here that thermal data – when corrected to radiance temperature in °C, and further on to kinetic temperature in °C – negative temperature (values) can occur, which is not possible for reflectance data from the VIS or NIR domain. While reflectance data is usually stored as ‘unsigned’ data (unsigned 8-bit, unsigned 12-bit etc.) thermal data should always be written as ‘signed’ (signed 8-bit, signed 12-bit, etc.) data, to allow for below 0 (negative) values.

### ***1.5.3 Mapping Approaches Based on Varying TIR Emissivity***

As already mentioned, emissivity is a wavelength-dependent term. Materials have different emissivity within the TIR domain. This means that objects have very distinct spectral signatures (spectral ‘fingerprints’) also in the TIR. The TIR spectra look similar to the continuous spectra in the VIS, NIR or MIR, and enable the distinction of materials. Sensors with multiple bands in the TIR, such as ASTER or MODIS, allow for the discriminative mapping of materials based on emissivity spectra due to differing emissivity at different wavelength in the TIR. ASTER, for example, records five thermal bands between 8.125 and 11.65 μm at 90 m spatial resolution each. Therefore, the user receives five measurements of an object’s radiant exitance in the TIR domain, and can plot a discrete emissivity spectral signature. MODIS has 36 spectral bands, of which bands 20–36 are located within the TIR domain between 3.66 and 14.385 μm. However, due to absorption bands in some of these areas, especially bands 20–23 (3.66–3.98) and bands 31 and 32 (10.78–12.27 μm) are suitable for LST and SST retrieval. Mapping approaches based on varying TIR emissivity have often been presented for geologic surface discrimination employing ASTER thermal bands (Coll et al. 2007; Haselwimmer et al. 2011).

### 1.5.4 Artefacts in Thermal Images

Artefacts in thermal imagery are clouds (usually very cold objects in thermal data) and cloud shadows (leading to a decrease of LST in the areas influenced by these shadows), wind smear and wind streak effects, as well as smears of high temperature events, as presented in Fig. 1.13 below.

### 1.5.5 Ground Truth and Validation

The accuracy of the temperatures retrieved after sensor calibration and atmospheric correction can be assessed based on ground truth temperatures (radiance and kinetic temperatures, depending on the desired final products) measured during the overflight of the airborne or spaceborne thermal sensor (Coll et al. 2005). It is then possible to measure in situ kinetic temperature directly via a contact thermometer, or without contact with the object, if its emissivity is known.

Most suitable are surfaces with a high thermal inertia (e.g., water) to prevent temperature changes during even slight temporal offsets between exact overflight time and in-situ measurement time. With water surfaces also the terrain-related (aspect, slope) uneven solar heating is omitted and its emissivity is very close to

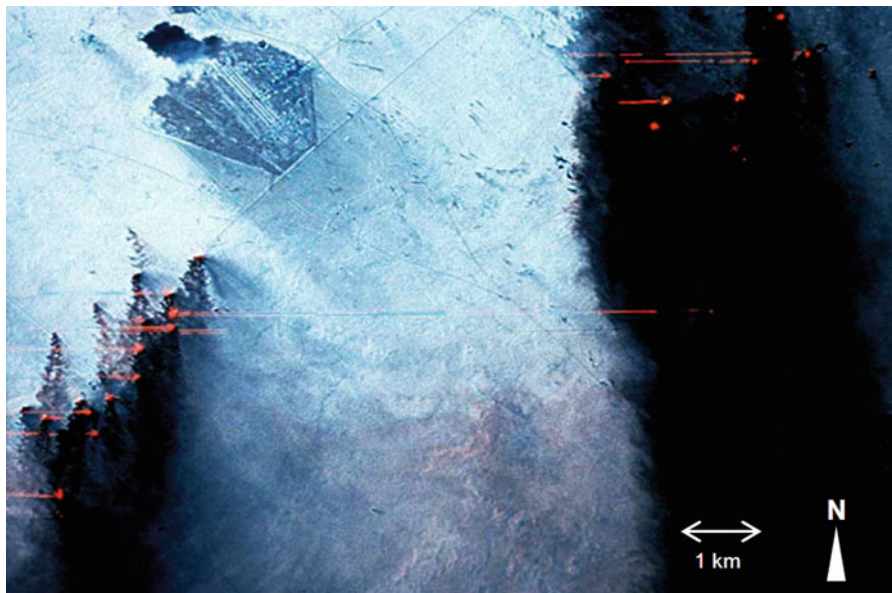


**Fig. 1.13** Smear effect due to oscillating mirror motion and extreme high temperature events (burning oil and gas flares in the gulf region) can be traced all the way into the *red band* of Landsat TM imagery (Wien's displacement)

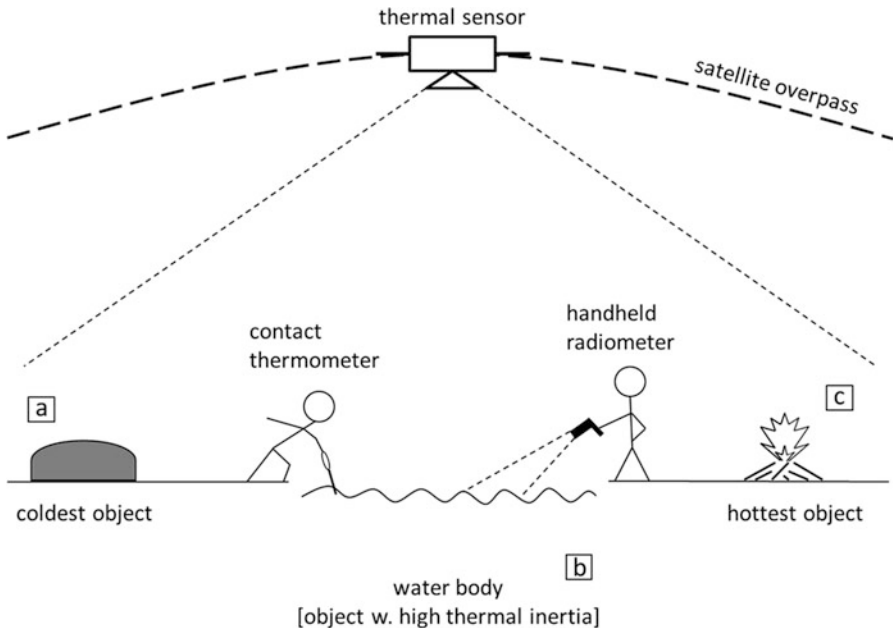


**Fig. 1.14** Schematic sketch of a thermal ground truthing campaign during sensor overflight

one. At the same time, the assumedly hottest and coldest objects within the area of image acquisition should also be measured, to have ground truth for both ends of the temperature range of the data set. The measurements must all be undertaken at exact overflight time. If the objects are too far apart for one person to reach within a few minutes, several persons with several instruments need to perform the validation measurements. If, e.g., three persons measure with three radiometers and three contact thermometers, it must be ensured beforehand that these instruments are intercalibrated. Furthermore, the ground objects (e.g., water body and the hot and cold object) must be large enough to be easily recognizable in the imagery; they should each cover several image pixels (Fig. 1.14). This condition is especially difficult to meet for medium-resolution TIR data, such as from AVHRR, MODIS or MSG SEVIRI. Only few regions show homogeneous surface behavior (similar topography and roughness, same material, same reflectance, same emittance, etc.) over an area of, e.g.,  $5 \text{ km}^2$ . If such areas are found, then one single in-situ temperature measurement will not be representative, and several measurements have to be averaged to validate one pixel (Hulley et al. 2009; Tang et al. 2010; Wan 2008).

If one aims at the validation of more than one scene (e.g., validation of time series of thermal data), then permanently installed measurement devices with temperature data loggers (e.g., in situ on the ground, in the air, etc.) usually coupled with a climate station also measuring wind speed, humidity, etc. are employed.

## 1.6 Conclusions

The chapter gave a short overview of the main physical principles of thermal infrared remote sensing. It also illustrated some principles behind typical applications which will be further detailed in the application chapters of this book. The interested reader is also referred to textbooks dealing with the thermal infrared domain, such as Monteith and Unsworth (2007), Sabins (1996), Jones and Vaughan (2010), Tipler (2000), and Walker (2008).

**Acknowledgements** The authors thank two anonymous reviewers for their valuable comments on the manuscript. Further thanks go to Clement Atzberger (BOKU, Vienna) for a critical discussion of this chapter.

## References

- Baroncini F, Castelli F, Caparrini F, Ruffo S (2008) A dynamic cloud masking and filtering algorithm for MSG retrieval of land surface temperature. *Int J Remote Sens* 29(12):3365–3382
- Batra N, Islam S, Venturini V, Bisht G, Jiang L (2006) Estimation and comparison of evapotranspiration from MODIS and AVHRR sensors for clear sky days over the Southern Great Plains. *Remote Sens Environ* 103:1–15
- Becker F (1987) The impact of emissivity on the measurement of land surface temperature from a satellite. *Int J Remote Sens* 8(10):1509–1522
- Coll C, Caselles V, Galve JM, Valor E, Niclòs R, Sánchez JM, Rivas R (2005) Ground measurements for the validation of land surface temperatures derived from AATSR and MODIS data. *Remote Sens Environ* 97:288–300
- Coll C, Caselles V, Valor E, Niclòs R, Sanchez JM, Galve JM, Mira M (2007) Temperature and emissivity separation from ASTER data for low spectral contrast surfaces. *Remote Sens Environ* 110(2):162–175
- Dech SW, Tungalagsaikhan P, Preusser C, Meisner RE (1998) Operational value-adding to AVHRR data over Europe: methods, results, and prospects. *Aerosp Sci Technol* 2:335–346
- Eastwood S, Le Borgne P, Pérez S, Poulter D (2011) Diurnal variability in sea surface temperature in the Arctic. *Remote Sens Environ* 115(10):2594–2602
- Flynn LP, Harris AJL, Wright R (2001) Improved identification of volcanic features using Landsat 7 ETM+. *Remote Sens Environ* 78(2):180–193
- Freitas SC, Trigo IF, Bioucas-Dias JM, Gottsche FM (2010) Quantifying the uncertainty of land surface temperature retrievals from SEVIRI/meteosat. *IEEE Trans Geosci Remote Sens* 48 (1 Part: 2):523–534
- Frey C, Kuenzer C, Dech S (2012) Quantitative comparison of the operational NOAA AVHRR LST product of DLR and the MODIS LST product V005. *Int J Remote Sens* 33(22):7165–7183
- Gleason ACR, Prince SD, Goetz SJ, Small J (2002) Effects of orbital drift on land surface temperature measured by AVHRR thermal sensors. *Remote Sens Environ* 79(2–3):147–165
- Haselwimmer CE, Riley TR, Liu JG (2011) Lithologic mapping in the Oscar II Coast area, Graham Land, Antarctic Peninsula using ASTER data. *Int J Remote Sens* 32(7):2013–2035
- Heald MA (2003) Where is the ‘Wien peak’? *Am J Phys* 71(12):1322–1323
- Hook SJ, Gabell AR, Green AA, Kealy PS (1992) A comparison of techniques for extracting emissivity information from thermal infrared data for geologic studies. *Remote Sens Environ* 42(2):123–135

- Hulley GC, Hook SJ, Baldrige AM (2009) Validation of the North American ASTER Land Surface Emissivity Database (NAALSED) version 2.0 using pseudo-invariant sand dune sites. *Remote Sens Environ* 113(10):2224–2233
- Hulley GC, Hook SJ, Schneider P (2011) Optimized split-window coefficients for deriving surface temperatures from inland water bodies. *Remote Sens Environ* 115(12):3758–3769
- Huth J, Kuenzer C, Wehrmann T, Gebhardt S, Dech S (2012) Land cover and land use classification with TWOPAC: towards automated processing for pixel- and object-based image classification. *Remote Sens* 4:2530–2553
- Idso SB, Jackson RD, Reginato RJ (1975) Detection of soil moisture by remote surveillance. *Am Sci* 63:549–557
- Iwasaki S, Kubota M, Tomita H (2008) Inter-comparison and evaluation of global sea surface temperature products. *Int J Remote Sens* 29(21):6263–6280
- Jang K, Kang S, Kim J, Lee CB, Kim T, Kim J, Hirata R, Saigusa N (2010) Mapping evapotranspiration using MODIS and MM5 four-dimensional data assimilation. *Remote Sens Environ* 114(3):657–673
- Jones HG, Vaughan RA (2010) Remote sensing of vegetation: principles, techniques, and applications. Oxford University Press, Oxford, 380pp. ISBN 10: 0199207798
- Kahle AB, Gillespie AR, Goetz AFH (1976) Thermal inertia imaging: a new geological mapping tool. *Geophys Res Lett* 3(1):26–28
- Kant Y, Bharath BD, Mallick J, Atzberger C, Kerle N (2009) Satellite-based analysis of the role of land use/land cover and vegetation density on surface temperature regime of Delhi, India. *J Indian Soc Remote* 37(2):201–214
- Kealy PS, Hook SJ (1993) Separating temperature and emissivity in thermal infrared multispectral scanner data: implications for recovering land surface temperatures. *IEEE Trans Geosci Remote Sens* 31(6):1155–1164
- Kirchhoff G (1860) Ueber das Verhältniss zwischen dem Emissionsvermögen und dem Absorptionsvermögen der Körper für Wärme und Licht. *Annalen der Physik und Chemie* (Leipzig) 109:275–301
- Klein I, Gessner U, Kuenzer C (2012) Regional land cover mapping in Central Asia using MODIS time series. *Appl Geogr* 35:1–16
- Kuenzer C (2005) Demarcating coal fire risk areas based on spectral test sequences and partial unmixing using multi sensor remote sensing data. Ph.D. thesis, Technical University Vienna, Vienna, 199pp
- Kuenzer C, Zhang J, Li J, Voigt S, Mehl H, Wagner W (2007) Detection of unknown coal fires: synergy of coal fire risk area delineation and improved thermal anomaly extraction. *Int J Remote Sens* 28:4561–4585
- Kuenzer C, Hecker C, Zhang J, Wessling S, Wagner W (2008) The potential of multi-diurnal MODIS thermal bands data for coal fire detection. *Int J Remote Sens* 29:923–944
- Li F, Jackson TJ, Kustas WP, Schmugge TJ, French AN, Cosh MH, Bindlish R (2004) Deriving land surface temperature from Landsat 5 and 7 during SMEX02/SMACEX. *Remote Sens Environ* 92:521–534
- Lillesand TM, Kiefer RW (1994) Remote sensing and image interpretation, 3rd edn. Wiley, New York, 748pp
- Lillesand TM, Kiefer RW, Chipman JW (2008) Remote sensing and image interpretation, 6th edn. Wiley, New York, 768pp. ISBN 10: 0470052457
- Löffler, E (1994) Geographie und Fernerkundung, 3rd edn. Teubner, 251p, ISBN 3-519-13423-3. <http://www/lehmanns.de/shop/technik/183801-9783519134237-geographie-und-fernerkundung>
- McNider RT, Song AJ, Casey DM, Wetzel PJ, Crosson WL, Rabin RM (1994) Toward a dynamic-thermodynamic assimilation of satellite surface temperature in numerical atmospheric models. *Mon Weather Rev* 122:2784–2803
- Monteith J, Unsworth M (2007) Principles of environmental physics, 3rd edn. Academic, London, 418 pp. ISBN 10: 0125051034

- Nerry F, Labed J, Stoll MP (1990) Spectral properties of land surfaces in the thermal infrared – laboratory measurements of absolute spectral emissivity signatures. *J Geophys Res* 95 (B5):7027–7044
- Norwood VT, Lansing JC (1983) Electro-optical imaging sensors. In: Colwell RN, Simonett DS, Ulaby FT (eds) *Manual of remote sensing, 1: theory, instruments and techniques*, 2nd edn. American Society of Photogrammetry, Falls Church, pp 335–367
- Panda SK, Choudhury S, Saraf AK, Das JD (2007) MODIS land surface temperature data detects thermal anomaly preceding 8 October 2005 Kashmir earthquake. *Int J Remote Sens* 28 (20):4587–4596
- Pipunic RC, Walker JP, Western A (2008) Assimilation of remotely sensed data for improved latent and sensible heat flux prediction: a comparative synthetic study. *Remote Sens Environ* 112(4):1295–1305
- Planck M (1900) Entropie und Temperatur strahlender Wärme. *Ann Phys* 306(4):719–737
- Richards JA (1986) *Remote sensing digital image analysis – an introduction*. Springer, Berlin, 281pp
- Richter R (2003) Atmospheric and topographic correction for satellite imagery. ATCOR-2/3 User guide. Version 5.5. DLR-I3 564-02/03. Wessling, 57pp
- Sabins FF (1996) *Remote sensing*, 3rd edn. Wiley, New York, 450pp
- Schwarz N, Lautenbach S, Seppelt R (2011) Exploring indicators for quantifying surface urban heat islands of European cities with MODIS land surface temperatures. *Remote Sens Environ* 115(12):3175–3186
- Sobrino JA, Li ZL, Stoll MP (1994) Improvements in the splitwindow technique for land surface temperature determination. *IEEE Trans Geosci Remote Sens* 32:243–253
- Streutker DR (2003) Satellite-measured growth of the urban heat island of Houston, Texas. *Remote Sens Environ* 85:282–289
- Tang R, Li ZL, Tang B (2010) An application of the Ts–VI triangle method with enhanced edges determination for evapotranspiration estimation from MODIS data in arid and semi-arid regions: implementation and validation. *Remote Sens Environ* 114(3):540–551
- Tiangco M, Lagmay AMF, Argete J (2008) ASTER-based study of the night-time urban heat island effect in Metro Manila. *Int J Remote Sens* 29(10):2799–2818
- Tipler PA (2000) *Physik*, 3rd edn. Spektrum Akademischer Verlag, Heidelberg, 1520pp
- Vidal A (1991) Atmospheric and emissivity correction of land surface temperature measured from satellite using ground measurements or satellite data. *Int J Remote Sens* 12(12):2449–2460
- Walker J (2008) *Fundamentals of physics*, 8th edn. Wiley, New York, 891pp. ISBN 9780471758013
- Wan ZM (2008) New refinements and validation of the MODIS land-surface temperature/emissivity products. *Remote Sens Environ* 112(1):59–74
- Zhang J, Kuenzer C (2007) Thermal surface characteristics of coal fires 1: results of in-situ measurements. *J Appl Geophys* 63:117–134
- Zhang J, Kuenzer C, Tetzlaff A, Oettl D, Zhukov B, Wagner W (2007) Thermal characteristics of coal fires 2: results of measurements on simulated coal fires. *J Appl Geophys* 63:135–147

# Chapter 2

## Geometric Calibration of Thermographic Cameras

Thomas Luhmann, Johannes Piechel, and Thorsten Roelfs

**Abstract** This chapter presents an overview of thermal imaging sensors for photogrammetric close-range applications. In particular, it presents results of the geometric calibration of thermographic cameras as they are used for building inspection and material testing. Geometric calibration becomes evident for all precise geometric image operations, e.g. mosaicking of two or more images or photogrammetric 3D modelling with thermal imagery. Two different test fields have been designed providing point targets that are visible in the thermal spectral band of the cameras.

Five different cameras have been investigated. Four of them have solid state sensors with pixel sizes between 25 and 40 µm (i.e. size of single sensor element on the chip). One camera is working in scanning mode. The lenses for thermographic cameras are made of Germanium, which is, in contrast to glass, transparent to thermal radiation. Conventional imaging configurations (typically 20 images) have been used for camera calibration. Standard parameters for principal distance, principal point, radial distortion, decentring distortion, affinity and shear have been introduced into the self-calibrating bundle adjustment. All measured points are introduced as weighted control points. Image coordinates have been measured either in the professional software package AICON 3D Studio (ellipse operators), or in the software system Stereomess (least-squares template matching), developed by the Institute for Applied Photogrammetry and Geoinformatics of the Jade University of Applied Sciences Oldenburg.

The calibration results differ significantly from camera to camera. All lenses show relatively large decentring distortion and deviations from orthogonality of the image coordinate axes. Using a plane test field with heated lamps, the average image precision is 0.3 pixel while a 3D test field with circular reflecting targets results in imaging errors of 0.05 pixel.

---

T. Luhmann (✉) • J. Piechel • T. Roelfs  
Institute for Applied Photogrammetry and Geoinformatics (IAPG),  
Jade University of Applied Sciences, Oldenburg, Germany  
e-mail: [Luhmann@jade-hs.de](mailto:Luhmann@jade-hs.de)

## 2.1 Camera Technology

Thermographic cameras are widely used in the fields of material testing, quality control and building monitoring. In all of these cases the radiometric information about temperature distribution is of major interest. Geometric applications are still rare, hence camera developers and suppliers still show little interest in photogrammetric techniques. Accordingly, the geometric calibration of these systems is neglected – except for a few contributions dealing with this topic (Buyuksalih and Petrie 1999; Luhmann et al. 2010). However, with increasing resolution of thermographic cameras the geometric processing of the image data will become more important.

For accurate geometric modeling of an image sensor, it is essential to understand the imaging process not only in geometrical terms but also with respect to radiometric properties. Below the basic physical principles are explained briefly. More details can be found, for example, in (Wolfe and Zissis 1985).

### 2.1.1 Physical Background

The specific spectral emission  $M_\lambda$  of an object is defined by Planck's emission law as a function of absolute temperature and wavelength (Planck 1900) formula notation according to (Schuster and Kolobrodov 2004):

$$M_\lambda \left[ \frac{W}{10^{-10} \cdot m} \right] = \frac{c_1}{\lambda^5} \frac{1}{\exp\left(\frac{c_2}{\lambda \cdot T}\right) - 1} \quad (2.1)$$

where

$c_1$ : 1. emission constant =  $3,7418 \cdot 10^{-16} \text{ W} \cdot \text{m}^2$

$c_2$ : 2. emission constant =  $1,4388 \cdot 10^{-2} \text{ K} \cdot \text{m}$

$T$ : absolute temperature [K]

$\lambda$ : wavelength [ $\mu\text{m}$ ]

Figure 2.1 shows the well known diagram of specific spectral emission for different absolute temperatures according to Eq. (2.1). It depicts that only objects with a temperature of more than about 1,000 K are emitting electro-magnetic radiation visible for the human eye or conventional cameras. The maximum of the specific emission is described by Wien's displacement law:

$$\lambda_{\max} = \frac{2897.8[K \cdot \mu\text{m}]}{T} \quad (2.2)$$

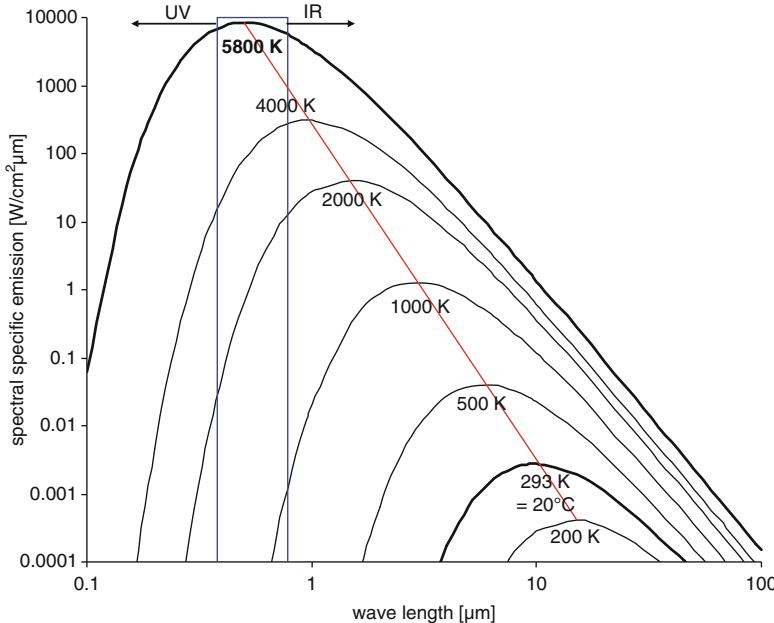


**Fig. 2.1** Spectral specific emission for different temperatures

In Eq. (2.2) the value 2897.8 is denoted as the Wien displacement constant. The formula states that the wavelength of maximum emission of an object is a reciprocal function of the temperature (red line in Fig. 2.1), hence higher temperatures yield lower wavelengths of peak emission (Dereniak and Boreman 1996). As an example, the sun has an average temperature of about 5,800 K, the resulting peak emission wavelength is 0.5  $\mu\text{m}$ , thus in the yellow band of the visible light spectrum (blue interval in Fig. 2.1). As a second example, an object of 20  $^{\circ}\text{C}$  (=293 K), the resulting wavelength is about 10  $\mu\text{m}$ .

Thermographic cameras consist of imaging sensors that are sensitive to wavelengths usually between 2.5 and 15  $\mu\text{m}$  (temperature: 880 ... –80  $^{\circ}\text{C}$ ). Depending on detector technology and camera model (see section below) temperatures between –30 and +400  $^{\circ}\text{C}$  can be detected (wavelength: 12 ... 4  $\mu\text{m}$ ).

The geometric resolution of imaging devices is limited by diffraction. The diameter of the Airy disk  $d$  (best focused spot of light that a perfect lens with a circular aperture can image) depends on the aperture  $k$  and the wavelength  $\lambda$ :

$$d = 2.44 \cdot \lambda \cdot k \quad (2.3)$$

As an example, geometric resolution at a wavelength of  $\lambda = 10 \mu\text{m}$  and aperture  $k = 2$  is limited to about 48  $\mu\text{m}$ . Equation (2.3) reveals that the pixel sizes of thermal sensors must be much larger than for standard RGB cameras. In fact most thermal imaging sensors provide pixel sizes between 30 and 50  $\mu\text{m}$ .

### 2.1.2 Detectors

Sensors for thermal cameras are either quantum detectors or thermal detectors (Nolting 2007). Quantum detectors are based on the inner photo-electric effect where electrons are set free between two layers of a semi-conductor device. Quantum detectors are very sensitive ( $\pm 0.01$  K) and fast, but need an external cooling system (Peltier or Sterling elements) (Fouad and Richter 2008).

Thermal detectors use the effect that a temperature change of the detector element leads to a change of the electrical properties of the detector, e.g. resistance or charges (Hierl 2008). These changes can be measured and transformed into intensity values. Different designs are available such as pyro-electric detectors or bolometers. Thermal detectors are less sensitive ( $\pm 0.1$  K) and slower than quantum detectors, but do not need any cooling elements. Hence they are less expensive und usually applied for applications like building monitoring.

Typical state-of-the-art thermal array sensors are available with  $320 \times 240$  pixels up to  $640 \times 320$  pixels. Sensor sizes then yield about up to 20–30 mm in each direction. Newest camera developments show pixel numbers of up to  $1,280 \times 960$ , achieved by microscanning technique (Le Noc et al. 2010).

In principle thermographic cameras built on solid state sensors can be handled as standard photogrammetric cameras. In order to be transparent in the range of longer wavelengths (8–14  $\mu\text{m}$ ) the lenses of thermographic cameras are made of Germanium or other crystalline materials which makes them more expensive. These lenses are optimized for radiometric resolution, thus geometric precision or minimal distortion are of less interest in most applications.

## 2.2 Test Fields for Calibration

### 2.2.1 Plane Test Field with Lamps

A plane reference field provided by the University of Dessau consists of 57 small lamps that warm up when switched on. The dimension of the wooden plate is about 1,000 mm  $\times$  1,000 mm (Fig. 2.2). The positions of the lamps have been measured by a theodolite system with an accuracy of about 0.2 mm.

The quality of the active targets is quite poor (Fig. 2.3). It is obvious that these targets are not circles (ellipses), and central points of maximum temperature are difficult to discern and cannot be measured with a precision as usually provided by photogrammetric targets. In addition, camera calibration with plane test fields is less accurate and less significant, i.e. statistically uncertain, compared to 3D reference fields and shows higher correlations between the parameters of the interior and exterior orientation (Fraser 1997; Luhmann 2010).



**Fig. 2.2** Plane test field with active lamps (size: 1 m × 1 m)

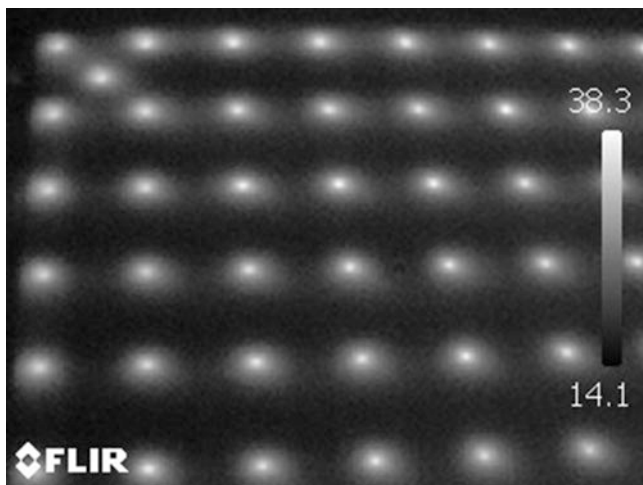


**Fig. 2.3** Imaging quality of the target points (section of the test field)

### 2.2.2 *Spatial Test Field with Coded Targets*

Since the plane reference field is not ideal for camera calibration a new design was investigated. The basic idea was to create spatially distributed targets that generate sufficient image contrast in the thermal spectrum. In addition, the new test field should be mobile, easy to calibrate, and cost effective without any need for artificial heating of targets. Several experiments have been carried out in order to find a

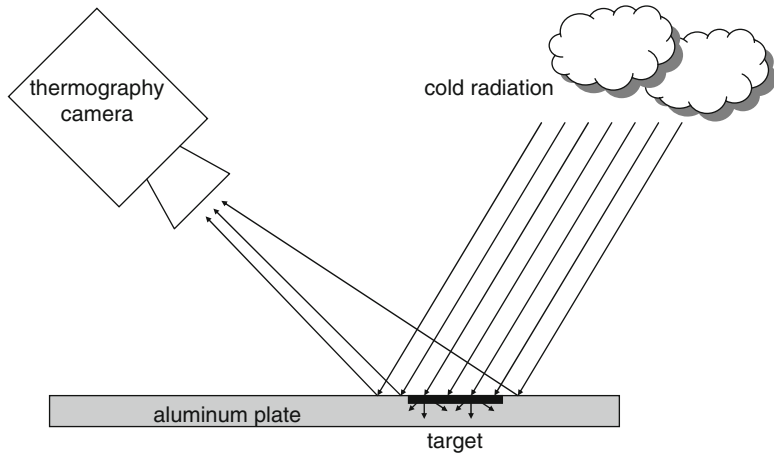


**Fig. 2.4** Target absorption of cold sky radiation

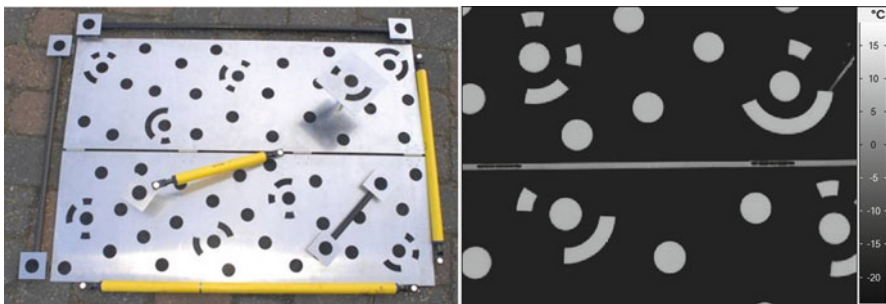


**Fig. 2.5** *Left:* new test field (color image, size: 1 m × 0.7 m, yellow: scale bars); *right:* thermal image of targets (section of the test field, size: 0.4 m × 0.3 m); parts of circles: binary code of target points

suitable combination of target material and lighting. Finally, the effect of reflecting cold sky radiation (Luhmann et al. 2010) has been used to create a test field design that fulfills the above mentioned specifications. The spatial distribution of targets is mainly required for the accurate determination of the focal length.

Figure 2.4 shows the reflectance principle. Assuming diffuse reflectance of the metal test field plate the cold temperature of space reflects on the metal surface. The targets are made of self-adhesive foil and emit radiation dependent only on their own temperature. With this principle the acquired image displays a strong contrast because targets appear bright while the surrounding areas appear dark (Fig. 2.5).

Based on the new design of target points, a mobile test field has been developed. It consists of 17 coded targets and 35 uncoded targets, and additional height points. Furthermore temperature-stable scale bars, made of carbon-fiber-reinforced polymer with the same type of targets (dark grey rods), can be mounted onto the test

field. Due to the target design a conventional photogrammetric calibration of the test field is possible which yields control points coordinates.

Because of the movable assembly and the thermal expansion of the metal the test field must be calibrated directly before and/or after each use by conventional photogrammetry. Using high precision calibrated scales (yellow), a high resolution camera and bundle adjustment, precise coordinates of the control points are derived. The size of the test field is about 1,000 mm × 700 mm × 200 mm. The accuracy of control points after measurement with a high-resolution digital camera and bundle adjustment is estimated to 8 µm in object space.

The new reference field can be used with almost no restrictions – at all temperatures, under cloudy skies, as well as in sunshine –, because the upper layers of the atmosphere (and the clouds) are always colder than objects on the ground. No power supply is required, just a clear view upward, so that no houses, trees, etc. are reflected on the metal plate. However, indoor use of the test field is not feasible.

## 2.3 Calibration Results

### 2.3.1 *Cameras*

Table 2.1 summarizes the technical data of four thermographic cameras that are included in the test. A fifth camera works with a rotation mirror device for image scanning. Due to the instable mechanical rotation and the non-perspective imaging model this camera has been eliminated from further tests for the time being.

The investigated cameras (Fig. 2.6) show more or less similar technical data. However, due to the different detector elements their performance differs as well as their market prices.

### 2.3.2 *Results*

Each camera was calibrated according to standard imaging configurations (Godding 1993; Luhmann et al. 2006) with about 20 multi-convergent images. Both reference fields as explained before have been used. The plane test field with burning lamps can be measured inside a lab while the reflective 3D test field has to be used open air.

Image measurement and bundle adjustment were performed with AICON 3D Studio. The calibration results, derived from the spatial test field, are listed in Tables 2.2 and 2.3. The plane test field leads to similar results. However, the precision of the estimated parameters is reduced and therefore they are not listed here.

**Table 2.1** Investigated thermographic cameras

	FLIR InfraCAM	FLIR B200	Testo 880-3	InfraTec VarioCAM
Pixels	$240 \times 240$	$320 \times 240$	$320 \times 240$	$384 \times 288$
Pixel size	0.025 mm	0.04 mm	0.035 mm	0.035 mm
Focal length	10 mm	30 mm	10 mm	11 mm
Thermal resolution	$\pm 0.2^\circ\text{C}$	$\pm 0.08^\circ\text{C}$	$<0.3^\circ\text{C}$	0.08–0.05 $^\circ\text{C}$
Price [€]	ca. 4,000	ca. 9,000	ca. 6,500	ca. 19,000

**Fig. 2.6** Investigated thermographic cameras (forward looking infrared, FLIR)**Table 2.2** Calibrated camera parameters (FLIR InfraCAM, FLIR B200)

Parameter	FLIR InfraCAM	FLIR B200
c [mm]	$-13.8971 \pm 0.0104$	$-36.9443 \pm 0.0223$
x'0 [mm]	$-0.2940 \pm 0.0188$	$1.4445 \pm 0.0574$
y'0 [mm]	$-0.3430 \pm 0.0197$	$-1.8332 \pm 0.0420$
A <sub>1</sub>	$-2.80 \cdot 10^{-3} \pm 1.33 \cdot 10^{-4}$	$-2.69 \cdot 10^{-4} \pm 1.94 \cdot 10^{-5}$
A <sub>2</sub>	$6.86 \cdot 10^{-7} \pm 2.03 \cdot 10^{-5}$	$-7.47 \cdot 10^{-7} \pm 6.94 \cdot 10^{-7}$
A <sub>3</sub>	$7.76 \cdot 10^{-7} \pm 9.52 \cdot 10^{-7}$	$2.79 \cdot 10^{-9} \pm 7.40 \cdot 10^{-9}$
B <sub>1</sub>	$1.91 \cdot 10^{-5} \pm 2.10 \cdot 10^{-5}$	$-2.78 \cdot 10^{-4} \pm 5.21 \cdot 10^{-6}$
B <sub>2</sub>	$-2.69 \cdot 10^{-5} \pm 2.25 \cdot 10^{-5}$	$-1.72 \cdot 10^{-5} \pm 6.18 \cdot 10^{-6}$
C <sub>1</sub>	$6.84 \cdot 10^{-4} \pm 1.99 \cdot 10^{-4}$	$-6.11 \cdot 10^{-4} \pm 2.60 \cdot 10^{-4}$
C <sub>2</sub>	$-2.22 \cdot 10^{-4} \pm 2.21 \cdot 10^{-4}$	$-8.66 \cdot 10^{-4} \pm 2.61 \cdot 10^{-4}$

The cameras FLIR InfraCAM, FLIR B200, and Testo 880-3 show relatively weak results in terms of image measurement precision ( $2.6\text{--}3.8 \mu\text{m}$ ) compared to the InfraTec VarioCAM ( $0.6 \mu\text{m}$ ), degrading also the standard deviations of principal point and principal distance. In contrast to the given focal length as taken from data sheets, the principal distance differs significantly. In the case of the FLIR B200 the principal point shift amounts to more than 1.4 mm in x and 1.8 mm in y, which corresponds to more than 35 respectively 45 pixels.

All cameras show relatively large radial distortion values as depicted in Fig. 2.7. The value of the radial-symmetric parameter A<sub>1</sub> is comparatively high and is determined significantly, while the remaining parameters are more or less weakly determined (standard deviations in the same order of magnitude as the parameters themselves). In practice the final adjustment should be limited to the relevant

**Table 2.3** Calibrated camera parameters (Testo 880-3, InfraTec VarioCAM)

Parameter	Testo 880-3	InfraTec VarioCAM
c [mm]	$-19.9373 \pm 0.0297$	$-11.8188 \pm 0.0014$
x'0 [mm]	$-0.1571 \pm 0.0524$	$0.0201 \pm 0.0013$
y'0 [mm]	$0.2110 \pm 0.0376$	$0.1400 \pm 0.0012$
A1	$-7.25 \cdot 10^{-4} \pm 1.20 \cdot 10^{-4}$	$-2.41 \cdot 10^{-3} \pm 4.93 \cdot 10^{-6}$
A2	$-9.59 \cdot 10^{-6} \pm 7.19 \cdot 10^{-6}$	$8.76 \cdot 10^{-6} \pm 1.83 \cdot 10^{-7}$
A3	$1.86 \cdot 10^{-7} \pm 1.28 \cdot 10^{-7}$	$-2.67 \cdot 10^{-8} \pm 2.05 \cdot 10^{-9}$
B1	$5.12 \cdot 10^{-5} \pm 1.22 \cdot 10^{-5}$	$5.23 \cdot 10^{-5} \pm 1.11 \cdot 10^{-6}$
B2	$-3.51 \cdot 10^{-5} \pm 1.72 \cdot 10^{-5}$	$-1.29 \cdot 10^{-5} \pm 1.14 \cdot 10^{-6}$
C1	$7.50 \cdot 10^{-4} \pm 3.16 \cdot 10^{-4}$	$-7.79 \cdot 10^{-5} \pm 2.47 \cdot 10^{-5}$
C2	$8.18 \cdot 10^{-4} \pm 2.96 \cdot 10^{-4}$	$1.85 \cdot 10^{-4} \pm 1.91 \cdot 10^{-5}$

The parameters are as follows (Luhmann et al. 2006):

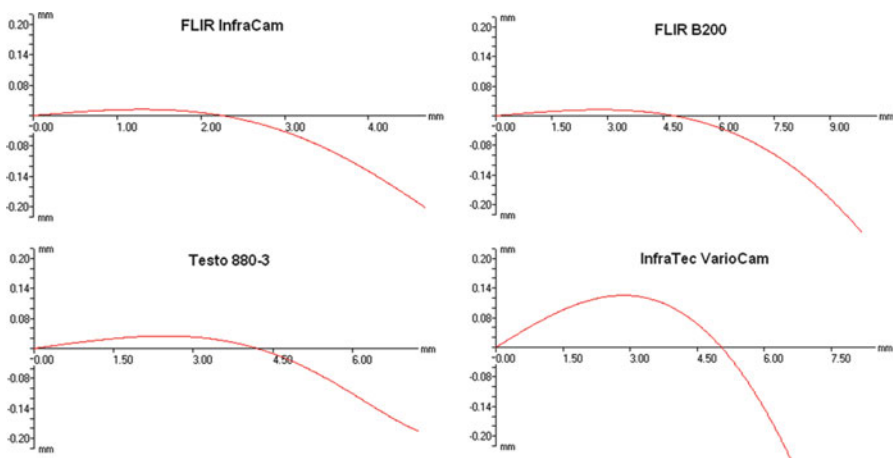
c principal distance ( $\approx$  focal length)

$x'_0, y'_0$  principal point shift, with respect to image center

$A_1, A_2, A_3$  radial-symmetric distortion, expressed in polynomial series

$B_1, B_2$  radial-asymmetric (tangential) distortion

$C_1, C_2$  affinity and shear

**Fig. 2.7** Distortion curves (radialsymmetric aberrations as a function of the image radius)

parameters, while this work aimed to examine the geometric properties of the cameras as comprehensively as possible.

The camera InfraTec VarioCAM yields the best results in terms of precision of the estimated parameters. The precision of image point measurement lies in the order of  $1 \mu\text{m}$  or  $1/30$ th of a pixel. For this camera the principal point shows moderate shift with respect to the centre of the image, and the principal distance is close to the given focal length.

The resulting precision in object space is estimated by root mean square values (RMS) of adjusted object coordinates. External reference values, for instance calibrated lengths, are not available in this test. Table 2.4 summarizes the results

**Table 2.4** RMS 1-sigma values of object coordinates

Camera	X (mm)	Y (mm)	Z (mm)
FLIR InfraCAM	0.110	0.118	0.143
Testo 880-3	0.137	0.160	0.236
FLIR B200	0.148	0.185	0.145
InfraTec VarioCam	0.038	0.029	0.062

in object space. As expected from the calibration quality discussed above, the first three cameras yield RMS values (1 sigma) of about 0.11–0.24 mm, which corresponds to about 1:6,000 of the largest object diameter. The InfraTec VarioCam results in RMS values of 0.03–0.06 mm, corresponding to about 1:20,000.

## 2.4 Applications

### 2.4.1 2D Processing

If thermographic cameras are calibrated in terms of the geometric imaging model they can be used for a variety of practical applications (Kaplan 2007). For two-dimensional purposes thermal images can be resampled to distortion-free images. As an example Fig. 2.8 shows the original thermal image of a facade (approx. 19 m × 11 m) taken with the InfraTec VarioCam. Radial distortion is clearly visible. Figure 2.9 shows the same image after correction of distortion. Geometrically corrected thermographic imagery can be used as thermal orthophotos, maps or mosaics, or as precise texture images for 3D city or building models.

It has to be pointed out that modified thermographic images often can not be processed by those software packages that are provided with a specific camera system. As an example, the FLIR software package solely allows post-processing of original FLIR imagery, e.g. changing temperature scales or colour tables.

### 2.4.2 3D Processing

Three-dimensional applications are also possible since thermographic images can be used in the same way as conventional photogrammetric images. For example it is possible to derive 3D building models from thermal imaging, if no other image or measurement data are available.

However, in many cases it is required to match corresponding points serving as tie or control points. It should be noted that most objects do not behave as diffuse Lambert reflectors. Therefore identical areas are displayed in different colors (temperatures).

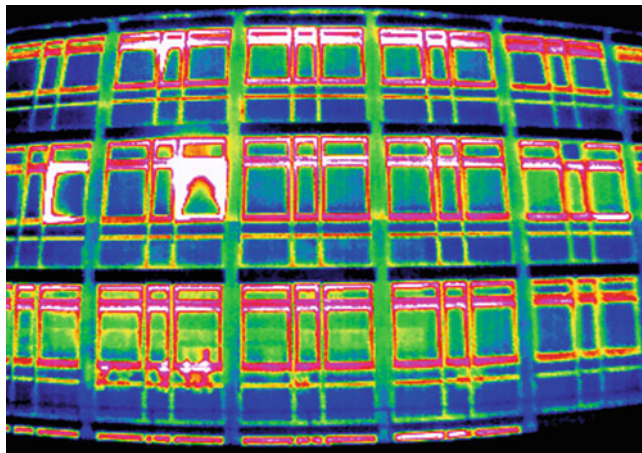


**Fig. 2.8** Original thermal image

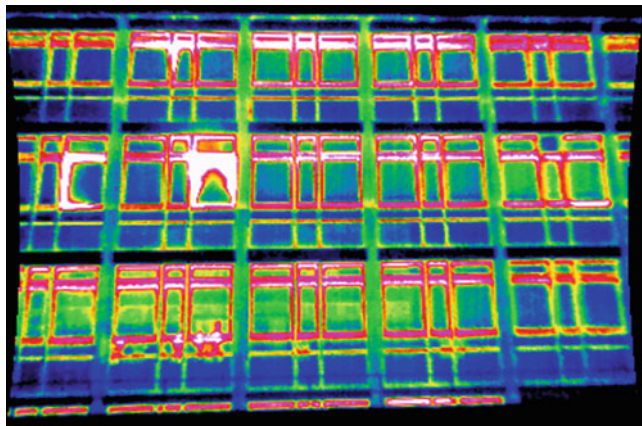


**Fig. 2.9** Distortion-free thermal image

Figure 2.10 shows three overlapping thermal images of a building and the derived mosaic. The next example presents a 3D building model (Fig. 2.11) with roof textures generated from aerial thermal images. Future investigations will concentrate on 3D modelling under consideration of radiometric object models.

### 2.4.3 Pan-Sharpening

If a high resolution panchromatic or RGB image is available in addition to a (low resolution) thermal image it is possible to apply pan-sharpening. Both image sources have to be registered (rectified) to the same geometric reference system.

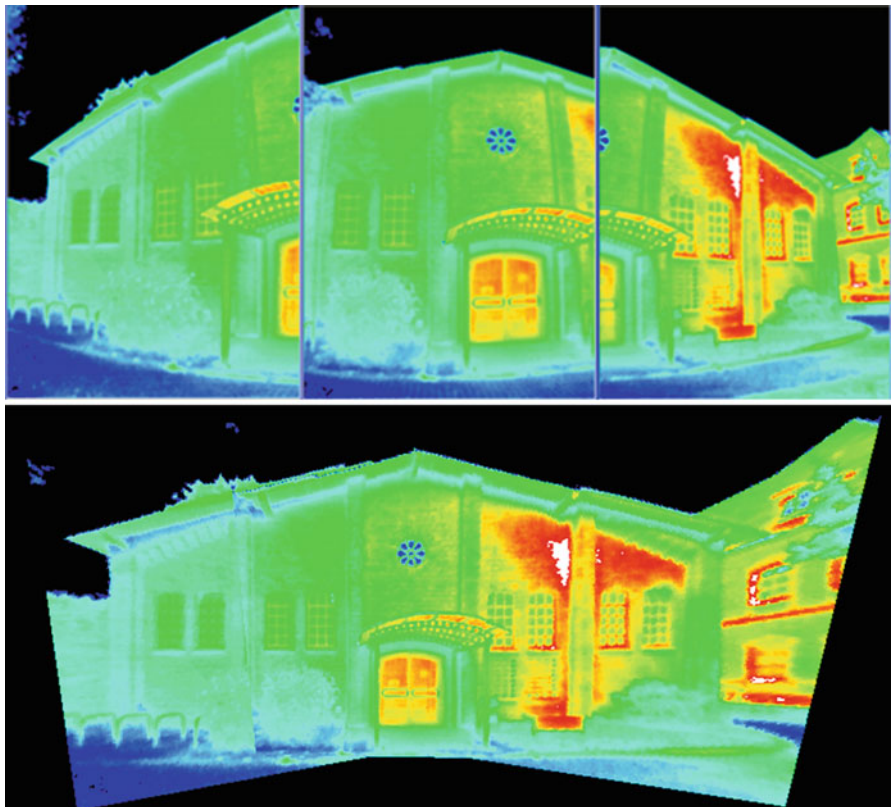


**Fig. 2.10** Multi-image thermography (size of the facade:  $20\text{ m} \times 8.5\text{ m}$ )

Figure 2.12 shows the principle image data flow for thermal pan-sharpening as it has been applied to the images shown below. In the drawing two different cases are displayed: If a colour photo (RGB) is available, the intensities of the three channels are computed and averaged. On the other hand, one-channel panchromatic images do not need any pre-processing.

To illustrate the benefits Fig. 2.13 shows original thermal images of a roof surface and a building façade. Figure 2.14 displays the results of pan-sharpening using a high-resolution digital image taken with a Trimble AIC Pro and a Nikon D2x, respectively. In contrast to standard methods in remote sensing (e.g. Toet et al. 1989; Ehlers et al. 2010), applying pan-sharpening to non-planar objects in close-range photogrammetry either requires identical perspectives for each image source, or given 3D object models and full orientation parameters of each image.

It should be noted that the colours will change by this processing and an attribution of temperature levels in a following step might lead to erroneous values in small structures. However, the method of pan-sharpening, meanwhile a standard technique in image processing, is quite suitable for presentation purposes of thermographic inspections in order to illustrate details of the object.

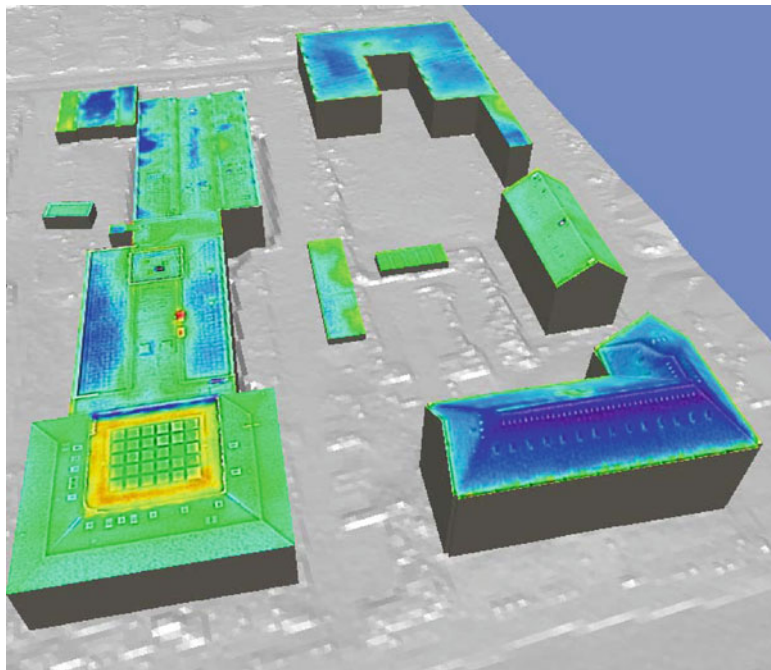


Fig. 2.11 3D building model, based on thermal images (section of 120 m × 160 m)

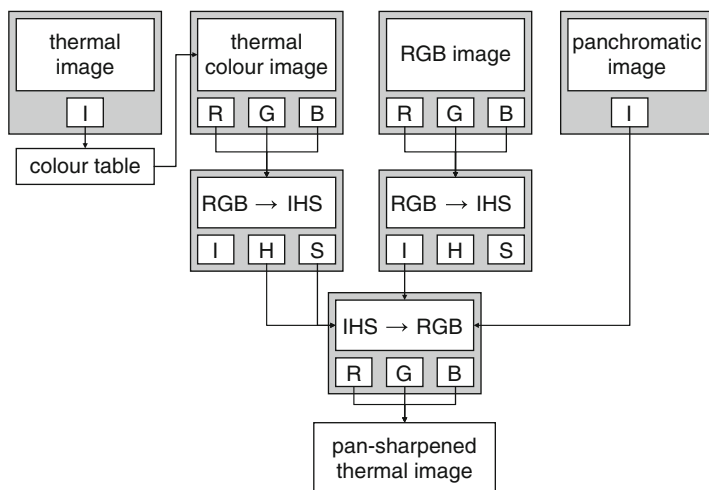
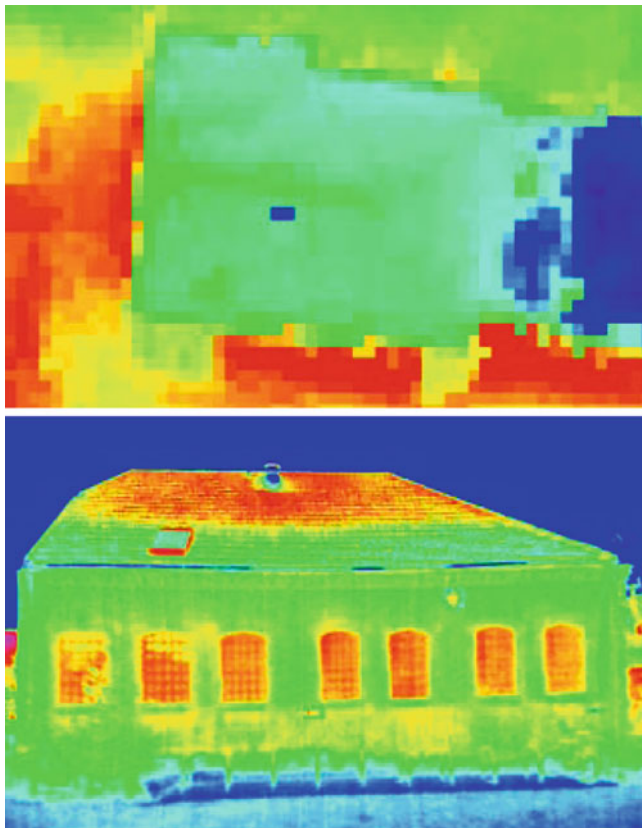


Fig. 2.12 Image data flow for thermal pan-sharpening



**Fig. 2.13** Original thermal images

## 2.5 Summary

We have investigated the performance of thermographic cameras with respect to their geometric image model and accuracy performance. Standard procedures for camera calibration can be applied to close-range thermal imagery if the cameras consist of array imaging sensors. In addition, the observed object must provide target points that are visible in the thermal spectrum. For this purpose a new test field has been designed that uses the cold temperature from sky in order to create sufficient image contrast.

The results of camera calibration show that standard thermographic cameras yield high distortion values, and large shifts of principal point. Only one camera (Infratec VarioCam) provides an accuracy level that is comparable to RGB cameras.

Some example applications are discussed ranging from 2D image modification purposes (rectification, image mosaics) and pan-sharpening approaches up to 3D

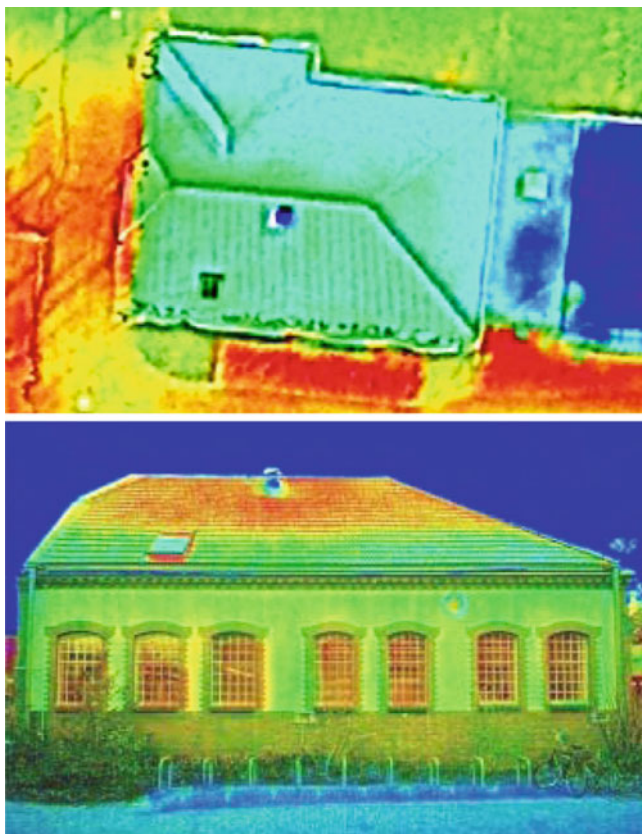


**Fig. 2.14** Thermal pan-sharpening results

modeling tasks that uses thermographic imagery in the same way as multi-image photogrammetry. However, the radiometric models of thermal object emission have to be investigated in more detail for a better understanding of the imaging process in convergent cases.

## References

- Buyuksalih G, Petrie G (1999) Geometric and radiometric calibration of frame-type infrared imagers. ISPRS joint workshop sensors and mapping from space 1999, Hannover
- Dereniak EL, Boreman GD (1996) Infrared detectors and systems. Wiley-Interscience, New York, 561pp
- Ehlers M, Klonusa S, Åstrand PJ, Rosso P (2010) Multi-sensor image fusion for pansharpening in remote sensing. *Int J Image Data Fusion* 1(1):25–45
- Fouad NA, Richter T (2008) Leitfaden Thermografie im Bauwesen. Fraunhofer IRB Verlag, Stuttgart, 127pp

- Fraser CS (1997) Digital camera self-calibration. *ISPRS J Photogramm Remote Sens* 52:149–159
- Godding R (1993) Ein photogrammetrisches Verfahren zur Überprüfung und Kalibrierung digitaler Bildaufnahmesysteme. *Z Photogramm Fernerkund* 2:82–90
- Hierl T (2008) Hochauflösende Infrarot-Detektormatrizen. In: Bauer N (ed) *Handbuch zur Industriellen Bildverarbeitung*. Fraunhofer IRB Verlag, Stuttgart, pp 41–46
- Kaplan H (2007) Practical applications of infrared thermal sensing and image equipment. SPIE Publications, Bellingham, 192pp
- Le Noc L, Tremblay B, Martel A, Chevalier C, Blanchard N, Morissette M, Mercier L, Duchesne F, Gagnon L, Couture P, Lévesque F, Desnoyers N, Demers M, Lamontagne F, Jerominek H, Bergeron A (2010) 1280 × 960 pixel microscanned infrared imaging module. In: *Infrared technology and applications XXXVI*. Proceedings of SPIE, vol 7660: 766021-766021-10, Orlando, 2010
- Luhmann T (2010) Erweiterte Verfahren zur geometrischen Kamerakalibrierung in der Nahbereichsphotogrammetrie, Habilitationsschrift, Deutsche Geodätische Kommission, Reihe C, Nr. 645. Verlag der Bayerischen Akademie der Wissenschaften in Kommission beim Verlag C. H. Beck, München
- Luhmann T, Robson S, Kyle S, Harley I (2006) Close range photogrammetry. Whittles Publishing, Dunbeath, 500pp
- Luhmann T, Ohm J, Piechel J, Roelfs T (2010) Geometric calibration of thermographic cameras. In: *International archives of photogrammetry, remote sensing and spatial information sciences*, vol XXXVIII, Part 5 Commission V symposium, Newcastle upon Tyne, 2010, pp 411–416
- Nolting J (2007) Detektoren für optische Strahlung. DOZ Optometrie 4-2007:50–56
- Planck M (1900) Zur Theorie des Gesetzes der Energieverteilung im Normalspectrum. *Verhandlungen der Deutschen physikalischen Gesellschaft* 2(17):237–245, Berlin
- Schuster N, Kolobrodov VG (2004) *Infrarothermographie*. Wiley-VCH Verlag, Weinheim, 354pp
- Toet A, van Ruyven JJ, Valeton JM (1989) Merging thermal and visual images by a contrast pyramid. *Opt Eng* 28(7):789–792
- Wolfe WL, Zissis GJ (1985) The infrared handbook. Environmental Research Institute of Michigan, Ann Arbor, 1700pp

# Chapter 3

## Thermal Infrared Spectroscopy in the Laboratory and Field in Support of Land Surface Remote Sensing

Christoph A. Hecker, Thomas E.L. Smith, Beatriz Ribeiro da Luz,  
and Martin J. Wooster

**Abstract** Thermal infrared (TIR) spectra of Earth surface materials are used in a wide variety of applications. These applications can fall into either of two groups: (a) where the TIR emissivity spectra themselves are the primary interest, and are used to determine the chemical/physical parameters of minerals and rocks, soil, vegetation and man-made materials, or (b) where the primary interest is in the temperature of the objects under study, and where emissivity spectra are required in order to best determine kinetic from radiant temperature. Unlike visible-near infrared (VNIR) and shortwave infrared (SWIR) instruments, TIR spectroscopy instrumentation often requires customization in order to acquire reliable and reproducible data, making thermal spectroscopy a potentially complex process. Within this chapter we intend to provide a simple starting point for the new user of thermal infrared spectroscopy, and a synoptic overview of the technique for the more experienced practitioner. We discuss the theoretical background, give examples of instrument setups and provide typical measurement scenarios for a number of land applications.

### 3.1 Introduction

Contrary to spectrometers that operate in the visible-near infrared (VNIR) and shortwave infrared (SWIR) spectral regions, thermal infrared (TIR) instruments often require customization before they are fully capable of supporting land surface

---

C.A. Hecker (✉)

Faculty of Geo-Information Science and Earth Observation (ITC), University of Twente,  
Enschede, The Netherlands  
e-mail: [c.hecker@utwente.nl](mailto:c.hecker@utwente.nl)

T.E.L. Smith • M.J. Wooster

Department of Geography, King's College London (KCL), Strand, London, UK

B. Ribeiro da Luz

University of Sao Paulo, Sao Paulo, Brazil  
e-mail: [beatrizrluz@gmail.com](mailto:beatrizrluz@gmail.com)

remote sensing applications. These applications can fall into either of two groups: (a) where the TIR spectra themselves are the primary interest, and are used to determine the chemical/physical parameters of minerals and rocks, soil, vegetation and man-made materials, or (b) where the primary interest is in the temperature of the objects under study, and where emissivity spectra are required in order to best determine kinetic from radiant temperature. The group of organizations involved in TIR spectroscopy has historically been rather small. However, recent developments in airborne and spaceborne TIR sensors (e.g., HyTES (Hyperspectral Thermal Emission Spectrometer), HypsIRI (Hyperspectral Infrared Imager), TASI (Thermal Airborne Spectrographic Imager), AISA OWL, MAKO, MAGI (Aerospace's Mineral and Gas Identifier), ASTER (Advanced Spaceborne Reflection and Emission Radiometer), MASTER (MODIS-ASTER Airborne Simulator)) have triggered increasing interest in TIR field and laboratory spectroscopy for calibration/validation of airborne and spaceborne data as well as for algorithm testing in ground-based pilot studies. In the past 10 years numerous organizations (for examples see later sections) have begun to utilize TIR spectroscopy methods in the field and laboratory, and have either purchased or designed custom instrumentation for the acquisition of TIR spectra. Although acquiring reliable and reproducible TIR spectral data is not as straightforward as in the VNIR and SWIR spectral regions, measurement techniques have been greatly improved throughout the past decade, and the use of TIR spectroscopy for remote sensing applications is becoming more widespread (e.g., Hecker et al. 2011; Ribeiro da Luz and Crowley 2010; Vaughan et al. 2005). For the remainder of the chapter, we focus on (1) measurement techniques that are quantitatively comparable to multi- and hyper-spectral TIR Earth observation data and (2) applications related to analysis of Earth's surface materials (soils, rocks, vegetation and man-made materials). Whilst thermal infrared spectroscopy has also been used for the characterization of water (e.g., Minnett et al. 2005), we do not deal with that application here and concentrate only on the solid land surface. Furthermore, TIR spectroscopy is a widely used technique in relation to analysis of gaseous atmospheric compounds, but the techniques and applications are very different (e.g., see reviews by Bacsik et al. 2004, 2005) and so these will not be treated here.

### ***3.1.1 Application Examples***

Field or laboratory thermal infrared spectra of Earth surface materials obtained in the mid-wave infrared (MWIR; 3–5  $\mu\text{m}$ ) and/or long-wave infrared (LWIR; 8–14  $\mu\text{m}$ ) atmospheric windows are used in a wide variety of applications, sometimes alone but often as part of a larger study making use of airborne or spaceborne datasets collected within the same wavelength range. These include applications focused on identification of surface composition, such as geologic mapping on Earth and other planets, where the spectral features corresponding to vibrational motions occurring within a crystal lattice at specific wavelengths are directly

related to the crystal structure and elemental composition (i.e., the mineralogy; e.g., Christensen et al. 2000; Salisbury et al. 1991; Lyon 1965). Use of thermal infrared data can be extremely useful in these types of studies, since many common minerals (e.g. silicates and carbonates) show distinctive spectral features in the TIR but can be relatively indistinct and difficult to unambiguously identify in the VNIR spectral region (Vaughan et al. 2003). The thermal IR spectra of plants and soils also contain potentially useful information, related to (plant) species, their chemical constituents, structure and moisture content (Ullah et al. 2012; Ribeiro da Luz and Crowley 2007; Salisbury 1986; Hulley et al. 2010). The mapping of surface temperature and the estimation of surface energy budgets using data from airborne or spaceborne imaging radiometers also requires knowledge of the surface emissivity, since this has a direct control on the amount of thermal radiation emitted (Jacob et al. 2004; Dash et al. 2002; Xu et al. 2008). Surface temperature retrieval methods based on a prescribed emissivity derived via TIR laboratory or field spectral measurements and a land cover classification are often used in such approaches (Voogt and Oke 2003). For some multi-band imaging radiometers operating at thermal wavelengths (e.g. TIMS (Thermal Infrared Multispectral Scanner), MASTER, ASTER), temperature-emissivity separation algorithms exist that retrieve a surface emissivity estimate as part of the calculation, but these methods are also generally based around algorithms derived and validated using laboratory or field emissivity spectra (Sabol et al. 2009; Gillespie et al. 1998; Coll et al. 2003). Indeed, in some circumstances it may still be beneficial to prescribe emissivity when analyzing these type of multispectral TIR data (e.g., in highly heterogeneous locations such as urban areas; Mitraka et al. 2011; Ramsey 2003). The mapping of atmospheric properties like temperature, humidity and trace gas concentration also often relies on TIR measurements made from space or aircraft, both when studying the ambient atmosphere and ‘plumes’ such as those emanating from industrial sources, fires or active volcanoes (Burrows et al. 2011). Knowledge of the underlying surface emissivity is often important here, since it imparts features within the measured spectra of downward viewing instruments that impact the atmospheric retrievals (Thomas et al. 2009; Hulley et al. 2009).

TIR emissivity spectra for use in these and other applications, such as studies of environmental pollution effects (Lammoglia and de Souza Filho 2011) can be measured by the user in the field or laboratory setting using the methods outlined in this chapter, and which are discussed in more detail in the referenced papers. If users do not have the capability to measure such spectra themselves, then example spectra of a very wide variety of surface materials can be obtained from (online) spectral databases, the most widely used of which are the Johns Hopkins Spectral Library (Salisbury et al. 1991), the Arizona State University library (Christensen et al. 2000), the spectral library of the United States Geologic Survey (USGS)(Clark et al. 2007) as well as the Jet Propulsion Laboratory’s (JPL) ASTER spectral library (Baldridge et al. 2009; Fig. 3.1).

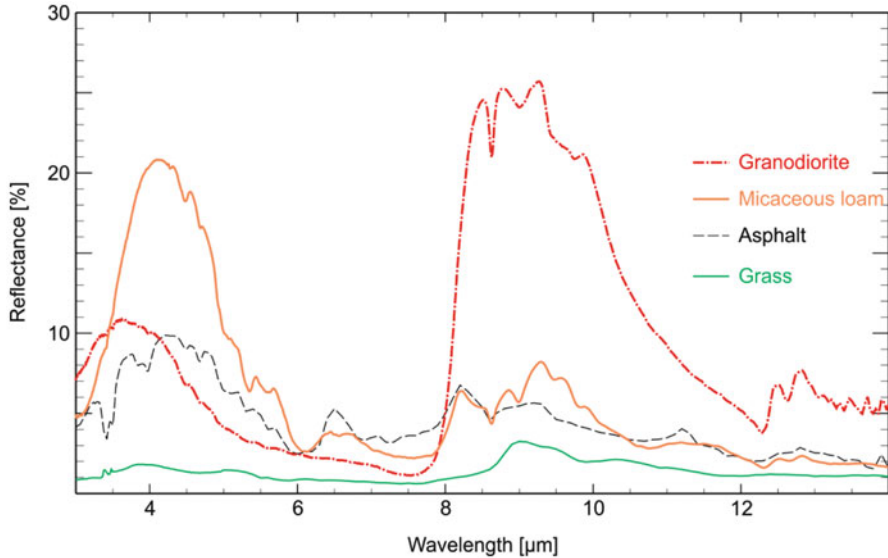


**Fig. 3.1** Examples of DHR reflectance spectra for a series of different land surface materials, in the MWIR and LWIR spectral regions (Reproduced from the ASTER Spectral Library through the courtesy of the Jet Propulsion Laboratory, California Institute of Technology, Pasadena, California. Copyright © 1999, California Institute of Technology. The ASTER Spectral Library is available at <http://speclib.jpl.nasa.gov/> and is described in Baldridge et al. (2009))

## 3.2 Theoretical Background

TIR spectrometers can operate across the MIR and LWIR spectral range, covering both the 3–5 and 8–14  $\mu\text{m}$  Earth's atmospheric windows. However, not all of the field or laboratory spectral measurement geometries shown in Fig. 3.2 are suitable for quantitative comparison with airborne or spaceborne remote sensing data. All currently operating air- and spaceborne TIR remote sensors detect the energy emitted by the object itself. Spectrometers that measure in emission mode mimic this type of remote sensing data most closely, but several studies have shown that directional-hemispherical reflectance (DHR) measurements are equivalent to emission measurements in most terrestrial situations (Korb et al. 1999; Salisbury et al. 1994). For the remainder of this chapter, therefore, we focus on TIR spectroscopic measurements in emission and DHR mode.

### 3.2.1 Directional-Hemispherical Reflectance (DHR)

Spectrometric measurements using the DHR geometry are relative reflectance measurements involving a high temperature emitter and a reference material of

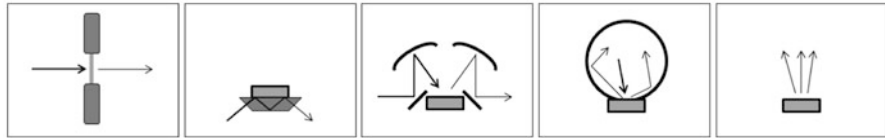


**Fig. 3.2** Sketches illustrating examples of different measurement geometries for TIR spectroscopy: transmission, attenuated total reflectance, bi-conical reflectance, directional–hemispherical reflectance, emission (from left to right) (Modified from Hecker et al. (2010))

known reflectance. In practice, a ceramic globar source is heated to 1,500 K and radiates energy onto the sample material. The directional-hemispherical reflectance (see Fig. 3.2) of the sample is measured and the reflectance and emissivity spectra are calculated. The calculations involved in DHR measurements are straight forward and essentially identical to those used in the VNIR and SWIR wavelength ranges. Reflectance of the sample ( $R_{\text{Sample}}$ ) is defined as

$$R_{\text{sample}}(\lambda) = \frac{L_{r,\text{sample}}(\lambda)}{L_i(\lambda)} \quad (3.1)$$

where  $L_i$  is the incoming radiance and  $L_{r,\text{sample}}$  is the radiance reflected off the sample. The measured energy at the detector ( $V_{\text{sample}}$ ) depends on the radiance leaving the sample ( $L_{r,\text{sample}}$ ), and the instrument's spectral response function ( $F$ ).

$$V_{\text{sample}}(\lambda) = L_{r,\text{sample}}(\lambda) * F \quad (3.2)$$

Since the energy impinging on the sample and the spectrometer's response function are not known, one also measures a well-characterized diffuse reference material, such as Labsphere Infragold® where

$$R_{\text{reference}}(\lambda) = \frac{L_{r,\text{reference}}(\lambda)}{L_i(\lambda)} \quad (3.3)$$

and

$$V_{\text{reference}}(\lambda) = L_{r,\text{reference}}(\lambda) * F \quad (3.4)$$

where  $R_{\text{reference}}$  is the calibrated reflectance spectrum of the reference material,  $L_{r,\text{reference}}$  is the radiance reflected off the reference and  $V_{\text{reference}}$  is the energy spectrum measured during the reference measurement. Combining (3.1), (3.2), (3.3) and (3.4), the instrument response function and incoming radiation terms are eliminated and

$$R_{\text{sample}}(\lambda) = \frac{V_{\text{sample}}(\lambda) * R_{\text{reference}}(\lambda)}{V_{\text{reference}}(\lambda)} \quad (3.5)$$

which is a simple ratio of the sample and reference spectral measurements, with a correction factor ( $R_{reference}$ ) for the imperfect reflectance behavior of the gold standard.

Equation (3.5) is based on the assumption that (a) there is no additive energy component, and (b)  $L_i$  and  $F$  do not vary between reference and sample measurements. If tests indicate assumption (a) to be invalid, a background radiation removal can be performed (see Hecker et al. 2011). Assumption (b) is usually true if reference and sample measurements are done in close succession. How frequently the reference measurement needs repeating has to be determined for a given spectrometer setup, as it depends on the stability of the globar source and of the atmospheric composition under which the measurement is made (mainly H<sub>2</sub>O and CO<sub>2</sub>; the latter of which can rapidly change indoors for example). The sampling area is often enclosed in an enclosing box and the spectrometer and box purged with N<sub>2</sub> gas (or H<sub>2</sub>O and CO<sub>2</sub>-scrubbed air) to reduce the effect of these atmospheric gases on the measured spectra.

Depending on the application, the reflectance spectra obtained from (3.5) may not be the desired format for further use, and so emissivity spectra ( $\epsilon_{sample}$ ) can be calculated from reflectance spectrum ( $R_{sample}$ ) of the sample using Kirchhoff's Law (Nicodemus 1965), which in its simplest form can be written as

$$\epsilon_{sample}(\lambda) = 1 - R_{sample}(\lambda) \quad (3.6)$$

### 3.2.2 Emissive Systems

Unlike the DHR approach, retrieving emissivity spectra using emissive systems does not require a separate source of infrared radiation; instead, the radiation emitted by the surface is compared with the amount of radiation emitted by a blackbody at the same kinetic temperature (Fig. 3.3). Early emissive systems (e.g., Lyon 1965) performed a direct comparison between measured samples and blackbodies. Recent approaches, however, calibrate sample radiance and, assuming a known sample temperature, compare this calibrated radiance with that of a modeled blackbody (e.g., Hoover and Kahle 1987). As this method does not rely upon keeping samples and blackbodies at a fixed temperature, the method is appropriate for field use.

The emissivity ( $\epsilon$ ) of the sample is the ratio of radiated energy by the sample ( $L_S$ ) to the radiated energy of a blackbody ( $L_{BB}$ ) at the same kinetic temperature ( $T$ ):

$$\epsilon(\lambda) = \frac{L_S(\lambda, T)}{L_{BB}(\lambda, T)} \quad (3.7)$$

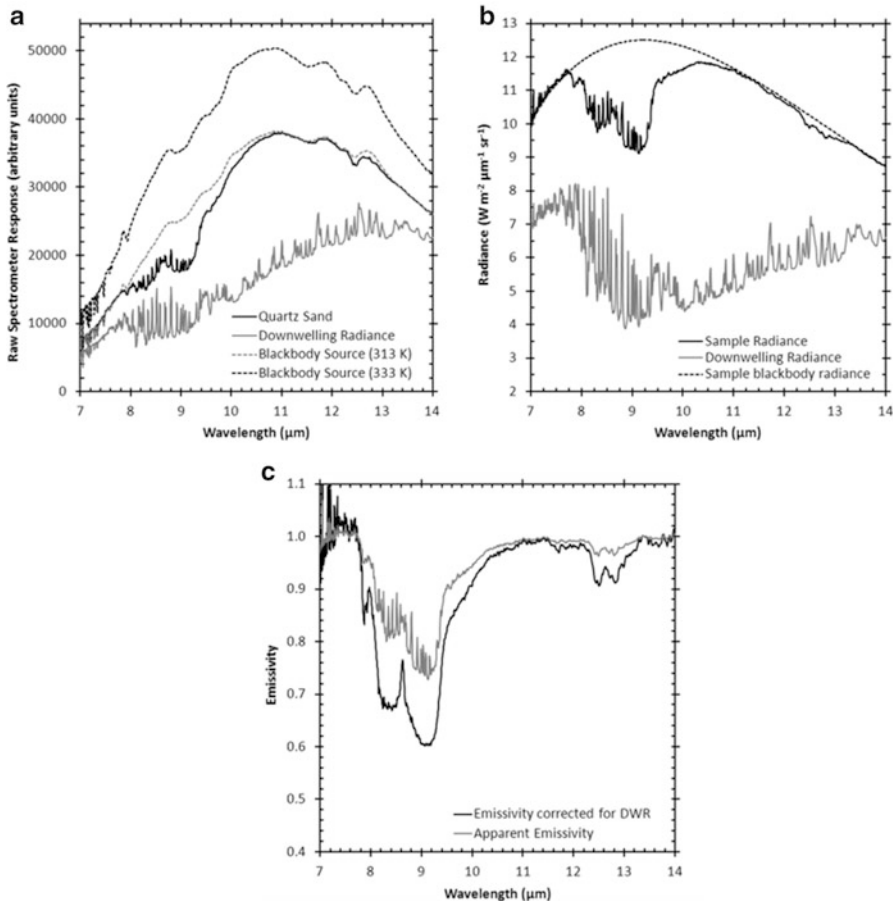


**Fig. 3.3** (a) Raw spectra for a sample of quartz sand, the two blackbody calibration sources, and the down-welling radiance (DWR) measured using the InfraGold plate; (b) calibrated radiance for both the sample and the DWR. Also shown is the blackbody curve used to calculate sample emissivity; (c) apparent emissivity (without subtracting the DWR), and emissivity after DWR correction (For a discussion of DWR and its importance, see section later in the text)

The spectral radiance of a blackbody ( $\text{W m}^{-2} \mu\text{m}^{-1} \text{sr}^{-1}$ ) ( $L_{BB}$ ) can be calculated using Planck's law of blackbody radiation, in relation to wavelength ( $\lambda$ ):

$$L_{BB}(\lambda, T) = \frac{2hc^2}{\lambda^5} \frac{1}{e^{\frac{hc}{kT\lambda}} - 1} \quad (3.8)$$

where  $h$  is Planck's constant ( $6.626068 \times 10^{-34} \text{ J s}^{-1}$ ),  $c$  is the speed of light ( $299,792,458 \text{ m s}^{-1}$ ) and  $k$  is Boltzmann's constant ( $1.38066 \times 10^{-23} \text{ J K}^{-1}$ ).

### 3.2.2.1 Spectrometer Calibration

For any spectrometer calibration process, a mathematical model must describe the raw spectrum provided by the spectrometer as a function of the radiation that enters the spectrometer. As radiation leaves the target surface (i.e., the sample or the calibration surface), it interacts with the atmosphere before entering the spectrometer, upon which it interacts with mirrors, beam splitters and lenses before impinging on the detector. Furthermore, self-emission by each of these components, and noise introduced by electronic constituents of the system, such as filters and amplifiers, all influence the final measured spectrum. A model of each of these components cannot be theoretically achieved. Therefore, a calibration procedure is required to determine the collective effect of these influences. To this end, calibration usually involves measuring the spectra of known radiation sources, such as blackbodies.

The basic mathematical model for describing the target radiance as a function of the spectrum measured by the spectrometer is given below:

$$L(\lambda) = G(\lambda)V(\lambda) + O(\lambda) \quad (3.9)$$

where  $L$  is the spectral radiance emitted by the target surface (i.e., the sample or the calibration surface),  $G$  is the spectral response (gain) of the spectrometer,  $V$  is the uncalibrated energy spectrum measured by the spectrometer, and  $O$  is the spectral radiance emitted by the spectrometer's inner parts (offset). By measuring the spectra of two blackbodies at different known temperatures (usually just below ambient and just above sample temperature), there is enough information to solve the above equation for  $G$  and  $O$  (see Hook and Kahle 1996).

Although the aforementioned two-temperature method has been widely used, Lindermeir et al. (1992) address a fundamental problem with the approach: that it requires an accurate knowledge of the blackbody temperatures that are used in the calibration. By measuring a third blackbody, there is enough information to treat the three blackbody temperatures as unknown variables. A nonlinear least squares fitting algorithm is used to determine the three temperatures and instrument parameters  $G$  and  $O$ .

### 3.2.2.2 Retrieving Emissivity: Downwelling Radiance Correction

The first problem encountered when retrieving surface emissivity from measured TIR spectra is the fact that the measured upwelling sample radiance is in fact composed of both sample thermal emission and reflected downwelling radiance (*DWR*). The latter originates from the atmosphere above (and the objects around) the sample. It is necessary to make measurements of *DWR* using a diffuse reflective surface ( $\epsilon < 0.1$ ), usually Infragold®, or crinkled aluminium. Since these reference materials have a non-zero emissivity, some authors adjust the measured DWR for the reference materials imperfect reflectance, as well as the (small) contribution of

the reference panel self-emission. The *DWR* ( $L_{DWR}$ ) is subsequently subtracted from the measured upwelling sample radiance to isolate the sample thermal emission (Fig. 3.3c):

$$\epsilon_S(\lambda) = \frac{L_s(\lambda) - L_{DWR}(\lambda)}{L_{BB}(T_s, \lambda) - L_{DWR}(\lambda)} \quad (3.10)$$

where  $\epsilon_S$  is the sample emissivity spectrum of interest,  $L_s$  the radiance spectrum from the sample measurement,  $L_{DWR}$  the downwelling radiance from the reference plate measurement and  $L_{BB}(T_s, \lambda)$  the blackbody radiance from the Planck function at the kinetic temperature of the sample.

Importantly, the *DWR* signal must be significantly less intense than the upwelling sample radiance for the method to work effectively. Therefore, measurements in a laboratory situation (where *DWR* will be the result of the ceiling and walls at ambient temperature) should be of a relatively hot sample surface, which generally necessitates heating of the sample (Salisbury 1998). Similarly, when measuring surfaces in the field, it is important to ensure that there is a clear ('cold' at IR wavelengths) sky, since the presence of many low clouds can result in sky temperatures similar to the ambient sample temperature. Of course, appropriate application of Eq. (3.10) requires knowledge of the sample kinetic temperature ( $T_s$ ), which is not always easy to measure at the necessary precision.

### 3.2.2.3 Retrieving Emissivity: Sample Temperature

Many materials and surface types are not amenable to high quality kinetic temperature measurements for use in Eq. (3.10). Separating temperature and emissivity effects is therefore the second problem encountered in the emissivity retrieval process. This temperature-emissivity separation problem has been tackled using a wide variety of methodologies, the most common of which are summarised below.

#### Reference Channel

The simplest approach to the temperature-emissivity separation problem is to assume that sample emissivity is equal to that of a blackbody (i.e., to *unity*) at one or more wavelengths within the measured TIR spectrum (Murcray et al. 1970). The wavelength itself can be prescribed during the analysis or can be determined as that which gives the highest temperature when the measured spectral radiance is used within the inverse of Eq. (3.8). Given that the sample radiance and its emissivity are then known at this specific wavelength, it is possible to calculate the surface kinetic temperature and thus use the spectral measurements at the other wavelengths to calculate the emissivity spectrum. This reference channel method can also be modified so that maximum assumed emissivity can be less than unity (e.g., Kahle et al. 1980).

### Blackbody Fit

A slightly less restrictive approach assumes a known emissivity maxima at a specified *waveband*, rather than at a specific wavelength (e.g., Kahle and Alley 1992). An iterative process fits a Planck blackbody radiance curve to the measured sample spectrum within the specified waveband. The temperature of the Planck curve with the best fit to the specified maximum emissivity waveband is then used to calculate emissivity for the remainder of the spectrum.

A limitation of both methods is that the maximum emissivity of a sample must be known. Whilst laboratory measurements exist for many materials (Salisbury and D'Aria 1992, 1994), only samples with identical surface characteristics to those in the reference spectra will have the same spectral-thermal properties; therefore, the required *a priori* knowledge of emissivity maxima is usually lacking.

### Spectral Smoothness

The spectral smoothness method proposed by Horton et al. (1998) does not require any assumptions about the magnitude (or spectral position) of the sampled emissivity maxima. The method relies upon detecting any residual atmospheric emission line artifacts (e.g., water vapour emission lines apparent in Fig. 3.3b at 7.5–9.5  $\mu\text{m}$ ) in emissivity spectra retrieved using Eq. (3.10), and adjusting the assumed sample temperature until these are removed. Horton et al. determined that when sample temperature is underestimated, the effect of atmospheric emission lines is to introduce positive ‘spikes’ into the emissivity spectra; and when overestimated to introduce negative ‘spikes’. Identifying a region of the TIR spectrum where atmospheric emission lines are strongest (e.g., at 7.5–9.5  $\mu\text{m}$ ), and using a curve-fitting algorithm to determine the temperature at which such ‘spikes’ were minimized, allows for the production of the emissivity spectrum (and determination of the sample temperature).

The spectral smoothness method has been adopted by a number of subsequent studies of the emissivity of a range of surfaces, from asphalt (Bower et al. 2001) to leaves (Ribeiro da Luz and Crowley 2007) and is considered to be the most accurate field method available (Salvaggio and Miller 2001). However, the approach does not work in the indoor laboratory environment, since the measured spectra do not contain the necessary atmospheric line features. Therefore, another method for measuring or estimating sample temperature needs to be used in this particular case.

## 3.3 Instrumentation

In this section we treat a few examples of existing spectrometer setups as they are operated by various organizations. It is not our purpose to provide a complete listing, but rather a summary of some of the existing base systems, modification approaches and their respective advantages.

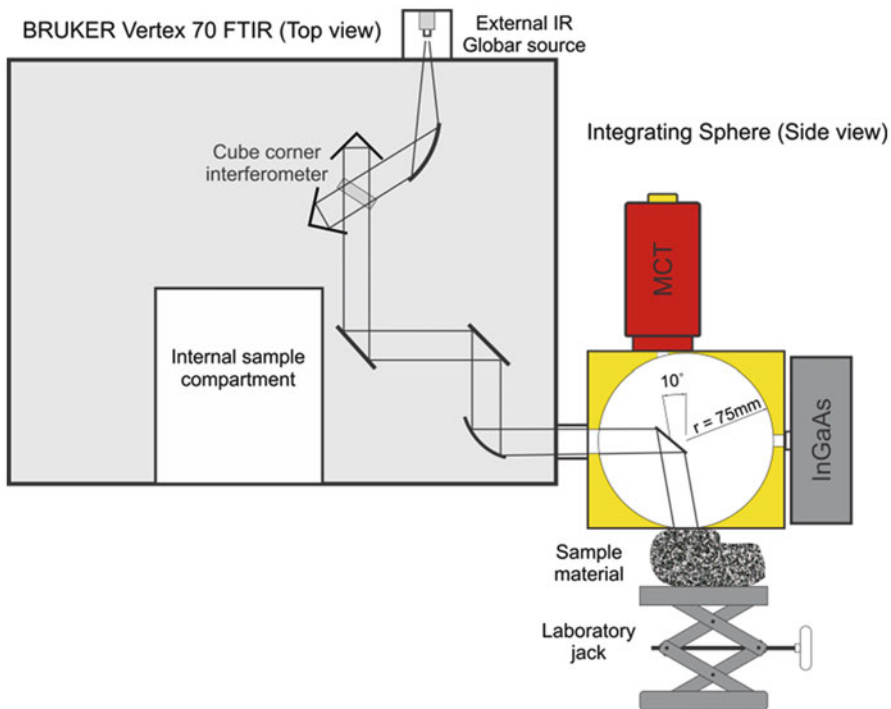


**Fig. 3.4** Sketch of the UT-ITC laboratory spectrometer as an example of a DHR instrument setup with an external integrating sphere. This instrument has a mid infrared (MCT) as well as a near infrared (InGaAs) detector on the sphere (Modified from Hecker et al. (2011))

### 3.3.1 Laboratory Environment

In the indoor laboratory environment, the typical TIR spectrometer is based on an off-the-shelf desktop Fourier-transform infrared (FTIR) spectrometer with external, customized sampling equipment. Several manufacturers of laboratory FTIR systems exist, and the differences between them are mostly relatively minor. A prerequisite is a model with high energy throughput, and possibilities to attach customized external sampling equipment.

If the FTIR is operated in the active *DHR mode*, the customizations include an external integrating sphere, one or several detectors that sit on the outside of the sphere, as well as a system of mirrors to bring the energy from the globar source via the interferometer and inside of the sphere onto the sample itself. The sample port is usually situated at the bottom of the sphere (Fig. 3.4). Similar systems exist at several other organizations (e.g., Jet Propulsion Laboratory, German Research Centre for Geosciences, Johns Hopkins University (JHU)) but all are ultimately based on Jack Salisbury's initial integrating sphere instrument as used since the

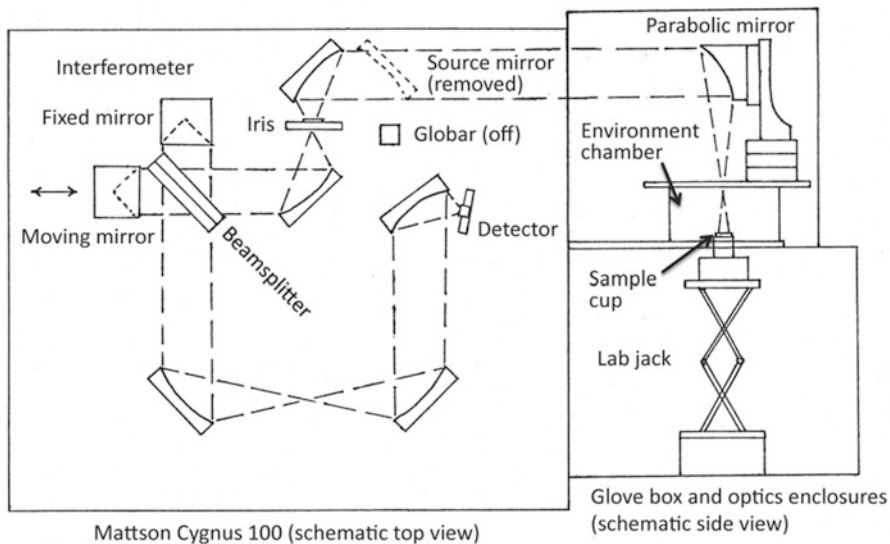


**Fig. 3.5** Sketch of the ASU laboratory spectrometer as an example of an emissive instrument setup with an external sample environment chamber (Modified from Ruff et al. (1997))

1980s at the US Geologic Survey (USGS). Advantages of these setups are high repeatability, and no need to control the sample temperature or calibrate the system with blackbodies. On the downside, measurements with good signal-to-noise ratio (SNR) can take very long (10–60 min depending on exact setup), and the sample has to have a reasonably flat measurement surface that can be in close contact with the sampling port.

If the FTIR is operated in the passive *emission mode*, the spectrometer box does not require a source. The energy comes from the sample itself, which sits outside of the spectrometer, often in a thermally controlled environment. The necessary customizations for this measurement approach include a thermally controlled sample holder, a mirror system that focuses the sample-emitted radiation via the interferometer onto the detector, and heatable blackbody emitters to calibrate the spectrometer's response to energy. Figure 3.5 shows the schematics of the Arizona State University setup as an example of such an emissive system. Small and particulate samples are pre-heated in the oven and placed in the heated sample holder during measurements (larger rock samples often do not require heating during measurements due to higher thermal inertia). As long as samples can be heated to a temperature considerably above that of the room (sample temperatures of 60–80 °C are often used) emissive systems have a much higher energy throughput than DHR systems, and measurement times are therefore generally shorter, usually totaling 0.5–10 min per sample.

**Fig. 3.6** DnP 102F  $\mu$ FTIR field spectrometer measuring vegetation detached from the canopy. The black barrel at the end of the gray power cord is the single calibration blackbody



### 3.3.2 *Field Equipment*

Early versions of TIR field spectrometers were very heavy, and needed several people to haul them into the field or a cart construction to carry them. As an example, JPL's early Portable Field Emission Spectrometer (Hoover and Kahle 1987) weight a total of 37 Kg (including a bottle of compressed Argon gas for cooling) and required 2–3 operators to carry backpacks and operate the system. Other organizations used laboratory FTIR spectrometers and customized them for field use (e.g., Salisbury 1998). Due to their heritage, these systems needed a generator for power supply and were mounted on a cart construction to move them around. In 1992 the US company Design and Prototypes built a dedicated thermal infrared field spectrometer based on a set of requirements from spectroscopists at JPL and JHU (Korb et al. 1996; Hook and Kahle 1996). After several iterations, the latest production model is the  $\mu$ FTIR 102F (Fig. 3.6) which has been adopted by many organizations worldwide as their field instrument. It is the first off-the-shelf TIR field emission spectrometer with a rather transportable

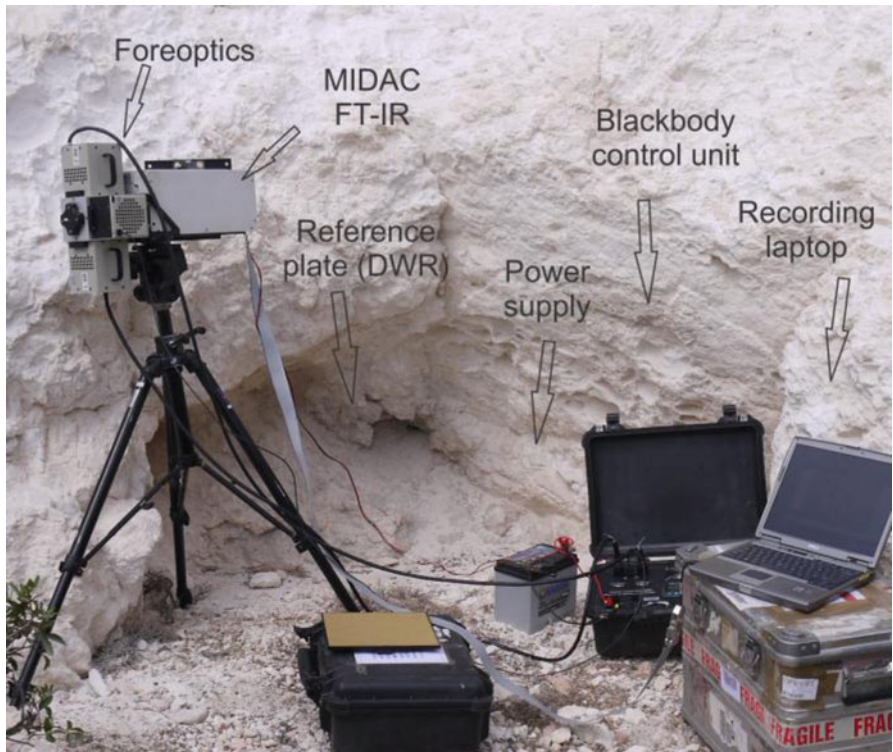


**Fig. 3.7** MIDAC Illuminator at a vertical outcrop with blackbody control unit, laptop and battery (Photo courtesy Chris MacLellan, NERC-FSF)

weight of  $<7$  kg (not including accessories). The spectral resolution of  $4\text{ cm}^{-1}$  is just sufficient for determining the sample temperature via the spectral smoothness method (see Sect. 3.2). However, we consider the major drawback of the  $\mu\text{FTIR}$  102 F to be the use of a single blackbody radiator for instrument calibration, requiring heating/cooling to two different temperatures for each calibration cycle. As field measurements are very sensitive to changes in atmospheric conditions, as well as to changes in the temperature of the spectrometer itself, most operators of field FTIRs prefer to calibrate their spectrometer frequently (if not for each sample measurement). With a single blackbody, the waiting involved to stabilize the calibration source at the lower and upper calibration temperatures results in a measurement cycle (cold blackbody, sample, down-welling radiance, hot blackbody) that can easily take up to 10 min. In anything but perfect conditions the atmosphere may have changed enough in 10 min to put numerous residual atmospheric features in the emissivity spectra.

Other organizations (e.g., King's College London, University of Twente-ITC, NERC-FSF) have chosen a different path and have modified a MIDAC Illuminator FTIR spectrometer for TIR spectral emissivity measurements (Fig. 3.7). The standard instrument housing is hermetically sealed cast aluminium (instrument

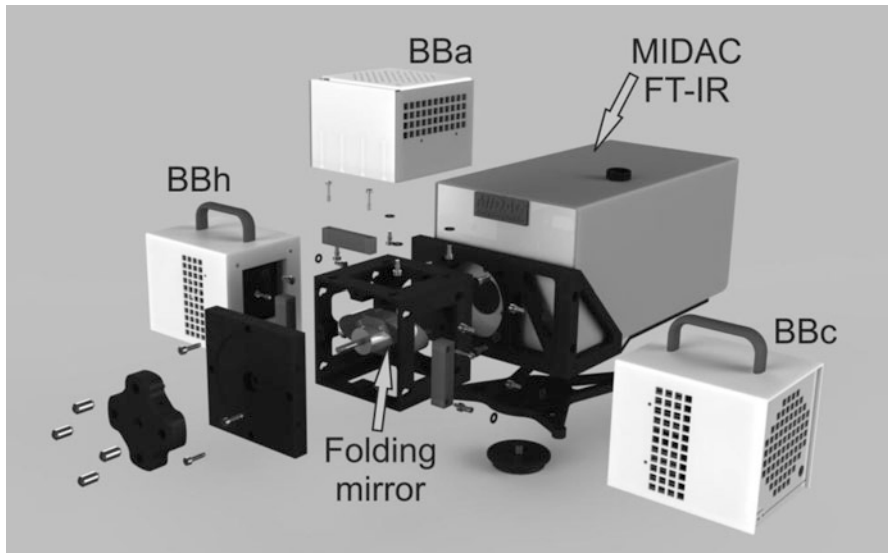


**Fig. 3.8** Detailed view of NERC-FSF foreoptics with a folding mirror and three blackbodies (hot, ambient and cold). The position of the individual blackbodies can be swapped if the application demands it. The folding mirror is rotated manually with the help of the dial (*dark gray handle on the left*) in order to view the different blackbodies or the sample (Drawing courtesy Chris MacLellan, NERC-FSF)

weight is 16 kg), which can be essential in overly dusty or chemically aggressive (e.g., volcanic) environments. For most other applications, a sheet metal option is available, which reduces the instrument weight by 50 %. Since this spectrometer was initially intended for open path atmospheric measurements, it typically has to be customized with down-looking foreoptics to support Earth surface observations.

One of the latest iterations in the design of such downward viewing foreoptics (subsequently built by Advanced Photonics International) is shown in Fig. 3.8. This contains a folding mirror that directs the spectrometer's field-of-view either onto the sample or onto three calibration blackbodies at different temperatures that are integrated into the foreoptics. With several blackbodies in place, there is no need to wait for temperature changes and stabilization, thus allowing a fast measurement sequence. A complete calibration and measurement cycle can be achieved in under a minute with this system. The MIDAC instrument also offers up to a  $0.5 \text{ cm}^{-1}$  resolution, allowing any atmospheric lines to be well-resolved during the spectral smoothness approach.

### 3.3.3 Other Developments

Recent developments in thermal spectrometers show a trend towards imaging systems as well as active reflectance systems. Below we mention a few of these

**Fig. 3.9** Optical head of the Hyper-Cam imaging field FTIR. The front shows two calibration blackbodies that can be swung into the optical path (Photo courtesy Telops)



emerging systems for reference, even though some are strictly speaking not quantitatively comparable to TIR remote sensing data due to their measurement geometry.

*Drill core loggers* are not based on a FTIR spectrometer, but rather on pushbroom-style, focal plane array TIR cameras. They allow hyperspectral imaging of the samples resulting in a spectral datacube with high spectral resolution. The Hylogger3 (Huntington et al. 2010) and the sisuRock ([URL1](#)) are examples of this group. Both systems were developed for the measurement of drill cores, and the capabilities of the systems have recently been extended into the thermal infrared spectral range. To guarantee a short measurement time and a high sample throughput, these systems are forced to use a *bi-conical reflectance* setup with high intensity lamps to illuminating the sample that are moving relative to the camera by a translation mechanism. Since the systems' primary application is on drill core data, comparison to remote sensing data is often not required and quantitative compositional as well as textural information can be extracted from the core logging imagery when compared to other bi-conical reference datasets.

The Hyper-Cam ([URL2](#); Fig. 3.9) is a field imaging spectrometer that is based on an entire focal plane array of individual FTIR elements. Contrary to the core loggers, each pixel of the Hyper-Cam records an entire interferogram which results in an array of 320 by 256 pixels emission spectra. The thermal infrared version



**Fig. 3.10** ExoScan 4100 during field use in a soil sampling pit (Photo courtesy Agilent Technologies)

records images in the 7.7–11.5  $\mu\text{m}$  spectral range and has two integrated blackbodies (see Fig. 3.9) for radiometric calibration.

The Hyper-Cam's optical head (without accessories) weights 29 or 32 kg for the normal and the weatherproof versions, respectively. The main advantage over a traditional field spectrometer is the possibility of seeing the measurements in their spatial context. If, as an example, the Hyper-Cam is deployed in an active mining environment and pointed towards the mine face, one receives an entire array of spectral measurements, rather than a single, averaged spectrum. The resulting image shows spatial patterns of quantitative mineralogic composition differences, which are crucial information for planning the future mine operations. Apart from field use, the Hyper-Cam can also be mounted on a special mounting module for airborne acquisitions.

The *ExoScan 4100* ([URL3](#); producer formerly known as “A2 Technologies”) is a lightweight handheld FTIR (Fig. 3.10) that measures diffuse reflectance spectra of materials in the field. The entire instrument is about 3 kg in weight and has the look and feel of a portable XRF system (Fig. 3.10).

The system produces diffuse reflectance spectra, which are not quantitatively comparable to remote sensing derived emissivity spectra, thus making the ExoScan unsuitable for ground truthing and calibration of airborne and spaceborne data. If comparison to earth observation data is not required, the instrument can be used for

material identification and quantification with the help of a spectral library of known diffuse reflectance spectra. This makes the ExoScan 4100 (for some applications) a truly portable alternative to the bulky emission systems.

### 3.4 Measurement Examples

The specific procedures used in TIR field and laboratory spectroscopy depend on the application field concerned. In the following sections we will describe a number of particular applications and discuss typical measurement approaches as well as sample preparation methods.

#### 3.4.1 *Solid Rocks*

TIR spectroscopy of rocks results in spectra with high spectral contrast as most rocks contain a sizeable quantity of silicate minerals or glassy fragments with strong and distinctive spectral features in the thermal infrared spectral region. Furthermore, the minerals are bound in a rock fabric, thus keeping porosity between mineral grains very low. This prevents moisture and the cavity effect (e.g., Ramsey and Fink 1999; Kirkland et al. 2002) from reducing the spectral contrast. However, interesting rocks outcrops tend to be located in remote and rugged terrains. With the currently available emission spectrometer technology it is almost always more sensible to haul a large amount of samples to the laboratory than transport a large amount of equipment to the field. This is especially true for instruments that depend on liquid nitrogen cooling, making them difficult to move in between measurement locations.

The laboratory measurements with DHR systems are rather uncomplicated. The most crucial step is to find a flat, representative sample spot for a given specimen. In very coarse grained samples (e.g. granite with phenocrysts) a single measurement of 2–3 cm diameter spot may not be sufficient to represent the average composition, and the measurement may need to be repeated at different spots. If a sample is not flat enough, a blow with a chisel and hammer should be sufficient to create a fresh, flat sampling area.

Rocks are also highly suitable for laboratory measurements in emission mode, even with field emission spectrometers that have no facility to heat the rocks during the measurements. If the samples are heated to ca. 70 °C in a forced-air oven overnight, the high heat capacity of the solid rock sample generally prevents errors due to cooling during the spectral measurements.

A novel type of geological TIR measurement is conducted at the University of Pittsburgh (Lee 2011). An emission spectrometer is combined with a miniature furnace to collect in-situ emission spectra of actively melting and cooling silicate lava. One to two grams of sample are melted at a time, and emission spectra are

collected at various set point temperatures. The furnace is only opened for about 10 s per measurement in order to protect surrounding equipment from the high furnace temperatures (up to 1,600 °C).

### 3.4.2 Soils

Measurements of soils and other particulate materials are more complex than those of solid rocks. The loose particles trap moisture, cause cavity effects, as well as volume scattering (e.g., Vincent and Hunt 1968; Kirkland et al. 2002; Salisbury and Wald 1992), all of which reduce the spectral contrast and change the spectral shape of the retrieved TIR spectra. Very fine-grained samples show mainly features of clay minerals, which have small spectral contrast themselves. TIR spectroscopy of undisturbed soils by necessity often means measurements must be conducted in the field. Whilst coherent soils can be sampled with sample rings (similar to a cookie cutter with plastic caps at both ends), sandy soils and fine surface crusts will always suffer from the sampling process and the soil moisture content may change even with the ends capped. Airborne/spaceborne calibration measurements, as well as measurements of soil and vegetation combinations, or textures of soil with coarser pebbles, are all more practically done directly in the field rather than bringing the sample to the laboratory. In order to not disturb the surface to be measured, care has to be taken when approaching the spot and setting up the spectrometer. Furthermore, the sample should be measured before the down-welling radiance measurement, as the placing of the reference plate on the sample area may disturb the surface.

Laboratory measurements of incoherent, disturbed soil samples require a sample preparation that guarantees an appropriate sample at the surface. Before and during the pouring into the sample container, the sample needs to be homogenized to prevent grain-size fractionation. Sample surfaces are often flattened with a spatula and a small amount of sample material sprinkled on top to prevent preferential orientation of the mineral grains. If an emissive system without the ability to keep the sample warm is used, measurement times should be kept as short as possible, since too much cooling of the hot sample during the measurements can create a tilt in the final emissivity spectrum.

### 3.4.3 Vegetation

Plant leaves are strongly coupled to TIR radiation, emitting and absorbing as near-blackbodies, having  $\epsilon$  close to 0.95. However, complex chemical and structural aspects of leaves produce subtle features superimposed on their broadly emissive TIR spectra. These features can be characterized using appropriate laboratory and field methods, and be utilized for species identification and remote spectral mapping (Salisbury 1986; Ribeiro da Luz 2006; Ribeiro da Luz and Crowley 2007, 2010).

Leaves can be collected by using a pruner, slingshot or shotgun, put inside plastic bags, and stored in a cooler with ice until measurements can be completed. If the plant is from a humid environment, a wet cotton ball or a sprinkle of water should be placed inside the bag before closing it. Laboratory samples should be kept in a refrigerator until they are measured to avoid fungus growth on the leaf surfaces, and to limit leaf desiccation. Samples showing excess surface moisture should be air dried prior to measurement.

In the laboratory, leaves can be placed directly under the sphere sample port when they are large enough. Smaller leaves, such as pine needles, must be detached from their branches and arranged side by side, either alone or over an adhesive tape (with care not to include the tape in the field of view). To reduce noise, three or more measurements of 500–1,000 scans apiece can be averaged. These measurements can be made of three different leaves of the same individual, or, if the leaves are very small, three different small branches from the same individual can be used. The entire sample port should be filled in any case. Ideally, one would collect at least 2 or 3 individuals of the same species for comparison, and if appropriate, perform spectral averaging.

TIR field spectral data can be taken directly over the plant, or, by using leaves that have been detached from the canopy and placed flat underneath the field spectrometer (Fig. 3.6), assuring that the leaves cover the entire field of view. Usually, leaf temperature is approximately equal to the air temperature, but on very warm days, when stomata are closed, leaf temperatures can be several degrees above ambient temperature (Gates 1980).

Remote sensing of vegetation in the TIR has been utilized to identify plant species but does present a variety of challenges. These challenges include the attenuation of signal by voids within canopies (which respond like blackbodies), and the difficulty of accurate atmospheric compensation (Ribeiro da Luz and Crowley 2010). Remote identification is most successful for species that have broad leaves, good spectral contrast, and relatively closed, planophile canopies. Identification of species with erectophile or drooping canopies tends to be much more difficult due to canopy blackbody effects.

### **3.4.4 Man-Made Materials**

In contrast to rocks, soils and vegetation, investigation of the thermal infrared spectral properties of man-made materials has been quite limited. Man-made materials for buildings, roofs and artificial open spaces consist of a great variety of material types (Anderson et al. 1976), including mineral materials (e.g. concrete, cement, glass, asbestos, bitumen), hydrocarbon materials (e.g., PVC, Plexiglas, painted materials), materials of biological origin (e.g., wood chippings, thatch) and some materials (e.g., metals) that have particularly low emissivities (e.g. copper, lead, tin, aluminium).

TIR spectroscopy of man-made materials in pristine condition is often simple, as most such surfaces are flat and impervious. As was the case for most solid rocks, this prevents the effects of moisture and surface cavities appearing in the measured spectra. However, most man-made materials are not in pristine condition, and will often show signs of chemical or physical weathering, sedimentary deposition and/or growth of biomass (e.g. lichen or mosses). It is therefore very difficult to make reproducible measurements of most urban surfaces given the relative effects of these influences on their TIR spectra. Unlike the case of rock outcrops discussed earlier, man-made surfaces are usually readily accessible and generally flat and navigable. During a recent acquisition of airborne TIR imagery over London, ground truth spectral measurements were made by wheeling an adapted MIDAC FTIR spectrometer on a trolley about London's urban environment. Considerations must be made concerning the DWR, particularly when measurements are made within urban canyons having low sky view factors, when a large component of the DWR may come from the surrounding buildings.

Man-made materials are also suitable for laboratory measurement using both DHR and emissive systems. Flat samples can be used for DHR measurements, although it can often be difficult to find a representative sample spot considering the heterogeneous nature of weathered man-made materials. For weathered materials, it can often be useful to compare pristine with progressively weathered conditions to develop a spectral index of weathering (e.g., Bassani et al. 2007; Pascucci et al. 2008). Laboratory measurements in the emissive mode also permit the measurement of the sensitivity of spectral emissivity to viewing angle (Sobrino and Cuenca 1999), which may be an important consideration for the remote sensing of man-made landscapes (e.g., slanted roofs, vertical walls and corrugated materials). One difficulty with measuring man-made materials using an emissive system in the laboratory is that materials with a low heat capacity (e.g. metals and hydrocarbon-based materials) are particularly difficult to keep at a constant temperature; without consistent heating of these samples, good quality spectral measurements cannot be made.

### 3.5 Outlook

It is clear that the thermal infrared spectral region contains important spectral features that respond to characteristics of the materials that may have little or no manifestations in the more commonly measured VNIR wavelengths. Furthermore, many applications of TIR airborne or spaceborne imaging radiometers, operating within or even outside of the MWIR (3–5  $\mu\text{m}$ ) and/or LWIR (8–14  $\mu\text{m}$ ) atmospheric windows, require information on the surface spectral emissivity if they are to perform to best effect. This is the case for developing the algorithms and/or evaluating their performance. In this chapter we have shown how the TIR spectra of land surface materials such as rock, vegetation, soils and man-made materials can be obtained, both in the field and in laboratory situations. As the availability of

thermal datasets collected by airborne and satellite radiometers continues to increase, and as future instruments such as the Hyperspectral Infrared Imager (HypSIRI) which work in the TIR region of the electro-magnetic spectrum are developed, the need for such spectral measurements is only expected to increase.

**Acknowledgements** The authors would like to thank Steve Ruff and Chris MacLellan, as well as the companies Telops and Agilent Technologies for providing illustrations of their spectrometer setups.

## References

- Anderson, JR, Hardy EE, Roach JT, Witmer RE (1976) A land use and land cover classification system for use with remote sensor data. Geologic survey professional paper, USGS, Washington, DC, p28
- Bacsik Z, Mink J, Kereszty G (2004) FTIR spectroscopy of the atmosphere. I. Principles and methods. *Appl Spectrosc Rev* 39(3):295–363. doi:[10.1081/asr-200030192](https://doi.org/10.1081/asr-200030192)
- Bacsik Z, Mink J, Kereszty G (2005) FTIR spectroscopy of the atmosphere part 2. Applications. *Appl Spectrosc Rev* 40(4):327–390. doi:[10.1080/05704920500230906](https://doi.org/10.1080/05704920500230906)
- Baldridge AM, Hook SJ, Grove CI, Rivera G (2009) The ASTER spectral library version 2.0. *Remote Sens Environ* 113(4):711–715. doi:[10.1016/j.rse.2008.11.007](https://doi.org/10.1016/j.rse.2008.11.007)
- Bassani C, Cavallini RM, Cavalcante F, Cuomo V, Palombo A, Pascucci S et al (2007) Deterioration status of asbestos-cement roofing sheets assessed by analyzing hyperspectral data. *Remote Sens Environ* 109(3):361–378. doi:[10.1016/j.rse.2007.01.014](https://doi.org/10.1016/j.rse.2007.01.014)
- Bower N, Lynch MJ, Knuteson RO, Revercomb HE (2001) High spectral resolution land surface temperature and emissivity measurement in the thermal infrared using Fourier transform spectroscopy. In: Sawchuk A (ed) Optical remote sensing, vol 52 of OSA trends in optics and photonics. Optical Society of America, paper OWA5. <http://www.opticsinfobase.org/abstract.cfm?URI=ORS-2001-OWA5>
- Burrows JP, Platt U, Borrell P (2011) The remote sensing of tropospheric composition from space, Physics of earth and space environments 15. Springer, Heidelberg
- Christensen PR, Bandfield JL, Hamilton VE, Howard DA, Lane MD, Piatek JL et al (2000) A thermal emission spectral library of rock-forming minerals. *J Geophys Res Planets* 105 (E4):9735–9739
- Clark RN, Swayze GA, Wise RA, Livo KE, Hoefen TM, Kokaly RF et al (2007) USGS digital spectral library splib06a. U.S. Geological Survey, Denver
- Coll C, Caselles V, Valor E, Rubio E (2003) Validation of temperature-emissivity separation and split-window methods from TIMS data and ground measurements. *Remote Sens Environ* 85 (2):232–242. doi:[10.1016/s0034-4257\(03\)00003-8](https://doi.org/10.1016/s0034-4257(03)00003-8)
- Dash P, Götsche FM, Olesen FS, Fischer H (2002) Land surface temperature and emissivity estimation from passive sensor data: theory and practice-current trends. *Int J Remote Sens* 23(13):2563–2594. doi:[10.1080/01431160110115041](https://doi.org/10.1080/01431160110115041)
- Gates DM (1980) Biophysical ecology. Springer, New York
- Gillespie A, Rokugawa S, Matsunaga T, Cothern JS, Hook SJ, Kahle AB (1998) A temperature and emissivity separation algorithm for Advanced Spaceborne Thermal Emission and Reflection Radiometer (ASTER) images. *Geosci Remote Sens IEEE Trans* 36(4):1113–1126
- Hecker C, van der Meijde M, van der Meer FD (2010) Thermal infrared spectroscopy on feldspars – successes, limitations and their implications for remote sensing. *Earth Sci Rev* 103(1–2):60–70. doi:[10.1016/j.earscirev.2010.07.005](https://doi.org/10.1016/j.earscirev.2010.07.005)

- Hecker C, Hook SJ, van der Meijde M, Bakker W, van der Werff H, Wilbrink H et al (2011) Thermal infrared spectrometer for earth science remote sensing applications-instrument modifications and measurement procedures. *Sensors* 11(11):10981–10999 doi:[10.3390/s111110981](https://doi.org/10.3390/s111110981)
- Hook SJ, Kahle AB (1996) The micro Fourier transform interferometer ( $\mu$ FTIR) – a new field spectrometer for acquisition of infrared data of natural surfaces. *Remote Sens Environ* 56 (3):172–181. doi:[10.1016/0034-4257\(95\)00231-6](https://doi.org/10.1016/0034-4257(95)00231-6)
- Hoover G, Kahle AB (1987) A thermal emission spectrometer for field use. *Photogramm Eng Remote Sens* 53:627–632
- Horton KA, Johnson JR, Lucey PG (1998) Infrared measurements of pristine and disturbed soils 2. Environmental effects and field data reduction. *Remote Sens Environ* 64(1):47–52
- Hulley GC, Hook SJ, Manning E, Lee SY, Fetzer E (2009) Validation of the Atmospheric Infrared Sounder (AIRS) version 5 land surface emissivity product over the Namib and Kalahari deserts. *J Geophys Res* 114(D19), D19104. doi:[10.1029/2009jd012351](https://doi.org/10.1029/2009jd012351)
- Hulley GC, Hook SJ, Baldridge AM (2010) Investigating the effects of soil moisture on thermal infrared land surface temperature and emissivity using satellite retrievals and laboratory measurements. *Remote Sens Environ* 114(7):1480–1493. doi:[10.1016/j.rse.2010.02.002](https://doi.org/10.1016/j.rse.2010.02.002)
- Huntington J, Whitbourn L, Mason P, Berman M, Schodlok MC (2010) HyLogging – voluminous industrial-scale reflectance spectroscopy of the earth's subsurface. In: Huntington JF (ed) Art, science and applications of reflectance spectroscopy symposium, Boulder, 23–25 Feb 2010, II, p 14
- Jacob F, Petitcolin F, Schmugge T, Vermote É, French A, Ogawa K (2004) Comparison of land surface emissivity and radiometric temperature derived from MODIS and ASTER sensors. *Remote Sens Environ* 90(2):137–152. doi:[10.1016/j.rse.2003.11.015](https://doi.org/10.1016/j.rse.2003.11.015)
- Kahle AB, Alley RE (1992) Separation of temperature and emittance in remotely sensed radiance measurements. *Remote Sens Environ* 42(2):107–111. doi:[10.1016/0034-4257\(92\)90093-y](https://doi.org/10.1016/0034-4257(92)90093-y)
- Kahle AB, Madura DP, Soha JM (1980) Middle infrared multispectral aircraft scanner data: analysis for geological applications. *Appl Opt* 19(14):2279–2290
- Kirkland L, Herr K, Keim E, Adams P, Salisbury JW, Hackwell J et al (2002) First use of an airborne thermal infrared hyperspectral scanner for compositional mapping. *Remote Sens Environ* 80(3):447–459
- Korb AR, Dybwad P, Wadsworth W, Salisbury JW (1996) Portable Fourier transform infrared spectroradiometer for field measurements of radiance and emissivity. *Appl Opt* 35 (10):1679–1692
- Korb AR, Salisbury JW, D'Aria DM (1999) Thermal-infrared remote sensing and Kirchhoff's law 2. Field measurements. *J Geophys Res Solid Earth* 104(B7):15339–15350
- Lammoglia T, de Souza Filho CR (2011) Spectroscopic characterization of oils yielded from Brazilian offshore basins: potential applications of remote sensing. *Remote Sens Environ* 115 (10):2525–2535. doi:[10.1016/j.rse.2011.04.038](https://doi.org/10.1016/j.rse.2011.04.038)
- Lee RJ (2011) Thermal emission spectroscopy of silicate glasses and melts: applications to remote sensing of glassy volcanic environments. Ph.D., University of Pittsburgh, Pittsburgh
- Lindermeir E, Haschberger P, Tank V, Dietl H (1992) Calibration of a Fourier transform spectrometer using three blackbody sources. *Appl Opt* 31(22):4527–4533
- Lyon RJP (1965) Analysis of rocks by spectral infrared emission (8–25 microns). *Econ Geol* 60:715–736
- Minnett PJ, Szczodrak M, Key EL (2005) Surface-based infrared interferometers – versatile sensors for the IPY. In: Proceedings of the 8th conference on polar meteorology and oceanography, San Diego, 10–13 Jan 2005
- Mitraka Z, Chrysoulakis N, Kamarianakis Y, Partsinevelos P, Tsouchlaraki A (2011) Improving the estimation of urban surface emissivity based on sub-pixel classification of high resolution satellite imagery. *Remote Sens Environ* 117:125–134. doi:[10.1016/j.rse.2011.06.025](https://doi.org/10.1016/j.rse.2011.06.025)
- Murcay FH, Murcay DG, Williams WJ (1970) Infrared emissivity of lunar surface features 1. Balloon-borne observations. *J Geophys Res* 75(14):2662–2669. doi:[10.1029/JB075i014p02662](https://doi.org/10.1029/JB075i014p02662)

- Nicodemus FE (1965) Directional reflectance and emissivity of an opaque surface. *Appl Opt* 4:767–773
- Pascucci S, Bassani C, Palombo A, Poscolieri M, Cavalli R (2008) Road asphalt pavements analyzed by airborne thermal remote sensing: preliminary results of the Venice highway. *Sensors* 8(2):1278–1296
- Ramsey MS (2003) Mapping the city landscape from space: the advanced spaceborne thermal emission and reflectance radiometer (ASTER) urban environmental monitoring program. In: Heiken G, Fakundiny R, Sutter J (eds) *Earth science in the city: a reader*. AGU, Washington, DC, pp 337–361
- Ramsey MS, Fink JH (1999) Estimating silicic lava vesicularity with thermal remote sensing: a new technique for volcanic mapping and monitoring. *Bull Volcanol* 61(1):32–39. doi:[10.1007/s004450050260](https://doi.org/10.1007/s004450050260)
- Ribeiro da Luz B (2006) Attenuated total reflectance spectroscopy of plant leaves: a tool for ecological and botanical studies. *New Phytol* 172(2):305–318. doi:[10.1111/j.1469-8137.2006.01823.x](https://doi.org/10.1111/j.1469-8137.2006.01823.x)
- Ribeiro da Luz B, Crowley JK (2007) Spectral reflectance and emissivity features of broad leaf plants: prospects for remote sensing in the thermal infrared (8.0–14.0 [mu]m). *Remote Sens Environ* 109(4):393–405. doi:[10.1016/j.rse.2007.01.008](https://doi.org/10.1016/j.rse.2007.01.008)
- Ribeiro da Luz B, Crowley JK (2010) Identification of plant species by using high spatial and spectral resolution thermal infrared (8.0–13.5 [mu]m) imagery. *Remote Sens Environ* 114 (2):404–413. doi:[10.1016/j.rse.2009.09.019](https://doi.org/10.1016/j.rse.2009.09.019)
- Ruff SW, Christensen PR, Barbera PW, Anderson DL (1997) Quantitative thermal emission spectroscopy of minerals: a laboratory technique for measurement and calibration. *J Geophys Res* 102(B7):14899–14913
- Sabol JDE, Gillespie AR, Abbott E, Yamada G (2009) Field validation of the ASTER temperature–emissivity separation algorithm. *Remote Sens Environ* 113(11):2328–2344. doi:[10.1016/j.rse.2009.06.008](https://doi.org/10.1016/j.rse.2009.06.008)
- Salisbury JW (1986) Preliminary measurements of leaf spectral reflectance in the 8–14 µm region. *Int J Remote Sens* 7(12):1879–1886. doi:[10.1080/01431168608948981](https://doi.org/10.1080/01431168608948981)
- Salisbury JW (1998) Spectral measurements field guide. Defense Technology Information Center, Fort Belvoir, p 91
- Salisbury JW, D’Aria DM (1992) Emissivity of terrestrial materials in the 8–14 µm atmospheric window. *Remote Sens Environ* 42(2):83–106
- Salisbury JW, D’Aria DM (1994) Emissivity of terrestrial materials in the 3–5 µm atmospheric window. *Remote Sens Environ* 47(3):345–361. doi:[10.1016/0034-4257\(94\)90102-3](https://doi.org/10.1016/0034-4257(94)90102-3)
- Salisbury JW, Wald A (1992) The role of volume scattering in reducing spectral contrast of restrahlen bands in spectra of powdered minerals. *Icarus* 96(1):121–128. doi:[10.1016/0019-1035\(92\)90009-v](https://doi.org/10.1016/0019-1035(92)90009-v)
- Salisbury JW, Walter LS, Vergo N, D’Aria DM (1991) Infrared (2.1–25 µm) spectra of minerals. The Johns Hopkins University Press, Baltimore/London
- Salisbury JW, Wald A, D’Aria DM (1994) Thermal-infrared remote sensing and Kirchhoff’s Law 1. Laboratory measurements. *J Geophys Res Solid Earth* 99(B6):11897–11911
- Salvaggio C, Miller CJ (2001) Comparison of field- and laboratory-collected midwave and longwave infrared emissivity spectra/data reduction techniques. In: Proceedings of the SPIE 4381, Algorithms for multispectral, hyperspectral, and ultraspectral imagery VII, Orlando, 2001, pp 549–558
- Sobrino JA, Cuenca J (1999) Angular variation of thermal infrared emissivity for some natural surfaces from experimental measurements. *Appl Opt* 38(18):3931–3936
- Thomas HE, Watson IM, Kearney C, Carn SA, Murray SJ (2009) A multi-sensor comparison of sulphur dioxide emissions from the 2005 eruption of Sierra Negra volcano, Galápagos Islands. *Remote Sens Environ* 113(6):1331–1342. doi:[10.1016/j.rse.2009.02.019](https://doi.org/10.1016/j.rse.2009.02.019)

- Ullah S, Schlerf M, Skidmore AK, Hecker C (2012) Identifying plant species using mid-wave infrared (2.5–6  $\mu\text{m}$ ) and thermal infrared (8–14  $\mu\text{m}$ ) emissivity spectra. *Remote Sens Environ* 118:95–102. doi:[10.1016/j.rse.2011.11.008](https://doi.org/10.1016/j.rse.2011.11.008)
- Vaughan RG, Calvin WM, Taranik JV (2003) SEBASS hyperspectral thermal infrared data: surface emissivity measurement and mineral mapping. *Remote Sens Environ* 85(1):48–63
- Vaughan RG, Hook SJ, Calvin WM, Taranik JV (2005) Surface mineral mapping at Steamboat Springs, Nevada, USA, with multi-wavelength thermal infrared images. *Remote Sens Environ* 99(1–2):140–158
- Vincent RK, Hunt GR (1968) Infrared reflectance from mat surfaces. *Appl Opt* 7:53–59
- Voogt JA, Oke TR (2003) Thermal remote sensing of urban climates. *Remote Sens Environ* 86 (3):370–384. doi:[10.1016/s0034-4257\(03\)00079-8](https://doi.org/10.1016/s0034-4257(03)00079-8)
- Xu W, Wooster MJ, Grimmond CSB (2008) Modelling of urban sensible heat flux at multiple spatial scales: a demonstration using airborne hyperspectral imagery of Shanghai and a temperature–emissivity separation approach. *Remote Sens Environ* 112(9):3493–3510. doi:[10.1016/j.rse.2008.04.009](https://doi.org/10.1016/j.rse.2008.04.009)
- URL1: <http://www.specim.fi/products/sisu-hyperspectral-scanners/sisurock.html>
- URL2: <http://www.telops.com>
- URL3: <http://www.agilent.com>

# Chapter 4

## Challenges and Opportunities for UAV-Borne Thermal Imaging

Margarete Vasterling and Uwe Meyer

**Abstract** UAV-borne thermal imaging involves the determination of ground surface temperature from thermal infrared measurements deploying an unmanned airborne vehicle (UAV). A large variety of UAVs is available and applied for different military and civil tasks. UAV-borne thermal imaging provides spatially distributed information of the ground surface temperature. In contrast to satellite or ground based measurement, the usage of a UAV allows us to obtain spatially distributed and geometrically highly resolved information on the ground surface temperature without the need to access the ground. The area can be flat or hilly, and steep walls and hillsides can be investigated easily. However, some problems, especially tasks related to mosaicking of the images, are not fully resolved to date. We address the detection of the anomalies in ground surface temperature induced by underground burning coal seams as example and describe the challenges and opportunities of UAV-borne thermal imaging, based on our experiences in this field.

### 4.1 Introduction

UAV-borne thermal imaging is the determination of ground surface temperature from thermal infrared measurements deploying a UAV. UAV stands for unmanned airborne vehicle (alternatively: UAS, unmanned airborne systems), which is a flying platform capable to carry different measurement devices (van Blyenburgh 1999). It is either controlled by a pilot on the ground or flies autonomously. There is

---

M. Vasterling (✉)

Sub-Department B4.3 – Central Seismological Observatory, Nuclear Test Ban,  
Federal Institute for Geosciences and Natural Resources (BGR), Hannover, Germany  
e-mail: [Margarete.vasterling@bgr.de](mailto:Margarete.vasterling@bgr.de)

U. Meyer

Sub-Department B2.1 – Geophysical Exploration – Technical Mineralogy, Federal Institute  
for Geosciences and Natural Resources (BGR), Hannover, Germany

**Table 4.1** Overview on different types of UAVs available

	Blimp	Helicopter-like	Fixed-wing
Stability against wind	– Susceptible to wind	+ Stable against wind	+ Stable against wind
Maximum payload	+ High e.g. 900 g (Blimp 2C) (SurveyCopter 2012)	– Varying e.g. 650 g (Falcon 8) (AscTech 2012)	+ High e.g. 5.4 kg (Wolverine III) (VikingAero 2012)
Start/landing	+ Vertical takeoff (zeppelin) + Gas needed (zeppelin)	+ Vertical takeoff	– Might need a runway or a catapult for launching
Positioning	– Difficult	+ Exact (GPS)	+ Exact (GPS)
Survey speed	○ Slow	+ Defined by pilot	– Extremely fast
Example of manufacturer	Survey Copter (France) SKIVE Aviation AG (Switzerland) Aero Drum Ltd. (Serbia)	Ascending Technologies (Germany) Microdrones (Germany) ESKY Beijing (China)	BAE Systems (USA) Viking Aerospace (USA)

a variety of UAVs available which are employed for various military missions (Yeh 2011) as well as for civil applications, for example, industrial or agricultural inspections (Sullivan et al. 2007; Laliberte et al. 2011), and research (Hartmann 2011; Sheng et al. 2010; Cress et al. 2011). A common application is fire fighting, which employs UAVs for surveillance of wildfire areas that are not safely accessible to obtain information for the design of extinguishing works (van Persie et al. 2011; Hinkley and Zajkowski 2011; Pastor et al. 2011). Another application of UAV-borne thermal imaging is the detection of roe deer fawn in the meadows to protect these animals at harvest time (Israel 2011). UAV sizes vary from as small as a hummingbird to as large as an airplane, while different types of UAVs are also available (Eisenbeiß 2009): blimp (e.g. zeppelin), parachute, kite, fixed-wing or helicopter-like with a different number of propellers (e.g. four or eight propellers, called quadrocopter and octocopter, respectively) each having different advantages (Table 4.1). In principle, every method can be applied that does not need direct contact to the ground.

UAV applications have several advantages:

- The desired area can be investigated – also repeatedly – in a relatively short amount of time.
- It is possible to obtain data from areas with no safe access options.
- UAVs are not very expensive.

All experiences and results described here have been obtained during a field campaign within the framework of the Sino-German research initiative “Innovative

technologies for exploration, extinction and monitoring of coal fires in Northern China” funded by the German Federal Ministry of Education and Research, BMBF.

The task was to obtain a spatial image of the ground surface temperature patterns at a survey site with many hill slopes. In addition it was not possible to access the site safely at all points of interest. We used the UAV “Falcon 8” (Ascending Technologies) equipped with a small thermal infrared (TIR) camera (mobileIR M4, InfraTec). In what follows, we describe the challenges and summarize our experiences during this UAV-borne thermal imaging campaign.

## 4.2 Unmanned Aerial Vehicle

### 4.2.1 *Advantages and Disadvantages of UAVs as Sensor Platform*

Ground surface temperature can be determined by ground-based as well as by air- or satelliteborne measurements. Each system has different advantages and disadvantages. Methodologies and routines have been developed to detect and quantify thermal anomalies at the topographic surface by using TIR satellite data (Kuenzer et al. 2007; Tetzlaff 2004). From Table 4.2 it is obvious, that thermal imaging with an UAV has several advantages compared to satellite as well as ground-based measurements. It is the only method appropriate for steep walls (Fig. 4.1) and can be used even on areas that are not accessible at ground level, e.g. in areas with coal fires were hot gas emission, increased surface temperature and roughness, as well as unstable ground (Kuenzer and Stracher 2011) occur. At the same time UAVs generate spatial data with good geometric resolution without the need to interpolate the data which might cause additional (interpolation) errors. For satellite data, either advanced sub-pixel methods or very costly high resolution data have to be used in order to obtain a high geometric accuracy. The necessary atmospheric corrections, however, provide the opportunity to compare data collected at different times and locations and thus aim at monitoring and comparing different targets. Each measurement taken remotely must be validated by ground measurements which can be obtained only from sites with safe access routes, however.

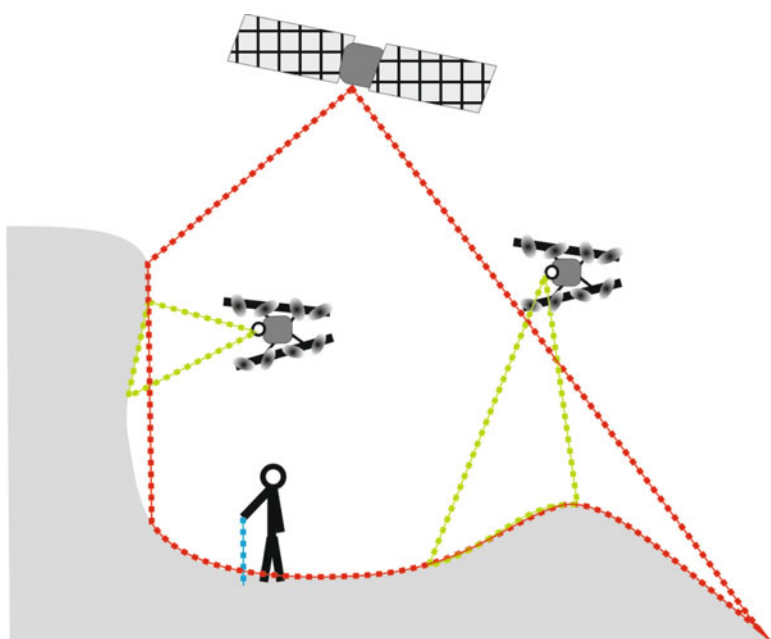
A disadvantage of many UAV concepts is the very limited payload, thus only simple light-weight sensor systems can be used.

### 4.2.2 *Selection Criteria*

As an example, we compare the data recorded by UAV, satellite (ASTER, Advanced Spaceborne Thermal Emission and Reflection Radiometer), and by a handheld

**Table 4.2** Comparison of satellite, UAV- and ground based measurements

	Satellite	UAV	Ground based
Survey area characteristics	○ Flat, hilly, walls	○ Flat, hilly	+ Flat, hilly, walls
Survey area/ Coverage	++ Very large area	○ Medium (depends on flight height)	- Small
Ground accessibility	+ Not necessary	+ Not necessary	- Necessary
Geometric resolution (thermal)	- Coarse	+ Fine	○ Point distance
Data type	+ Spatial	+ Spatial	- Point + Spatial (handheld camera)
Measuring progress	+ Very high	○ Medium/slow	- Very slow
Data processing	<ul style="list-style-type: none"> <li>○ Georeferencing (transformation, orthorectification)</li> <li>○ Atmospheric correction</li> <li>○ Emissivity correction</li> </ul>	<ul style="list-style-type: none"> <li>○ Emissivity correction</li> <li>○ Georeference (transformation, orthorectification)</li> </ul>	<ul style="list-style-type: none"> <li>○ Emissivity correction</li> <li>- Interpolation</li> </ul>

**Fig. 4.1** Application of satellite, UAV-borne and ground based thermal imaging

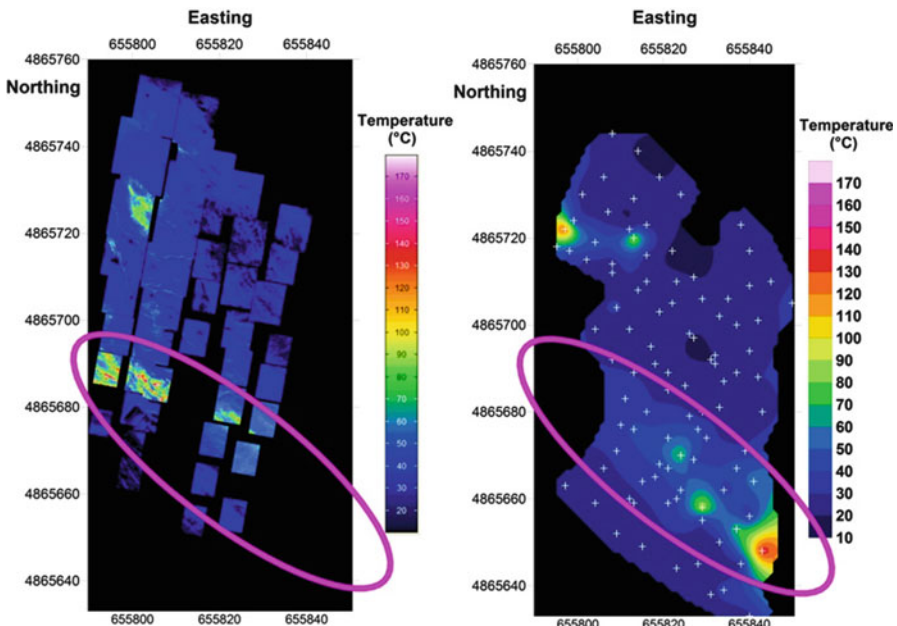


**Fig. 4.2** *Left:* mosaic of thermal images taken by UAV; *right:* spatial interpolated surface temperature from ground based measurements. The thermal anomaly marked with the pink ellipse indicates the burning coal seam. Both measurements cover an area of about  $50 \times 100$  m and were taken during the same survey in October 2009

infrared device at the coal fire site of Shuixigou (Xinjiang Province, P.R. China). Figure 4.2 shows the mosaicked UAV images and the interpolated ground based data. The gaps in the UAV imagery are caused by technical problems of the TIR camera, or occur when the UAV does not fly parallel to the topography of the survey area (see Sect. 4.6.3). A prominent feature in both images is the area of increased temperature (pink ellipse) which indicates the subsurface burning coal seam. For the left part only UAV-images exist as this part was not accessible (on ground) due to fractures emitting hot gasses. If we compare the ground surface temperatures we see that in both methods the main temperature anomalies are detected but located at slightly different positions. The offset, however, is within the precision of GPS which is used by both methods for positioning. It is obvious that the ground surface temperature patterns are portrayed in much more detail by the mosaicked UAV images compared to the interpolated ground based measurements.

A comparison of satellite and UAV-borne results illustrates clearly that these two methods work on different scales with respect to the geometric resolution (Fig. 4.3). Even though the satellite image is not transferred into exact values of the ground surface's temperature (light colors correlate to higher temperature, darker colors to lower temperature) the Shuixigou fire zone seems to be resolved. This is indicated by the increased temperatures in the section of the UAV survey

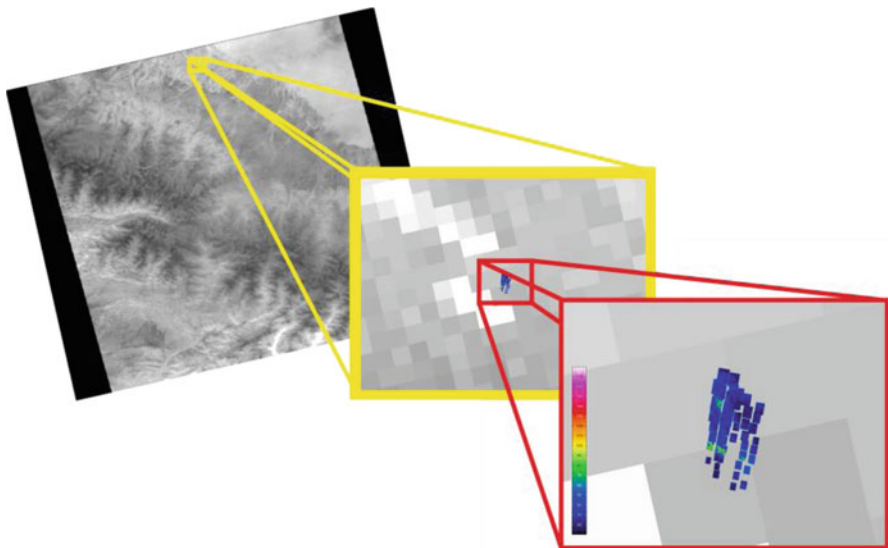


**Fig. 4.3** Thermal ASTER scene (90 m pixel resolution) with overlay of mosaicked thermal images (UAV) (20th Feb. 2007). Light grey corresponds to higher temperatures, darker grey to lower temperatures

area marked by a yellow frame (zoom into scene). Since the pixel size of the sensor is relatively large neither the single fire itself is detected and details of the fire cannot be identified.

#### 4.2.3 Selected System – Falcon 8

Within the Sino-German coal fire research initiative the octocopter “Falcon 8” manufactured by Ascending Technologies GmbH (Germany) was used. The Falcon basically consists of two rails, each equipped with four propellers, and the central unit (Fig. 4.4). Four out of eight propellers are turning left or right, respectively, which enables a stable flight together with a precise flight control. The distance between the rails decreases from the front to the back and results in a v-shaped design. As the camera is mounted in front of the central unit, this design results in a field of vision for the camera which is completely free of undesirable objects. The camera can be panned by 180° from as far as “looking up” to “looking down”. Consequently it is possible to survey plane areas as well as sloping sites such as gentle hills or even steep walls where the camera position is perpendicular to the target surface (Fig. 4.1). Altitude, speed and direction are internally controlled by regulation of each propeller’s speed. For positioning, the Falcon 8 is equipped with GPS, IMU (Inertial Measuring Unit), three orthogonal magnetic field sensors and a barometric height sensor. The position parameters pitch, yaw, and roll are

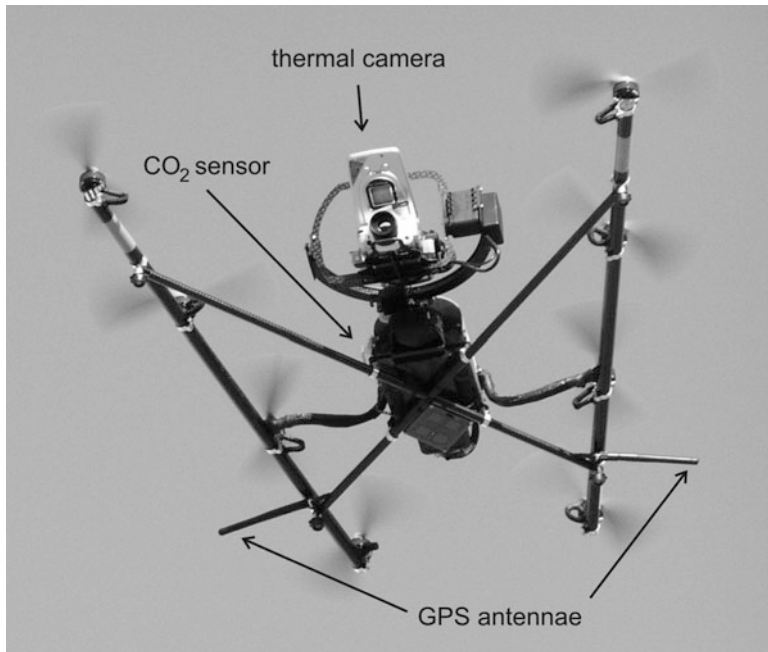


**Fig. 4.4** Falcon 8 equipped with thermal camera mobilIR M4 and CO<sub>2</sub> sensor

determined. All flight parameters (e.g. longitude, latitude, time, GPS altitude, position etc.) are stored in a log-file together with UAV status parameters (e.g. battery status, flight modus and GPS signal quality). Additionally, the camera parameters (position, timestamp, image number, GPS altitude, pressure altitude relative to launching area etc.) are also stored in the log-file and thus are available for mosaicking the individual images.

The UAV is powered by an 800 mA Lithium ion rechargeable battery pack allowing for a maximum flight time of as much as 45 min without payload. The maximum payload (in addition to the battery) of the Falcon 8 is 300 g, resulting in a flight time of about 15 min. The flight time depends on payload but is also strongly influenced by wind conditions. The Falcon 8 allows for stable flight under conditions with a wind speed up to 10 m/s (AscTech 2012; Friedli 2010).

Besides flying the Falcon manually it is possible to plan missions ahead. Therefore, position, altitude, heading, position accuracy, camera angle time at waypoint, and action (trigger camera or not) at waypoints, profiles or grids can be defined using waypoint software. For flying planned missions the remote control is connected via USB cable<sup>1</sup> to the mobile computer where the waypoint software is installed. The remote control for manual flights is connected with the Falcon via

---

<sup>1</sup> Ascending Technologies is recently (11/2011) working on changing the connection via cable to a wireless connection, e.g. via Bluetooth.

2.4 GHz Link. This theoretically allows for a range of a few kilometres. However, for safety reasons it is regulated by law to operate the UAV only within sight distance. For a successful field campaign it is mandatory to work with a well trained and experienced pilot.

In terms of the UAV itself the challenge of UAV-borne thermal imaging is the selection of the most suitable UAV to perform the given task under the given circumstances.

### 4.3 TIR Camera

All bodies with a temperature greater than 0 K radiate electromagnetic waves of different wavelengths (Gaussorgues 1994). The Stefan Boltzmann law describes the radiation power  $P_{bb}$  (W) of a black body depending on temperature  $T$  (K) and the area of radiation  $A$  ( $\text{m}^2$ )

$$P_{bb} = \sigma AT^4 \quad (4.1)$$

where  $\sigma$  is the Stefan Boltzmann constant. The wavelength of the maximal radiation power depends on the temperature of the body as stated by Wien's law. A more realistic object, a so called gray body, emits only a certain portion  $P = \varepsilon \cdot P_{bb}$  of the radiation power, which is described by the scaling factor, the emissivity  $\varepsilon$ . The emissivity describes the ability of a material to emit electromagnetic radiation. It depends on the wavelength and on the composition of a material and its surface structure and varies between 0 and 1 (mainly between 0.85 and 0.95 for geological materials). For  $\varepsilon = 1$ , which is the case for a black body only, the brightness temperature has the same value as the kinetic temperature. For real media the emissivity is smaller than 1 and thus, the temperature emitted by the body and registered by the sensor is smaller than the kinetic temperature. The radiance recorded at the TIR camera's sensor is also influenced by climatic parameters (e.g. transmittance of the atmosphere, path radiances between surface and sensor system, thermal downwelling flux) and surface emissivity. To calculate kinetic temperatures based on Planck's law, the emissivity must always be taken into account. Special care is required to ensure calibration and stability of the thermal sensor (Salisbury 1992; Sugiura et al. 2007; Kiwamoto et al. 1997).

#### 4.3.1 TIR Camera Types for Application on UAVs

Cameras for the (8–14)  $\mu\text{m}$  bandwidth generally do not have a cooled sensor resulting in a low signal to noise ratio. However, these camera systems are relatively light weight which is an essential advantage for the usage together with a UAV. Table 4.3 lists two examples for small infrared cameras and their parameters.

**Table 4.3** Overview on camera parameters

	mobilIR M4	Quark 336
Spectral band	(8–14) $\mu\text{m}$	(7.5–13.5) $\mu\text{m}$
Extent of the picture frame	160 $\times$ 120 pixel	336 $\times$ 256 pixel
Operating temperature range	(0 … 50) $^{\circ}\text{C}$	(–40 … +80) $^{\circ}\text{C}$
Sensitivity	<0.12 K	<0.05 K
Weight	265 g	28.5 g (19 mm lens)
Reference	InfraTec (2012)	FLIR (2012)

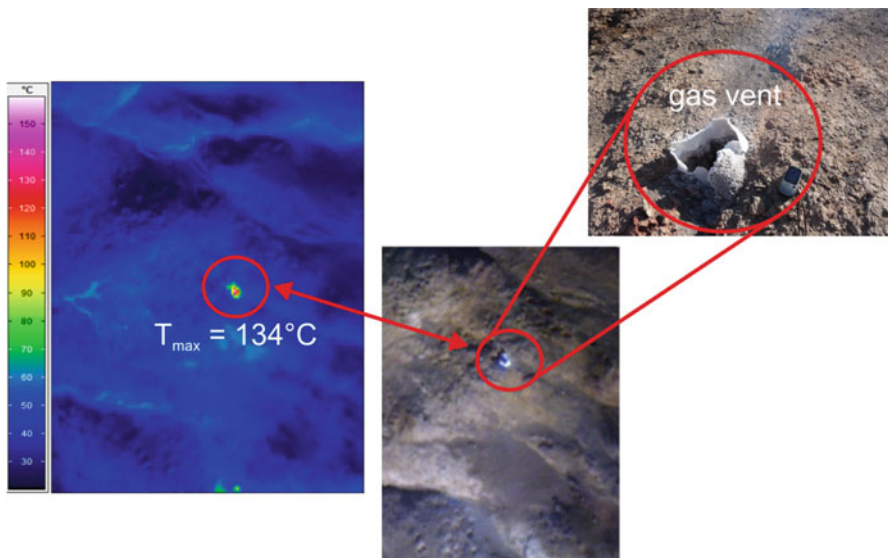


**Fig. 4.5** Correlation of thermal anomaly with a geological feature. *Left:* thermal image, *middle:* image taken simultaneously with the thermal image, *right:* photo showing the gas vent releasing hot gasses from the underground burning coal fire

### 4.3.2 Selection Criteria

For application on an UAV the camera has to be sufficiently light weight as the camera's weight is a limiting criterion due to the limited payload of the UAV. It also has to be robust in terms of being operated from an UAV (e.g. insensitivity towards vibrations and dust). Different targets might require a different dynamic range and/or temperature resolution. A careful evaluation of all requirements regarding the desired target is essential for the choice of the camera.

Video output to a remote control and/or laptop is recommended for visual flight control. The recording of the infrared video stream via downlink to a remote control or a connected computer, respectively, allows extracting single frames in the post processing which helps to optimize the spatial coverage. In addition, a visual picture or video should be recorded at the same time as the thermal image. This allows mapping thermal anomalies and geological features (Fig. 4.5).

Note that for certain countries the import and export of some cameras is restricted.

### 4.3.3 *Selected System – mobileIR M4*

In the example presented (Sect. 4.6) the “mobileIR M4” (InfraTec, Dresden) was chosen due to its light weight, sufficient resolution, and wide dynamic range of  $-20$  to  $250$  °C. A visual image is recorded at the same time as the thermal image. In our application of coal fire temperature imaging we calculate the brightness temperature for comparison with ground based data.

## 4.4 Field Application

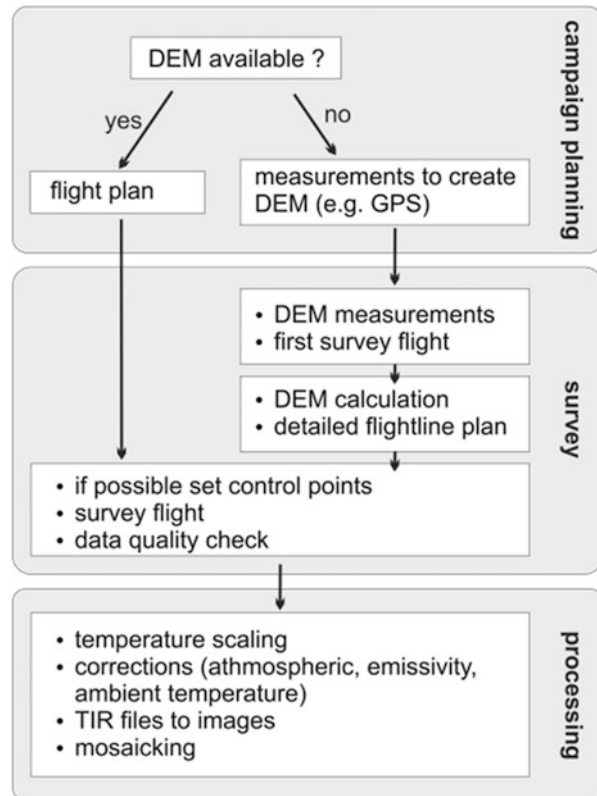
### 4.4.1 *Planning the Field Campaign*

For a successful and safe field campaign good preparation is as important as skilful handling of the equipment in the field. Having chosen the most suitable UAV and camera, the next step is to plan the flight. Before the actual flight it is necessary to check with the authorities whether flight permission is required for the desired area. According to German regulations light weighted UAVs (less than 5 kg) for non commercial use are allowed to fly without special permission (Luftverkehrsordnung §16, as at June 2012). However, for commercial use authorization has to be granted by the responsible office (for Germany this is the Luftfahrtbundesamt). Operation of the UAV (in Germany) is allowed only within sight for safety reasons. An experienced pilot is mandatory for a safe and successful flight campaign. A simplified workflow for UAV mission planning, survey and processing is given in Fig. 4.6.

The aim is to get a georeferenced, spatially covering, undistorted set of thermal images of the target showing the true (kinetic) ground surface temperature without any distortions. The georeference in terms of location within a coordinate system can be derived from the GPS system of the UAV. However it is necessary to make corrections like shift, rotation, scaling and orthorectification (correction of terrain-induced distortion). A very useful and advantageous feature of UAVs is the fact that these can be used in areas which are not safely accessible or even inaccessible, for example, steep walls. As a consequence, however, it is in general impossible to set or measure ground control points for photogrammetric analyses. Thus, alternative ways for transforming and correcting the individual images must be considered and developed (see next section).

Before planning the flight details it should be checked which height is actually recorded logged by the UAV. The Falcon 8 measures the height above ground calibrated at launching area. Thus, the recorded “height above ground” is the height

**Fig. 4.6** Scheme of workflow for UAV mission planning, survey and processing



above launching area only (position (a) in Fig. 4.7). If the survey area is not a flat plane or wall but has some topographic features, this “height above ground” might significantly differ from the actual UAV flight altitude (position b in Fig. 4.7). Therefore it is necessary to have a proper digital elevation model (DEM) with a resolution which is at least in the same range as the camera’s footprint. If such an elevation model is not available it must be calculated using differential GPS, a laser scanner, or equivalent measurements. A good alternative would be the application of a sensor (e.g. laser altimeter) to measure the distance towards ground (respectively image target in general). To obtain a thermal image for the whole area in a survey area with topographic features either the profile distance and point spacing or the flight altitude (relative barometric height and/or absolute GPS height) have to be adapted (Table 4.4).

Most light weight infrared cameras do not have an autofocus. Thus, before mounting the camera onto the UVA the focus hast to be adjusted manually by focusing at an object at the same distance as the planned flight altitude.

The camera’s footprint then depends on the distance towards the target. A scheme for the calculation of the area depicted by a single image is given in

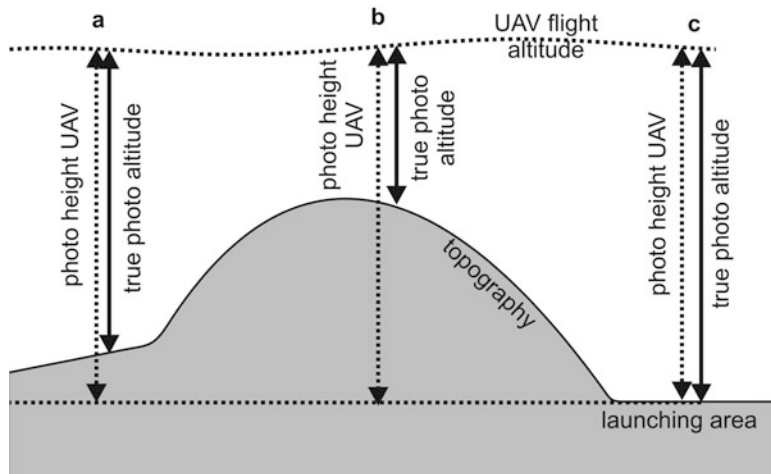


**Fig. 4.7** Relation between flight altitude, topography and photo height

**Table 4.4** Image size, point distance and line spacing for different photo heights for 50 % overlap

Flight (photo) height (m)	Image size (m × m)	Point distance (m)	Line spacing (m)	Images to cover a (100 × 50) m area	Pixel resolution (cm × cm)
30	10 × 13	7.5	5	15 × 09	8.3 × 8.1
15	05 × 07	3.5	2.5	28 × 17	4.2 × 4.4

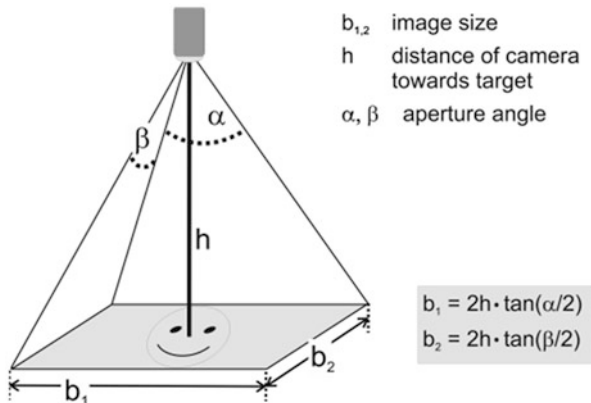
The geometric resolution is given for an image of 120 × 160 pixels

Fig. 4.8. Thus, the flight altitude has to be chosen by making a compromise between resolution and efficiency. If the data are not recorded continuously (video), then for satisfactory mosaicking the overlap of individual neighbouring pictures should be at least 50 %. Thus, only the central part of the images is used which improves the quality of the composite image.

Should the target area allow for setting ground control points for photogrammetric processing, these points should preferably be visible in thermal and visual bandwidth. Therefore a material with an emissivity as well as visual contrast to the survey area has to be chosen (e.g. aluminum foil).

We strongly suggest to carry additional batteries for UAV, camera, and laptop (and/or the opportunity to recharge them in the field) along as flight time and camera operation are limited by the available power supply (number of batteries). It is also recommended to have a good amount of spare parts available in the field as crashes might happen (a first aid kit might be good to have in this case, too). It is a very good idea to wear sunglasses since watching the UAV means looking into the bright sky.

**Fig. 4.8** Scheme for calculating pictured scene size (camera footprint) from aperture angles ( $\alpha, \beta$ ) and distance towards target (h)



#### 4.4.2 Conduction of the Field Campaign

In the field several points must be considered to guarantee a safe and successful survey. As any UAV is more or less susceptible to wind the current weather conditions cannot be ignored. It is not recommended to fly the UAV in strong winds. Also, it is recommended to stay away from systems like e.g. power lines or other model aircrafts as they might cause problems with communication between remote control and UAV. It is advised to cover sandy or dusty launching and landing areas to protect the motors from rising sand and dust. Over extremely hot areas an increased flight altitude might be necessary depending on operating temperature of UAV and camera. Atmospheric effects on the thermal sensor are considered negligible for the low flight altitude compared to measurements conducted by plane or satellite. However, barometric height will decrease when the UAV flies through a vapor plume (as occurs e.g. when the water from extinguishing work at a coal fire site evaporates and is emitted at distinct spots). Here some experience in manual flight control is essential in order to adjust the UAV flight altitude.

After each flight the data should be transferred from the camera to the computer and the data quality should be checked if the data are not sent to a computer via downlink during flight. If the data quality is poor, the flight should be repeated. In addition to the thermal images taken from the UAV the ambient temperature should also be measured to allow for corrections of temperature changes between different days of the survey. For measurement of emissivity in the field see e.g. Hook and Gabell (1992) and Tian et al. (2008).

For stereographic analyses the automatic autofocus of the camera must be deactivated.

If an additional sensor is installed on the UAV it should be checked if the boundary conditions for these measurements are also satisfying. E.g. the time at

waypoint has to be at least as long as t90-time<sup>2</sup> in order to obtain reliable CO<sub>2</sub> measurements.

In terms of field application the challenge of UAV-borne thermal imaging is to set up the flight campaign in a way such that good quality images and all information necessary for proper data processing can be obtained by a safe survey flight.

## 4.5 Data Processing

After the field campaign the individual thermal image files have to be processed to obtain the ground surface temperature for the whole survey area. Therefore the single thermal images are transferred from the camera to a computer and exported as image files for further processing.

To ensure comparability all individual thermal images have to be scaled to a common temperature range and scale first. Minimum and maximum of the temperature range can be determined from the statistics of each pixel's temperature. Different ambient temperatures at different days of survey have to be corrected. The influence of climatic parameters such as transmittance of the atmosphere, path radiances between surface and sensor system and thermal downwelling flux are considered comparatively small for UAV application of thermal infrared imaging (8–14 µm) and thus might be neglected as the influence of surface emissivity is dominant when the actual ground surface temperature is measured. For the calculation of the brightness temperature the emissivity is set to  $\epsilon = 1$ . Information on the emissivity for geological materials is given in literature, e.g. Rivard et al. (1995).

### 4.5.1 Georeference

Georeferencing a picture means to provide information on position, transformation (scaling, rotating, shifting) and orthorectification (possible terrain-induced distortions that will have to be corrected). Position, rotation, and shifting can be derived from the UAV flight log. The scaling depends on the distance of the camera from the target (flight altitude above ground). As described earlier (see the Sect. 4.4), the logged height above ground and the true flight altitude might differ. To compensate this effect a digital elevation model of the survey area's topography is needed. The geometrical resolution has to be in the range of the point distance for proper scaling of the images. If there is no such digital elevation model (DEM) available it has to be derived from corresponding measurements in the survey area. For the Shuixigou coal fire at several points within the survey area the position (x, y, z) was taken with a handheld GPS device. A simple DEM was than obtained from interpolation of these

---

<sup>2</sup>The t90 time is defined as the time it takes for the sensor to get 90 % of the final reading.

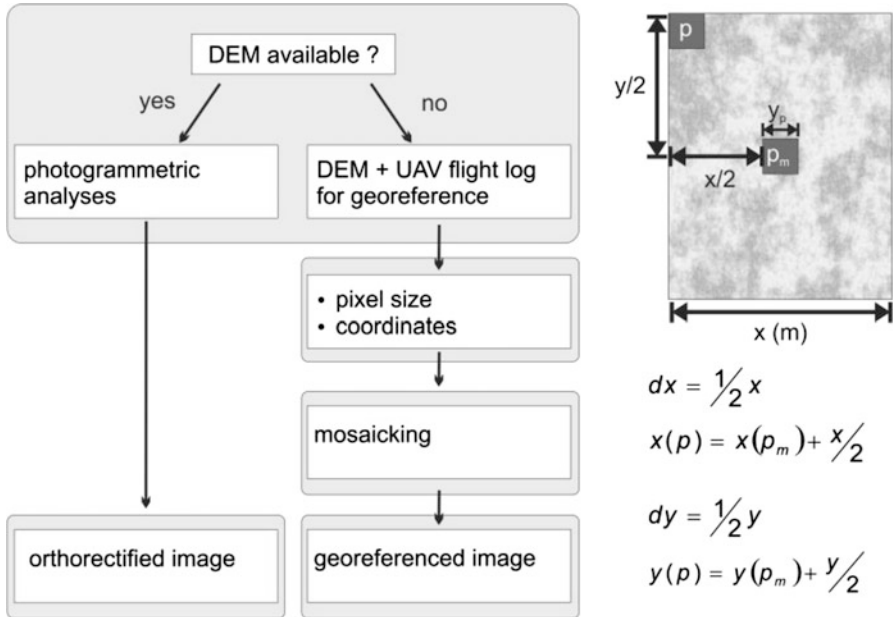


**Fig. 4.9** Schematic workflow for data processing (left), coordinates of upper left pixel from UAV position (middle pixel  $p_m$ ) and image size (right)

point data. The height above ground is then the difference of height logged by the UAV and DEM. The resolution per pixel in x- and y-direction can be derived from the image size and the camera's footprint (Fig. 4.8), precisely it is the quotient of side length (m) and number of pixels. For converting an individual TIR-image from e.g. a tif-file to a georeferenced image a corresponding world-file (.tfw) has to be written, which contains the resolution per pixel in x- and y-direction and the coordinates x(p) and y(p) of the upper left pixel (right side of Fig. 4.9).

#### 4.5.2 Mosaicking

To get an image of the surface temperature covering the whole survey area, the individual images have to be stitched together (mosaicked). Depending on the target basically two different approaches are feasible (Fig. 4.9, left panel): Patch the images manually or use automatic algorithms utilizing the images' georeference. Automatic mosaicking uses ground control points determined by photogrammetry. Therefore markers which are visible in the thermal (and also in the visual) image have to be positioned in the field and its positions have to be determined accurately. The images than are stretched to fit with the markers to the respective coordinate. This gives not only information on scaling, rotation and positioning of the images but also distortions

are taken into account. This is only feasible if it was possible to position and measure control points in the survey area. Also, automatic algorithms like professional software for processing satellite images (e.g. ENVI) are based on this spatial reference of the individual images. For steep areas or hillsides the profiles are not horizontal but vertical (since the UAV flies up and down) to be parallel to the hillside. Thus, the position with respect to Easting and Northing (respectively longitude and latitude) is about the same for all images and the mosaicking algorithm would stack the images on top of each other. Algorithms for automatic splicing without control points are currently being investigated for UAV-borne images in the visual bandwidth (Li et al. 2011).

Alternatively the images might be patched together manually using common graphic software. Orientation is provided by obvious features that can be traced over different images and the positions of the UAV when the images are taken. A coordinate grid built from these coordinates can be used as overlay for the final mosaic thus yielding the georeference of the surface temperature distribution. This method can only give a rough picture of temperature distribution as distortions are not accounted for.

## 4.6 Example: Thermal Imaging of Coal Fires

### 4.6.1 *Thermal Anomaly of Coal Fires*

Coal fires are a worldwide problem as they deplete the coal reserves and contribute to global warming and pollution by releasing large amounts of greenhouse gases (Stacher 2008; UNESCO 2005; van Dijk et al. 2011). The ignition of a coal seam is mainly caused by spontaneous combustion as a result of exposure to oxygen. This typically happens in small and/or not properly sealed mines. The knowledge of the ground surface temperature and the released energy is essential for fire fighting and monitoring, as well as for calculations regarding CDM (Clean Development Mechanism) purposes (Meyer et al. 2009, 2010; Prakash and Vekerdy 2004; van Dijk et al. 2011; Zhang et al. 2004).

The heat of the burning coal seam moves towards the surface by conductive transport within the host rock and by convective heat transport by pore fluids and combustion gases as simulations confirm (Wessling et al. 2008; Zhang et al. 2007). This process increases the surface temperature locally (Fig. 4.10). Thermal satellite and airborne sensor systems register the heat radiated from the surface (Prakash et al. 1995) which can be converted to surface temperatures using statistical approaches or physical models validated by ground reference measurements (Zhang and Kuenzer 2007). Within our research we surveyed two fires zones with UAV-borne thermal imaging (Vasterling et al. 2010).

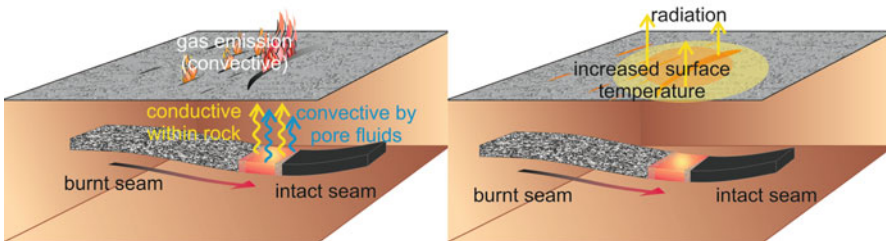


**Fig. 4.10** Development of the surface temperature anomaly tailing the burning coal seam. *Left:* Heat transfer, *right:* surface temperature anomaly

For the application to coal fires the Falcon 8 was equipped with a thermal camera “mobilIR M4” (InfraTec) and a CO<sub>2</sub> sensor. However, the implementation of a different camera as well as (additional) sensors is possible if the maximum payload is not exceeded.

#### 4.6.2 Coal Fire on a Hillside (*QueerGou, Xinjiang Province P.R. China*)

The QueerGou fire zone is situated at both sides of a valley. The hills are covered with vegetation, however, during the ongoing extinguishing works terraces were cut into the hillsides. Water from a nearby creek is used to cool the fire as well as the host rock. The last step is to cover the terraces with loess to stop the oxygen supply for the fire (Fig. 4.11).

Within two field campaigns (May and October 2009) two different terraces were surveyed by a UAV. The lower terrace which was first investigated in May was already covered completely with loess in October. Consequently a different terrace had to be surveyed and monitoring the changes was not possible as the two mosaics do not represent the same area. In May an area of approximately 53 m × 31 m was investigated and an area of 34 m × 8 m in October. The areas of interest were not flat but feature steep hillsides and neither satellite nor ground based measurements were available. Several vertical trajectories were followed up and down the hillside with a few meters distance towards the wall.

As the position with respect to Easting and Northing is about the same for all images of the same profile, the mosaicking algorithm would lay the images on top of each other. Thus, the images are patched together manually to obtain the surface temperature distribution from the mosaic of thermal images. Emissivity was set to  $\epsilon = 1$  for all pictures.

In the pictures taken in May (Fig. 4.12) the terrace’s base and the water hoses for cooling appear as structures of decreased temperature. In large areas the

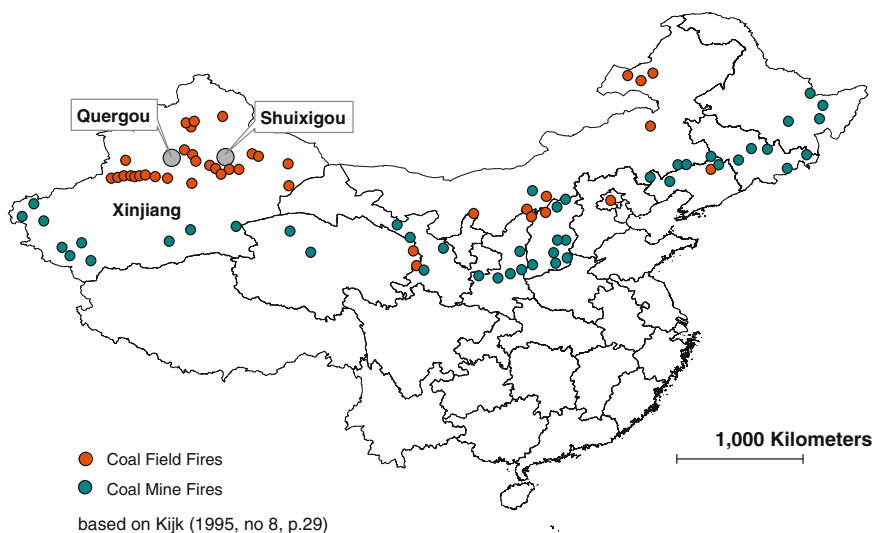


**Fig. 4.11** Xinjiang Province in Northwest China

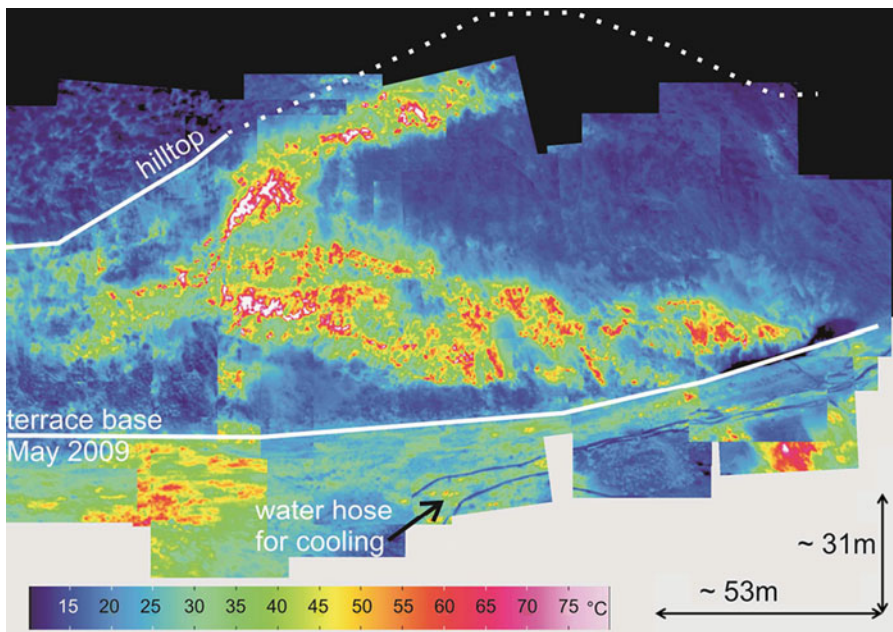


**Fig. 4.12** Thermal image (brightness temperature) of the terrace surveyed in May 2009. The images were taken till noon while the sun was behind the hill

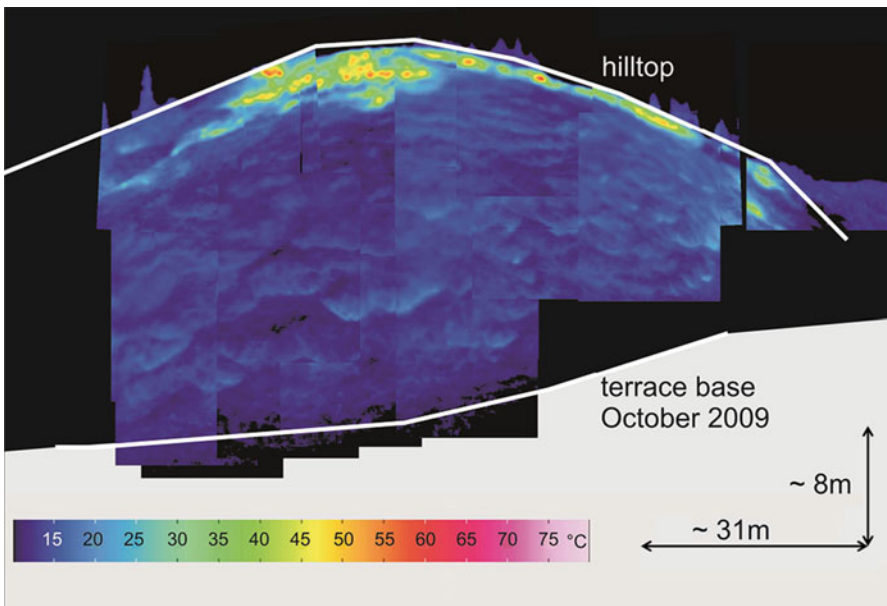


**Fig. 4.13** Thermal image (brightness temperature) of the terrace surveyed in October 2009. The images were taken till noon while the sun was behind the hill

temperature is significantly increased and is as high as 70 °C. In October (Fig. 4.13), however, the brightness temperatures are lower (maximum about 55 °C) and much more homogenous in almost all parts of the terrace. It is only near the hilltop where a band of increased temperature is visible.

#### 4.6.3 Coal Fire on a Hilltop (*Shuixigou, Xinjiang Province P.R. China*)

The surveyed area's topography includes a hill as well as cracks and vents emitting hot gases. The soil is colored by condensates (Fig. 4.5). As there is no vegetation growing at the survey area, it is suitable for a comparison of ground based, UAV-borne and satellite measurements of the ground surface temperature. At the Shuixigou fire no extinguishing works have been conducted so far.

Using the Falcon 8, 53 images were taken along six parallel profiles. As no high resolution DEM was available, in a first attempt an overview flight at constant height was conducted. This height refers to the starting area as base, which results in not flying parallel to the topography. Consequently, the flight altitude of 30 m above the starting area is reduced to a height above ground of approximately 15 m at the hilltop. Thus, the camera's footprint is reduced from 10 m × 13 m to only 5 m × 7 m

causing the obvious gaps between neighbouring images. The plan was to create a DEM from GPS measurements taken during the overview flight by a handheld GPS sensor. Then, a more sophisticated flight plan should be prepared utilizing this DEM for height reference and also taking the results from the first flight into account. However, during the first survey flight technical problems with the camera occurred that could not be fixed. This results in the large gap starting at the centre and extending to the south that could not be filled by using data collected by an additional flight.

A digital elevation model was created from the height measured by a handheld GPS. This is just a rough approximation to the true topography and it has shown that the resulting photo height is not accurate enough for georeference based mosaicking. The thermal images are scaled to a common temperature range of 10–180 °C and are patched together manually. A coordinate grid was used as overlay for the final mosaic to yield the georeference of the calculated surface temperature distribution.

In Fig. 4.2 the mosaic of the manually patched thermal images taken by the UAV is shown. It portraits the ground surface temperature in detail. Despite some large temperature anomalies smaller features like linear structures in the central part are observed. In the southern part of the survey area the increased surface temperature (pink ellipse) is caused by the burning coal in the subsurface.

## 4.7 Summary and Outlook

UAV-borne thermal imaging is the measurement of ground surface temperature by a small unmanned airborne vehicle equipped with a TIR camera. Compared to satellite measurements the geometric resolution is much better. In contrast to ground based measurements, UAV-borne thermal imaging provides spatial data which provides a very detailed picture of the temperature distribution. At the same time interpolation is not necessary. The method is suitable for almost any kind of topography without ground accessibility being necessary. The costs for the required equipment are moderate. Any method that does not need ground contact and is operated by applying a light weighted instrument might theoretically be mounted onto a UAV for a fast survey even on difficult terrain. Thus, UAV-borne surveys can be used in a large variety situations and applications.

A variety of different types and sizes of UAVs are available. In our example of coal fire temperature measurements, the helicopter like system Falcon 8 was used and carried a thermal camera with the desired properties regarding weight, temperature range, resolution (both spatial as well as temperature dynamic range) and footprint.

For the field application a well trained pilot is mandatory. A good preparation of the mission is necessary, including the check on possible legal restrictions, provision of spare parts, and planning the flight mission. Information regarding the local topography should be used for planning the flight profiles and setting the waypoints.

Mosaicking of the individual images has to be considered. For photogrammetric analyses control points are necessary. As the terrain might not allow for positioning ground control points, alternative approaches for patching the images together should be considered. The georeference can be deduced from the UAV's position, a known or derived DEM, and the flight altitude. However, this approach does not consider orthorectification. The emissivity has to be taken into account to retrieve the true ground surface temperature.

Thus, the main challenges of UAV-borne thermal imaging are first to select the most suitable system of UAV and camera, then plan and perform a successful field campaign and finally derive a large image mosaic of the ground surface temperature patterns based on the acquired individual images.

Based on our experience further development might be necessary to optimize the technique of UAV-borne thermal imaging. To improve georeference based mosaicking it is necessary to either register the distance of the camera to the target using a digital elevation model or work with ground control points. A possible solution of this problem might be the implementation of a light weight altitude sensor to determine the height above ground level (for flat survey areas) or a sensor recording the distance of the camera to the target in general. If it is difficult to get a powerful sufficiently light weighted distance meter, then the TIR flight and altimeter flight must be carried out separately. The distance to the ground level can then be determined by performing a first flight in a constant height with respect to the launching area. Point and profile distance then have to be adapted to guarantee an overlapping of the individual images for the whole survey area. This can be done in advance of the field campaign if a proper elevation model of the targeted area is available. For automatic mosaicking, the development of an algorithm that takes not only easting and northing into account but also height and spatial orientation as derived from camera angle might be an asset. Also, a continuous recording of thermal images by recording a TIR video is possible. At this moment the position accuracy is now in the range of GPS accuracy. For working with georeference based algorithms the position accuracy should be improved (Bláha et al. 2011).

The comparison of UAV- and satellite-borne data shows the different scale both methods work on which makes a direct upscaling of UAV- to satellite data impossible. The linking scale could be provided by using a large airborne system.

The implementation of additional methods, for example gas measurement sensors, is potentially viable. If thermal imaging and gas measurements are conducted simultaneously during one flight, the gas sensor has to be sufficiently fast to determine the amount of the gas in the column while the UAV hovers over the observation point. If the removal and reattachment of the various measurement devices is sufficiently easy, then separate flights for thermal imaging and other methods might be considered.

In conclusion, UAV-borne thermal imaging is a promising method to retrieve highly resolved spatial information on the ground surface temperature within a short amount of time; however, some challenges are still unresolved and need further research.

**Acknowledgements** The presented results were gained within the framework of the Sino-German research initiative “Innovative technologies for exploration, extinction and monitoring of coal fires in Northern China” funded by the Federal Ministry of Education and Research, BMBF, Germany.

The authors would like to thank the Chinese and German partners in particular for their help during the field campaign. Many thanks go to Christian Fischer and Christoph Ehrler for providing the satellite data and to Stefan Schlömer for sharing the ground based temperature measurements. The comments of the reviewers and Elisabeth Ullmann were much appreciated and have improved the manuscript.

## References

- Ascending Technologies (2012) AscTec Falcon 8. Production information, available at [www.asctec.de/asctec-falcon-system](http://www.asctec.de/asctec-falcon-system). Accessed 02 Nov 2012
- Bláha M, Eisenbeiss H, Grimm D, Limpach P (2011) Direct georeferencing of UAVs. In: Proceedings of the international archives of the photogrammetry, remote sensing and spatial information sciences, vol XXXVIII-1/C22 UAV-g 2011, Conference on unmanned aerial vehicle in geomatics, Zurich, 14–16 Sept 2011
- Cress JJ, Sloan JL, Hutt ME (2011) Implementation of unmanned aircraft systems by the U.S. Geological Survey. *Geocarto Int* 26(2):133–140
- Eisenbeiß H (2009) UAV photogrammetry. Dissertation, Institut für Geodäsie und Photogrammetrie ETH Zürich, 237 pp
- FLIR (2012) Quark data sheet, available at [www.flir.com](http://www.flir.com). Accessed 13 Mar 2012
- Friedli E (2010) Evaluierung der Oktokopters Falcon 8. Bachelorarbeit, Institut für Geodäsie und Photogrammetrie ETH Zürich, 70 pp
- Gaussorges G (1994) Infrared thermography. Microwave technology series 5, Chapman and Hall, London, 560p
- Hartmann W (2011) Untersuchung der Positionierungs- und Orientierungsgenauigkeit von UAVs mit Hilfe einer Thermalkamera, Masterprojektarbeit, Institut für Geodäsie und Photogrammetrie, ETH Zürich
- Hinkley EA, Zajkowski T (2011) USDA forest service – NASA: unmanned aerial systems demonstrations – pushing the leading edge in fire mapping. *Geocarto Int* 26(2):103–111
- Hook JS, Gabell AR (1992) A comparison of techniques for extracting emissivity information from thermal infrared data for geologic studies. *Remote Sens Environ* 42:123–135
- InfraTec (2012) InfraTEc mobileIR M4 – Mobile Miniatur-Thermographiekamera. Production information, available at [www.infratec.de](http://www.infratec.de). Accessed 26 Feb 2012
- Israel M (2011) A UAV-based Roe Deer Fawn detection system. In: Eisenbeiss H, Kunz M, Ingensand H (eds) Proceedings of the international conference on unmanned aerial vehicle in Geomatics (UAV-g), vol XXXVIII. ISPRS, Zurich, 2011, pp 1–5
- Kiwamoto Y, Abe H, Tatematsu Y, Saito T, Kurata M, Kajiwara K, Kikuchi Y, Takahashi T, Tamano T (1997) Thermographic temperature determination of gray materials with an infrared camera in different environments. *Rev Sci Instrum* 68(6):2422–2427
- Kuenzer C, Stracher GB (2011) Geomorphology of coal seam fires. *Geomorphology* 138:209–222
- Kuenzer C, Zhang J, Li J, Voigt S, Mehl H, Wagner W (2007) Detection of unknown coal fires: synergy of coal fire risk area delineation and improved thermal anomaly extraction. *Int J Remote Sens* 28:4561–4585
- Laliberte AS, Winters C, Rango A (2011) UAS remote sensing missions for rangeland applications. *Geocarto Int* 26(2):141–156
- Li C, Zhang G, Lei T, Gong A (2011) Quick imageprocessing method of UAV without control points data in earthquake disaster area. *Trans Nonferrous Metals Soc China* 2:523–528

- Meyer U, Chen-Brauchler D, Schloemer S, Kus J, Lambrecht A, Rueter H, Fischer C, Bing K (2009) Geophysics and clean development mechanisms (CDM): applications to coal fires. In: *Geophysical research abstracts 11, Proceedings on EGU general assembly*, Vienna, 2009, 19–24 April, p 9847
- Meyer U, Rueter H, Chen-Brauchler D, Schloemer S, Kus J, Wuttke MW, Fischer C (2010) Alternative methods for baseline estimations – political and scientific aspects. In: *Latest developments in coal fire research– bridging the science, economics, and politics of a global disaster/ICCFR2 2010; Proceedings published by Federal Ministry of Education and Research*, Berlin, 19–21 May 2010, pp 371–377
- Pastor E, Barrado C, Royo P, Santamaría E, Lopez J, Salami E (2011) Architecture for a helicopter-based unmanned aerial systems wildfire surveillance system. *Geocarto Int* 26 (2):113–131
- Prakash A, Vekerdy Z (2004) Design and implementation of a dedicated prototype GIS for coal fire investigations in North China. *Int J Coal Geol* 59(1–2):107–119
- Prakash A, Saraf AK, Gupta RP, Dutta M, Sundaram RM (1995) Surface thermal anomalies associated with underground fires in Jharia coal mines, India. *Int J Remote Sens* 16 (12):2105–2109
- Rivard B, Thomas PJ, Giroux J (1995) Precise emissivity of rock samples. *Remote Sens Environ* 54:152–160
- Salisbury JW (1992) Emissivity of terrestrial materials in the 8–14/tm atmospheric window. *Remote Sens Environ* 42:83–106
- Sheng H, Chao H, Coopmans C, Han J, McKee M, Chen Y (2010) Low-cost UAV-based thermal infrared remote sensing: platform, calibration and applications. In: *Proceedings of the international conference on mechatronics and embedded systems and applications (MESA)*, 2010 IEEE/ASME, Conference proceedings, Qingdao, 15–17 July 2010, pp m38–43
- Stacher GB (ed) (2008) *Geology of coal fires: case studies from around the world*. The Geological Society of America, Boulder, 283 pp
- Sugiura R, Noguchi N, Ishii K (2007) Correction of low-altitude thermal images applied to estimate soil water status. *Biosyst Eng* 96(3):301–313
- Sullivan DG, Fulton JP, Shaw JN, Bland G (2007) Evaluating the sensitivity of an unmanned thermal infrared aerial system to detect water stress in a cotton canopy. *Trans ASABE* 50 (6):1955–1962
- SurveyCopter (2012) The Blimp 2C. Production information, available at [www.surveycopter.fr](http://www.surveycopter.fr). Accessed 26 Feb 2012
- Tetzlaff A (2004) Coal fire quantification using Aster, ETM and Bird instrument data. Dissertation, Geosciences, Maximilians-University, Munich, 155 pp
- Tian J, Zhang R, Su H, Sun X, Chen S, Xia S (2008) An automatic instrument to study the spatial scaling behavior of emissivity. *Sensors* 2008(8):800–816
- UNESCO (Ed) (2005) Spontaneous coal seam fires: mitigating a global disaster. In: *International research for sustainable control and management. ERSEC ecological book series – 4*. Tsinghua University Press and Springer, Beijing
- van Blyenburgh P (1999) UAVs: an overview. *Air Space Eur* 1(5):43–47
- van Dijk P, Zhang J, Jun W, Kuenzer C, Wolf KH (2011) Assessment of the contribution of in-situ combustion of coal to greenhouse gas emission; based on a comparison of Chinese mining information to previous remote sensing estimates. *Int J Coal Geol* 86:108–119
- van Persie M, Oostdijk A, Fix A, van Sijl MC, Edgardh L (2011) Real-time UAV based geospatial video integrated into the fire brigades crisis management GIS system. In: *International archives of the photogrammetry, remote sensing and spatial information sciences*, vol XXXVIII-1/C22 UAV-g 2011, Proceedings of the conference on unmanned aerial vehicle in geomatics, Zurich, 14–16 September, pp 173–175
- Vasterling M, Schloemer S, Ehrler C, Fischer, F (2010) Correlation of surface temperature and remote thermal infrared measurements using an unmanned aerial vehicle. In: *Latest developments in coal fire research– bridging the science, economics, and politics of a global*

- disaster/ICCFR2 2010; Conference Proceedings published by Federal Ministry of Education and Research, Berlin, 19–21 May 2010, pp 221–228
- VikingAero (2012) Wolverine III – helicopter unmanned system. Production information, available at [www.vikingaero.com](http://www.vikingaero.com). Accessed 26 Feb 2012
- Wessling S, Kuenzer C, Kessels W, Wuttke M (2008) Numerical modeling to analyze underground coal fire induced thermal surface anomalies. *Int J Coal Geol* 74:175–184
- Yeh SS (2011) A failure of imagination: unmanned aerial vehicles and international security. *Comp Strategy* 30(3):229–241
- Zhang J, Kuenzer C (2007) Thermal surface characteristics of coal fires 1: results of in-situ measurements. *J Appl Geophys* 63:117–134
- Zhang X, Zhang J, Kuenzer C, Voig S, Wagner W (2004) Capability evaluation of 3–5 and 8–12.5  $\mu\text{m}$  airborne thermal data for underground coal fire detection. *Int J Remote Sens* 25 (12):2245–2258
- Zhang J, Kuenzer C, Tetzlaff A, Oettl D, Zhukov B, Wagner W (2007) Thermal characteristics of coal fires 2: result of measurements on simulated coal fires. *J Appl Geophys* 63:135–148

# Chapter 5

## NASA's Hyperspectral Thermal Emission Spectrometer (HyTES)

Simon J. Hook, William R. Johnson, and Michael J. Abrams

**Abstract** The Hyperspectral Thermal Emission Spectrometer (HyTES) is being developed as part of the risk reduction activities associated with the Hyperspectral Infrared Imager (HyspIRI). HyspIRI is one of the NASA's Tier 2 Decadal Survey Missions for earth science. HyTES will provide information on how to place the spectral filters on the HyspIRI Thermal Infrared Instrument as well as provide antecedent science data. The HyTES pushbroom design has 512 spatial pixels over a 50-degree field of view and 256 contiguous spectral bands between 7.5 and 12  $\mu\text{m}$  in the thermal infrared (TIR) wavelength region. HyTES includes many key enabling state-of-the-art technologies including a high performance concave diffraction grating, a quantum well infrared photodetector (QWIP) focal plane array, and a compact Dyson-based optical design. The Dyson optical design allows for a very compact and optically fast system (F/1.6). It also minimizes cooling requirements due to the fact it has a single monolithic prism-like grating design which allows baffling for stray light suppression. The monolithic configuration eases mechanical tolerancing requirements which are a concern since the complete optical assembly is operated at cryogenic temperatures. The QWIP allows for optimum spatial and spectral uniformity and provides adequate responsivity or D-star to allow 200 mK noise equivalent temperature difference (NEDT) operation across the TIR passband. The system uses two mechanical cryocoolers to maintain instrument temperature. The first cooler holds the focal plane array at 40 K and the second cooler holds the remainder of the cryovacuum system at 100 K. Assembly of the system is now complete and the system is undergoing alignment and laboratory testing. Once laboratory testing is complete the system will be used to acquire airborne data from a Twin Otter aircraft over the southwestern USA in late 2012.

---

S.J. Hook (✉) • W.R. Johnson • M.J. Abrams  
Jet Propulsion Laboratory, California Institute of Technology, National Aeronautics  
and Space Administration (NASA), Pasadena, CA, USA  
e-mail: [Simon.hook@jpl.nasa.gov](mailto:Simon.hook@jpl.nasa.gov)

## 5.1 Introduction

This chapter describes the Hyperspectral Thermal Emission Spectrometer (HyTES) which is being developed as part of the risk reduction activities associated with the thermal infrared (TIR) instrument on the Hyperspectral Infrared Imager (HyspIRI). HyspIRI is one of the missions recommended by the Earth Science Decadal Survey. HyTES will be used to provide information on how to place the spectral filters on the HyspIRI-TIR instrument as well as provide antecedent science data. Initially the Decadal Survey is described followed by the Heritage and Science Objectives for HyspIRI-TIR and HyTES. The remainder of the chapter provides a detailed description of HyTES and QWEST (Quantum Well Earth Science Testbed) which was the prototype for HyTES. Finally some recent results from laboratory tests are presented together with a discussion of future activities.

### 5.1.1 The Decadal Survey

In 2004, the National Aeronautics and Space Administration (NASA) requested the National Research Council (NRC) conduct a Decadal Survey (DS) for Earth science and applications from space. The 2007 report is titled *Earth Science and Applications from Space: National Imperatives for the next Decade and Beyond* (NRC 2007). The purpose of DS study was to provide NASA with a blueprint for the subsequent 10 years, prioritizing science missions, in response to community inputs and recommendations. The report identified key science measurements and recommended a small number of missions to acquire those measurements. The topical areas included earth science applications and societal benefits; land use change, ecosystem dynamics, and biodiversity; weather; climate variability and change; water resources and the global hydrologic cycle; human health and security; and solid earth hazards, resources and dynamics. The missions were arranged in three groups or tiers and are referred to as the Tier I, Tier II or Tier III missions. It was the intention of the DS that the three tiers represent a succession of mission starting with Tier I. The Hyperspectral and Infrared Imager (HyspIRI) is one of the missions in the Tier II group.

HyspIRI will provide global observations at local and landscape scales (10s of meters to 100s of kilometers). The mission includes a hyperspectral visible-near infrared-shortwave infrared (VSWIR) imaging spectrometer, and a multispectral thermal infrared (TIR) scanner. Operating from low earth orbit, the instruments will provide global coverage, frequent repeat revisits, and data at moderate to high spatial resolution (60 m). The DS laid out a timeline to implement the missions with launch dates for the Tier II missions recommended between 2013 and 2016. Subsequent to the community driven DS a study was undertaken by members of the US Climate Change Research Program and published as “Responding to the Challenge of Climate and Environmental Change: NASA’s Plan for a Climate-Centric Architecture for

Earth Observations and Applications from Space" (NASA 2010). This study inserted additional missions and re-assigned the priority of certain missions adjusting the sequence in which the Decadal Survey missions were implemented. The Tier II missions, including HyspIRI will be launched in the 2020+ timeframe according to the current NASA schedule. NASA assigned the Jet Propulsion Laboratory (JPL) to lead a concept study with support from the Goddard Space Flight Center (GSFC). Dr. Robert Green headed up the studies for the VSWIR hyperspectral instrument, Dr. Simon Hook was responsible for the TIR instrument and Dr. Elizabeth Middleton was responsible for the onboard processing and distribution of a subset of the data through a system referred to as the intelligent payload module (IPM). This chapter describes the Hyperspectral Thermal Emission Spectrometer (HyTES) which is being developed as part of the risk reduction activities associated with the TIR component of HyspIRI. HyTES will be used to provide information on how to place the spectral filters on the HyspIRI Thermal Infrared Instrument as well as provide antecedent science data.

### 5.1.2 *Heritage*

TIR aircraft instruments have been operating since the early 1970s. The first work was with a two-band instrument (Vincent 1972). By ratioing values from two thermal bands, emissivity differences could be detected in the resulting image, and these were related to differences in rock type. In the early 1980s, NASA started operating the Thermal Infrared Multispectral Scanner (TIMS), a 6-band airborne instrument with bands in the 8–12  $\mu\text{m}$  wavelength region (Kahle and Rowan 1980). TIMS was the first operational scanner that acquired multispectral TIR data allowing separation of temperature and emissivity (T-E). Many researchers developed techniques to solve the under-determined T-E problem, and accurate retrievals of both values is now routine. TIMS flew for more than 15 years before being replaced by the MODIS/ASTER (MASTER) airborne instrument (Hook et al. 2001). MASTER is a 50 band instrument with 25 bands in the VSWIR, 15 bands in the mid infrared (3–5  $\mu\text{m}$ ) and 10 bands in the TIR. In Europe, the 102-band MIVIS (Multispectral Infrared Visible Imaging Spectrometer) scanner, owned and operated by Italy's National Research Council, has acquired data since 1994 for many researchers. MIVIS has 10 bands in the 8.2–12.7  $\mu\text{m}$  region (Bianchi et al. 1994). The U.S. Aerospace Corporation developed the SEBASS (Spatially Enhanced Broadband Array Spectrograph System) scanner and first deployed it in 1995 (Hackwell et al. 1996). SEBASS has 128 bands in each of the 3.0–5.5  $\mu\text{m}$  and 7.8–13.5  $\mu\text{m}$  regions. The instrument images 128 pixels cross-track with an instantaneous field of view (IFOV) of 1 mrad. All the aforementioned instruments with the exception of SEBASS have a relatively small number of spectral channels in the thermal infrared but a fairly wide swath. Such instruments are useful for providing precursor science data provided that the spectral bands closely match those of the spaceborne sensor being developed. Conversely, SEBASS has many spectral bands

but a narrow swath. The many spectral bands allow the creation of broader spectral bands by aggregating narrow bands to simulate another instrument with fewer broader bands. The difficulty with SEBASS is any such simulations are limited by its narrow swath width and small pixel size. Therefore it was decided to develop a new generation of imaging spectrometers with much higher spectral resolution and a wide swath. This began with the laboratory implementation of a prototype instrument termed the Quantum Well Earth Science Testbed (QWEST) which was used to develop many of the technologies which are now part of the airborne HyTES instrument. JPL has a long history of developing science-grade imaging spectrometers for remote sensing applications. Recent examples include the Airborne Visible Infrared Imaging Spectrometer (AVIRIS), the Carnegie Airborne Observatory (CAO), and the imaging spectrometer on board the Moon Mineralogical Mapper (M3) (<http://aviris.jpl.nasa.gov> and <http://m3.jpl.nasa.gov>). HyTES brings together numerous in-house specialties such as optical design and general spectrometer alignment optimization, precision slit fabrication, high efficiency and low scatter concave diffraction grating design and fabrication, precision mechanical and machining capability and quantum well infrared photo detectors (QWIP) focal plane arrays.

HyTES will operate between 7.5 and 12  $\mu\text{m}$  and have a dual use in that as well as being used to determine the band positions for HyspIRI it will also be used to provide antecedent science data for research purposes. Over the last 40 years, a large and growing research community has developed to study and expand the applications of TIR data over a wide range of earth science disciplines. Working with laboratory measurements, field spectrometers, aircraft data, and data from spaceborne instruments, researchers have compiled spectral libraries of surface materials (Christensen et al. 2000; Baldridge et al. 2009); developed techniques to extract surface compositional information from airborne hyperspectral TIR data (Kirkland et al. 2002; Hook et al. 1992); detected canopy water stress in coniferous forests (Pierce et al. 1990); and refined determination of land surface temperature and emissivity (Hulley and Hook 2011), to name just a few. HyTES will allow the continued development of the research community by providing the first ever high spatial, high spectral wide swath freely available thermal infrared data.

### **5.1.3 *Science Objectives***

The science objectives of HyTES are the same as those of HyspIRI which are described in the 2008 HyspIRI Whitepaper and Science Workshop Report and subsequent workshop reports available online (see URL1). The science objectives for HyspIRI are summarized as a set of questions which data from the instrument will address. These questions were originally articulated in the Decadal Survey and have been further developed by the HyspIRI Science Study Group (SSG). The SSG was established by NASA to provide community guidance for the HyspIRI mission. The SSG is intended to be a dynamic group with individuals rotating in and out

depending on the activities of its members. There are separate science questions that will be addressed by either the VSWIR, TIR or both instruments. HyTES will be used to help address the TIR questions which are arranged as five main science themes:

- **Volcanoes**

How can we help predict and mitigate earthquake and volcanic hazards through detection of transient thermal phenomena?

- **Wildfires**

What is the impact of global biomass burning on the terrestrial biosphere and atmosphere, and how is this impact changing over time?

- **Water Use and Availability**

How is consumptive use of global freshwater supplies responding to changes in climate and demand, and what are the implications for sustainable management of water resources?

- **Urbanization**

How does urbanization affect the local, regional and global environment? Can we characterize this effect to help mitigate its impact on human health and welfare?

- **Land Surface Composition and Change**

What is the composition and temperature of the exposed surface of the Earth? How do these factors change over time and affect land use and habitability?

## 5.2 Instrument Description

In late 2006, JPL began the development of a breadboard thermal infrared pushbroom-spectrometer termed the Quantum Well infrared photodetector Earth Science Testbed (QWEST) as an end to end laboratory demonstration of both the thermal Dyson spectrometer as well as the quantum well infrared focal plane technology. The testbed was the precursor to the airborne HyTES. QWEST brought together numerous in-house specialties such as optical design and general spectrometer alignment optimization, precision slit fabrication, high efficiency and low scatter concave diffraction grating design and fabrication, precision mechanical and machining capability and QWIP focal plane arrays. The specifications for both QWEST and HyTES are given in Table 5.1.

### 5.2.1 *Optical Design*

Both QWEST and HyTES utilize a concentric optical design which allows a point to be mapped perfectly to a focal plane array. Past and future planned imaging spectrometer systems have successfully implemented the Offner design (Offner

**Table 5.1** QWEST and HyTES specifications, QWEST is a laboratory technology demonstration testbed while HyTES is the IIP funded airborne sensor

Instrument characteristics	QWEST	HyTES
Number of cross track pixels	320	512
Number of bands	256	256
Spectral range	8–12 $\mu\text{m}$	7.5–12 $\mu\text{m}$
Typical dwell time	30 ms	30 ms
Total field of view	40°	50°
Calibration (preflight)	Full aperture blackbody	Full aperture blackbody
QWIP array size	640 $\times$ 512	1,024 $\times$ 512
QWIP pixel pitch	25 $\mu\text{m}$	19.5 $\mu\text{m}$
QWIP temperature	40 K	40 K
Spectrometer temperature	40 K	100 K
Slit width	50 $\mu\text{m}$	39 $\mu\text{m}$
Pixel size at 2,000 m flight altitude	4.5 m	3.64 m
Pixel size at 20,000 m flight altitude	45 m	36.4 m

1973; Chrissp 1999). The idea behind the Offner concentric design was to provide a relay unit magnifier to alleviate distortion and third order system aberrations while having an accessible object and image plane. The first published supplementary idea for an all reflecting or 2-mirror concentric imaging spectrometer was cast by Thevenon and Mertz (Mertz 1977). Subsequent work was also done by Kwo et al. (1987) and Lobb (1994). A concentric design like the Offner is well-suited to spectrometers. Smile and keystone distortion are nearly eliminated using proper alignment and design techniques. Although an excellent performer, for the TIR the Offner design would be relatively large and would require a bulky temperature controlled dewar and large power supplies to maintain adequate thermal control. J. Dyson published a paper in 1959 outlining a Seidel-corrected unit magnifier which was composed of a single lens and concave mirror. It was used to project groups of lines for emulsion photography and also phase contrast microscopy. Mertz also proposed the Dyson principle in the same paper where he discussed the Offner. Wynne (1987) proposed a Dyson design for microlithography in the visible and ultraviolet and Mouroulis et al. (2000), considered Dyson designs for visible spectrometry and for coastal ocean applications. A thorough treatment of these designs as well as a working infrared system is described in work by Warren et al. (2008). Kuester et al. (2007) discuss an airborne platform which uses a visible transmitting Dyson.

Both QWEST and HyTES use the same Dyson principle but extend the Dyson design to work optimally with the LWIR (long-wave infrared). The savings in physical size for similar F/# systems is dramatic as shown in Fig. 5.1. Both QWEST and HyTES were designed to minimize smile and keystone distortion (Mouroulis et al. 2000) while simultaneously virtually eliminating ghosting. The slit width of QWEST is 50  $\mu\text{m}$  and the slit width of HyTES is 39  $\mu\text{m}$ , which corresponds to two detector pixels. QWEST has 25  $\mu\text{m}$  pixels whereas HyTES has 19.5  $\mu\text{m}$  pixels. Smile and keystone distortions were kept to no more than 1–2 % of this or  $\sim$ 2  $\mu\text{m}$ .

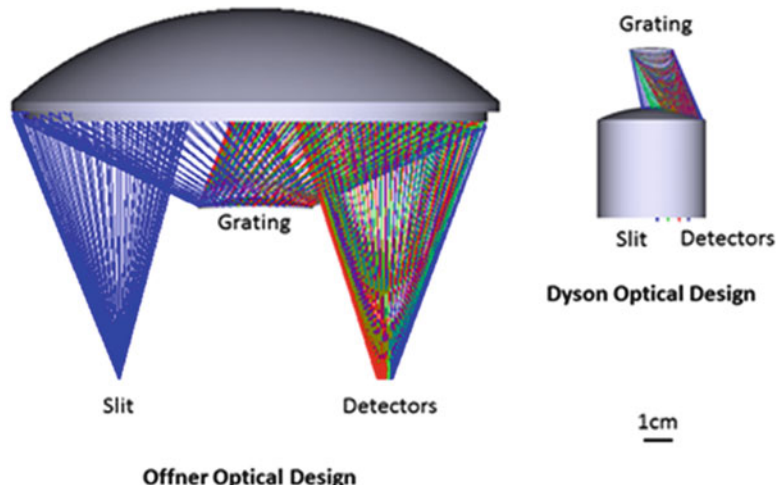


**Fig. 5.1** Ray trace of larger Offner spectrometer (*left*) and smaller Dyson spectrometer (*right*). Designs are for comparable F/#'s and slit width and represent the relative difference in size of the full optical path between the two spectrometer designs

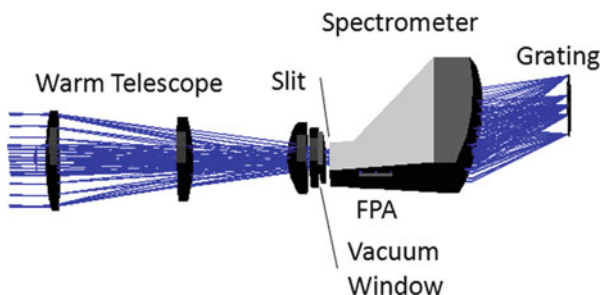


**Fig. 5.2** Optical ray trace of the QWEST Dyson spectrometer and objective lens elements. Thermal radiation passes through the slit and is dispersed by the grating. The dispersion is reimaged ultimately back at the focal plane array (*FPA*) which is kept at 40 K to obtain the optimum performance from the detector

JPL can fabricate ultra precision slits using reactive ion etching which can be kept straight to an order of magnitude better than this. For this reason the slit straightness is not typically the limiting factor in spectrometer performance. As shown in Fig. 5.2 (QWEST) and Fig. 5.3 (HyTES), a single monolithic block is used in double pass where light from the slit enters at a narrow optical passageway and is transmitted through the rear power surface, diffracts off the grating and re-enters the block to totally internally reflect off the back surface which guides the spectrally dispersed radiation to focus at the QWIP detector location, labeled as the Focal Plane Array (FPA) in Figs. 5.2 and 5.3. The FPA is kept at 40 K in both instruments. This design minimizes the travel and form factor of the system.

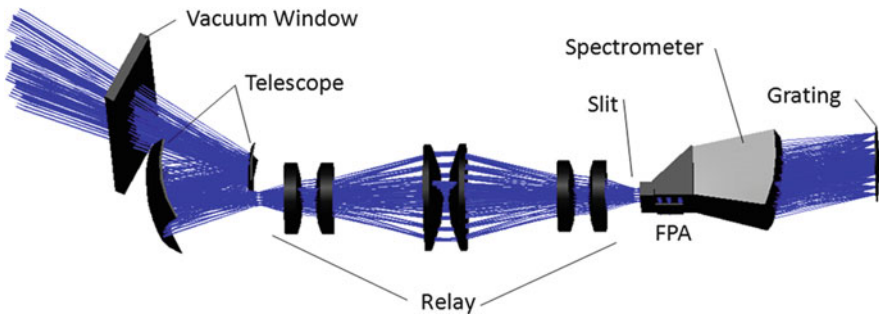


**Fig. 5.3** Optical ray trace of Dyson spectrometer and objective lens elements. Thermal radiation passes through the slit and is dispersed by the grating. The dispersion is reimaged ultimately back at the focal plane array

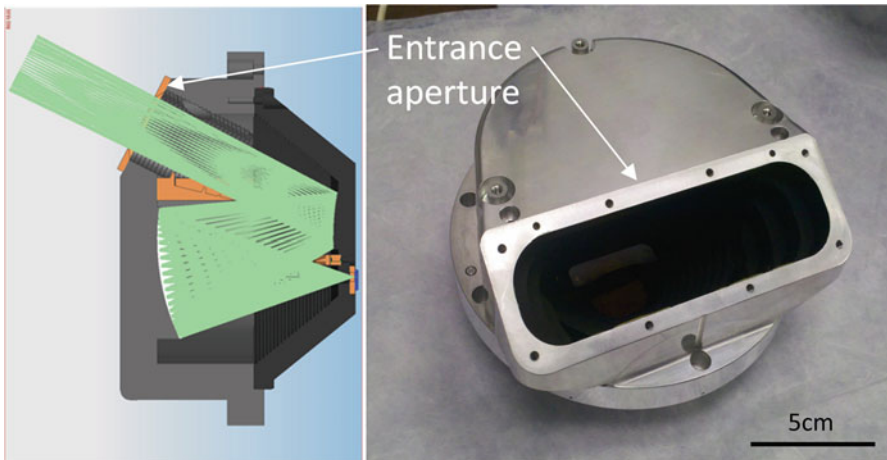


**Fig. 5.4** Light path through telescope (*left*) and front view of actual snap-together self aligning telescope used with HyTES

### 5.2.2 Telescope

The telescope for QWEST was operated warm whereas the telescope for HyTES is kept cold (100 K). Keeping the telescope cold on HyTES minimizes any self emission which would negatively impact the dynamic range, uniformity, and linearity of the data. HyTES uses a reflective off-axis two mirror anastigmat telescope which is a two-piece, self-aligning, all aluminum design by B. Van Gorp, JPL. It consists of two oblate ellipsoids, diamond-turned Al (Fig. 5.4). There was special attention to internal baffling which was also diamond turned into the aluminum structure. The aluminum mirror surfaces were over coated with gold for maximum reflectivity, and all other internal surfaces were painted with

**Fig. 5.5** Top image shows how HyTES Germanium and Zinc Selenide relay elements were bread boarded at room temperature using a test camera in the laboratory to confirm image quality. Bottom image shows the final titanium housing for the six optical elements. The enclosure is kinematic allowing repeatable and stable alignment while being thermal cycled. See Fig. 5.2 for a ray trace of the assembly



high emissivity black, hence, minimizing stray reflections. The outside of the telescope was brought to a mirror-like look from the diamond tip. This fine surface treatment also helps in eliminating thermal buildup from local radiation loading since radiation from the warm outer vacuum housing will be reflected away.

### 5.2.3 Relay

A key difference between QWEST and HyTES is HyTES has a relay assembly prior to the spectrometer housing. This minimizes stray light and allows for a fixed aperture stop position for the telescope. A photo of the relay is shown in Fig. 5.5. The assembly uses six total lens elements. All surfaces are coated with highly transmissive interference layers in order to maximize light throughput. The lens elements are held in a kinematic mount to minimize distortions during flight

operation. As shown in the figure, all internal surfaces are coated with black paint. This includes the stop aperture which is symmetrically placed between the two stacks of lenses. This symmetric design allows the focused field rays from the telescope to be re-imaged at the spectrometer slit with essentially zero chromatic aberration. The goal is to have the diffraction grating introduce the dispersion, not the other optical elements.

#### 5.2.4 Slit

Both QWEST and HyTES use a slit to limit the field angle. JPL can fabricate ultra precision slits. The slits are kept straight to an order of magnitude better than needed. This is one of the keys to enable high performance imaging spectrometers. The slit uses Reactive ion etching (RIE) of silicon nitride ( $\text{Si}_3\text{N}_4$ ) films formed by low pressure chemical vapor deposition (LPCVD). A schematic of the etching process is shown in Fig. 5.6a with the finished product for HyTES shown in Fig. 5.6b.

#### 5.2.5 Dyson Spectrometer

Both QWEST and HyTES use a Dyson spectrometer machined from a ZnSe block. The Dyson spectrometer blocks for QWEST and HyTES are shown in Fig. 5.7. Broadband area coatings are used on all applicable light transmitting surfaces. The coatings allow 99.0 % or better LWIR light to transmit per surface. The block is fabricated from ZnSe, a robust material with a transparent wavelength region from 0.4 to 23  $\mu\text{m}$  and an absorption coefficient between  $10^{-3}$  and  $10^{-4}$  cm. The ZnSe slab is produced by chemical vapor deposition in large chucks and usually cut to small line slices for lens fabrication. A block large enough to support HyTES is difficult to find in practice, since it requires large dimensions ( $>30$  mm) in all 3-axes.

Baffling the Dyson spectrometer in practice is challenging. Notice the grooves in the block used with HyTES which provide additional baffling to avoid stray light effects.

#### 5.2.6 Grating

Both QWEST and HyTES use a diffraction grating. Grating design and fabrication are key enabling technologies for these spectrometers. JPL has developed electron-beam lithography techniques that allow fabrication of precisely blazed

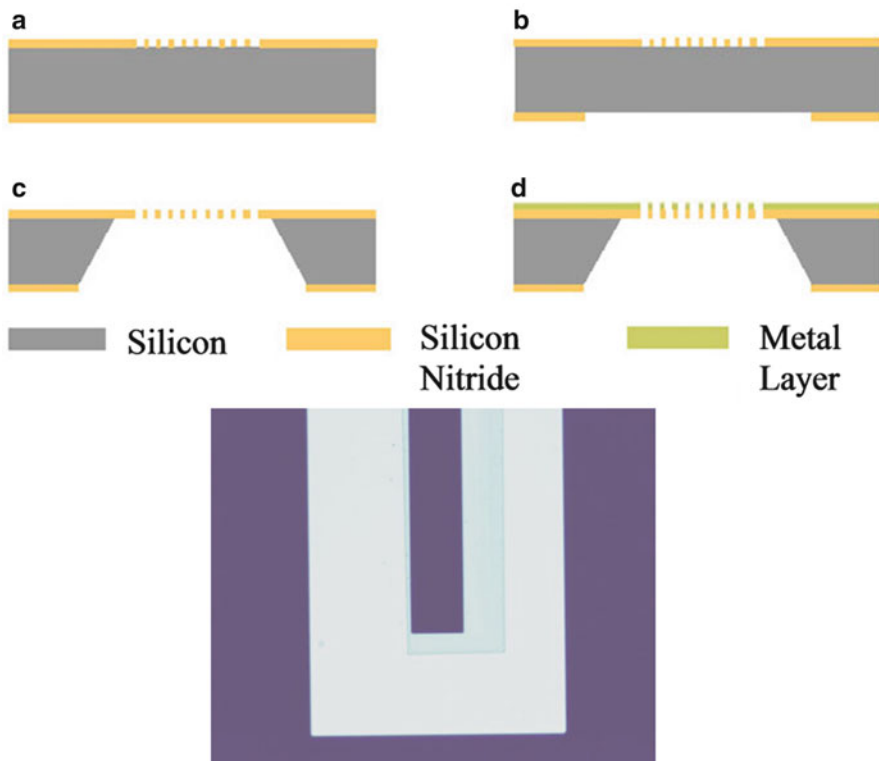


**Fig. 5.6** (a) A generalized process for etching away silicon nitride to expose a clear opening. The etching is done using an ion beam so that precise features and edges can be formed. After etching away the material, the opening is used as the slit for HyTES. (b) A microscope image of the completed HyTES slit edge. The 50  $\mu\text{m}$  wide slit is shown near the center of the photo

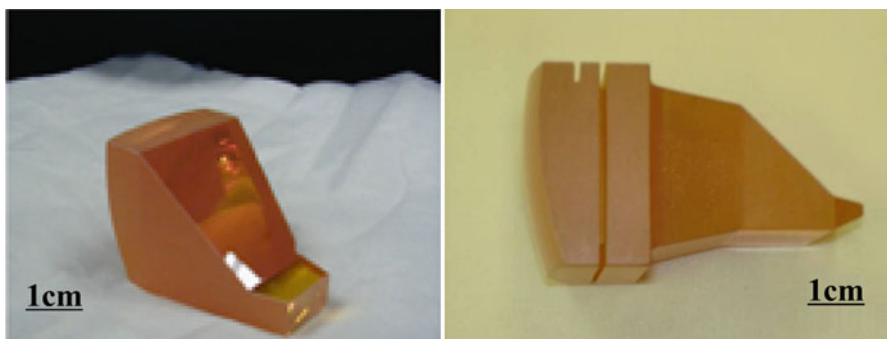


**Fig. 5.7** Monolithic ZnSe optical block with broadband anti-reflection (BBAR) coatings used in double pass for the Dyson spectrometer. QWEST on the *left* and HyTES on the *right*

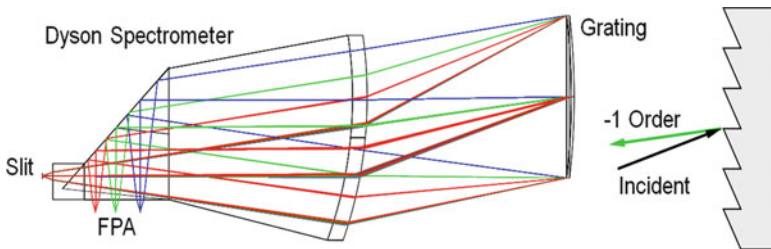


**Fig. 5.8** Illustration of the HyTES grating. The grating is a standard saw-tooth blaze. The  $-1$  order makes it back through the Dyson spectrometer and is focused on the focal plane array

gratings on curved substrates having several millimeters of height variation (Wilson et al. 2003; Perry and Dereniak 1993). To date, JPL is the only facility capable of producing electron beam fabricated gratings on curved substrates. Gratings fabricated in this manner provide high efficiency combined with low scatter. Figure 5.8 illustrates the optical path through the Dyson spectrometer and grating and return path of the dispersed light back through the Dyson to the focal plane. Figure 5.9 shows an electron microscope measurement of the actual grating and picture of the grating. Figure 5.10 shows the assembled grating, relay and spectrometer housing.

### 5.2.7 QWIP Detector

Both QWEST and HyTES use QWIP detectors (Gunapala et al. 2007). QWIP utilizes the photoexcitation of electrons between the ground state and the first excited state in the conduction band quantum well (QW). QWIPs have been successfully integrated into commercial handheld field units for more than a decade. This is the first integration of the QWIP with a spectrometer system for earth science studies requiring accurately calibrated data. The detector pixel pitch of the FPA is  $20\text{ }\mu\text{m}$  and the actual pixel area is  $19.5 \times 19.5\text{ }\mu\text{m}$ . Indium bumps were evaporated on top of the detectors for hybridization with a silicon readout integrated circuit (ROIC). These QWIP FPAs were hybridized (via indium bump-bonding process) to a  $1,024 \times 1,024$  pixel complementary metal-oxide semiconductor (CMOS) ROIC and biased at  $-1.25\text{ V}$ . At temperatures below  $72\text{ K}$ , the signal-to-noise ratio of the system is limited by array nonuniformity, readout multiplexer (i.e., ROIC) noise, and photocurrent (photon flux) noise. At temperatures above  $72\text{ K}$ , the temporal noise due to the dark current becomes the limitation. We are currently running the system at  $40\text{ K}$  to have a SNR advantage. The QWIP is known for its high spatial uniformity ( $<1\text{ \%}$ ). This is a clear advantage over other detector technologies such as Mercury Cadmium Telluride (HgCdTe) and Indium Antimonide (InSb). QWIP's are typically known to be

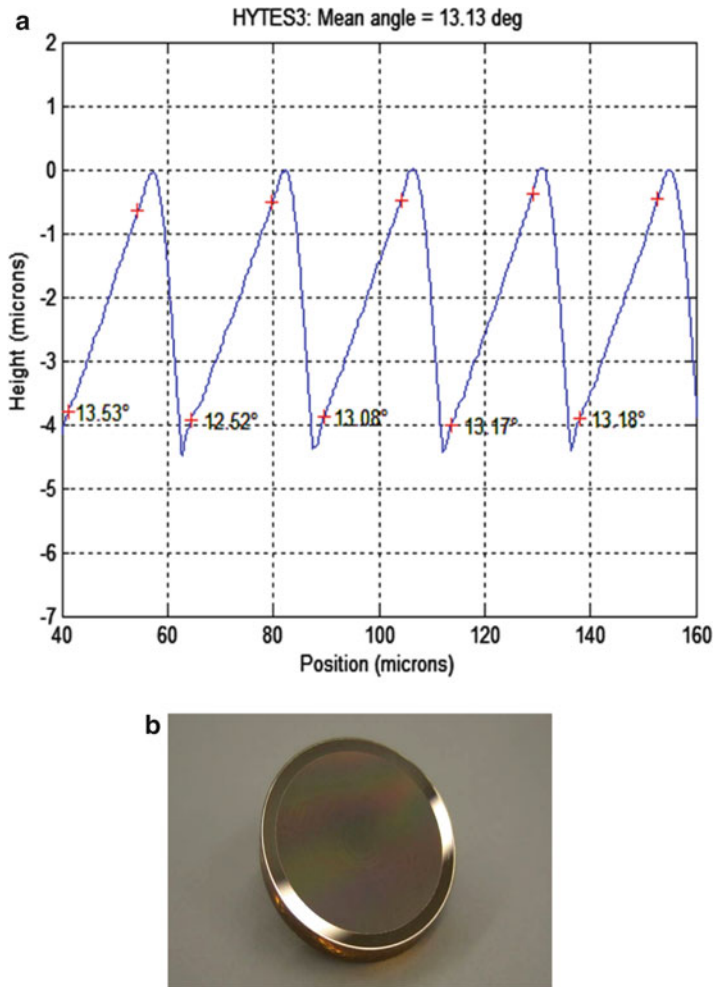


**Fig. 5.9** (a) Measurement of saw-tooth blaze (b) macroscopic photo of grating. The actual microscopic blaze is only written on the center part of the part. The edge is clear. A slight roughness can be seen in the photo towards the center while the edge is shiny. The grating substrate is 38.1 mm in diameter

narrow band in nature and a single QWIP stack was used for QWEST which limited the spectral range to 8–9  $\mu\text{m}$ . HyTES used a 2-stack QWIP which allowed the spectral range to be extended from 7.5 to 12  $\mu\text{m}$  (Fig. 5.11).

Figure 5.12 shows the packaged HyTES Focal Plane Array and flex cable attachment. The QWIP focal plane is split into two regions to cover the system bandwidth requirements. Region one is sensitive to the 7.5–10  $\mu\text{m}$  region while region 2 is sensitive to the 10–12  $\mu\text{m}$  region. Figure 5.13 shows two pictures taken using the full QWIP array in an external camera.

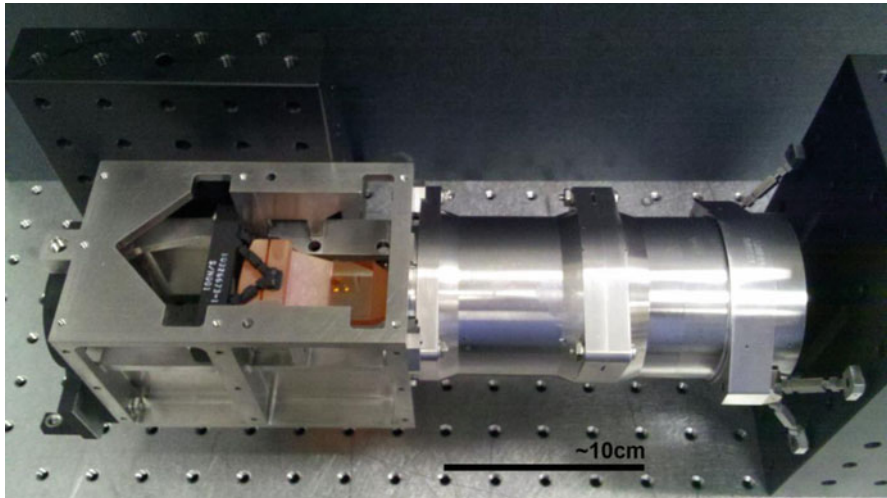


**Fig. 5.10** Assembled grating, relay and spectrometer housing. See Fig. 5.2 for a ray trace of the assembly

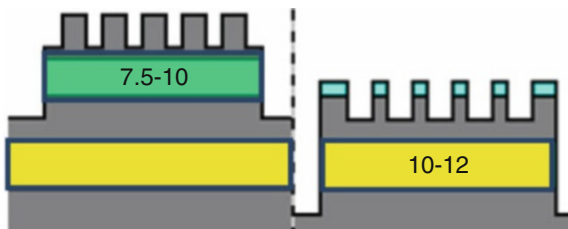


**Fig. 5.11** HyTES pixel design – cross-sectional zoom at the transition point, showing two bands with  $\frac{1}{4}$  lambda gratings on each. Light enters from the *bottom* of the diagram and is diffracted by the grating on *top*. The grating diffracts the light at a nearly horizontal direction. It is absorbed by the intervening material (shown as two different colors on the figure), converted to electrical signal and sent to the readout

### 5.2.8 System Integration

Both QWEST and HyTES used a vacuum chamber to keep the focal plane and system cold. The QWEST chamber used liquid helium whereas the HyTES system uses two mechanical cryocoolers. In QWEST the telescope was external to the vacuum chamber and therefore contributed considerable self emission to the measurement whereas in HyTES the telescope is incorporated in the cryovacuum system thereby minimizing any self emission. In QWEST, the focal plane was held at 40 K and the surrounding components allowed to self equilibrate with the vacuum chamber which resulted in strong thermal gradients in the system. The HyTES vacuum chamber uses two cryocoolers (Fig. 5.14). The chamber has

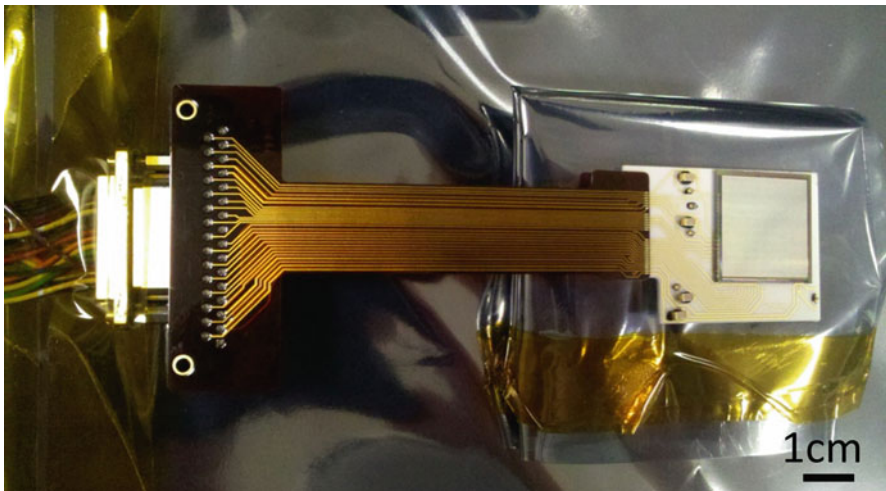


**Fig. 5.12** Small form factor HyTES focal plane array analog electronics. Traces on a single layer ceramic board is used to send all electrical signals from the readout electronics to the analog-to-digital converters. A flex cable is used to minimize the thermal footprint, since this is the coldest part of the instrument



**Fig. 5.13** Two images taken with the HyTES 1 K  $\times$  1 K QWIP array, the first author is on the *left*. The images show that most pixels appear to be active. There's very little “dead” pixels. The image on the *left* uses a single point correction and the image on the *right* uses a two point correction. A single point correction typically takes out any offset present in the system while the 2-point correction typically removes bias and gain. There's an obvious improvement in terms of image uniformity between the two images

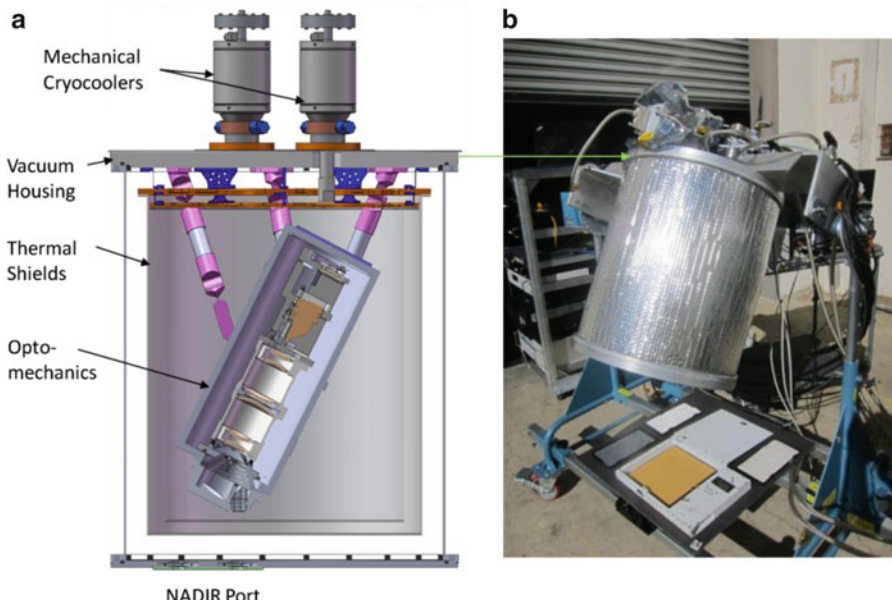


**Fig. 5.14** (a) Schematic of the HyTES system showing two cryocoolers. (b) HyTES system is shown during field operation. Various mineralogical targets are positioned at the NADIR port. Emissivity spectrum is recovered as a function of field angle to show system performance

already been proven to support airborne operation for other VSWIR instruments while maintaining rigidity of its inner precision optical components.

The focal plane reaches its operating temperature in about 4 h whereas the rest of the system takes about 26 h to reach operating temperature.

### 5.2.9 System Testing

QWEST has been tested extensively whereas the HyTES system is complete and under test prior to the first airborne flights expected in late 2012. The radiometric performance of QWEST and HyTES was assessed by performing a National Institute of Standards and Technology (NIST) traceable transfer calibration, using an electro-optic blackbody to verify performance, between two end bracket temperatures of 5 and 30 °C. JPL has multiple NIST traceable blackbodies with a stability at 25 °C of  $\pm 0.0007$  °C and a thermistor standard probe with an accuracy of 0.0015 °C over 0–60 °C and stability/yr of 0.005 °C. A 2-point non-uniformity correction was then applied using the blackbody measurements at 5 and 30 °C (Perry and Dereniak 1993; Mooney et al. 1989). In order to evaluate the instrument performance the external blackbody was then ramped from 5 to 30 °C in 5 °C and

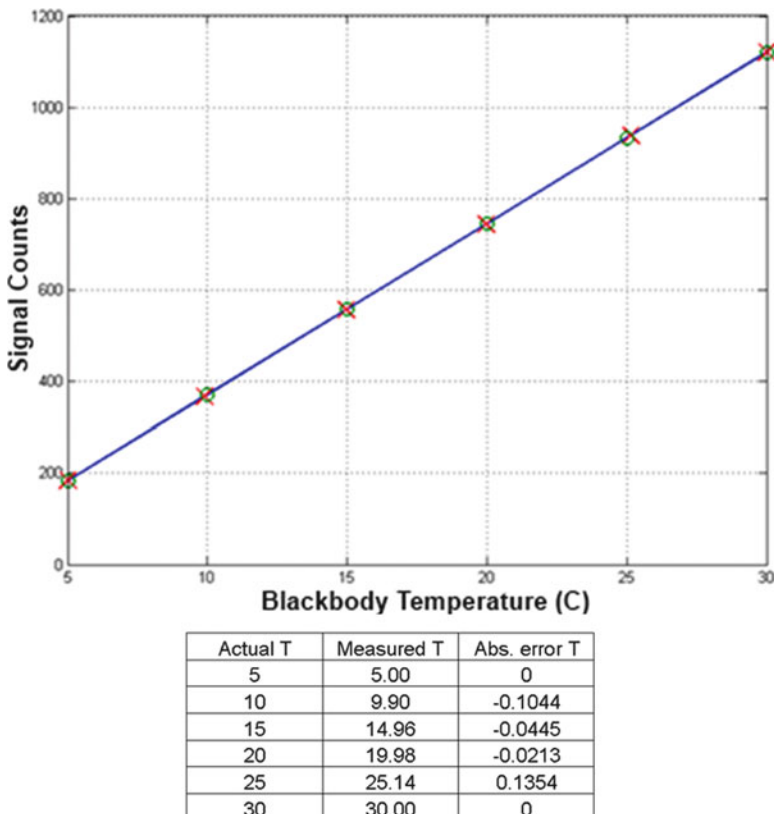


**Fig. 5.15** Basic QWEST linearity, (Top) Chart plotted with respect to a straight line showing deviation of the QWEST measurement from the blackbody measurement and (Bottom) actual readings and absolute error

its radiation measured with the sensor (HyTES or QWEST) after the blackbody is stable at each of the temperature increments. Frames are taken at each interval to check for both temporal artifacts and single frame noise equivalent temperature difference per spectral band as well as determining any spectral non-linearity.

Two tests were performed to characterize the instrument performance. Test one was for spectral linearity while the other determined the spectral noise equivalent delta temperature (NEdT). Figure 5.15 shows that QWEST has very good linearity with many temperature measurements showing absolute errors below 0.1 °C. Figure 5.16 shows the noise equivalent delta temperature for spectral channels at blackbody temperatures between 5 and 30 °C. This implies that for a given temperature between this range QWEST has a mean NEdT of 124.7 mK.

The QWEST system was then operated outdoors under direct sunlight to understand and characterize the science usefulness of the instrument towards remote sensing earth science applications. Testing involved using the same approach as

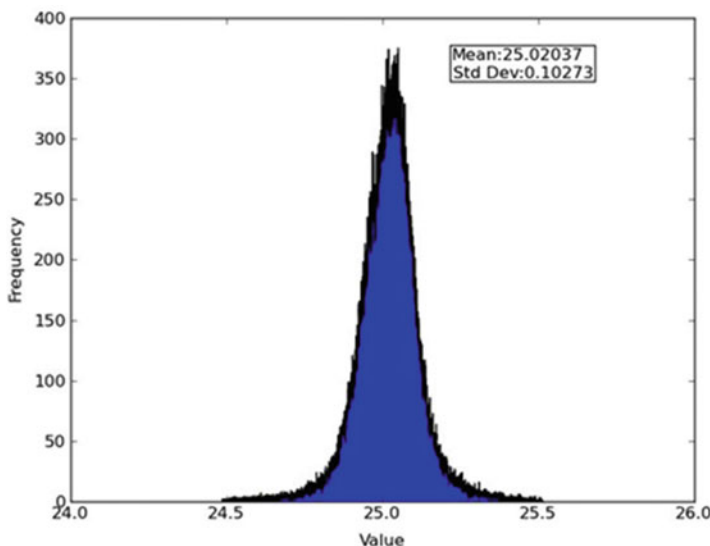


**Fig. 5.16** Frame (Temporal) Mean Histogram. The mean value shown corresponds well with the expected linearity and the standard deviation is a measure of the noise equivalent temperature difference

outlined in Hook and Kahle (1996). A spectral calibration of the system is performed by observing a gold plate illuminated with direct sunlight; the reflected sky radiation shows the atmospheric water lines and these can then be matched with their known positions. An assessment of a retrieval was then performed by looking at a laboratory sample of quartz and retrieving the quartz spectrum. The data shown uses an integration time of 30 ms and the measurements were made around solar noon. Figure 5.17 shows the radiance calculated for a gold standard; the atmospheric water lines are clearly apparent. The data were proven to be both spectrally and radiometrically accurate.

These data are then used in part to further reduce data taken with the system in direct sunlight. Once the atmospheric water lines are removed the spectral features present in a sample of Quartz are clearly apparent (Fig. 5.18). This spectrum compares favorably with previously taken data in the laboratory using a reflectance measurement and provided in the ASTER spectral library (Baldridge et al. 2009).

As noted above HyTES laboratory testing is still underway but initial results are very promising. Figure 5.19 shows the NEdT performance of HyTES using the same approach described with QWEST.

Figure 5.19 shows that HyTES has a good NEdT from 7.5 to 11.5  $\mu\text{m}$  and meets the desired specification of better than 0.2 K. The NEdT plot was generated using an integration time similar to that required for the lowest altitude flights. Higher altitude flights would have more integration with further improvement. Figures 5.20 and 5.21 provide examples of measurements made with HyTES in the laboratory by

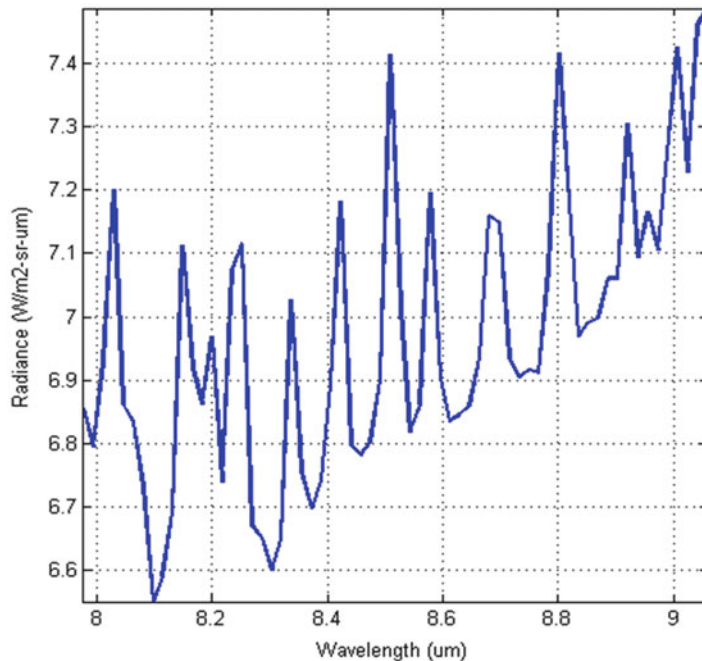


**Fig. 5.17** Radiance of gold standard with superimposed atmospheric bands as measured in direct sunlight

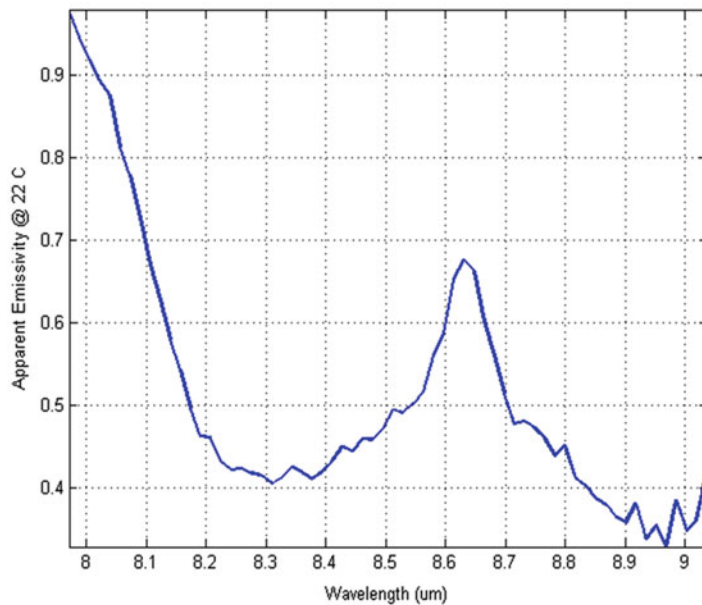


**Fig. 5.18** Apparent emissivity of quartz as measured by QWEST in direct sunlight

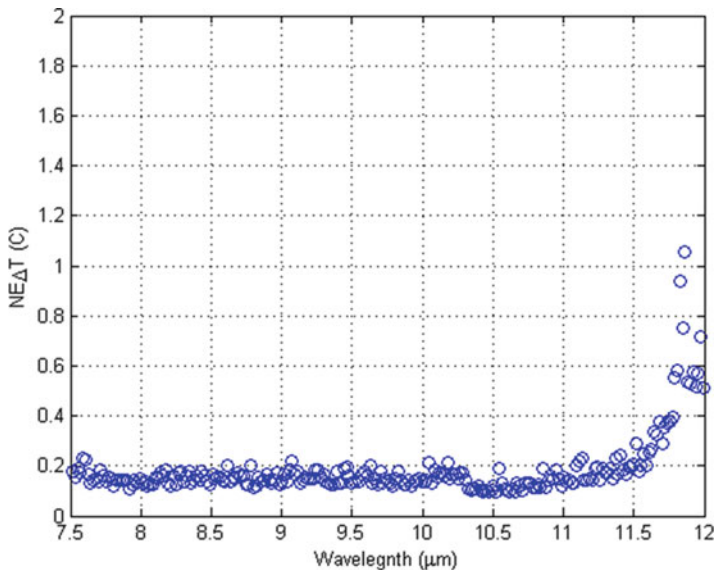


**Fig. 5.19** HyTES spectral noise equivalent temperature difference (NE $\Delta$ T). The distribution is shown for all spectral channels. The scene was composed of a 25 °C blackbody target. Measurements were made for a calibrated blackbody between 5 and 45 °C

first calibrating HyTES and then placing the sample at the entrance. These spectra clearly indicate that HyTES can be used to measure emissivity spectra but further work is needed to establish the full instrument performance in the laboratory before flights later in 2012.

### 5.3 Future Perspective

The HyTES system represents a major step forward in airborne thermal infrared (TIR) remote sensing and will provide the first ever high spatial, spectral and wide swath thermal infrared imagery that will be routinely available to the research community. This contrasts with similar high spectral, spatial and wide swath imaging instruments operating in the visible to shortwave infrared (VSWIR) such as AVIRIS which have been available for over a decade. This discrepancy arose due to the additional technological challenges that needed to be overcome to make equivalent measurements in the TIR compared with the VSWIR. QWEST and HyTES demonstrate that these technological challenges have been largely overcome but further work is needed, especially in the detector arena, to obtain the highest possible quality data. QWEST and HyTES represent the culmination of many years of research. We fully expect that HyTES will provide a wealth of new scientific data which will open new avenues of research in a similar way that

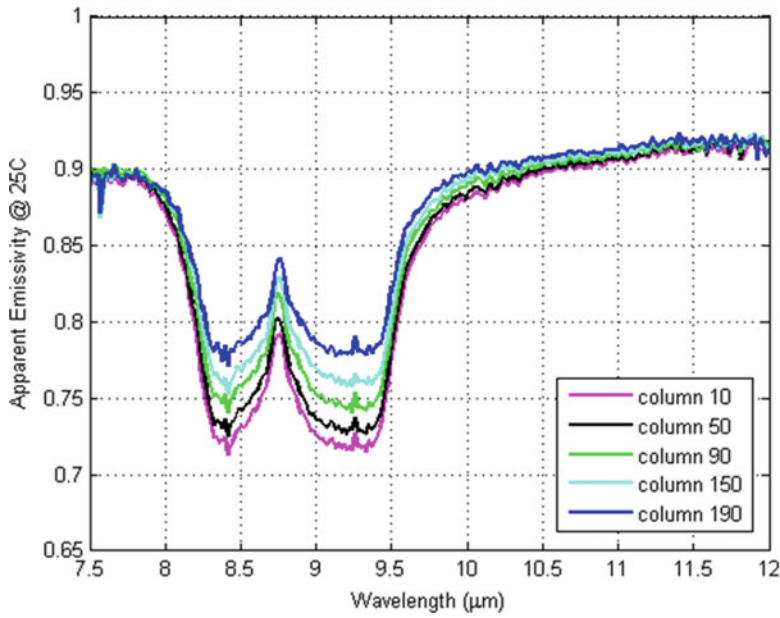


**Fig. 5.20** Example emissivity spectra retrieved from samples of quartz with HyTES in the laboratory. Ottawa sand is mostly composed of quartz. The quartz doublet is clearly visible in the emissivity spectrum. Different pixel values are shown. Each pixel value represents a different cross track field angle. The absolute value of the spectra differs due to an artifact in the measurement process

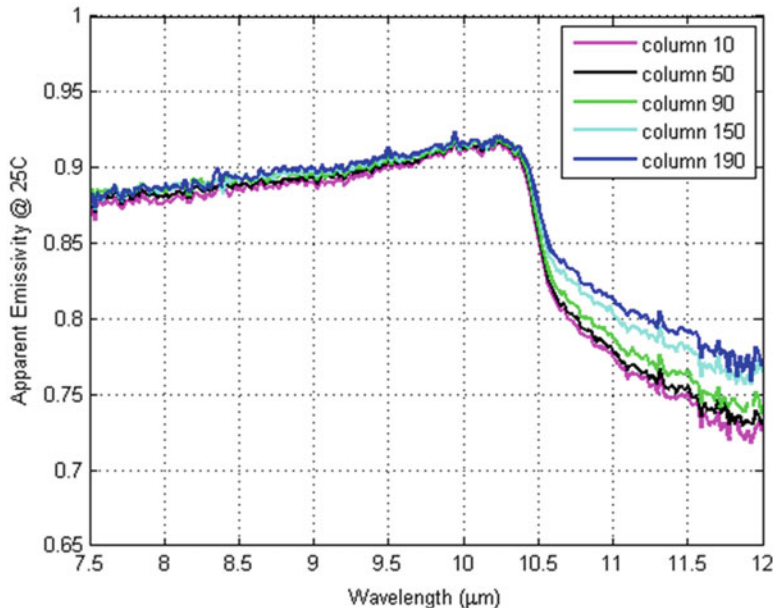


**Fig. 5.21** Example emissivity spectra retrieved from samples of Silicon Carbide with HyTES in the laboratory. The absolute value of the spectra differs due to an artifact in the measurement process

AVIRIS opened up new research avenues for Earth and Planetary research. While HyTES represents the state of the art in terms of airborne measurements, the multichannel HypsIRI TIR represents the next step in spaceborne measurements and it seems likely that in the future we will see both VSWIR and TIR hyperspectral land imagers in space.

**Acknowledgements** Work by Hook, Johnson and Abrams was performed at the Jet Propulsion Laboratory, California Institute of Technology, under contract with the National Aeronautics and Space Administration.

## References

- Baldridge A, Hook S, Grove C, Rivera R (2009) The ASTER spectral library version 2.0. *Remote Sens Environ* 113:711–715
- Bianchi R, Marino C, Pignatti S (1994) Airborne hyperspectral remote sensing in Italy. *SPIE* 2318:29–37
- Chrisp MP (1999) Convex diffraction grating imaging spectrometer. US Patent 5,880,834
- Christensen PR, Bandfield JL, Hamilton VE, Howard DA, Lane MD, Piatek JL, Ruff SW, Stefanov WL (2000) A thermal emission spectral library of rock-forming minerals. *J Geophys Res-Planet* 105:9735–9739
- Gunapala SD, Bandara SV, Liu JK, Mumolo JM, Hill CJ, Kurth E, Woolaway J, LeVan PD, Tidrow MZ (2007) Towards dualband megapixel QWIP focal plane arrays. *Infrared Phys Technol* 50:217–226
- Hackwell J, Warren D, Bongiovi R, Hansel S, Hayhurst T, Mabry D, Sivjee M, Skinner J (1996) LWIR/MWIR imaging hyperspectral sensor for airborne and ground based remote sensing. *SPIE* 2819:102–107
- Hook SJ, Kahle AB (1996) The micro Fourier transform interferometer. *Remote Sens Environ* 56:172–181
- Hook S, Gabell A, Green A (1992) A comparison of techniques for extracting emissivity information from thermal infrared data for geologic studies. *Remote Sens Environ* 42:123–135
- Hook SJ, Myers J, Thome K, Fitzgerald M, Kahle A (2001) The MODIS/ASTER airborne simulator (MASTER) – a new instrument for earth science studies. *Remote Sens Environ* 76:93–102
- Hulley GC, Hook SJ (2011) Generating consistent land surface temperature and emissivity products between ASTER and MODIS data for earth science research. *IEEE Trans Geosci Remote Sens* 49:1304–1315
- HypsIRI Group (2009) NASA 2008 HypsIRI Whitepaper and workshop report. JPL Publication 09-19. Jet Propulsion Laboratory, Pasadena
- Kahle A, Rowan L (1980) Evaluation of multispectral middle infrared images for lithologic mapping in the East Tintic Mountains, Utah. *Geology* 8:234–239
- Kirkland L, Herr K, Keim E (2002) First use of an airborne hyperspectral scanner for compositional mapping. *Remote Sens Environ* 80:447–459
- Kuester MA, Lasnik JK, Ramond T, Lin T, Johnson B, Kapchen P, Good W (2007) Airborne prototype instrument suite test flight of a low-light high-dynamic range imager and visible spectrometer, *SPIE* 6677:667710
- Kwo D, Lawrence G, Chrisp M (1987) Design of a grating spectrometer from a 1:1 Offner mirror system. *SPIE* 818:275–279
- Lobb DR (1994) Theory of concentric designs for grating spectrometers. *Appl Opt* 33:2648–2658
- Mertz L (1977) Concentric spectrographs. *Appl Opt* 16:3122–3124

- Mooney JM, Shepard ED, Ewing WS, Murguia JE, Silverman J (1989) Response nonuniformity limited performance of infrared staring cameras. *Opt Eng* 28:1151–1161
- Mouroulis P, Green RO, Chrien TG (2000) Design of pushbroom imaging spectrometers for optimum recovery of spectroscopic and spatial information. *Appl Opt* 39:2210–2220
- NRC (2007) Earth Science and applications from space: national imperatives for the next decade and beyond. Committee on Earth Science and Applications from Space: a Community Assessment and Strategy for the Future. National Academies Press. Referred to as the Decadal Survey or NRC 2007, 456pp
- Offner A (1973) Unit power imaging catoptric anastigmat. U.S. Patent No. 3,748,015
- Ormsby J (1982) The use of Landsat-3 thermal data to help differentiate land covers. *Remote Sens Environ* 12:97–105
- Perry DL, Dereniak EL (1993) Linear theory of non uniformity correction in infrared staring sensors. *Opt Eng* 32:1853–1859
- Pierce L, Running R, Riggs G (1990) Remote detection of canopy water-stress in coniferous forests using the NS001 thematic mapper simulator and the thermal infrared multispectral scanner. *Photogramm Eng Remote Sens* 56:579–586
- Vincent R (1972) Rock-type discrimination from ratioed infrared scanner images of Pisgah Crater, California. *Science* 175:986–988
- Warren DW, Gutierrez DA, Keim ER (2008) Dyson spectrometers for high-performance infrared applications. *Opt Eng* 47:103601
- Wilson D, Maker WPD, Muller RE, Mouroulis PZ, Backlund J (2003) Recent advances in blazed grating fabrication by electron-beam lithography. *SPIE* 5173:115–126
- Wynne CG (1987) Monocentric telescopes for microlithography. *Opt Eng* 26:300–303
- URL1: <http://hyperspectral.jpl.nasa.gov/documents>
- URL2: [http://science.nasa.gov/media/medialibrary/2010/07/01/Climate\\_Architecture\\_Final.pdf](http://science.nasa.gov/media/medialibrary/2010/07/01/Climate_Architecture_Final.pdf)

# Chapter 6

## NASA's Hyperspectral Infrared Imager (HyspIRI)

Michael J. Abrams and Simon J. Hook

**Abstract** NASA's Hyperspectral and Infrared Imager (HyspIRI) mission is one of the missions recommended in the National Research Council Earth Science Decadal Survey. HyspIRI will fly two instruments: a hyperspectral visible to short wave infrared imaging spectrometer, and a multispectral thermal infrared (TIR) imager. In this study we discuss the expected performance and use of the TIR instrument. The TIR instrument will have eight spectral channels, seven of the channels are between 7 and 12  $\mu\text{m}$ , with one additional channel at 4  $\mu\text{m}$ . The TIR instrument will have a swath width of 600 km, and pixel size of 60 m. HyspIRI TIR will provide two visits every 5 days (one day and one night) at the equator, and more frequently at higher latitudes. The TIR instrument will always be on and full resolution (60 m) data will be downlinked for the entire land surface including the coastal oceans (shallower than 50 m depth). Data over the deeper ocean will also be downlinked but at a reduced spatial resolution of 1 km. In response to the Decadal Survey, HyspIRI has been designed to answer important science questions in the areas of coastal, ocean and inland aquatic environments; wildfires; volcanoes; ecosystem function and diversity; land surface composition and change; and human health and urbanization. NASA's Distributed Active Archive Center will archive and distribute Level 0 to Level 2 products. In addition a direct broadcast capability will allow users to capture and process a subset of HyspIRI data in near real time.

---

M.J. Abrams (✉) • S.J. Hook

Jet Propulsion Laboratory, California Institute of Technology, National Aeronautics and Space Administration (NASA), Pasadena, CA, USA  
e-mail: [Mjabrams@jpl.nasa.gov](mailto:Mjabrams@jpl.nasa.gov)

## 6.1 Introduction

### 6.1.1 *The Decadal Survey*

In 2004, the U.S. NASA (National Aeronautics and Space Administration) commissioned the National Research Council (NRC) to conduct a Decadal Survey (DS) for Earth science and applications from space. The 2007 report is titled *Earth Science and Applications from Space: National Imperatives for the next Decade and Beyond* (NRC 2007). The purpose of this study was to provide NASA with a blueprint for the next 10 years, prioritizing science missions, in response to community inputs and recommendations. The report identified key science measurements and recommended a small number of missions to acquire those measurements. The topical areas included earth science applications and societal benefits; land use change, ecosystem dynamics, and biodiversity; weather; climate variability and change; water resources and the global hydrologic cycle; human health and security; and solid earth hazards, resources and dynamics.

Included in the recommended missions was the Hyperspectral and Infrared Imager (HyspIRI) that would provide global observations at local and landscape scales (10s of meters to 100s of kilometers). The mission would include a hyperspectral visible-near infrared-shortwave infrared (VSWIR) imaging spectrometer, and a multispectral thermal infrared (TIR) scanner. Operating from low earth orbit, the instruments would provide global coverage, frequent repeat revisits, and data at adequate spatial resolution. The DS laid out a timeline to implement the missions: HyspIRI was included in the second tier, with recommended launch dates in the 2013–2016 timeframe. NASA assigned preliminary study activities for HyspIRI to the Jet Propulsion Laboratory (JPL). Dr. Robert Green headed up the studies for the VSWIR hyperspectral instrument, and Dr. Simon Hook was responsible for the TIR instrument. This chapter describes the TIR component of HyspIRI.

### 6.1.2 *Heritage*

HyspIRI's thermal infrared sensor draws its heritage from several spaceborne missions, and airborne instruments. Acquisition of moderate spatial resolution TIR data from satellite instruments ( $\sim$ 100 m) with TIR capability are dominated by two instruments. The long series of Landsat scanners, operated by NASA, have provided global data since 1972. In 1978, the Landsat Multispectral Scanner added a 240 m 10–12  $\mu\text{m}$  channel (Ormsby 1982). Since 1982, all the versions of the Landsat Thematic Mapper scanner have included a single broad band TIR channel, typically covering the 8–12  $\mu\text{m}$  wavelength region. Pixel sizes have varied from 60 to 120 m. Single channel instruments measure brightness temperature, which includes the temperature and emissivity of the surface being observed. Single channel instruments cannot be used to recover the surface temperature unless the

emissivity is assumed or the emissivity unless the temperature is assumed. For perfect blackbodies, the brightness and kinetic temperatures are the same. For bare areas in the real world (i.e., rocks and soils, and excluding water and vegetation), the difference between brightness and kinetic temperatures can be several degrees Celsius. Since 1999, NASA and METI (Japan's Ministry of Economy, Trade and Industry) have jointly operated the ASTER (Advanced Spaceborne Thermal Emission and Reflection Radiometer) instrument on NASA's Terra platform (Yamaguchi et al. 1998). ASTER includes a multispectral thermal scanner, with five channels in the 8–12  $\mu\text{m}$  region, 90 m pixel size, and 60 km swath width. Because of its multispectral data, surface kinetic temperature and emissivity can be recovered from ASTER data. This information can then be used to map surface composition, and as accurate inputs to climate models.

Both Landsat and ASTER have operational shortcomings: either they have a single TIR channel, and are not multispectral (Landsat), or they do not provide systematic global coverage (ASTER). HyspIRI seeks to improve on both of these scanners by providing multispectral TIR data, and global coverage with frequent revisits.

Several other spaceborne instruments have had a relatively short lifetime, and limited capabilities. The DLR's (German Aerospace Center) BIRD (Bi-Spectral Infrared Detection) scanner (Briess et al. 2000) had two MWIR (mid-wave infrared)/TIR channels (3.4–4.2  $\mu\text{m}$  and 8.5–9.3  $\mu\text{m}$ ), designed to detect and measure elevated temperatures produced by, for example, forest fires and volcanic eruptions. BIRD was designed with a 290 m pixel size, and 145 km swath width. BIRD operated nominally from 2002 to 2004, and irregularly for several years after. The U.S. Department of Energy sponsored the Multispectral Thermal Imager (MTI), launched in 2000 with highly restricted access to data. The instrument had a 12 km swath width, 20 m pixel size, 2 bands in the 3.5–5  $\mu\text{m}$  region, and 3 bands in the 8–10.7  $\mu\text{m}$  region (Szymanski and Weber 2005). Several members of the HyspIRI study team were investigators with access to MTI data; their experiences went into the HyspIRI TIR concept.

It is ironic that the most advanced spaceborne multi-band TIR instrument is currently orbiting Mars. The Thermal Emission Imaging System (THEMIS) is a scanner on the Mars Odyssey spacecraft. It combines a 5-band visual imaging system with 20 m pixels; and a 9-band TIR imaging system with 100 m pixels (Christensen et al. 2003). THEMIS data have helped to unlock Martian mysteries related to presence of water on the planet, composition of rocks, and the geologic history of the planet.

TIR aircraft instruments have been operating since the early 1970s. The first work was with a two-channel instrument (Vincent 1972). By ratioing values from two thermal bands, emissivity differences could be detected in the resulting image, and these were related to differences in rock type. In the early 1980s, NASA started operating the Thermal Infrared Multispectral Scanner (TIMS), a 6-channel airborne instrument with bands in the 8–12  $\mu\text{m}$  wavelength region (Kahle and Rowan 1980). TIMS was the first operational scanner that acquired multispectral TIR data allowing separation of temperature and emissivity (T-E). Many researchers

developed techniques to solve the under-determined T-E problem, and accurate retrievals of both values is now routine. TIMS flew for more than 15 years before being replaced by a 10-channel TIR instrument, the MODIS (Moderate Resolution Imaging Spectrometer)/ASTER (MASTER) 50 channel instrument (Hook et al. 2001). In addition to 10 bands in the 8–12  $\mu\text{m}$  region, MASTER has channels in the 3–5  $\mu\text{m}$  region. In Europe, the 102-channel MIVIS (Multispectral Infrared Visible Imaging Spectrometer) scanner, owned and operated by Italy’s National Research Council, has acquired data since 1994 for many researchers. MIVIS has 10 channels in the 8.2–12.7  $\mu\text{m}$  region (Bianchi et al. 1994). The U.S. Aerospace Corporation developed the SEBASS (Spatially Enhanced Broadband Array Spectrograph System) scanner and first deployed it in 1995 (Hackwell et al. 1996). SEBASS has 128 bands in each of the 3.0–5.5  $\mu\text{m}$  and 7.8–13.5  $\mu\text{m}$  regions. The instrument images 128 pixels cross-track with an instantaneous field of view (IFOV) of 1 mrad.

In the last 40 years, a large and growing research community has developed to study and expand applications of TIR data over a wide range of earth science disciplines. Working with laboratory measurements, field spectrometers, aircraft data, and data from spaceborne instruments, researchers have compiled spectral libraries of surface materials (Christensen et al. 2000; Baldridge et al. 2009); developed techniques to extract surface compositional information from airborne hyperspectral TIR data (Kirkland et al. 2002; Hook et al. 1992); detected canopy water stress in coniferous forests (Pierce et al. 1990); and refined determination of land surface temperature and emissivity (Hulley and Hook 2011), to name just a few. It was the combined voice of this TIR user community that convinced the NRC of the need for HyspIRI.

### **6.1.3 Science Objectives**

The following description of the HyspIRI mission draws heavily on the 2008 HyspIRI Whitepaper and Science Workshop Report available online ([URL1](#)).

HyspIRI is a science-driven mission, developed to address the science questions called out in the Decadal Survey. These have been further developed by the HyspIRI Science Study Group under six topic areas. Both the TIR and VSWIR instruments are required to answer important science questions:

1. Coastal, Ocean and Inland Aquatic Environments: The oceans and inland aquatic environments are a critical part of global climate, the hydrologic cycle, and biodiversity. HyspIRI will allow for greatly improved separation of phytoplankton pigments, better retrievals of chlorophyll content, more accurate retrievals of biogeochemical constituents of the water, and more accurate determination of physical properties, including water temperature derived from TIR channels (GEO 2007).
2. Wildfires: The 4  $\mu\text{m}$  channel will greatly improve determination of fire temperatures, since it will not saturate like almost all other sensors with a similar

wavelength channel. Coupling the multispectral TIR data with the VSWIR data will improve understanding of the coupling between fires and vegetation and associated trace gas emissions (Dennison et al. 2006).

3. Volcanoes: HyspIRI's TIR channels will allow combined measurement of temperature, surface composition, and SO<sub>2</sub> emissions. These three parameters are critical to understand changes in a volcano's behavior that may herald an impending eruption. Fumaroles, lava lakes, and crater lakes often undergo characteristic increases in temperature associated with upwelling magma; SO<sub>2</sub> emissions both increase and decrease before some eruptions. Prediction of lava flow progress depends entirely on knowledge of effusion rate and temperature (Wright et al. 2008).
4. Ecosystem Function and Diversity: HyspIRI will provide improved measures of plant physiological function through simultaneous estimates of surface temperature and plant biochemistry, improved estimates of surface biophysical properties (e.g. albedo or crown mortality) and energy balance and improved discrimination of plant species and functional types. No current sensor can simultaneously retrieve canopy temperature and quantify physiological or compositional changes in response to stress.
5. Land Surface Composition and Change: Combining information from the hyperspectral VSWIR and TIR scanners will greatly improve our ability to discriminate and identify surface materials: rocks, soils and vegetation. This is the first step to be able to quantitatively measure change of the land surface, whether naturally caused or of anthropogenic origin. Change detection, monitoring, and mapping forms the basis for formulating numerous policy decisions, from controlling deforestation to open-pit mining. HyspIRI will provide a greatly improved tool to make more informed and intelligent decisions.
6. Human Health and Urbanization: It appears that the world's urban population will grow by over 60 % by 2030 (UNIS 2004). Because of its enhanced hyperspectral capabilities in the VSWIR bandwidths and its multiple channels in the TIR, HyspIRI will provide much better data to improve measurement and modeling of urban characteristics around the world. One of the issues that has been problematic in the past is retrieving accurate measurements of temperature, albedo, and emissivity for specific surfaces across the complex and heterogeneous urban landscape. HyspIRI has the spatial resolution, spectral coverage, and repeat cycle to greatly improve these retrievals.

## 6.2 Instrument Description

HyspIRI TIR is a science driven instrument. A science study group, representing a broad range of science disciplines, formulated the important science questions that a TIR (and combined TIR-VSWIR) instrument could address. The questions were used to help formulate instrument requirements and mission operation parameters (HyspIRI Group 2009). Through a series of trade-offs with the engineering experts,

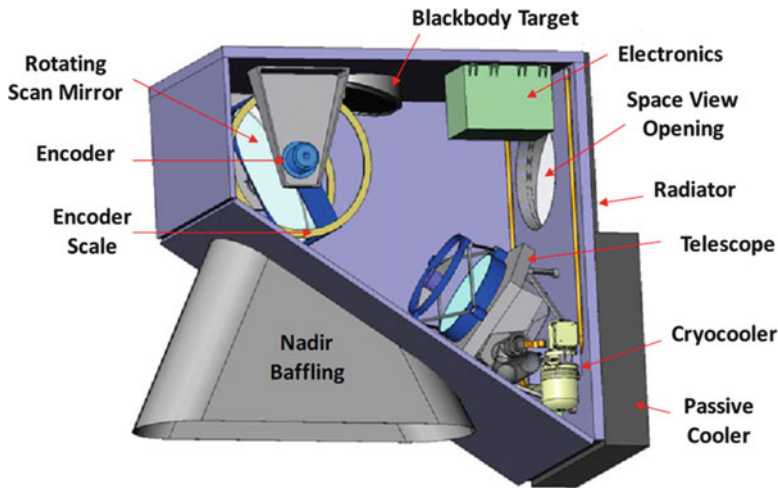


**Fig. 6.1** Conceptual drawing showing cutaway view of HypsIRI TIR instrument

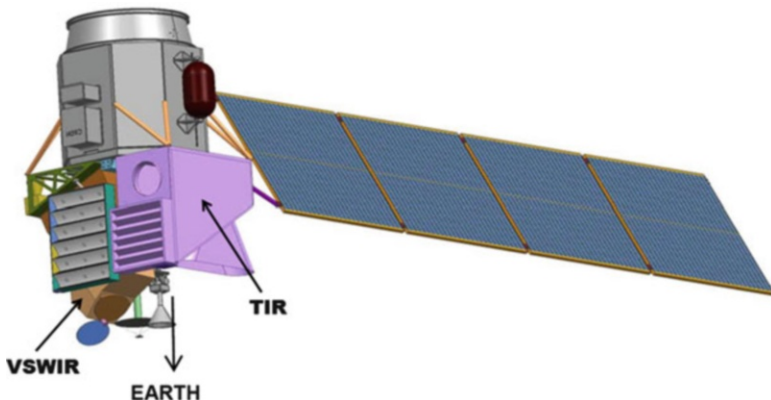


**Fig. 6.2** Conceptual drawing of HypsIRI TIR and VSWIR instruments in orbit

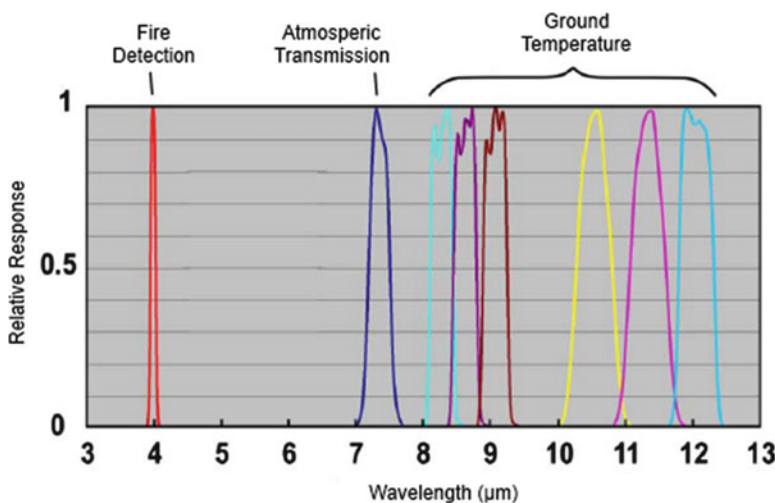
a TIR instrument was designed that met the great majority of the science requirements, while satisfying budgetary constraints on mission costs.

Based on these considerations, the TIR instrument was designed as a whisk-push broom scanner with reflective optics to image a 600 km swath width at 60 m pixel size (Fig. 6.1). It has an on-board blackbody and an opening to look towards deep space at every scan; both of these are for calibration. The TIR and VSWIR instruments are configured together on a single spacecraft bus (Fig. 6.2).

The number and position of the spectral bands were considered based on experience gained from the heritage instruments (primarily spaceborne ASTER and MODIS, and airborne TIMS and MASTER), and systematic studies of saturation levels for hot target measurement. Table 6.1 summarizes the spectral and

**Table 6.1** Instrument characteristics

<b>Spectral</b>	
Bands (8) um	3.98, 7.35, 8.28, 8.63, 9.07, 10.53, 11.33, 12.05 $\mu\text{m}$
Bandwidth	0.084, 0.32, 0.34, 0.35, 0.36, 0.54, 0.54, 0.52 $\mu\text{m}$
Accuracy	<0.01 $\mu\text{m}$
<b>Radiometric</b>	
Range	Bands 2–8 = 200–500 K; band 1 = 1,200 K
Resolution	<0.05 K, Linear quantization to 14 bits
Accuracy	<0.5 K 3-sigma at 250 K
Precision (NEdT)	<0.2 K
Linearity	>99 % characterized to 0.1 %
<b>Spatial</b>	
IFOV	60 m
MTF	>0.65 at FNy
Scan type	Push-whisk
Scan width	600 km ( $\pm 25.5^\circ$ at 623 km altitude)
Cross track samples	10,000
Swath length	15.4 km ( $\pm 0.7^\circ$ at 623 km altitude)
Down track samples	256
Band to band co-registration	0.2 pixels (12 m)
Pointing knowledge	1.5 arcsec (0.1 pixels)

**Fig. 6.3** Proposed HyspIRI TIR spectral band positions in the 4–12  $\mu\text{m}$  wavelength region

radiometric characteristics of TIR: 8 bands, with 7 in the 7.3–12.1  $\mu\text{m}$  thermal infrared region, and one band at 4  $\mu\text{m}$  in the mid infrared region (Fig. 6.3). It is expected that while the number of bands will remain at eight the exact position of the bands within the 4–12  $\mu\text{m}$  window will shift based on ongoing science studies.

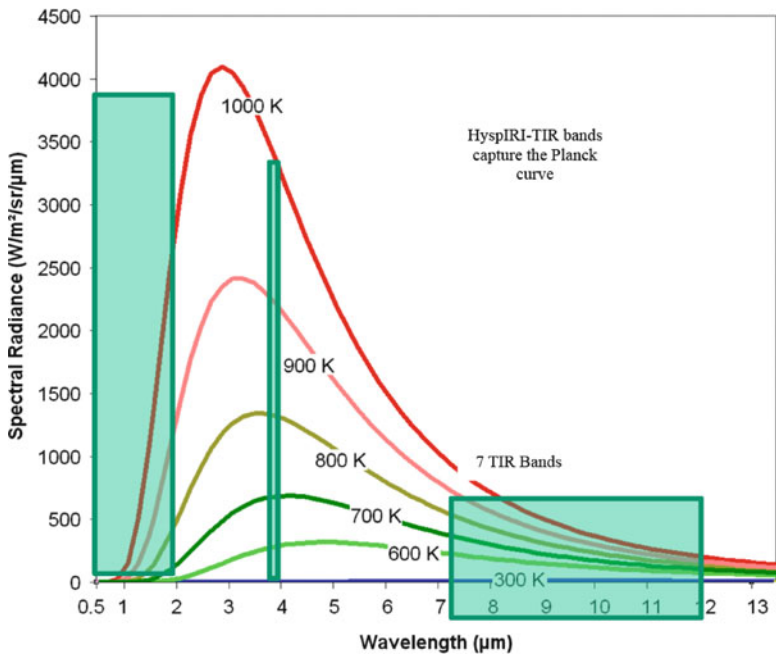


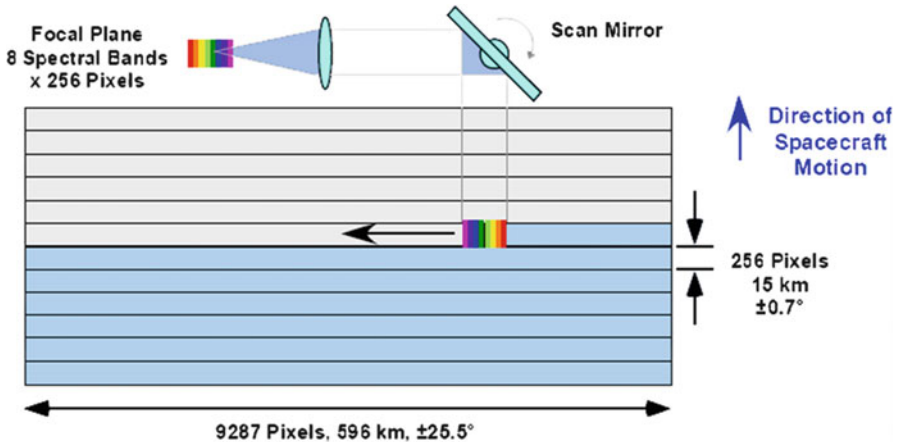
**Fig. 6.4** Thermal emission peaks in the MWIR (3–5  $\mu\text{m}$ ) region for fire temperatures ranging from  $\sim 650$  K (weak smoldering) to  $>1,200$  K (strong flaming). MIR is far more sensitive to hot targets than TIR

These studies will capitalize on new data from the Hyperspectral Thermal Emission Spectrometer (HYTEs – see subsequent chapter).

The current placement of 3 of the TIR bands closely matches the first 3 thermal bands of ASTER (8.28, 8.63, 9.07  $\mu\text{m}$ ); the position of 2 of the thermal bands is patterned after MODIS's bands 31 and 32 (7.35, 12.05  $\mu\text{m}$ ) used for split window applications. The study of hot targets is a key objective of HyspIRI TIR (volcanoes and wildfires). An exhaustive study (Realmuto et al. 2011) of all of the historic measurements made with instruments having a 4  $\mu\text{m}$  channel indicated that saturation was a problem for the hottest targets. Systematic simulations of peak lava flow and wildfire temperatures led to setting the saturation temperature of the 4  $\mu\text{m}$  band at 1,200 K, far higher than the  $\sim 500$  K value used by all previous instruments. The saturation temperature for the TIR channels was set at 500 K to provide excellent resolution and sensitivity to a wide range of terrestrial temperatures (Fig. 6.4). Quantization was set at 14-bits to fully capture information provided by a precision (NEDT or Noise Equivalent Delta Temperature) of  $<0.2$  K. Radiometric accuracy will be assured by using an on-board blackbody and view to deep space included as part of every 256-line scan. In addition, ground-based validation field campaigns will be performed several times per year; and periodic lunar views will be used to characterize imaging anomalies (Table 6.2).

**Table 6.2** Instrument characteristics (continued)

<b>Temporal</b>	
Orbit crossing	11 a.m. sun synchronous descending
Global land repeat	5 days at equator
<b>On orbit calibration</b>	
Lunar views	1 per month (radiometric)
Blackbody views	1 per scan (radiometric)
Deep space views	1 per scan (radiometric)
Surface cal experiments	2 (d/n) every 5 days (radiometric)
Spectral surface cal experiments	1 per year
<b>Data collection</b>	
Time coverage	Day and night
Land coverage	Land surface above sea level
Water coverage	Coastal zone –50 m and shallower
Open ocean	Averaged to 1 km spatial sampling
Compression	2:1 lossless

**Fig. 6.5** Diagram of cross-track scan and data rate for HyspIRI

The instrument employs a rotating scan mirror to sweep across the scene as the spacecraft advances. A swath of 256 lines, covering 15 km, is captured at each scan and imaged onto the  $8 \times 256$  element focal plane (Fig. 6.5).

With its 9,287 cross track pixels, and 60 m pixel size, the TIR instrument will image a swath of 600 km along its near-polar orbit. This will permit a revisit interval of 5 days at the equator during the daytime, and similar repeat coverage at nighttime. Band-to-band co-registration is expected to be 0.2 pixels (12 m). The time-averaged science data rate is 0.024 Gbps, based on the following assumptions: 14 bits data, 2:1 compression, 40 % of data over land, scan mirror rotation rate of 14.2 RPM, and pixel dwell time of 32 microseconds.

### 6.3 Mission Concept

HyspIRI will fly in a sun-synchronous, near polar ( $83^{\circ}$  inclination), low earth orbit (625 km); the overpass time will be late morning. At the equator, the TIR scanner provides a 5 day revisit in the daytime, and another 5 day revisit at night. At higher latitudes, the combined day-night revisit times are more frequent; for example, Alaska can be imaged 1–2 times per day (Fig. 6.6).

The acquisition strategy for HyspIRI TIR is controlled by target maps. The instrument is always on, but there are two modes of data storage: high resolution mode data are acquired over the land area and coastal waters; low resolution mode data are acquired over the open oceans. In the low resolution mode the data are reduced to 1 km spatial resolution. With a dual-mode strategy, mission operations costs are reduced and the instrument can obtain data in a near-autonomous fashion.

The data rate for both instruments combined is 65 Mbps (continuous and averaged), resulting in a daily data volume of 5.5 Tb. This is comparable to currently operating satellites, such as WorldView-1. The HyspIRI satellite will be equipped with 3 Tb of onboard storage capacity. Downlink will be by Dual X band or Ka band.

The satellite also includes an Intelligent Payload Module (IPM) with direct broadcast capability. The IPM taps into the data feed from the instruments and allows a small subset of the data to be downloaded in real time. The IPM is independent of the on board data recording and storage system and connects to the data stream to pull out the desired wavelengths for direct broadcast. Onboard

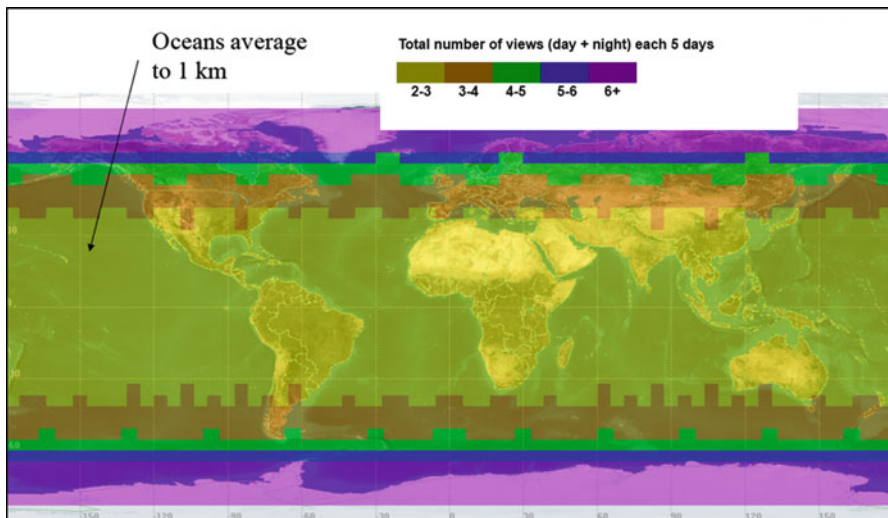


**Fig. 6.6** TIR imaging opportunities: total number of views per day including both day and night observations

computing can address issues to downselect and process data to fit within the reduced downlink bandwidth of 10 Mbps, since the IPM has no storage capacity. Spatial and spectral subsampling can be tailored for many quasi-operational applications, such as observing floods, fires, volcanoes, and other natural disasters. This capability is similar to that provided by NASA's MODIS project. Users will be provided software to process the HyspIRI data at their own receiving sites, thus reducing data latency to a minimum. This scenario has proved enormously effective and popular with the MODIS community, where 150+ users participate with their own receiving stations and processing facilities.

## 6.4 Data Products

HyspIRI is using the same product level definitions as used by NASA's Earth Observing System data systems. Briefly, the levels are described below:

- Level 0—Reconstructed and unprocessed instrument data at full resolution
- Level 1A—Reconstructed unprocessed instrument data at full resolution, time referenced, and annotated with ancillary information such as radiometric and geometric calibration coefficients. These are appended to, but not applied to, the Level 0 data
- Level 1B—Level 1A data with calibration coefficients applied; data are in sensor units (radiance at the sensor)
- Level 2—Derived geophysical variables at the same resolution and location as Level 1
- Level 3—Variables mapped on uniform time-space grid scales
- Level 4—Model output or results from analyses of lower level data (average time series, for example)

It is planned that the HyspIRI project will provide the Level 0 through Level 2 data products. Higher level (Level 3 and 4) products will be provided by the scientific community. The Level 2 data products will include surface radiance, surface reflectance, surface temperature, and surface emissivity. There will also be two cloud masks, one for the VSWIR and the other for the TIR. The Level 0 through Level 2 products will be created for every data granule acquired, and archived for distribution to users.

Data products will be developed at the HyspIRI Science Data System under the control and operation of the mission. For each product, an Algorithm Theoretical Basis Document is prepared, and sent out for peer review. Only when this procedure is satisfied will NASA approve the data products for distribution to the user community. Archiving, storage, and distribution of the Level 0–2 products will be done by one of NASA's Distributed Active Archive Centers.

## 6.5 Future Perspective

As of this writing (November 2011), there are two new NASA-funded aircraft TIR instruments completed, funded by the Earth Science Technology Office (ESTO) in support of the HyspIRI-TIR related activities. The Mineral and Gas Identifier Instrument (MAGI) was developed by the Aerospace Corporation. It has 32 bands covering the 7–12.7  $\mu\text{m}$  region: the higher spectral resolution compared to existing TIR sensors will improve discrimination of rock types, greatly expand the gas detection capability, and result in more accurate land-surface temperature retrieval (Hall et al. 2011). It was funded more specifically to address HyspIRI-type measurement applications such as rock type identification and volcano monitoring. First aircraft flights took place in the fall of 2011.

The second instrument funded by NASA is HyTES (Hyperspectral Thermal Emission Spectrometer), a 256-spectral channel imaging spectrometer. HyTES is being developed at the Jet Propulsion Laboratory (HyTES 2011). Test flights with the completed instrument took place in July, 2012. See the chapter on HyTES in this book for a full description.

Analyses of data from both MAGI and HyTES will be used to refine the positions of HyspIRI's spectral bands. The position and spectral width of HyspIRI's bands have not yet been fixed; changes can still be made based on analysis of data with narrower bands (MAGI), or simulating an infinite range of possible bands (HyTES). It is expected that NASA will fund investigators to use data from these instruments in science research projects related to HyspIRI's primary mission objectives.

What does the immediate future hold for HyspIRI-like spaceborne instruments? The chart in Table 6.3 summarizes related future instrument launches by space-capable countries. Included are hyperspectral VSWIR instruments, and instruments with moderate spatial resolution TIR capability.

Germany (Stuffler et al. 2007), Italy (Prisma 2011), and Japan (Matsunaga et al. 2011) plan to launch VSWIR imaging spectrometers into polar orbits. Their three instruments are all fairly similar, providing ~250 bands in the 0.4–2.5  $\mu\text{m}$  wavelength region with pixel sizes of ~30 m, and swath widths of ~30 km. None of these missions include instruments with any thermal channels. Because of the limited swath widths, none of these missions can provide global coverage. They can be used to target small areas on a repeat basis, allowing for very limited spatial sampling, but fairly frequent temporal coverage. The U.S. launched LDCM (Landsat Data Continuity Mission, or Landsat-8) in 2013 (Irons and Masek 2006), continuing the long series of Thematic Mapper Scanner instruments. Unlike its predecessors, LDCM will have multispectral thermal infrared capability, with two bands at 120 m pixel size. Quantum Well Infrared Photodetectors (QWIP) with saturation temperature set at 360 K (Jhabvala et al. 2009) will limit the usefulness for wildfire and volcanic eruption observations due to saturation over these hot targets.

**Table 6.3** HyspIRI-like instruments scheduled for launch in the next 5 years. HyspIRI's two swath widths are for the VSWIR and the TIR

Country	Instrument	Swath, km	Dates	Coverage in 19 days, %	Mission type	Repeat interval, days	TIR
USA	HyspIRI	150/600	TBD	100	Global	19/5	8 bands
USA	LDCM	185	2013	100	Global	16	2
Germany	EnMAP	30	2017	<1	Sampling/ application	–	No
Italy	PRISMA	30	2013?	~1	Demo/ sampling/ application	–	No
Japan	HISUI	30	2015+	~1	Sampling/ application	–	No

HyspIRI is part of NASA's planned Earth Observation missions, as defined in the Decadal Survey. Budgetary constraints have slowed down the pace of development and launch of satellites compared to the NRC's recommendations. Nevertheless, work continues on refining the TIR instrument design, moving forward with airborne simulators, funding research projects to improve algorithms, and enlarging the user community applying TIR data. We hope to see HyspIRI in orbit within the next 10 years.

**Acknowledgment** Work by Abrams and Hook was performed at the Jet Propulsion Laboratory, California Institute of Technology, under contract with the National Aeronautics and Space Administration.

## References

- Baldridge A, Hook S, Grove C et al (2009) The ASTER spectral library version 2.0. *Remote Sens Environ* 113:711–715
- Bianchi R, Marino C, Pignatti S (1994) Airborne hyperspectral remote sensing in Italy. *SPIE* 2318:29–37
- Briess K, Barwald W, Gerlich T, Jahn H, Lura F, Studemund H (2000) The DLR small satellite mission BIRD. *Acta Astronaut* 46:111–120
- Christensen P, Bandfield J, Hamilton V et al (2000) A thermal emission spectral library of rock-forming minerals. *J Geophys Res Planet* 105:9735–9739
- Christensen P, Bandfield J, Bell J, Gorelick N, Hamilton V, Ivanov A, Jakosky B, Kieffer H, Lane M, Malin M, Mehal G (2003) Morphology and composition of the surface of Mars: Mars Odyssey THEMIS results. *Science* 300:2056–2061
- Dennison P, Charoensiri K, Roberts D, Peterson S, Green R (2006) Wildfire temperature and land cover modeling using hyperspectral data. *Remote Sens Environ* 100:212–222
- GEO (2007) GEO Inland and nearshore coastal water quality remote sensing workshop, Geneva. [http://www.earthobservations.org/meeting/20070327\\_29\\_water\\_quality\\_workshop\\_report.pdf](http://www.earthobservations.org/meeting/20070327_29_water_quality_workshop_report.pdf)
- Hackwell J, Warren D, Bongiovi R, Hansel S, Hayhurst T, Mabry D, Sivjee M, Skinner J (1996) LWIR/MWIR imaging hyperspectral sensor for airborne and ground based remote sensing. *Proc SPIE* 2819:102–107

- Hall J, Gutierrez D, Tratt D, Warren D, Young S, Ramsey M (2011) Mineral and gas identification using a high performance thermal imaging spectrometer. Earth Science Technology Forum 2011, NASA, Pasadena, <http://esto.nasa.gov/conferences/estf2011/index.html>
- Hook S, Gavell A, Green A (1992) A comparison of techniques for extracting emissivity information from thermal infrared data for geologic studies. *Remote Sens Environ* 42:123–135
- Hook S, Myers J, Thome K, Fitzgerald M, Kahle A (2001) The MODIS/ASTER airborne simulator (MASTER) – a new instrument for earth science studies. *Remote Sens Environ* 76:93–102
- Hulley G, Hook S (2011) Generating consistent land surface temperature and emissivity products between ASTER and MODIS data for earth science research. *IEEE Trans Geosci Remote Sens* 49:1304–1315
- HyspIRI Group (2009) NASA 2008 HyspIRI Whitepaper and workshop report. JPL Publication 09-19. Jet Propulsion Laboratory, Pasadena
- HyTES (2011) <http://airbornescience.jpl.nasa.gov/hytes/>
- Irons J, Masek J (2006) Requirements for a Landsat Data Continuity Mission. *Photogramm Eng Remote Sens* 72:1102–1108
- Jhabvala M, Reuter D, Choi K et al (2009) QWIP-based thermal infrared sensor for the Landsat Data Continuity Mission. *Infrared Phys Technol* 52:424–429
- Kahle A, Rowan L (1980) Evaluation of multispectral middle infrared images for lithologic mapping in the East Tintic Mountains, Utah. *Geology* 8:234–239
- Kirkland L, Herr K, Keirn E et al (2002) First use of an airborne hyperspectral scanner for compositional mapping. *Remote Sens Environ* 80:447–459
- Matsunaga T, Yamamoto S, Kato S et al (2011) Simulation of operation of future Japanese spaceborne hyperspectral imager: HISUI. *Proc SPIE*. doi:[10.1117/12.898376](https://doi.org/10.1117/12.898376)
- NRC (2007) Earth science and applications from space: national imperatives for the next decade and beyond. Committee on Earth Science and Applications from Space: A Community Assessment and Strategy for the Future. National Academies Press. Referred to as the Decadal Survey or NRC 2007, 456pp
- Ormsby J (1982) The use of Landsat-3 Thermal data to help differentiate land covers. *Remote Sens Environ* 12:97–105
- Pierce L, Running S, Riggs G (1990) Remote detection of canopy water-stress in coniferous forests using the NS001 thematic mapper simulator and the thermal infrared multispectral scanner. *Photogramm Eng Remote Sens* 56:579–586
- Prisma (2011) [http://www.asi.it/en/activity/earth\\_observation/prisma](http://www.asi.it/en/activity/earth_observation/prisma)
- Realmuto V, Hook S, Foote M, et al. (2011) HyspIRI high-temperature saturation study. JPL Publication 11-2. Jet Propulsion Laboratory, Pasadena, 51pp
- Stuffler T, Kaufmann C, Hofer S et al (2007) The EnMAP hyperspectral imager – an advanced optical payload for future applications in Earth observation programs. *Acta Astronaut* 61:115–120
- Szymanski J, Weber P (2005) Multispectral Thermal Imager: mission and applications overview. *IEEE Trans Geosci Remote Sens* 43:1943–1949
- UNIS (2004) UN report says world urban population of 3 billion today expected to reach 5 billion by 2030. URL: <http://www.unis.univie.ac.at/unis/pressrels/2004/pop899.html>. United Nations Information Service, Vienna
- Vincent R (1972) Rock-type discrimination from ratioed infrared scanner images of Pisgah Crater, California. *Science* 175:986–988
- Wright R, Garbeil H, Harris A (2008) Using infrared satellite data to drive a thermo-rheological/stochastic lava flow emplacement model: a method for near-real-time volcanic hazard assessment. *Geophys Res Lett* 35, L19307
- Yamaguchi Y, Kahle A, Tsu H, Kawakami T, Pniel M (1998) Overview of Advanced Spaceborne Thermal Emission and Reflection Radiometer (ASTER). *IEEE Trans Geosci Remote Sens* 36:1062–1071
- URL1: <http://hyspiri.jpl.nasa.gov/documents>

# **Chapter 7**

## **Spaceborne Thermal Infrared Observation – An Overview of Most Frequently Used Sensors for Applied Research**

**Claudia Kuenzer, Huadong Guo, Marco Ottinger, Jianzhong Zhang,  
and Stefan Dech**

**Abstract** This chapter presents an overview of the most commonly used spaceborne sensors for thermal infrared research applications. There is a large fleet of international sensors available which allow for the acquisition of data in the thermal infrared. Depending on spatial coverage, some sensors are more suitable for mapping large areas, while others support observations at a local scale. Temporal resolution defines whether temperature patterns or phenomena can be monitored on a daily, weekly, monthly, or even only an annual basis. A wide variety of thermal sensors will be introduced in overview tables. However, as certain sensors with thermal infrared bands have established themselves as ‘work horses’ for certain types of applications, they will be especially highlighted and presented in depth. A comprehensive overview of typical thermal infrared application studies and the sensors particularly favored rounds off this chapter.

### **7.1 Introduction**

Thermal remote sensing over land and ocean has always been a discipline with a relatively small analyst and user community compared to the fields of multispectral remote sensing or even radar remote sensing (see Table 7.1). Typical applications for thermal remote sensing over land are: large scale land surface temperature (LST) mapping for model input in the fields of vegetation monitoring, agriculture,

---

C. Kuenzer (✉) • M. Ottinger • S. Dech  
German Remote Sensing Data Center (DFD), Earth Observation Center (EOC),  
German Aerospace Center (DLR), Oberpfaffenhofen, Germany  
e-mail: [Claudia.kuenzer@dlr.de](mailto:Claudia.kuenzer@dlr.de)

H. Guo  
Center for Earth Observation and Digital Earth (CEODE), Beijing, China

J. Zhang  
Beijing ESKY Technology Limited, Beijing, China

**Table 7.1** Number of publications related to thermal infrared research in four selected remote sensing journals in the years 2009, 2010, and 2011, with respect to the overall number of publications and different fields of application

Topic	International Journal of Remote Sensing				Remote Sensing of Environment				International Journal of Applied Earth Observation and Geoinformation				IEEE Transactions on Geoscience and Remote Sensing			
	2009	2010	2011		2009	2010	2011		2009	2010	2011		2009	2010	2011	
All articles	387	387	523	21 (5 %)	23 (4 %)	36 (14 %)	256	330	56	91	106	374	383	424	12 (3 %)	13 (3 %)
Thermal articles	—	—	3	4	1	4	—	—	—	2	2	2	—	—	—	—
LST retrieval	1	3	1	3	5	5	—	—	—	—	—	—	—	—	—	—
SST retrieval	1	2	—	—	2	7	1	1	1	1	1	1	1	1	1	2
Urban climatology, UHI	2	2	2	2	2	5	1	—	—	—	—	—	—	—	—	1
Other climatology	2	1	2	2	—	—	—	—	—	—	—	—	—	—	—	—
Clouds, snow and ice	1	2	2	2	—	—	—	—	—	—	—	—	—	—	—	—
Agriculture modeling	3	—	—	—	4	4	1	—	—	—	—	—	—	—	—	—
Volcano analyses	—	1	1	2	1	1	—	—	—	—	—	—	1	1	—	—
Earthquake analyses	—	1	—	—	—	—	—	—	1	1	—	—	—	—	—	—
Geothermal research	1	—	1	—	—	—	—	—	—	—	1	—	—	—	—	—
Forest fire analyses	2	2	2	6	4	6	1	1	1	1	—	—	—	—	—	—
Peat fire detection	—	—	1	—	—	—	—	—	—	—	—	—	—	—	—	—
Coal fire analyses	—	1	—	—	—	—	—	—	—	—	—	—	—	—	—	—
Soil moisture	—	—	—	1	1	2	—	—	—	1	1	—	—	—	—	—
Mineral discrimination	—	—	—	1	1	—	1	—	—	—	—	—	—	—	—	—
Land cover	—	—	1	2	—	—	—	—	—	—	—	—	—	—	—	—
Emissivity and inertia	—	—	3	2	1	—	—	—	1	1	—	—	—	—	—	—

climatology and hydrology; analysis of thermal heat island and heat sink patterns in urban areas; urban area climatology; volcano monitoring; geothermal analysis; forest fire, peat fire, and burned area detection; observation of industrial areas, investigation of coal fire and mining areas worldwide; security applications such as pipeline monitoring; the retrieval of soil moisture data; and rock type and mineral discrimination. In the field of ocean or water surface observation, water temperature patterns, water mixing, and freeze-thaw processes are of special interest to the community focusing on sea surface temperature (SST). Despite the limited number of scientists engaged in thermal infrared (TIR) remote sensing and (compared to optical, multispectral or radar sensors) a relatively narrow choice of really suitable spaceborne thermal sensors, the applications listed above still indicate a large potential for quantitative analysis and product generation, which should not be underestimated. This chapter presents an overview of the currently available sensors with bands in the thermal infrared which are most commonly used for thermal earth observation applications.

Table 7.1 presents the number of publications related to thermal infrared research in four selected remote sensing journals for the years 2009, 2010, and 2011, with respect to the overall number of publications and sorted according to different fields of application. We can see that with respect to LST analysis, especially the application fields of general LST retrieval over land, forest fire analysis, cloud/snow/ice detection, and image classification and accuracy mapping are well represented. The latter fields are especially strong as many scientists publish work demonstrating that the inclusion of the thermal band can improve the distinction of land cover and land use classes and can therefore positively influence classification accuracy. Other field such as geothermal analyses, coal and peat fire investigations, or geo-health – to give only three examples – are less extensively dealt with. However, one has to keep in mind that in certain fields, thermal-infrared-related research findings are not published in typical remote sensing journals, but in those of other disciplines (energy, geology, environment, etc.) (ESA 2012).

## 7.2 Thermal Infrared Sensors

Table 7.2 gives a detailed overview of typical sensors and their characteristics (spatial resolution, revisit time, swath width, platform, agency operating the sensor and launch year) employed for the analysis of land and sea surface temperatures and related applications. Currently, most instruments stem from the USA. However, Europe also had and has several suitable sensors in space, and the upcoming Sentinel 3 satellite will have on board a thermal sensor named ‘Sea and Land Surface Temperature Radiometer’, SLSTR, providing 1 km resolution. Also, China’s fleet of spaceborne sensors, including those with thermal infrared bands, has expanded rapidly in recent years. All sensors presented are operational (unless indicated otherwise, marked grey) and deliver data.

**Table 7.2** Selected sensors often used for the analysis of land surface temperature and related applications

Sensor	Spatial res.	Revisit	Swath width	Platform/satellite	Agency	Launch year
ETM+	60 m	16 d	185 km	Landsat-7	USGS, NASA	1999
TM	120 m	16 d	185 km	Landsat 5	USGS, NASA	1984
TIRS	100 m	16 d	185 km	Landsat 8 (LDCM)	USGS, NASA	2013
ASTER	90 m	4–16 d	60 km	Terra	NASA	1999
IRMSS	160 m	26 d	120 km	CBERS-1, 2, 2b	CRESDA, INPE	1999–2003, 2003, 2007–2010
IRSCAM	80 m	26 d	120 km	CBERS-3 and 4, 4b	CRESDA, INPE	2012, 2014, 2016
MERIS	250 m	1 d	2800 km	FY-3A, FY-3B	NRSCC, CAST, NSM a.o.	2008, 2010
InfraredCam	300 m	31 d	720 km	HJ-1B	CRESDA, CAST, NRSCC	2008
NIRST	351 m	<1–2 d	182–1,060 km	Aquarius	NASA, CONAE	2011
BIRD	370 m	10 d	190 km	BIRD	DLR	2001–2004
TET-1	356 m	10 d	180 km	TET-1	DLR	2012
VIIIRS	1.6 km	<1 d	3,000 km	Suomi NPP	NASA/NOAA	2011
CrIS	14 km	<1 d	2,200 km	Suomi NPP	NASA/NOAA	2011
CERES	20 km	<1 d	3,000 km	Suomi NPP	NASA/NOAA	2011
IIR	1 km	16 d	64 km	CALIPSO	CNES	2006
MODIS	1 km	4 per day	2,330 km	Terra, Aqua	NASA	1999, 2002
ATSR-2	1 km	3 d	512 km	ERS-2	ESA, UKSA, CSIRO	1995–2011
AATSR	1 km	35 d	500 km	Envisat	ESA, UKSA	2002–2012
AVHRR/1	1.1 km	<1 d	2,600 km	TIROS-N, NOAA 6, 8, 10	NOAA	1978–1986
AVHRR/2	1.1 km	<1 d	3,000 km	NOAA9, 10, 11, 12, 13, 14	NOAA	1984–2005
AVHRR/3	1.1 km	<1 d	3,000 km	NOAA15–19, Metop A,B	NOAA, EUMETSAT	1998, 2000, 2002, 2005, 2006, 2012

MSG-SEVIRI	1–3 km	<1 d	Full earth disk	Meteosat-8/9/19	ESA/EUMETSAT	2002, 2005, 2012
MVIRI	5 km	ev. 30 min	Full earth disk	Meteosat-3/4/5/6/7	EUMETSAT, ESA	1988, 1989, 1991, 1993, 1997
MSU-MR	1 km	37 d	3,000 km	Meteor 3 M, and -M N1	ROSHYDROMET a.c.	2001, 2009
MSU-GS	4 km	geost. <1 d	Full earth disk	Elektro-L N1	ROSHYDROMET a.c.	2011
IMAGER	4 km	geost., <1 d	Full earth disk	MTSAT-1,2,3	JMA	1999, 2006, 2013
MVISR	1.1 km	3–4 d	3,200 km	FY-1C, ID	CMA, NRSCC	1999, 2002
IVISSR	5 km	1 d	Full earth disk	FY-2C, 2D, 2E, 2 F	NRSCC, CAST, NSMC	2004, 2006, 2008, 2012
VHRR	8 km	ev. 30 min	Full earth disk	Insat-2A,B,E, -3A	ISRO	1992, 1993, 1999, 2003
IASI	25 km	29 d	2,052 km	MetOP-A/B	CNES, EUMETSAT	2006, 2012
HIRS/3	20.3 km	<1 d	2,240 km	NOAA 15,16,17	NOAA	1998, 2000, 2002
HIRS/4	20.3 km	<1 d	2,240 km	NOAA 18/19, MetOp A/B	NOAA, EUMETSAT	2005, 2006, 2009, 2012
ScaRaB	40 km	1 d	2,200 km	Meteor-3, Resurs-01, Megha Tropiques	CNES	1994, 1998, 2011

Spatial resolution is presented for the commonly used TIR domain above 8  $\mu\text{m}$ . Agency Code for Table 7.2: USA: NASA National Aeronautics and Space Administration, USGS United States Geological Survey, NOAA National Oceanic and Atmospheric Administration, Europe: ESA European Space Agency, EUMETSAT European Organization for the Exploitation of Meteorological Satellites, UKSA UK Space Agency, DLR German Aerospace Center, CNES Centre National d'Etudes Spatiales, China: CRESDA China Centre for Resources Satellite Data and Application, CNSA Chinese Meteorological Administration, NRSCC National Remote Sensing Center China, CNSA Chinese National Space Administration, CAST Chinese Academy of Science and Technology, Japan: JAXA Japan Aerospace Exploration Agency, JMA Japan Meteorological Administration, India: ISRO Indian Space Research Organisation, Australia: CSIRO Commonwealth Scientific and Industrial Research Organisation. *a.o.* amongst others

### 7.2.1 Overview of Selected Sensors with Thermal Infrared Instruments

The following list presents the full names of sensors listed in Table 7.2.

- ETM+: Enhanced Thematic Mapper (on board the U.S. Landsat 7)
- TM: Thematic Mapper (on board the U.S. Landsat 5)
- TIRS: Thermal InfraRed Sensor (on board the U.S. Landsat DCM)
- ASTER: Advanced Spaceborne Thermal Emission & Reflection Radiometer (on board the American-Japanese sensor of the same name, on the Terra platform)
- IRMSS: InfraRed MultiSpectral Sensor (on board the Chinese CBERS 1, 2, and 2b)
- IRSCAM: Infrared Medium Resolution Camera (on board the Chinese CBERS 3, and future CBERS 4 and 4b)
- InfraredCamera (on board the Chinese HJ-1B satellite)
- MERSI: Medium Resolution Spectral Imager (on board the Chinese FengYun satellites)
- NIRST: New Infrared Sensor Technology (on board the American Aquarius)
- BIRD: Bi-spectral Infrared Detection (on board the German sensor of the same name)
- TET: Technologie Entwicklungsträger (on board the German sensor of the same name)
- VIIRS: Visible/Infrared Imager Radiometer Suite (on board the U.S. Suomi NPP)
- CrIS: Cross-track Infrared Sounder (on board the U.S. Suomi NPP)
- CERES: Cloud's and Earth's Radiant Energy System (on board the U.S. Suomi NPP)
- IIR: Imaging Infrared Radiometer (on board the French CALIPSO satellite)
- MODIS: Moderate Resolution Imaging Spectroradiometer (on the U.S. platforms Terra and Aqua)
- AATSR: Advanced Along-Track Scanning Radiometer (on board the European Envisat)
- AVHRR: Advanced Very High Resolution Radiometer (on board the U.S. NOAA satellites)
- MSG-SEVIRI: Meteosat Second Generation – Spinning Enhanced Visible and InfraRed Imager (on board the European METEOSAT Second Generation satellites)
- MVIRI: Meteosat Visible and InfraRed Imager (on board the geostationary European METEOSAT satellites)
- MSU-MR: Multispectral scanning imager-radiometer (on board the Russian orbiting Meteor-M N1 meteorological satellite)
- MSU-GS: Multispectral scanning imager-radiometer (on board the Russian geostationary Elektro-L N1 meteorological satellite)

- Imager: Multiband Imager (on board the MTSAT Japanese meteorological satellites)
- MVISR: Multispectral Visible and Infra-red Scan Radiometer (on board the Chinese FengYun meteorological satellites)
- IVISSR: Improved Multispectral Visible and Infra-red Scan Radiometer (on board the operating Chinese FengYun meteorological satellites)
- VHRR: Very High Resolution Radiometer (on board the Indian National Satellite System INSAT)
- IASI: Infrared Atmospheric Sounding Interferometer (on board the European Metop-A, Metop-B satellites)
- HIRS: High Resolution Infrared Radiation Sounder (in different versions as HIRS/2/3/4 on board the U.S. NOAA and European Metop series)
- ScaRaB: Scanner for Earth's Radiation Budget (on board the French satellite Megha Tropiques)

In Table 7.2 some sensors or satellites are marked in grey. These are no longer operational, but they are listed here as they were extensively used by the thermal infrared community, and as we want to indicate the availability of the relevant data archives for long term monitoring purposes. Concerning spatial resolution, the pixel resolution in the TIR band(s) (usually located somewhere in the 8–14  $\mu\text{m}$  domain) is given. Furthermore, we elaborate on some of the thermal instruments in detail. Here we selected the most commonly employed satellites such as Landsat-7, ASTER, CBERS, HJ-1B, MODIS, and AVHRR/3. These (amongst other) have been – or are currently – widely used in the application studies presented in SCI journals.

### 7.2.2 *Landsat-7 ETM+ Thermal Infrared Data*

The Landsat ETM+ characteristics were already briefly introduced in Chap. 1 of this book. However, as Landsat-7 ETM+ has been – for many years – a work horse for the thermal infrared community, and as this chapter might be read independently of the remaining chapters of this book, some facts are repeated here. The new Landsat DCM (Data Continuity Mission) sensor is covered in a separate chapter of this book. The ETM+ sensor has one thermal band in the 10.4–12.5  $\mu\text{m}$  domain delivering data at a spatial resolution of 60 m. For ETM+ all bands are acquired in either a low- or high-gain mode. Gain selection is defined in the gain strategy of the former Long Term Acquisition Plan (LTAP), depending on acquisition time and the dominant surface types in a scene (percentages of land, desert, ice/snow, water, sea ice, etc.). These are known a priori, based on maps. Except for very specific requests the user has no influence on the gain setting in the reflective modes. Nevertheless, LS-7 band 6 will always be recorded and delivered in the low-gain and high-gain mode. These double gain settings extend the temperature range. However, detector saturation can occur if a surface has extremely high temperatures, or – vice versa – a surface will not be

**Table 7.3** Temperature of saturation in the low- and high-gain bands of Landsat-7 ETM+ with an 8 bit dynamic range

Part of the EMS	Band width/EMR-area [μm]	Minimum temperature [°C]	Maximum temperature [°C]
1 (VIS, blue)	0.45–0.51	1,051 (1,075)	1,483 (1,526)
2 (VIS, green)	0.52–0.60	900 (922)	1,301 (1,340)
3 (VIS, red)	0.63–0.69	755 (775)	1,119 (1,156)
4 (NIR)	0.75–0.90	595 (613)	926 (961)
5 (SWIR)	1.55–1.75	206 (217)	417 (440)
6 (TIR)	10.40–12.50	−33 (−134)	51 (77)
7 (SWIR)	2.09–2.35	92 (101)	258 (276)
8 (PAN)	0.52–0.90	702 (721)	1,056 (1,092)

Source: Flynn et al. (2001), modified

detected thermally if its temperature is below a certain threshold. Table 7.3 lists the minimum and maximum temperatures in the low-gain and high-gain setting, indicating the lowest or highest pixel integrated temperature which can be detected in a certain wavelength region. It also shows that the mid-infrared band 5 can be used to detect thermal anomalies of very high temperatures leading to saturation in band 6. Even the near-infrared channel 4 offers options for the detection of extremely high temperatures.

Although the low-and high-gain options are new compared to the former Landsat-TM, the thermal bands of ETM+ are less suitable for high temperature studies. They saturate at 51 and 77 °C, respectively, while TM band 6 saturates at around 90 °C. It is also often stated that ETM+ still suffers from an antiquated 8 bit dynamic range, limiting radiance steps to 256 instead of, e.g., 4,096 if a 12 bit system is used (Flynn et al. 2001). However, the major difference to ETM+ data is the lower spatial resolution in the thermal band (120 m, no double gain setting) and the lack of a panchromatic channel for the visible domain. Furthermore, Landsat TM data have a weaker SNR ratio and radiometric sensitivity. However, Landsat-5 TM is still acquiring up-to-date images of the earth's surface and provides an important data source for many thermal applications.

Figure 7.1 presents a subset of a multispectral combination and a thermal band of Landsat-7 ETM+ acquired over the Wuda coal mining area in Inner Mongolia, China. The Yellow River in the center of the subset runs from south to north. It is frozen in most parts and temperatures range between −2 to 1 °C. Coal surfaces (which can be recognized as black spots in the ‘ear-shaped’ coal mining syncline west of the river, as well as in some locations in the south-eastern quarter of the subset) and sun-exposed geologic surfaces are the warmest areas (15–29 °C), while the deeply incised valleys on the eastern side of the Yellow River and the northwest exposed slopes in the northern Helan Mountains in the southwestern quarter are the coldest regions (−13 to 0 °C). When radiometrically correcting winter scenes it has to be taken into account that negative temperature values may occur, and therefore the data has to be handled as “signed” bit instead of “unsigned” bit data; otherwise all negative temperatures will appear as 0 °C.

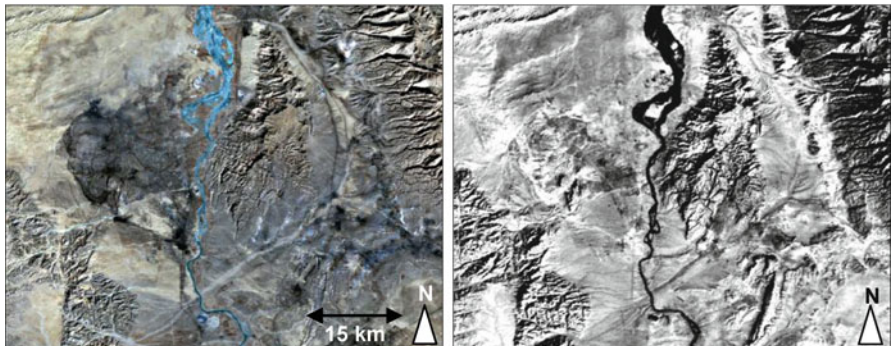


**Fig. 7.1** Subset of a multispectral and a thermal daytime scene acquired by Landsat-7 ETM+ on 12.02.2003, 2 months before the scan mirror failure. *Left:* false color infrared image, *right:* DNs converted to temperature in °C. *Light:* high temperatures, *dark:* lower temperatures. Temperature range: –13 to 29 °C. Center location: 650695E, 4373295N, UTM, Z48N

Upon special request it is possible to plan specific nighttime acquisitions of Landsat (thermal only). The scheduling of nighttime acquisition is usually only possible for selected projects and users. Only a limited amount of nighttime data can be acquired during a satellite's path around the world, since acquisition on the nighttime side (descending orbit) requires more energy than a daytime acquisition. The acquisition of one nighttime scene will lead to the skipping of seven daytime frames in the ascending daytime orbit. However, nighttime data acquired in the past is usually available in the worldwide data archives and can be ordered by every user.

ETM+ thermal data has been available since 1999. In May 2003 the ETM+ sensor had a technical failure in a scan mirror. However, according to the Landsat science team 78 % of the data sets are unaffected and can be ordered. However, many scientists have stopped using ETM+ instead of analyzing whether the scan mirror problem even affects their area of interest or the data quality for their purposes. The new sensor Landsat Data Continuity Mission, LDCM, with its TIRS instrument acquiring data in the thermal domain, is presented in its own chapter in this book. Unfortunately, the thermal infrared band comes at a spatial resolution of 100 m, which is lower than the 60 m resolved thermal band of the foregoing ETM+ sensor.

### 7.2.3 ASTER Thermal Infrared Data

The spectral and spatial properties of the ASTER sensor, installed on the Terra platform and flying 30 min behind Landsat-7, are briefly introduced in Table 7.4. Since December 1999 ASTER has traveled in a near polar, sun synchronous orbit, acquiring data since February 24, 2000 with a repetition rate of 16 days. Data is down-linked in frames covering an area of approximately 60 km × 60 km at

**Table 7.4** Spectral and spatial properties of ASTER data

Part of the electromagnetic spectrum	Band width/EMR-area [μm]	Spatial resolution [m]	Depth [bit]
(1) VNIR	0.52–0.60	15	8
(2) VNIR	0.63–0.69	15	8
(3) VNIR nadir looking	0.76–0.86	15	8
(3) VNIR backward looking	0.76–0.86	15	8
(4) SWIR	1.6–1.7	15	8
(5) SWIR	2.145–2.185	30	8
(6) SWIR	2.185–2.225	30	8
(7) SWIR	2.235–2.285	30	8
(8) SWIR	2.295–2.365	30	8
(9) SWIR	2.360–2.430	30	8
(11) TIR	8.125–8.475	90	12
(12) TIR	8.475–8.825	90	12
(13) TIR	8.925–9.275	90	12
(14) TIR	10.25–10.95	90	12
(15) TIR	10.95–11.65	90	12

10:30 a.m. local time. Unlike Landsat-7, which acquires (acquired) data constantly and therefore provided near-worldwide coverage of frames (except the poles), ASTER only scans the earth's surface when specifically requested by a customer. Thus it does not grant sufficient areal coverage (Earth Remote Sensing Data Analysis Center. 2000, 2001; Abrams and Hook 1995). Nighttime data with five thermal bands, acquired at 10:30 p.m. local time, can also be requested by users. A major advantage of such thermal nighttime data is that at that time only a few solar effects modify the thermal signal. Influences of uneven heating due to slope and aspect are minimized (Kuenzer 2005; Zhang and Kuenzer 2007; Zhang et al. 2007). However, the optimal time for thermal data acquisition would be around 5 a.m., shortly before sunrise, when objects on the earth's surface have the lowest temperature and the solar effect is least accentuated (Zhang and Kuenzer 2007).

A large advantage and unique feature of the ASTER sensor is the availability of five bands in the TIR between 8.125 and 11.65 μm at 90 m spatial resolution at a 12 bit dynamic range. Even MODIS has only two bands in the TIR domain and only at 1 km resolution. ASTER therefore allows discrete emissivity-influenced spectra of surfaces to be mapped based on five measurements. As elaborated in Chap. 1, emissivity of a surface varies depending on wavelength. Therefore, an object with a certain kinetic temperature depicts different amounts of emitted radiation at different wavelengths in the thermal domain. If thorough atmospheric correction and emissivity normalization is performed, it is possible to utilize data of these five bands for emissivity-based surface mapping and surface discrimination. ASTER thermal bands are thus very widely used for mineral mapping in arid areas, as presented by Tangestani et al. (2005), Mars and Rowan (2006), and Pour and Hashim (2012), amongst many others.

**Table 7.5** Infrared Scanner, IRS on board CBERS-3

Part of the EMS	Band width/EMR-range [μm]	Spatial resolution	Technical characteristics
MIR	6: 0.5–0.9	40 m	8 bit
SWIR	7: 1.55–1.75	40 m	120 km swath
	8: 2.08–2.35	40 m	No side looking option
TIR	9: 10.4–12.5	80 m	

### 7.2.4 CBERS Thermal Infrared Data

The China-Brazil Earth Resources Satellite CBERS-1 was launched in October 1999, followed by CBERS-2 in October 2003. CBERS-1 operated from 1999 until 2003, but CBERS-2 is still delivering data with its three instruments: the Charge Coupled Device Camera (CCD), the Wide Field Imager (WFI) and the Infrared Multi-Spectral Scanner (IRMSS). The latter also includes a thermal band at 10.40–12.5 μm at 156 m resolution. CBERS-2b was launched in 2007 and operated for 3 years. CBERS-3 was launched ahead of schedule in fall 2012, and it has an improved infrared scanner on board which delivers thermal data in the 10.40–12.5 μm range covering a swath width of 120 km at now 80 m resolution. The resolution is thus better than that of the Landsat DCM thermal band. A panchromatic band at 5 m resolution, and multispectral bands at 10 m resolution are also available and cover a swath of 60 km. CBERS-4 and CBERS-4b are currently in the assembly phase and due to be launched in 2014 and 2016, respectively. CBERS is widely used by the Chinese thermal remote sensing community, amongst others purposes also to fill existing data gaps in thermal Landsat ETM+ data (Chen et al. 2011) (Table 7.5).

### 7.2.5 HJ-1B Thermal Infrared Data

HJ stands for HuanJing, which means “environment” in Chinese. The HJ-1B satellite belongs to a fleet of three (and in the future more) satellites which were launched in September 2006 (HJ-1A, and HJ-1B) and November 2012 (HJ-1C). The three satellites were and are mainly used for national disaster and environmental monitoring and can acquire multispectral and radar imagery. HJ-1A, which covered two bands in the TIR at 1.1 km spatial resolution, is no longer operational. However, HJ-1B has an infrared camera on board which acquires data in the thermal domain from 10.5 to 12.5 μm at 300 m spatial resolution, covering a swath of 720 km. One band in the 3.50–3.90 μm MIR domain collects data at 150 m resolution and allows for the detection of extremely hot thermal events. HJ-1B thermal data is mainly used for general LST retrieval and the analysis of LST patterns. Due to the novelty of the HJ series, thermal data from HJ-1B has furthermore extensively been compared with other spaceborne thermal data, airborne data, and in-situ calibration measurements. Publications in English SCI journals on HJ-1B thermal data utilization are still rare, which can be attributed to the novelty of the sensor, as well as the mainly national data analyses for Chinese territory.

**Table 7.6** Spectral and spatial characteristics of the MODIS mid-infrared (MIR) and thermal infrared (TIR) bands suitable for thermal earth-surface analyses

Part of the EMS	Band width/ EMR-range [μm]	Spatial resolution [km]	Technical characteristics
MIR	20: 3.660–3.840	1	12 bit
	21: 3.929–3.989	1	2,330 km swath
	22: 3.929–3.989	1	FOV ±55°
	23: 4.020–4.080	1	
TIR	31: 10.780–11.280	1	
	32: 11.770–12.270	1	

It should be noted that MODIS has more channels in the MIR and TIR. However, due to water absorption they are not employable for land temperature investigations

### 7.2.6 MODIS Thermal Infrared Data

The MODIS sensor acquires data in 36 spectral bands ranging from 0.62 to 14.385 μm. Spatial resolution at nadir is 250 m for bands 1 and 2 (VIS), 500 m for bands 3–7 (VIS and NIR) and 1,000 m for bands 8–36 (visible (VIS), near infrared (NIR), middle infrared (MIR), TIR). At the sensor's maximum scan angle of 55° near the far end of a swath the pixel sizes can reach almost 2 km \* 5 km. However, large swath widths grant a higher revisiting frequency so that MODIS data is available daily for most spots on the earth's surface. Due to the installation of the sensor on the TERRA platform (launched 1999) and an identical instrument on the AQUA platform (launched 2002), most areas can be covered 4–5 times daily: in the morning, afternoon, evening, and pre-dawn. This grants frequent cloud-free observations and continuous monitoring of a desired area. For thermal research especially bands 20–23 (ranging from 3.66 to 4.08 μm) as well as bands 31 and 32 (ranging from 10.78 to 12.27 μm) are of interest. These bands were designed for land surface temperature analysis and are shown in Table 7.6.

Kuenzer et al. (2008) have demonstrated the potential of MODIS multi-diurnal thermal observation. Four observations per day allow the discrimination of clear thermal daytime versus nighttime patterns, and can even support the analysis of hot spot dynamics over the course of a 24 h cycle. The availability of several MIR and TIR bands furthermore allows for the creation of ratio images and therefore the delineation of exceptional versus ‘normal’ hot spots.

MODIS thermal bands data have been widely used for land surface temperature pattern analyses, sea surface temperature studies, as well as forest fire detection (see the application section).

### 7.2.7 NOAA-AVHRR/3 Thermal Infrared Data

The Advanced Very High Resolution Radiometer/3 (AVHRR/3), launched for the first time in 1998, consists of six channels with a spectral range from 0.58 to

**Table 7.7** Spectral and spatial characteristics of the NOAA-AVHRR/3 sensor

Part of the EMS	Band width/EMR-range [μm]	Spatial resolution [km]	Technical characteristics
VIS	1: 0.58–0.68	1.1	10 bit, 1,090 m spatial resolution at nadir, 2,900 km swath width
NIR	2: 0.725–1.00	1.1	
SWIR	3a: 1.58–1.64	1.1	
MIR	3b: 3.55–3.93	1.1	
TIR	4: 10.30–11.30 5: 11.50–12.50	1.1	

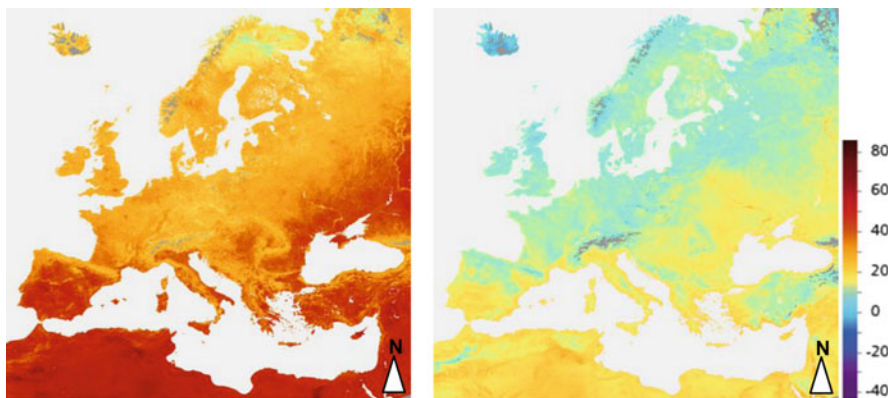


**Fig. 7.2** Land surface temperature monthly composite derived from NOAA-18 AVHRR/3 data for Europe, June 2009. *Left:* daytime composite, *right:* nighttime composite. Daytime temperatures range between 10 °C in northern Norway and Finland, up to around 70° and more in northern Africa. Nighttime temperature range between 5 and 30 °C. *Grey:* no values

12.5 μm. Nadir resolution of all bands is 1.1 km. With a swath of approx. 2,900 km, it ensures full global coverage twice daily. Thermal data from AVHRR have been widely used for applications related to land surface and sea surface temperature. A large advantage of the AVHRR is its daily (actually twice daily) revisit time, and the availability of data covering the last three decades. It is therefore the only sensor in space which allows for real trend analyses (Table 7.7 and Fig. 7.2).

### 7.3 Selected Fields of TIR Applications and Selected Publications Sorted by Sensor

We provide below a compilation of application studies in typical application fields for thermal infrared data, sorted by field of application and most common sensors used. All references are from remote sensing SCI journals. They are not additionally included in the references section of this book chapter for reasons of space.

However, interested readers will find the respective source when searching in the Internet for the application field, sensor, and author name. For each field of application the studies are presented in a sequence from lower to higher spatial resolution TIR sensors. Please note that there is no claim of completeness, neither for the selected application fields nor the sensor lists, and that the emphasis has been placed on selecting references from the past decade.

### **Land surface temperature retrieval, LST**

**MSG SEVIRI** (Stisen et al. 2007; Götsche and Olesen 2009; Lu et al. 2011; Freitas et al. 2010; Sun and Pinker 2007; Schroedter-Homscheidt et al. 2011), **NOAA-AVHRR** (Czajkowski et al. 1998; Gleason et al. 2002; Han et al. 2004; Kerenyi and Putsay 2000; Price 1983; Sobrino et al. 1994; Bhattacharya et al. 2009; Reynolds et al. 2008), **MODIS** (Petitcolin and Vermote 2002; Wan and Li 1997; Wan et al. 2002; Mito et al. 2006; Momeni and Saradjian 2007; Pinheiro et al. 2007; Agam et al. 2007; Nonaka et al. 2007; Wang et al. 2007; Song and Zhao 2007; Bhattacharya et al. 2009; Hulley and Hook 2009a; Wang and Liang 2009a; Coops et al. 2009; Vancutsem et al. 2010; Yang et al. 2011; Westermann et al. 2011; Albright et al. 2011; Hulley and Hook 2011; Wan 2008; Hashimoto et al. 2008; Wang et al. 2008; Huang et al. 2008; Mostovoy et al. 2008; McCabe et al. 2008; Langer et al. 2010), **AATSR** (Sòria and Sobrino 2007), **HJ-1B** (Zhou et al. 2010; Zhao et al. 2010; Hua et al. 2010; Xiaoguang et al. 2009), **FengYun** (Tang and Li 2012; Tang et al. 2008), **CBERS-2** (Zhang et al. 2006; Shi 2009; Yu et al. 2009), **Landsat-5 TM** (Li et al. 2004; Nichol 1998; Okwen et al. 2011; Jiménez-Muñoz et al. 2009), **Landsat 7 ETM+** (Li et al. 2004; Wloczyk et al. 2011; Okwen et al. 2011; Yue et al. 2007; Weng and Lu 2008), **ASTER** (Sobrino et al. 2007b; Mao et al. 2011; Wang and Liang 2009; Yang et al. 2011; Mira et al. 2009; Wang et al. 2011; Hulley and Hook 2011; Mao et al. 2008)

### **Sea surface temperature retrieval, SST**

**MSG SEVIRI** (Clerici 2009; Merchant et al. 2009; Petrenko et al. 2011; Le Borgne et al. 2011), **NOAA-AVHRR** (Romo et al. 2007; Sousa et al. 2008; Sun et al. 2008; Chang et al. 2008; Iwasaki et al. 2008; Wang et al. 2010; Williams et al. 2010; Miliarexis and Seymour 2011; Breaker et al. 2010; Castro et al. 2010; Hulley et al. 2011; Eastwood et al. 2011), **MODIS** (Panda et al. 2007; Cai et al. 2007a; Reinart and Reinhold 2008; Cai et al. 2010; Crosman and Horel 2009; Alcantara et al. 2010; Hulley et al. 2011), **HJ-1B** (Hu et al. 2011; Huang et al. 2011; Zhou et al. 2011), **FengYun** (Wan Kadir and Rasib 2007; Zhou et al. 2008), **CBERS-2** (Wang et al. 2011), **Landsat TM/ ETM+** (Isoguchi et al. 2009), **ASTER** (Sentlinger et al. 2008; Cai et al. 2010; Hulley et al. 2011; Matsuoka et al. 2011)

### **Clouds, snow, ice, and glaciers**

**MSG-SEVIRI** (Mackie et al. 2010a; Mackie et al. 2010b; Pérez et al. 2011; Guo and Wang 2008; Turk et al. 2010), **NOAA-AVHRR** (Laine 2008; Turk et al. 2010; Berque et al. 2011; Fontana et al. 2009; Pérez et al. 2011), **MODIS** (Genkova et al. 2007; Starnes et al. 2007; Aoki et al. 2007; Hori et al. 2007; Yu et al. 2007; Hall et al. 2008; Luo et al. 2008; Guo and Wang 2008; Turk et al. 2010; Fraser et al.

2010; Fraser et al. 2009), **CBERS-2** (Ribeiro et al. 2007), **Landsat** (Hall et al. 2008; Hilker et al. 2009; Helmer et al. 2010; Hagolle et al. 2010; Huang et al. 2010), **ASTER** (Genkova et al. 2007; Hall et al. 2008; Bhambri et al. 2011; Shukla et al. 2010), **Ground based TIR cameras** (Rees et al. 1993; Rees and James 1992; Leppäranta and Lewis 2007)

### **Climatology and evaporation**

**MSG-SEVIRI** (Stisen et al. 2008; De Paepe et al. 2008; Sobrino and Romaguera 2008; Nieto et al. 2011; Chaurasia et al. 2010), **GOES** (Han et al. 2010; McNider et al. 1994), **FY-2** (Shu et al. 2011), **NOAA-AVHRR** (Rotach et al. 2005; Owen et al. 1998; Latifovic and Pouliot 2007; Sobrino et al. 2007a; Choudhury et al. 2007; Han et al. 2004; Han et al. 2010), **MODIS** (Cleugh et al. 2007; Rotach et al. 2005; Sánchez et al. 2007; Mallick et al. 2007; Song and Zhao 2007; Tang et al. 2010; Jang et al. 2010; Mu et al. 2011; Pouteau et al. 2011; Shu et al. 2011; Vinukollu et al. 2011; McCabe et al. 2008; Ghoneim 2008), **FengYun** (Shu et al. 2011; Shu 2010; Yun-Qiao 2011), **Landsat TM/ ETM+** (Rotach et al. 2005; Chavez et al. 2009), **ASTER** (Sarwar and Bill 2007; Nichol and Wong 2008; Bawazir et al. 2009; Galleguillos et al. 2011; Gangopadhyay et al. 2009).

### **Soil moisture**

**NOAA-AVHRR** (Van den Hurk 2001; Verstraeten et al. 2006), **MODIS** (Cai et al. 2007b; Merlin et al. 2009; Hulley et al. 2010; Merlin et al. 2010; Van doninck et al. 2011), **Landsat TM** (Van den Hurk 2001), **ASTER** (Merlin et al. 2009; Hulley et al. 2010; Mira et al. 2010)

### **Urban climatology, heat islands**

**NOAA-AVHRR** (Rigo et al. 2006; Gallo et al. 1993; Streutker 2003; Gallo and Owen 2002; Stathopoulou and Cartalis 2009), **MODIS** (Rigo et al. 2006; Imhoff et al. 2010; Keramitsoglou et al. 2011; Schwarz et al. 2011), **HJ-1B** (Yang et al. 2010; Luo et al. 2011), **CBERS-2** (Ji et al. 2009), **Landsat TM/ ETM+** (Rigo et al. 2006; Kim 1992; Yuan and Bauer 2007; Pena 2008; Cai et al. 2011; Amiri et al. 2009; Imhoff et al. 2010; Li et al. 2011; Zhang et al. 2009; Ma et al. 2010; Leak and Venugopal 1990; Munier and Burger, 2001), **ASTER** (Kato and Yamaguchi 2007; Frey et al. 2007; Tiangco et al. 2008; Weng et al. 2009; Cai et al. 2011; Dominguez et al. 2011; Weng et al. 2011), **Airborne TIR camera** (Lagouarde et al. 2010), **Ground based TIR cameras** (Rigo et al. 2006; Meier et al. 2010)

### **Agriculture modeling**

**NOAA-AVHRR** (Hurtado et al. 1994; Salazar et al. 2008; Biradar et al. 2009), **MODIS** (Jonna et al. 2007; Sims et al. 2008; Merlin et al. 2010; Tang et al. 2010; Jeganathan et al. 2011), **HJ-1B** (Klaasse and Jarman 2011), **ASTER** (Sepulcre-Canto et al. 2007; Courault et al. 2009; Merlin et al. 2010; Jeganathan et al. 2011), **Airborne Camera** (Suárez et al. 2010)

### **Forest fire detection and burnt area delineation**

**MSG-SEVIRI** (Roberts et al. 2011; Amraoui et al. 2010; Freeborn 2009; Calle et al. 2009), **NOAA-AVHRR** (Galindo et al. 2003; Kucera et al. 2005; Smith et al.

2007; Leblon et al. 2007; Ressl et al. 2009), **MODIS** (Kazi et al. 2006; Kiran Chand et al. 2006; Morisette et al. 2005; Mazzoni et al. 2007; Smith et al. 2007; Koltunov and Ustin 2007; Kiran Chand et al. 2007; Miettinen and Liew 2008; Bromley 2010; Quintano et al. 2010; He and Li 2011; Giglio et al. 2009; Ressl et al. 2009; Freeborn 2009; Libonati et al. 2010; Libonati et al. 2011; Veraverbeke et al. 2011; Dennison and Matheson 2011; Roberts et al. 2011; Freeborn et al. 2011; Siljander 2009), **BIRD** (Oertel et al. 2003; Oertel et al. 2004), **HJ-1B** (Qian et al. 2009; Yonggang et al. 2008), **FengYun** (Zhang et al. 2011; Frantzova et al. 2010), **CBERS-2** (Zhang et al. 2011), **Landsat TM/ ETM+** (Schroeder et al. 2008), **ASTER** (Morisette et al. 2005; Schroeder et al. 2008; Giglio et al. 2008; Eckmann et al. 2009; Dennison and Matheson 2011; Veraverbeke et al. 2011), **Airborne Camera** (Riccio et al. 2011)

### **Coal and peat fire detection and analysis**

**NOAA-AVHRR** (Mansor et al. 1994; Zhang et al. 2004), **MODIS** (Kuenzer et al. 2007; Kuenzer et al. 2008), **BIRD** (Siegert et al. 2004), **Landsat TM/ ETM+** (Kuenzer et al. 2007; Kuenzer 2005; Zhang et al. 2004a; Chen et al. 2007; Martha et al. 2010), **ASTER** (Kuenzer et al. 2007; Martha et al. 2010), **Ground measurements** (Zhang and Kuenzer 2007; Yunhao et al. 2007; Zhang et al. 2004; Prakash et al. 1999)

### **Volcano analysis**

**MSG-SEVIRI** (Hirn et al. 2009), **NOAA-AVHRR** (Van Manen et al. 2011; Marchese et al. 2011), **MODIS** (Thomas et al. 2009), **Landsat TM/ EM+** (Deroin et al. 1995; Ganas and Lagios 2003), **SPOT** (Deroin et al. 1995), **ASTER** (Ganas et al. 2010; Carter and Ramsey 2009), **Ground based TIR camera** (Corradini et al. 2010)

### **Earthquake (precursor) analysis**

**NOAA-AVHRR** (Saraf et al. 2009), **MODIS** (Saraf et al. 2009), **ASTER** (Yang et al. 2010), **Landsat ETM+** (Yang et al. 2010), **MTSAT** (Yang and Guo 2010)

### **Land cover discrimination**

**MSG-SEVIRI** (Fensholt et al. 2011), **MODIS** (French and Inamdar 2010), **Landsat TM/ ETM+** (Xian et al. 2009; Fernández et al. 2010; Xian and Homer 2010; Roy et al. 2010; Wu et al. 2010; Southworth 2004).

### **Rock type/mineral discrimination**

**MSG-SEVIRI** (Li et al. 2007; Klüser and Schepanski 2009), **ASTER** (Ninomiya et al. 1997; Katra and Lancaster 2008; Moore et al. 2008; Öztan and Süzen 2011; Vicente and Souza Filho 2011), **Ground based TIR camera** (Wu et al. 2011)

### **Emissivity and inertia studies**

**NOAA-AVHRR** (Cracknell and Xue 1996a; Cracknell and Xue 1996b; Badenas 1998; Stathopoulou et al. 2007), **MODIS** (Niclòs et al. 2007; Pipunic et al. 2008; Renzullo et al. 2008; Tang and Li 2008), **HJ-1B** (ShanShan et al. 2012), **FengYun** (Jiang and Zhou 2011), **ASTER** (Gangopadhyay et al. 2005; Coll et al. 2007; Hulley and Hook 2009b; Hulley et al. 2009; Sabol et al. 2009).

### Accuracy assessments/Sensor calibration

**MSG-SEVIRI** (Niclòs et al. 2011; Baraldi et al. 2010), **ASTER** (Gillespie et al. 2011; Yang et al. 2010; Mira et al. 2011), **NOAA-AVHRR** (Devasthale and Grassl 2009; Casciello et al. 2011; Baraldi et al. 2010), **MODIS** (Hao and Qu 2009; Wang and Liang 2009b; Chander et al. 2010; Xiaoxiong et al. 2009a; Xiaoxiong et al. 2009b); **AATSR** (Shi 2011; Baraldi et al. 2010), **HJ-1B** (Du et al. 2011), **FengYun** (Tong et al. 2010; Xiuqing et al. 2001), **CBERS-2** (Zhang et al. 2005; Zhang et al. 2002), **Landsat** (Jing and Cheng 2010; Chander et al. 2009; Chander et al. 2010; Wulder et al. 2011; Baraldi et al. 2010), **Airborne camera** (Houborg et al. 2011)

### Vegetation/Forest

**NOAA-AVHRR** (Bhuiyan and Kogan 2010; Julien and Sobrino 2009), **MODIS** (Wu et al. 2010; Waring et al. 2011; Xu et al. 2011), **Landsat** (Potapov et al. 2011), **Airborne camera** (Zarco-Tejada et al. 2009; Ribeiro da Luz and Crowley 2010; Berni et al. 2009b)

### Atmospheric correction

**MODIS** (Jiménez-Muñoz et al. 2010; Ellicot et al. 2009), **Landsat ETM+** (Coll et al. 2010), **ASTER** (Chrysoulakis et al. 2010).

### Drought events

**NOAA-AVHRR** (Shamsipour et al. 2011), **MODIS** (Caccamo et al. 2011), **FengYun** (Frantzova et al. 2010), **Landsat TM/ ETM+** (Gao et al. 2011).

## 7.4 Conclusion

A large variety of instruments acquiring data in the thermal infrared domain (TIR) exist. They span a broad range: from sensors acquiring data for the whole earth disk at a temporal resolution allowing daily or even hourly observations at low spatial resolutions of several tenths of kilometers to one kilometer up to sensors delivering thermal data with a spatial resolution of up to 60 m at swath widths well below 200 km and repetition rates enabling only one to two observations per month. Sensors of high value for long term observation allowing a look into the past for up to nearly 30 years are Landsat-TM, Landsat-ETM+ continued by the new Landsat DCM, as well as NOAA-AVHRR data. Under cloud-free conditions the latter enables daily temperature monitoring of the earth's surface at a spatial resolution of 1.1 km reaching back to 1978, while the Landsat fleet enables observations at a higher resolution of 120 m (TM), 60 m (ETM+), and 100 m (LDCM) – although only at a 16 day revisit interval. The largest fleet of sensors supporting TIR research is currently operated by the USA, whereas the availability of European instruments monitoring the thermal domain has decreased in recent years due to the loss of the Envisat satellite (including the AATSR instrument). Currently, Europe acquires thermal data via the Meteosat satellites and is in the midst of preparing the launch of the Sentinel 3 mission with a thermal instrument on board. However, after the USA,

it is China which has the most operational thermal instruments in orbit. The Chinese fleet enabling temperature observations from 5 km down to 80 m spatial resolution in the TIR (CBERS-3) is foreseen to grow further. Data from these sensors hold a large potential for the thermal remote sensing community – especially if made more widely available internationally.

**Acknowledgements** The authors thank I. Schlegel and N. Lütge for checking the references. Further thanks go to two anonymous reviewers for valuable suggestions which helped to improve the manuscript.

## References

- Abrams M, Hook SJ (1995) Simulated ASTER data for geologic studies. *IEEE Trans Geosci Remote Sens* 33(3):692–699
- Chen F, Tang L, Wang C, Qiu Q (2011) Recovering of the thermal band of Landsat 7 SLC-off ETM+ image using CBERS as auxiliary data. *Adv Space Res* 48(6):1086–1093
- European Space Agency, ESA (2012) The earth observation handbook: special edition for Rio +20. Available at: <http://www.eohandbook.com/>. Accessed Dec 2012
- Flynn LP, Harris AJL, Wright R (2001) Improved identification of volcanic features using Landsat 7 ETM+. *Remote Sens Environ* 78(2):180–193
- Kuenzer C (2005) Demarcating coal fire risk areas based on spectral test sequences and partial unmixing using multi sensor remote sensing data. Ph.D. thesis, Technical University Vienna, Vienna, 199pp
- Kuenzer C, Hecker C, Zhang J, Wessling S, Wagner W (2008) The potential of multi-diurnal MODIS thermal bands data for coal fire detection. *Int J Remote Sens* 29:923–944
- Mars JC, Rowan LC (2006) Regional mapping of phyllitic- and argillic-altered rocks in Zagros magmatic arc, Iran, using advanced spaceborne thermal emission and reflection radiometer (ASTER) data and logical operator algorithms. *Geosphere* 2(3):161–186
- Pour AB, Hashim M (2012) The application of ASTER remote sensing data to porphyry copper and epithermal gold deposits. *Ore Geol Rev* 44:1–9
- Tangestani MH, Mazhari N, Agar B (2005) Mapping the porphyry copper alteration zones at the meiduk area, SE Iran, using the advanced spaceborne thermal emission and reflection radiometer (ASTER) data. In: Ehlers M, Michel U (eds) *Remote sensing for environmental monitoring, GIS applications, and geology*, vol 5983, SPIE, Brugge, p 59830
- Zhang J, Kuenzer C (2007) Thermal surface characteristics of coal fires 1: results of in-situ measurements. *J Appl Geophys* 63:117–134
- Zhang J, Kuenzer C, Tetzlaff A, Oettl D, Zhukov B, Wagner W (2007) Thermal characteristics of coal fires 2: results of measurements on simulated coal fires. *J Appl Geophys* 63:135–147

# **Chapter 8**

## **Thermal Remote Sensing with Small Satellites: BIRD, TET and the Next Generation BIROS**

**Eckehard Lorenz**

**Abstract** High sensitive infrared detectors normally require more resources than comparable instruments in the visible spectral bands. Although the un-cooled detector arrays achieved in the last years a remarkably quality, their detection principle is inferior to the cooled quantum detectors. The price for the higher sensitivity of the cooled quantum detectors are higher efforts in mass, volume, power consumption, and costs. Therefore it is of interest to examine the compatibility of high sensitive infrared systems with the limited resources of small satellites which could be utilized for affordable space missions. The FIRES (Fire Recognition System) study was a first attempt to examine the accommodation of a challenging infrared mission on a small satellite. Based on this concept the BIRD (Bi-spectral Infra-Red Detection) satellite was launched in 2001, this satellite was mainly dedicated to the detection and monitoring of high temperature events. Following the success of the BIRD satellite a further constellation of two satellites called FIREBIRD (Fire Recognition with Bi spectral Infra-Red Detector) is currently in preparation.

### **8.1 The FIRES Study**

In the beginning of the 1990s various discussions about low-cost, small satellite technologies as an alternative to the cost-intensive, large systems were intensified (Jahn n.a.; Brieß et al. 1996). Due to the limited resources offered by a small system one of the main problems is to design adequate useful application concepts. In parallel to this trend the technological sciences offered more and more miniaturized solutions which triggered the trend for using small satellites. For example, the use of the un-cooled infrared bolometer arrays at this time could be referred to Lorenz and Sandau (2002).

---

E. Lorenz (✉)  
Optical Information Systems, DLR, Berlin, Germany  
e-mail: [Eckehard.lorenz@dlr.de](mailto:Eckehard.lorenz@dlr.de)

Following those discussions about small satellite applications a related study was initiated by the German company OHB in Bremen and the German Aerospace Center (Deutsche Zentrum für Luft- und Raumfahrt e. V. DLR) (FIRES 1994). One of the basic theses for the study was the realization, that the most convincing concept for the usage of small satellites would be the implementation of a powerful infrared detector system, which would have the advantage to gather huge amounts of information related to the detected objects, and at the same time test the technological limits of the small carrier system.

Whereas the mentioned bolometer arrays represent a remarkable technological breakthrough, they cannot achieve for physical reasons the sensitivity of cooled quantum detectors (Kingston 1978). The detectivity of a bolometer is limited to  $1.8 \times 10^{10} \text{ cm}^* \text{Hz}^{1/2}/\text{W}$  whereas the detectivity of a cooled quantum detector is more than an order higher. Therefore the main attention in this study was paid to the miniaturization of cooled quantum detectors.

A second aspect described in the study was the fact, that the systematic investigation on global fire events was not available at that time due to the fact that the information required was not retrievable from the fire management agencies. It has to be pointed out that the impacts of global wild fires have a massive contribution to greenhouse emissions, and to climate conditions (Wooster et al. 2005).

For these reasons it was decided to investigate the implementation of an infrared fire monitoring system on a small satellite.

### ***8.1.1 Fire Monitoring, Fire Ecology and Climate Change***

Normally only large fires in the vicinity of densely populated areas are of public interest. The fire-fighting management agencies, in these cases, have a difficult and demanding task because such fire events consist of many different types of fires with different intensities, and expansion properties. For the fire-fighting management agency it is important to know these characteristics to decide where the limited fire-fighting resources can be deployed most efficiently. Such an overview can be given only by special airborne or spaceborne systems. A spaceborne system has a much larger field of view than an airborne system and can deliver this overview much faster. The image delivered by the infrared system of BIRD in 2003 showing the monstrous fires in Portugal (Fig. 8.1) can be mentioned as a typical example. This image was delivered to the Global Fire Monitoring Center GFMC in Freiburg half an hour after being downloaded to the ground station, and was according to the Portuguese Fire Monitoring Center the main basis for their decisions on fire fighting strategies.

However the decisions of the fire-fighting management are not only depending on the location of the fire, but also on its strength, and magnitude, the burning fuel and other factors. Therefore it is not only necessary to detect the fires, and to find out their geo- location but also to measure the main fire parameters in detail. This is

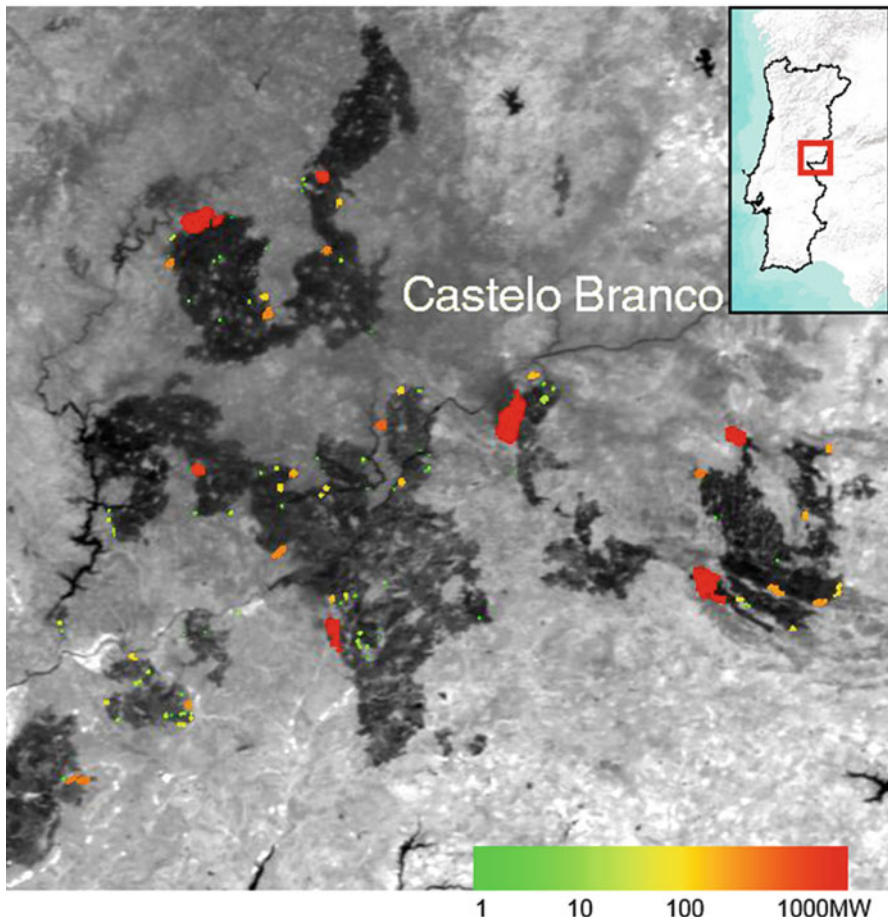


**Fig. 8.1** Fragment of the BIRD image of 4th August 2003: hotspots with their fire radiative energy release projected on NIR image (0.84–0.90  $\mu\text{m}$ ) published in this form by the GFMC in Freiburg

a demanding measurement task which requires a sophisticated space based infrared instrument.

The fire-fighting management agencies are also very interested in detailed quantitative fire parameters. Fires have a major impact on the ecological systems. In some cases fires are a part of the ecologic systems, and in other cases the fires are of a fully destructive nature causing loss of life and damage to the environment. And last but not least, the combustion of organic fuels generates CO<sub>2</sub> and other greenhouse gases. Different studies show that more than 30 % of the greenhouse gas emissions are caused by wild fires (DLR 2005).

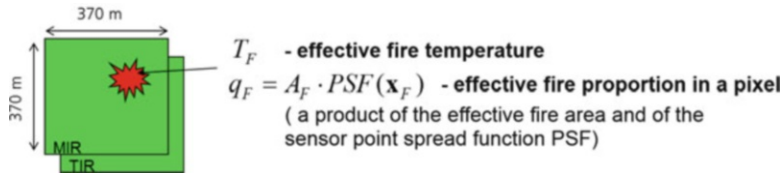


**Fig. 8.2** Application of bi-spectral technique (Dozier 1981) for the retrieval of effective fire temperature and area

### 8.1.2 Description of Fire Observation Scenarios

From the human point of view fires are a very impressive light event coupled with extreme high temperatures. For these reasons the measurement of fires seems to be a very simple task. But in the praxis using remote sensing very different aspects have to be considered.

At a first glance a wild fire seems to be huge for an observer on Earth. However using detailed imagery it can be seen, that an assumed large-area fire consists of a multitude of small fire fronts, with gaps and intervals of some meters, and a distance from each other up to 100 m. Furthermore, a huge amount of the thermal energy will be propagated by convection via the atmosphere (Freeborn et al. 2009).

This should not be a problem for airborne measurements as the instruments have a ground resolution of for examples 3 m, and the infrared instruments can partly ‘feel’ the convection process.

Spaceborne measurements have a completely different scenario. They have a very low ‘feeling’ for the convection processes ,and have normally a ground resolution greater than 100 m, where a single fire front fills only a part of the area seen by a single detector element as shown in Fig. 8.2. The result is the brightness temperature measured by the related detector element which is indeed higher than the values of the surrounding detector elements, but does not reflect the real fire temperature.

This situation is analytically described by Dozier’s model (1981).

$$L_j = q_F B_j(T_F) + (1 - q_F) L_{j,bg} \quad (8.1)$$

Where:

$L_j$  and  $L_{j,bg}$  are hot pixel and background radiances in channel  $j$  ( $j = \text{MW, LW}$ ).

(MW – 3–5 μm; LW > 8 μm)

$B_j(T)$  is the black body radiance in channel  $j$ .

$q_F = \rho_j(\mathbf{x}_F - \mathbf{x}_p)A_F$  is the effective fire proportion in the pixel (for small fires).

$\rho_j(\mathbf{x}_F - \mathbf{x}_p)$  is the point-spread function (PSF) of channel  $j$ .

$x_F$  and  $x_p$  are the fire and pixel centre coordinates.

$T_F$  is the fire temperature.

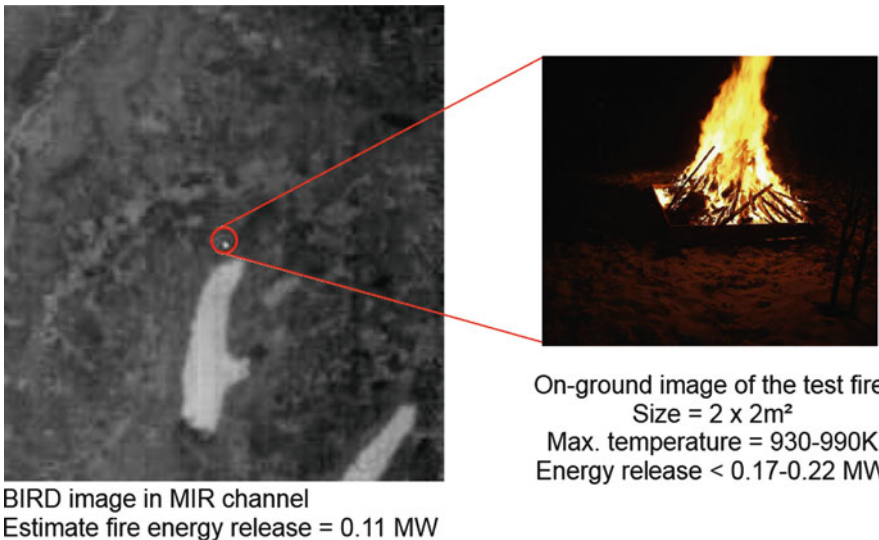


**Fig. 8.3** Measurement of a very small fire with the BIRD satellite. On ground verification of nighttime BIRD fire detection (18 January 2003, Ammersee area, Germany)

In this model the two unknown parameters  $q_F$  and  $T_F$  can be calculated if the radiances  $L_j$  are measured in two different spectral bands, so that the same scenario will be represented by two independent measurements.

In the result it is possible to measure the real temperature and the size of a fire from space with an instrument which has a ground pixel size of 370 m as in the case of the BIRD satellite (see Fig. 8.3).

Clarifying that two different spectral bands are necessary for a measurement in the sub pixel range, it has to be find which spectral band is optimal for the fire detection.

The general characterization of different remote sensing objects is shown for the spectral interval between 0.4 and 15  $\mu\text{m}$  in Fig. 8.4.

Depending on the spectral band in which the dedicated instrument is used the received radiation has different origins. At smaller wavelengths up to 2  $\mu\text{m}$  the signal consists mainly of reflected sun light having its maximum at  $\sim 0.5 \mu\text{m}$  (the temperature of the sun surface is 5,778 K). High reflecting objects like clouds or water surfaces can cause very high signal levels (sun glints). For a fire with a temperature of 1,000 K the maximum is located around  $\sim 2.9 \mu\text{m}$ . For larger wavelengths more and more fractions come from the thermal emission of the observed objects having its maximum at  $\sim 10 \mu\text{m}$  for a temperature of 300 K.

The categories vegetative background, and warm soil are typical objects of interest for remote sensing. The signal caused by a fire in the spectral band 3–5  $\mu\text{m}$  is much higher than the signal of these objects, and can be easily detected. Sun glints can deliver a signal much higher than a fire event and can be confused by this.

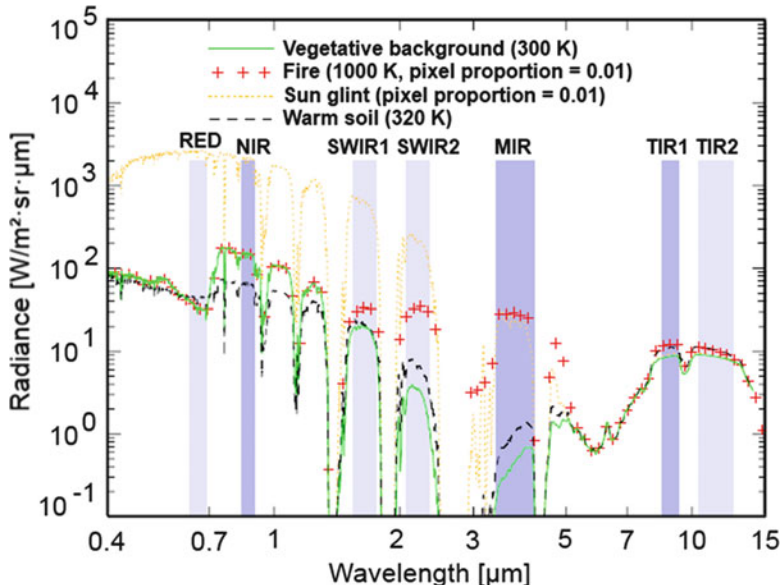


**Fig. 8.4** Simulated top-of-atmosphere spectral radiances of a 1,000 K sub pixel-sized fire in comparison to that of a vegetation background, sun glints from water surfaces, and homogeneous warm soil

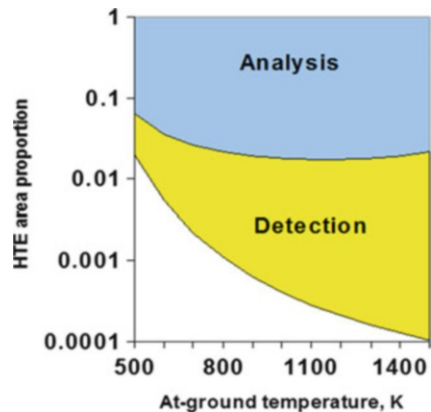
To fully understand the curves in Fig. 8.4 it is important to consider the absorption of the atmosphere which is strongly depending on the wavelength. The result of the radiation is observable in a spectral band up to 2.5  $\mu\text{m}$ . The next atmospheric windows are located between 3 and 5  $\mu\text{m}$ , and between 8 and 15  $\mu\text{m}$ .

Within the atmospheric windows weaker absorption lines are seen which can vary with the actual atmospheric conditions. It is recommended to limit the spectral sensitive bands of the instruments, and thus minimizing the influence of these absorption lines.

For the detection of fires, even if they are small, it is essential to have an as high as possible signal level compared to other objects like vegetation. Obviously the MW band marked in gray in Fig. 8.4 is the best choice. Only the sun glint signal deliver a signal comparable to the ones of a fire. For smaller wavelengths the sun glint signal becomes more and more dominating and the fire signal could not be detected in the wavelength region  $<1.5 \mu\text{m}$ . Therefore an additional instrument which is sensitive in a spectral band  $<1.0 \mu\text{m}$  would detect a sun glint, but not a fire, thus delivering a unique criteria which distinguished between a fire and a sun glint.

Considering the role of the sun glints it is obvious that for a numerical calculation of the fire parameters according to Eq. (8.1) the LW band in Fig. 8.4 is the only usable spectral band where the influence of the sun glint is small enough. In addition a measurement at a wavelength  $<1 \mu\text{m}$  can confirm that the object is a fire and not a sun glint, because a fire cannot be detected at this wavelength (see Fig. 8.4).

**Fig. 8.5** Minimum fire proportion in a hot cluster required for fire detection (yellow) and a quantitative analysis with an accuracy of better than 30 %



Discussing Fig. 8.4 in connection with Eq. (8.1) it must be considered that in the figure the case is depicted, that each class of objects fills the whole pixel. In difference to this in Fig. 8.2 is shown the case that the received signal is a mixture of two different components – the fire and the background signal.

At a given extension lower than the pixel size the fire must have a minimal temperature to be identified as a possible candidate for further analysis. The signal difference to the signal of surrounding pixels not affected by fire must exceed the signal noise as well as the variation of the surrounding background signal. This situation is shown in Fig. 8.5. To detect fires in small areas the temperature of the fires must be higher in order to analyze its thermal structure (analysis). This figure is a basic guideline for the design of sensitive fire detectors.

The second aspect is the measurement of the fire parameters in the sub pixel range using formula (8.1). For quantitative calculations the measurements in the LW band have to be used. As seen from Fig. 8.4 the differences between the background signal (vegetation) and the fire signal are much lower than in the MW band. With respect to Fig. 8.5 it is clear, that the related curve describing the conditions for a reliable estimation of the fire parameters must be located considerably higher than the one describing the detection because of the smaller difference in the LW band. Detection is possible earlier than a quantitative analysis. It is however important to mention that numerical limits for the analysis will be defined in difference to the detection mainly by the signal to noise ratio of the LW instrument, whereas the detection limit is depending on the variations in the background signal (see ESA/ESTEC 2007, program flow chart in Chapter 4.6.2).

The equation system (8.1) can be solved only if the difference of the hot pixel radiance  $L_j$  and the background radiance  $L_{j,bg}$  is higher than the signal noise. According to Fig. 8.4 this difference is quite low in the LW band. Therefore one of the most important conclusions is that an excellent fire monitoring system has to be also an excellent instrument for normal environmental temperatures.

The final parameter characterizing the fires is not the fire temperature but mostly the so-called Fire Radiative Power (FRP), as a measure of the intensity of burning. The FRP can be roughly described by Eq. (8.2).

$$FRP = \sigma(T_F^4 - T_b^4)A_F \quad (8.2)$$

- where  $\sigma$  is the Stefan-Boltzmann constant,  $T_b$  is the background temperature that is assumed to be equal to the mean at surface LW temperature in the vicinity of the hot cluster,  $T_F$  is the fire temperature and  $A_F$  the extent of the fire.

### 8.1.3 Spaceborne Fire Observation Systems

Whereas the impact of fires on the earth's environment is known, a dedicated satellite Fire Observation Remote Sensing System does not exist at the present time. Future systems like ESA's Sentinel 3 with the Sea and Land Surface Temperature Radiometer (SLSTR) or the German System Enmap with the SWIR (short wave infrared  $<2.5\text{ }\mu\text{m}$ ) do not have the MW band essential for the fire detection. Other existing spaceborne systems are capable to detect and to measure fire events due to their infrared channels. In the previous chapter it was mentioned that a fire observation system must have all features of a system measuring thermal environmental scenarios with high accuracy. However one additional important feature identifies an infrared instrument optimized for fire detection: In case of very large fires a 'normal' system will be saturated especially in the MW band. Therefore the infrared system should be equipped with special features to avoid the saturation e.g. electronic real time saturation prevention within the detector control. In all other aspects the fire detection system has to fulfill all requirements necessary for an infrared system serving all traditional applications for such a system.

The first dedicated fire observation system equipped with an anti-saturation mechanism was the Hotspot Recognition Sensor (HSRS) instrument on the BIRD satellite.

Other systems have a lower ground resolution compared to BIRD (370 m) and therefore the probability of saturation is lower, so an anti-saturation mechanism is of less concern. On the other hand a smaller ground resolution reduces the possibility to observe small size fires (see Fig. 8.5a).

In Table 8.1 parameters of different systems capable to generate fire products are shown. Except for the BIRD satellite all have a ground resolution  $\geq 1,000\text{ m}$ . This results in different fire observation capabilities as shown in Fig. 8.6.

The fire radiative power FRP shown in the abscissa characterizes the strength of the fire and is an important basic parameter in developing higher fire-observation products. The number of hot clusters describes the observation occurrence of fires characterized by the FRP. The observation of small fires (low FRP) is important in terms of an early warning system. The BIRD instrument system is the only system

**Table 8.1** Parameters of different systems capable to generate fire products

Instrument	Resolution (m)	Swath	IR1 ( $\mu\text{m}$ )	IR2 ( $\mu\text{m}$ )	IR3
AVHRR	1,100	2,928 km	3.55–3.93	10.3–11.3	11.5–12.5
GOES I-M	4,000	3,000 km	3.80–4.00	10.2–11.2	11.5–12.5 $\mu\text{m}$
SEVIRI	3,000	Earth disc	3.48–4.36	9.8–11.8	11.0–13.0 $\mu\text{m}$
MODIS	1,000	2,330 km	3.93–3.99	10.8–11.3	11.77–12.27 $\mu\text{m}$
HSRS	370	190 km	3.4–4.2	8.5–9.3	

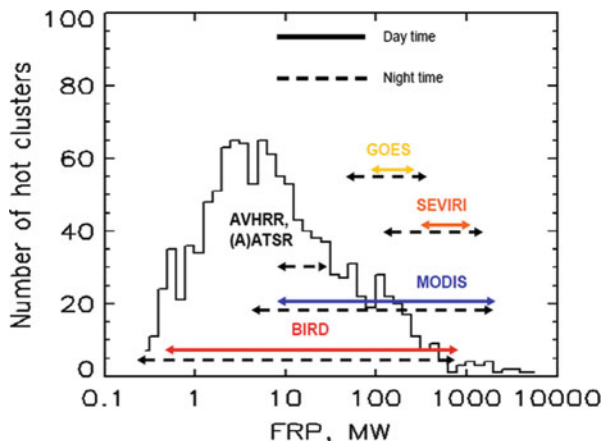


**Fig. 8.6** Histogram distribution of FRP (Fire Radiative Power) obtained from BIRD HTE observations and arrows for the FRP (with  $<\pm 30\%$  accuracy) ranges which are covered by BIRD, MODIS, SEVIRI, GOES at day and night and by AVHRR and (A)ATSR – only at night (ESA/ESTEC 2007)

which can cover the whole range of the different fire scenarios. In the case of AVHRR for instance the lower resolution does not allow the observation of small fires, whereas larger fires cannot be measured because of early saturation.

### 8.1.4 Worldwide Usage of Fire Monitoring Data in National GIS Systems

The usage of space based fire-observation data is of great interest for many national and international organizations (Ahern et al. 2001; Altan et al. 2010). The motivation for the usage may be different according to individual needs. The fire-fighting management agencies have a key need which requires a strategic area overview. This overview can be delivered mainly by satellites. Furthermore the same instruments can provide a lot of information for the early warning systems, and prevention procedures (see URL1).

The other important aspect is the previously mentioned strong influence of global wild-fire events, and the impact on the climate change processes. This last aspect requires the knowledge of well-established statistical data about the worldwide wild-fire events as well as a better understanding of the mechanisms of the ongoing processes (Boehm and Siegert 2001).

Examples for related national GIS systems are the Sentinel Portal in Australia (see [URL2](#)) and the South Africa Fire Services (see [URL3](#)). These are national bushfire monitoring systems that provide timely information about hotspots to emergency service managers.

The Global Fire Monitoring Center (GFMC) in Freiburg (see [URL4](#)) coordinates many international activities on behalf of the United Nations. The GFMC is responsible for the coordination of the Global Wildland Fire Networks.

## 8.2 Concept and Characteristics of the IR Instruments on Board the BIRD Satellite

Under the slogan “Faster Better Cheaper (FBC)” (NASA 1999) in the 1990s the developments of small satellite technologies were intensified. A small satellite was defined at this time as a satellite with a mass in the order of 100 kg or less. It is obvious that the costs for a small satellite are lower than the costs for a big satellite. Last but not least a small satellite can be launched piggy-back reducing the launch costs drastically and minimizing the negative outcome of a possible loss of the satellite.

Due to its size small satellites can accommodate only small instruments and provide only limited resources. Following this logic it is necessary to develop specific instruments capable to serve the challenging remote sensing tasks.

In Germany the first small satellite called BIRD (Fig. 8.7) was designed and built by DLR (Briess et al. 2002). The satellite was launched on October 21st 2001, and was in service to 2004. The BIRD mission was a technology demonstrator with the following primary mission objectives:

- Test of small satellite technologies, such as an attitude control system using new star sensors and new actuators, an on-board navigation system based on a new orbit predictor and others.
- Test of a new generation of infrared array sensors with an adaptive radiometric dynamic range.
- Detection and scientific investigation of High Temperature Events (HTE) such as forest fires, volcanic activities, and coal seam fires.

### 8.2.1 Basic Requirements to the Detector System

According to the criteria given in Sect. 8.1.2 a demanding fire-observation instrument needs at least two different, highly sensitive infrared detectors. One must be



**Fig. 8.7** Configuration of the BIRD satellite

sensitive in the mid-wave infrared (MW, 3–5  $\mu\text{m}$ ) and one in the long-wave infrared (LW, >8  $\mu\text{m}$ ). The required high sensibility of the infrared detectors presupposes the usage of active cooled quantum detectors.

Additionally at least one detector in the visible spectral region is required to handle the false alarms.

The detectors should be equipped with optics capable of realizing a ground resolution notably better than 1,000 m. According to Fig. 8.5 the ground resolution defines the size of the detectable fires. To avoid saturation in case of larger fires the IR camera should have an electronic saturation prevention capability (Zhukov et al. 2006).

The optical design for the infrared detectors has to be adapted to the design of the detector units in order to protect the detector against thermal radiation from the surroundings which would decrease the accuracy of the measurements.

All detector arrays were arranged as long linear arrays. The area monitored by the satellite should be as large as possible. Therefore the number of the detector elements across the flight path of the satellite should be as large as possible. Large satellites often uses an across-track scanning mirror to enlarge the number of image points in this direction, but it is not possible to use this item on a small satellite and thus long linear arrays are the best choice. A linear array delivers a one-dimensional image; the second dimension will be realized by the movement of the satellite scanning in fly direction a certain area on the earth. This method constructing an image is called push broom imaging.

According to these specifications a special infrared detector design has to be developed which is compatible to the satellite bus. In Fig. 8.8 is shown the infrared detector unit including the dedicated optics as designed and built for the BIRD satellite.

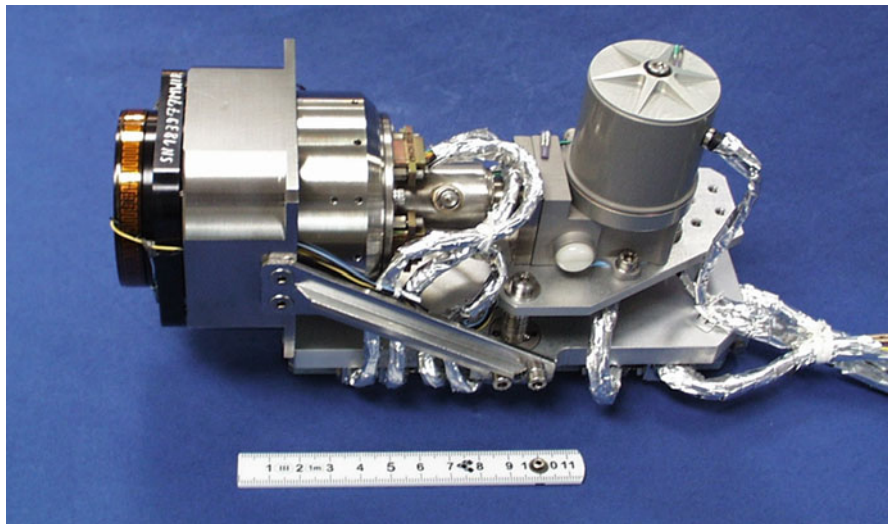


**Fig. 8.8** Infrared detector unit for the BIRD satellite (primary aperture (*left*), focal plane array (*middle part*), Cooler (*right*)) (scale bar in cm)

The complete BIRD payload compartment is shown in Fig. 8.9a, and details of the infrared payload in Fig. 8.9b.

The specific parameters of the instruments are given in Table 8.2.

The NEDT (noise equivalent differential temperature) for the infrared (IR) instruments is in the order of 0.1 K.

### 8.2.2 *Technical Limitations Caused by the Satellite*

In the previous chapters limitations were highlighted especially in the design of the infrared instruments which were caused by the limited resources of a small satellite.

It should be considered for the BIRD mission, that BIRD was launched 10 years ago. The technical knowhow was different compared to today, and due to these limitations there were only a few chances on how to overcome the related problems. The BIRD mission was a precursor with the purpose to verify new technological approaches.

The first evident item in this context is the usage of cryogenic coolers cooling down the two infrared detector units down to  $-200^{\circ}\text{C}$ . Un-cooled infrared detector technologies like bolometers do not have the necessary sensitivity to fulfill all requirements (Kingston 1978).

The cooling engines offered 10 years ago were large, heavy and power consuming. With respect to the very low temperature which has to be achieved and a required long lifetime the design was restricted to certain criteria. Additionally

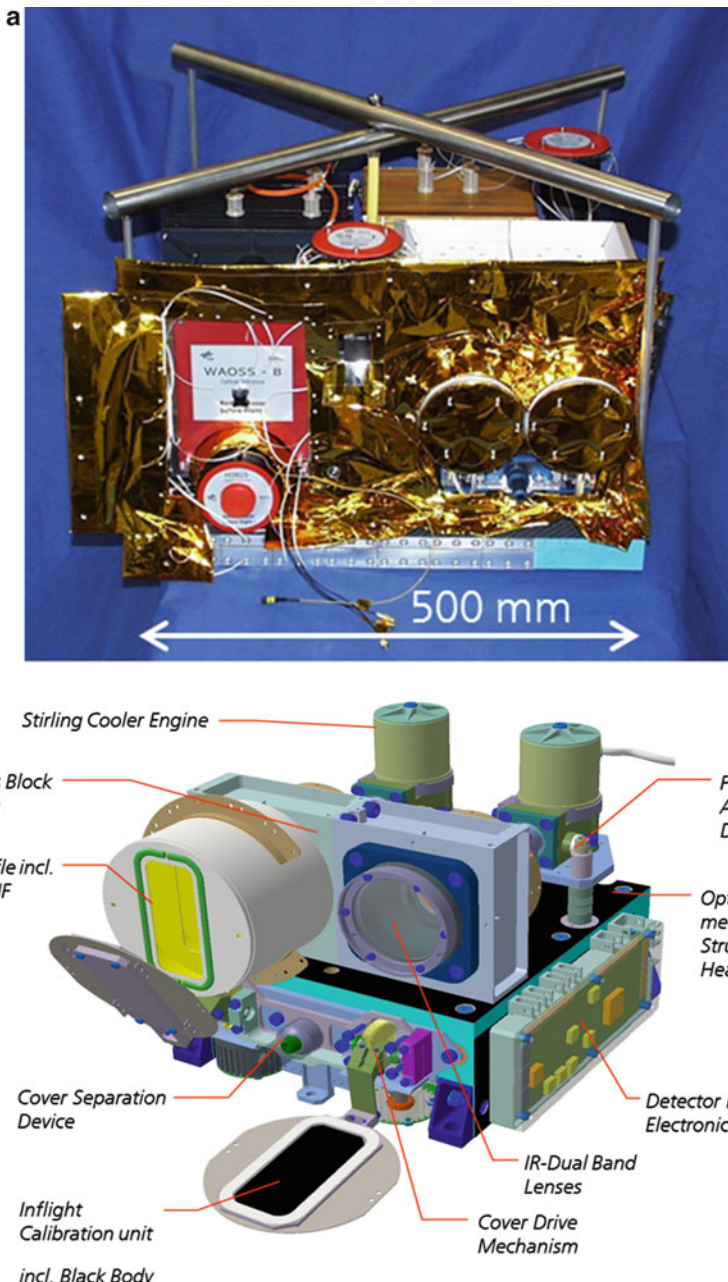


**Fig. 8.9** (a) The complete BIRD payload compartment. On the *left side* the WAOSS camera is located, on the *right* the two infrared cameras. (b) Details of the BIRD infrared payload

**Table 8.2** Parameters of the BIRD instruments

	WAOSS-B	MW	LW
Wavelength	600–670 nm 840–900 nm	3.4–4.2 $\mu\text{m}$	8.5–9.3 $\mu\text{m}$
Focal length	2.65 mm	46.39 mm	46.39 mm
Field of view	50°	18.8°	18.8°
f number	2.8	2.0	2.0
Detector	CCD line	CdHgTe arrays	CdHgTe arrays
Detector cooling	passive, 20 °C	Stirling, 90 K	Stirling, 80 K
Pixel size	7 × 7 $\mu\text{m}$	30 × 30 $\mu\text{m}$	30 × 30 $\mu\text{m}$
Pixel number	2,880	2 × 512 staggered	2 × 512 staggered
Quantization	11 bit	14 bit	14 bit
Ground pixel size	185 m	370 m	370 m
Swath width	533 km	190 km	190 km

smaller cooling engines to meet constraints regarding the lifetime were developed, especially for military applications. Because the planned lifetime of the BIRD mission was 1 year the detector provider was mandated to investigate the applicability of these small space coolers. The results based on these constraints were satisfactory (on ground run time tests over 9,000 h) and confirmed by a life time in orbit of more than 10 years. The relatively low duty cycle (30 min per day) could question this design philosophy, nevertheless it had to be decided what is more dangerous for the life span – a continuously operating mode or a consequent switch on – switch off only when a measurement is desired.. The main part of the cooling system of the BIRD detectors is the cylindrical part in the right upper side of the picture in Fig. 8.8.

The described cooling engines have a rotatory drive which influences the angular momentum of the satellite and with this the stability. Due to its small size the disturbing forces are low compared to the inertial momentum of the satellite. Last but not least the impact of this disturbance is dependent also on the ground resolution of the instruments. With the resolution shown in Table 8.2 the cooling engines do not impact the data performance.

For similar reasons the use of mechanical scanning mirrors on small satellites is not possible because the disturbing angular momentum would be too large. Therefore the usage of the infrared technology on small satellites is closely connected with the development of large infrared detector arrays which can collect the desired image data without moving mechanical devices.

Very similar to a domestic refrigerator the cooling engine generates an adequate amount of heat on its back side. This must be dissipated away from the detector unit. A direct coupling to a radiator is not advisable due to the fact that this may cause a not allowable under cooling of the system. Here a very balanced concept is necessary which uses heat buffering objects like the mechanical structure of the satellite bus. Numerical Thermal Models can be used to maintain the necessary conditions for a balanced thermal control.

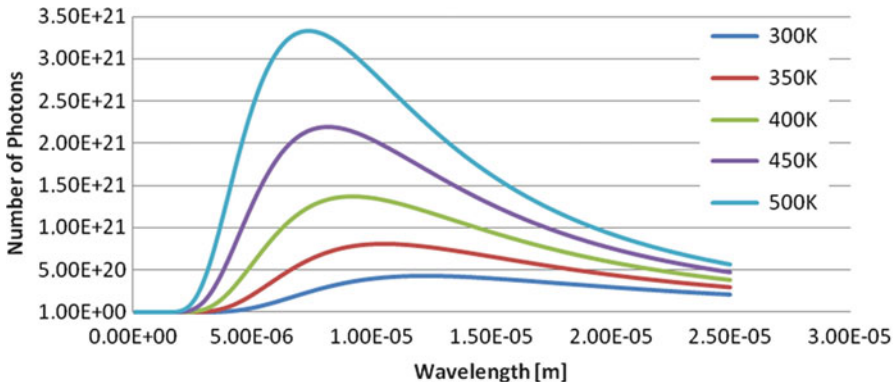


**Fig. 8.10** Numbers of photons emitted by a black body at different temperatures

### 8.2.3 Calibration Requirements

The calibration procedures have to provide as well the radiometric measurement process for the geometrical processes of the image formation.

After receiving a certain input radiation power a detector element generates a related electrical output signal. In digital camera systems this output signal will be converted to a digital number. It is the task of the calibration procedure to reconstruct this relationship between the input power and the respective digital number using a well specified reference source. For infrared systems the ideal reference source is a black body which generates for a given temperature a heat radiation according to Planck's law as shown in Fig. 8.10.

On the BIRD satellite cooled quantum detectors are used which work like a photon counter with a quantum efficiency  $\text{QE} < 30\%$  ( $\text{QE}$ : incident photon to converted electron ratio). It is expected that the output signal is proportional to the number of photons falling on the detector. The calibration procedure has to establish this linear dependency between the calculated number of photons and the related detector output signal.

In principle it would also be possible to calculate the dependency of the output signal on the temperature settings of the black body. But this dependency is nonlinear and the handling of the fitting procedures is quite problematic whereas the calculation of the number of incident photons is simple knowing the spectral characteristic of the detector and the temperature setting of the black body. Last but not least the radiometric calibration procedure should describe the detection process correctly and this is the linear dependence of the number of photo electrons on the number of incident photons.

The radiometric on-ground calibration is a standard procedure similar to the ones used for commercial thermography cameras. But the detector parameters have also to be controlled continuously on board because of possible degradations caused by radiation, out gassing deposits and other effects. Considering the linearity of the fit



**Fig. 8.11** Test assembly for geometrical measurements. On the *left side* the manipulator to simulate the satellite movements is located, on the *right side* the collimator to realize the imaging of objects in fare distances

procedure for the on-board calibration procedure the black body measurement for at least two different temperatures is necessary. Tilt mirrors changing alternately the illumination source for the detectors are often used for this purpose. On-board black bodies with a stable temperature and the deep space usually serve as calibration sources (Rataj et al. 2011).

Because the tilt mirror devices are quite voluminous and heavy another method was developed for BIRD. Figure 8.9a shows that the optics of the infrared instruments is covered by small flaps. These flaps are little black body devices shown in Fig. 8.9b. Under the black lacquer coating inside of the flaps there is installed a heating foil, and temperature sensors. The flaps will be opened before a measurement and closed after the measurement heating up continuously the black lacquer coating inside to a given maximal temperature. By using this method the measuring data for the calibration gather more information than the two-point method.

As well as the radiometric calibration it is important to verify the geometrical properties of the payload. Here different aspects are to be considered. All components of the payload are imaging systems. Therefore the first task is the validation of the imaging properties taking into consideration that the objects of interest will be observed from an orbit altitude of several hundred kilometers. The optics is designed for imaging of distant objects; images of objects in distance of some meters are blurred. Collimator optics between the test objects and the cameras as shown in Fig. 8.11 creates a scenario equivalent to the imaging of far away objects.

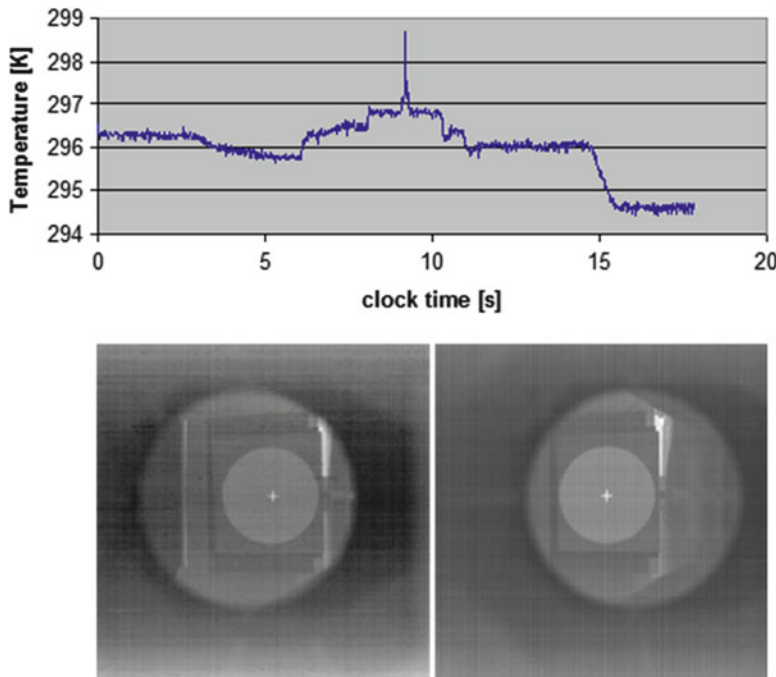


**Fig. 8.12** Crosshair target image simultaneously measured by the LW (*lower left*) and the MW (*lower right*) camera ( $1,024 \times 1,024$  pixels). The *top* picture shows the temperature profile measured by a detector element of the MW camera

In Sect. 8.1.2 the Push Broom principle of the BIRD instruments is discussed. The Push Broom principle implies a movement of the camera relatively to the object in direction across the orientation of the detector line array. For this reason the payload was mounted on a manipulator with two perpendicular rotary axes (to the left in Fig. 8.11) simulating the movement of the satellite. In Fig. 8.12 the images show a cross-hair target located in the focus of the collimator. The left picture in this figure demonstrates the application of the radiometric calibration to the target images illustrating this with the overall calibration complex.

### 8.3 BIRD Infrared Data Processing Procedures

To conclude and summarize the discussion of all design aspects for the BIRD instrumentation a validation of the overall concept and design is necessary.

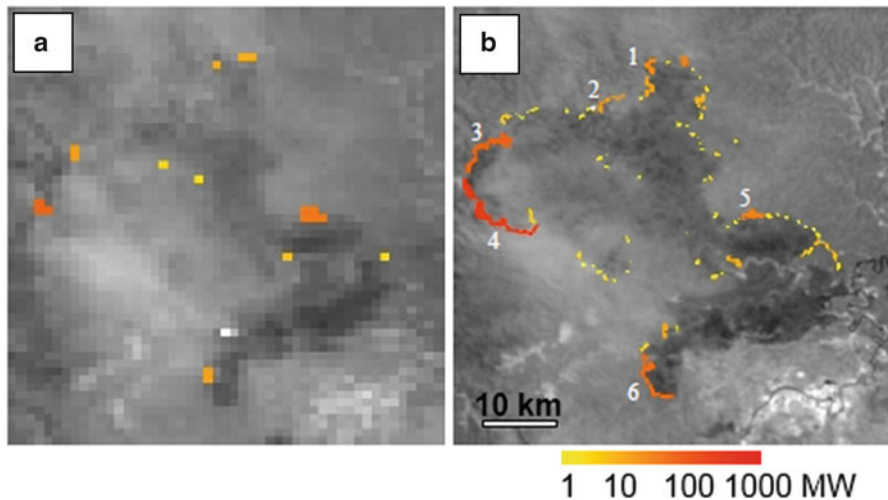


**Fig. 8.13** Zoomed fragments of images showing hot clusters detected in the bush fire images of Australia, NSW obtained on 5 January 2002 by MODIS (a) and BIRD (b)

### 8.3.1 Fire Detection and Monitoring Application

In Fig. 8.3 there is shown an example detecting an extreme small fire.

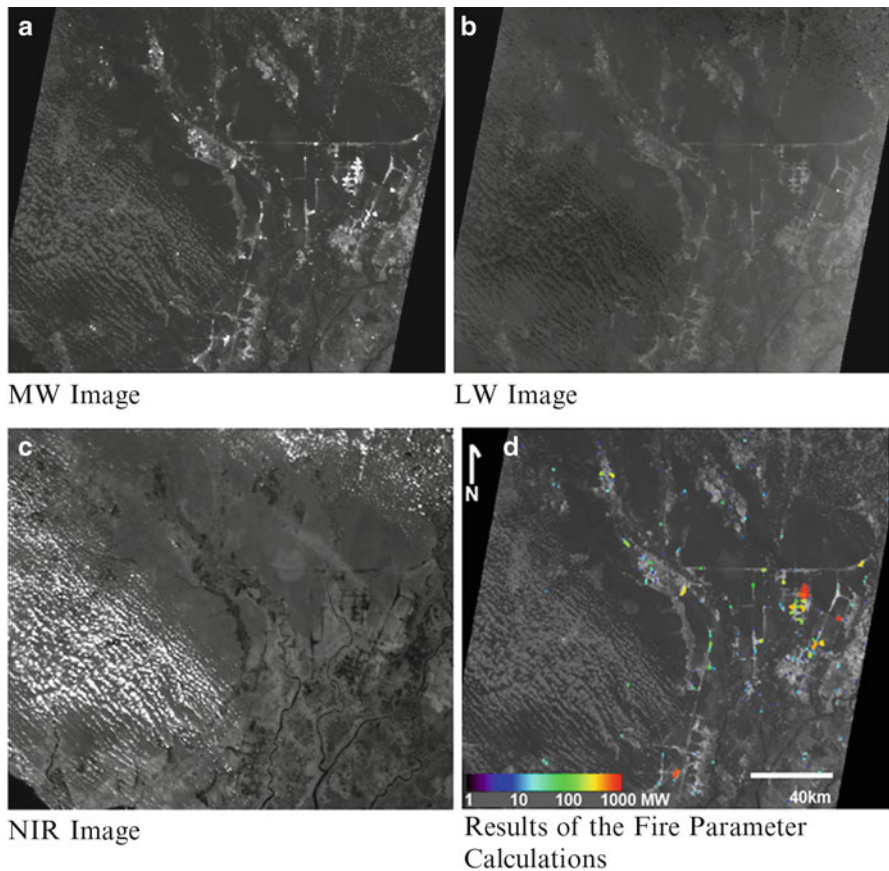
The surrounding background of the fire has a quite low temperature ( $-9^{\circ}\text{C}$ ). The data take was captured at night time drastically reducing the background variations caused by reflected sun light. Both aspects promote a good contrast of the fire pixel to the background. The BIRD instruments have an outstanding performance as is demonstrated by a comparison with MODIS (Moderate Resolution Imaging Spectroradiometer) data in Fig. 8.13 (related BIRD results are shown in Table 8.3 (DLR 2005)). The time delay between the BIRD and MODIS image capture was 20 min, which makes the comparison representative by this kind of highly dynamic phenomena.

Figure 8.14 illustrates the classification and calculation procedures for high temperature events using the Bi-Spectral Method as described in Sect. 8.1.2. In the MW image (a) the bright areas and spots are possible candidates for high temperature events, mainly fires. But it is also possible that some of these spots are sun glints from water or clouds. The clouds (left lower corner in the images) are bright objects in the NIR image (c) because the sun light reflected and scattered by the clouds is dominating in this band. In the LW image (b) the clouds appear as dark objects because the LW band is mainly sensitive to the low temperatures of the clouds. Considering these relationships it is possible to disregard the false alarms caused by the sun glints from the original data (ESA/ESTEC 2007).

Another reason for false alarms may be warm soil areas as shown in Fig. 8.4. In this case the signal intensity in the LW band is higher than the MW band. For fire events this situation is inverted, and these events can also be distinguished from the

**Table 8.3** Characteristics of selected bush fire fronts in the BIRD image Fig. 8.13b of Australia, 5 January 2002 (the confidence intervals for these parameters are indicated in brackets)

Hot cluster see Fig. 8.13b	Effective fire temperature, K	Flaming ratio	Effective fire area, Ha	FRP, MW	Front length, km	Front radiative intensity, kW/m
1	1,163 (896–1,500)	1.0 (0.42–1.0)	0.10 (0.09–0.28)	103 (103–105)	2.9	36
2	1,500 (933–1,500)	1.0 (0.56–1.0)	0.07 (0.06–0.16)	71 (71–71)	4.2	17
3	874 (754–1,186)	0.36 (0.13–1.0)	0.66 (0.20–1.35)	217 (210–222)	6.8	32
4	956 (830–1,500)	0.68 (0.25–1.0)	0.99 (0.42–1.86)	465 (464–492)	12.9	36
5	1,084 (863–1,500)	1.0 (0.33–1.0)	0.16 (0.11–0.40)	122 (122–128)	3.1	39
6	1,107 (800–1,500)	1.0 (0.20–1.0)	0.22 (0.17–0.89)	190 (190–198)	9.6	20



**Fig. 8.14** Peat fires in Kalimantan taken by BIRD at 24 August 2002. In the MW image (a) the bright areas and spots are candidates for high temperature events or sun glints. These can be deselected comparing the MW image with the NIR image (c) and the LW image (b). The verified fire spots will be processed according Eq. (8.1) using the related pixel of the MW and the LW images. The result is shown in the image (d)

fires with a high probability. This classification procedure is driven by a well justified threshold parameter as described in ESA/ESTEC (2007).

By eliminating all false alarms the remaining events can be classified with a high probability as fires. The parameters can be calculated according to Eq. (8.1). In Figs. 8.13b and 8.14d the color of a fire sector represents its FRP value.

### 8.3.2 Environmental Temperature Applications and Their Relationship to Fire Applications

The classical application fields for infrared systems in space are thermal processes on Earth within a temperature region  $250 \text{ K} < T_b < 350 \text{ K}$ . Many of these

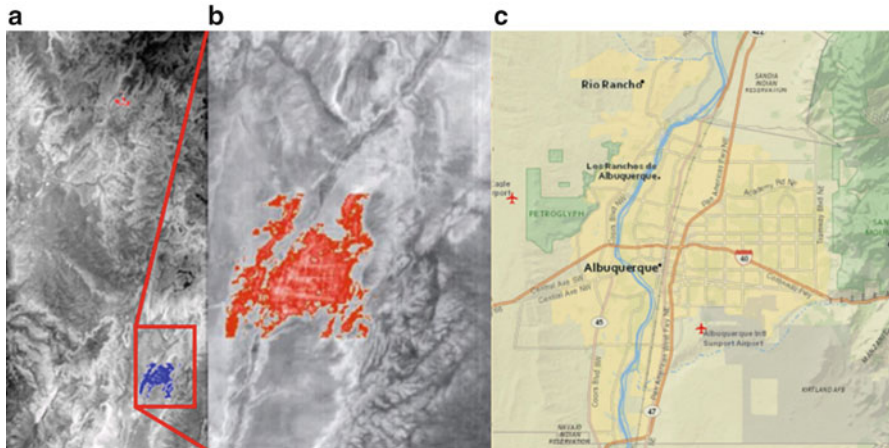


**Fig. 8.15** A thermal image taken by BIRD on 17 June 2002. In picture (a) in the northern part a large fire area near Denver (*red colored*) is shown and in the south the area of Albuquerque (*blue colored*). Picture (b) depicts the area of Albuquerque in a larger scale and using a more subtle coloration. Picture (c) shows a rough map of Albuquerque

applications like sea surface temperature do not need a high resolution because they have a regional character. Other applications like moisture of dedicated agriculture areas may require a higher resolution (Melesse et al. 2007).

Figure 8.15 demonstrates the capability of the BIRD instruments to measure fire scenarios as well as urban heat scenarios.

In principle the bi-spectral method for measurements in the sub pixel region is not restricted to high temperature events. But for moderate temperatures close to the background temperature it is quite problematic to estimate a representative background temperature, and the resulting error is often not acceptable. An exception is the detection of objects on water because the water temperature is sufficiently uniform to detect a ship with a temperature slightly different from the water temperature.

A good example is shown in Fig. 8.15. The picture (a) demonstrates that BIRD is capable to handle within one data take very high temperature differences (fires near Denver) as well as quite low high temperature differences. The areal of Albuquerque is large enough to estimate a representative background temperature for the surrounding areas. All temperatures higher than this background temperature were mapped using a color table. The blue color indicates lower temperatures, red indicates higher temperatures. In picture (a) the fires near Denver are displayed and therefore the area of Albuquerque is depicted in blue. The temperature resolution represented by the different color shades is relatively coarse. In picture (b) the fires are not included and therefore the area of Albuquerque is the warmest part and the temperature resolution represented by the different color shades is excellent. A comparison of the colored region in picture (b) with the map of Albuquerque in picture (c) demonstrates the effect of the urban heat. In picture (b) there are also bright lines seen in Albuquerque

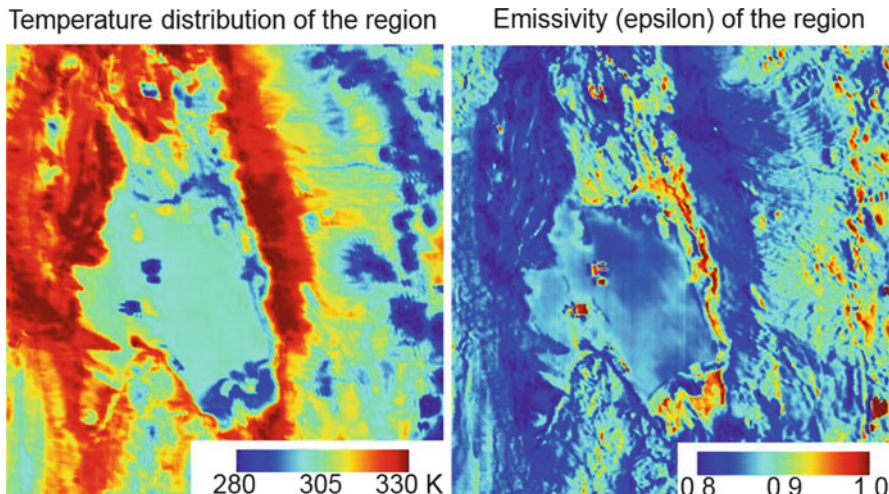


**Fig. 8.16** Epsilon T separation within the region of the Salar de Atacama

which can be identified with the road network. Taken into account that the ground resolution of the infrared cameras is 370 m it is obvious that the roads are sub pixel objects and can be handled by the bi-spectral method. The bi-spectral method is independent on the temperature of the object to be analyzed. Based on the previous data it becomes clear that all fire specific terms where used in the classification process to identify an object as a fire. The final application of Eq. (8.1) doesn't have any fire specific terms.

The bi-spectral method is one application based on the merging of two or more infrared channels. The retrieving of emissivity is another one.

Planck's law describes the heat radiation of an ideal black body with a given temperature. A black body is an idealized physical body that absorbs all incident electromagnetic radiation. The most natural objects are not a black body and the heat radiation emitted by them is less than that emitted by a black body with the same temperature. This can be described by a multiplicative factor in Planck's law which is less than 1. This factor is called emissivity and can be depend on the wavelength. With this the emissivity characterizes a material property. A black body has an emissivity of 1, an ideal mirror has an emissivity of 0 because a mirror reflects all incident electromagnetic radiation.

Figure 8.16 shows an example for the emissivity mapping. The infrared radiation coming from any natural objects is normally not identical to a black body radiation. If the temperature of a natural object will be measured by a contact thermometer, and parallel with an infrared camera than the measurement with the infrared camera normally offers a lower temperature. A natural object is emitting only a part of the heat quantity compared to that of an ideal black body. This will be described by a multiplicative factor in Planck's law called emissivity. The emissivity normally varies also with the wavelength. Assuming that the emissivity is not depending on

the wavelength a temperature measurement with an infrared camera will be described by two parameters- the temperature and the emissivity. Similar to the bi-spectral method it is possible to measure these two parameters using two infrared cameras with a different spectral response. The result of related calculations is shown in Fig. 8.16. It is surprising that the temperature picture (left) is blurred and the emissivity picture (right) is quite sharp. The temperature picture reflects all thermal processes like convection and atmospheric flicker in the vicinity of heated objects. The emissivity is a property of the objects and therefore the emissivity picture appears sharper. But this is only a side effect which can be used to improve the image quality. The quantitative measurement of the emissivity is more relevant for the characterization and classification of observed objects.

### 8.3.3 *BIRD Results and ESA's ECOFIRE Study*

The most detailed analysis of the BIRD data is presented in ECOFIRE Study (DLR 2005) financed by ESA. In Sect. 8.1.3 the specification of the BIRD instruments was compared with other systems. Two outstanding features are characteristic for the BIRD instruments: the higher ground resolution and their special technical design which considers a large variety of measurement scenarios.

The quality of the BIRD data demonstrated new opportunities to study new aspects of the worldwide fire processes, especially the impact of the wild fires on the atmospheric and climate processes as described in the executive summary of the study:

Wildfires and volcanic eruptions have trans-national impacts, most notably via the pyrogenic formation of gaseous and particle emissions that influence the composition and functioning of the atmosphere and the global climate system. Fires produce direct land-atmosphere carbon fluxes estimated to be about 2 Gigatonnes/year (Gt/y), compared to 6.5 Gt/y from fossil fuel consumption and cement production.

Using the BIRD data this statement could be verified. Furthermore, capability gaps in the current remote sensing programs could be identified.

A second part of this study was finished in 2007 (ESA/ESTEC 2007). A central statement of this second part was the following sentence:

A direct quantitative observation of the HTE plumes, HTE thermal characteristics and rates of heat output, which should relate more directly to the carbon, trace gas and aerosol emissions fluxes, are highly desirable and should allow current methods of emissions estimation to be significantly improved upon in terms of increasing the temporal frequency, accuracy and precision.

An experimentally derived relationship between the temporal integral of fire radiative power (the so-called fire radiative energy) and the fuel biomass combusted found by M. Wooster et al. (2005) who was involved in this second part could be investigated in more details using the BIRD data.

## 8.4 FIREBIRD as a BIRD Follow-On Small Satellite Constellation

As previously mentioned the BIRD satellite was an experimental satellite with limited capabilities. A single small satellite cannot replace a large satellite with the same applications. But it is worth discussing the advantage of a constellation of small satellites as far as the costs for the constellation do not exceed the costs of one large satellite. In this context it is important to consider not only the Hardware costs but in particular also the satellite operation costs. The main criteria for a comparison should be the operational aspects.

FUEGO (Martin-Rico et al. 1997) was a first proposal for a fire observation constellation with small satellites. Unfortunately the requirements regarding the operational aspects were unrealistic (15 min revisit time) so that this proposed concept did not find funding.

### 8.4.1 *Advantages of Small Satellite Constellations*

After the success of BIRD different approaches for small satellite constellations were discussed. To reduce costs it was decided to use the spare models of BIRD for the IR cameras because a development of new infrared detector devices would be very expensive and have a major impact on the overall costs.

Currently in discussion is the FIREBIRD constellation consisting of the two satellites TET-1 (Technologie Entwicklungsträger) and BIROS (Berlin InfraRed Optical System). TET-1 was launched on June 22nd 2012. BIROS is planned to be launched in 2014.

For an improved spatial and temporal coverage, the two satellites will circle the Earth at an altitude of about 520 km in solar-synchronous orbits with varying local equator crossing times as illustrated in Fig. 8.17. Furthermore the small satellites have a higher agility turning the line of sight slightly away from the nadir pointing which makes it possible to widen the swath width. This is an equivalent to the tilt mirror mechanisms of the large satellites.

Furthermore a satellite constellation has lower financial risks in case of defects in key components because the loss of one small satellite would result in a lower financial loss, however at the same time retaining at least one half of the mission capabilities.

### 8.4.2 *Future Infrared Instrument Concepts for Small Satellites*

Whereas it was mentioned in the beginning of this chapter that the FIREBIRD constellation uses BIRD spare models for the infrared cameras a comparison of

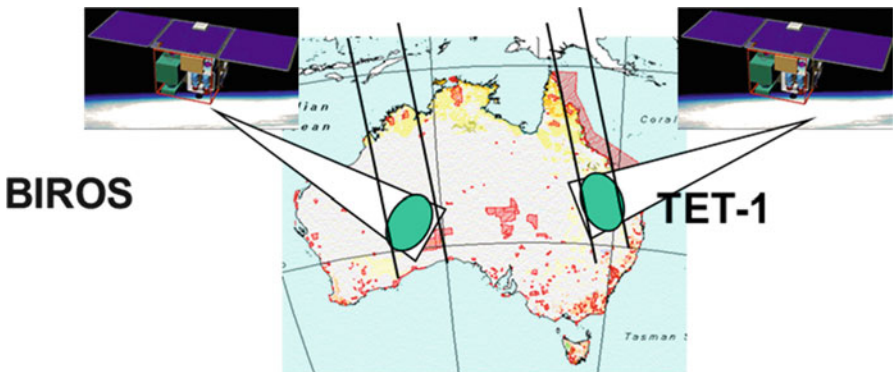


**Fig. 8.17** Improvement of spatial and temporal coverage using a constellation of two small satellites

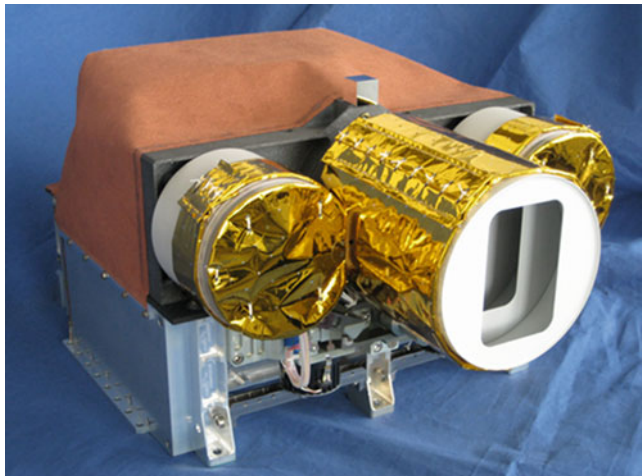


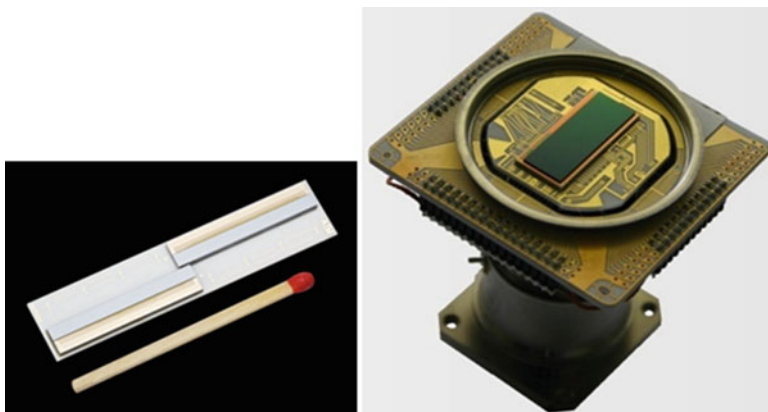
**Fig. 8.18** The optical payload for TET-1 and BIROS the next steps after FIREBIRD is that it will be necessary to specify and realize the next generation of infrared detector arrays

Figs. 8.9a and 8.18 demonstrates remarkable changes in the overall design of the payload caused by the joint BIRD experiences, and the advancement of satellite technology.

The parameters of the FIREBIRD mission are shown in Table 8.4. Noticeable are the changes for the visible camera. The choice of the spectral bands and the improved ground resolution (42 m) allow testing different new methods combining the visible and the infrared bands, and also improving the classification of the fire events.

**Table 8.4** Parameters of the FIREBIRD payload

	VIS	2 infrared cameras
Wavelength	0.5, 0.6, 0.8 $\mu\text{m}$	
Green, Red, NIR	MW: 3.4–4.2 $\mu\text{m}$ ; LW: 8.5–9.3 $\mu\text{m}$	
Focal length	90.9 mm	46.39 mm
FOV	19.6°	19°
Aperture	3.8	2.0
Detector	CCD lines	CdHgTe arrays
No. of pixel	3 $\times$ 5,164	2 $\times$ 512 staggered
Quantization	14 bit	14 bit
Ground resolution	42.4 m	356 m
Sampling size	42.4 m	178 m
Swath width	211 km	178 km
In-flight calibration	No	Black body flap
Accuracy of location	100 m at ground	100 m at ground

**Fig. 8.19** Design of a long linear array with 2,400 elements (© AIM Germany) (*Left* – the focal plane array, *right* – the focal plane array in the dewar housing without the entrance window)

The first step should be the application of longer line array thus improving either the ground resolution or the swath width or both. Figure 8.19 shows the design of a long linear array with 2,400 elements. The second step could be the construction of an infrared detector chip containing a MW band as well as the LW band on the same focal plane array. In this case only one infrared camera would be sufficient. This would also improve the geometrical co-alignment of the two spectral bands.

Last but not least would be to change over from the multispectral payload to a hyper spectral payload. Figure 8.20 shows the imaging spectrometer MERTIS (MErcury Radiometer and Thermal Infra-red Spectrometer) for the Mercury Mission BepiColombo (launch date 2015). It covers a spectral band from 7 to

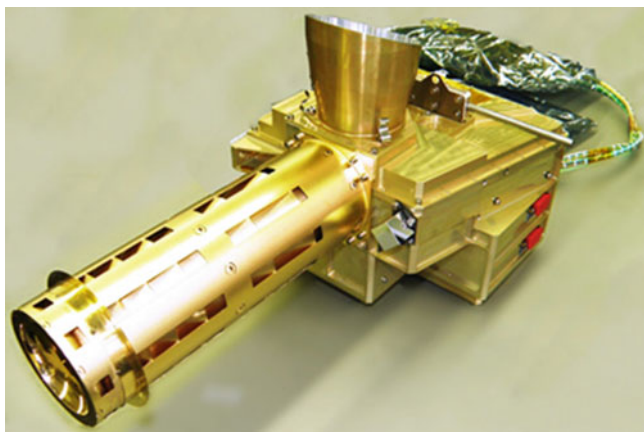


**Fig. 8.20** The imaging spectrometer MERTIS for the mercury mission BepiColombo is working in the LW band (7–14  $\mu\text{m}$ ), 180  $\times$  180  $\times$  130 mm $^3$  (excl. Baffles)

14  $\mu\text{m}$ . In combination with a similar instrument in the MW band it would be possible to gain more knowledge on global wildfires, and in addition give a better insight, and much more information about burning biomass and the emitted Greenhouse gases.

## References

- Ahern FJ, Goldammer JG, Justice CO (eds) (2001) Global and regional vegetation fire monitoring from space: planning a coordinated international effort. SPB Academic Publishing, The Hague
- Altan O, Backhaus R, Boccardo P, Zlatanova S (eds) (2010) Geo-information for disaster and risk management. Joint Board of Geospatial Information Societies (JB GIS). United Nations Office for Outer Space Affairs (UNOOSA)
- Boehm HDV, Siegert F (2001) Ecological impact of the one million hectare rice project in Central Kalimantan, Indonesia, using remote sensing and GIS. In: Proceedings of the ACRS 2001 – 22nd Asian conference on remote sensing, 5–9 Nov 2001, Singapore, vol 1, pp 439–444
- Briess K, Bärwald W, Hartmann M, Kayal H, Krug F, Lorenz E, Lura F, Maibaum O, Montenegro S, Oertel D, Röser HP, Schlotzhauer G, Schwarz J, Studemund H, Turner P, Zhukov B (2002) Orbit experience and first results of the BIRD mission. In: Proceedings of the 53rd international astronautical congress, 10–19 Oct 2002, Houston
- Brieß K, Jahn H, Röser HP (1996) A DLR small satellite mission for the investigation of hot spots, vegetation and clouds. *Acta Astronaut* 39:899–908
- DLR (2005) ECOFIRE study on scientific assessment of space-borne high temperature event observing mission concepts. ESTEC Contract No. 17690/03/NL/FF, Final report, December 2005
- Dozier J (1981) A method for satellite identification of surface temperature fields of sub pixel resolution. *Remote Sens Environ* 11:221–229

- ESA/ESTEC (2007) ECOFIRE study II on scientific assessment of space-borne high temperature event observing mission concepts. Contract change notice N-2, ESA/ESTEC Contract 17690/30/NL/FF, Feasibility of a Fire Monitoring Product Information System, October 2007
- FIREs (1994) Fire recognition system for small satellites, phase a study. DLR Institute of Space Sensor Technology/OHB-System, Berlin/Bremen
- Freeborn PH, Wooster MJ, Roberts G, Malamud BD, Xu W (2009) Development of a virtual active fire product for Africa through a synthesis of geostationary and polar orbiting satellite data. *Remote Sens Environ* 113(8):1700–1711. doi:[10.1016/j.rse.2009.03.013](https://doi.org/10.1016/j.rse.2009.03.013)
- Jahn H (n.a.) Affordable Space Missions (ASM). [http://www.dlr.de/os/desktopdefault.aspx/tabid-7064/5402\\_read-8110/](http://www.dlr.de/os/desktopdefault.aspx/tabid-7064/5402_read-8110/). Accessed 27 Feb 2012
- Kingston RH (1978) Detection of optical and infrared radiation. Springer, Berlin/Heidelberg/New York
- Lorenz E, Sandau R (2002) Planned applications of bolometer arrays at DLR. Workshop on uncooled infra-red detector technologies, 24 June 2002, ESA/ESTEC, Noordwijk
- Martin-Rico C, Gonzalo J, Leibrandt W, Mariani A (1997) The FUEGO system concept. In: Proceedings of the 48th international astronautical congress, 6–10 Oct 1997, Turin, IAF-97-C.2.02
- Melesse AM, Weng Q, Thenkabail PS, Senay GB (2007) Remote sensing sensors and applications in environmental resources mapping and modelling. *Sensors* 7:3209–3241
- NASA (1999) NASA FBC task final report. <http://mars.jpl.nasa.gov/misp98/misc/fbctask.pdf>. Accessed 27 Feb 2012
- Rataj M, Walter I, Schmidt J, Habermeier J (2011) Design and tests of the selected part of the pointing unit of the MERTIS/BEPPI Colombo experiment for the mission severe environmental conditions. In: Proceedings of the 14th European space mechanisms and tribology symposium – ESMATS 2011, Constance, 28–30 Sept 2011, pp 455–462
- Wooster MJ, Roberts G, Perry G, Kaufman YJ (2005) Retrieval of biomass combustion rates and totals from fire radiative power observations: calibration relationships between biomass consumption and fire radiative energy release. *J Geophys Res* 110, D21111. doi:[10.1029/2005JD006318](https://doi.org/10.1029/2005JD006318)
- Zhukov B, Lorenz E, Oertel D, Wooster MJ, Roberts G (2006) Spaceborne detection and characterization of fires during the bi-spectral infrared detection (BIRD) experimental small satellite mission (2001–2004). *Remote Sens Environ* 100:29–51
- URL1: <http://activefiremaps.fs.fed.us>
- URL2: <http://sentinel.ga.gov.au/acres/sentinel/index.shtml>
- URL3: <http://www.fireservices.gov.za/>
- URL4: <http://www.fire.uni-freiburg.de/>

# Chapter 9

## Landsat and Thermal Infrared Imaging

Terry Arvidson, Julia Barsi, Murzy Jhabvala, and Dennis Reuter

**Abstract** The purpose of this chapter is to describe the collection of thermal images by Landsat sensors already on orbit and to introduce a new Landsat thermal sensor. The chapter describes the Landsat 4 and 5 thematic mapper (TM) and Landsat 7 enhanced thematic mapper plus (ETM+) sensors, the calibration of their thermal bands, and the design and prelaunch calibration of the new thermal infrared sensor (TIRS). The TIRS will be launched in February 2013 on the Landsat Data Continuity Mission (LDCM) satellite, which will be renamed to Landsat 8 after it reaches orbit. Continuity of the data record has always been a priority for the Landsat project. The TIRS will extend the unique Landsat thermal data archive begun in 1978 that supports, among other applications, water resource management in the western United States and global agricultural monitoring studies. The TIRS also introduces improved technology and data quality, both of which are discussed in the chapter.

### 9.1 Background

The current Landsat mission is to systematically image the Earth's landmasses, building an essentially cloud-free global archive that is refreshed seasonally. However, the original mission was a demonstration of the value of space technology to Earth applications. The first satellite, Earth Resources Technology Satellite 1 (later

---

T. Arvidson (✉)

Information Systems and Global Solutions, Lockheed Martin, Greenbelt 20770, MD, USA  
e-mail: [Terry.arvidson@nasa.gov](mailto:Terry.arvidson@nasa.gov)

J. Barsi

Science Systems and Applications Inc. (SSAI), Lanham 20706, MD, USA

M. Jhabvala • D. Reuter

Goddard Space Flight Center (GSFC), National Aeronautics and Space Administration  
(NASA), Greenbelt 20770, MD, USA

renamed Landsat 1) was launched in 1972 with instruments covering the solar reflective band regions. Six years later, the first thermal capability was introduced on Landsat 3's multispectral scanner (MSS). The thermal band's on-orbit performance was disappointing and its operation was terminated in March 1979, 1 year after launch (NASA 1979). No further discussion is provided for the MSS thermal band due to its poor performance.

Although very little good data were acquired from the MSS thermal band, applications using thermal data were starting to emerge—including thermal mapping, plant stress, and urban/non-urban land use differentiation—and there were firm plans to try again with a thermal band on the TM (Thermal Mapper), the next generation Landsat instrument. Launched in 1982 on Landsat 4 and 1984 on Landsat 5, the TM thermal band improves upon the MSS and, in general, does not suffer from the same problems. Landsat 4 operated successfully for over 10 years, with data collection terminated in 1993. The Landsat 5 TM acquired data for over 27 years until communication system failures essentially ended the TM data collections in November 2011. Landsat 6 never reached its operational orbit after launching in 1993. In 1999, Landsat 7 was launched with the ETM+ instrument.

The newest Landsat mission, Landsat Data Continuity Mission (LDCM, or Landsat 8 after launch), will launch in February 2013 and carry the next generation Landsat thermal imaging capability.

## 9.2 TM and ETM+ Design and Operation

The TM and ETM+ instruments are whiskbroom radiometers, with an oscillating scan mirror in front of the telescope optics that sweeps back and forth across the field of view, roughly perpendicular to the direction of spacecraft travel (Fig. 9.1). The scan mirror sweeps the ground, projecting the energy through the telescope and onto the focal plane, which consists of four detectors in the TM or eight detectors in the ETM+. A scan-line corrector assembly compensates for the forward motion of the spacecraft during each sweep, returning adjacent sweeps to a parallel alignment.

The TM and ETM+ on-board calibration systems consist of a single on-board cavity blackbody and a black, highly emissive shutter (Fig. 9.1) (Markham et al. 1997). The blackbody sits off the optical axis at a constant temperature. The shutter, which carries the calibration lamps across the optical axis for the reflective band calibration, has on it a toroidal mirror. As the shutter sweeps across the optical axis, the mirror reflects the radiation from the blackbody onto the optics and through to the cold focal plane. The non-mirror part of the shutter is coated with a high-emissivity paint and sits at the instrument ambient temperature. Outputs from thermistors located within TM and ETM+—monitoring temperatures of the individual components such as the shutter and the mirrors—are included in the downlinked data.

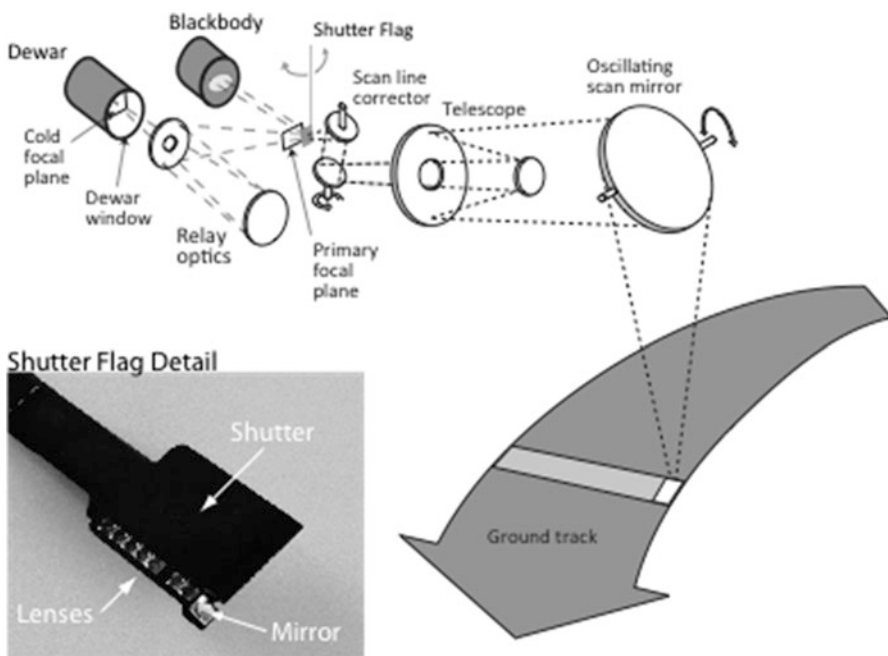


**Fig. 9.1** The thematic mapper optical layout, from the scan mirror that whisks across the field of view to the focal planes. The shutter flag is shown in the calibration position, blocking energy from the ground and reflecting the blackbody radiance onto the cold focal plane. The shutter flag detail (*inset*) shows the dark surface used as a cool target and the mirror that reflects energy emitted by the blackbody onto the focal plane. The lenses pipe the light from the calibration lamps onto the focal planes for reflective band calibration

The cold focal plane, which includes the thermal band detector array as well as those of the shortwave infrared bands, is housed in a dewar to isolate and control the thermal environment. There is a zinc selenide window in the dewar, with an antireflective coating, to allow light to reach the detector array with maximum transmission. In the TM instruments, a contaminant, most probably ice, builds up on the dewar window over time (Helder et al. 2004). Periodically, outgassing is performed wherein the cold focal plane is warmed up to remove the contaminant.

The TM and ETM+ thermal bands improve upon the MSS design (Table 9.1). The TM instruments increase the spatial resolution and correct the features that led to the poor quality of the MSS thermal data. The TM radiometric resolution has been well below 0.5 K (Table 9.2). For additional radiometric resolution, the ETM+ outputs two versions of the thermal data, one in high gain to improve radiometric sensitivity and one in low gain to prevent saturation. The ratio of high gain to low gain is approximately a factor of two. The actual spectral response of the thermal bands has varied due to manufacturing processes, but the TM and ETM+ thermal band requirement has always been a wide bandpass, from approximately 10.5 to 12.5  $\mu\text{m}$  (Fig. 9.2).

**Table 9.1** Landsat thermal band characteristics; Landsats 3–7 were implemented with mercury-cadmium-telluride detectors. LDCM uses quantum well infrared photodetectors

Satellite and sensor	Number of detectors	Focal plane temperature (K)	Resolution (m)
Landsat 3 MSS	2	90	240
Landsat 4, 5 TM	4	90	120
Landsat 7 ETM+	8	91	60
LDCM TIRS	1,850	40	100

**Table 9.2** Comparison of noise equivalent change in brightness temperature ( $\text{NE}\Delta\text{T}$ ) and radiometric ranges of the thematic mapper class instruments. For the TM instruments, the smaller  $\text{NE}\Delta\text{T}$  is when the dewar window is clear of contaminant, the larger is when contaminant build-up is at its peak. ETM+ operates in two gain states simultaneously, so the values for both states are provided here. The radiance and temperature ranges are the ranges to which the TM and ETM+ data are scaled during processing, not necessarily the native sensitivity of the instruments. The TIRS numbers are derived from requirements and pre-launch measurements

Satellite instrument	NE $\Delta\text{T}$ at 285 K (K)	Radiometric scaling range (W/m <sup>2</sup> sr $\mu\text{m}$ )	Useful temperature range (K)
Landsat-4 TM	0.22–0.32	1.238–15.300	200–340
Landsat-5 TM	0.17–0.30	1.238–15.300	200–340
Landsat-7 ETM+	0.26 0.21	0.00–17.04 3.20–12.65	130–350 240–320
LDCM TIRS	< 0.1	(to be determined)	240–360

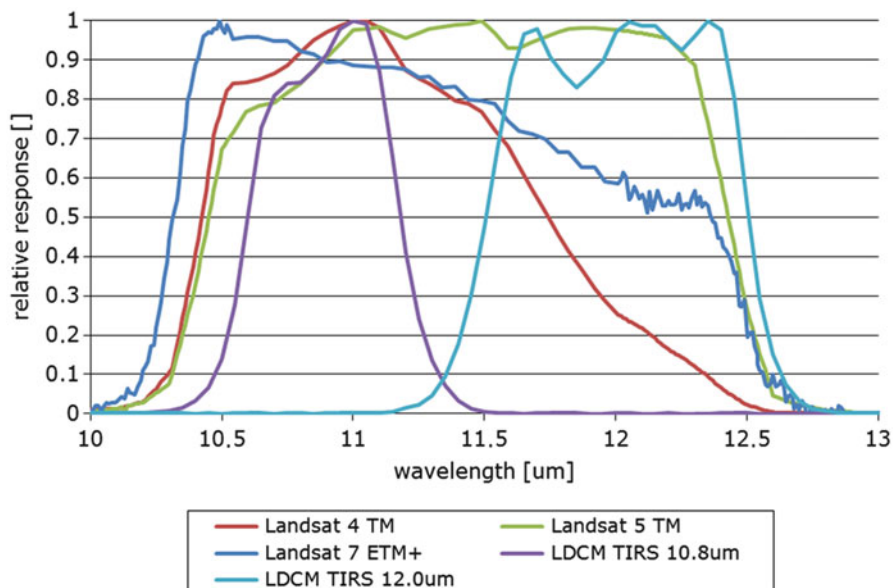


**Fig. 9.2** Relative spectral responses of the Landsat thermal bands, including the new TIRS sensor

### 9.3 TM and ETM+ Calibration

Calibration relates the radiance received by the sensor to the digital output of that sensor. Calibration parameters are applied during image processing to create products where the corrected digital numbers are linearly scaled to at-sensor radiance. In the thermal bands, apparent brightness temperature can be calculated from radiance.

The calibration parameters are initially determined from pre-launch laboratory calibration with external National Institute of Standards and Technology (NIST)-traceable radiance sources. Instrument gains and biases are used to calibrate the data so that users can convert the data to radiance using fixed calibration coefficients. These gains and biases are determined using the calibration parameters, along with the responses to the blackbody and shutter flag in the internal calibration system of the sensor and the temperatures of the blackbody and shutter flag.

The development of an Image Assessment System (IAS) has been essential to the knowledge of the calibration of the ETM+ (Storey et al. 1999). Developed by the United States Geological Survey (USGS) Earth Resources Observation and Science center, the IAS includes all the functionality of the primary processing system for ETM+ data, but it also features additional analysis tools and a trending database to record calibration information. Some data from every scene processed through the primary processing system is recorded to the IAS database. An additional four scenes per day are further processed through the IAS's analysis tools and statistics on each detector for each scan of both scene content and internal calibrators are recorded to the database. In this way, the instrument gains and biases can be monitored on a very short time scale, to reveal abrupt changes or slow degradations.

Initially developed for Landsat 7, the IAS has proven to be invaluable in monitoring the stability of the ETM+ and in 2008, the capability to process TM data was added (Micijevic and Morfitt 2010). Early attempts at long-term TM trending involved using one scene every 60 days; with the TM IAS, data from at least one scene per day are available. The populated TM IAS database increased the knowledge of the instruments' long-term behavior, in absolute gain and offset for example, and allowed for the monitoring of short-term trends in relative gain and outgassing behavior.

Thermal band vicarious calibration provides an independent means of measuring on-orbit sensor performance using well-instrumented water bodies. There was a single attempt at vicarious calibration for each of the TM instruments soon after their launches (Schott 1988) though further validation attempts were not regularly scheduled again until the launch of Landsat 7. Vicarious calibration was performed immediately after the ETM+ launch and continues to this day. Since 1999, four unmanned instrumented buoys on Lake Tahoe record the surface-leaving radiance every 2 min (Hook et al. 2004). Another unmanned station was established in 2007 on the Salton Sea. Manned campaigns on Lakes Ontario and Erie in support of ETM+ began just after launch and, soon after, teams were deploying in support of Landsat 5 TM as well (Barsi et al. 2003).

More recently, the network of the National Buoy Data Center archive has been used to increase the extent of the vicarious calibration capabilities, both spatially and temporally. These buoys record hourly subsurface water temperature as well as meteorological data. Padula and Schott (2010) developed methods for using this archive for Landsat 5 TM and Schott et al. (2012) extended the vicarious calibration method for use with Landsat 4 TM.

The vicarious calibrations track the absolute calibration of the sensor data and have spawned several updates of the calibration parameters. Adding the relatively hot Salton Sea site expanded the temperature range of the vicarious data and uncovered gain errors in the prelaunch calibration parameters that had been previously undetected.

## 9.4 TM and ETM+ Performance

Beginning with Landsat 4, the Landsat thermal bands have been generally well-behaved. The TM and ETM+ thermal systems are designed to rely on the stability of the internal calibration systems as opposed to the bands themselves, though in most cases the thermal band focal planes are as stable as the calibration system. For the TM, it is necessary to rely on scene-by-scene calibration of the thermal bands using the calibration systems, due to the dewar window contamination. Outgassing restores the system to its previous sensitivity, indicating that the focal plane itself is stable. Because of the contamination, the gain of the TM instruments could drop as much as 40 % between outgassings (Barsi et al. 2007). The effect of the decreasing gain is accounted for in the calibration processing, so the decrease does not inherently result in a calibration error. It does, however, reduce the sensitivity of the detectors; thus the NE $\Delta$ T is presented as a range for Landsats 4 and 5 in Table 9.2.

For ETM+, the contamination is not an issue and the average responsivity of the cold focal plane has been stable since launch to within 0.2 % for gain and 0.4 % for offset (Barsi et al. 2009). One thermal band detector did change relative to the others by about 1 %, perhaps due to a localized contamination.

Only two updates to the calibration parameters have been made as a result of actual instrument change. The Landsat 5 TM offset was updated to reflect a  $0.092 \text{ W/m}^2 \text{ sr } \mu\text{m}$  bias error seen in the vicarious calibration results starting in 1999 (Barsi et al. 2007). With the addition of the historical buoy data, this change was determined to have actually occurred in the early part of 1997 and was revised to  $0.11 \text{ W/m}^2 \text{ sr } \mu\text{m}$  (Schott et al. 2012). Records of spacecraft and instrument behavior from that time period are incomplete, so while it is suspected that an event occurred within the instrument to cause the offset change, there is no definitive proof of what it was. The Landsat 4 TM bias was also updated as a result of a change in the instrument (Schott et al. 2012). The simple calibration model used for TM does not account for changing instrument temperatures and so a change in the Landsat 4 TM instrument operating temperature, resulting after a long period of

**Table 9.3** Current calibration status of the Landsat thermal bands

Instrument	Residual uncertainty in calibration (K)
Landsat-7 ETM+	0.48
Landsat-5 TM	0.66
Landsat-4 TM	0.98

non-use, manifested itself as a change in instrument offset. The  $0.43 \text{ W/m}^2 \text{ sr } \mu\text{m}$  offset error was corrected in the processing system in 2011.

With the current calibration parameters and processing algorithms, all three thermal bands are calibrated to within 1 K (Table 9.3).

These tools—an on-board calibrator, vicarious calibration sites, and the IAS—will be used by LDCM to characterize and calibrate the TIRS instrument and track its stability.

## 9.5 LDCM (Landsat 8) TIRS Instrument Description

The Landsat Data Continuity Mission (Fig. 9.3) is scheduled to launch in February 2013 with two instruments that will be operated simultaneously: (1) the operational land imager (OLI) that images in the visible, near-infrared, and short-wave infrared; and (2) the thermal infrared sensor (TIRS). In keeping with the Landsat continuity directive, the LDCM specifications are compatible and comparable with most of the heritage Landsat specifications, including ground resolution, swath width, radiometric and geometric accuracy, and bandwidths.

Both instruments introduce a technology new to the Landsat program—pushbroom sensor operation—in which rows of detectors for each channel are swept in the along-track direction by spacecraft motion. For each channel, an image is built-up by concatenating successive single-row measurements. Previous Landsat instruments used whiskbroom operations, in which a few detectors for each channel are swept across track by a system of moving mirrors as the spacecraft travels in the along-track direction. Because, in a pushbroom sensor, each spatial element has its own detector, integration times can be much longer, which leads to improved noise performance. Furthermore, unlike in whiskbroom sensors, in pushbroom sensors there is no need for a large, continuously moving scan mirror or for the scan-line corrector, eliminating sources of jitter and possible failure modes.

TIRS is the first Landsat instrument built in-house at the National Aeronautics and Space Administration (NASA) Goddard Space Flight Center (GSFC). Although design and development of the OLI instrument began in 2007, work on the TIRS did not start until mid-2008, reducing the time from design to delivery for integration on the spacecraft to about 3 years. To facilitate the shortened schedule, TIRS was built as a Class C instrument (NASA 2004)—reducing the required end-of-life reliability somewhat and simplifying the review process—and with a 3.25-year design life. In contrast, the OLI is a Class B instrument with a 5-year design life. Technology improvements over previous Landsat thermal capabilities



**Fig. 9.3** The Landsat Data Continuity Mission will extend the 40-year record of moderate-resolution reflective and thermal measurements of the Earth's surface

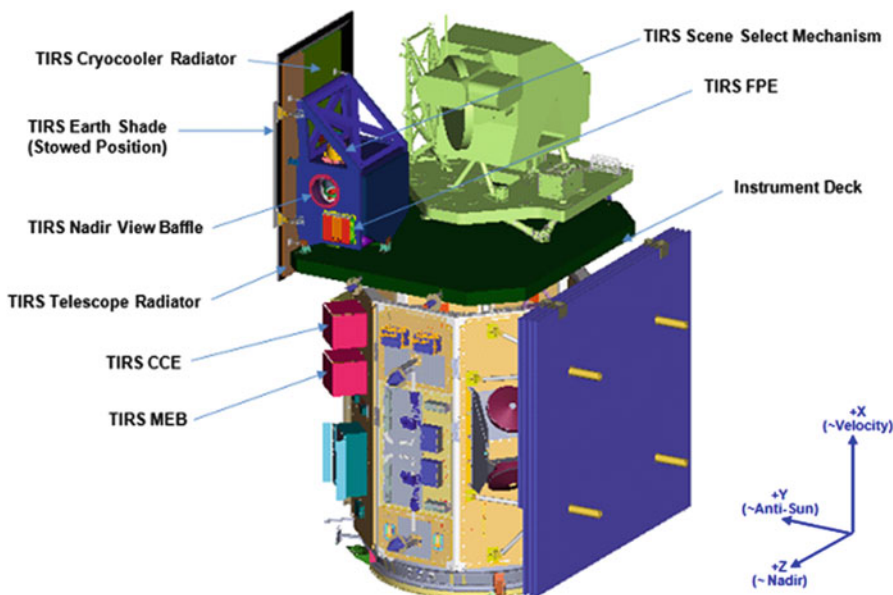


**Fig. 9.4** The TIRS sensor unit is mounted on the LDCM spacecraft instrument deck alongside the OLI sensor. The TIRS main electronics box (*MEB*) and cryocooler electronics (*CCE*) are mounted on the spacecraft body, below the deck (*FPE* focal plane electronics)

include: pushbroom mode, two spectral channels, a cooled optical path to reduce background noise, and quantum well infrared photodetector (QWIP) arrays.

Structurally, the TIRS consists of the sensor unit—including the telescope assembly, focal plane array and electronics, cryocooler, blackbody calibrator, scene select mechanism, Earth shield, radiators, and heat pipes—and two electronics boxes, the main electronics box (*MEB*) and the cryocooler electronics (*CCE*) (Figs. 9.4 and 9.5). The *MEB* provides command, telemetry, and image data interfaces to the spacecraft; provides power to and controls all functions of the

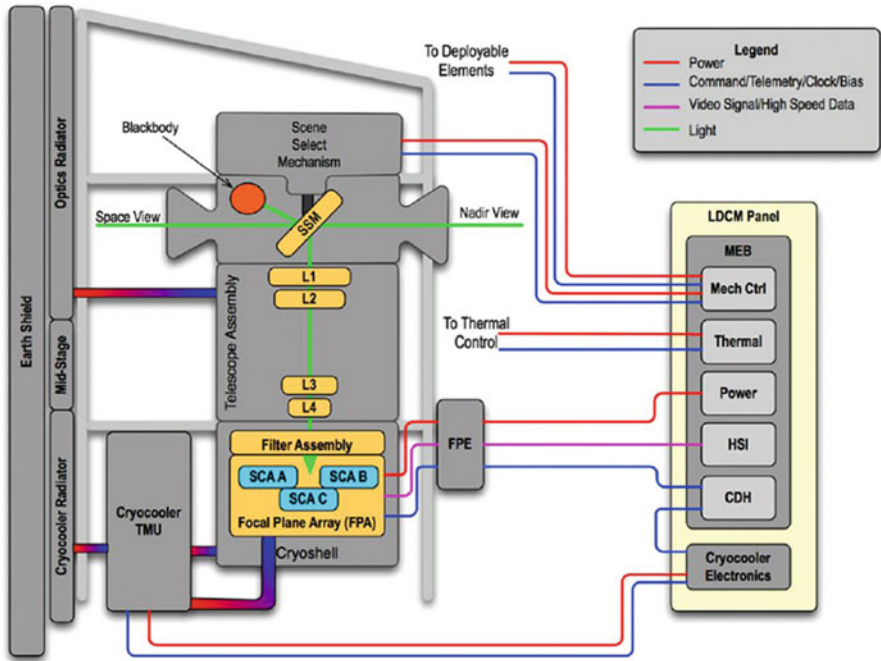


**Fig. 9.5** Block diagram showing interfaces among major parts of TIRS and the spacecraft, including light paths and relative temperatures along the heat pipes (SSM scene select mirror, SCA sensor chip assembly, TMU thermal unit, HSI high speed interface, L lens, CDH command and data handling)

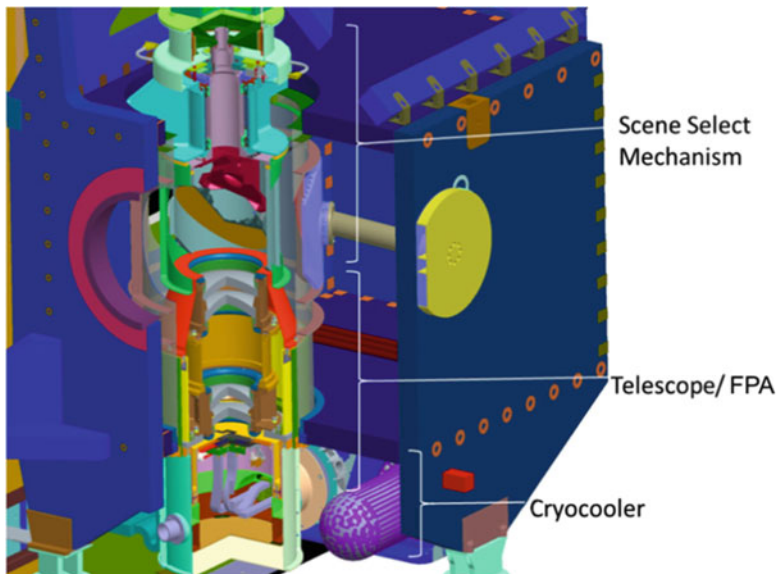
instrument; controls the thermal zones on the instrument (except the cryocooler); and commands the cryocooler electronics. The CCE provides power to the cryocooler and controls its operations and temperature.

TIRS has 100 m spatial resolution, not as fine as the ETM+ at 60 m, but better than the TM sensors at 120 m thermal band resolution (Table 9.1). To produce the 185 km swath width of TIRS, 1,850 pixels are required for each row in each channel. At a ground speed of 7 km/s, it requires approximately 0.014 s to move 100 m and 70 effective rows of pixels are produced in each second for each channel. TIRS uses a 3.4 ms integration time and the resultant 25 m image motion, when convolved with the instrument spatial function, does not excessively broaden the spatial resolution. The 12-bit digitized output data are required to produce precise temperature measurements over the range of 240–360 K—a temperature range slightly larger than previous Landsat thermal bands.

There are two spectral channels, centered near 10.9 and 12  $\mu\text{m}$ , effectively splitting the heritage TM/ETM+ band into two (Fig. 9.2, Table 9.4). The two channels—a “split-window” approach—allow for compensation of the thermal effects of the atmospheric column in transforming at-satellite radiances into surface temperatures (Prabhakara et al. 1974; Kerr et al. 1992). To accomplish this with the ETM+ single thermal band, an atmospheric propagation model and supplementary atmospheric data must be used.

**Table 9.4** TIRS band definitions and maximum radiance error (Reuter et al. 2010, 2011)

Channel	Band	50 % response lower band edge (μm)	50 % response upper band edge (μm)	Center wavelength (μm)	Maximum allowed Radiance error W/ (m <sup>2</sup> sr μm)
10	Thermal 1	10.6	11.2	10.9	0.059
11	Thermal 2	11.5	12.5	12	0.049

**Fig. 9.6** TIRS optics showing the SSM, lens, focal plane and cryocooler assemblies (FPA focal plane array)

The TIRS telescope uses a temperature-stabilized four-element refractive lens system—three germanium (Ge) elements and one zinc selenide element—to produce nearly diffraction-limited images at the focal plane (Fig. 9.6). A scene select mechanism (SSM) allows the field of regard to be pointed in the nadir direction for surface imaging, to a temperature-controlled on-board blackbody for radiometric calibration, and to a deep space view for thermal background subtraction.

To reduce the thermal background, the TIRS optics are cooled to 185 K and temperature-stabilized to  $\sim 0.1$  K, using a radiative cooler and heaters controlled by the MEB. In addition, the first stage of the cryocooler is used to cool the focal plane enclosure to  $\sim 100$  K. The optics temperature directly affects the focus of the Ge elements, because the Ge index of refraction is a strong function of temperature (Reuter et al. 2010, 2011). This coupling provides a means of adjusting the focus. The blackbody calibrator temperature is controlled by the MEB and can be set from

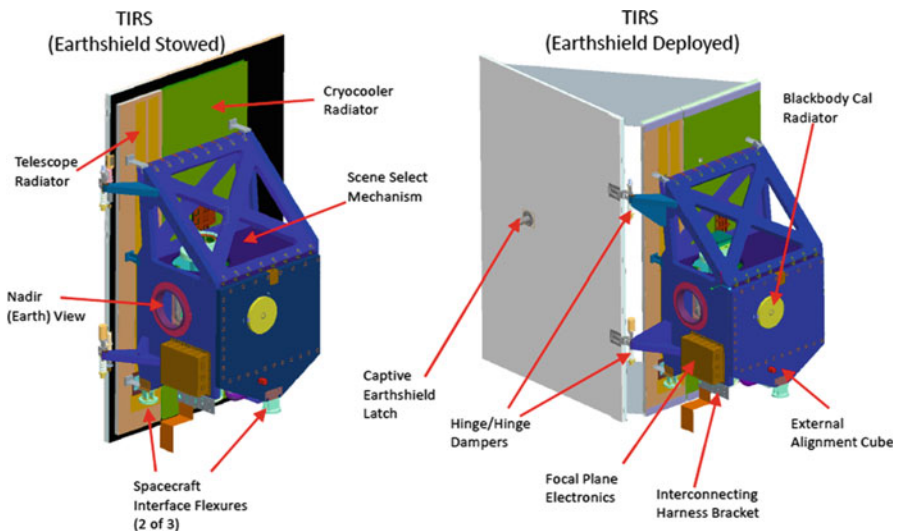


**Fig. 9.7** The TIRS with Earth shield stowed for launch (*left*) and with Earth shield deployed for on-orbit operations (*right*)

270 to 330 K, within an accuracy of 0.1 K. The focal plane array is cooled to about 40 K by the second stage of the two-stage mechanical cryocooler controlled by the CCE. The focal plane temperature is stable to better than 0.01 K. The radiators required to cool the optics and to dump the heat generated by the cryocooler are protected from heating by the Earth by a shield that deploys soon after launch (Fig. 9.7).

The focal plane consists of three QWIP arrays, arranged in a staggered configuration, that provide a 185 km swath image of the Earth (Fig. 9.8). Each QWIP has two filters mounted 300  $\mu\text{m}$  above it. These filters provide the spectral shapes described in Table 9.1. Each of the three QWIP arrays contains 327,680 pixels—25 by 25  $\mu\text{m}$  each—arranged in a grid of 640 columns by 512 rows (Fig. 9.9). The QWIP detectors are fabricated by growing many (in excess of 60) alternating layers of gallium arsenide (GaAs) quantum wells and aluminum gallium arsenide (AlGaAs) barriers. The thickness of the GaAs and AlGaAs and the concentration of aluminum in the AlGaAs primarily determine the band structure in the wells and hence the spectral response of the material structure (Jhabvala et al. 2009). Once this “superlattice” is grown, the QWIP arrays are fabricated using photolithography, reactive ion etching, and vacuum deposition processes similar to those used by the semiconductor industry.

Photons of the appropriate energy will excite an electron out of the GaAs quantum well that is then detected by an external circuit. The QWIP arrays are hybridized, or attached—using indium bump bonding technology—to a commercially available readout integrated circuit (ROIC). The ROIC contains the integrated electronics that detect the photo-generated electrons and convert the

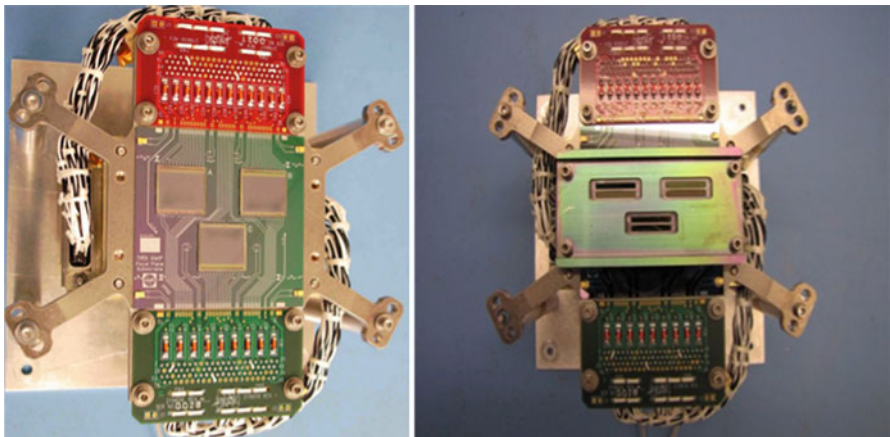


**Fig. 9.8** The actual TIRS flight focal plane with the three QWIP arrays exposed (*left*) and the focal plane with the filter assembly installed (*right*) (Photos courtesy of NASA)

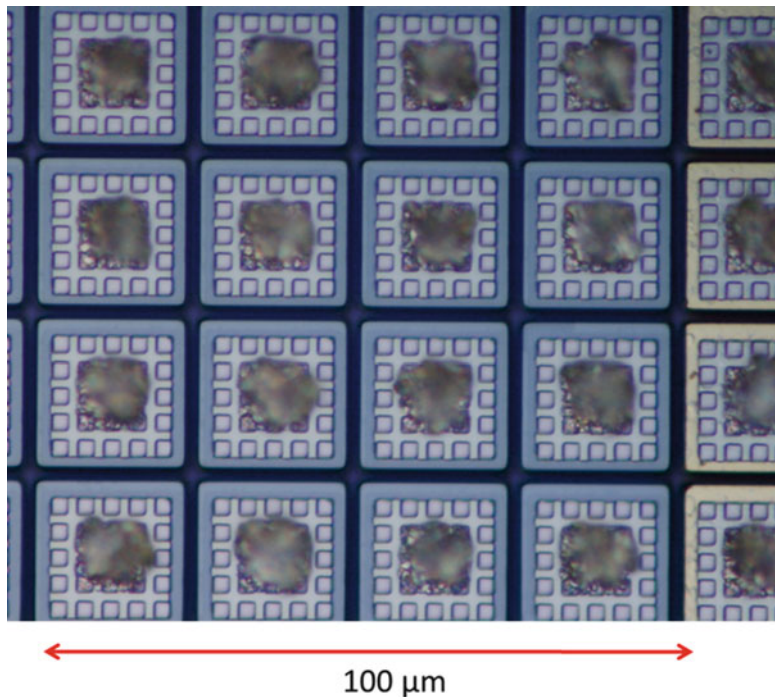


**Fig. 9.9** A highly magnified image of 9 pixels of one of the QWIP arrays. Each QWIP array contains 327,680 such pixels (Photo courtesy of NASA)

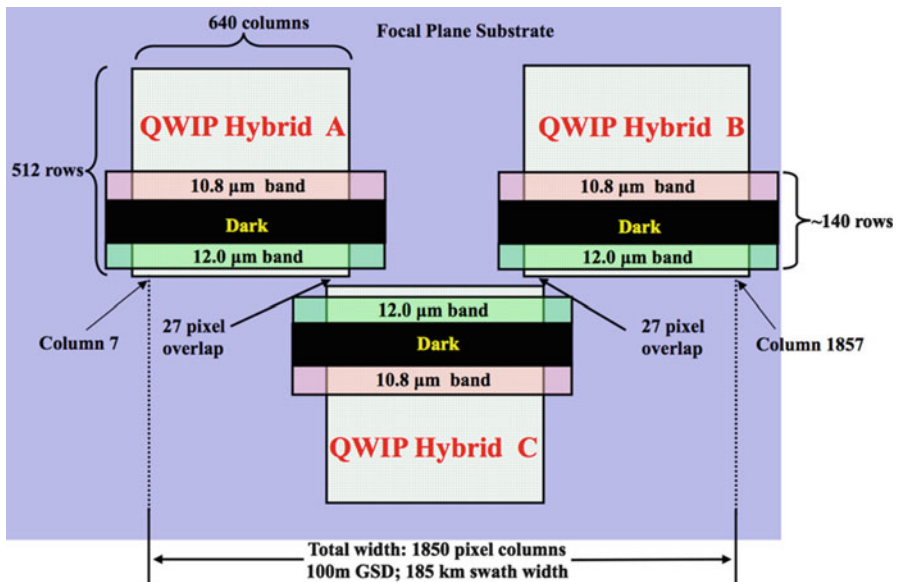


**Fig. 9.10** The focal plane layout illustrating the infrared band locations and the specific pixel columns that participate in the image collection and reconstruction. The 1,920 total row pixels ( $3 \times 640$ ) are reduced to 1,850 pixels by including array overlap and eliminating the first and last 8 columns. The areas of the hybrids not directly under the filters are shielded from illumination (GSD ground sample distance)

electrons to a voltage. This voltage is proportional to the number of detected photons. The QWIP/ROIC hybrid is then bonded to a custom-developed silicon substrate that contains metal traces. The QWIP hybrids are wire bonded to the traces on the silicon substrate and this subassembly is attached to an invar baseplate. Also mounted on the baseplate are two printed circuit (PC) boards located at either end of the silicon substrate. Wire bonds connect the silicon substrate traces to these PC “daughter” boards. Connectors on these daughter boards provide the interface between the QWIP hybrids and the external focal plane electronics.

Once the filters are positioned over the focal plane, the two infrared bands and the dark pixel regions are precisely defined in each QWIP hybrid—down to the individual pixels as shown in Figs. 9.10 and 9.11 (Jhabvala et al. 2010).

In each of the 70 samples produced per second, six rows are read out from each hybrid: two illuminated rows from the unvignetted region under each filter (four rows altogether) and two dark rows from an area on the hybrid that is far removed from the filters. The pixels from the illuminated rows in each channel in each hybrid are projected onto the Landsat Worldwide Reference System-2 grid during ground processing. Should a detector fail in a pushbroom instrument like TIRS, a complete column of data is lost. Capturing two rows from each infrared channel on each hybrid allows the ground processing software to combine the two rows into a single “effective” 1,850-pixel row that has no inoperable pixels and covers the entire

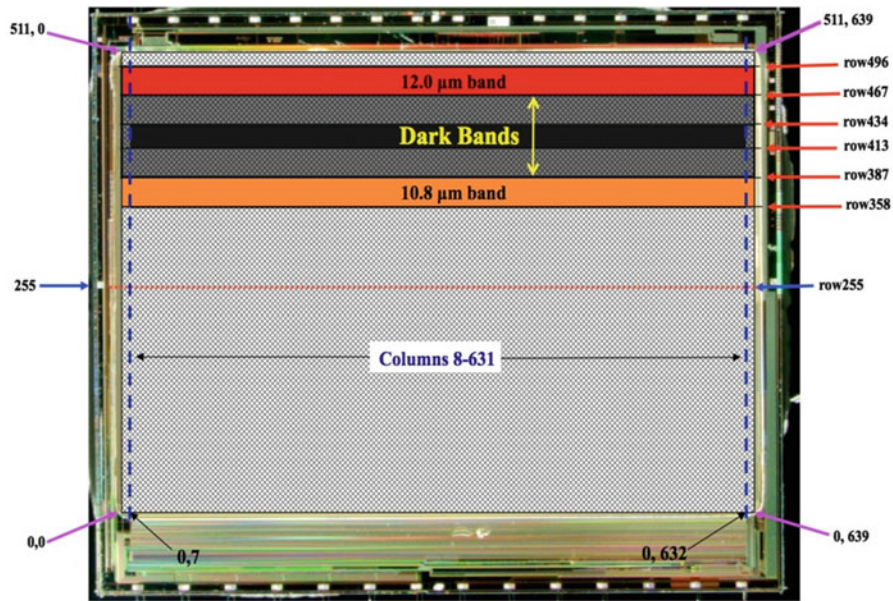


**Fig. 9.11** Once the filters are positioned over the QWIP hybrids, the arrays are precisely partitioned, down to the pixel level, as shown in the illustration. The first and last 8 columns are not used to avoid edge-related defects

185-km swath. The dark pixels are read out to provide a measure of the dark current of the QWIP hybrids. This is done to mitigate the effect of variable dark current on the image data in the unlikely event that the temperature of the focal plane is not controlled to sufficient precision by the CCE. Under normal conditions, the dark pixels are not used in data processing.

The arrays receive clock signals and biases from the focal plane electronics (FPE). The FPE contain an applications-specific integrated circuit (ASIC) chip to gather image data from the QWIP arrays. The ASIC controls the read pattern on the hybrids and performs analog-to-digital conversion of the image data. The FPE adds header information, formats these data, and sends them to the main electronics box. The MEB packetizes the digitized image data and forwards the packets to the spacecraft communications system to downlink.

The MEB controls the scene mirror position and provides mirror position data to the spacecraft for incorporation into the telemetry. The scene mirror can be positioned with an accuracy better than  $10 \mu\text{rad}$  ( $3\sigma$ ) in order to meet the geodetic requirement that pixel location on the ground be known to 18 m ( $27 \mu\text{rad}$ ).

The FPE, ASIC, and CCE software are loaded from electrically erasable programmable read-only memory, which can be updated from the ground. The MBE uses field-programmable gate arrays for its operations.

Once turned on, the TIRS instrument continually gathers image data but these data are recorded and brought to the ground only on command. Nominally, this will be whenever the OLI is acquiring data. The two data sets are merged onboard,

downlinked in a single data stream, and processed into a single product. None of the calibration modes of the TIRS require maneuvering of the satellite, although TIRS will collect image data during OLI calibrations that do require maneuvers.

The LDCM will collect and archive the global, synoptic, and repetitive OLI and TIRS imagery and will electronically distribute data products to the general public on a no-cost basis. USGS is responsible for the ground system, including the Ground Network Element, the Mission Operations Element, and the Data Processing and Archive System (DPAS). The DPAS consists of several subsystems that produce the Level 0 data and associated metadata, and generate the Level 1 radiometrically calibrated and orthorectified images of the Earth's surface. It also includes the IAS developed for OLI and TIRS. The processing algorithms are being developed by USGS and NASA GSFC calibration and validation teams.

## 9.6 TIRS Calibration and Pre-launch Performance

The existing suite of thermal data calibration and validation tools will be applied to the TIRS data set. Vicarious calibrations will continue to play an important role. The IAS has been updated to process pushbroom data, after proving the concept with data from the Earth Observer-1 advanced land imager, also a pushbroom instrument (Micijevic and Morfitt 2010). Additionally, there are new capabilities on the LDCM for calibration and for validation of TIRS. Table 9.5 lists the types of calibrations that will be used by TIRS on orbit.

For normal radiometric calibration, the scene mirror uses the scene select mechanism to change its field of view from a nadir Earth view to the on-board blackbody calibrator for 60 s and then to deep space for 60 s. This is done twice each orbit, before the first imaging interval and after the last imaging interval (the Landsat 4–7 thermal bands perform similar calibrations twice each data line). The TIRS is capable of imaging up to 35 min between calibration sequences. The data acquired during these calibration cycles is used during ground processing to correct offsets and gains that may vary over time. There is a requirement for less than 0.7 % drift between calibrations. As noted by Reuter et al. (2010, 2011), the QWIP array is in itself temporally stable, thus facilitating radiometric stability between calibrations.

The normal calibration sequence described above is replaced on a periodic basis by two other calibration modes: (1) an integration time sweep calibration during the blackbody portion of the normal calibration, and (2) a series of normal calibrations during a blackbody temperature sweep. If required, a stability calibration may be performed in which the normal calibration sequence is repeated, every 5 min, for a total of ten times across 50 min.

As the TIRS will image coincidentally with the OLI, the TIRS will collect data during the OLI calibrations. TIRS-driven acquisitions will include ocean and night collects. The IAS performs long-term trending, characterization, and calibration of the TIRS data and updates the processing parameters as needed.

**Table 9.5** TIRS calibration data types and their application

	Detector-to-detector relative calibration	Long term stability (Change monitoring)	Absolute calibration (Geophysical parameter retrieval)
Dark (Deep space)	X	X	X
Blackbody	X	X	X
Vicarious sites		X	X
	Band-to-band registration (Within and between sensors)	Geodetic accuracy	Focus
Geometric super-sites	X	X	
Focus check sites			X

Calibration has been performed at the component, subsystem, and instrument level throughout the TIRS fabrication process. Comprehensive requirements verification, and calibration and measurements, were made in a thermal vacuum environment prior to shipment of TIRS for integration on the spacecraft. These measurements employed NIST-traceable radiometric sources. A detailed description of the results of these tests is beyond the scope of this chapter and will be published later. In general, all requirements were met with a few minor exceptions. Modeling studies indicate that these exceptions will not impact the TIRS data quality. A high level summary of the overall performance is as follows:

**Radiometric accuracy:** The requirements of 2 % accuracy for temperatures between 260 and 330 K and 4 % for the rest of the range from 240 to 360 K appear to be met. The absolute accuracy is obtained using NIST-traceable laboratory sources in instrument-level thermal vacuum testing. Final verification of the radiometric accuracy will take place on orbit through vicarious methods.

**Noise:** This measure includes noise equivalent radiance, banding, streaking, and the like. The noise is typically less than the requirements shown in Table 9.4 by a factor of 5 or more. This corresponds to a NEAT of <0.1 K at 285 K. The banding, streaking, stability, and coherent noise performance is similarly good.

**Spatial:** There are slight deficiencies in some pixels' edge slope and edge extent, but these do not significantly degrade the image quality and will not affect the science results.

**Geometric:** The various geometric requirements are generally met, although the measured pointing stability as the instrument temperature is varied over its qualification range is somewhat worse than desired. The stability requirements, however, are near the limits of measurement capability and it is probable that chamber vibrations and ground support equipment effects are contributing to the instability.

**Spectra:** The majority of the spectral requirements are met, although there are some very minor deficiencies in the pixel average response and in-band spectral variation.

These are mitigated by the spectral uniformity of the atmosphere and surface in the TIRS spectral bands and no science impact is expected.

**Scattering, stray light, etc.:** These parameters meet requirements. In some cases, the calibration equipment was not capable of illuminating the extended focal array area but analytical modeling results indicate that the regions not included will not contribute to the signal in flight.

Except where indicated above, all the instrument parameters were stable over the range of thermal conditions and electrical variability expected in flight.

## 9.7 Conclusions

The TM and ETM+ instruments have proven to be very stable. With the current calibration data, TM and ETM+ products are accurate with respect to thermal radiance.

The TIRS provides thermal data continuity with previous Landsat sensors. As of August 2012, the TIRS is in Arizona at the spacecraft contractor, Orbital Sciences Corporation (Figs. 9.12 and 9.13). It has been integrated with the spacecraft and is undergoing final testing before shipment to the launch site. The TIRS promises improved performance and more challenging calibration.

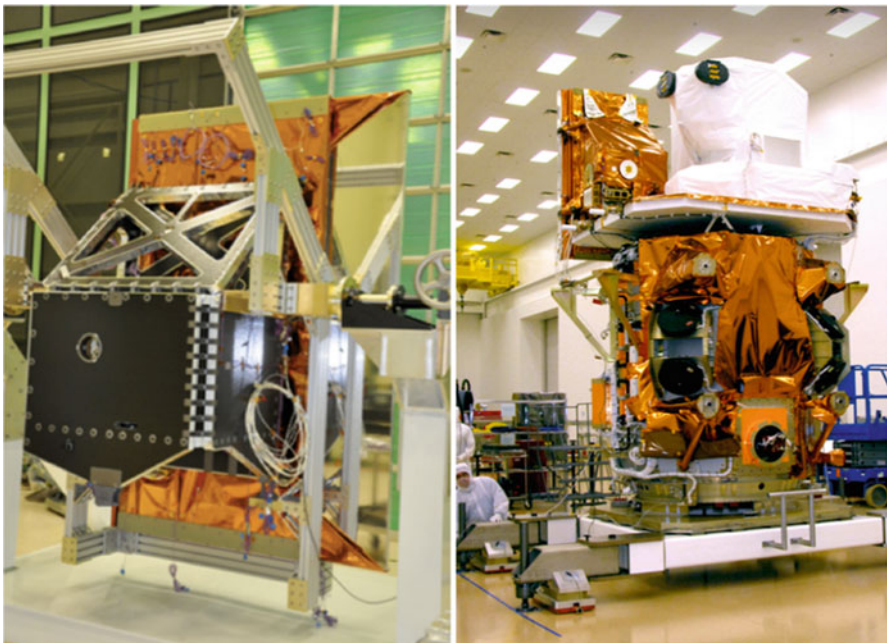


**Fig. 9.12** (Left) The fully assembled TIRS primary structure, with radiators and Earth shield (Photo courtesy of NASA). (Right) The TIRS, shrouded in gold thermal blanketing, is mounted on the top left of the LDCM spacecraft (nadir view is to the left). The OLI is on the right of the payload deck, with white blanketing (Photo credit: Orbital Sciences Corp)

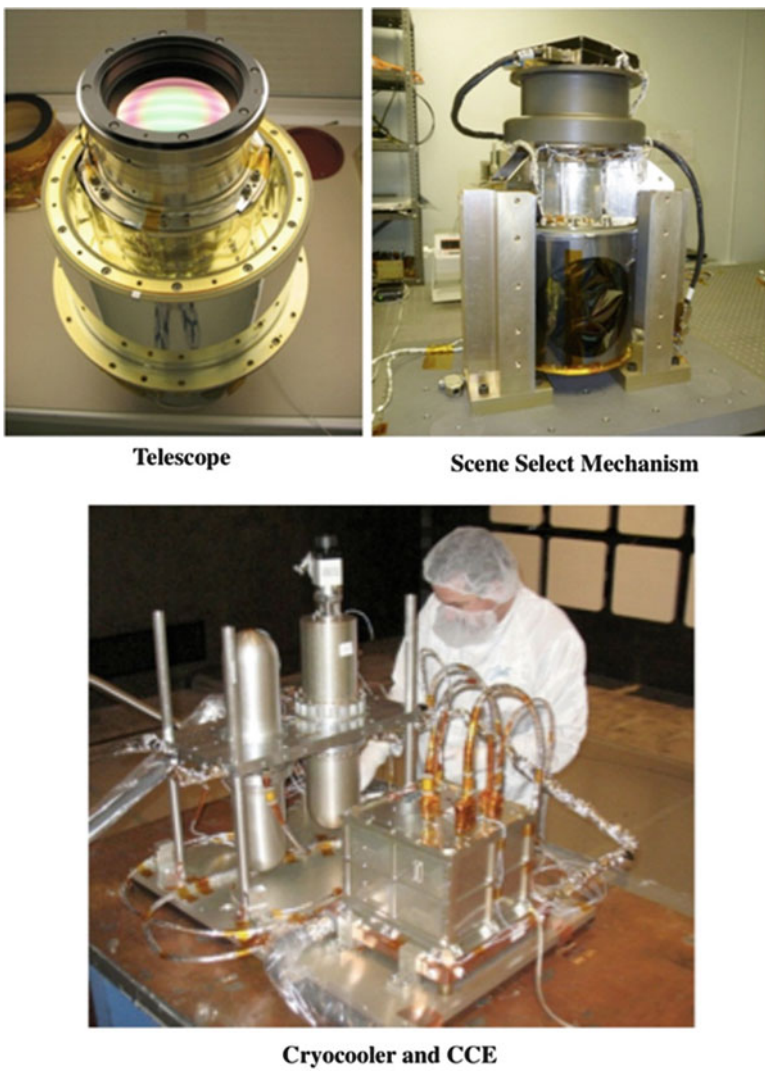


**Fig. 9.13** Montage of actual photographs of TIRS hardware (Photos courtesy of NASA)

**Acknowledgements** Work described in this chapter was performed under NASA Contracts NNG09HP18C/Task 061 and NNG09HP08C. The authors would like to thank all partners in the LDCM mission. In particular, they would like to express their deepest gratitude to the members of the TIRS development, analysis, fabrication, and test teams without whose exceptional efforts TIRS would not exist.

## References

- Barsi JA, Schott JR, Palluconi FD, Helder DL, Markham BL, Chander G (2003) Landsat TM and ETM+ thermal band calibration. *Can J Remote Sens* 29(2):141–153
- Barsi JA, Hook SJ, Schott JR, Raqueno NG, Markham BL (2007) Landsat-5 thematic mapper thermal band calibration update. *IEEE Geosci Remote Sens Lett* 4(4):552–555. doi:[10.1109/LGRS.2007.896322](https://doi.org/10.1109/LGRS.2007.896322)
- Barsi JA, Markham BL, Schott JR, Hook SJ, Raqueno NG (2009) Landsat-7 and Landsat-5 thermal band calibration updates. Paper presented at SPIE Earth Observing Systems XIV. In: Butler JJ, Xiong X, Gu X (eds) Proceedings SPIE Vol. 7452, 21 Aug 2009. doi: [10.1117/12.828501](https://doi.org/10.1117/12.828501)
- Helder DL, Micijevic E (2004) Landsat-5 thematic mapper outgassing effects. *IEEE Trans Geosci Remote Sens* 42(12):2717–2729. doi:[10.1109/TGRS.2004.839086](https://doi.org/10.1109/TGRS.2004.839086)
- Hook SJ, Chander G, Barsi JA, Alley RE, Abtahi A, Palluconi FD, Markham BL, Richards RC, Schladow SG, Helder DL (2004) In-flight validation and recovery of water surface temperature with Landsat-5 thermal infrared data using an automated high-altitude lake validation site at Lake Tahoe. *IEEE Trans Geosci Remote Sens* 42(12):2767–2776. doi:[10.1109/TGRS.2004.839092](https://doi.org/10.1109/TGRS.2004.839092)
- Jhabvala M, Reuter D, Choi K, Jhabvala C, Sundaram M (2009) QWIP-based thermal infrared sensor for the Landsat Data Continuity Mission. *Infrared PhysTechnol* 52(6):424–429
- Jhabvala M, Reuter D, Choi K, Sundaram M, Jhabvala C, La AT, Waczynski A, Bundas J (2010) The QWIP focal plane assembly for NASA's Landsat Data Continuity Mission. Paper presented at SPIE Defense, Security, and Sensing. In: Andresen BF, Gulop GG, Norton PR (eds) Proceedings SPIE Vol. 7660, Infrared Technology and Applications XXXVI, 3 May 2010
- Kerr YH, Lagourde JP, Imbernon J (1992) Accurate land surface temperature retrieval from AVHRR data with use of an improved split window algorithm. *Remote Sens Environ* 41 (2–3):197–209. doi:[10.1016/0034-4257\(92\)90078-X](https://doi.org/10.1016/0034-4257(92)90078-X)
- Markham BL, Bonycky WC, Helder DL, Barker JL (1997) Landsat-7 Enhanced Thematic Mapper Plus radiometric calibration. *Can J Remote Sens* 23(4):318–332
- Micijevic E, Morfitt R (2010) Operational calibration and validation of Landsat Data Continuity Mission (LDCM) sensors using the Image Assessment System (IAS). Paper presented at IGARSS 2010, Honolulu, 25–30 July 2010
- NASA (1979) Landsat-3 MSS band 5 (thermal) data. *NASA Landsat Newsl* 25:1–2
- NASA (2004) Risk classification for NASA payloads. *NASA Procedural Requirement 8705.4 Appendix B*, NASA Office of Safety and Assurance. [http://nодis3.gsfc.nasa.gov/displayDir.cfm?Internal\\_ID=N\\_PR\\_8705\\_0004\\_&page\\_name=AppendixB](http://nодis3.gsfc.nasa.gov/displayDir.cfm?Internal_ID=N_PR_8705_0004_&page_name=AppendixB). Accessed 29 June 2012
- Padula FP, Schott JR (2010) Historic calibration of the thermal infrared band of Landsat-5 TM. *Photogramm Eng Remote Sens* 76(11):1225–1238
- Prabhakara C, Dalu G, Kunde VG (1974) Estimation of sea surface temperature from remote sensing in the 11 to 13- $\mu$ m window region. *J Geophys Res* 79:5039–5044. doi:[10.1029/JC079i033p05039](https://doi.org/10.1029/JC079i033p05039)
- Reuter D, Richardson C, Irons J, Allen R, Anderson M, Budinoff J, Casto G, Coltharp C, Finnigan P, Forsbacka B, Hale T, Jennings T, Jhabvala M, Lunsford A, Magnuson G, Mills R, Morse T, Otero V, Rohrbach S, Smith R, Sullivan T, Tesfaye Z, Thome KJ, Unger G, Whitehouse P (2010) The Thermal Infrared Sensor on the Landsat Data Continuity Mission. In Proceedings of IEEE International Geoscience and Remote Sensing Symposium (IGARSS) 2010, 754–757, doi:[10.1109/IGARSS.2010.5653746](https://doi.org/10.1109/IGARSS.2010.5653746)
- Reuter D, Irons J, Lunsford A, Montanaro M, Pellerano F, Richardson C, Smith R, Tesfaye Z, Thome K (2011) The Operational Land Imager (OLI) and the Thermal Infrared Sensor (TIRS) on the Landsat Data Continuity Mission (LDCM). In: Shen SS, Lewis PE (eds) Algorithms and Technologies for Multispectral, Hyperspectral, and Ultraspectral Imagery XVII. Proceedings Of SPIE, 804812, 20 May 2011. doi:[10.1117/12.885963](https://doi.org/10.1117/12.885963)

- Schott JR (1988) Thematic Mapper, Band 6, radiometric calibration and assessment. In Proceedings, recent advances in sensors, radiometry, and data processing for remote sensing. SPIE 924(6–8):72–88
- Schott JR, Hook SJ, Barsi JA, Markham BL, Miller J, Padula FP, Raqueno NG (2012) Thermal infrared radiometric calibration of the entire Landsat 4, 5, and 7 archive (1982–2010). *Remote Sens Environ.* doi:[10.1016/j.rse.2011.07.022](https://doi.org/10.1016/j.rse.2011.07.022)
- Storey JC, Morfitt RA, Thorson PR (1999) Image processing on the Landsat 7 image assessment system. Paper presented at 1999 ASPRS annual conference, from image to information, Portland, Oregon, 17–21 May 1999. *Proceedings: American Society of Photogrammetry and Remote Sensing*, Bethesda, Maryland, CD-ROM, 1 disc, pp 743–758

# **Chapter 10**

## **Review of High Resolution Thermal Infrared Applications and Requirements: The Fuegosat Synthesis Study**

**José A. Sobrino, Fabio Del Frate, Matthias Drusch, Juan C. Jiménez-Muñoz, and Paolo Manunta**

**Abstract** High resolution thermal infrared remote sensing can have a wide range of applications. In this chapter we describe the different applications and requirements identified after a revision study in the framework of the Fuegosat Synthesis Study (FSS). This project was funded by the European Space Agency (ESA), and the three main objectives were: (i) review of applications and analyses for user requirements, (ii) consolidation of user requirements over a broad range of applications, and (iii) matching of user requirements and industry concepts to identify and outline a set of potential mission scenarios and their corresponding requirements. This chapter focuses on issues (i) and (ii). These objectives were achieved by means of integrated studies within literature and ancillary documentation, and also by consultation of external experts. As a result, more than 30 applications were identified within three different fields: (i) Land and Solid Earth, (ii) Health and Hazards and (iii) Security and Surveillance. A complete set of requirements (spatial, temporal, and radiometric resolution, algorithms used, supporting data, among others) were also provided.

---

J.A. Sobrino (✉) • J.C. Jiménez-Muñoz  
Global Change Unit, Image Processing Laboratory (IPL), University of Valencia,  
Valencia, Spain  
e-mail: [Sobrino@uv.es](mailto:Sobrino@uv.es)

F. Del Frate  
GEO-K, Tor Vergata University, Rome, Italy

M. Drusch  
European Space Research and Technology Centre (ESTEC), European Space Agency (ESA), Noordwijk, The Netherlands

P. Manunta  
PLANETEK Italia, Bari, Italy

## 10.1 Introduction

The Fuegosat Consolidation Element is part of the Earth Watch Programme approved by the European Space Agency (ESA) Council at Ministerial Level in November 2001. The work plan for Fuegosat included two steps; the first step proposed to implement an Infra-Red (IR) element in the form of passenger payloads in all Sentinels suited to carry it. The target application was risk management related to natural hazards with a special focus on fire risk management. However, the reassessment of the mission requirements confirmed the weakness in the traceability to Global Monitoring for Environment and Security (GMES) operational services, and in particular that fire monitoring capabilities were not traceable to services required under GMES as defined via GMES Service Elements, or via preliminary documentation produced for Fast-Track or Core Services. Since high applications of infrared observations have been identified as potentially relevant for GMES, the programme is currently undergoing a re-orientation.

In this framework, the Fuegosat Synthesis Study (FSS) project contributed to the identification of applications for high resolution Thermal Infra-Red (TIR) remote sensing and the analysis of user requirements in three different topics: Land and Solid Earth, Health and Hazards, and Security and Surveillance. The FSS project included also the matching of user requirements and industry concepts to identify and outline a set of potential mission scenarios and their corresponding requirements. In this chapter we focus on the applications identified during the literature review and also the requirements for each application.

The methodology employed to identify the different applications and to extract the user requirements is based mainly on available reports and especially on papers published in international journals or proceedings presented in international symposiums, i.e., these results were mainly based on a literature review process. This is true except for “Security and Surveillance” related applications, since these types of applications are not commonly published and divulged, a literature review did not provide useful information. In this case, most of the applications and requirements were extracted from personal communications. In this chapter we provide a brief description of each topic and also detailed tables of user requirements.

## 10.2 Land and Solid Earth

Applications included in the “Land and Solid Earth” topic were volcano and fire monitoring, which are based on the detection of High Temperature Events (HTE), and evapotranspiration retrieval, and water stress detection, both of them related to water management issues. Other secondary applications such as the role of TIR data in Earthquake events, detection of coal mine fires, and growing degree-days were also considered. Requirements for all these applications are provided in Sect. 10.5 (Table 10.2).

### ***10.2.1 Volcano Monitoring***

Volcanic eruptions pose serious hazards to sensitive ecosystems, transportation and communication networks, and to populated regions. Knowing the mineralogy of a rock or alluvial surface is critically important to a geologist trying to interpret the geologic, climatic, or volcanic history of the surface. Spectroscopy and remote sensing in the TIR region has lagged behind that of other wavelength regions for numerous reasons. However, the utility of TIR remote sensing for geology and mineralogy has become clear in the past decades and numerous air- and space-based instruments have become available.

### ***10.2.2 Fire Monitoring***

Fires are a major security hazard in numerous countries around the world, which affect vegetated resources, as well as the species that they shelter, not to mention human housing. In this section, the term “fire” will be dedicated to any wildland fire in the natural environment, including farmland fires (CEOS 2003). Wildland fire is any non-structural fire, other than prescribed fire, that occurs in the wildland (vegetated areas such as whether forests, savannas or Mediterranean vegetation). In Europe, the Southern countries (Portugal, Spain, France, Italy, and Greece) are the most affected by fires, with an average of almost 50,000 fires between 1980 and 2008, corresponding to an average burnt area of more than 480,000 ha per year (JRC 2008). The total cost of fires can be estimated at around 1 % of global Gross Domestic Product (WFSC 2009), including the costs of direct and indirect fire losses, the cost of fire fighting organizations, the cost of fire insurance administration and the cost of fire protection to buildings.

Fires are characterized by their plumes, their temperature, and their luminosity. Most in-situ daytime fire sightings result from the observation of smoke generated by fuel combustion, while most nighttime sightings result from high and unusual luminosity of the burning areas. The high temperature of the burning areas make the fires detectable from satellite under clear-sky conditions.

### ***10.2.3 Water Management***

Detection of water stress and evapotranspiration retrieval are key applications for water management purposes. Thermal infrared remote sensing has been recognized for a long time one of the most feasible means to detect and evaluate water stress and to quantify evapotranspiration over large areas and in a spatially distributed manner.

Water stress is considered to be a major environmental factor limiting plant productivity world-wide. Water stress develops in plants as evaporative losses cannot be sustained by the extraction of water from the soil by the roots.

Evapotranspiration (ET) is a term used to describe the loss of water from the Earth's surface to the atmosphere by the combined processes of evaporation from surface and transpiration from vegetation. Evapotranspiration depends on the presence of water and is regulated by the availability of energy, needed to convert liquid water to water vapor, and to transport vapor from the land surface to the atmosphere. Physiological regulations also occur in plants through mechanisms controlling water extraction by the roots, water transport in plant tissue, and water release to the atmosphere via the stomata at the leaf surface (in direct relation with the mechanisms of CO<sub>2</sub> assimilation and photosynthesis).

#### **10.2.4 Other Applications**

Other applications using TIR remotely sensed data were identified within the “Land and Solid Earth” topic, such as earthquakes, coal mine fires, and growing degree-days. However, during the duration of the project, these applications were considered as a medium to low priority compared to the other applications. This does not mean that these applications are not important, but they were not the main driver in the elaboration of technical requirements of a future high TIR resolution sensor.

### **10.3 Health and Hazards**

The last two decades have witnessed the increasing use of remote sensing for understanding the geophysical phenomena underlying natural hazards. The scientific knowledge gained along with the ability to disseminate timely geospatial information that can be integrated with demographic and socioeconomic data are contributing to comprehensive risk mitigation planning and improved disaster response. Observations from Earth orbiting satellites are complementary to local and regional airborne observations, and to traditional in situ field measurements and ground-based sensor networks. The contributions of satellite remote sensing to Earth science, ranging from high-resolution topography (using e.g. Interferometric SAR (Synthetic Aperture Radars), Lidar (Light Detection And Ranging) and digital photogrammetry) and geodesy to passive multispectral thermal sensor, such as ASTER (Advanced Spaceborne Thermal Emission and Reflection Radiometer) or MODIS (Moderate Resolution Imaging Spectroradiometer), and active microwave imaging have transformed the discipline. This transformation is leading to define a rapidly growing field of applied research that increasingly will provide geospatial information products addressing the operational requirements of multi-hazard decision support tools and systems. Policy makers, emergency managers and responders

from international and federal to state, regional and local jurisdictions use these tools and systems to generate scenarios, devise mitigation plans and implement effective response measures.

In this section two major applications are considered: the Urban Heat Island effect and Epidemiology. Other applications such as industrial risks, coastal inundations, and asbestos-cement detection are also presented. Requirements for all these applications are provided in Sect. 10.5 (Table 10.3). Note that fire risk could be also considered as a “Health and Hazard” application, but it was presented in the previous section (Land and Solid Earth applications, Sect. 10.2).

### ***10.3.1 Urban Heat Island***

Thermal remote sensing has been used over urban areas to assess urban heat island effects, to perform land cover classifications, and as input for models of urban surface atmosphere exchange. The main surface parameter to be extracted from thermal remote sensing is the so-called Land Surface Temperature (LST) or simply surface temperature, which is of prime importance to the study of urban climatology. It modulates the air temperature of the lowest layers of the urban atmosphere, is central to the energy balance of the surface, helps to determine the internal climates of buildings and affects the energy exchanges that affect the comfort of city dwellers. Surface and atmospheric modifications due to urbanization generally lead to a modified thermal climate that is warmer than the surrounding non-urbanized areas, particularly at night. This phenomenon is the Urban Heat Island (UHI). UHIs have long been studied by ground-based observations taken from fixed thermometer networks or by traverses with thermometers mounted on vehicles. With the advent of thermal remote sensing technology, remote observation of UHIs became possible using satellite and aircraft platforms and has provided new avenues for the observation of UHIs and the study of their causation through the combination of thermal remote sensing and urban micrometeorology (Voogt and Oke 2003). Since thermal remote sensors observe the spatial patterns of thermal radiance at the surface, the term Surface Urban Heat Island (SUHI) is usually employed to distinguish between UHI (when air temperature is considered) and SUHI (when LST is considered). In this field, most of the information was extracted from the UHI project funded by ESA under the DUE program (URL1).

### ***10.3.2 Epidemiology***

There is a growing international consciousness about the importance of the epidemiology of diseases. It is recognized that improved up to date information of the environment, in which infectious diseases occur, will help epidemiologists to study, understand, and predict threats to human health and hazards. Earth observations by

satellites open up new opportunities to predict and help combat epidemic outbreaks, as well as joining the search for the origin of pathogens. In fact, several diseases can be analyzed using determined remotely sensed factors, a detailed list of them was studied by Beck et al. (2000) and references therein.

Remote sensing data creates an important opportunity to evaluate risk areas or determine the spatial distribution for some epidemic or vector outbreaks which affect human health. In fact, during the past three decades, remote sensing improvements have contributed to health science since 1970. After that, some free or low cost environmental and meteorological data sets (e.g. low resolution images) have been used to assess epidemic risks at global, regional, and local levels. Therefore, remote sensing data presents valuable information to determine risk factors and mapping risk areas, and their uses can also be integrated into models, which are based on ecological analyses (Herbretau et al. 2007).

### ***10.3.3 Other Applications***

Other operational contexts in the framework of “Health and Hazards” applications can benefit from TIR remote sensing. Among them, industrial risks, coastal inundation, and detection of asbestos-cement were considered. These applications were also considered as a lower priority level.

## **10.4 Security and Surveillance**

Applications and user requirements for security and surveillance related issues are currently only vaguely defined, probably due to that security and surveillance are normally related to military and politically sensitive applications. In addition, these applications require mainly a very high spatial resolution TIR data, paying less attention to spectral configurations or algorithms to extract geophysical variables. Since operational TIR systems at very high-resolution data are rarely accessible to the scientific community, security and surveillance applications have been poorly developed and access to this knowledge by scientific community is limited. This fact implies that a review of peer-reviewed literature (as considered in the case of “Solid Earth” and “Health and Hazards” applications) is not possible in order to provide a list of applications and user requirements (only vague and poor information have been found in the different international journals explored).

Most of the information found included applications using hand-held thermal cameras or Unmanned Aerial Vehicles (UAVs), with spatial resolutions of centimeters. In particular, handheld thermal infrared cameras play an important role. It is worth to mention the Multi-spectral Thermal Imager (MTI) sensor, developed in Los Alamos National Laboratory (Sandia National Laboratory). The sensor has a spatial resolution of 5 m in the visible bands and 20 m in the thermal bands. MTI is an American quasi-military reconnaissance sensor mounted in a

spacecraft and launched in March, 2000. The program was cosponsored by the Department of Energy, Office of Nonproliferation and National Security (USA). The 587 kg spacecraft carried visible and infrared sensors in 15 spectral bands to spot cooling ponds adjacent to nuclear reactors and dust content associated with uranium ore processing. The collected data also have spin-off benefits to civilian research involving atmospheric ozone, water vapor, etc.

It is worth to mention the security service included in the GMES initiative ([URL2](#)). The pre-operational security service of GMES is currently provided through the FP7 project G-MOSAIC (GMES services for Management of Operations, Situation Awareness and Intelligence for regional Crises) ([URL3](#)) and the FP6 project LIMES (Land and Sea Monitoring for Environment and Security) ([URL4](#)). These two projects, which combine Earth observation technologies with communication and positioning technologies, address the following domains:

- Maritime surveillance: sea border surveillance in and outside Europe, illegal immigration and illegal trafficking surveillance, safety sea lane/piracy/sensitive cargo...)
- Infrastructure surveillance: land border surveillance, critical infrastructure (e.g. pipelines...)
- Support to peace-keeping: population monitoring, resources (water)...
- Support intelligence and early warning
- Support crisis management operations

Despite that these GMES activities were consulted by the Fuegosit Synthesis Study project to identify applications in the security and surveillance topic, it should be noted that applications found in the former G-MOSAIC and LIMES projects use high resolution VNIR (Very Near Infrared) imagery (e.g. IKONOS, QUICKBIRD) and SAR data, but no application using high resolution TIR data has been found. This is probably due to the fact that no TIR sensor with high resolution and revisit time is currently available.

Different applications were suggested by the military organisms consulted by the Fuegosit project team, who also provided basic requirements. As stated before, since information was provided through personal communication, a strong justification of requirements cannot be provided in some cases. Requirements for all these applications are provided in Sect. 10.5 (Table 10.4).

## 10.5 Summary of Requirements

In order to offer a global vision of applications and user requirements identified during the FSS project, we include in this section a summary of the reviewing process. Table 10.1 provides a list of all the applications presented in this chapter. For the “Land and Solid Earth” topic 18 applications were identified, whereas for the “Health and Hazards” topic 17 applications were considered. The number of applications is reduced significantly in the case of “Security and Surveillance”, with only 6 applications.

**Table 10.1** Summary of TIR remote sensing applications

Topic	Subtopic	Application
Land and Solid Earth	Volcanoes	Eruption clouds
		Tropospheric Plumes
		Hot spots and active lava flows
		Post eruptive studies on lava flows
	Fires	Detection of fires
		Estimation of fire risk
		Estimation of burnt area
	Water management	Detection of water stress in crops
		Detection of water stress in forest
		Detection of evapotranspiration in crops
		Detection of evapotranspiration in River Basin
	Earthquakes	Detection of evapotranspiration in continents
		Detection of earthquakes
Health and Hazards	Coal mine fires	Detection of coal mine fires
		Delineation of potential coal fires and coal fire risk areas
	Growing degree-day	Growing degree day estimations
		Growing degree day mapping
		Cooling degree day Estimations
	Urban heat island	Vegetation maps
		Land cover/land use
		Building information
		Air quality
	Epidemiology	Mapping malaria potential regions
		Arthropod vector ecology and disease distribution
		Mapping cholera potential regions
		Mapping meningitis outbreak
	Industrial risks	Air pollution
		Differentiate between urban and industrial zone
		Oil spill detection
		Plume detection
	Coastal inundations	Prediction of floods
		Monitoring of floods
		Asbestos-cement detection over non-accessible areas
Security and Surveillance	Ship/port monitoring	Detection of minefields and landmines
		Border security
		Object monitoring and detection
		Piracy/drug smuggling/Illegal Immigration
		Industrial/power plant monitoring
		Trafficability (off-road soil moisture content)

The user requirements for all these applications are included in Tables 10.2, 10.3 and 10.4 or the “Solid Earth”, “Health and Hazards” and “Security and Surveillance” topics, respectively. Note that these tables also include the main references consulted to extract the information presented in this chapter.

**Table 10.2** Summary of user requirements for Land and Solid Earth applications

Application (Source)	EO Level 2/3 product	Spatial resolution	Geographical coverage	Temporal resolution	Accuracy	Algorithms	TIR spectral resolution	Other spectral ranges	Supporting data
Eruption clouds (Pugnagh et al. 2006; Corradini et al. 2003)	Geophysical variables	1–3 km	Large 1,000–2,000 km	3–4 hours	Time series	Two bands (10–12 $\mu$ m)	UV-VIS	Physical models	
Tropospheric Plumes (Pugnagh et al. 2006; Corradini et al. 2003)	Geophysical variables	30–100 m	Medium 100–500 km	daily	BTD, LUT	Multispectral ( $\geq$ 3 bands in 8–12 $\mu$ m)	UV-VIS	Physical models, DEM	
Hot spots and active lava flows (Wright et al. 2002)	Geophysical variables	10–50 m	Small 60–100 km	daily	Saturation above 60°	Threshold	11 $\mu$ m	4 $\mu$ m – Deformation maps – DEM	
Post eruptive studies on lava flows (Harris et al. 2003; Oppenheimer 1998)	Geophysical variables	10–50 m	Small 100–200 km	15 days	Saturation above 60°	Threshold	11 $\mu$ m	SWIR-MIR – SAR DEM	
Detection of fires (CEOS 2003; Zhukov et al. 2006)	Geophysical variables (LST)	100 m	Global	15 min	Not critical (hot spots are at least 200 K higher than background)	Temperature threshold from a single image	Multispectral ( $\geq$ 3 bands in 8–12 $\mu$ m)	SWIR (1.5–2.5 $\mu$ m) MIR (3–5 $\mu$ m)	Atmospheric constituents for atm correction
Estimation of fire risk (CEOS 2003)	Geophysical variables (Vegetation Index)	30 m	Global	Daily–Weekly	2 % (usual accuracy of NDVI estimations)	Multitemporal: Vegetation Condition Index (VCI)	—	VNIR (Red, Green, NIR@0.8 $\mu$ m)	—
Estimation of burnt area (CEOS 2003; Giglio et al. 2009)	Geophysical variables (Vegetation Index)	30 m	Global	Daily–Weekly	2 % (usual accuracy of NDVI estimations)	Multitemporal: comparison of reflectance or vegetation index with time series	Split-window (SW) method: Temperature and Emissivity Separation (TES) method	VNIR (Red, NIR@0.8 $\mu$ m); Multispectral ( $\geq$ 3 bands in 8–12 $\mu$ m)	Atmospheric water vapor content; Atmospheric constituents for atm correction
Detection of earthquakes – LST (Tronin 2000; Tramutoli et al. 2005; Saraf and Choudhury 2005)	LST	0.5–5 km	200 km – global	Daily	< 1 K	Two bands (10–12 $\mu$ m); Temperature and Emissivity Separation (TES) method	VNIR (Red, NIR@0.8 $\mu$ m)	Atmospheric constituents	
Detection of earthquakes – Emissivity (Tronin 2000; Tramutoli et al. 2005;	Emissivity	0.5–5 km	200 km – global	Weekly–monthly	<0.01	Threshold method; TES	Multispectral ( $\geq$ 3 bands in 8–12 $\mu$ m)	VNIR (Red, NIR@0.8 $\mu$ m)	Atmospheric constituents

(continued)

Table 10.2 (continued)

Application (Source)	EO Level 2/3 product	Spatial resolution	Geographical coverage	Temporal resolution	Accuracy	Algorithms	TIR spectral resolution	Other spectral ranges	Supporting data
Saraf and Choudhury <a href="#">(2005)</a>	Detection of coal mine fires (Zhang et al. 2004a, b; Kuenzer et al. 2007)	Geophysical variables (LST)	1–100 m	Local to Regional	Daily–Monthly	Not critical (hot spots are 20 K higher than background)	Temperature threshold from a single image	1 broad-band (8–12 $\mu\text{m}$ ) VNIR (Red, Green, NIR@0.8 $\mu\text{m}$ )	In-situ temperature to select the threshold is for atm correction
Multispectral $\geq 3$ bands in 8–12 $\mu\text{m}$	Delineation of potential coal fires and coal fire risk areas (Gao et al. 2006, 2009)	MIR (3–5 $\mu\text{m}$ )	Land cover	100 m	Local to Regional	Monthly	Classification techniques from a single image	Multispectral ( $\geq 3$ bands in 8–12 $\mu\text{m}$ ) VNIR (Red, Green, NIR@0.8 $\mu\text{m}$ )	–
Detection of water stress in crops (Sepulcre-Cantó et al. (2006, 2007))	Detection of water stress in forest (Vidal and Daux- Ros 1995; Duchemin et al. 1999)	Level 3 (classifications, consider also visible, near infrared and meteorological data)	Land cover	2–7 m	Local	Daily	1 K	Temperature threshold, classification techniques	SWIR (1.5–2.5 $\mu\text{m}$ )
Detection of evapotranspiration in crops (Sobrino et al. 2005, 2008)	Detection of evapotranspiration in River Basin (Sanchez et al. 2008; Jia et al. 2009)	Level 3 (classifications, consider also visible, near infrared and meteorological data)	Land cover	100 m	Local to Regional	Daily–Monthly	1 K	Temperature threshold, classification techniques	Meteorological data (air temperature)
		Level 3 (classifications, consider also visible, near infrared and meteorological data)	Local	1–10 m	Instantaneous–Daily	1 K	Energy Balance Models	Two bands (10–12 $\mu\text{m}$ ) VNIR	Meteorological data (Air temperature, relative humidity)
		Level 3 (classifications, consider also visible, near infrared and meteorological data)	Local to Regional	100 m	Daily–Monthly	1 K	Energy Balance Models	Two bands (10–12 $\mu\text{m}$ ) VNIR	Meteorological data (Air temperature, relative humidity)

Detection of evapotranspiration in continents (Fisher et al. 2008)	Level 3 classifications, consider also visible, near infrared and meteorological data	1 km Continental-Global	Daily-Monthly	1 K	Energy Balance Models	Two bands (10–12 $\mu\text{m}$ )	VNIR	Meteorological data (Air temperature, relative humidity, precipitation)
Growing Degree Day estimations (Vancu et al. 2010; Hassan et al. 2007a)	Level 3 Land surface temperature; Vegetation Index (NDVI)	20–1,000 m Local scale	Daily/Sub-daily	1–2 K	Multivariate Statistical correlation	Two bands (10–12 $\mu\text{m}$ ) for Split-Window; Multispectral $\geq 3$ bands in 8–12 $\mu\text{m}$	VNIR for NDVI 0.63–0.69 $\mu\text{m}$ 0.76–0.90 $\mu\text{m}$	Weather station network & Land cover map
Growing Degree Day mapping (Mikkelsen and Olesen 1984; Blair et al. 2002; Hassan et al. 2007b)	Level 3 LST & Land cover maps	20–1,000 m Regional to local scale	Daily/Sub-daily	1–2 K	Multivariate Statistical correlation & Spatial Analysis using Computational approach	Two bands (10–12 $\mu\text{m}$ ) for Split-Window; Multispectral $\geq 3$ bands in 8–12 $\mu\text{m}$ for TES	VNIR for NDVI 0.63–0.69 $\mu\text{m}$ 0.76–0.90 $\mu\text{m}$	Weather station network & Land cover map
Cooling Degree Day Estimations (Stathopoulou et al. 2006)	Level 3 Land surface temperature	20–1,000 m Local scale	Daily/Sub-daily	1–2 K	Method proposed by Stathopoulou et al. (2006)	Two bands (10–12 $\mu\text{m}$ ) for Split-Window; Multispectral $\geq 3$ bands in 8–12 $\mu\text{m}$ for TES	VNIR for NDVI 0.63–0.69 $\mu\text{m}$ 0.76–0.90 $\mu\text{m}$	Weather station network & Land cover map

**Table 10.3** Summary of user requirements for Health and Hazards applications

Application (Source)	EO Product	Level 2/3	Spatial resolution	Geographical coverage	Temporal resolution	Accuracy	Algorithms	TIR spectral resolution	Other spectral ranges	Supporting data
UHI – Vegetation maps (UHI Proj. 2009)	Maps	10–100 m	Local-Regional	Monthly		Multivariate statistical	Two bands (10–12 $\mu\text{m}$ )	Multispectral	Land cover maps	
UHI – Land cover/Land use Maps (UHI Proj. 2009)	Maps	10–100 m	Local-Regional	Monthly		Multivariate statistical	Two bands (10–12 $\mu\text{m}$ )	Multispectral-SAR	GIS	
UHI – Building information (UHI Proj. 2009)	Temperature	1–10 m	Local	Monthly	1–2 K	LST	Two bands (10–12 $\mu\text{m}$ )	SAR	City maps	
UHI – Air Quality (UHI Proj. 2009)	Temperature	20 m–1 km	Local-Regional	Daily-monthly		Statistical	(10–12 $\mu\text{m}$ )	UV-VIS	Atmo models	
Air pollution (Bowman et al. 2006; Barret et al. 2005)	Radiance	100 m	Local-Regional	Daily (at noon) –		Inversion techniques from IR sounding	Hyperspectral (3–15 $\mu\text{m}$ )	–	–	
Differentiate between urban and industrial zone (Kato and Yamaguchi 2007)	Storage heat flux	100 m	Local	Monthly	LST: 1.5 K Emissivity: 0.015	TES for LST/energy balance	FTIR spectroscopy Multispectral ( $\geq 3$ bands in 8–12 $\mu\text{m}$ )	VNIR data for albedo	Meteorological data and surface roughness	
Oil spill detection (Shcherbak et al. 2008; Tseng and Chiu 1994)	Temperature CLD	100 m–1 km	Local-Regional	Few hours	1 K	Temperature threshold (LST from split-window)	Two bands (10–12 $\mu\text{m}$ )	Combination between VNIR and RADAR		
Plume detection (Chrysoulakis 2002; Chrysoulakis and Cartalis 2003; Chrysoulakis et al. 2005)	Temperature	100 m–1 km	Local	Few hours	1 K	Classification and temperature threshold (LST from split-window)	Two bands (10–12 $\mu\text{m}$ )	VNIR for NDVI 0.63–0.69 $\mu\text{m}$ 0.76–0.90 $\mu\text{m}$		
Prediction of floods (Billa et al. 2006; Feidas et al. 2000; Morales et al. 2003)	Level 3 classifications, consider also visible and near-infrared)	500 m–1 km	Regional	Daily	–	Temperature threshold, classifications techniques	Two bands (10–12 $\mu\text{m}$ )	VNIR or Passive microwave	Lighting information from long-range network	
	Level 3 (thresholds)	1 m–1 km					1 K	–	–	

Monitoring of floods (Roshier et al. 2004; Lakshmi et al. 2001)	Local to regional	Daily (Noon-Midnight)	Temperature threshold from a single image	Multispectral ( $\geq 3$ bands in 8–12 $\mu\text{m}$ )
Mapping malaria potential regions Green and Hay 2002; Gemperli et al. 2004; Rahman et al. 2006)	Level-3 Land surface temperature; Vegetation Index (NDVI)	100–1,000 m Continental to regional scale	Daily/sub-daily <2 K	Split-window
Arthropod vector ecology and disease distribution (Mari et al. 2008; Gemperli et al. 2004)	Level-3 LST & Land cover maps	100–1,000 m Continental to regional scale	10 days composite/sub-daily <2 K	Split-window
Mapping cholera potential regions Gil et al. 2004; Lobitz et al. 2000; Emech et al. 2008)	Level-3 : SST and Chlorophyll concentrations	100–1,000 m Continental to regional scale	Daily/sub-daily <1 K	Split-window
Meteorological data Mapping meningitis outbreak (Gemperli et al. 2004)	Level-3 : LST and Dust Blown map	100–5,000 m Continental to regional scale	Daily/sub-daily <2 K	Split-window
Asbestos-cement detection over non-accessible areas (Bassani et al. 2007)	Level-2 (radiance) Level 3 Emissivity at high spatial level	3–20 m Local scale	Monthly/daily Not critical, only relative values are used	Temperature and Emissivity Separation algorithms
recommendable	Laboratory analysis, mineralogical composition, in-situ measurements		Hyperspectral (with a band in 9.44 $\mu\text{m}$ )	VNIR for visual inspection
				VNIR for NDVI

**Table 10.4** Summary of user requirements for Security and Surveillance applications

Application (Source)	EO Level	Spatial resolution	Geographical coverage	Temporal resolution	Accuracy	Algorithms	TIR spectral resolution	Other spectral ranges	Supporting data
Detection of minefields and landmines (Maathuis and van Genderen 2004)	LST	2–8 cm		(landmines) 1–5 m (minefields)	Local		Overpass time: sunrise, sunset	<0.5 °C	
Two bands (10–12 µm); Multispectral ( $\geq 3$ bands in 8–12 µm)	VNIR (Red, SW);		Split-window (SW);		Temperature and Emissivity Separation (TES)				
Border security (Personal Interview)	2 = TOA Brightness Temp	~15 m	Europe + N Africa to 5°N	1–2 days			SAR	DEM	
Object monitoring and detection (Personal Interview)	2 = TOA Brightness Temp	~10 m	Local	1–2 days		Two dimensional MRTD models	1 band: 0.8–2.5 µm	SAR	DEM
Ship & port monitoring: Piracy/drug smuggling/illegal Immigration (Personal Interview)	2 = TOA Brightness Temp	~15 m	Lat.: 60° N to 35° S	1–2 days		Two dimensional MRTD models	1 band: 0.8–2.5 µm	SAR, VIS	AIS
Industrial/power plant monitoring (Wu et al. 2007; Tang et al. 2003)	3 = Surface Temp	10–15 m	Lat.: 60° N to 35° S	1–2 days	1–2 K	TES, models, statistics	UV/VIS/NIR	Sonde measurements	
Trafficability (off-road soil moisture content) (Personal Interview)	3 = Surface Temp	30 m	Lat.: 60° N to 35° S	1–2 days	1–2 K	TTM	Two bands (10–12 µm)	SAR	DEM, ECMWF, LSE
			Lon. 70° W to 70° E						

## 10.6 Conclusions

The Fuegasat Synthesis Study identified several high-resolution thermal remote sensing applications and requirements in three different topics: Land and Solid Earth, Health and Hazards, and Security and Surveillance. Results presented in this chapter were extracted from the literature, although personal communication in the case of the Security and Surveillance topic was also helpful. Main applications in the Land and Solid Earth topic included volcano and fire monitoring, as well as detection of water stress and retrieval of evapotranspiration for water management purposes. In the case of the Health and Hazards topic, main applications identified were urban heat islands and epidemiology. Applications related to the Security and Surveillance topic were only vague defined, since poor information was found in the literature.

We conclude observing that a clear perception was registered about the fact that a high-resolution TIR mission with a nearly daily revisit time might have significant consensus among the users community, since existing high resolution TIR sensors (e.g. Landsat/TM-ETM+, Terra/ASTER) do not meet most of the user requirements. In this sense, it is worth to mention on-going activities such as MicroSatellite for Thermal InfraRed Ground Surface Imaging (MISTRIGRI) and Thermal Infrared Explorer (TIREX). MISTRIGRI is a project of microsatellite in the TIR conducted by the Centre National D'Études Spatiales (CNES) (France) in cooperation with Spain, currently in Phase-A. TIREX is a proposal presented in a recent (2010) ESA's call for Earth Explorer Opportunity Missions, although it was finally rejected for Phase-A. The originality of MISTRIGRI and TIREX is to combine a high spatial resolution (~50 m) with high revisit capabilities of 1 or 2 days over selected sites. Another significant initiative refers to the HypsI<sup>R</sup>I (Hyperspectral Infrared Imager) mission operated by NASA/JPL (Jet Propulsion Laboratory) (a dedicated chapter is included in this book). We also would like to remind the importance of complementary mission activities such as ground truth collections and data simulations for algorithm development and testing.

To sum up, a number of high resolution TIR applications were analyzed and technical requirements for a potential TIR sensor were identified. The results extracted from this study could be considered in part as a reference for the design of such a sensor in order to fill-in the currently existing gap in the acquisition of high spatial and temporal resolution TIR data.

## References

- Barret B, Turquety S, Hurtmans D, Clerbaux C, Hadji-Lazaro J, Bey I, Auvray M, Coheur PF (2005) Global carbon monoxide vertical distributions from spaceborne high-resolution FTIR nadir measurements. *Atmos Chem Phys* 5:2901–2914
- Bassani C, Cavalli RM, Cavalcante F, Cuomo V, Palombo A, Pascucci S, Pignatti S (2007) Deterioration status of asbestos-cement roofing sheets assessed by analyzing hyperspectral data. *Remote Sens Environ* 109:361–378

- Beck LR, Bradley ML, Wood BL (2000) Remote sensing and human health: new sensor and new opportunities. *Emerg Infect Dis* 6(3):217–225
- Billa L, Mansor S, Mahmud AR, Ghazali AH (2006) Modelling rainfall intensity from NOAA AVHRR data for operational flood forecasting in Malaysia. *Int J Remote Sens* 27(23):5225–5234
- Blair R, Blair-Fitzharris B, Richards K (2002) Interpolation of growing degree-days in non-homogeneous terrain. The 14th annual colloquium of the Spatial Information Research Centre University of Otago, Dunedin, New Zealand
- Bowman KW, Rodgers CD, Kulawik SS, Worden J, Sarkissian E, Osterman G, Steck T, Lou M, Elderling A, Shephard M, Worden H, Lampel M, Clough S, Brown P, Rinsland C, Gunson M, Beer R (2006) Tropospheric emission spectrometer: retrieval method and error analysis. *IEEE Trans Geosci Remote Sens* 44:1297–1307
- CEOS (2003) The use of earth observing satellites for hazard support: assessments and scenarios. Final report of the CEOS Disaster Management Support Group (DMSG), November
- Chrysoulakis N (2002) Thermal detection of plumes produced by industrial accidents in urban areas based on the presence of the heat island. *Int J Remote Sens* 23(14):2909–2916
- Chrysoulakis N, Cartalis C (2003) A new algorithm for detection of plumes caused by industrial accidents, based on NOAA/AVHRR imagery. *Int J Remote Sens* 24(17):3353–3367
- Chrysoulakis N, Adaktylou N, Cartalis C (2005) Detecting and monitoring plumes caused by major industrial accidents with JPLUME, a new software tool for low-resolution image analysis. *Environ Model Softw* 20:1486–1494
- Corradini S, Pugnaghi S, Teggi S, Buongiorno MF, Bogliolo MP (2003) Will ASTER see the Etna SO<sub>2</sub> plume? *Int J Remote Sens* 24(6):1207–1218
- Duchemin B, Goubier J, Courrier G (1999) Monitoring phenological key stages and cycle duration of temperate deciduous forest ecosystems with NOAA/AVHRR data. *Remote Sens Environ* 67:68–82
- Emch M, Feldacker C, Yunus M, Streatfield PK, Vu DT, Cahn DG, Alí M (2008) Local environmental predictors of cholera in Bangladesh and Vietnam. *Am J Trop Med Hyg* 78(5):823–832
- Feidas HN, Cartalis C, Cracknell AP (2000) Use of Meteosat imagery to define clouds linked with floods in Greece. *Int J Remote Sens* 21(5):1047–1072
- Fisher JB, Tu K, Baldocchi DD (2008) Global estimates of the land–atmosphere water flux based on monthly AVHRR and ISLSCP-II data, validated at 16 FLUXNET sites. *Remote Sens Environ* 112:901–919
- Gao Y, Mas JF, Maathuis BHP, Zhang X, Van Dijk PM (2006) Comparison of pixel-based and object-oriented image classification approaches – a case study in a coal fire area, Wuda, Inner Mongolia, China. *Int J Remote Sens* 27(18):4039–4055
- Gao Y, Kerle N, Mas JF (2009) Object-based image analysis for coal fire-related land cover mapping in coal mining areas. *Geocarto Int* 24(1):25–36
- Gemperli A, Vounatsou P, Anderegg D, Pluschke G (2004) EPIDEMIO: Earth observation in epidemiology. In: Proceedings of the 2004 Envisat & ERS Symposium, Salzburg, Austria, 6–10 Sept 2004 (ESA SP-572, April 2005), <http://www.epidemio.info>
- Giglio L, Loboda T, Roy DP, Quayle B, Justice CO (2009) An active-fire based burned area mapping algorithm for the MODIS sensor. *Remote Sens Environ* 113(2):408–420
- Gil AI, Louis VR, Rivera ING, Lipp E, Huq A, Lanata CF (2004) Occurrence and distribution of *Vibrio cholerae* in the coastal environment of Peru. *Environ Microbiol* 6:699–706
- Green RM, Hay SI (2002) The potential of Pathfinder AVHRR data for providing surrogate climatic variables across Africa and Europe for epidemiological applications. *Remote Sens Environ* 79:166–175
- Harris AJL, Rose WI, Flynn LP (2003) Temporal trends in lava dome extrusion at Santiaguito 1922–2000. *Bull Volcanol* 65:77–89
- Hassan Q, Bourque CPA, Meng FR, Richards W (2007a) Spatial mapping of growing degree days: an application of MODIS-based surface temperatures and enhanced vegetation index. *J Appl Remote Sens* 1(1):013511

- Hassan Q, Bourque CPA, Meng FR (2007b) Application of Landsat-7 ETM+and MODIS products in mapping seasonal accumulation of growing degree days at an enhanced resolution. *J Appl Remote Sens* 1(1):013539
- Herbretau V, Salem G, Souris M, Hugot JP, Gonzalez JP (2007) Thirty years of use and improvement of remote sensing, applied to epidemiology: from early promises to lasting frustration. *Health Place* 13:400–403
- Jia L, Xi G, Liu S, Huang C, Yan Y, Liu G (2009) Regional estimation of daily to annual regional evapotranspiration with MODIS data in the Yellow River Delta wetland. *Hydrol Earth Syst Sci* 13:1775–1787
- JRC (2008) Forest fires in Europe 2008, Report no 9, Joint Research Centre. Available at <http://effis.jrc.ec.europa.eu/download/forest-fires-in-europe-2008.pdf>
- Kato S, Yamaguchi Y (2007) Estimation of storage heat flux in an urban area using ASTER data. *Remote Sens Environ* 110:1–17
- Kuenzer C, Zhang J, Li J, Voigt S, Mehl H, Wagner W (2007) Detecting unknown coal fires: synergy of automated coal fire risk area delineation and improved thermal anomaly extraction. *Int J Remote Sens* 28(20):4561–4585
- Lakshmi V, Schaaf K (2001) Analysis of the 1993 midwestern flood using satellite and ground data. *IEEE Trans Geosci Remote Sens* 39(8):1736–1743
- Lobitz B, Beck L, Huq A, Wood B, Fuchs G, Faruque ASG, Colwell R (2000) Climate and infectious disease: use of remote sensing of detection of *Vibrio cholerae* by indirect measurement. *Proc Natl Acad Sci USA* 97:1438–1443
- Maathuis BHP, Van Genderen JL (2004) A review of satellite and airborne sensors for remote sensing based detection of minefields and landmines. *Int J Remote Sens* 25(23):5201–5245
- Marj A, Mobasher MR, Valadan zouje MJ, Rezaei Y, Abaei MR (2008) Using satellite images in determination of Malaria outbreaks potential region. *Nature Precedings* hdl:10101/npre.2008.2325.1
- Mikkelsen SA, Olesen JE (1984) Computer-aided mapping of growing degree days for Denmark, calculated from monthly temperature normals. *Acta Agr Scand* 34(3):330–338
- Morales CA, Anagnostou EN (2003) Extending the capabilities of high-frequency rainfall estimation from geostationary-based satellite infrared via a network of long-range lightning observations. *J Hydrometeorol* 4:141–159
- Oppenheimer C (1998) Volcanological applications of meteorological satellites. *Int J Remote Sens* 19:2829–2864
- Pugnagh S, Gangale G, Corradini S, Buongiorno MF (2006) Mt. Etna sulfur dioxide flux monitoring using ASTER-TIR data and atmospheric observations. *J Volcanol Geotherm Res* 152:74–90
- Rahman A, Kogan F, Roytman L (2006) Short report: analysis of malaria cases in Bangladesh with remote sensing data. *Am J Trop Med Hyg* 74(1):17–19
- Roshier DA, Rumbachs RM (2004) Broad-scale mapping of temporary wetlands in arid Australia. *J Arid Environ* 56:249–263
- Sanchez JM, Scavone G, Caselles V, Valor E, Copertino VA, Telesca V (2008) Monitoring daily evapotranspiration at a regional scale from Landsat-TM and ETM+ data: application to the Basilicata region. *J Hydrol* 351:58–70
- Saraf AK, Choudhury S (2005) Cover: NOAA-AVHRR detects thermal anomaly associated with the 26 January 2001 Bhuj earthquake, Gujarat, India. *Int J Remote Sens* 26(6):1065–1073
- Sepulcre-Cantó G, Zarco-Tejada PJ, Jiménez-Muñoz JC, Sobrino JA, de Miguel E, Villalobos FJ (2006) Detection of water stress in an olive orchard with thermal remote sensing imagery. *Agr Forest Meteorol* 136:31–44
- Sepulcre-Cantó G, Zarco-Tejada PJ, Jiménez-Muñoz JC, Sobrino JA, Soriano MA, Fereres E (2007) Monitoring yield and fruit quality parameters in open-canopy tree crops under water stress. Implications for ASTER. *Remote Sens Environ* 107:455–470

- Shcherbak SS, Lavrova OY, Mityagina MI, Bocharova TY, Krovotyntsev VA, Ostrovskii AG (2008) Multisensor satellite monitoring of seawater state and oil pollution in the northeastern coastal zone of the Black Sea. *Int J Remote Sens* 29(21):6331–6345
- Sobrino JA, Gomez M, Jimenez-Muñoz JC, Olioso A, Chehbouni G (2005) A simple algorithm to estimate evapotranspiration from DAIS data: application to the DAISEX campaigns. *J Hydrol* 315:117–125
- Sobrino JA, Jiménez-Muñoz JC, Sória G, Gómez M, Barella-Ortiz A, Romaguera M, Zaragoza M, Julien Y, Cuenca J, Atitar M, Hidalgo V, Franch B, Mattar C, Ruescas A, Morales L, Gillespie A, Balick L, Su Z, Nerry F, Peres L, Libonati R (2008) Thermal remote sensing in the framework of the SEN2FLEX project: field measurements, airborne data and applications. *Int J Remote Sens* 29(17–18):4961–4991
- Stathopoulou M, Cartalis C, Chrysoulakis N (2006) Using midday surface temperature to estimate cooling degree-days from NOAA-AVHRR thermal infrared data: an application for Athens, Greece. *Sol Energy* 80:414–422
- Tang D, Kester DR, Wang Z, Lian J, Kawamura H (2003) AVHRR satellite remote sensing and shipboard measurements of the thermal plume from the Daya Bay, nuclear power station, China. *Remote Sens Environ* 84:506–515
- Tramutoli V, Cuomo V, Filizzola C, Pergola N, Pietrapertosa C (2005) Assessing the potential of thermal infrared satellite surveys for monitoring seismically active areas. The case of Kocaeli (İzmit) earthquake, August 17, 1999. *Remote Sens Environ* 96:409–426
- Tronin AA (2000) Thermal IR satellite sensor data application for earthquake research in China. *Int J Remote Sens* 21(16):3169–3177
- Tseng WY, Chiu LS (1994) AVHRR observations of Persian Gulf oil spills. In: Proceedings of IGARSS'94, 2:779–782
- UHI Project (2009) Requirements baseline Document, pkt258-25-2.0
- Vancutsem C, Ceccato P, Dinku T, Connor SJ (2010) Evaluation of MODIS land surface temperature data to estimate air temperature in different ecosystems over Africa. *Rem Sens Environ* 114:449–465
- Vidal A, Devaux-Ros C (1995) Evaluating forest FIRE hazard with a Landsat TM derived water stress index. *Agr Forest Meteorol* 77:207–224
- Voogt JA, Oke TR (2003) Thermal remote sensing of urban climates. *Remote Sens Environ* 86:370–384
- WFSC World Fire Statistics (2009) Information Bulletin of the World Statistics Centre. Available at <http://www.genevaassociation.org/PDF/WFSC/GA2009-FIRE25.pdf>
- Wright R, Flynn L, Garbeil H, Harris A, Pilger E (2002) Automated volcanic eruption detection using MODIS. *Remote Sens Environ* 82:135–155
- Wu C, Wang Q, Yang Z, Wang W (2007) Monitoring heated water pollution of the DaYaWan nuclear power plant using TM images. *Int J Remote Sens* 28(5):885–890
- Zhang J, Wagner W, Prakash A, Mehl H, Voigt S (2004a) Detecting coal fires using remote sensing techniques. *Int J Remote Sens* 25(16):3193–3220
- Zhang X, Zhang J, Kuenzer C, Voigt S, Wagner W (2004b) Capability evaluation of 3–5 μm and 8–12.5 μm airborne thermal data for underground coal fire detection. *Int J Remote Sens* 25 (12):2245–2258
- Zhukov B, Lorenz E, Oertel D, Wooster M, Roberts G (2006) Spaceborne detection and characterization of fires during the bi-spectral infrared detection (BIRD) experimental small satellite mission (2001–2004). *Remote Sens Environ* 100:29–51
- URL1: <http://www.urbanheatisland.info>
- URL2 <http://www.gmes.info>
- URL3: <http://www.gmes-gmosaic.eu>
- URL4: <http://www.fp6-limes.eu>

# Chapter 11

## Cross-Comparison of Daily Land Surface Temperature Products from NOAA-AVHRR and MODIS

Corinne Myrtha Frey, Claudia Kuenzer, and Stefan Dech

**Abstract** Land surface temperature (LST) products retrieved from two different sensors – AVHRR (Advanced Very High Resolution Radiometer) and MODIS (Moderate Resolution Imaging Spectroradiometer) – were cross-compared. The analysis was conducted on a daily basis for 4 different years. Only pixels that followed a certain homogeneity criteria were chosen. Furthermore a time criterion defining the maximal time difference between two acquisitions was considered. The differences of the two products showed diurnal and annual patterns with LST of AVHRR being higher than MODIS at high surface temperatures and AVHRR being lower than MODIS at lower temperatures. Additionally some irregular patterns were identified and attributed to the different algorithm approaches. However, mean annual absolute differences were relatively low: 2.2 K for the daytime and 1.4 K for the nighttime scenes, indicating a general good agreement between the two products. The  $r^2$  between the LST of AVHRR and MODIS for both day and night scenes was about 0.99.

### 11.1 Introduction

Land Surface Temperature (LST) is an important parameter in the climate system, being the interface between the long- and shortwave radiation fluxes on one side and the turbulent heat fluxes or the ground heat flux on the other side. Air temperature is further strongly dependent on LST. This central position in the

---

C.M. Frey (✉)

Department of Remote Sensing in cooperation with the German Aerospace Center (DLR)

Department of Geography and Geology, University of Würzburg, Würzburg, Germany  
e-mail: [Corinne.frey@dlr.de](mailto:Corinne.frey@dlr.de)

C. Kuenzer • S. Dech

German Remote Sensing Data Center (DFD), Earth Observation Center (EOC),  
German Aerospace Center (DLR), Oberpfaffenhofen, Germany

climatological system puts LST in the position of a useful variable for a variety of studies ranging from in depth analyses of energy balance and evaporation to global climate change studies. In fact LST, as part of the surface radiation budget or the fire disturbance, belongs to the essential climate variables defined in WMO-GCOS (World Meteorological Organization – Global Climate Observing System) World Meteorological Organization ([URL1](#)). However, satellite-derived LST is very dynamic and the current uncertainty in relating it to other in situ measurements makes LST unsuitable for global, long-term monitoring (GCOS [2010](#)). Effectively, the quality assessment of LST products is a challenging task. Uncertainties in the calibration constants and algorithm adequacy ask for an after-launch validation of the data. Validation campaigns tailored for the requirements of space-born measurements are conducted (Kabsch et al. [2008](#); Coll et al. [2005](#)). However, the validation of LST products with a spatial resolution of 1 km makes great demands. The campaigns should offer as homogeneous sites as possible. But in most cases, still small scale irregularities occur. Multiple measurements inside a plot may help to overcome this problem. The operation of validation sites is cost and time intensive, so usually only shorter periods of measurements are available, not allowing the comparison of longer time series of satellite data. At higher latitudes the problem aggravates, as many satellite scenes are cloud contaminated, limiting additionally the number of available comparison times. Therefore, usually only few dates and times are available for validation. For example Zhong et al. ([2010](#)) compared AVHRR (Advanced Very High Resolution Radiometer) and MODIS (Moderate Resolution Imaging Spectroradiometer) LST with in situ data of the Tibetan plateau. They compared LST data retrieved with a split window algorithm for four validation sites. They compared the data at four cloud-free days in the year 2003. The mean absolute differences between their satellite results and in situ data were 2.2 K for the AVHRR LST and 1.4 K for the MODIS LST.

If no in situ data is available, there is also the option of a cross-comparison of the products of two different satellites. This method is not a real validation, but allows identifying weak points in a product. Comparison of longer time series of satellite datasets is possible, given that the satellites have equal times of acquisition. However, also this method entails several constraints. In some cases different spatial resolutions lead to scaling issues. Different view zenith angles impose thermal anisotropy effects on the data (Liu et al. [2007, 2009](#)). Batra et al. ([2006](#)) compared MODIS and AVHRR LST. The comparison was part of an evaporation study, covering only a few days. They did not consider the time of overflight, though mean differences were in the range of 2–5 K only. Such low mean differences can occur, when the absolute differences are not considered in the averaging process, so that the single differences can be positive as well as negative.

Some authors have combined the two approaches. Noyes et al. ([2006](#)) for example validated the AATSR (Advanced Along-Track Scanning Radiometer) LST product. They compared 1 year series with in situ data as well as with MODIS and SEVIRI (Spinning Enhanced Visible and Infrared Imager) data and found a seasonal bias in all comparisons. Also Yang and Yang ([2006](#)) validated 10-day composite LST from AVHRR with MODIS LST and 257 in situ datasets

from weather stations over China. They found AVHRR being 2–3 K larger than the MODIS LST and explained it by the used emissivity approaches. Also, they found the RMSE (Root Mean Square Error) of the in situ and the AVHRR LST ranging from 3.5 to 3.9 K for their three observation periods with AVHRR LST being higher than the in situ measurements. No information about the suitability of the in situ stations for such a comparison is given.

Future LST systems ambitiously try to achieve an accuracy of <1 K (GMES Sentinel-3 MRD 2007), which is set for example by the need to model the fluxes of the energy balance with an accuracy better than  $10 \text{ Wm}^2$  (NCDC LST-Workshop Summary 2008).

This study is an example piece of quality assessment focussing on the method of cross-comparison. The product to analyse is the AVHRR LST time series of DLR (German Aerospace Center) (Dech et al. 1998; Tungalagsaikhan et al. 1998), the correspondent truth data is the MODIS LST product. The MODIS LST product was chosen due to its ongoing improvements in the algorithm and careful maintenance (Wan et al. 2002). The comparison was conducted using 4 years of daily daytime and nighttime data, acquired at similar times and viewing angles. The use of the final product level for LST ensured that no pre-selection of ‘optimal’ scenes was done.

## 11.2 Satellite Data

### 11.2.1 AVHRR LST

In this study the AVHRR LST product provided by DLR (Dech et al. 1998; Tungalagsaikhan et al. 1998) was used. It will be further referred to as AHVRR LST. The product is generated based on the split window algorithm (SWA) developed by Becker and Li (1990) which includes a general atmospheric correction. Emissivity is estimated following van de Griend and Owe (1992). The NDVI (Normalized Difference Vegetation Index) which is used by the emissivity estimation is taken from a 10 days maximum composite from DLR (Holben 1986; Dech et al. 1998). Clouds are detected by the APOLLO (AVHRR Processing scheme Over cLoud Land and Ocean) cloud detection scheme (Saunders and Kriebel 1988; Gesell 1989) and affected pixels are set to a missing value. The LST product is delivered with a spatial resolution of 1.1 km.

The AVHRR LST product is a spatial and temporal composite of three consecutive scenes over Europe and Northern Africa. This is comprehensible, as the NOAA (National Oceanic and Atmospheric Administration) satellites are on a sun-synchronous orbit. However, the time deviation in one scene from the subsatellite track to the image border is 45 min at the equator due to the large swath width of 2,500 km. At higher latitudes the time differences increase even to more than an hour.

The spatial merging of the three scenes creates zones of overlapping. A maximum NDVI condition for the daytime scenes and a maximum LST criterion for the nighttime scenes, both based on daily values, are used defining the appropriate input scene for each pixel (Holben 1986; Dech et al. 1998). The two criteria shall favour the selection of the pixel that is least distorted by the atmosphere or clouds that were not recognized by APOLLO. Through this merging process as well as through the high time difference between subsatellite track and image border, temperature leaps can occur inside the composite as surface temperature shows high diurnal amplitudes. Especially in non-vegetated sites (bare ground, sealed surfaces) strong differences in LST occur within few hours (Frey et al. 2011). The AVHRR LST product is provided without pixel-based time information and only the day of acquisition is given in the metadata. In order to compare the AVHRR LST with the MODIS product, acquisition time information had to be reconstructed. It was done using the geographical information of the original HRPT (High Resolution Picture Transmission) files. The geographical extent of each original HRPT scene was reconstructed and projected in the composite. Through this approach, pixels in the composite that were only covered by one scene could be identified. Such pixels are often found at the West and East of Europe and in North Africa. Local time images were generated for these HRPT scenes using the geographical information as well as the start time of acquisition. Thereby first the acquisition time of the ground track line was generated in dependence on the speed of the satellite and following the local time information was included using the longitude information of the generated images. Finally the scenes were warped into the geometry of the composite. To avoid large viewing angles, a border of 500 pixels was cut from the scenes before the warping process. Considering the simplified geometry of the approach, we estimate that only pixels with a satellite viewing angle lower than about  $\sim 30^\circ$  were left.

Four years of data were considered for comparison: Data from 2003 with input scenes from AVHRR-16, from 2005 with scenes from AVHRR-17, from 2008 with scenes from AVHRR-18 and from 2010 with scenes from AVHRR-19. In case scenes of other AHVRR models were used than given before, then these dates were excluded from the comparison.

### **11.2.2 MODIS LST**

MODIS data were obtained from the Land Processes Distributed Active Archive Center (LP DAAC), located at the U.S. Geological Survey (USGS) Earth Resources Observation and Science (EROS) Center ([lpdaac.usgs.gov](http://lpdaac.usgs.gov)) for the same years as the AVHRR selected data. To have the best temporal matching of the MODIS measurements to the daily composites of AVHRR, the MOD11A1/MYD11A1 Daily LST products of the collection 5 (v005) have been selected. It will be further referred to as MODIS LST.

Like the AVHRR LST, MODIS LST is also generated using a split-window algorithm. However, the approach is more sophisticated and the coefficients are not only depending on the atmospheric conditions and the ranges of surface temperature, but also on the viewing angle (Wan and Dozier 1996; Wan 2008). The emissivity is estimated on a classification-based look-up table derived from land-cover types and dynamic and seasonal factors (Snyder and Wan 1998). The spatial resolution of the product is 0.928 km.

The MODIS LST product is constantly reviewed. A versioning system has been introduced to account for modifications in the processing chain (Wan 2008). The MODIS team claims the accuracy of the LST product to be better than 1 K ([URL2](#)). However, at larger viewing angles, as well as in semi-arid and arid regions some higher errors were detected. Hulley and Hook (2009) compared the emissivity of the collection 4, 4.1, and 5 and validated them with laboratory measurements of sand samples from the Namib Desert. They found the collection 5 to overestimate the emissivity and therefore suggest considering using collection 4 or 4.1 for studies in arid areas. Nevertheless, collection 5 seemed to be better suited for this comparison due to its fewer missing pixels and lesser artefacts in the product.

The most suitable pixels for comparison are found in the West and East of Europe and in North Africa. Two tiles of the fixed grid of MODIS LST with the centre coordinates of 35.0° Lat, –6.5319° Lon (western tile) and 35.0° Lat, 31.1236° Lon (eastern tile, see also Fig. 11.1) cover the region of interest. The tiles were warped into the same projection as the AVHRR LST scenes. Only data with the MODIS quality flag “good quality” were used in the comparison.

### 11.3 Choice of Comparison Sites

To minimize the geolocation errors in the comparison, only pixels that exhibit a certain homogeneity were chosen. The selection criteria for the homogeneity filter used in the comparison were as follows:

- The LST and NDVI data values should not exceed certain variability in a  $5 \times 5$  pixel box. So, the maximum threshold for the standard deviation of LST is set as 1 K and the maximum threshold for the standard deviation of NDVI is set as 0.1.
- The maximum slope of topography inside a  $5 \times 5$  pixel box should not be larger than 2°. The slope parameter is calculated using the 250 m SRTM DEM (Shuttle Radar Topography Mission – Digital elevation model) from the CGIAR-CSI GeoPortal (Consultative Group on International Agricultural Research – Consortium for Spatial Information) ([URL3](#)).

Setting these criteria, most pixels selected were found in Northern Africa. The selected MODIS tiles cover the Western and Eastern South of Europe and Northern Africa, so a sufficient number of pixels was available for the comparison (see Fig. 11.1).

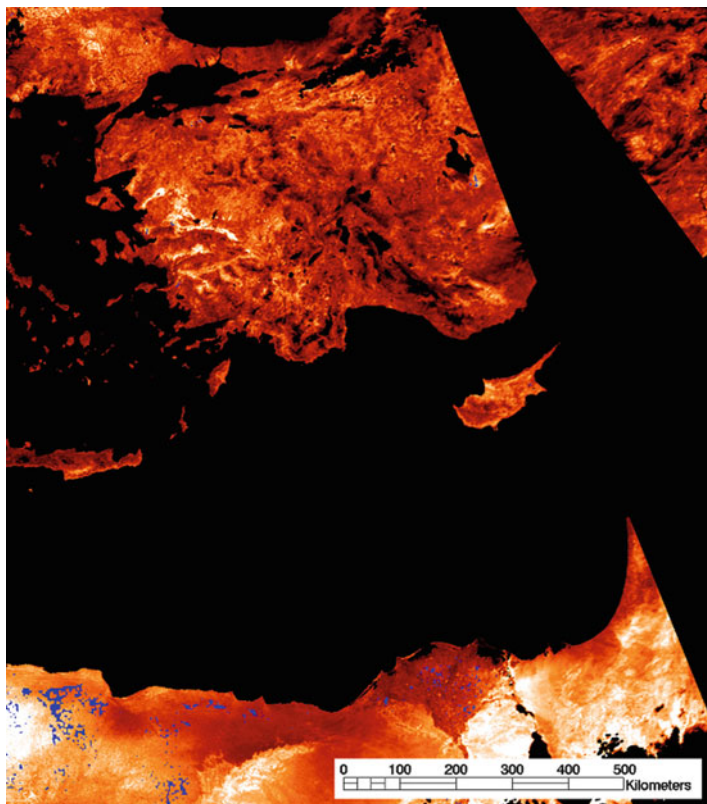


**Fig. 11.1** AVHRR composite of 3rd May 2003 resampled to the Eastern MODIS tile. Notice that a part in the East of the cut-out is not available due to AVHRR scene overlapping. Pixels plotted in blue indicate the selected areas after the homogeneity filter

By applying a less strict homogeneity filter (e.g.  $3 \times 3$  pixels and  $3^\circ$  DEM slope), the difference between AVHRR and MODIS LST values tend to increase. A stricter filter in turn (e.g.  $7 \times 7$  pixel and  $1^\circ$  DEM slope) reduces the differences. However, considering such stricter filter reduces the number of pixels available for comparison. A  $5 \times 5$  pixel with a  $2^\circ$  slope criterion was found to be a good compromise between homogeneous pixels and available number of pixels.

## 11.4 Results

The analysis was done using all pixels left over after applying the homogeneity and MODIS quality filter and after removing the overlapping areas of AVHRR scenes. In this way, the number of pixels representing one day might be different from the number of pixels representing another day. The LST of AVHRR and MODIS agree

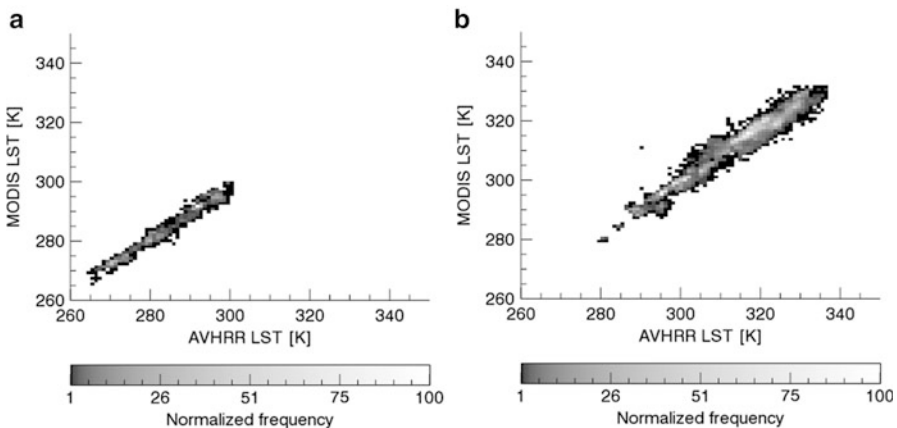


**Fig. 11.2** 2D histograms of AVHRR and MODIS LST for all 4 years. Only pixels with viewing angles lower than  $30^\circ$  were used. The maximal time difference was 30 min for the nighttime scenes (a) and 5 min for the daytime scenes (b)

well with an  $r^2$  equal to 0.99 and the mean absolute difference (MAD) of 1.90 K. The MAD is given by

$$MAD = \frac{1}{n} \sum_{i=1}^n |LST_{AVHRR_i} - LST_{MODIS_i}| \quad (11.1)$$

Looking only at the nighttime data, the MAD improves even to 1.4 K, while the daytime data have a MAD of 2.2 K. Figure 11.2 shows 2D histograms of AVHRR and MODIS LST separated for nighttime (Fig. 11.2a) and daytime (Fig. 11.2b) scenes. The daytime scenes feature a much stronger scattering than the nighttime scenes, which can be statistically expressed by the standard deviation: In the daytime scenes the standard deviation is 2.0, in the nighttime scenes it is 1.1 K.

Analysing the single years, similar statistical values are found (Tables 11.1 and 11.2). Annual MADs range from 1.2 to 3.4 K. Maximal annual values are found in the daytime scenes of the year 2008 and 2010 with MADs of 3.00 and 3.41 K. In these years also the standard deviation is high ( $>2$  K), whereas the other 2 years and all nighttime scenes have annual mean standard deviations lower than 2 K.  $r^2$  are usually very high, except of the daytime scenes of 2005, where also the number of observations is very low (35 pixels only). In 2008 also the number of observations is low (70 pixels) but there the correlation is good though.

The strong diurnal fluctuation of LST requires a strict time limitation for the comparison of the two products. For the selection of pixels in the comparison analysis, the maximum allowed acquisition time difference between scenes was set to 5 min for daytime and 30 min for nighttime scenes. Including all pixels for comparison, the MADs would increase considerably. For example for the daytime scenes, the MAD rises from 2.1 to 4.6 K and 3.4 to 4.5 K in the years 2003 and 2010 respectively if the time filter is not used. In the nighttime scenes, the effect of

**Table 11.1** Statistical attributes of the differences between LST of AVHRR and MODIS for the daytime scenes

Year	Number of analysed pixels	MAD	SAD	$r^2$
2003	14,796	2.12	1.91	0.96
2005	35	2.26	1.51	0.59
2008	70	3.00	2.24	0.92
2010	833	3.41	2.50	0.97

*MAD* stands for mean absolute difference and *SAD* for standard deviation of the absolute differences

**Table 11.2** Statistical attributes of the differences between LST of AVHRR and MODIS for the nighttime scenes

Year	Number of analysed pixels	MAD	SAD	$r^2$
2003	0	—	—	—
2005	4,396	1.32	1.11	0.99
2008	2,532	1.15	0.80	0.99
2010	1,504	1.91	1.30	0.97

*MAD* stands for mean absolute difference and *SAD* for standard deviation of the absolute differences

acquisition time difference is not significant. For example, for the nighttime scenes, the MAD increases from 1.15 to 2.15 K in 2008, but in 2010 the MAD remains at 1.9 K even after the exclusion of time filter. However, the relation between the LST MAD and the acquisition time difference is not linear due to the highly variable course of LST during the year. So, correlation coefficients  $r^2$  between the MAD and the time difference must be low (0.21 for all daytime scenes and 0.12 for all nighttime scenes).

All in all, the nighttime scenes match better than the daytime scenes. Such pattern is found throughout the year. But especially in summer the daytime scattering of differences is high. Figures 11.3 and 11.4 show the differences between AVHRR and MODIS LST grouped into monthly clouds. Single values are plotted in grey; the monthly means are given in bold black. The monthly means show an annual course with highest differences in summer and lowest differences in winter. This trend can be found in the both daytime and nighttime scenes. However, in the daytime scenes the means are mostly positive, while in the nighttime scenes, the differences tend to be negative in winter and positive in summer.

The Eastern tile generally shows a better agreement between AVHRR and MODIS LST than the western tile. In the Eastern tile the daytime/nighttime MADs of all years are 1.56 and 0.63 K only, while in the Western tile the respective MADs are 2.55 and 1.71 K. Also the standard deviations are higher in the Western tile due to the strong scattering occurring in the data of the Western tile. Especially in the night scenes, the difference is evident. There, the annual course is not existent in the Eastern tile and scattering is very low. Unfortunately, the data availability of the nighttime data in the Western tile is too low to deduct a proper annual course. Therefore, the filter restrictions had to be relaxed to a  $3 \times 3$  pixel environment for

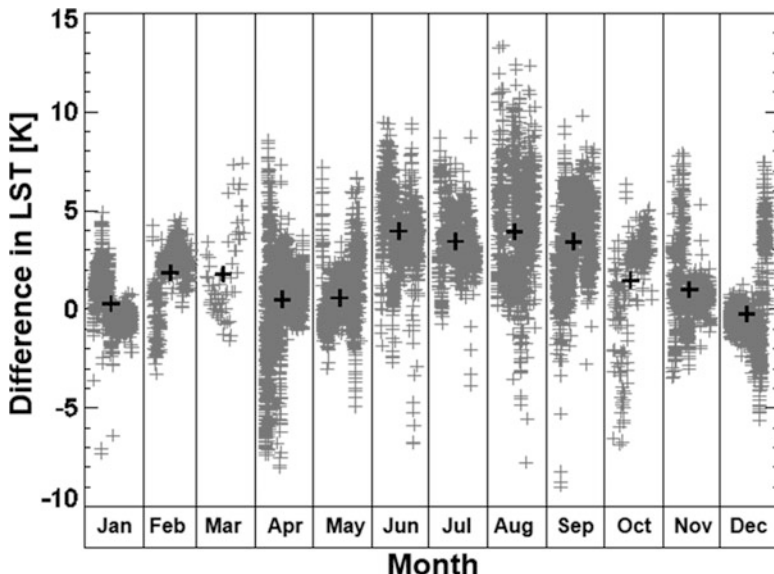


**Fig. 11.3** Daytime AVHRR LST minus MODIS LST for all 4 years and both MODIS tiles, grouped into monthly clouds. Only pixels with viewing angles lower than  $30^\circ$  were used and the maximal time difference was 5 min. Single values are plotted in grey; monthly means are given in black

these findings. Looking at the slope of a linear regression between the AVHRR and MODIS LST nighttime data sets (normal filter), then the value of the Western tile is 0.84, the slope of the Eastern tile is 0.98. This speaks for stronger temperature dependence in the data of the Western tile.

Like other missing metadata, the Viewing Zenith Angle (VZA) is not given in the AVHRR product. However, through the exclusion of the across track border areas of the input scenes, wide AVHRR VZA are automatically eliminated from this comparison. It is estimated that only VZA lower than  $30^\circ$  are taken. Similarly, the MODIS VZA is restricted to  $30^\circ$  in this study. Allowing higher MODIS VZA, e.g. up to  $50^\circ$ , then the MAD of all daytime scenes will increase from 2.2 to 3.1 K. Similarly the  $r^2$  will drop from 0.96 to 0.95. However, the relation between the differences and the MODIS VZA is not linear and the  $r^2$  between the two is low, only 0.14. In case of the nighttime scenes, no correlation can be found at all. However, the  $r^2$  between AVHRR and MODIS LST remains similar high (0.98) after inclusion of MODIS VZA up to  $50^\circ$ . And the MAD of the night scenes is even decreasing from 1.4 to 1.2 K.

Fifty-eight percent of all considered daytime pixels in this study show lower differences than 2 K. Even 72 % show lower differences than 3 K. However, 18 % of all absolute differences are higher than 4 K, which is out of an accepted accuracy. And 5 % of all absolute differences are higher than 6 K.

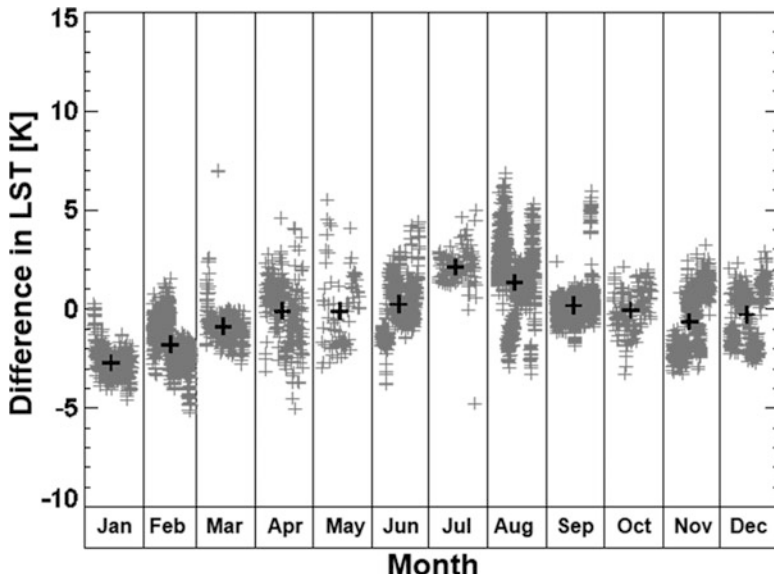


**Fig. 11.4** Nighttime AVHRR LST minus MODIS LST for all 4 years and both MODIS tiles, grouped into monthly clouds. Only pixels with viewing angles lower than  $30^\circ$  were used and the maximal time difference was 30 min. Single values are plotted in grey; monthly means are given in black

In the night scenes, these values are better: 92 % of all considered nighttime pixels show lower differences than 2 K and 96 % show lower differences than 3 K. Only 2 % of all absolute differences are higher than 4 K.

#### 11.4.1 Detailed Analysis

In the analysis above only low MADs are found, which is due to the high number of input values into the averaging process. However, a more detailed analysis of the data revealed that there are occasions, where very strong deviations between AVHRR and MODIS occur. As stated before, the western tile shows the higher differences. Figure 11.5 shows the variation of differences between AVHRR and MODIS, plotted for each day of the year 2003 in the western tile. It gets obvious that for a single day some pixels have almost no difference, while at other pixels in the same scene, strong deviations occur. The reason for such discrepancies might be explained by different land cover leading to variations in surface emissivity or else by different illumination conditions induced by small-scale inhomogeneities of the surface in combination with the viewing zenith angle VZA of the sensor – favouring or disfavouring a comparison. Another reason can be the insufficient atmospheric correction and masking of clouds.

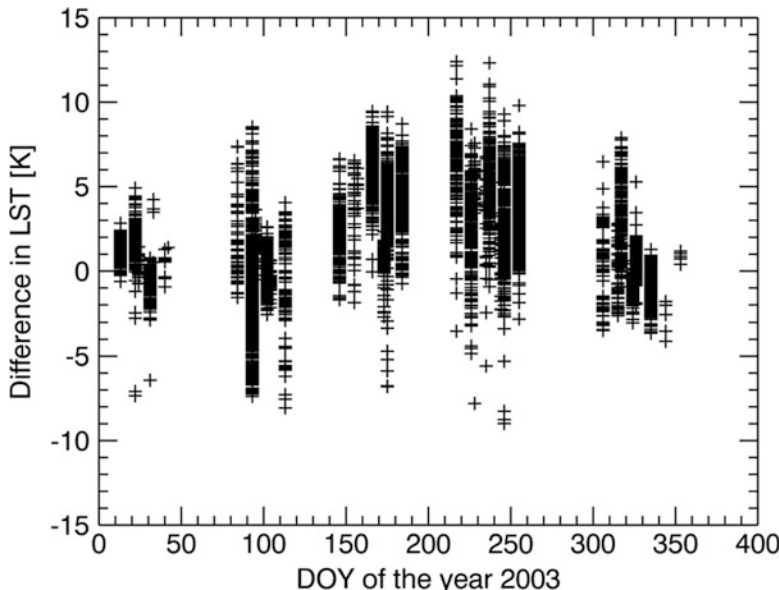


**Fig. 11.5** Variation of daytime differences occurring in the western tile of the year 2003 per day

An example of insufficient cloud masking is given on the example of the 24th June 2003 (DOY 175). Most differences in the western daytime scene are positive – indicating that AVHRR LST values are higher than MODIS LST. However, there are some pixels, where the opposite is true: there MODIS LST is clearly higher than the AVHRR LST, resulting in negative differences. These pixels are located in the Western part of the Algerian desert, where an area of cumulus clouds extends. Due to the allowed time difference (maximal 5 min), the location of the clouds is not exactly the same in the MODIS and the AVHRR scene, hence also the cloud masks are not identical. Additionally, the selection of only MODIS pixels with the quality flag “good” resulted in a much larger masked area than the cloud masking in the AVHRR product (Fig. 11.6). In the AVHRR product the cloud masking reflects the structure of the cumulus clouds. However, it seems that some of the clouds were not detected by the APOLLO algorithm, resulting in pixels with low LST. Some of these pixels are not cloudy in the MODIS product, so that before mentioned negative differences are produced. In the West of the described cumulus area, a faint layer of translucent clouds is present (not shown in Fig. 11.6). This area is neither detected by the AVHRR nor by the MODIS cloud detection scheme, resulting in both cases in low LST.

Such unreliable masking of clouds was detected at several days. It is therefore anticipated that the AVHRR product has some pixels with a strong underestimation of LST due to cloudiness. However, these pixels are often masked out in this study due to the fact that only MODIS pixels with the quality flag “good” were taken.

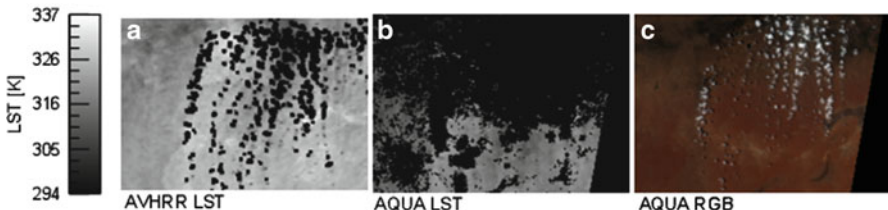


**Fig. 11.6** Daytime LST of part of the Algerian desert on 24 June 2003. (a) AVHRR LST, (b) MODIS AQUA LST, (c) RGB image of MODIS AQUA. Pixels printed in black are cloud masked areas

The cloud masking in the AVHRR product is done using the APOLLO software (Gesell 1989). APOLLO is a robust and well validated tool (Triebel et al. 2003). However, in the case of the AVHRR LST series, cases of unreliable cloud discrimination were found, which may be related to the general problem of discrimination of clouds over desert surfaces.

## 11.5 Discussion

The results retrieved for the whole dataset are good. LST of AVHRR and MODIS show a high correlation and their averaged long-term differences are in the range of the accuracy for LST of most thermal scanners (2 K). But in all years, nighttime differences have a lower scattering than daytime differences. Similarly, the scattering in the winter month is lower than the scattering in the summer month. Figure 11.3 shows that scattering increased with higher temperatures, both in day and in night scenes.

There are two obvious explanations for this behaviour:

1. There is always a slight time difference in the acquisition of the two scenes. A maximum of 5 min for the daytime and 30 min for the nighttime scenes are allowed. During this time LST change will probably occur due to the strong diurnal course of LST. Generally, the LST change per time unit is much higher during the day than during the night.
2. Induced by the roughness of the surface, there is a variation of LST with the VZA, called thermal anisotropy. Such effects can produce a diurnal variation in LST. As the view angles of the two acquisitions are not the same and the filtering DEM has a spatial resolution of 250 m only, it follows that higher differences must occur during daytime due to different surfaces sensed by the AVHRR and MODIS sensors (compare: Liu et al. 2009).

It is assumed that a considerable part of the scattering and therewith a certain part of the diurnal and annual patterns found in the data is due to these two explanations. So, this part of deviations is not a result of the product generation

of AVHRR and MODIS, but it is a result of the comparison method in this research, which cannot eliminate completely the factors ‘LST change per time unit’ and ‘thermal anisotropy’.

Another factor leading to scattering is the insufficient masking of clouds. This factor can lead to high deviations. It is assumed that scattering is increased in cloudy seasons.

Disregarding the scattering, the differences between AVHRR and MODIS LST tend to be higher in summer than in winter. This feature was found in all years and both tiles. In the daytime scenes, differences are mostly positive; with highest positive differences during the summer months (see Fig. 11.3). In the nighttime scenes, the differences are negative in winter, but positive in summer (Fig. 11.4). The interpretation of this finding is complicated by the fact that the choice of pixels is different for each month and day. But generally, the AVHRR LST tends to be higher than the MODIS LST during the day, especially during summer, while in the night, mostly the MODIS LST is higher than the AVHRR LST. However, in the summer month, the AVHRR LST might also exceed the MODIS LST also in the nighttime scenes.

Like in the scattering phenomenon, differences seem to follow the LST. At low LST, MODIS delivers higher values, but at high LST AVHRR estimates the higher values. Indeed, the  $r^2$  between the differences of LST of AVHRR and MODIS and the LST of MODIS itself is 0.28. The  $r^2$  of the night scenes only is even 0.35, as the scattering at night is much less. So, there is a dependence – even if not linear – of the differences on the LST itself, manifesting in an annual curve. Above mentioned two factors (‘LST change per time unit’ and ‘thermal anisotropy’) do not explain this behaviour, therefore other factors have to be investigated.

1. It is likely that different approaches to calculate the emissivity produce seasonal differences. For example Pozo Vázquez et al. (1997) found that in the Becker&Li-algorithm there is an emissivity effect: At high temperatures, an error in emissivity results in a LST difference of 1.2–1.8 K, while at low temperatures this difference is lower. Supposed that the two approaches from AVHRR and MODIS do not produce exactly the same emissivities, a seasonal and diurnal dependence of LST is possible.
2. The AVHRR uses the NDVI to deduce the emissivity using a logarithmic algorithm from van de Griend and Owe (1992). This algorithm produces very low emissivities for NDVI values close to zero. This might actually imply that emissivity is underestimated in most of considered pixels in this study as a huge part of the selected regions consist of many bare soil, rock and sandy surfaces. This effect goes along with the MODIS algorithm that seems to underestimate LST in arid and semi-arid areas due to an overestimation of the emissivity in such regions (Wan et al. 2002).
3. Another factor which produces differences between AVHRR and MODIS might be the atmospheric correction using the split window approach (SWA). MODIS uses a generalized SWA, accounting for different states of the atmosphere. AVHRR in turn uses a single set of coefficients for the SWA, standing for a

ing le tandar d atmop here. Due to changing atmoph eric condition in the annual cour e, it i poi ble that the difference in the SWA approach lead to annual variation in LST.

4. Calibration finally i uppo ed to influence the quality of the AVHRR product. AVHRR thermal calibration i done uing two reference target: A cold target (pa ce) and a warm blackbody onboard (internal calibration target ICT). The temperature of the ICT i not fixed but varie according to Tri hchenko and Li (2001) at temperature clearly lower than 300 K. From thi it can be aumed that urface temperature in the very high range might be le correct than temperature le than 300 K. However, 86 % of all daytime pixel ued in thi tud y feature LST higher than 300 K. In the nighttime cene only 1 % of the pixel are affected though. Such, a diurnal and ea onal effect could evolve. The calibration i further affected by non-linearity effect.

It wa found that the difference in the Eatern tile were lower than in the Weter n tile. Alo, the annual cour e wa le diti nct in the Wetern tile and even aben t in the nighttime cene of the Weter n tile. One reaon for thi behaviour can be found in the urface characteritic of the two tile. Indeed, the analyi of the co-occurrence meaur e ‘homogeneity’, ‘diimilari ty’, and ‘entropy’ of the lope of the 250 m SRTM DEM howed that the urface of the Eatern tile i much more homogeneou than the Weter n tile. The applied filter of a maximum of 2° in the lope probably left over pixel with a high urface roughne in the ma ller cale. However, maximum difference between the Eat ern and the Weter n tile were found at night, where thermal ani otropy i minimal. Another reaon could be that in the Weter n tile more vegetation i available than in the Eatern tile, foterig an annual cour e in emiivity a wa how n before. It i alo poibl e that atmop heric condition (e.g. cloudine) in the Wetern tile are different from the Eatern tile, leading to uch different pattern.

## 11.6 Conclusions

The AVHRR and the MODIS LST product how a general good agreement. The two dataet, conit ing of pixel pair elected according to acquii tion time difference and homogeneity criteria, have a high correlation  $r^2$  of 0.99. The mean absolut e difference (MAD) i 1.89 K only. Separating for daytime and nighttime data, the  $r^2$  are 0.96 and 0.98 and the MAD are 2.2 and 1.4 K. Neverthele, diurnal and annual pattern were found in the calculated difference of the two product , a well a temporal and pat ial irregularitie. Firtly, the cattering i trongl y enhanced in the daytime and umme r time data in contra t to the nighttime and winter time data. Beide the inu fficient making of cloud, the cat tering i attributed to the fact that the cene to be compared are hardly taken at exactly the am e time. Time difference of up to 5 min in the daytime cene and up to 30 min in the nighttime cene were allowed. Conid ering that LST ha a strong

diurnal course, such time differences will introduce errors in the comparison especially during the day. Another explanation for the scattering pattern is the thermal anisotropy of not perfectly flat surfaces, sensed by different viewing angles of the two sensors. Most real surfaces are not completely flat but are consisting of small-scale irregularities. Therefore, the thermal anisotropy will lead to increased scattering in occasions of different viewing angles.

Secondly: Besides the scattering, AVHRR and MODIS LST showed a slightly different diurnal and annual behaviour, which could be attributed to the LST itself: The higher the LST, the higher are AVHRR LST compared to MODIS LST. Explanations for this behaviour can be found in the different steps of the processing chain: Calibration issues, atmospheric correction, and emissivity correction. These factors can be used to explain a general offset, short term and spatially varying irregularities as well as annual patterns.

A general assumption of this study was that the MODIS produces higher quality LST than AVHRR due to its up to date algorithm. Additionally, the lack of available metadata layers in the AVHRR LST product (time of acquisition, satellite view zenith and azimuth angle, quality flags) introduced difficulties in the use and interpretation of the data. However, ignoring some temporal and spatial variations, and considering the whole set of available data, the AVHRR LST does compare well with the MODIS LST with an overall MAD of 1.9 K.

**Acknowledgements** The authors thank P. Seifert, P. Tungalagsaikhan, K. Günther, T. Ruppert and W. Ebke from DLR for the valuable comments and support of the study.

## References

- Batra N, Islam S, Venturini V, Bisht G, Jiang L (2006) Estimation and comparison of evapotranspiration from MODIS and AVHRR sensors for clear sky days over the Southern Great Plains. *Remote Sens Environ* 103:1–15
- Becker F, Li ZL (1990) Towards a local split window method over land surfaces. *Int J Remote Sens* 11:369–393
- Coll C, Caselles V, Galve JM, Valor E, Niclòs R, Sánchez JM, Rivas R (2005) Ground measurements for the validation of land surface temperatures derived from AATSR and MODIS data. *Remote Sens Environ* 97:288–300
- Dech SW, Tungalagsaikhan P, Preusser C, Meissner RE (1998) Operational value-adding to AVHRR data over Europe: methods, results, and prospects. *Aerospace Sci Technol* 2:335–346
- Frey CM, Parlow E, Vogt R, Abdel Wahab M, Harhash M (2011) Flux measurements in Cairo. Part 1: In situ measurements and their applicability for comparison with satellite data. *Int J Climatol* 31:218–231
- GCOS (2010) Implementation plan for the global observing system for climate in support of the UNFCCC (2010 update). WMO, Intergovernmental Oceanographic Commission. <http://www.wmo.int/pages/prog/gcos/Publications/gcos-138.pdf>. Accessed 8 Dec 2011
- Gesell G (1989) An algorithm for snow and ice detection using AVHRR data: an extension to the APOLLO software package. *Int J Remote Sens* 10:897–905

- GMES Sentinel-3 MRD (2007) Sentinel-3: Mission Requirements Document, V2.0, ESA. [http://esamultimedia.esa.int/docs/GMES/GMES\\_Sentinel3\\_MRД\\_V2.0\\_update.pdf](http://esamultimedia.esa.int/docs/GMES/GMES_Sentinel3_MRД_V2.0_update.pdf). Accessed 9 Dec 2011
- Holben BN (1986) Characteristics of maximum-value composite images from temporal AVHRR data. *Int J Remote Sens* 7:1417–1434
- Hulley GC, Hook SJ (2009) Intercomparison of versions 4, 4.1 and 5 of the MODIS land surface temperature and emissivity products and validation with laboratory measurements of sand samples from the Namib desert, Namibia. *Remote Sens Environ* 113:1313–1318
- Kabsch E, Olesen FS, Prata F (2008) Initial results of the land surface temperature (LST) validation with the Evora, Portugal ground-truth station measurements. *Int J Remote Sens* 29:5329–5345
- Liu Y, Yamaguchi Y, Ke C (2007) Reducing the discrepancy between ASTER and MODIS land surface temperature products. *Sensors* 7:3043–3057
- Liu Y, Noumi Y, Yamaguchi Y (2009) Discrepancy between ASTER- and MODIS- derived land surface temperatures: terrain effects. *Sensors* 9:1054–1066
- NCDC LST-Workshop Summary (2008) International workshop on the retrieval and use of land surface temperature: bridging the gaps. Summary report. [http://rain.atmos.colostate.edu/GRP/reports/NCDC-LSTWorkshopReport\\_final.pdf](http://rain.atmos.colostate.edu/GRP/reports/NCDC-LSTWorkshopReport_final.pdf). Accessed 9 Dec 2011
- Noyes E, Good S, Corlet G, Kong X, Remedios J, Llewellyn-Jones D (2006) AATSR LST product validation. In: Proceedings of the second working meeting on MERIS and AATSR calibration and geophysical validation, 20–24 Mar 2006, ESRIN, Frascati, Italy
- Pozo Vázques D, Olmo Reyes FJ, Alados Arboledas L (1997) A comparative study of algorithms for estimating land surface temperature from AVHRR data. *Remote Sens Environ* 62:215–222
- Saunders RW, Kriebel KT (1988) An improved method for detecting clear-sky and cloudy radiances from AVHRR-data. *Int J Remote Sens* 9:123–150
- Snyder W, Wan Z (1998) BRDF models to predict spectral reflectance and emissivity in the thermal infrared. *IEEE Trans Geosci Remote Sens* 36:214–225
- Triebel KT, Gesell G, Kästner M, Mannstein H (2003) The cloud analysis tool APOLLO: improvements and validations. *Int J Remote Sens* 24:2389–2408
- Trishchenko AP, Li Z (2001) A method for the correction of AVHRR onboard IR calibration in the event of short-term radiative contamination. *Int J Remote Sens* 22:3619–3624
- Tungalagsaikhan P, Meissner RE, Dech SW (1998) Operational generation of AVHRR-based land surface temperatures (LST) – a new values adding product from the German Remote Sensing Data Center. In: Proceedings of the 1998 International Geoscience and Remote Sensing Symposium IGARSS'98, vol 4, 6–10 July, Seattle, WA, USA, pp 2116–2118
- van de Griess AA, Owe M (1992) On the relationship between thermal emissivity and the normalized difference vegetation index for natural surfaces. *Int J Remote Sens* 14(6):1119–1131
- Wan Z (2008) New refinements and validation of the MODIS land-surface temperature/emissivity products. *Remote Sens Environ* 112:59–74
- Wan Z, Dozier J (1996) A generalized split-window algorithm for retrieving land-surface temperature from space. *IEEE Trans Geosci Remote Sens* 34:892–905
- Wan Z, Zhang Y, Zhang Q, Li ZL (2002) Validation of the land-surface temperature products retrieved from Terra Moderate Resolution Imaging Spectroradiometer data. *Remote Sens Environ* 83:163–180
- Yang H, Yang Z (2006) A modified land surface temperature split window retrieval algorithm and its applications over China. *Glob Planet Chang* 52:207–215
- Zhong L, Yaoming MA, Zhongbo SU, Salama MS (2010) Estimation of land surface temperature over the Tibetan Plateau using AVHRR and MODIS data. *Adv Atmos Sci* 27:1110–1118
- URL1: WMO-GCOS (World Meteorological Organization – Global Climate Observing System) World Meteorological Organization <http://www.wmo.int/pages/prog/gcos/index.php?name=EssentialClimateVariables>

URL2: NASA, Goddard Space Flight Center, MODIS land team, Validation <http://landval.gsfc.nasa.gov/ProductStatus.php?ProductID=MOD11>

URL3: CGIAR-CSI GeoPortal (Consultative Group on International Agricultural Research – Consortium for Spatial Information) <http://srtm.csi.cgiar.org>

# Chapter 12

## Comparison of the Thermal Sensors of SEVIRI and MODIS for LST Mapping

Caixia Gao, Xiaoguang Jiang, Zhao-Liang Li, and Françoise Nerry

**Abstract** This study aims to evaluate quantitatively the land surface temperature (LST) from SEVIRI data (Spinning Enhanced Visible and Infrared Imager, onboard MSG-2 satellite) with the MODIS (Moderate Resolution Imaging Spectroradiometer, onboard Terra)-derived LST extracted from the MOD11B1 V5 product. Two SEVIRI-derived LST level-2 products are used for this purpose: the LSTs retrieved using the generalised split-window method with the emissivities estimated using the day/night TISI (Temperature Independent Spectral Indices)-based method and the LSTs generated by the Land Surface Analysis of the Satellite Application Facility. The results show that (1) higher discrepancies are observed during the daytime, especially for bare areas, with a maximum of 5.7 K; (2) these differences are time- and land cover-dependent; (3) these differences strongly depend on the view zenith angle differences; and (4) the two LST retrieval algorithms for SEVIRI present the higher discrepancy for bare areas, with a maximum difference of 6.1 K.

---

C. Gao

College of Resources and Environment, Graduate University of Chinese Academy of Sciences,  
Beijing 100049, China

Image Sciences, Computer Sciences and Remote Sensing Laboratory (LSIIT), UdS,  
CNRS, Bld Sébastien Brant, BP 10413, 67412 Illkirch, France

X. Jiang

College of Resources and Environment, Graduate University of Chinese Academy of Sciences,  
Beijing 100049, China

Z.-L. Li (✉)

Engineering, Computing and Imaging Laboratory (ICube), UdS,  
CNRS, Bld Sébastien Brant, BP 10413, 67412 Illkirch, France

Key Laboratory of Resources and Environment Information System, Institute of Geographic  
Science and Natural Resources Research, CAS, Beijing, China  
e-mail: [lizl@unistra.fr](mailto:lizl@unistra.fr)

F. Nerry

Engineering, Computing and Imaging Laboratory (ICube), UdS,  
CNRS, Bld Sébastien Brant, BP 10413, 67412 Illkirch, France

## 12.1 Introduction

Land surface temperature (LST) is one of the key parameters in the physics of land surface processes, combining the results of surface-atmosphere interactions and the energy fluxes between them (Mannstein 1987; Sellers et al. 1988). It can be used to improve the understanding of the quantifications of the surface fluxes and water availability, to aid resource management and to improve numerical weather forecasts (Sun 2008). Therefore, acquiring LST over large spatial and temporal scales is crucial. Remote sensing is a unique way of providing LST measurements globally at different spatial and temporal resolutions. Compared with microwave-based LST retrievals, thermal infrared (TIR)-based retrievals are more accurate because of the lower variation of land surface emissivity (LSE) in the TIR and the stronger dependence of the radiance on temperature (Sun 2008). In the last two decades, various methods have been published in the open literature to estimate LST from TIR data with the goal of reaching an accuracy better than 1 K, such as the single-channel method (Price 1983; Ottlé and Vidal-Madjar 1992; Qin et al. 2001; Jiménez-Muñoz and Sobrino 2003), the split-window (SW) method (Price 1984; Becker and Li 1990a; Kerr et al. 1992; Prata 1993; Coll et al. 1994; Sobrino et al. 1994; Wan and Dozier 1996; Jiang and Li 2008, among others) and the multi-angle method (Sobrino et al. 1996).

The single-channel method was developed to retrieve LST from the radiance measured in a single atmospheric window channel, and it requires good knowledge of LSE and accurate atmospheric profiles. Because accurate atmospheric profiles are not available with sufficient spatial density or at the time of the passage of the satellite, the split-window method was developed to correct atmospheric effects based on the different absorptions in the two adjacent channels, without the knowledge of detailed atmospheric profiles. The split-window method was first proposed by McMillin (1975) to determine the sea surface temperature and was extended to LST retrieval from space (Price 1984). Since then, a variety of split-window algorithms have been developed and improved to retrieve LST with some success from space instruments, such as MODIS (Moderate Resolution Imaging Spectroradiometer), AVHRR (Advanced Very High Resolution Radiometer) and SEVIRI (Spinning Enhanced Visible and Infrared Imager). The multi-angle method is based on a principle similar to the split-window method but uses different absorptions resulting from different atmospheric path-lengths for different observation angles. This method, however, assumes that LST is angular independent.

The MODIS onboard Terra and Aqua marks a new era of remote sensing. It captures data in 36 spectral bands, ranging in wavelength from 0.4 to 14.4  $\mu\text{m}$ , at varying spatial resolutions. Its daily LST products are generated on a global scale by NASA's Terra and Aqua Earth Observation System and have been used in various studies (Mostovoy et al. 2006; Nagler et al. 2005; Sun et al. 2005; Tran 2006; Wan et al. 2004; Wang et al. 2006). Because this satellite has a polar orbit, these data do not provide information about the diurnal cycle. The MSG (Meteosat Second Generation) satellite, which represents the new generation of geostationary meteorological

satellites, was developed by the European Space Agency (ESA) in close co-operation with the European Organisation for the Exploitation of Meteorological Satellites (EUMETSAT). Its main payload – SEVIRI – provides image data in four visible and near infrared (VNIR) channels and eight TIR channels every 15 min, thus offering the possibility to provide more frequent LST to study the diurnal LST cycle and to improve the forecasting of natural hazards, such as extreme temperatures. Therefore, many studies have been performed on LST retrieval from SEVIRI data. Sobrino and Romaguera (2004) and Atitar et al. (2008) retrieved LST using the split-window method proposed by Sobrino et al. (1996) from MSG-1/SEVIRI and MSG-2/SEVIRI data, respectively. Jiang and Li (2008) retrieved LST from MSG-1/SEVIRI data using the method proposed by Becker and Li (1990a) and improved by Wan and Doizer (1996). Peres et al. (2010) also estimated LST from MSG/SEVIRI over Brazil using emissivity maps derived from MODIS data. Due to the differences in retrieval algorithms and input data, however, inconsistencies among the LST products from different sensors – even from the same sensor – could occur, which restricts the widespread applications of LST products. Therefore, this study aims to evaluate LST retrieved from MSG-2/SEVIRI (denoted as SEVIRI LST1) and the LSTs extracted from MOD11B1 V5 product (denoted as MODIS LST). In addition, an operational MSG/SEVIRI LST product (denoted as SEVIRI LST2) generated by the Land Surface Analysis of Satellite Application Facility (LSA SAF) is compared with MODIS derived-LST used as a reference.

This chapter is organised as follows. Section 12.2 describes the study area. Section 12.3 presents the LST retrieval methods for the three LST products mentioned above. Section 12.4 describes the evaluation procedure. Section 12.5 provides the results of the inter-comparison of different LST products generated from different satellite data or from the same satellite data using different algorithms. The conclusions are given in the last section.

## 12.2 Study Area

In terms of surface types, a study area, mainly encompassing the Iberian Peninsula and part of the Maghreb, was selected, with geospatial coverage of latitude 30°N–45°N and longitude 15°W–15°E. The Iberian Peninsula is located in Western Europe and includes Portugal and Spain, with an area of approximately 580,000 km<sup>2</sup>. It is divided into two macro-bioclimatic areas: the Temperate zone, mainly in the north, and the Mediterranean zone, occupying a large area of the centre and south of the peninsula (Gomes 2007). The Iberian Peninsula is dominated by traditional and newly developed agriculture (approximately 49 %) embedded in a matrix of natural and semi-natural vegetation (approximately 47 %) (Del Barrio et al. 2010). The Maghreb, a region in North Africa that includes Morocco, Algeria and Tunisia, is divided into a Mediterranean climate region in the north and the arid Sahara to the south. Its variations in elevation, rainfall, temperature, and soil type give rise to distinct communities of plants and animals.

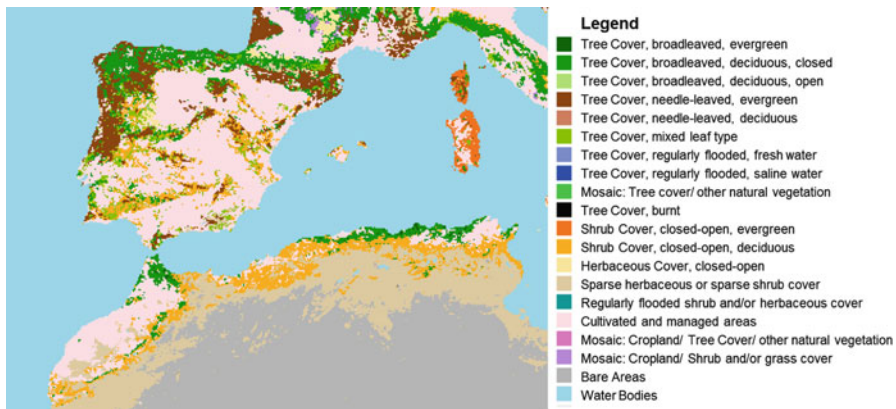


**Fig. 12.1** Land cover map of the study area generated from the Global Land Cover 2000 ([URL 2](#))

As displayed in the land use/land cover (LULC) map (see Fig. 12.1) generated from the global land cover 2000 produced by the Institute for Environment and Sustainability (IES), the study area in Maghreb is mainly dominated by shrub cover (approximately 9 %), herbaceous cover (approximately 26 %) and bare areas (approximately 52 %).

According to the MOD11B1 sinusoidal grid ([URL 1](#)), the study area is covered with the tiles h17v04, h17v05, h18v04 and h18v05. The study period comprises five clear-sky days covering March 2008 to August 2009. Because of the long period of cloud contamination over the study area, the data during the winter season are not included in this study.

## 12.3 Sensor Characteristics and LST Retrieval Methods

### 12.3.1 Sensor Characteristics

MSG is a series of four geostationary satellites, with the latest satellite, MSG-2, launched in December 2005. Its main payload, SEVIRI, observes an Earth disk with a view zenith angle (VZA) ranging from 0 to 80° and a 3-km nadir spatial resolution. The instrument provides data in 12 spectral bands every 15 min. The spectral responses for SEVIRI channels 4, 7, 9 and 10 are shown in Fig. 12.2.

Launched in 1999, MODIS onboard Terra scans  $\pm 55^\circ$  from the nadir in 36 spectral bands, with 16 thermal bands from 3 to 15  $\mu\text{m}$ . It is designed to provide long-term global observation every 1–2 days. The TIR bands have an instantaneous field of view of approximately 1 km at the nadir. In addition, MODIS has an onboard calibrator, and the sensor is assumed to be well calibrated with an accuracy of approximately 1 % for the TIR bands. The calibration for the surface temperature bands ranges up to 0.75 %

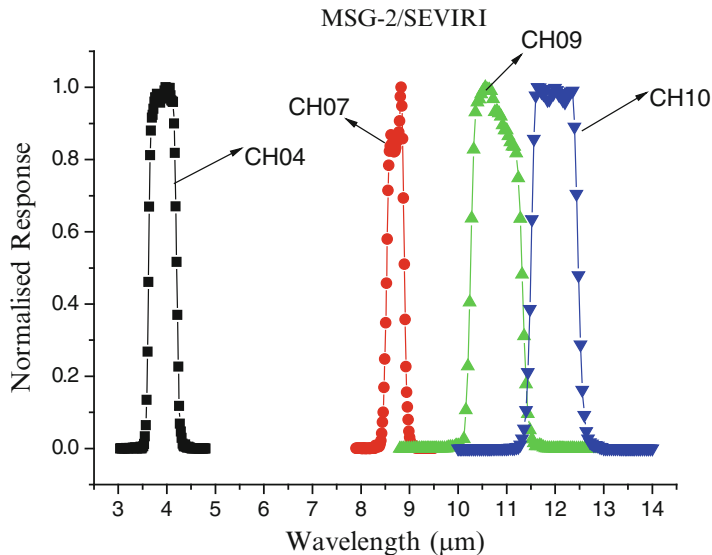


**Fig. 12.2** Normalised spectral response function for MSG-2/SEVIRI channels 4, 7, 9 and 10

(band 20) and 0.5 % (bands 31 and 32) (Guenther et al. 1995). Specifically, TIR bands 20, 22, 23, 29, and 31–33 are used to correct for atmospheric effects and retrieve LSE and LST. Their spectral responses are presented in Fig. 12.3.

### 12.3.2 LST Retrieval Methods

#### 12.3.2.1 Retrieval Method for SEVIRI LST1

In this study, the generalised split-window (GSW) method with a similar formulation to those proposed by Becker and Li (1990a) and improved by Wan and Dozier (1996) is used to retrieve LST from the SEVIRI data. According to the GSW method, the LST for clear skies can be expressed as:

$$\begin{aligned} LST = & \left( A_1 + A_2 \frac{1 - \varepsilon}{\varepsilon} + A_3 \frac{\Delta\varepsilon}{\varepsilon} \right) \frac{T_9 + T_{10}}{2} \\ & + \left( B_1 + B_2 \frac{1 - \varepsilon}{\varepsilon} + B_3 \frac{\Delta\varepsilon}{\varepsilon} \right) \frac{T_9 - T_{10}}{2} + C \end{aligned} \quad (12.1)$$

where  $T_9$  and  $T_{10}$  are the brightness temperatures at the top of atmosphere (TOA) in SEVIRI channels 9 (10.8  $\mu\text{m}$ ) and 10 (12.0  $\mu\text{m}$ ), respectively;  $\varepsilon$  and  $\Delta\varepsilon$  are the averaged emissivity and emissivity difference of these two channels; and  $A_1, A_2, A_3, B_1, B_2, B_3$ , and  $C$  are unknown coefficients that need to be pre-determined for a

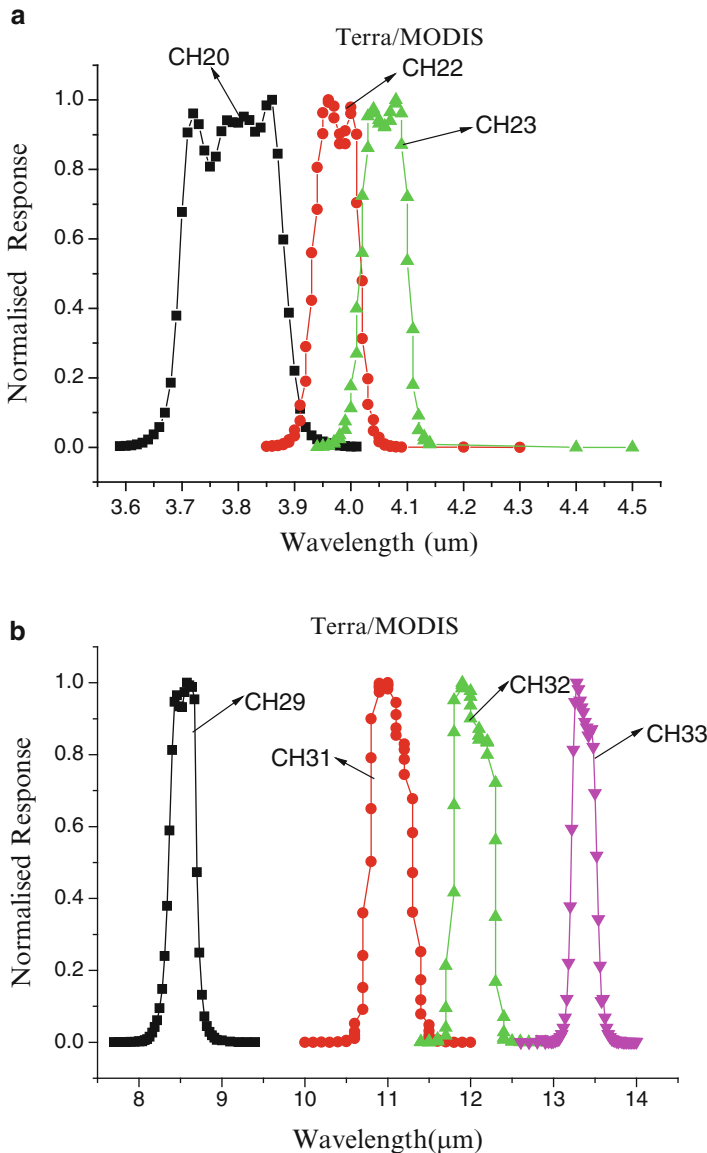


**Fig. 12.3** (a) Normalised spectral response function for MODIS bands 20, 22 and 23 (b) Normalised spectral response function for MODIS bands 29 and 31–33

given VZA and a given sub-range of atmospheric water vapour content (WVC),  $\varepsilon$  and LST.

To determine the coefficients  $A_1$ ,  $A_2$ ,  $A_3$ ,  $B_1$ ,  $B_2$ ,  $B_3$ , and  $C$ , simulations are performed with the aid of the atmospheric radiative transfer model MODTRAN 4.0 (MODerate resolution atmospheric TRANsmision) and the thermodynamic initial

guess retrieval (TIGR) dataset (denoted as TIGR2000) built by the laboratoire de météorologie dynamique (LMD), which represents a worldwide set of atmospheric situations (2311 radiosoundings) from polar to tropical atmospheres. Combined with the clear-sky atmospheric profiles extracted from TIGR2000, various surface conditions (different LSTs and LSEs) are used to drive MODTRAN 4.0 to simulate TOA radiances or brightness temperatures under various atmospheric conditions for each VZA (from  $0^\circ$  to  $67^\circ$ ). Furthermore, for each VZA, to improve LST retrieval accuracy, the WVC,  $\epsilon$  and LST are divided into several sub-ranges with a partial overlap at two extremes of each sub-range, i.e.,  $\epsilon$ : 0.90–0.96 and 0.94–1.0; WVC: 0–1.5, 1.0–2.5, 2.0–3.5, 3.0–4.5, 4.0–5.5 and 5.0–6.5 g/cm<sup>2</sup>; LST:  $\leq$ 280.0 K, 275–295 K, 290–310 K, 305–325 K, and  $\geq$ 320 K. For each sub-range, the unknown coefficients  $A_i$ ,  $B_i$  ( $i = 1, 3$ ) and  $C$  are constant and can be determined by the minimisation procedure with these simulated data. In practice, LST is estimated in two steps. First, the approximate LST is estimated with the coefficients for the whole LST range, and then a more accurate LST is determined with the coefficients for the LST sub-range in which the approximate LST has fallen. The results show that the root mean square errors (RMSEs) of the retrieved LSTs vary with the VZA and the atmospheric WVC and that the RMSEs are within 1.0 K for all sub-ranges in which  $VZA \leq 30^\circ$  and  $WVC < 4.25$  g/cm<sup>2</sup>.

For LSE determination, the day/night temperature-independent spectral indices (TISI)-based method proposed by Becker and Li (1990b) is used in consideration of the multi-spectral characteristics (see Fig. 12.2) and the high temporal resolution of SEVIRI (15 min). The principle of the TISI-based method is to first extract the bi-directional reflectivity in the MIR (middle infrared) channel by eliminating the emitted radiance during the day using a particular inter-comparison between day and night TISI. As SEVIRI provides image data every 15 min, various bi-directional reflectivities in MIR with different solar illuminated directions are estimated. Subsequently, the directional emissivity in the MIR channel can be estimated as a complement to the hemispheric-directional reflectivity, which is the integration of bi-directional reflectivities in the MIR channel described by the RossThick-LiSparse-R model (Lucht and Roujean 2000). Finally, with respect to the concept of TISI, the directional emissivities for the TIR channels are obtained from the two-channel TISIs and directional emissivity in the MIR channel. More details about this method can be found in Li et al. (2000), Jiang et al. (2006), and Tang et al. (2009).

It is worth noting that the atmospheric corrections need to be performed for the SEVIRI MIR and TIR channels to construct the TISI. In this study, the atmospheric profiles at a spatial resolution of  $0.25^\circ/0.25^\circ$  latitude/longitude provided by the European Centre for Median-Range Weather Forecasts (ECMWF) are employed to correct for the atmospheric effects of the SEVIRI MIR and TIR images at synoptic times (00:00; 06:00; 12:00; 18:00) with the aid of MODTRAN 4.0. Because of the lack of corresponding atmospheric profiles for the other SEVIRI data, time-nearest atmospheric data are used to correct for the atmospheric effects for the images in the MIR channel due to its reduced sensitivity to WVC. For the images in TIR channels, a two-part, physics-based temperature diurnal cycle model with six

unknown parameters (Göttsche and Olesen 2001) is used to obtain the atmospherically corrected radiance at the times other than the synoptic times. Spatially, a bilinear interpolation method is used to estimate the atmospheric quantities for each SEVIRI pixel (Jiang et al. 2006).

In addition to the LSE determination, atmospheric WVC is required in GSW method. However, as atmospheric WVC is only used to select the optimal coefficients  $A_1, A_2, A_3, B_1, B_2, B_3$ , and  $C$  in the GSW method, accurate WVC is not required as long as the estimated WVC is within the same range as the actual WVC. The method proposed by Li et al. (2003) is used to estimate the WVC at the spatial resolution of several pixels from the SEVIRI measurements of channels 9 and 10. If this method fails (the square of the correlation coefficient is less than 0.95), the WVCs provided by the ECMWF data are used to obtain the WVC corresponding to the relevant pixel by a temporal and spatial linear interpolation.

### 12.3.2.2 Retrieval Method for SEVIRI LST2

The SEVIRI LST generated by the LSA SAF is based on a GSW method with a similar formulation as Eq. (12.1) ([URL 3](#)). In this method, the brightness temperatures were simulated with MODTRAN 4.0 to obtain the algorithm coefficients. The atmospheric database was composed of 77 atmosphere profiles to cover a broad variety of WVC. Several simulations were performed for each profile with different surface emissivities, VZAs and LSTs. LST varied from  $T_o - 15 \text{ K}$  to  $T_o + 15 \text{ K}$  ( $T_o$  being the air temperature at the first layer of atmosphere), and emissivity values  $\epsilon$  from 0.94 to 1.0 and  $\Delta\epsilon$  from  $-0.0135$  to  $0.022$  were initially used, and then  $0.96 < \epsilon_{10} < 0.995$  (LSE in channel 10 of SEVIRI) and  $\epsilon_{10}-0.030 < \epsilon_9 < \epsilon_{10} + 0.018$  (LSE in channel 9 of SEVIRI) were considered. WVC is divided into eight sub-ranges ( $0.0-0.75, 0.75-1.5, 1.5-2.25, 2.25-3.0, 3.0-3.75, 3.75-4.5, 4.5-5.25$ , and  $5.25-6.0 \text{ g/cm}^2$ ) for each VZA (total of 11 VZAs, up to  $75^\circ$ ), and the coefficients  $A_1, A_2, A_3, B_1, B_2, B_3$ , and  $C$  for a given VZA and a given sub-range of WVC are obtained by regression of the LSTs with the simulated brightness temperatures (Freitas et al. 2010).

In addition, the WVC which is required to select the most suitable coefficients of the GSW is obtained from the ECMWF data. The LSEs are estimated with the vegetation cover method (VCM) published by Caselles and Sobrino in 1989 and Peres and DaCameara in 2005. This method produces effective LSEs using information on the proportion of vegetation and exposed surfaces with the knowledge of the LSEs for each component, vegetation and bare soil.

### 12.3.2.3 Retrieval Method for the MODIS LST

Considering the spatial resolution of SEVIRI (3 km at nadir), the daily LSTs at the spatial resolution of 5 km stored in the MOD11B1 product are used to evaluate the SEVIRILST in this study. MOD11B1 product is tile-based, gridded in the sinusoidal

projected LST product and constructed with the results produced by the day/night LST method from the pairs of day- and nighttime observations in seven MODIS TIR bands (bands 20, 22, 23, 29, and 31–33, whose spectral characteristics are shown in Fig. 12.3) (Wan and Li 1997). Some refinements were made in the latest V5 MOD11B1 LST product to provide more high-quality LST data. This LST product has been validated through field campaigns in 47 clear-sky cases, indicating that its accuracy is better than 1 K in most cases (Wan 2008a). Because the split-window algorithm provides initial LST values for the LST retrieval in the V5 of day/night algorithm, large errors in the LSTs retrieved by the split-window algorithm in desert regions also affect the final LST retrieved by the day/night algorithm (Wan 2008b).

In addition to LST, information on LSE, VZA, view time, and quality control (QC) is included in this product. They are the key input parameters for the LST comparison.

## 12.4 Data Processing and Comparison Method

Because LST strongly varies over space and time, the LST inter-comparison between different sensors must be conducted on the same sites and within time period as short as possible. Taking into account the facts that the SEVIRI provides LSTs every 15 min, and the SEVIRI measurements closest in view time to MODIS are eligible for this inter-comparison, therefore, in this study, only pixels with view time differences less than 7.5 min (15/2 min) between two LST products are considered for the inter-comparison. For the MOD11B1 LST product, the view time (local solar time) of each pixel is stored, and it can be extracted from the product file, while the view time in UTC for the SEVIRI data is given in the file name.

As two LST products have different spatial resolutions, to inter-compare these two products, they must be aggregated to the same spatial resolution using the area-weighted pixel aggregation algorithm (Jiang 2007) based on the following equation:

$$R_i = \sum_{j=1}^N w_{j,i} R_j / \sum_{j=1}^N w_{j,i} \text{ with } w_{j,i} = S_{j,i} / S_j \quad (12.2)$$

where  $R_i$  is the aggregated radiance of a target pixel  $i$ ,  $N$  is the total number of pixels  $j$  within the aggregated pixel  $i$ ,  $w_{j,i}$  is the weight of pixel  $j$  in the aggregated pixel  $i$ ,  $S_{j,i}$  is the area of the overlapping region between pixels  $i$  and  $j$ ,  $S_j$  is the total area of pixel  $j$ , and  $R_j$  is the radiance of the pixel  $j$ .

Coordinates derived from the product generally represent the pixel centroid location of each pixel. The coordinates of the four corners of a pixel are easily

calculated using the centroid coordinates of the neighbouring pixels. In this study, the SEVIRI LST products are aggregated to the same spatial resolution as the MODIS B1 V5 LST product.

Other considerations are taken into account in the inter-comparison procedure, such as the VZA restriction. In our study area, the SEVIRI sun-satellite viewing geometry leads mostly to sunlit observed scenes, while for MODIS onboard the polar satellite, its sun-satellite viewing geometry can result in some fraction of shadow surfaces being observed. To reduce the observed LST difference resulting from the effect of shadow surfaces, only pixels with MODIS VZAs less than 30° are considered in the following analysis. In addition, according to the QC criteria, only the MODIS LST pixels with a value of 0 in the QC bit flags, which indicates good quality and cloud-free, are used in this study. Respecting these considerations, spatially aggregated SEVIRI-derived LST products will be compared with time coincidentally MODIS-derived LST products (within a 7.5 min time frame). To quantify the discrepancies of the LST products derived from the SEVIRI and MODIS data, mean differences (MDs), mean absolute differences (MADs), along with standard deviations of the differences (SDs), are calculated as quantitative measures of these discrepancies:

$$MD_{LST} = \frac{1}{M} \sum_{i=1}^M (LST_{i,SEVIRI} - LST_{i,MODIS}) \quad (12.3)$$

$$MAD_{LST} = \frac{1}{M} \sum_{i=1}^M |LST_{i,SEVIRI} - LST_{i,MODIS}| \quad (12.4)$$

$$SD_{LST} = \sqrt{\frac{1}{M-1} \sum_{i=1}^M [(LST_{i,SEVIRI} - LST_{i,MODIS}) - MD_{LST}]^2} \quad (12.5)$$

where  $LST_{SEVIRI}$  and  $LST_{MODIS}$  are the SEVIRI-derived LST and MODIS derived-LST, respectively, and  $M$  is the number of pixels qualified for inter-comparison.

The workflow procedure for the LST inter-comparison is presented in Fig. 12.4. After data preparation, such as supplying the LST products, coordinates (latitudes and longitudes), view times, VZAs, QCs and land cover information for each pixel, the pixels with a view time difference less than 7.5 min are first selected. Considering the spatial relationship between the SEVIRI pixel and MODIS pixel, the derived SEVIRI radiance data are then aggregated into the MODIS spatial resolution in a sinusoidal grid projection with Eq. (12.2). Finally, in terms of the MODIS VZAs, QCs and land cover information, the inter-comparison between registered SEVIRI and MODIS LSTs is performed with qualified pixels meeting the conditions described above.

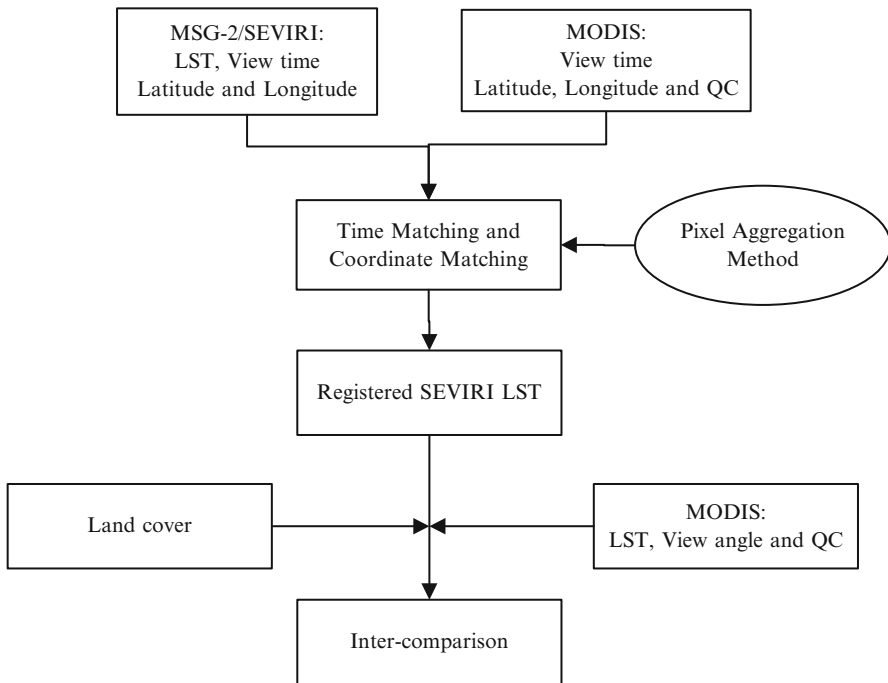


**Fig. 12.4** Procedure for the inter-comparison of LST products derived from SEVIRI and MODIS data

## 12.5 Comparison Results

### 12.5.1 *Inter-comparison Between SEVIRI LST<sub>1</sub> and MODIS LST*

The inter-comparison is first carried out between SEVIRI LST<sub>1</sub> and MODIS LST over the entire study area. Five pairs of cloud-free SEVIRI and MODIS data from 2008 to 2009 (June 18, 2008, July 3, 2008, August 9, 2008, May 2, 2009, and August 22, 2009) are collected and pre-processed. The statistics of this inter-comparison are summarised in Table 12.1, with the pixel number being the number of qualified pixels in this study. The MD<sub>LST</sub> between the SEVIRI LST<sub>1</sub> and MODIS LST ( $LST_{SEVIRI\ 1} - LST_{MODIS}$ ) varies from 0.93 to 3.43 K, the MAD<sub>LST</sub> varies from 1.36 to 3.52 K, and the SD<sub>LST</sub> varies from 1.22 to 2.48 K. Moreover, the SD<sub>LST</sub> during daytime is larger than that during nighttime. This result could be explained by the relatively homogeneous thermal behaviour of the Earth's surface at night, as indicated by the standard deviation of MODIS LST in column 8 of Table 12.1.

**Table 12.1** Means, absolute means and standard deviations of temperature differences in Kelvin between the SEVIRI LST1 and MODIS LST over the study area

Date	Day/Night	Pixel number	LST <sub>SEVIRI 1</sub> – LST <sub>MODIS</sub> (K)			LST <sub>MODIS</sub> (K)	
			MD <sub>LST</sub>	MAD <sub>LST</sub>	SD <sub>LST</sub>	Mean <sub>LST</sub>	Stdev <sub>LST</sub>
June 18, 2008	Day	16,366	1.63	2.30	2.48	313.16	7.65
	Night	12,440	1.73	1.86	1.55	291.44	3.67
July 3, 2008	Day	861	1.34	1.66	1.57	321.58	3.70
	Night	2,210	1.36	1.49	1.22	298.33	2.46
August 9, 2008	Day	9,011	3.43	3.52	1.61	321.74	3.89
	Night	5,803	2.06	2.11	1.17	298.96	4.05
May 2, 2009	Day	1,981	2.17	2.35	2.14	302.66	4.43
	Night	3,788	2.45	2.49	1.40	283.49	3.05
August 22, 2009	Day	4,168	2.12	2.56	2.60	314.66	7.01
	Night	5,323	0.93	1.36	1.54	294.72	3.62

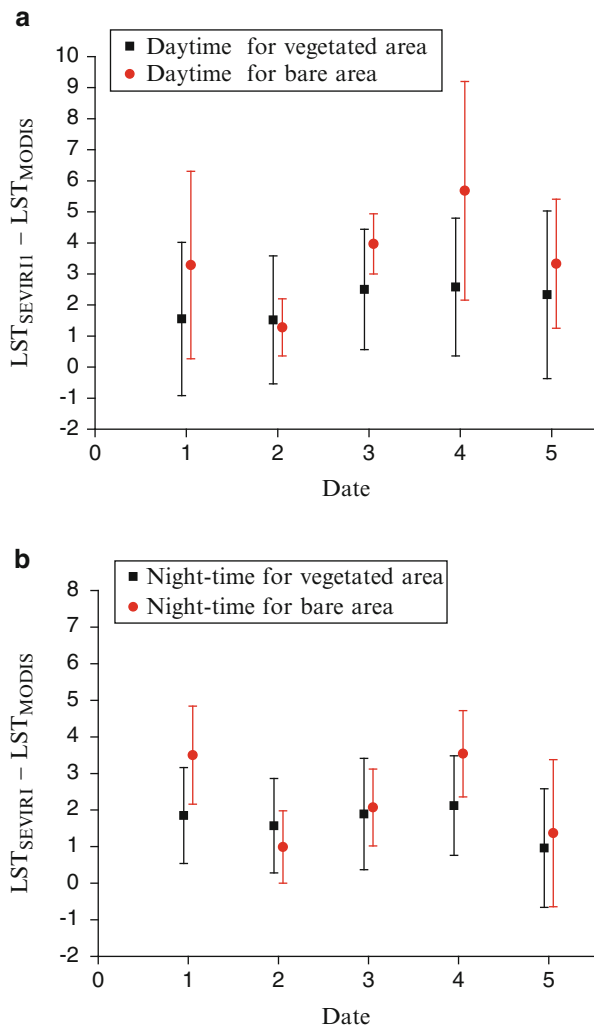
LST<sub>SEVIRI 1</sub> is the LST retrieved using the GSW algorithm, with LSE estimated using the TISI-based method and LST<sub>MODIS</sub> is the LST extracted from the V5 MOD11B1 product

To analyse the impact of local land cover on these calculated differences, the land cover in the study area is divided into bare areas and vegetated areas (<http://bioval.jrc.ec.europa.eu/products/glc2000>), and their MD<sub>LST</sub> and SD<sub>LST</sub> for these 5 days are shown in Fig. 12.5. The LST differences between two LST products appear to be correlated with land cover types, and bare soils show the higher LST discrepancies on average with a maximum of 5.8 K, particularly for daytimes. This can be explained that LSTs for bare soils during daytimes are higher and have a large spatial variation (as indicated in columns 7 and 8 of Table 12.1) due to the contribution of direct solar radiation.

To further investigate the land cover-dependence of LST differences for vegetated areas, according to the land cover map of the study area generated from the Global Land Cover 2000, the land surfaces in the study area were classified into five types, which are tree cover, shrub cover, herbaceous cover, cultivated and managed areas and bare areas. For these five different surface types, the MD<sub>LSTs</sub> and SD<sub>LSTs</sub> of the 5 days are displayed in Fig. 12.6. Surfaces dominated by a tree cover produce slightly higher MD<sub>LST</sub> than other vegetated surfaces during daytime, while the MD<sub>LST</sub> for herbaceous surfaces is slightly higher during nighttime. As for the SD<sub>LST</sub>, shrub areas show a particularly higher SD<sub>LST</sub> during daytime, exceeding 2.5 K, but there are almost no differences between different land cover types of vegetated surfaces during nighttime data acquisition.

The VZA mainly influences the estimated LST in two ways: (1) pixels with different VZAs contain different land surface components due to the three-dimensional structure of land surfaces, and (2) the intrinsic error of the LST retrieval methods is usually proportional to the VZA (Jiang and Li 2008). In order to investigate the impact of VZA differences on the LST differences between SEVIRI LST1 and MODIS, the VZA differences (|VZA<sub>SEVIRI</sub> – VZA<sub>MODIS</sub>|) were divided into three sub-ranges, which are 0°–20°, 20°–40° and 40°–60°. The MD<sub>LST</sub> and SD<sub>LST</sub> between these two products are displayed for each VZA sub-range in Fig. 12.7. It is

**Fig. 12.5** Means and standard deviations of temperature differences between SEVIRI LST and MODIS LST for vegetated areas and bare areas. The deviation bars are centred on the mean of the temperature difference (denoted by the symbols in the figure), and the half-length of the bar is equal to the standard deviation of the temperature difference. The X-axis scale, 1–5, represents the dates of June 18, 2008, July 3, 2008, August 9, 2008, May 2, 2009, and August 22, 2009, respectively. (a) In the daytime; (b) In the nighttime



worth noting that  $MD_{LST}$  depends on the VZA differences and is inversely proportional to the VZA differences. This may be explained by the fact that the MODIS views the surface with smaller view angles and observes more bare soil surfaces than the large view angles when the VZA differences between SEVIRI and MODIS increase as the VZA of SEVIRI for viewing the study areas is about  $45^\circ$ . In addition, due to the 3-dimensional structure of vegetation, higher MODIS LSTs are observed at the near nadir viewing than these at oblique viewing for daytime. However, as showed in Tables 12.1 and 12.2, compared with MODIS derived LSTs, SEVIRI derived LSTs are overestimated in this study, leading to lower LST differences when the VZA differences increase.

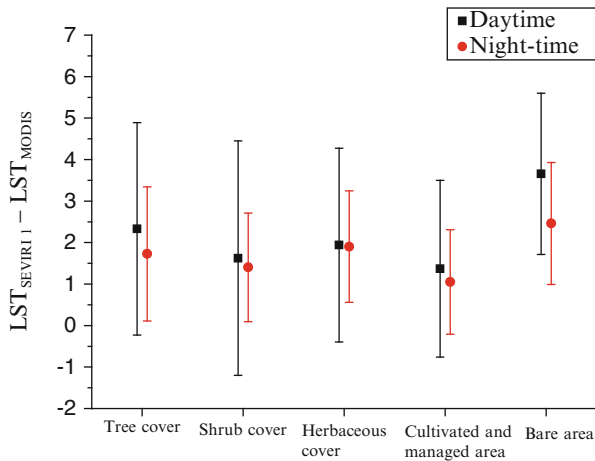


**Fig. 12.6** Means and standard deviations of temperature differences for the 5 days between the SEVIRI LST1 and MODIS LST for different land cover types. The mean differences and standard deviations are denoted as in Fig. 12.5

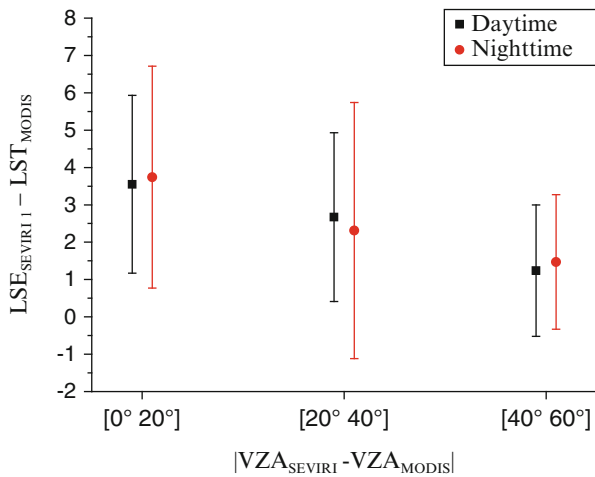


**Fig. 12.7** Means and standard deviations of temperature differences for the 5 days between the SEVIRI LST1 and MODIS LST for different VZA sub-ranges. Mean differences and standard deviations are denoted as in Fig. 12.5

### 12.5.2 Inter-comparison Between SEVIRI LST2 and MODIS LST

A similar inter-comparison is carried out for SEVIRI LST2 ( $LST_{SEVIRI\ 2}$ ) and MODIS LST ( $LST_{MODIS}$ ) over the entire study area, and results are summarised in Table 12.2. The mean LST differences ( $MD_{LST}$ ) are within 2.61 K, the mean

**Table 12.2** Means, absolute means and standard deviations of temperature differences between the SEVIRI LST2 and MODIS LST over the entire study area

Date	Day/Night	Pixel number	LST <sub>SEVIRI 2</sub> – LST <sub>MODIS</sub> (K)		
			MD <sub>LST</sub>	MAD <sub>LST</sub>	SD <sub>LST</sub>
June 18, 2008	Day	16,366	1.68	2.36	2.46
	Night	12,440	0.04	0.89	1.13
July 3, 2008	Day	861	2.12	2.46	2.01
	Night	2,210	0.34	0.75	0.91
August 9 2008	Day	9,011	2.48	2.56	1.33
	Night	5,803	0.38	0.63	0.80
May 2, 2009	Day	1,981	0.40	1.35	1.83
	Night	3,788	0.04	0.95	1.19
August 22, 2009	Day	4,168	2.61	2.72	1.65
	Night	5,323	0.26	0.86	1.14

LST<sub>SEVIRI 2</sub> is the SEVIRI LST provided by LSA-SAF, and LST<sub>MODIS</sub> is the LST extracted from the V5 MOD11B1 product

absolute differences (MAD<sub>LST</sub>) are within 2.72 K, and the standard deviations (SD<sub>LSTs</sub>) range from 0.80 to 2.5 K. In addition, the MD<sub>LST</sub> and SD<sub>LST</sub> during daytime are higher than those during nighttime.

Similar to Fig. 12.5, Fig. 12.8 shows the MD<sub>LST</sub> and SD<sub>LST</sub> of the vegetated and bare surfaces in the study area and presents similar behaviours to those in Fig. 12.5, i.e., bare areas generally produce higher LST discrepancies than vegetated areas.

As in Fig. 12.6, the MD<sub>LST</sub> and SD<sub>LST</sub> for the five surface types are shown in Fig. 12.9, but the results differ slightly from those shown in Fig. 12.6. The surfaces dominated by the herbaceous cover present higher MD<sub>LST</sub> than other vegetated areas. However, these discrepancies during daytime are also larger than those during nighttime.

Similar to Fig. 12.7, Fig. 12.10 displays the MD<sub>LST</sub> and SD<sub>LST</sub> between two products for each VZA sub-range and also indicates that MD<sub>LST</sub> decreases as the VZA differences increase.

### 12.5.3 Inter-comparison Between the Two LST Algorithms for SEVIRI LST1 and SEVIRI LST2

As described in Sect. 12.3.2, different algorithms are applied for the LST retrievals from the SEVIRI data. To examine how the LST difference results from the different GSW algorithms using the same input data, new LSTs (LST<sub>SEVIRI-Revised</sub>) are retrieved using Eq. (12.1) with the LSE provided by LAF-SAF, instead of those retrieved with the TISI-based method, and LST<sub>SEVIRI-Revised</sub> are compared with SEVIRI LST2 (LST<sub>SEVIRI 2</sub>). The MD<sub>LST</sub> and SD<sub>LST</sub> between LST<sub>SEVIRI-Revised</sub> and LST<sub>SEVIRI 2</sub> (LST<sub>SEVIRI-Revised</sub> – LST<sub>SEVIRI 2</sub>) for vegetated areas and bare areas are shown in Table 12.3. Different GSW algorithms result in a large difference of

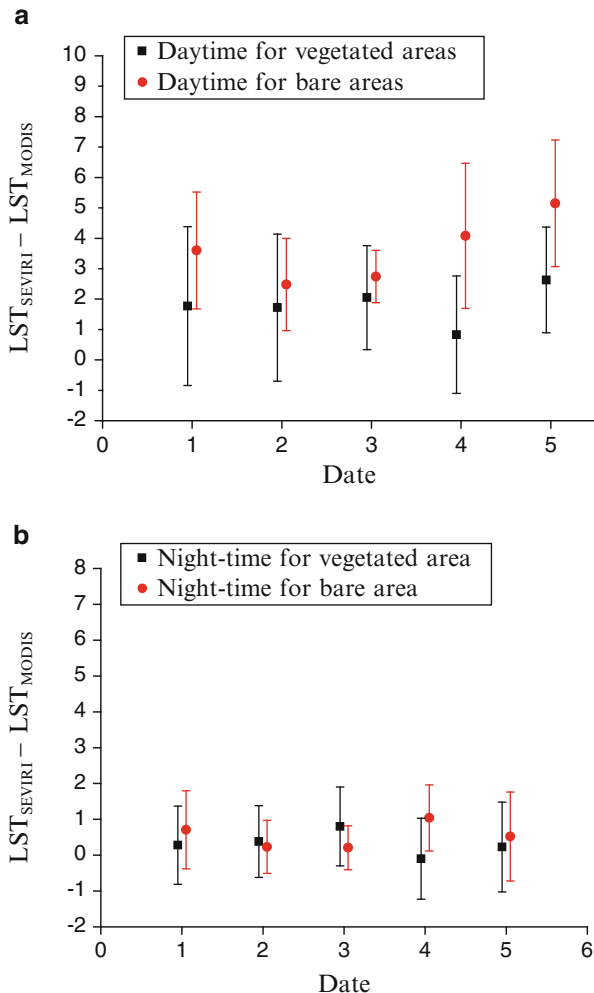


**Fig. 12.8** Same as Fig. 12.5, but for the inter-comparison of SEVIRI LST2 and MODIS LST

LST even though the same LSEs are used. For bare surfaces during daytime, the MD<sub>LST</sub> in the case of this study is  $-6.09\text{ K}$ . These results also demonstrate that the LST differences shown in Tables 12.1 and 12.2 are due to the combined effects of the different emissivity and different GSW algorithms used in the different LST products.

This analysis demonstrates that collected and calculated LST differences are algorithm-dependent, and mainly result from the accuracies of the applied LSEs and LST retrieval algorithms.

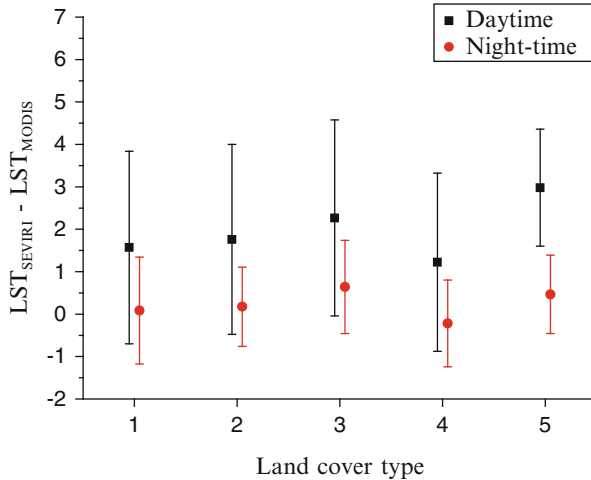


**Fig. 12.9** Same as Fig. 12.6, but for the inter-comparison of SEVIRI LST2 and MODIS LST

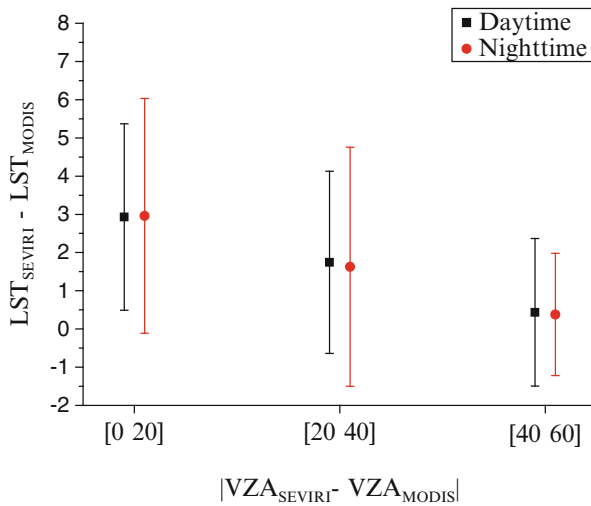


**Fig. 12.10** Same as Fig. 12.7, but for the inter-comparison of SEVIRI LST2 and MODIS LST

## 12.6 Conclusions

This study aims to evaluate SEVIRI LST quantitatively with MODIS LST. The study area encompasses the Iberian Peninsula and part of the Maghreb. After time matching and coordinate matching, on the basis of the VZAs and QC indicators of MODIS, two SEVIRI LST products (SEVIRI LST1 and SEVIRI LST2) are evaluated over the study area during five clear-sky days with MODIS LST used

**Table 12.3** Means and standard deviations of temperature differences between the SEVIRI LSTs derived using two different GSW algorithms and based on the same LSEs (LAF-SAF LSEs) for vegetated and bare areas

$LST_{SEVIRI\text{-Revised}} - LST_{SEVIRI\text{ 2}} (\text{K})$			
Vegetated areas		Bare areas	
	$MD_{LST}$	$SD_{LST}$	$MD_{LST}$
Daytime	-3.35	1.69	-6.09
Nighttime	-1.27	1.22	-3.58

$LST_{SEVIRI\text{-Revised}}$  is retrieved for the MSG-2/SEVIRI data using the LST retrieval method of SEVIRI LST1 with the LSE provided by LAF-SAF, and  $LST_{SEVIRI\text{ 2}}$  is the same as that in Table 12.2

as a reference. The results show that there are discrepancies between the two SEVIRI LST1/2 and MODIS LST, with a maximum mean difference of 3.43 K. The two inter-comparisons applied demonstrate that standard deviation during nighttime tend to be lower than ones obtained during daytime, which would be caused by the homogeneous thermal behaviour of the Earth's surface at night. The mean LST differences seem to be correlated with the land cover type, with the mean LST differences for bare surfaces being higher than those for vegetated areas. However, there are a few exceptions (the LST differences on July 3, 2008), which should be investigated further. In addition, the LST differences strongly depend on the VZA differences and are inversely proportional to the VZA differences.

The comparison of SEVIRI LST2 with LST retrieved from SEVIRI data using Eq. (12.1) with the same LSEs used in the SEVIRI LST2 shows that the mean LST difference can reach up to 6.09 K for bare surfaces in the daytime. This indicates that the different GSW algorithms can result in a large difference in the LST retrievals even though they use the same LSEs as inputs. Moreover, the LST differences between the different products observed in this study result mainly from the effects of the different emissivities and different GSW algorithms. To further investigate LST differences between these different products, more detailed analyses should be performed in the future to investigate these factors affecting the LST differences between SEVIRI LST1/2 and MODIS LST.

**Acknowledgements** The authors would like to thank Mr. N. Albalat at the University of Strasbourg for providing atmospheric data and Dr. Genming Jiang at Fudan University and Ms. Shi Qiu at the University of Strasbourg for their support in the LST retrieval activities. We also thank EUMETSAT for providing the MSG-2/SEVIRI data.

## References

- Atitar M, Sobrino JA, Soria G, Wigneron JP, Jimenes-Munoz JC, Julien Y, Belen Ruescas A (2008) Land surface temperature retrieval from SEVIRI/MSG2 data: algorithm and validation. EUMETSAT meteorological satellite conference, Darmstadt (Alemania), 8–12 Sept 2008  
 Becker F, Li ZL (1990a) Towards a local split window method over land surfaces. Int J Remote Sens 11:369–393

- Becker F, Li ZL (1990b) Temperature independent spectral indices in thermal infrared bands. *Remote Sens Environ* 32:17–33
- Caselles V, Sobrino JA (1989) Determination of frosts in orange groves from NOAA-9 AVHRR data. *Remote Sens Environ* 29:135–146
- Coll C, Caselles V, Sobrino JA, Valor E (1994) On the atmospheric dependence of the split-window equation for land surface temperature. *Int J Remote Sens* 15:105–122
- Del Barrio G, Puigdefabregas J, Sanjuan ME, Stellmes M, Ruiz A (2010) Assessment and monitoring of land condition in the Iberian Peninsula, 1989–2000. *Remote Sens Environ* 114:1817–1832
- Freitas SC, Trigo IF, Bioucas-Dias JM, Götsche FM (2010) Quantifying the uncertainty of land surface temperature retrievals from SEVIRI/Meteosat. *IEEE Trans Geosci Remote* 48:523–534
- Gomes JPRT (2007) Late-quaternary landscape dynamics in the Iberian Peninsula and Balearic Islands. Dissertation, University of Porto, Porto
- Götsche FM, Olesen FS (2001) Modeling of diurnal cycles of brightness temperature extracted from METEOSAT data. *Remote Sens Environ* 76:337–348
- Guenther B, Barnes W, Knight E, Barker F, Harnden J, Weber R, Roberto M, Godden G, Montgomery H, Abel P (1995) MODIS calibration: a brief review of the strategy for the at-launch calibration approach. *J Atmos Ocean Technol* 13:274–285
- Jiang GM (2007) Retrievals of land surface emissivity and land surface temperature from MSG1-SEVIRI data. Dissertation, University of Strasbourg, Strasbourg
- Jiang GM, Li ZL (2008) Split-window algorithm for land surface temperature estimation from MSG1-SEVIRI data. *Int J Remote Sens* 29:6067–6074
- Jiang GM, Li ZL, Nerry F (2006) Land surface emissivity retrieval from combined mid-infrared and thermal infrared data of MSG-SEVIRI. *Remote Sens Environ* 105:326–340
- Jiménez-Muñoz JC, Sobrino JA (2003) A generalized single-channel method for retrieving land surface temperature from remote sensing data. *J Geophys Res* 108:4688–4697. doi:[10.1029/2003JD003480](https://doi.org/10.1029/2003JD003480)
- Kerr YH, Lagourde JP, Imbernon J (1992) Accurate land surface temperature retrieval from AVHRR data with the use of an improved split-window algorithm. *Remote Sens Environ* 41:197–209
- Li ZL, Petelin F, Zhang RH (2000) A physically based algorithm for land surface emissivity retrieval from combined mid-infrared and thermal infrared data. *Sci China Ser E* 43:22–33
- Li ZL, Jia L, Su ZB, Wan Z, Zhang RH (2003) A new approach for retrieving precipitable water from ATSR2 split-window channel data over land area. *Int J Remote Sens* 24:5059–5117
- Lucht W, Roujeau JL (2000) Considerations in the parametric modeling of BRDF and albedo from multiangular satellite sensor observations. *Remote Sens Environ* 18:343–379
- Mannstein H (1987) Surface energy budget, surface temperature, and thermal inertia. In: Vaughan RA, Reidel D (eds) *Remote sensing applications in meteorology and climatology*, vol 201, NATO AS1 series C: math and physical science. A Reidel Publishing Co., Dordrecht, pp 391–410
- McMillin LM (1975) Estimation of sea surface temperature from two infrared window measurements with different absorptions. *J Geophys Res* 20:5113–5117
- Mostovoy GV, Filippova MG, King RL, Reddy KR, Kakani VG (2006) Statistical estimation of daily maximum and minimum air temperatures from MODIS LST data over the state of Mississippi. *Gisci Remote Sens* 43:78–110
- Nagler PL, Cleverly J, Glenn E, Lampkin D, Huete A, Wan Z (2005) Predicting riparian evapotranspiration from MODIS vegetation indices and meteorological data. *Remote Sens Environ* 94:17–30
- Ottlé C, Vidal-madjar D (1992) Estimation of land surface temperature with NOAA –9 data. *Remote Sens Environ* 40:27–41
- Peres LF, DaCamara CC (2005) Emissivity maps to retrieve land surface temperature from MSG/SEVIRI. *IEEE Trans Geosci Remote* 43:1834–1844

- Peres LF, Dacamara CC, Trigo IF, Freitas SC (2010) Synergistic use of the two-temperature and split-window methods for land-surface temperature retrieval. *Int J Remote Sens* 31:4387–4409
- Prata A (1993) Land surface temperature derived from the advanced very high resolution radiometer and the along-track scanning radiometer 1. Theory. *J Geophys Res* 98:16689–16702
- Price JC (1983) Estimating surface temperature from satellite thermal infrared data—a simple formulation for the atmospheric effect. *Remote Sens Environ* 13:353–361
- Price JC (1984) Land surface temperature measurements from the split window channels of the NOAA 7 AVHRR. *J Geophys Res* 89:7231–7237
- Qin ZH, Karnieli A, Berliner A (2001) A mono-window algorithm for retrieving land surface temperature from landsat TM and its application to the Israel-Egypt border region. *Int J Remote Sens* 22:3719–3746
- Sellers PJ, Hall FG, Asrar G, Strebel DE, Murphy RE (1988) The First ISLSCP Field Experiment (FIFE). *J Bull Am Meteorol Soc* 69:22–27
- Sobrino JA, Romaguera M (2004) Land surface temperature retrieval from MSG1-SEVIRI data. *Remote Sens Environ* 92:247–254
- Sobrino JA, Li ZL, Stoll MP, Becker F (1994) Improvements in the split window technique for land surface temperature determination. *IEEE Trans Geosci Remote* 32:243–253
- Sobrino JA, Li ZL, Stoll MP, Becker F (1996) Multi-channel and multi-angle methods for estimating sea and land surface temperature with ATSR. *Int J Remote Sens* 17:2089–2114
- Sun Y (2008) Retrieval and application of land surface temperature. <http://www.geo.utexas.edu/courses/387h/PAPERS/Term%20paper-Sun.pdf>. Accessed 10 July 2011
- Sun YJ, Wang JF, Zhang RH, Gillies RR, Xue Y, Bo YC (2005) Air temperature retrieval from remote sensing data based on thermodynamics. *Theor Appl Climatol* 80:37–48
- Tang BH, Li ZL, Bi YY (2009) Estimation of land surface directional emissivity in mid-infrared channel around 4.0  $\mu\text{m}$  from MODIS data. *Opt Express* 17:3173–3182
- Tran H (2006) Assessment with satellite data of the urban heat island effects in Asian mega cities. *Int J Appl Earth Obs* 8:34–48
- Wan Z (2008a) New refinements and validation of the MODIS land-surface temperature/emissivity products. *Remote Sens Environ* 112:59–74
- Wan Z (2008b) Current status of the MODIS land-surface temperature/emissivity products. In: International workshop on the retrieval and use of land surface temperature: bridging the gaps, Asheville, NC, 7–9 April. [http://www.joss.ucar.edu/joss\\_psg/meetings/Meetings\\_2008/Bridging\\_the\\_Gaps/pdf/Monday\\_AM/Wan\\_presentation\\_ud.pdf](http://www.joss.ucar.edu/joss_psg/meetings/Meetings_2008/Bridging_the_Gaps/pdf/Monday_AM/Wan_presentation_ud.pdf). Accessed 15 Oct 2011
- Wan Z, Dozier J (1996) A generalized split-window method for retrieving land-surface temperature from space. *IEEE Trans Geosci Remote* 34:892–905
- Wan Z, Li ZL (1997) A physics-based method for retrieving land-surface emissivity and temperature from EOS/MODIS data. *IEEE Trans Geosci Remote* 35:980–996
- Wan Z, Wang P, Li X (2004) Using MODIS land surface temperature and normalized difference vegetation index products for monitoring drought in the southern Great Plains, USA. *Int J Remote Sens* 25:61–72
- Wang K, Li Z, Cribb M (2006) Estimation of evaporative fraction from a combination of day and night land surface temperatures and NDVI: a new method to determine the Priestley-Taylor parameter. *Remote Sens Environ* 102:293–305
- URL1: <http://remotesensing.unh.edu/modis>
- URL2: <http://bioval.jrc.ec.europa.eu/products/glc2000/products.php>
- URL3: <http://landsaf.meteo.pt/>

# Chapter 13

## A Water Vapor Scaling (WVS) Method for Improving Atmospheric Correction of Thermal Infrared (TIR) Data

Glynn Hulley

**Abstract** The thermal infrared (TIR) radiance at sensor measured by any spaceborne or airborne instrument will include atmospheric emission, scattering, and absorption by the Earth's atmosphere. These atmospheric effects need to be removed from the observation in order to isolate the land-leaving surface radiance contribution and retrieve important surface variables such as land surface temperature (LST) and emissivity. The accuracy of the atmospheric correction is dependent upon accurate characterization of the atmospheric state using independent atmospheric profiles of temperature, water vapor, and other gas constituents. The profiles are typically input to a radiative transfer model for estimating atmospheric transmittance, path, and sky radiances. Residual errors from incomplete atmospheric correction constitute one of the largest uncertainties in derived LST and emissivity products from the Advanced Spaceborne Thermal Emission and Reflection Radiometer (ASTER) and the Moderate Resolution Imaging Spectroradiometer (MODIS) sensors on NASA's Terra satellite. This chapter will describe a technique for improving the accuracy of the atmospheric parameters on a pixel-by-pixel basis using the Water Vapor Scaling (WVS) method. We have shown that using WVS can improve the accuracy of LST retrievals by up to 5 K for MODIS and 3 K for ASTER data in humid conditions.

### 13.1 Introduction

Atmospheric correction of data from thermal infrared (TIR) satellite sensors currently relies on two approaches. The first approach uses differential absorption characteristics of atmospheric water vapor between two bands in the longwave

---

G. Hulley (✉)

Jet Propulsion Laboratory, California Institute of Technology,  
National Aeronautics and Space Administration (NASA), Pasadena, CA, USA  
e-mail: [Glynn.Hulley@jpl.nasa.gov](mailto:Glynn.Hulley@jpl.nasa.gov)

spectral region (11–12  $\mu\text{m}$ ). Variations of this method include the split window (SW) approach (Coll and Caselles 1997; Prata 1994; Price 1984; Wan and Dozier 1996; Yu et al. 2008), the multichannel algorithm (Deschamps and Phulpin 1980), and the dual-angle algorithm (Barton et al. 1989). Sensors such as the Moderate Resolution Imaging Spectroradiometer (MODIS), Advanced Along-Track Scanning Radiometer (AATSR), and Advanced Very High Resolution Radiometer (AVHRR) all use variation of the split-window method to retrieve LST over land by assuming the emissivity can be estimated from land cover classification maps by assigning fixed emissivities based on cover type (Snyder et al. 1998).

The second approach uses full radiative transfer calculations to estimate atmospheric effects on a pixel-by-pixel and band-by-band basis. The atmospheric transmittance, path radiance, and downward sky irradiance are estimated using a radiative transfer model such as MODTRAN (MODerate resolution atmospheric TRANsmission) (Kneizys et al. 1996). The Advanced Spaceborne Thermal Emission and Reflection Radiometer (ASTER) uses this method to retrieve the LST and spectral emissivity simultaneously for TIR bands 10 (8.3  $\mu\text{m}$ ), 11 (8.6  $\mu\text{m}$ ), 12 (9.1  $\mu\text{m}$ ), 13 (10.6  $\mu\text{m}$ ), and 14 (11.3  $\mu\text{m}$ ) using the Temperature Emissivity Separation (TES) algorithm (Gillespie et al. 1998). The TES algorithm has been recently modified to retrieve LST and emissivity for MODIS bands 29 (8.55  $\mu\text{m}$ ), 31 (11  $\mu\text{m}$ ) and 32 (12  $\mu\text{m}$ ) (Hulley and Hook 2011).

Split-window based algorithms are generally tuned to have high LST accuracy over graybody surfaces where the emissivity is well known (e.g. water, vegetation), whereas the residual effects from incomplete atmospheric correction degrade the accuracy of TES LST products over graybody surfaces (Gustafson et al. 2006). Conversely, the TES retrieval is designed to have higher LST accuracy over geologic surfaces (e.g. bare rock, sand) (Hulley et al. 2009), whereas with split-window algorithms, errors in assigned emissivities can translate into large errors in LST (Galve et al. 2008). These errors can be due to a misclassification in the original cover type, a lack of fidelity in the cover type map, or a dynamic change in the cover type map for example from an increase in soil moisture.

The accuracy of the TES algorithm is limited by residual errors from incomplete atmospheric correction, which results in a larger apparent emissivity spectral contrast. This intrinsic weakness of the TES algorithm has been systematically analyzed by several authors (Coll et al. 2007; Gillespie et al. 1998; Gustafson et al. 2006; Hulley and Hook 2009; Li et al. 1999), and its effect is greatest over graybody surfaces that have a true spectral contrast that approaches zero. In order to minimize these errors, a Water Vapor Scaling (WVS) method has been introduced to improve the accuracy of the atmospheric parameters on a band-by-band basis for each observation using an Extended Multi-Channel/Water Vapor Dependent (EMC/WVD) algorithm (Tonooka 2005a), which is an extension of the Water Vapor Dependent (WVD) algorithm (Francois and Ottle 1996). The WVS method has already been incorporated in producing gridded ASTER emissivity maps, such as the North American ASTER Land Surface Emissivity Database (NAALSED) (Hulley and Hook 2009). It is also currently being incorporated with the TES algorithm to produce a 1 km MODIS LST and emissivity product (bands 29, 31, 32)

at the MODIS Adaptive Processing System (MODAPS). This chapter will describe the methodology of the WVS method, and show examples of its application to improving accuracy of MODIS and ASTER TIR data.

## 13.2 Thermal Infrared (TIR) Radiative Transfer

Assuming the spectral variation in emissivity is small, and using Kirchhoff's law to express the hemispherical-directional reflectance as directional emissivity  $\rho_\lambda = (1 - \varepsilon_\lambda)$  the clear sky at-sensor radiance can be written as:

$$L_\lambda(\theta) = [\varepsilon_\lambda B_\lambda(T_s) + (1 - \varepsilon_\lambda)L_\lambda^\downarrow] \tau_\lambda(\theta) + L_\lambda^\uparrow(\theta) \quad (13.1)$$

where:

$L_\lambda(\theta)$  – at-sensor radiance

$\lambda$  – wavelength

$\theta$  – observation angle

$\varepsilon_\lambda$  – surface emissivity

$B_\lambda(T_s)$  – Planck function

$T_s$  – surface temperature

$L_\lambda^\downarrow$  – downwelling sky irradiance

$\tau_\lambda(\theta)$  – atmospheric transmittance

$L_\lambda^\uparrow(\theta)$  – atmospheric path radiance

The at-sensor radiance for a discrete band  $i$  is obtained by weighting and normalizing the at-sensor spectral radiance calculated by Eq. (13.1) with the sensor's spectral response function for each band,  $Sr_\lambda$  as follows:

$$L_i(\theta) = \frac{\int Sr_\lambda(i) \cdot L_\lambda(\theta) \cdot d\lambda}{Sr_\lambda(i) \cdot d\lambda} \quad (13.2)$$

Using Eqs. (13.1) and (13.2), the surface radiance for band  $i$  can be written as a combination of two terms: the Earth-emitted radiance, and the reflected downward irradiance from the sky and surroundings:

$$L_{s,i} = \varepsilon_i B_i(T_s) + (1 - \varepsilon_i)L_i^\downarrow = \frac{L_i(\theta) - L_i^\uparrow(\theta)}{\tau_i(\theta)} \quad (13.3)$$

The atmospheric parameters:  $L_\lambda^\downarrow$ ,  $\tau_i(\theta)$ ,  $L_i^\uparrow(\theta)$  are estimated with a radiative transfer model such as MODTRAN (Berk et al. 2005; Kneizys et al. 1996) using input atmospheric fields of air temperature, relative humidity, and geopotential height.

### 13.3 Water Vapor Scaling (WVS) Method

The WVS method improves the accuracy of atmospheric parameters output by MODTRAN in Eq. (13.3) on a pixel-by-pixel basis using the EMC/WVD equation. The EMC/WVD equation models the at-surface brightness temperature, given the at-sensor brightness temperature, along with an estimate of the total water vapor amount as follows:

$$\begin{aligned} T_{g,i} &= \alpha_{i,0} + \sum_{k=1}^N \alpha_{i,k} T_k \\ \alpha_{i,k} &= p_{i,k} + q_{i,k} W + r_{i,k} W^2 \end{aligned} \quad (13.4)$$

where:

$i$  – band number

$n$  – number of bands

$W$  – estimate of total precipitable water vapor [cm]

$p, q, r$  – regression coefficients for each band

$T_k$  – brightness temperature for band  $k$  [K]

$T_{g,i}$  – brightness surface temperature for band  $i$

The coefficients of the EMC/WVD equation are determined using a global-based simulation model with profile data typically from numerical weather model data, such as the NCEP (National Centers for Environmental Prediction) Climate Data Assimilation System (CDAS) reanalysis project (Kalnay et al. 1990).

The scaling factor,  $\gamma$ , used for improving a water profile, is based on the assumption that the transmissivity,  $\tau_i$ , can be expressed by the Pierluissi double exponential band model formulation (Kneizys et al. 1996). The scaling factor is computed for each graybody pixel on a scene using  $T_{g,i}$  computed from Eq. (13.4) and  $\tau_i$  computed using two different  $\gamma$  values that are selected *a priori*:

$$\gamma^{\alpha_i} = \frac{\ln\left(\frac{\tau_i(\theta, \gamma_2)^{\gamma_1^{\alpha_i}}}{\tau_i(\theta, \gamma_1)^{\gamma_2^{\alpha_i}}} \cdot \left(\frac{B_i(T_{g,i}) - L_i^\uparrow(\theta, \gamma_1)/(1 - \tau_i(\theta, \gamma_1))}{L_i - L_i^\uparrow(\theta, \gamma_1)/(1 - \tau_i(\theta, \gamma_1))}\right)^{\gamma_1^{\alpha_i} - \gamma_2^{\alpha_i}}\right)}{\ln(\tau_i(\theta, \gamma_2)/\tau_i(\theta, \gamma_1))} \quad (13.5)$$

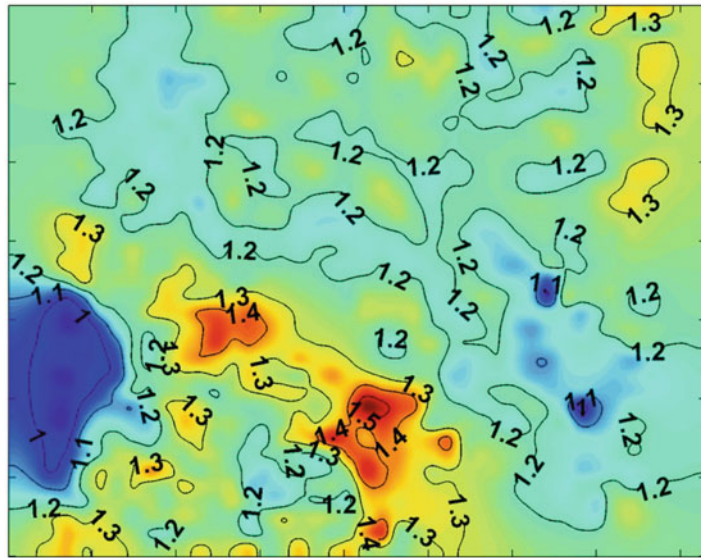


**Fig. 13.1** Water Vapor Scaling (WVS) factor,  $\gamma$ , computed using Eq. (13.5) for an ASTER scene on July 15, 2000 over the Salton Sea, CA. The atmospheric parameters were computed using MODIS MOD07 atmospheric profiles at 5 km spatial resolution and MODTRAN 5.2 radiative transfer code. The image has been interpolated and smoothed using methods discussed in Sect. 13.3.2

where:

$\alpha_i$  – band model parameter,

$\gamma_1, \gamma_2$  – two appropriately chosen  $\gamma$  values,

$\tau_i(\theta, \lambda_{1,2})$  – transmittance calculated with water vapor profile scaled by  $\gamma$ ,

$L_i^{\uparrow}(\theta, \gamma_{1,2})$  – path radiance calculated with water vapor profile scaled by  $\gamma$ .

Typical values for  $\gamma$  are  $\gamma_1 = 1$ , and  $\gamma_2 = 0.7$ . Tonooka (2005a) found that the  $\gamma$  calculated by Eq. (13.5) will not only reduce biases in the water vapor profile, but will also simultaneously reduce errors in the air temperature profiles and/or elevation. An example of the water vapor scaling factor,  $\gamma$ , is shown in Fig. 13.1 for an ASTER scene over the Algodones dunes area on July 15, 2000.

### 13.3.1 Gray Pixel Computation

It is important to note that  $\gamma$  is only computed for graybody pixels (e.g., vegetation, water, and some soils) with emissivities close to 0.99, and as a result, an accurate gray-pixel estimation method is required prior to processing. Vegetation indices such as the



**Fig. 13.2** Graybody-pixel map for the Salton Sea (black = gray, white = bare). A first guess graybody-pixel map was first estimated by thresholding ASTER reflectance indices to identify vegetated and water/snow pixels (e.g., NDVI), and then refined using the Thermal Log Residual (TLR) method described in the text

Normalized Difference Vegetation Index (NDVI), land cover databases (e.g., MODIS MOD12), and thermal log residuals (TLR) (Hook et al. 1992), are three different approaches that can be used in combination with each other to accomplish this. Typically, one classifies all green vegetation pixels first by thresholding NDVI computed from VIS/NIR bands. Water and snow/ice pixels are then classified using a land-water and snow-cover map. The MODIS product, for example, produces both a snow cover and water map at 1-km resolution (e.g., MOD10 and MOD44). A TLR approach can then be used to further refine the gray-pixel map. The TLR approach spectrally enhances images generated from multi-spectral data and removes dependence on band-independent parameters such as surface temperature. All gray pixels within a TLR image will have similar spectral shapes, and this characteristic is exploited in order to refine the gray-pixel map from the first guess gray pixels. Figure 13.2 shows an example of a gray-pixel map for an ASTER image on 15 July, 2000.

### 13.3.2 Interpolation and Smoothing

Once  $\gamma$  is computed for all gray pixels, the values are horizontally interpolated to adjacent bare pixels on the scene and smoothed before computing the improved atmospheric parameters. An inverse distance-weighted interpolation method is typically used to fill in bare pixel gaps. This is an interpolation method frequently

used in numerical weather forecasting with much success. The specific steps for interpolation of  $\gamma$  values are outlined in Tonooka (2001) and are as follows:

1. First all bare pixels are set to 1; in addition, all  $\gamma$  values less than 0.2 and greater than 3 are set to 1 for stability purposes and to eliminate possible cloud contamination.
2. Next, all cloudy pixels on the scene are set to NaN.
3. All bare pixels are then looped over, and optimum weights are found for all gray pixels within a given effective radius of the bare pixel. The  $\gamma$  value for the pixel is then computed using the weighted  $\gamma$  values surrounding the pixel and ignoring all NaN values as follows:

$$\gamma(x, y) = \sum_{i=1}^n w_i \gamma_i \quad (13.6)$$

Where  $n$  is the number of gray pixels, and  $w_i$  are the weight functions assigned to each gray pixel  $\gamma$  value:

$$w_i = \frac{d_i^{-p}}{\sum_{j=1}^n d_j^{-p}} \quad (13.7)$$

Where  $p$  is weighting factor called the power parameter, typically set to 2. Higher values give larger weights to the closest pixels.  $d_i$  is the geometrical distance from the interpolation pixel to the scattered points of interest within some effective radius:

$$d_i = \sqrt{(x - x_i)^2 + (y - y_i)^2} \quad (13.8)$$

Where  $x$  and  $y$  are the coordinates of the interpolation point, and  $x_i$  and  $y_i$  are coordinates of the scattered points.

4. If any bare pixels remain after the first pass, the bare pixels with a valid, calculated  $\gamma$  value are considered gray pixels, and the process is repeated until  $\gamma$  values for all bare pixels have been computed.

This interpolation method should not introduce large error, since gray pixels are usually widely available in any given scene and atmospheric profiles do not change significantly at the medium-range scale ( $\sim 50$  km). Figure 13.1 shows an example of a  $\gamma$  image after interpolation and smoothing.

### 13.3.3 Scaling Atmospheric Parameters

#### 13.3.3.1 Transmittance and Path Radiance

Once the MODTRAN run has completed and the  $\gamma$  image has been interpolated and smoothed, the atmospheric parameters transmittance  $\tau_i$  and path radiance  $L_i^\uparrow$  are modified as follows:

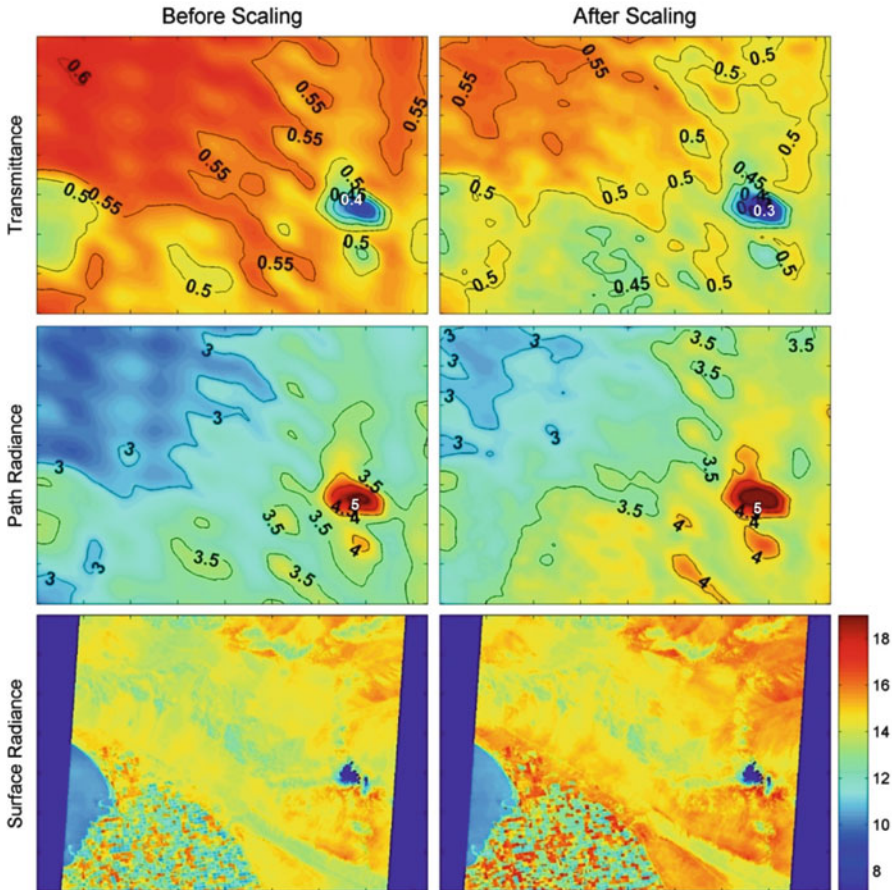


**Fig. 13.3** Comparisons between the atmospheric transmittance (top), path radiance (middle), and computed surface radiance (bottom), before and after applying the WVS scaling factor  $\gamma$  for the ASTER scene on July 15, 2000. Results are shown for ASTER band 10 (8.3  $\mu\text{m}$ )

$$\tau_i(\theta, \gamma) = \tau_i(\theta, \gamma_1)^{\frac{\gamma_1^{\alpha_i} - \gamma^{\alpha_i}}{\gamma_1^{\alpha_i} - \gamma_2^{\alpha_i}}} \cdot \tau_i(\theta, \gamma_2)^{\frac{\gamma_2^{\alpha_i} - \gamma^{\alpha_i}}{\gamma_1^{\alpha_i} - \gamma_2^{\alpha_i}}} \quad (13.9)$$

$$L_i^\uparrow(\theta, \gamma) = L_i^\uparrow(\theta, \gamma_1) \cdot \frac{1 - \tau_i(\theta, \gamma)}{1 - \tau_i(\theta, \gamma_1)} \quad (13.10)$$

Once the transmittance and path radiance have been adjusted using the scaling factor, the surface radiance can be re-computed with the updated atmospheric parameters using Eq. (13.3). Figure 13.3 shows an example of comparisons between ASTER band 10 (8.3  $\mu\text{m}$ ) atmospheric transmittance (top), path radiance (middle), and computed surface radiance (bottom), before and applying the WVS scaling factor,  $\gamma$ , for the ASTER scene on July 15, 2000. In this example, it is

clear that after scaling the transmittances are lower and path radiances higher (i.e. more opaque), meaning that the original water vapor estimate was too low for this scene. The result is a higher surface radiance in some regions of the scene due to the improved correction. Also note the very low transmittances and corresponding high path radiances in the southeast corner of the image due to the presence of cloud.

### 13.3.3.2 Downward Sky Irradiance

In the WVS simulation model, the downward sky irradiance can be modeled using the path radiance, transmittance, and view angle as parameters (Tonooka 2001). To simulate the downward sky irradiance in a MODTRAN run, the sensor target is placed a few meters above the surface, with surface emission set to zero, and view angle set at prescribed angles, e.g., Gaussian angles ( $\theta = 0^\circ, 11.6^\circ, 26.1^\circ, 40.3^\circ, 53.7^\circ$ , and  $65^\circ$ ). In this way, the only radiance contribution is from the reflected downwelling sky irradiance at a given view angle. The total sky irradiance contribution is then calculated by summing up the contribution of all view angles over the entire hemisphere:

$$L_i^{\downarrow} = \int_0^{2\pi} \int_0^{\pi/2} L_i^{\downarrow}(\theta) \cdot \sin \theta \cdot \cos \theta \cdot d\theta \cdot d\delta \quad (13.11)$$

Where  $\theta$  is the view angle and  $\delta$  is the azimuth angle. However, to minimize computational time in the MODTRAN runs, the downward sky irradiance can be modeled as a non-linear function of path radiance at nadir view (Tonooka 2005a):

$$L_i^{\downarrow}(\gamma) = a_i + b_i \cdot L_i^{\uparrow}(0, \gamma) + c_i \cdot L_i^{\uparrow}(0, \gamma)^2 \quad (13.12)$$

Where  $a_i$ ,  $b_i$ , and  $c_i$  are regression coefficients, and  $L_i^{\uparrow}(0, \gamma)$  is computed by:

$$L_i^{\uparrow}(0, \gamma) = L_i^{\uparrow}(\theta, \gamma_1) \cdot \frac{1 - \tau_i(\theta, \gamma)^{\cos \theta}}{1 - \tau_i(\theta, \gamma)} \quad (13.13)$$

Tonooka (2005a) found RMSEs of less than  $0.07 \text{ W/m}^2/\text{sr}/\mu\text{m}$  for ASTER bands 10–14 when using Eq. (13.12) as opposed to Eq. (13.11).

### 13.3.4 Determining EMC/WVD Coefficients

The EMC/WVD coefficients,  $p$ ,  $q$ ,  $r$  from Eq. (13.4) are determined using a global simulation model with input atmospheric parameters from either numerical weather model or radiosonde data. Radiosonde databases such as the TIGR, SeeBor, and

CLAR contain uniformly distributed global atmospheric soundings acquired both for day and night in order to capture the full-scale natural atmospheric variability.

Geophysical profiles of air temperature, relative humidity, and geopotential height are used in combination with surface temperature and emissivity to simulate at-sensor brightness temperatures for the global set of profiles distributed uniformly over land. The air temperature profiles are then shifted by  $-2$ ,  $0$ , and  $+2$  K, while the humidity profiles are scaled by factors of  $0.8$ ,  $1.0$ , and  $1.2$  to capture more variability for that specific atmospheric profile shape. These types of perturbations will help simulate a full range of atmospheric conditions. Furthermore, the surface temperatures are modified by  $-5$ ,  $0$ ,  $5$ , and  $10$  K, and the surface emissivity provided consists of a set of  $10$  spectra typically from gray materials selected from the ASTER spectral library; for example, water, vegetation, snow, ice, and some types of soils. These emissivity spectra typically have values greater than  $0.95$ . This ensures that the simulation results are not affected by uncertainties in surface emissivity, such as Lambertian effects. The at-sensor radiance is then computed using MODTRAN for the full set of profiles and perturbations ( $3 \times 3 \times 4 \times 10 = 360$ ). The surface elevation is taken from a global digital elevation model (DEM) (e.g. ASTER GDEM, or USGS GTOPO30), and the view angle is assumed to be nadir. Furthermore, a noise-equivalent differential temperature ( $NE\Delta T$ ) appropriate for the sensor is applied using a normalized random number generator. Using the simulated at-sensor  $T_k$ , at-surface  $T_g$  brightness temperatures, and an estimate of the total precipitable water vapor, the coefficients in Eq. (13.4) can be found by using a linear least squares method. WVS coefficients computed using MODTRAN4 for MODIS bands 29, 31 and 32 can be found in (Tonooka 2005b) and for ASTER bands 10–14 in (Tonooka 2005a). Updated coefficients for MODTRAN5.2 can be obtained by contacting the corresponding author of this chapter.

## 13.4 Impacts of WVS on Land Surface Temperature and Emissivity Retrievals

In this section we look at the impact of applying WVS to the accuracy of LST and emissivity retrievals using the TES algorithm for ASTER and MODIS observations over the Salton Sea on July 15, 2000. The emissivity of water is high ( $\sim 0.98$ ) and spectrally flat, and so this provides a good test for the accuracy of the emissivity retrieval, and consequently the LST retrieval. Any warping of the spectra is usually the result of incomplete atmospheric correction. The LST and emissivity was retrieved in the same manner for both ASTER and MODIS data using the methods outlined in Hulley and Hook (2011).

The results in Fig. 13.4 show that emissivity spectra from the Standard atmospheric correction (STD) method are too low for both ASTER and MODIS, especially in the  $8$ – $10$   $\mu\text{m}$  region when compared to the lab spectra from the ASTER spectral library. Applying the WVS coefficients results in a dramatic

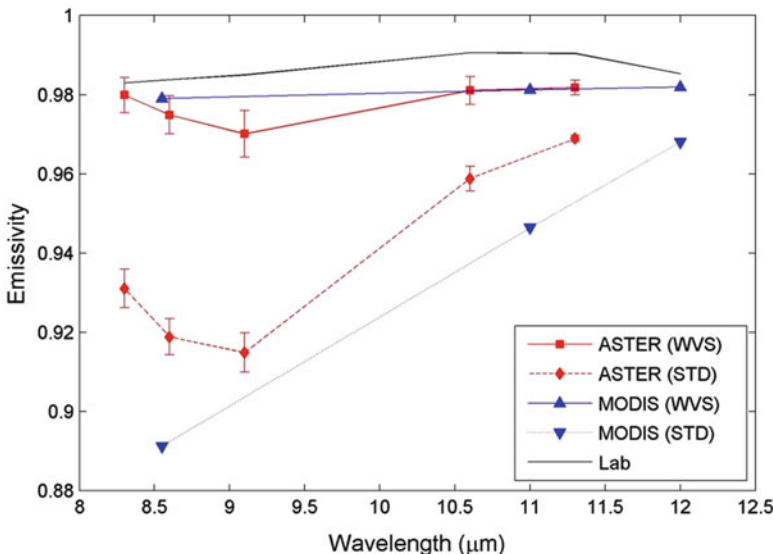


**Fig. 13.4** Emissivity spectra for the Salton Sea on 15 July 2000 for ASTER and MODIS data using the TES algorithm, and lab spectra of water from the ASTER spectral library. Results show improvements when using the Water Vapor Scaling (WVS) method as opposed to the standard (STD) atmospheric correction method. Total precipitable water estimated from the MOD07 atmospheric product on this day was high (4 cm), indicating very humid conditions

**Table 13.1** Land Surface Temperature (*LST*) and emissivity differences between using the Water Vapor Scaling (WVS) and Standard (STD) atmospheric correction methods for MODIS (1 km pixel) and ASTER ( $10 \times 10$ , 90 m pixels) data over the Salton Sea, CA, 15 July 2000

	ASTER		MODIS	
	STD	WVS	STD	WVS
Ts [K]	309.65	306.76	310.22	305.06
MMD	0.0522	0.0158	0.0597	0.0083
emin	0.9120	0.9611	0.91	0.97

*MMD* represents the minimum-maximum difference in emissivity for a water pixel spectrum, while *emin* is the minimum emissivity for the water spectrum

improvement in emissivity accuracy in both magnitude (up to 0.06 for ASTER band 11, and 0.09 for MODIS band 29) and spectral shape. Table 13.1 shows LST and emissivity differences between the WVS and STD approach for 1 MODIS pixel (1 km) and  $10 \times 10$  ASTER pixels (90 m) over the same area of the Salton Sea. LST differences between the STD and WVS method are as large as 5 K for MODIS and just under 3 K for ASTER. For water, the Minimum-Maximum Difference (MMD) in emissivity should approach near zero, and there is a significant decrease in MMD when using WVS as opposed to the STD approach. Humidity conditions on this day were very high, with total precipitable water values exceeding 4 cm (estimated from MOD07 product) making accurate atmospheric correction a

challenge. This is evident by the fact that the spectral contrast, or MMD in emissivity, for the STD correction are warped for both sensors (Fig. 13.4). With application of the WVS method, the ASTER emissivity spectra fall within 0.015 of the lab measured spectrum while MODIS emissivity spectra are within 0.005 at all wavelengths.

## References

- Barton II, Zavody AM, Obrien DM, Cutten DR, Saunders RW, Llewellyn-Jones DT (1989) Theoretical algorithms for satellite-derived sea-surface temperatures. *J Geophys Res-Atmos* 94:3365–3375
- Berk A, Anderson GP, Acharya PK, Bernstein LS, Muratov L, Lee J, Fox M, Adler-Golden SM, Chetwynd JH, Hoke ML, Lockwood RB, Gardner JA, Cooley TW, Borel CC, Lewis PE (2005) MODTRAN<sup>TM</sup> 5, a reformulated atmospheric band model with auxiliary species and practical multiple scattering options: update. In Sylvia SS, Lewis PE (eds) Algorithms and technologies for multispectral, hyperspectral, and ultraspectral imagery XI. Proceedings of SPIE, Bellingham
- Coll C, Caselles V (1997) A split-window algorithm for land surface temperature from advanced very high resolution radiometer data: validation and algorithm comparison. *J Geophys Res-Atmos* 102:16697–16713
- Coll C, Caselles V, Valor E, Niclos R, Sanchez JM, Galve JM, Mira M (2007) Temperature and emissivity separation from ASTER data for low spectral contrast surfaces. *Remote Sens Environ* 110:162–175
- Deschamps PY, Phulpin T (1980) Atmospheric correction of infrared measurements of sea-surface temperature using channels at 3.7, 11 and 12 Mu-M. *Bound-Layer Meteorol* 18:131–143
- Francois C, Ottle C (1996) Atmospheric corrections in the thermal infrared: global and water vapor dependent split-window algorithms – applications to ATSR and AVHRR data. *IEEE Trans Geosci Remote Sens* 34:457–470
- Galve JA, Coll C, Caselles V, Valor E (2008) An atmospheric radiosounding database for generating land surface temperature algorithms. *IEEE Trans Geosci Remote Sens* 46:1547–1557
- Gillespie A, Rokugawa S, Matsunaga T, Cothern JS, Hook S, Kahle AB (1998) A temperature and emissivity separation algorithm for advanced spaceborne thermal emission and reflection radiometer (ASTER) images. *IEEE Trans Geosci Remote Sens* 36:1113–1126
- Gustafson WT, Gillespie AR, Yamada GJ (2006) Revisions to the ASTER temperature/emissivity separation algorithm. In: 2nd international symposium on recent advances in quantitative remote sensing, Torrent (Valencia), Spain
- Hook SJ, Gabell AR, Green AA, Kealy PS (1992) A comparison of techniques for extracting emissivity information from thermal infrared data for geologic studies. *Remote Sens Environ* 42:123–135
- Hulley GC, Hook SJ (2009) The North American ASTER Land Surface Emissivity Database (NAALSED) version 2.0. *Remote Sens Environ* 113:1967–1975
- Hulley GC, Hook SJ (2011) Generating consistent land surface temperature and emissivity products between ASTER and MODIS data for earth science research. *IEEE Trans Geosci Remote Sens* 49:1304–1315
- Hulley GC, Hook SJ, Baldridge AM (2009) Validation of the North American ASTER Land Surface Emissivity Database (NAALSED) version 2.0 using pseudo-invariant sand dune sites. *Remote Sens Environ* 113:2224–2233
- Kalnay E, Kanamitsu M, Baker WE (1990) Global numerical weather prediction at the National-Meteorological-Center. *Bull Am Meteorol Soc* 71:1410–1428

- Kneizys FX, Abreu LW, Anderson GP, Chetwynd JH, Shettle EP, Berk A, Bernstein LS, Robertson DC, Acharya PK, Rothman LA, Selby JEA, Gallery WO, Clough SA (1996b) The MODTRAN 2/3 report & LOWTRAN 7 model, F19628-91-C-0132. Phillips Laboratory Hanscom AFB, Bedford
- Li ZL, Becker F, Stoll MP, Wan ZM (1999) Evaluation of six methods for extracting relative emissivity spectra from thermal infrared images. *Remote Sens Environ* 69:197–214
- Prata AJ (1994) Land-surface temperatures derived from the advanced very high-resolution radiometer and the along-track scanning radiometer.2. Experimental results and validation of Avhrr algorithms. *J Geophys Res-Atmos* 99:13025–13058
- Price JC (1984) Land surface temperature measurements from the split window channels of the NOAA 7 advanced very high resolution radiometer. *J Geophys Res* 89:7231–7237
- Snyder WC, Wan Z, Zhang Y, Feng YZ (1998) Classification-based emissivity for land surface temperature measurement from space. *Int J Remote Sens* 19:2753–2774
- Tonooka H (2001) An atmospheric correction algorithm for thermal infrared multispectral data over land – a water-vapor scaling method. *IEEE Trans Geosci Remote Sens* 39:682–692
- Tonooka H (2005a) Accurate atmospheric correction of ASTER thermal infrared imagery using the WVS method. *IEEE Trans Geosci Remote Sens* 43:2778–2792
- Tonooka H (2005b) Atmospheric correction of MODIS thermal infrared bands by water vapor scaling method. *IEEE Trans Geosci Remote Sens* 5979:152–163
- Wan ZM, Dozier J (1996) A generalized split-window algorithm for retrieving land-surface temperature from space. *Proc SPIE* 34:892–905
- Yu Y, Privette JL, Pinheiro AC (2008) Evaluation of split-window land surface temperature algorithms for generating climate data records. *IEEE Trans Geosci Remote Sens* 46:179–192

# Chapter 14

## Time Series Corrections and Analyses in Thermal Remote Sensing

José A. Sobrino and Yves Julien

**Abstract** The time span of surface thermal data bases now reaches a few decades. However, studies using surface thermal time series are seldom, due to the difficulty of obtaining temporally coherent estimations for this parameter. Applications for surface thermal multitemporal analysis range from climate change studies and modeling to anomaly detection for natural or industrial hazard detection. This chapter presents methods to improve the temporal coherence of temperature time series, through data reconstruction of atmospheric and cloud contaminated observations, and through the correction of the orbital drift effect which hinders the use of the longest data sets. Then, methods for the analysis of time series are presented, including both image to image comparison and trend detection, the choice between these methods depending on the spatial resolution of the dataset and the aims of the considered study.

### 14.1 Introduction

Although thermal remote sensing data have been available since the 1970s, the use of time series in remote sensing is recent, since the temporal coherence of thermal data records have been hindered by several flaws. Nonetheless, the potential of the applications is high, from climate change studies to environment monitoring.

As concern about the consequences of climate change grows, the need for reliable information on surface temperature has increased. For example, climate modelers need surface temperature as input for their models to adequately simulate past and future climate, in order to be able to quantify vegetation and plankton response to atmospheric CO<sub>2</sub> anthropogenic forcing (see for example Diak and

---

J.A. Sobrino (✉) • Y. Julien  
Global Change Unit, Image Processing Laboratory (IPL),  
University of Valencia, Valencia, Spain  
e-mail: [Sobrino@uv.es](mailto:Sobrino@uv.es)

Whipple 1993). As stated by Frey et al. (2012), “surface temperature is a key variable in the climatological system. It represents the interface between the incoming radiation fluxes and other terms of the energy balance, i.e. the sensible heat flux or the ground heat flux. Air temperature is directly triggered by Land Surface Temperature (LST). Because of this central position in the climatological system, LST can be used as an indicator of the energy balance at the Earth’s surface and the so-called greenhouse effect in climate change studies. As part of the surface radiation budget, LST belongs also to the essential climate variables of WMO-GCOS (World Meteorological Organization-Global Climate Observing System, URL1). In the Strategic Plan for the US Climate Change Science Program (CCSP 2006), the surface ground temperature is listed as a state variable and the long-wave surface energy budget (derived also from LST) is listed as one of its key external forcing or feedback observations” (Frey et al. 2012).

This need for reliable surface thermal estimations is also shared by studies on climate change’s current consequences. For example, it allows the identification of desertification (Lambin and Ehrlich 1996; Karnieli et al. 2010), whether under water stress or human pressure. Surface temperature is also a key parameter for ecosystem studies, since the suitability of temperature conditions for local flora and fauna species is endangered by climate change (see for example Bertrand et al. 2011).

Thermal estimations include both temperature and emissivity, which are intimately related (see for example Gillespie et al. 1998, for temperature and emissivity separation methods). Thermal emissivities have been monitored for their inclusion in global climate model surface schemes (Menglin and Liang 2006), and their seasonal variation analyzed (Ogawa et al. 2008). Thermal emissivities can also be used to monitor vegetation changes through time, as French et al. (2008) have presented for a semi-arid site in New Mexico (USA).

Another field of application of thermal remote sensing is thermal anomaly detection and monitoring. These approaches are carried out by comparing pixel temperatures against their background in uni-temporal satellite data (Kuenzer et al. 2007), or they consist in comparing a near-real time surface temperature estimation to past reference measurements, in order to identify departures from standard behaviors (Kuenzer et al. 2008). Some modern fire detection systems have been developed based on this principle, and are especially useful for detection of fire events in remote areas (Prins et al. 2004). Such alert systems can also be implemented for volcano monitoring, or for industrial hazard detection.

However, for such applications to be implemented, one key aspect has to be taken into account: when two thermal images are compared at two distinct dates, one has to make sure that both images are coherent. Some of the factors that decreases the temporal coherence in multitemporal thermal analysis are common to other remote sensing characterization, while others are more TIR (Thermal Infra Red) specific. All these factors are summarized in Table 14.1.

Common factors with other remote sensing applications are included in what is generally referred to as level 2 products, which include calibration, georeferencing, and atmospheric correction. Calibration is needed to transform sensor counts into brightness temperature, is sensor dependent, and calibration coefficients may need

**Table 14.1** Factors influencing time series coherence of thermal parameters

	Factors	Observations
Optical and TIR	Gas absorption bands	Dependent on sun-sensor-target geometry and atmospheric mass
	Water vapor disturbance	
	Aerosols	
	Clouds	
	Cloud shadows	
	Topography related adjacency effect	
	BRDF effects	
TIR	Topography related uneven solar heating	
	Variation in data acquisition times	Such as orbital drift or within scanline variations
	Emissivity effect	Such as metal roofs in urban areas

to be updated during the activity period of a given sensor. Georeferencing is crucial for time series analyses, in order to make sure that the same location is being monitored through time. Regarding atmospheric correction, some land and sea surface temperature algorithms (Jiménez-Muñoz and Sobrino 2008; Barton 1995) consider the absorption due to total atmospheric water content, while others only transform brightness temperatures to land surface temperature through the assignation of land surface emissivities (Sobrino et al. 2008a). Additionally, complex atmospheric correction may be needed, especially considering the impact of atmospheric depth, atmospheric mass, and also terrain on the thermal signal, such as provided by the ATCOR (atmospheric correction) tool, implemented for thermal bands of Landsat MSS (Multispectral Scanner), TM (Thematic Mapper) or ETM+ (Enhanced Thematic Mapper Plus), ASTER (Advanced Spaceborne Thermal Emission and Reflection Radiometer ) or BIRD (Bispectral Infra-Red Detection) instruments, and available in various software packages.

However, time series pre-processing of thermal remote sensing data also present more specific characteristics. The first one, which is shared with other optical remote sensing, is the presence of clouds, which mask the land surface and therefore prevent from the estimation of surface temperature. Additionally, in high resolution data, projected cloud shadows can also decrease the retrieved temperatures. Cloud masks are sometimes provided with temperature retrievals, although undetected clouds may still be present in the data. For example, thin cirrus clouds decrease the observed surface temperature, although their detection from remotely sensed data is problematic (Saunders and Kriebel 1988). Moreover, some regions of the globe are almost permanently covered with clouds during some seasons, and therefore cloud free observations are scarce, and time series gap filling has to be implemented.

Another specific aspect of time series analysis in thermal remote sensing is the orbital drift effect. This orbital drift effects all satellites which do not possess onboard fuel for orbit correction, such as engineless platforms, or ageing platforms

which fuel reserves have been exhausted. Orbital drift is evidenced mainly for polar satellites, and consists in a slow but steady change in the orbit characteristics of the considered satellite, which results in an increasing delay or advance in satellite overpass over a given reference geographic location. An example of such orbital drift can be observed in the case of the NOAA (National Oceanic and Atmospheric Administration) satellite series (Price 1991). The effect of the orbital drift combines both considerations on sun-target-sensor geometry (proportion of shade in a given pixel) as well as on daily temperature cycle characteristics, to which the resulting variations in the pathway length through the atmosphere can be added. Therefore, it is evidenced more easily for land covers with high daily amplitude (deserts, crops) than for low amplitudes (sea, evergreen forests). A similar effect can be evidenced for non-drifting platforms for which some pixels are observed for different paths. However, this effect is not correlated with time, and therefore can be assimilated as an additional noise in the time series which can be handled by the trend detection methods presented in Sect. 14.3.2.

Thermal anisotropy is another factor which can influence temperature retrieval, and therefore thermal time series (Lagouarde et al. 1995), for which a BRDF-type (Bidirectional Reflectance Distribution Function, see Tanré et al. 1983) correction could be developed. However, since such correction has not yet been developed in the case of thermal data, it will not be mentioned further here.

In order to be able to analyze thermal time series (whether emissivities or temperatures) correctly, all these aspects have to be taken into consideration. Then, change analysis can be conducted. To that end, this chapter is divided into two parts, the first part describing how to conduct these corrections, while the second one is focused specifically on change analysis.

## 14.2 Removal of Temporal Incoherence in Thermal Time Series

As stated in the introduction, the coherence of thermal time series can be hindered by several factors. Since factors such as calibration, geocorrection, and atmospheric correction are usually taken into account during data processing, they will not be elaborated on here. Instead, this first part will be devoted to the correction of two more specific factors, i.e. cloud contamination and orbital drift effects.

### 14.2.1 Cloud Contamination

The first step in cloud contamination removal is cloud identification. It is usually carried out through band ratio and/or band thresholding, with each band or band ratio threshold aiming at the detection of one particular type of cloud (high and low

thick clouds, thin cirrus) for both Land Surface Temperature and Sea Surface Temperature (SST). The key point here is the number of bands available for the considered sensor, which allow for more or less thresholds to be applied. When restricted to thermal infrared, the application of thresholds is less reliable, especially when the observed areas may present an ice or snow cover during part of the time series (mountains, temperate to polar areas). This is due to the fact that cloud tops have similar temperatures to snow or ice covered surfaces. Recent algorithms allow for a good assessment of cloud contamination (Ackerman et al. 1998; Derrien and Le Gléau 2005). Nevertheless, cloud masking may leave out cloud contaminated values in the time series, which is the reason why this section will focus on cloud reconstruction methods.

Cloud reconstruction methods are based on a few assumptions, which allow identifying cloud contaminated values within the temporal profile of the data, and then filling the gap corresponding to cloud contaminated values. Usually, the assumptions made for reconstruction are threefold (Julien and Sobrino 2010): continuity of the time series, which corresponds to the fact that observed natural processes show slow changes; clouds have an unidirectional effect on the signal, which is due to the fact that usually cloud contamination tend to decrease the signal values; and finally, cloud free dates are sufficient for time series reconstruction. Most methods for time series reconstruction have been developed for analyses of vegetation index time series (such as NDVI – Normalized Difference Vegetation Index, Tucker 1979, or EVI – Enhanced Vegetation Index, Huete et al. 2002). However, these methods can also be applied to sea or land surface temperature as well as to emissivity time series. Such methods are reviewed in the following paragraphs, to focus finally on three methods selected for their wide application or their novelty.

Numerous methods have been presented to identify and interpolate contaminated values in time series data (van Dijk et al. 1987; Viovy et al. 1992; Roerink et al. 2000; Jönsson and Eklundh 2002, 2004; Chen et al. 2004; Ma and Veroustraete 2006; Beck et al. 2006; Julien and Sobrino 2010), the latest methods usually performing better than the previous ones (Hird and McDermid 2009). The criteria usually followed to assess the best reconstruction method are its fidelity to the original cloud-free data and its ability to identify cloud contaminated values. Validation of the reconstructed time series is usually qualitative, since spatially extensive measurements (usually of the order of one square kilometer) would be needed for a quantitative validation. Readers have to keep in mind that such corrections reconstruct a “clear-sky” time series, which can differ substantially from ground truth, since cloudy LST for example would be lower than the reconstructed “clear-sky” value. However, estimation of cloudy LST would require the inclusion of models that would increase considerably the processing costs of the correction, which is the reason why such methods have not been developed widely. One example of such method can be found in Jin and Dickinson (2000). Note that these methods do not distinguish between clouds and other atmospheric contamination of the data.

The methods presented by van Dijk et al. (1987) and Viovy et al. (1992) were designed with their application to daily time series in mind, and therefore are difficult to apply on composited time series, due to their focus on the highest frequencies in the signal (up to a few days), which do not appear in composited time series. Indeed, most of the publicly available databases of remotely sensed data for Earth observation, such as Pathfinder AVHRR (Advanced Very High Resolution Radiometer) Land (Smith et al. 1997) or GIMMS (Global Inventory Modeling and Mapping Studies; Tucker et al. 2005) are composited. This compositing aims at lowering atmospheric and cloud influence, as shown in Holben (1986), with different compositing periods ranging usually from 8 to 15 days. Even though composite data present lower atmospheric contamination than raw time series, this composition process does not eliminate atmospheric contamination. For example, cloud cover can persist longer than the compositing period for some time periods (rainy season) or over some specific areas (tropical rainforests). Therefore, we present here three approaches for remaining atmospheric influences on composited time series:

**HANTS (Harmonic Analysis of NDVI Time Series):** This algorithm (Menenti et al. 1993; Verhoef et al. 1996; Roerink et al. 2000) was developed with the application to time series of NDVI images in mind. These images are usually composited by means of the so-called Maximum Value Compositing (MVC, Holben 1986) algorithm in order to suppress atmospheric effects. The HANTS algorithm exploits the negative effect of atmospheric contamination on NDVI values. In HANTS, a curve fitting is applied iteratively, i.e. first a least squares curve is computed based on all data points, and next the observations are compared to the curve. Observations that are clearly below the curve are candidates for rejection due to atmospheric contamination and the points that have the greatest negative deviation from the curve therefore are removed first. Next a new curve is computed based on the remaining points and the process is repeated. Pronounced negative outliers are removed by assigning a weight of zero to them, and a new curve is computed. This iteration eventually leads to a smooth curve that approaches the upper envelope of the data points. In this way, atmospheric contaminated observations have been removed and the amplitudes and phases computed are much more reliable than those based on a straightforward FFT (Fast Fourier Transform). An example of implementation of the HANTS algorithm for land surface temperature time series analysis can be found in Julien et al. (2006).

**Double logistic curve fitting:** The double logistic approach has been previously applied in Julien and Sobrino (2009) to global GIMMS data, as a generalization of the method presented by Beck et al. (2006) for Siberia.

NDVI yearly evolutions are fitted to the following double logistic function (Beck et al. 2006):

$$\begin{aligned} NDVI(t) = & (mNDVI - wNDVI) \times \left( \frac{1}{1 + e^{-mS \times (t-S)}} + \frac{1}{1 + e^{mA \times (t-A)}} - 1 \right) \\ & + wNDVI \end{aligned} \quad (14.1)$$

where  $\text{NDVI}(t)$  is the remotely sensed NDVI evolution for a given year ( $t = 0$  to 364, in day of year),  $w\text{NDVI}$  is the winter NDVI value,  $m\text{NDVI}$  is the maximum NDVI value,  $S$  is the increasing inflection point (spring date),  $A$  is the decreasing inflection point (autumn date),  $mS$  is related to the rate of increase at  $S$  inflection point, and  $mA$  is related to the rate of decrease at  $A$  inflection point. All these parameters are retrieved iteratively on a pixel-by-pixel basis, by using the Levenberg-Marquardt technique (More 1977). In order to remove eventual snow- or cloud-contaminated values, a preliminary fit is conducted in order to estimate the dormancy period as the period before spring date and after autumn date. During this period, all eventual negative NDVI values are set to the highest positive value over the whole dormancy period, labeled winter NDVI. Since surface temperatures usually present a high seasonality, this approach is also suitable for surface temperature time series. Although NDVI and LST annual curves may differ in shape (no constant LST during winter or summer), the double logistic approach can describe adequately the LST annual curves.

**IDR (iterative Interpolation for Data Reconstruction):** This method (Julien and Sobrino 2010), also exploits the tendency of cloud and atmospheric influence to lower NDVI values. Additionally, since NDVI is a proxy for vegetation greenness, its temporal variation should be smooth and continuous. Therefore, for each date of a given time series, an alternative NDVI value is computed as the mean between the immediately preceding and following observations. An alternative NDVI time series is therefore obtained, and compared to the original time series. The date corresponding to the maximum difference between the alternative and original time series is identified, and the corresponding NDVI value in the original time series is replaced with the corresponding NDVI value in the alternative time series. This replacement is carried out only when the maximum difference between both time series is higher than noise level (in that case 0.02 NDVI units). Then a new alternative time series is computed from the modified time series, and the process is iterated until convergence is reached. This process allows to progressively increase one by one the low and discontinuous NDVI values (corresponding to atmospherically contaminated values) until the upper envelope of the NDVI time series is reached. The methodology is somewhat similar to the one presented in Ma and Veroustraete (2006), with the difference that the IDR method is carried out from the data itself, and not from a comparison to an average of different years, which can be problematic for areas with high interannual variability, for areas suffering a land cover change, or when the acquired time series length is short.

Figure 14.1 presents an example of atmospheric contamination reconstruction using the IDR method with Meteosat Second Generation land surface temperature data, retrieved during one whole day by using the algorithm developed by Sobrino and Romaguera (2004). Cloud contamination appears as sudden decreases in retrieved land surface temperature from 10:00 to 13:00 (GMT), while atmospheric contamination is more easily evidenced at night (from 17:00 to 24:00 GMT for example).

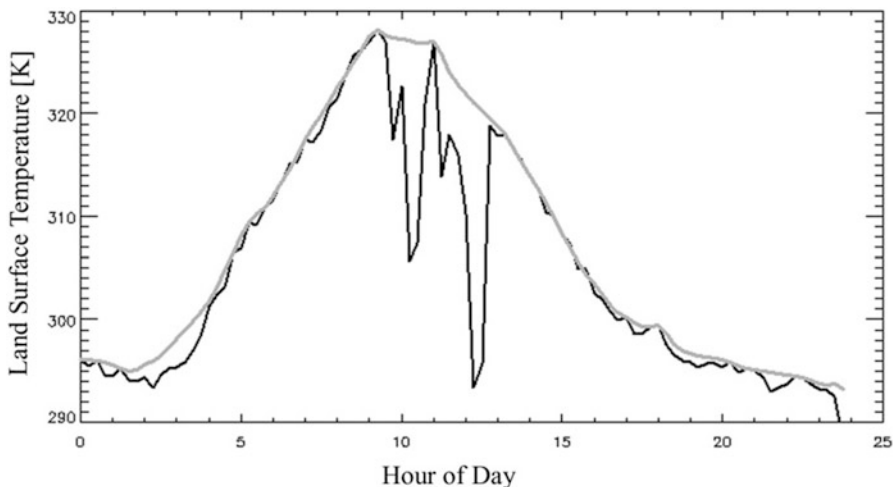


**Fig. 14.1** One-day (15th July 2010) land surface temperature (in Kelvin) for a pixel in eastern Turkey as retrieved by Meteosat Second Generation SEVIRI (Spinning Enhanced Visible and InfraRed Imager) sensor (black), and after IDR atmospheric contamination reconstruction (grey). See text for details on the IDR method

#### 14.2.2 *Orbital Drift Effect*

The orbital drift effect is evidenced only for a few platforms, although these platforms are the ones that provide one of the longest time series of surface temperature. Therefore, the following paragraph describes only methods developed to counterbalance this phenomenon for the NOAA-AVHRR sensor.

The first method, developed by Gutman (1999), relies on the previous calculations of temperature and SZA (Solar Zenithal Angle) time series anomalies, which are then averaged over homogeneous vegetation classes. A simple linear regression is then conducted between these averaged anomalies, and finally, the fitted SZA anomalies are removed from LST time series by simple difference. This method was applied and analyzed thoroughly in Gleason et al. (2002), showing that some hemispherical and local adaptations were needed for desert and crop classes respectively. These methods rely on a priori knowledge on land cover, which can (and should) not be considered in change studies through time series analysis.

Another method, developed by Jin and Treadon (2003), relies on modeling land surface temperature daily cycle, from which the difference of temperature between the nominal and actual satellite overpass times can be estimated, and then added to the data for the corresponding date. However, the daily cycles have been computed for 18 land covers, for all four seasons, and for latitude bands of  $5^{\circ}$ , which transforms temporal discontinuities in land surface temperatures at satellite transitions into spatial discontinuities at vegetation class and latitude band transitions.

Pinheiro et al. (2004) developed a model based on vegetation structural data and geometric optics, which allows for the estimation of the fraction of sunlit and shaded endmembers observed by AVHRR for each pixel of each overpass. This approach has been used to build a daily record of NOAA-14 AVHRR land surface temperature over Africa (Pinheiro et al. 2006). Due to the needed a priori knowledge of the land cover and to the model complexity this approach is difficult to implement for large datasets.

Pinzon et al. (2005) used an approach based on the Empirical Mode Decomposition (EMD) to correct NDVI data for the orbital drift. The decomposition uses the simple assumption that any data consists of different simple intrinsic modes of oscillations, which can be retrieved iteratively from the data itself. Therefore, a specific mode could be identified as orbital drift dependent, and removed from the signal. This approach was chosen for the correction of GIMMS NDVI as well as for the LTDR (Long Term Data Record) dataset.

Finally, Sobrino et al. (2008b) presented a simple and automated method to correct NOAA-AVHRR orbital drift, also using SZA anomaly information. The iterative character of this method results in increased processing times, and is thus difficult to implement for large databases.

All the methods presented above are unable to correct the orbital drift effect without introducing spurious trends in the data (Hou and Shi 2011), since the differentiation between orbital drift and trends included in the time series is not always obvious. However, Julien and Sobrino (2012) developed a data-driven method to correct this orbital drift, therefore avoiding the lack of information on NOAA-AVHRR acquisition times (although indirect approaches such as the ones presented in Frey et al. 2012, or Ignatov et al. 2004, allow for their estimation). The Julien and Sobrino (2012) approach is based on a pixel-by-pixel fit of LST anomalies against both time since launch and solar zenithal angle anomaly, which allows for the removal of orbital drift influence without removing eventual trends in the pixel time series. Figure 14.2 presents an example of the orbital drift influence on a barren pixel time series and its correction by the Julien and Sobrino (2012) approach.

### 14.3 Time Series Analyses

In the case of sea surface temperatures, the main application being climate modeling, basic approaches relying on anomaly estimation and linear regression have been generally applied (see for example Comiso 2003). Another case of time series analyses based on anomaly estimation is the coal fire detection method presented by Kuenzer et al. (2008), which also presents the particularity of using four observations per day, as a rare example of intra-daily time series application. Due to the scarcity of temporally coherent land surface temperature time series, few methods have been developed specifically for their analysis. However, methods developed for other optical wavelengths can easily be transposed to thermal

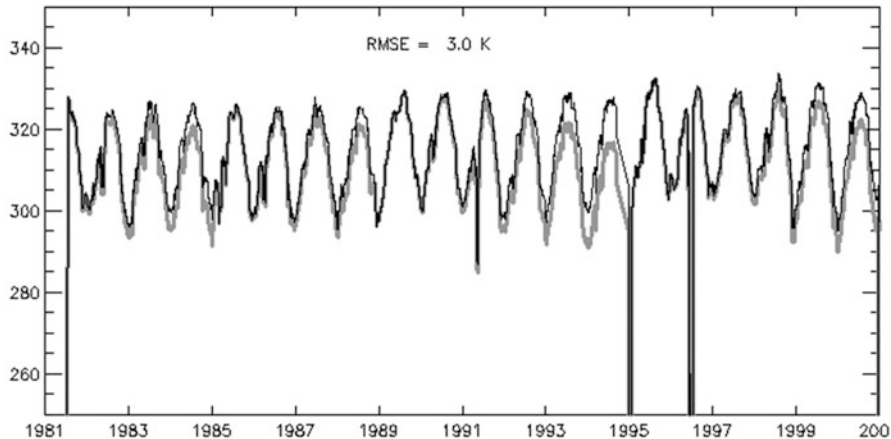


**Fig. 14.2** LST time series for a barren pixel before (grey) and after (black) the Julien and Sobrino (2012) orbital drift correction. The orbital drift effect on the uncorrected LST time series is clearly evidenced by the increasing difference between both curves from satellite launch to retirement dates

infrared applications. Therefore, the following methods could also perfectly be applied to LST time series as well. These methods are presented hereafter, divided in change detection and trend retrieval methods.

### 14.3.1 Change Detection

Coppin et al. (2004) have reviewed different methods for vegetation monitoring. This section summarizes the ones that are relevant to thermal time series, completed with other references. Detection of changes in remotely sensed images presupposes having access to similar data, whether regarding acquisition (cloud free images, atmospheric effects, illumination and observation geometry, similar wavelengths and spatial resolutions), time scale (comparable phenological state of the vegetation), data processing (similar methods, accurate georeferenciation). Change detection algorithms are mainly based on bi-temporal analysis, i.e. comparison of two sets of data, preferably from before and after the change.

- A first technique for change detection is univariate image differencing, which consists in the simple subtraction of two images previously co-georeferenced (Banner and Lynham 1981; Lyon et al. 1998; Nelson 1983). Negative differences can generally be attributed to increase in vegetation cover (which temperature is lowered by increased evapotranspiration), while positive differences evidence mainly a decrease in vegetation cover. An example of this method can be found in Fig. 14.3, where the difference between two land surface temperature estimates from airborne AHS (Airborne Hyperspectral

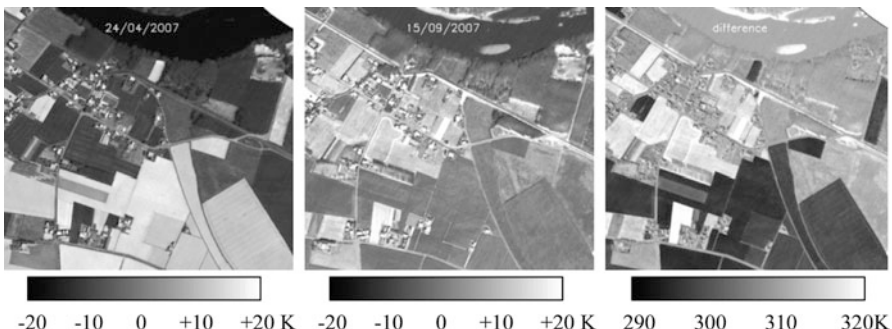


**Fig. 14.3** Land surface temperature as retrieved by the AHS (Airborne Hyperspectral Scanner) sensor over an agricultural area in Southern France on 24th April 2007 and 15th September 2007 (*upper images*) and their difference (*lower image*)

Scanner) sensor, acquired over an agricultural area in southern France in 2007 at 11:40 UTC, shows the land cover change between two dates. This difference image allows the identification of the changes suffered between these two dates: lower river (Garonne) level (top of the image, in white), increase in vegetation cover (as a decrease of LST in the lower part of the image, in dark grey) and decrease in vegetation cover (as an increase in LST in the left part of the image, in white). This method has the advantage of low cost in processing time.

- A second technique consists in image ratioing on a pixel by pixel basis, resulting in an image where change pixels have a value different to unity. This technique has been applied by Howarth and Wickware (1981), unfortunately without being able to make a quantitative assessment of the changes.
- A third technique is image regression, which consists in assuming that the “after” image is linearly related to the “before” image for all bands, implying that the spectral properties of most pixels have not changed between images. Changes are then identified by setting thresholds to the residuals. This technique has not been proven to reach high accuracies (Burns and Joyce 1981; Singh 1989; Ridd and Liu 1998).
- A fourth method is multi-temporal spectral mixture analysis, which supposes that the images (preferably with high spatial resolution) include pixels with pure spectral signatures or end-members, present in all pixels with different proportions. Then, change results in variation in end-member percentiles. This method was implemented successfully for Landsat images of Brazilian Amazon by Adams et al. (1995) and Roberts et al. (1998).
- Finally, a fifth technique is multidimensional temporal feature space analysis, which consists in overlaying selected bands of the “before” and “after” images in a composite image as red, green and blue bands, in which changes appear in unique colors. This technique does not provide any insight on the drivers of the changes, and is usually applied for mask building before change detection. For example, Alwashe and Bokhari (1993) and Wilson and Sader (2002) have applied this technique to Landsat bands or derived indices. Finally, combinations of those different techniques have also been used (Desclée et al. 2006).

Among all these techniques, users should choose which method is more adequate for their application. For example, methods 1, 2 and 5 are straightforward (these techniques can be carried out automatically for large amounts of data, with changes being identified through threshold definition.), while methods 3 and 4 are more difficult to implement. Therefore, methods 1, 2 and 5 can be used as an exploratory tool in order to identify where changes are occurring, while methods 3 and 4 can emphasize links between changes separated geographically. Moreover, method 4 is useful for determining the nature of the change which has been identified.

### **14.3.2 Trend Analyses**

Most of the methods presented above have been designed for high resolution images, such as those retrieved by SPOT (Satellite Pour l'Observation de la Terre) or Landsat sensors, for which temporal resolution is quite low. However, when temporal resolution is higher and spatial resolution is lower, surface temperature retrieval consists in an averaging of temperature over land covers and vegetation species, while abrupt events such as harvesting are smoothed due to their local character. Thus, different techniques have to be applied, which can be summarized as temporal trajectory analyses. These techniques include statistical analysis (departure from averages, optima, etc. – Lambin and Strahler 1994), simple anomalies (instantaneous departure from average corresponding period over the whole time series – Myneni et al. 1997; Plisnier et al. 2000; Comiso 2003), Fourier analysis (Andres et al. 1994), principal component analysis (PCA) (Eastman and Fulk 1993; Young and Wang 2001) and change-vector analysis (CVA) (Lambin and Strahler 1994; Lambin and Ehrlich 1997). As was the case with change detection methods, the last techniques (Fourier, PCA and CVA) are heavier to implement, although they allow for a better assessment of geographical correlation of the changes. Additionally, De Beurs and Henebry (2005a) designed a statistical framework for land cover change analysis.

Ordinary least squares (OLS) regression is the most common method applied for trend analysis in long image time series, as is the study of global trends in SST by Deser et al. (2010). However, four basic assumptions affecting the validity of trends summarized by OLS regression are often violated: (1) all the Y-values should be independent of each other; the residuals should be (2) random with (3) zero mean; and (4) the variance of the residuals should be equal for all values of X (De Beurs 2005). Since time series of biophysical parameters are temporally correlated, OLS regression retrieved trends are not reliable.

The approach described hereafter relies on the Mann-Kendall framework, which has been applied in a few previous studies of time series of remotely sensed data (De Beurs and Henebry 2004a, b, 2005a, b). The basic principle of Mann-Kendall (MK) tests for trend is to examine the sign of all pairwise differences of observed values (Libiseller and Grimvall 2002). An univariate form of such tests was first

published by (Mann 1945), and the theory of multivariate Mann-Kendall tests is due to Hoeffding (1948), Kendall (1975), Dietz and Killeen (1981). During the past two decades, applications in the environmental sciences have given rise to several new MK tests. Hirsch and Slack (1984) published a test for detection of trends in serially dependent environmental data collected over several seasons.

The Mann-Kendall statistic for monotone trend in a time series  $\{Z_k, k = 1, 2, \dots, n\}$  of data is defined as:

$$T = \sum_{j < i} \text{sgn}(Z_i - Z_j) \quad (14.2)$$

where

$$\text{sgn}(x) = \begin{cases} 1, & \text{if } x > 0 \\ 0, & \text{if } x = 0 \\ -1, & \text{if } x < 0 \end{cases} \quad (14.3)$$

If no ties are present and the values of  $Z_1, Z_2, \dots, Z_n$  are randomly ordered, this statistic test has expectation zero and variance:

$$\text{Var}(T) = \frac{n(n-1)(2n+5)}{18} \quad (14.4)$$

Furthermore, T is approximately normal, if n is large ( $n > 10$  – Kendall 1975).

Finally, the null trend hypothesis can be rejected at a confidence level  $\alpha$  if T (in absolute value) is greater than a corresponding threshold, which value is  $z_\alpha \cdot \sqrt{\text{Var}(T)}$ , with  $z_\alpha$  being retrieved from standard normal distribution tables.

This test determines whether trends are present in the data. However, it does not provide estimates of the trend magnitude. To that end, Sen's slope approach (Sen 1968) can be used. This approach consists in determining trend values for all pairs of data of the time series, and then in identifying the median value of all these estimated trends. This approach has been shown to be resistant to outliers (Sen 1968).

Figure 14.4 shows an example of Mann-Kendall significance level for MODIS (Moderate Resolution Imaging Spectroradiometer) TERRA maximum land surface temperature trends, as well as trend values estimated by Sen's slope approach for the whole globe, and a synthesis image which presents Sen's slope trend values for Mann-Kendall values above 90 % confidence level. These maps show a good spatial homogeneity, which confirms the validity of the applied pixel-based approach. Obviously, the relatively short time span of MODIS data (10 years) does not allow for climate studies, although the observed trends can easily be related to climate change impacts (increased air temperatures in boreal areas for example – IPCC 2007). In order to be able to analyze climate related trends, a longer time series is needed, from the AVHRR instrument for example, provided an adequate correction of the orbital drift effect (Sect. 2.3).

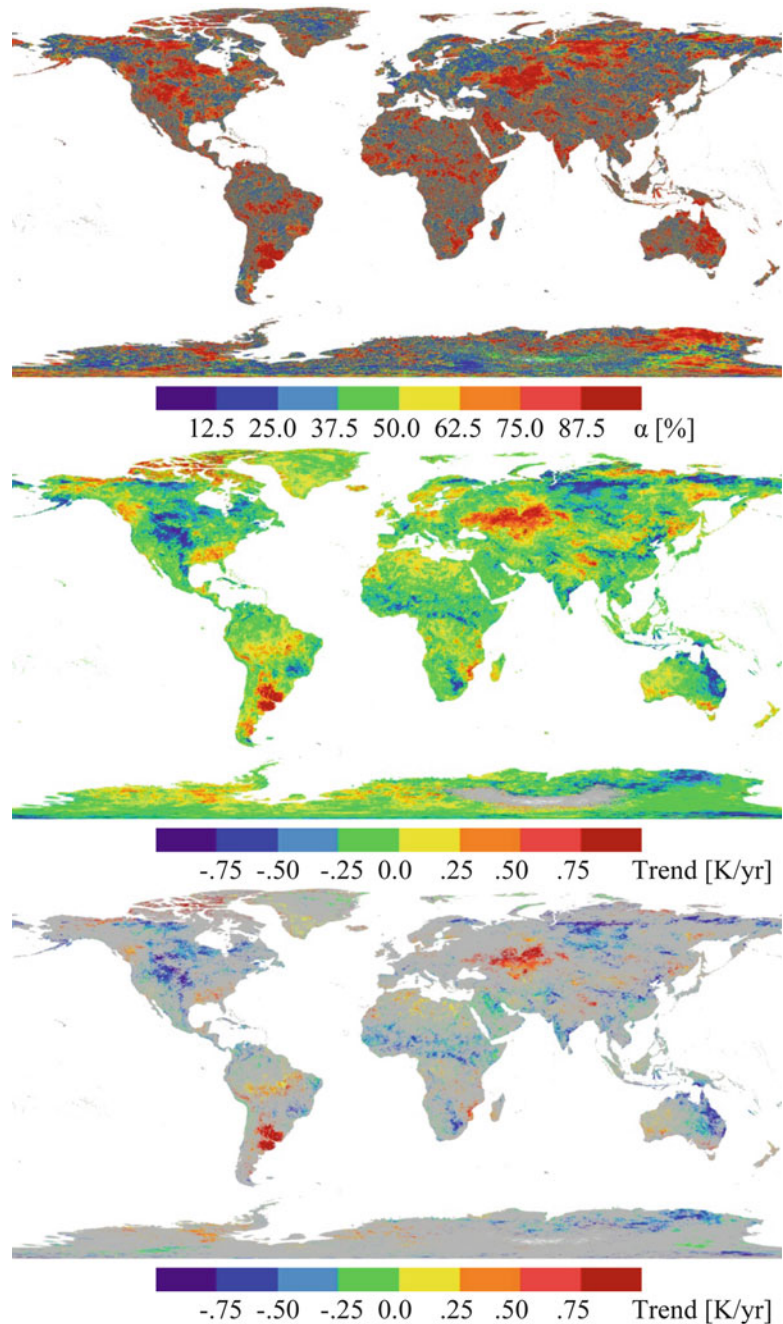


**Fig. 14.4** Global trends for MODIS TERRA land surface temperature between 2001 and 2010, as retrieved through the Mann-Kendall statistical framework. These maps correspond to significance level (top), trend values (middle), and trend values with a confidence level above 90 % (bottom)

Finally, a novel technique has been developed by Verbesselt et al. (2010), which consists in the detection of breakpoints in a time series (BFAST – Breaks For Additive Seasonal and Trend). Although this technique has been developed with the application to vegetation indices in mind, this technique can perfectly be applied to surface temperature time series, and can provide interesting insight on the timing of surface changes, which are useful for the attribution of causes of the observed changes.

## 14.4 Conclusions

Time series analysis for thermal data is a quite novel field, due to the low availability of temporally coherent datasets. However, recent advances in time series pre-processing (such as the ones presented here) and new sensors will result in an increased interest in this field. This has to be added to the general concern regarding global warming, based on trends observed from air temperatures, although surface temperature is a better indicator of ecosystem suitability for existing vegetation and animal species, whether aquatic or terrestrial. Therefore, thermal time series could allow for an improved assessment of global warming impacts (plant phenology, pests control, food security, etc.).

## References

- Ackerman S, Strabala K, Menzel W, Frey R, Moeller C, Gumley L (1998) Discriminating clear sky from clouds with MODIS. *J Geophys Res* 103:32141–32157
- Adams JB, Sabol DE, Kapos V, Almeida Filho R, Robers DA, Smith MO, Gillespie AR (1995) Classification of multi-spectral images based on fractions of end members: applications to land-cover change in the Brazilian Amazon. *Remote Sens Environ* 12:137–154
- Alwashe MA, Bokhari AY (1993) Monitoring vegetation changes in Al Madinah, Saudi Arabia, using Thematic Mapper data. *Int J Remote Sens* 14:191–197
- Andres L, Salas WA, Skole D (1994) Fourier analysis of multitemporal AVHRR data applied to a land cover classification. *Int J Remote Sens* 15:1115–1121
- Banner A, Lynham T (1981) Multi-temporal analysis of Landsat data for forest cutover mapping – a trial of two procedures. In: Proceedings of the 7th Canadian symposium on remote sensing, Winnipeg, Canada, pp 233–240
- Barton IJ (1995) Satellite-derived sea surface temperatures: current status. *J Geophys Res* 100(C5):8777–8790
- Beck P, Atzberger C, Høgda KA, Johansen B, Skidmore A (2006) Improved monitoring of vegetation dynamics at very high latitudes: a new method using MODIS NDVI. *Remote Sens Environ* 100:321–334
- Bertrand R, Lenoir J, Piedallu C, Riofrío-Dillon G, de Ruffray P, Vidal C, Pierrat JC, Gégot JC (2011) Changes in plant community composition lag behind climate warming in lowland forests. *Nature*. doi:[10.1038/nature10548](https://doi.org/10.1038/nature10548)

- Burns GS, Joyce AT (1981) Evaluation of land cover change detection techniques using Landsat MSS data. In: Proceedings of the 7th PECORA symposium, Sioux Falls, SD. ASPRS, Bethesda, MD, pp 252–260
- CCSP (Climate Change Science Program) (2006) Strategic plan for the U.S. Climate Change Science Program, chapter 12. In: Observing and monitoring the climate system. <http://www.climatescience.gov/Library/stratplan2003/final/ccspstratplan2003-chap12.pdf>. Accessed 13 Nov 2012
- Chen J, Jönsson P, Tamura M, Gu Z, Matsushita B, Eklundh L (2004) A simple method for reconstructing a high-quality NDVI time-series data set based on the Savitzky–Golay filter. *Remote Sens Environ* 91:332–334
- Comiso JC (2003) Warming trends in the Arctic from clear sky satellite observations. *J Climate* 16:3498–3510
- Coppin P, Jonckheere I, Nackaerts K, Muys B, Lambin E (2004) Digital change detection methods in ecosystem monitoring: a review. *Int J Remote Sens* 25(9):1565–1596
- De Beurs KM (2005) A statistical framework for the analysis of long image time series: the effect of anthropogenic change on land surface phenology. PhD dissertation, Faculty of The Graduate College, University of Nebraska
- De Beurs KM, Henebry GM (2004a) Land surface phenology, climatic variation, and institutional change: analyzing agricultural land cover change in Kazakhstan. *Remote Sens Environ* 89:497–509
- De Beurs KM, Henebry GM (2004b) Trend analysis of the Pathfinder AVHRR Land (PAL) NDVI data for the deserts of Central Asia. *IEEE Geosci Remote Sens Lett* 1(4):282–286
- De Beurs KM, Henebry GM (2005a) A statistical framework for the analysis of long image time series. *Int J Remote Sens* 26(8):1551–1573
- De Beurs KM, Henebry GM (2005b) Land surface phenology and temperature variation in the International Geosphere-Biosphere Program high-latitude transects. *Glob Chang Biol* 11:779–790
- Derrien M, Le Gléau H (2005) MSG/SEVIRI cloud mask and type from SAFNWC. *Int J Remote Sens* 26:4707–4732
- Desclée B, Bogaert P, Defourny P (2006) Forest change detection by statistical object-based method. *Remote Sens Environ* 102:1–11
- Deser C, Phillips AS, Alexander MA (2010) Twentieth century tropical sea surface temperature trends revisited. *Geophys Res Lett* 37:L10701. doi:[10.1029/2010GL043321](https://doi.org/10.1029/2010GL043321)
- Diak GR, Whipple MS (1993) Improvements to models and methods for evaluating the land-surface energy balance and effective roughness using radiosonde reports and satellite-measured skin temperature data. *Agr Forest Meteorol* 63(3–4):189–218
- Dietz EJ, Killeen TJ (1981) A nonparametric multivariate test for monotone trend with pharmaceutical applications. *J Am Stat Assoc* 76:169–174
- Eastman JR, Fulk M (1993) Long sequence time series evaluation using standardized principal components. *Photogramm Eng Remote Sens* 59:991–996
- French AN, Schmugge TJ, Ritchie JC, Hsu A, Jacob F, Ogawa K (2008) Detecting land cover change at the Jornada Experimental Range, New Mexico with ASTER emissivities. *Remote Sens Environ* 112:1730–1748
- Frey CM, Kuenzer C, Dech S (2012) Quantitative comparison of the operational NOAA-AVHRR LST product of DLR and the MODIS LST product V005. *Int J Remote Sens* 33(22):7165–7183
- Gillespie A, Rokugawa S, Matsunaga T, Cothern JS, Hook S, Kahle AB (1998) A temperature and emissivity separation algorithm for Advanced Spaceborne Thermal Emission and Reflection Radiometer (ASTER) images. *IEEE Trans Geosci Remote Sens* 36(4):1113–1126
- Gleason ACR, Prince SD, Goetz SJ, Small J (2002) Effects of orbital drift on land surface temperature measured by AVHRR thermal sensors. *Remote Sens Environ* 79:147–165
- Gutman GG (1999) On the monitoring of land surface temperature with the NOAA/AVHRR: removing the effect of satellite orbit drift. *Int J Remote Sens* 20(17):3407–3413

- Hird JN, McDermid GJ (2009) Noise reduction of NDVI time series: an empirical comparison of selected techniques. *Remote Sens Environ* 113:248–258
- Hirsch RM, Slack JR (1984) A nonparametric trend test for seasonal data with serial dependence. *Water Resour Res* 20:727–732
- Hoeffding W (1948) A class of statistics with asymptotically normal distribution. *Ann Math Stat* 19:293–325
- Holben BN (1986) Characteristics of maximum-value composite image from temporal AVHRR data. *Int J Remote Sens* 7:1417–1434
- Hou TY, Shi Z (2011) Adaptive data analysis via sparse time-frequency representations. *Adv Adapt Data Anal* 3(1&2):1–28
- Howarth PJ, Wickware GM (1981) Procedures for change detection using Landsat. *Int J Remote Sens* 2:277–291
- Huete A, Didan K, Miura T, Rodriguez EP, Gao X, Ferreira LG (2002) Overview of the radiometric and biophysical performance of the MODIS vegetation indices. *Remote Sens Environ* 83(1–2):195–213
- Ignatov A, Laszlo I, Harrod ED, Kidwell KB, Goodrum GP (2004) Equator crossing times for NOAA, ERS and EOS sun-synchronous satellites. *Int J Remote Sens* 25(23):5255–5266
- IPCC (2007) In: Parry ML, Canziani OF, Palutikof JP, van der Linden PJ, Hanson CE (eds) Climate change 2007: impacts, adaptation, and vulnerability, contribution of working group II to the fourth assessment report of the Intergovernmental Panel on Climate Change. Cambridge University Press, Cambridge
- Jiménez-Muñoz JC, Sobrino JA (2008) Split-window coefficients for land surface temperature retrieval from low-resolution thermal infrared sensors. *IEEE Geosci Remote Sens Lett* 5(4):806–809
- Jin M, Dickinson RE (2000) A Generalized algorithm for retrieving cloudy sky skin temperature from satellite thermal infrared radiances. *J Geophys Res* D22:27037–27047
- Jin M, Treadon RE (2003) Correcting the orbit drift effect on AVHRR land surface skin temperature measurements. *Int J Remote Sens* 24(22):4543–4558
- Jönsson P, Eklundh L (2002) Seasonality extraction by function fitting to time-series of satellite sensor data. *IEEE Trans Geosci Remote Sens* 40:1824–1832
- Jönsson P, Eklundh L (2004) TIMESAT – a program for analyzing time-series of satellite sensor data. *Comput Geosci* 30:833–845
- Julien Y, Sobrino JA (2009) Global land surface phenology trends from GIMMS database. *Int J Remote Sens* 30(13):3495–3513
- Julien Y, Sobrino JA (2010) Comparison of cloud-reconstruction methods for time series of composite NDVI data. *Remote Sens Environ* 114:618–625
- Julien Y, Sobrino JA (2012) Correcting long term data record V3 estimated LST from orbital drift effects. *Remote Sens Environ* 123:207–219
- Julien Y, Sobrino JA, Verhoef W (2006) Changes in land surface temperatures and NDVI values over Europe between 1982 and 1999. *Remote Sens Environ* 103:43–55
- Karnieli A, Agam N, Pinker RT, Anderson M, Imhoff ML, Gutman GG, Panov N, Goldberg A (2010) Use of NDVI and land surface temperature for drought assessment: merits and limitations. *J Climate* 23(3):618–663
- Kendall MG (1975) Rank correlation methods. Charles Griffin, London
- Kuenzer C, Zhang J, Li J, Voigt S, Mehl H, Wagner W (2007) Detecting unknown coal fires: synergy of automated coal fire risk area delineation and improved thermal anomaly extraction. *Int J Remote Sens* 28(20):4561–4585
- Kuenzer C, Hecker C, Zhang J, Wessling S, Wagner W (2008) The potential of multidurnal MODIS thermal band data for coal fire detection. *Int J Remote Sens* 29(3):923–944
- Lagouarde JP, Kerr YH, Brunet Y (1995) An experimental study of angular effects on surface temperature for various plant canopies and bare soils. *Agr Forest Meteorol* 77:167–190
- Lambin EF, Ehrlich D (1996) The surface temperature-vegetation index space for land cover and land-cover change analysis. *Int J Remote Sens* 17:463–487

- Lambin EF, Ehrlich D (1997) Land-cover changes in sub-Saharan Africa (1982–1991): application of a change index based on remotely sensed surface temperature and vegetation indices at a continental scale. *Remote Sens Environ* 61:181–200
- Lambin EF, Strahler AH (1994) Change-vector analysis in multitemporal space: a tool to detect and categorize land-cover change processes using high temporal-resolution satellite data. *Remote Sens Environ* 48:231–244
- Libiseller C, Grimvall A (2002) Performance of partial Mann-Kendall test for trend detection in the presence of covariates. *Environmetrics* 13:71–84
- Lyon GJ, Yuan D, Lunetta RS, Elvidge CD (1998) A change detection experiment using vegetation indices. *Photogramm Eng Remote Sens* 64:143–150
- Ma M, Veroustraete F (2006) Reconstructing pathfinder AVHRR land NDVI timeseries data for the Northwest of China. *Adv Space Res* 37:835–840
- Mann HB (1945) Non-parametric tests against trend. *Econometrica* 13:245–259
- Menenti M, Azzali S, Verhoef W, van Swol R (1993) Mapping agro-ecological zones and time lag in vegetation growth by means of Fourier analysis of time series of NDVI images. *Adv Space Res* 13:233–237
- Menglin J, Liang S (2006) An improved land surface emissivity parameter for land surface models using global remote sensing observations. *J Climate* 19:2867–2881
- More JJ (1977) The Levenberg-Marquardt algorithm: implementation and theory. In: Watson GA (ed) Numerical analysis, Lecture notes in mathematics 630. Springer, New York
- Myndeni RB, Keeling CD, Tucker CJ, Asrar G, Nemani RR (1997) Increased plant growth in the northern high latitudes from 1981 to 1991. *Nature* 386(6626):698
- Nelson RF (1983) Detecting forest canopy change due to insect activity using Landsat MSS. *Photogramm Eng Remote Sens* 49:1303–1314
- Ogawa K, Schmugge T, Rokugawa S (2008) Estimating broadband emissivity of arid regions and its seasonal variations using thermal infrared remote sensing. *Trans Geosci Remote Sens* 46(2):334–343
- Pinheiro ACT, Privette JL, Mahoney R, Tucker CJ (2004) Directional effects in a daily AVHRR land surface temperature dataset over Africa. *IEEE Trans Geosci Remote Sens* 42(9):1941–1954
- Pinheiro ACT, Mahoney R, Privette JL, Tucker CJ (2006) Development of a daily long term record of NOAA-14 AVHRR land surface temperature over Africa. *Remote Sens Environ* 103:153–164
- Pinzon J, Brown ME, Tucker CJ (2005) Satellite time series correction of orbital drift artifacts using empirical mode decomposition. In: Huang NE, Shen SSP (eds) EMD and its applications, vol 10. World Scientific, Singapore, pp 285–295
- Plisnier PD, Serneels S, Lambin EF (2000) Impact of ENSO on East African ecosystems: multivariate analysis based on climatologic and remote sensing data. *Glob Ecol Biogeogr Lett* 9:481–497
- Price JC (1991) Using spatial context in satellite data to infer regional scale evapotranspiration. *IEEE Trans Geosci Remote Sens* 28:940–948
- Prins EM, McNamara D, Schmidt CC (2004) Global geostationary fire monitoring system. In: AMS 13th satellite meteorology and oceanography conference, Norfolk, VA, 20–24 Sept 2004
- Ridd MK, Liu J (1998) A comparison of four algorithms for change detection in an urban environment. *Remote Sens Environ* 63:95–100
- Roberts DA, Batista GT, Pereira J, Waller EK, Nelson BW (1998) Change identification using multitemporal spectral mixture analysis: applications in eastern Amazonia. In: Elvidge C, Lunetta R (eds) Remote sensing change detection: environmental monitoring applications and methods. Ann Arbor Press, Chelsea, pp 137–161
- Roerink GJ, Menenti M, Verhoef W (2000) Reconstructing cloudfree NDVI composites using Fourier analysis of time series. *Int J Remote Sens* 21(9):1911–1917
- Saunders RW, Kriebel KT (1988) An improved method for detecting clear sky and cloudy radiances from AVHRR data. *Int J Remote Sens* 9:123–150

- Sen PK (1968) Estimates of the regression coefficient based on Kendall's tau. *J Am Stat Assoc* 63:1379–1389
- Singh A (1989) Digital change detection techniques using remotely-sensed data. *Int J Remote Sens* 10:989–1003
- Smith PM, Kalluri SNV, Prince SD, Defries R (1997) The NOAA/NASA pathfinder AVHRR 8-km land data set. *Photogramm Eng Remote Sens* 63(1):12–31
- Sobrino JA, Romaguera M (2004) Land surface temperature retrieval from MSG1-SEVIRI data. *Remote Sens Environ* 92:247–254
- Sobrino JA, Jiménez-Muñoz JC, Sòria G, Romaguera M, Guanter L, Moreno J, Plaza A, Martínez P (2008a) Land surface emissivity retrieval from different VNIR and TIR sensors. *IEEE Trans Geosci Remote Sens* 46(2):316–327
- Sobrino JA, Julien Y, Atitar M, Nerry F (2008b) NOAA-AVHRR orbital drift correction from solar zenithal angle data. *IEEE Trans Geosci Remote Sens* 46(12):4014–4019
- Tanré D, Herman M, Deschamps PY (1983) Influence of the atmosphere on space measurements of directional properties. *Appl Opt* 22:733–741
- Tucker CJ (1979) Red and photographic infrared linear combinations for monitoring vegetation. *Remote Sens Environ* 8:127–150
- Tucker CJ, Pinzon JE, Brown ME, Slayback DA, Pak EW, Mahoney R, Vermote EF, El Saleous N (2005) An extended AVHRR 8-km NDVI dataset compatible with MODIS and SPOT vegetation NDVI data. *Int J Remote Sens* 26(20):4485–4498
- van Dijk A, Callis S, Sakamoto C, Decker W (1987) Smoothing vegetation index profiles: an alternative method for reducing radiometric disturbance in NOAA/AVHRR data. *Photogramm Eng Remote Sens* 53:1059–1067
- Verbesselt J, Hyndman R, Newnham G, Culvenor D (2010) Detecting trend and seasonal changes in satellite image time series. *Remote Sens Environ* 114:106–115. doi:[10.1016/j.rse.2009.08.014](https://doi.org/10.1016/j.rse.2009.08.014)
- Verhoef W, Menenti M, Azzali S (1996) A colour composite of NOAA-AVHRR-NDVI based on time series analysis (1981–1992). *Int J Remote Sens* 17(2):231–235
- Viovy N, Arino O, Velward A (1992) The Best Index Slope Extraction (BISE): a method for reducing noise in NDVI time-series. *Int J Remote Sens* 13:1585–1590
- Wilson EH, Sader SA (2002) Detection of forest harvest type using multiple dates of Landsat TM imagery. *Remote Sens Environ* 80:385–396
- Young SS, Wang CY (2001) Land-cover change analysis of China using globalscale Pathfinder AVHRR Landover (PAL) data, 1982–92. *Int J Remote Sens* 22:1457–1477
- URL1: <http://www.wmo.int/pages/prog/gcos/index.php?name=EssentialClimateVariables>

# Chapter 15

## Thermal Remote Sensing of Sea Surface Temperature

Christopher J. Merchant

**Abstract** Sea surface temperature has been an important application of remote sensing from space for three decades. This chapter first describes well-established methods that have delivered valuable routine observations of sea surface temperature for meteorology and oceanography. Increasingly demanding requirements, often related to climate science, have highlighted some limitations of these approaches. Practitioners have had to revisit techniques of estimation, of characterising uncertainty, and of validating observations – and even to reconsider the meaning(s) of “sea surface temperature”. The current understanding of these issues is reviewed, drawing attention to ongoing questions. Lastly, the prospect for thermal remote sensing of sea surface temperature over coming years is discussed.

### 15.1 How Does Sea Surface Temperature Vary?

Thermal remote sensing is a powerful technique to obtain global, frequent observations sea surface temperature (SST). Surface temperature across the oceans varies with time (e.g., Robinson 2004), responding, for example, to the daily cycle in heating by the Sun (e.g., Fairall et al. 1996), to the passage of the seasons, and to changes in upwelling or vertical mixing driven by the wind blowing across the sea surface (e.g., Munk 1950). Surface waters are constantly moving: in ocean currents and eddies; and, near coasts, with tides and river outflows. Surface water advection changes SST over time at a given location.

Scales of a kilometre and upwards are globally observed with radiometers from space (e.g., Donlon et al. 2010). Viewing the thermal structure of the ocean surface at such scales, one may observe relatively sharp boundaries in SST (Fig. 15.1). These “fronts” are signatures in SST of the convergence of surface water masses,

---

C.J. Merchant (✉)

Department of Meteorology, University of Reading, Reading, UK

e-mail: [c.j.merchant@reading.ac.uk](mailto:c.j.merchant@reading.ac.uk)

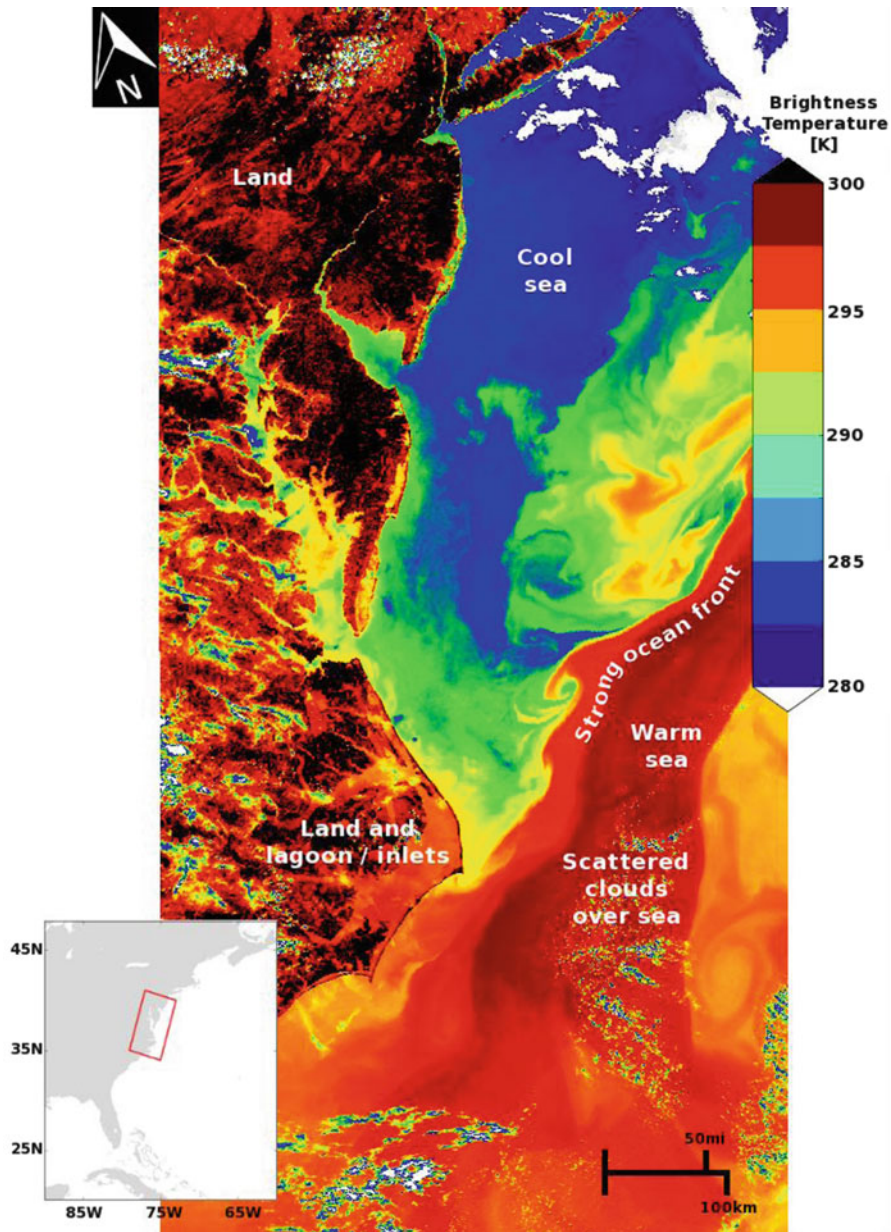


**Fig. 15.1** Image at thermal window wavelength of  $11\text{ }\mu\text{m}$  of US Eastern seaboard including Cape Hatteras and Pimlico Sound, obtained by the second Along Track Scanning Radiometer. The width of the image is about 512 km and the pixel resolution is 1 km. Ocean features are reasonably well resolved, with smooth contiguous variations in surface temperature reflected in the image brightness temperature, except where there are scattered, cooler clouds that are often not fully resolved. Land is also more heterogeneous, and, this being a day time image, warmer than the sea in many areas (Image obtained from [URL1](#) and adapted by the author)

**Table 15.1** Selected ocean phenomena and the magnitude and scales of their SST signature

Phenomenon	Magnitude/K	Length scale/km	Time scale
Climatological variation across oceans	35	$10^4$	
El Nino and interannual variability	0.5–5	500–5,000	Months to years
Tropical instability waves	0.5–5	200–2,000	Months to years
Meanders and eddies on major fronts and boundary currents	1–8	5–2,000	Weeks to months
Diurnal warming cycle	0.1–5	5–1,000	Hours
Coral bleaching events	0.3–3	20–200	Days
Coastal wind induced phenomena	0.2–2	1–100	Hours

Extracted and adapted from Robinson (2004), which provides a more complete listing

convergence that can arise from a number of processes of oceanographic interest. More generally, thermal remote sensing can reveal any phenomenon that measurably alters the radiometric SST, provided that the surface temperature signature occurs on a length scale longer than the sensor's spatial resolution and persists for long enough relative to the time-sampling properties of the observing system. Note that the relevant sampling rate is not the rate of acquisition of images, but rather the rate at which a cloud-free observation at a given location is typically obtained. Examples of oceanographic phenomena and their SST magnitude and spatiotemporal scales are given in Table 15.1.

## 15.2 Basis in Physics of Sea Surface Temperature Remote Sensing

All remote sensing depends on a remotely observable signal that reflects variations in the phenomenon of interest. To observe SST from space, the radiance at the top of atmosphere must change in response to changes in surface temperature (e.g., Deschamps and Phulpin 1980). Figure 15.2 shows the spectral sensitivity of the top-of-atmosphere brightness temperature (BT,  $y$ ) to SST ( $x$ ) variations – i.e., it is a plot of the variation with wavelength,  $\lambda$ , of  $\partial y_\lambda / \partial x$ . This has been simulated using the physics of thermal radiative transfer encapsulated in a radiative transfer model. Here, the radiative transfer (RT) model makes calculations of the emission, scattering, and absorption of thermal radiation at the surface and through the full vertical profile of the atmosphere, wavelength-by-wavelength. The spectral BT sensitivity has been calculated for an example of mid-latitude and of tropical conditions, in both cases for a cloud-free nadir view of the ocean. A change in temperature of 1 K of an ideal radiating surface (a black body) would change the spectral BT observed by a radiometer (under a vacuum) by 1 K – that is, the sensitivity would be  $\partial y_\lambda / \partial x = 1$ . A change in sea surface temperature leads to a change in BT observed at

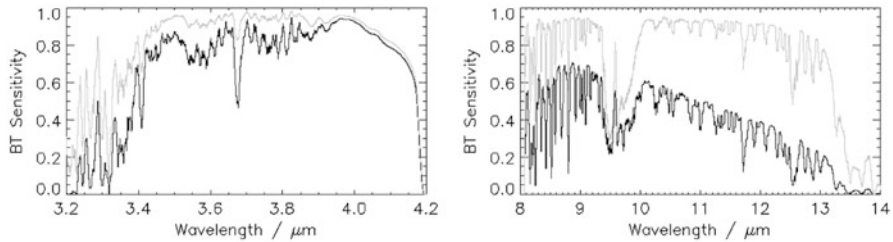


**Fig. 15.2** Spectral brightness temperature (BT) sensitivity (the response at the top of the atmosphere per unit change in surface temperature, in units of  $\text{K K}^{-1}$ ). Grey lines: for a mid-latitude case with low total column water vapour (TCWV). Black lines: for an equatorial case, high TCWV. *Left panel:* a near-infrared window used for SST remote sensing (usually for night-time scenes only), presented at a spectral resolution of  $10 \text{ cm}^{-1}$ . *Right panel:* the mid-infrared window, spectral resolution  $3 \text{ cm}^{-1}$

the top-of-atmosphere that is smaller, because of a number of factors listed and described in Table 15.2. The key point is that sensitivity is high at wavelengths where the atmosphere is relatively transparent to the passage of electromagnetic radiation.

Figure 15.2 presents two parts of the spectrum useful for SST remote sensing: the atmospheric windows in the near infra-red (around  $4 \mu\text{m}$ ), and the mid infra-red (between 8 and  $13 \mu\text{m}$ , albeit interrupted by an ozone absorption feature around  $9.7 \mu\text{m}$ ). Although described as windows, there is variability in sensitivity with wavelength, which would be even more striking if plotted with finer spectral resolution. Within the windows, individual molecular absorption features reduce spectral sensitivity close to zero over narrow intervals of wavelength, while there are also some intervals a few  $\text{cm}^{-1}$  without such lines. An example of the latter is the micro-window at  $2,616 \text{ cm}^{-1}$  ( $3.823 \mu\text{m}$ ). In such micro-windows, the clear-sky attenuation of temperature by the atmosphere can be just a few tenths of degree kelvin (except when the presence of atmospheric aerosols decreases the transmittance). Most sensors from which SSTs are derived, however, have channels of width of order  $100 \text{ cm}^{-1}$ . This allows higher spatial resolution with reasonable noise characteristics, but requires that atmospheric effects must be accounted for when inferring surface temperature (e.g., McMillin and Crosby 1984).

We can expect more accurate, less noisy estimates of SST when using observations with higher sensitivity, other factors being equal. This is because the SST signal is then greater in proportion to instrumental noise and signals associated with variations in the atmospheric state. Sensitivity to SST is greater in mid-latitude conditions than tropical conditions largely because there is less absorption related to water vapour in the atmosphere (Merchant et al. 2009). The near-infrared window maintains relatively high sensitivity even under tropical conditions, and is particularly useful for observing equatorial SSTs. However, this window is usually only used for night-time scenes, because of the complication of significant solar irradiance at these wavelengths during the day. The sensitivity across the mid-infrared window is highly responsive to the total amount of water vapour.

**Table 15.2** Factors that affect the top-of-atmosphere clear-sky spectral brightness temperature and its sensitivity to surface temperature variations

Factor	Nature of influence
Sea surface emissivity	If emissivity is less than 1, emitted radiance is correspondingly less than the ideal Planck (black body) radiance. Sea water emissivity is generally high (0.96–0.99) for near-nadir observations at wavelengths relevant to thermal remote sensing. For flat sea-water, spectral emissivity depends on temperature, salinity and the angle of view (emissivity reduces markedly at angles beyond about 55°). Under wind-roughened conditions the water is not flat, which modifies the effective emissivity as a function of wind speed
Sea surface reflectivity	Downward atmospheric and (for near infra-red) solar radiance can be reflected at the surface. Reflectivity depends on the same factors as emissivity, and increases as emissivity decreases
Radiatively active gases	The surface-leaving radiance is absorbed by gases in the atmosphere, to a greater or lesser degree according to wavelength. In decreasing order of impact on SST remote sensing, the most relevant gases are: water vapour, carbon dioxide, dinitrogen oxide, methane, CFC-12, nitrogen, CFC-11 and nitric acid. These gases also emit radiation by virtue of their temperature. For the most part, this does not wholly offset the absorption, since the atmosphere is mostly colder than the underlying surface. Nevertheless, the effect of the atmosphere is to introduce a source that is not directly dependent on the surface temperature, and therefore to reduce the BT sensitivity. At wavelengths where absorption is very efficient, the BT becomes independent of the surface temperature. Of the significant radiatively active gases, water vapour is by far the most variable
Aerosols	Particles in the atmosphere absorb and emit radiance, as with gases, and may also significantly scatter radiance (in to or out of the view of a satellite). The radiative properties and concentrations of aerosols are much more variable and much less understood than for gases. Aerosol impacts of BTs can range from negligible (in clean air), to highly significant (e.g., dust storms)
Solar radiance	Solar radiance can be reflected by the surface and scattered by the atmosphere into the view of a satellite. This is usually very significant for day time observations at near infra-red wavelengths, and can be marginally significant at longer thermal wavelengths when there is strong specular (mirror-like) reflection (known as sun glint)

Summarized from Embury et al. (2012a)

Thus, when relying on the mid-infrared window for day-time SST, we can expect larger uncertainties for regions of high total column water vapour (TCWV).

The physics of atmospheric radiative transfer for these wavelengths is quantified with great precision in the spectroscopic databases exploited by line-by-line RT models (Rothman 2010). Moreover, the sea surface is relatively simple and homogeneous. The thermal emission and reflection of the surface can also be well simulated. In the absence of significant aerosol, clear-sky RT modelling relevant to typical SST sensors gives BTs that seem to be physically realistic to of order 0.1 K. This is comparable to the calibration uncertainty and noise for “good” SST sensors. Therefore, RT-based approaches to SST estimation are feasible and are currently used in practice, in addition to empirical approaches.

## 15.3 Sea Surface Temperature Retrieval

### 15.3.1 Simple Empirical Estimators

The process of estimating SST from a number of clear-sky brightness temperature observations is usually termed SST retrieval. Most retrieval methods have been based on defining coefficients for a weighted combination of BTs. This is a simple, computationally efficient approach. At least two BTs are required (Anding and Kauth 1970), since it is necessary to infer both the SST (explicitly) and the impact of the atmosphere on BTs (implicitly). The difference SST minus BT is called the atmospheric correction, the idea being that this is the temperature that must be added to the BT to correct the net attenuating effect of the atmosphere. Despite the term, some of the difference is due to non-ideal emissivity of the sea surface.

The minimum of two BT observations required to retrieve SST must be at wavelengths that (i) have adequately high sensitivity to SST and (ii) are differentially absorbed by atmospheric water vapour. Of the relevant absorbing gases in the atmosphere, only water vapour is extremely variable, with total column water vapour (TCWV) varying from almost zero up to  $\sim 60 \text{ kg m}^{-2}$ . The atmospheric correction generally increases with increasing TCWV, and does so more rapidly for wavelengths that are more effectively absorbed by water vapour. Consequently, the atmospheric correction for either of the BTs is approximately linearly related to the difference between the BTs:

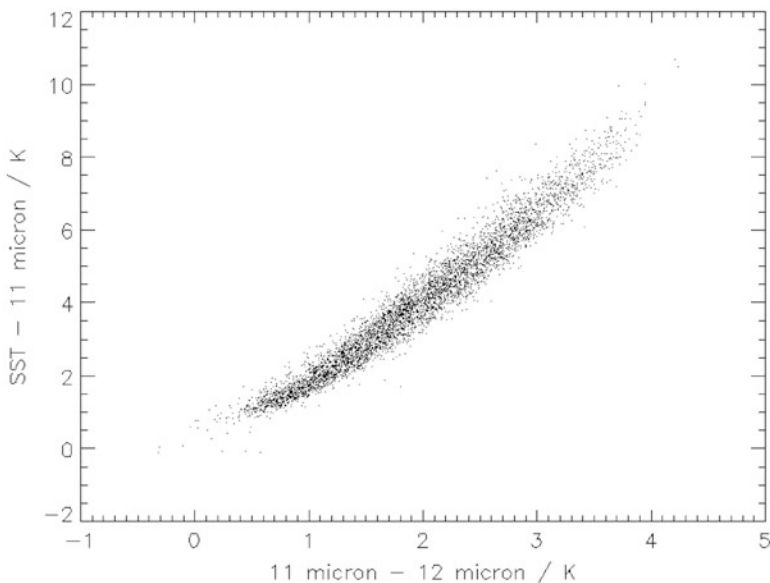
$$x - y_1 \propto y_1 - y_2 \quad (15.1)$$

Figure 15.3 illustrates the degree to which proportionality holds. The SST can thus be estimated by an expression:

$$\hat{x} = a_0 + a_1 y_1 + a_2 (y_1 - y_2) \quad (15.2)$$

where  $a_0$ ,  $a_1$  and  $a_2$  are retrieval coefficients.

Wavelengths between about 10 and 13  $\mu\text{m}$  have high sensitivity that varies progressively across that window (Fig. 15.2), reflecting differential water vapour absorption. This is the principal window used by SST sensors, and is usually split between two channels centred around 11 and 12  $\mu\text{m}$  respectively. Equation 15.2 in this case describes a split window retrieval. This equation and variants of it have been widely used to obtain SST from meteorological sensors (e.g., McClain et al. 1985; Walton et al. 1998). The coefficients need to be specified for each sensor, since the spectral responses of the nominal 11 and 12  $\mu\text{m}$  channels are inevitably somewhat different between sensors. The split window equation is appealing because it is physically intuitive (Barton 1995): the SST is the 11  $\mu\text{m}$  BT scaled up a little to compensate for non-ideal emissivity ( $a_1$  is usually a little more than 1.0), with an offset,  $a_0$ , added (interpreted as compensating for the absorption of non-varying trace



**Fig. 15.3** Nadir atmospheric correction for 11  $\mu\text{m}$  brightness temperatures against difference in brightness temperature between 11 and 12  $\mu\text{m}$  channels, for a typical split-window sensor. Each point represents an observation made at a particular location and time from a global sample. The distribution is close to linear for differences between the 11 and 12  $\mu\text{m}$  brightness temperatures greater than about 1 K. The scatter for a given brightness temperature difference arises from factors such as variable vertical distribution of water vapour, troposphere-sea temperature difference, etc. These factors have systematic geographical variations, which tends to create coherent geographical biases in any SST retrieval based on fitting a function to such a distribution

gases), plus a term that accounts for the highly variable water vapour absorption (whose impact is proportional to the difference between the BTs).

The values of the coefficients have usually been defined empirically, by regression between BTs and matched *in situ* SST observations. This is discussed further in a later section. Here, we review the ways in which the simple split window equation has been elaborated.

The first elaboration is with respect to satellite view angle. The total column of water vapour encountered by radiance passing through the atmosphere on a slant path exceeds the TCWV by an approximate factor of approximately  $\sec(\theta)$ , where  $\theta$  is the satellite zenith angle (angle of the slant path to the vertical at the surface). The degree to which sea surface emissivity is less than 1 increases markedly with angles beyond about 55°. A common approach has been to fit the combined BT impact of these effects by having some coefficients depend on  $S = \sec(\theta) - 1$ , such that  $a_0 \rightarrow a_0 + b_0 S$  etc. (e.g., Walton et al. 1998).

The second elaboration is adaptation to use additional channels. In addition to the split window channels of 11 and 12  $\mu\text{m}$ , BTs observed in the near-infrared window between about 3.6 to 4  $\mu\text{m}$  are useful for SST estimation. BTs in this region

have mainly been used for night-time scenes, when solar-reflected radiance is absent. There is a high degree of sensitivity in this range (Fig. 15.2) to surface temperature, and in addition the dependence of radiance on temperature is extremely steep for terrestrial temperatures  $T \sim 285$  K – around  $T^{14}$ . This strong non-linearity reduces the impact of non-unity emissivity, of contaminants in the field of view such as sub-pixel undetected clouds, and of radiometric noise of a given magnitude. Therefore, on a well-designed sensor, a channel centred at 3.7–3.9  $\mu\text{m}$  can be particularly “clean” for SST, which is a colloquial way of expressing that the information content on SST is very high. Compared to the near-infrared window, the high-sensitivity region around 8.7  $\mu\text{m}$  behaves more similarly to the usual 11 and 12  $\mu\text{m}$  channels. Nonetheless, it can be useful if present.

Inclusion of additional BTs has been done using various equations, most of which can be re-expressed in the form:

$$\hat{x} = a_0 + b_0S + \sum_i (a_i + b_iS)y_i \quad (15.3)$$

Some investigators impose additional restrictions on the empirical fit of the coefficients in Eq. 15.3 by choosing specific forms of equation (e.g., Li et al. 2001). For example, a three-channel algorithm with form:

$$\hat{x} = a_0 + b_0S + (a_1 + b_1S)y_{3.7\mu\text{m}} + a_2(y_{11\mu\text{m}} - y_{12\mu\text{m}}) \quad (15.4)$$

is Eq. 15.3 with the additional constraints that  $a_2 = -a_3$  and  $b_2 = b_3 = 0$ . Sometimes a physical argument is put forward to justify a specific form of equation. Imposing such additional constraints may seem at odds to adopting an empirical approach to determine coefficients, but if the empirical dataset relating BTs and SSTs is small, imposing such additional constraints may avoid over-fitting. Additional constraints can also modify the sensitivity of the estimator to factors such as atmospheric aerosols (discussed further below).

As well as observations at additional wavelengths, “channels” can be added by having sensors view the sea surface at more than one view angle, i.e., near-nadir and off-nadir (forwards or backwards along the track).

The third elaboration relates to use of non-linear terms. The residuals (retrieved minus *in situ* SSTs) of purely linear estimators such as Eq. 15.3 usually display coherent systematic variations if plotted against latitude, longitude-within-a-latitude-zone, TCWV, BT differences, and so on. These reflect the non-linearity evident in Fig. 15.3, and sensitivity to geographical variations in the broad vertical structure of water vapour and temperature in the atmosphere. A wide range of non-linear estimators have been proposed, for example:

- banding of coefficients by latitude or other regional optimisation (e.g., Minnett 1990)
- banding of coefficients by BT difference (e.g., Kilpatrick et al. 2001)

- banding of coefficients by prior TCWV or retrieved TCWV (e.g., Barton 2011)
- inclusion of a term that modifies coefficients via a prior SST (e.g., Pichel et al. 2001)
- quadratic dependence on BTs or prior TCWV (e.g., Emery et al. 1994)

These generally offer modest benefit to retrieval accuracy. Simple functional forms do not reflect the underlying origins of the systematic residuals, which are the non-linearity of the physics of RT and geographical variations in atmospheric structure (Merchant et al. 2006).

The final elaboration is to use alternative regression methods. The usual means of defining retrieval estimators empirically has been ordinary least squares fitting (multiple linear regression). Neural nets in principle seem an attractive way to deal with the non-linear aspects of the retrieval problem, but are yet to demonstrate good success. ‘Genetic’ algorithm identification seems to converge on a form rather similar to the split window formulation.

### **15.3.2 Approaches Involving Radiative Transfer Modelling**

Progress has been made in recent years using RT modelling to improve retrieval accuracy and precision.

The main use of RT has been to define coefficients that look rather like the simple empirical estimators discussed above. Instead of empirical matches between *in situ* SST measurements and satellite observations, RT-based coefficients are derived by regressing simulated BTs to the SSTs used as input to the simulations. The simulations are driven using atmospheric profiles obtained from radiosondes or numerical weather prediction (NWP) systems. The RT-based approach is compared to the empirical approach in Table 15.3.

One strength of approaching SST retrieval with RT simulations is the enhanced ability to diagnose and solve problems. An example is how to adapt SST retrieval to the presence of stratospheric aerosol (Merchant et al. 1999). Occasionally, major volcanic eruptions penetrate the stratosphere and create a haze of sulphuric acid droplets that persists at altitudes of order 20 km for a year or two. This stratospheric aerosol layer has climatic impacts, and also affects remote sensing at visible and infra-red wavelengths. The aerosol absorbs infra-red radiation, and causes BTs to be reduced. Let’s assume that the impact per unit aerosol optical depth,  $\tau$ , on the BTs of a typical three-channel sensor is  $\frac{\partial \mathbf{y}}{\partial \tau} = \left( \frac{\partial y_{3.7\mu m}}{\partial \tau} \frac{\partial y_{11\mu m}}{\partial \tau} \frac{\partial y_{12\mu m}}{\partial \tau} \right)^T$ . Here, and hereafter,  $\mathbf{y}$  is used for a column vector containing the BTs to be used in a SST retrieval. For a given observation (at a particular view angle etc.), the retrieval equation can be conveniently written also using vector notation as:

$$\hat{x} = a + \mathbf{a}^T \mathbf{y} \quad (15.5)$$

**Table 15.3** Contrasting advantages and disadvantages of deriving SST retrieval coefficients by empirical means compared with derivation by radiative transfer simulation

Aspect	Empirical approach	RT-based approach
Instrument calibration and characterisation	Reduced need to understand instrument characteristics and calibration, since many calibration issues are empirically accounted for in the coefficients	Need sensor to be well characterised (accurate spectral response functions available) and calibrated (ideally to $\sim 0.1$ K). In absence of this, significant effort is required to bias-correct simulated BTs to match observations
Spatio-temporal sampling (representativity)	Can only match locations where <i>in situ</i> measurements are already present. This gives no formal basis for assessing the accuracy of retrieved SSTs in areas/periods with few or no <i>in situ</i> measurements. <i>In situ</i> coverage has greatly improved since the early 2000s, but high latitude seas remain under-represented	The spatio-temporal sampling is in the control of the investigator. Access to an NWP re-analysis provides a consistent atmospheric data set that can be sampled across all epochs and with no gap regions
Nature of sea surface temperature	Satellite SSTs are regressed to the SST at the depth typical of the <i>in situ</i> measurements (tens of cm in the case of drifting buoys). However, BTs are sensitive to skin SSTs. Thus, empirical methods conflate different forms of SST that do not bear a simple relation to each other. An approach which addresses this issue is to restrict the regression cases to those where skin-depth differences are thought to be well understood (e.g., moderate wind stress at night)	The simulation can be done using skin SST. The coefficients are then unambiguously retrieval coefficients for skin-SST, the geophysical variable to which the BTs are sensitive
Independence from <i>in situ</i> data sets	No independence (fully tied to <i>in situ</i> )	Independence possible for best characterized instruments. For reasonably well calibrated instruments, RT-based coefficients can be tuned by adjusting only the offset coefficient
Difficulty of defining algorithm	Requires a statistically sound number of satellite- <i>in situ</i> matches (for every required stratum of latitude/TCWV/view angles/etc.). Implies no retrieval scheme is available at launch	Requires a RT simulation capability, sampled NWP profiles, and commensurate computing power. Retrieval scheme can be defined prior to launch

See also Merchant and Le Borgne 2004

where, compared to Eq. 15.3,  $a = a_0 + b_0S$ ; the first element of the coefficient column vector,  $\mathbf{a}$ , is equal to  $a_1 + b_1S$ ; and so on. The summation in Eq. 15.3 is achieved in Eq. 15.5 by the matrix multiplication of row vector  $\mathbf{a}^T$  and the column vector  $\mathbf{y}$ . Use of matrix algebra may at first seem unnecessary, but is a powerful tool for expressing and analysing retrieval algorithms. Written in this form, it is clear that the impact of the stratospheric aerosol on the retrieved SST will be:

$$\delta\hat{x} = \tau\mathbf{a}^T \frac{\partial\mathbf{y}}{\partial\tau} \quad (15.6)$$

at least over the range for which the BT depression is linear in the optical depth. Using radiative transfer,  $\partial\mathbf{y}/\partial\tau$  can be calculated from knowledge of the properties of the sulphuric acid droplets (concentration and size distribution). Knowing this, the different sensitivities to stratospheric aerosol of different retrieval formulations can be understood using Eq. 15.6. Moreover, we readily formulate the requirement for an SST retrieval algorithm to be robust (i.e., insensitive) to stratospheric aerosol. It is:

$$\mathbf{a}^T \frac{\partial\mathbf{y}}{\partial\tau} = 0 \quad (15.7)$$

This property can be designed into retrieval coefficients by imposing Eq. 15.7 as a linear constraint when deriving coefficients by regression. This has been done successfully for a dual view sensor in relation to the major eruption in 1991 of Mount Pinatubo in the Philippines (Merchant and Harris 1999). The addition of an extra constraint like this means that a useful set of robust coefficients can only be found for three or more channels (at different wavelengths and/or view angles). The relationships between other perturbations to observed BTs and the resulting SST bias can be analysed with a similar approach. This illustrates that understanding a retrieval problem by simulation can lead to useful insights.

More recent RT-based approaches emphasize simulation of BTs for the particular context of an observation (rather than for a spatio-temporal sample, as when defining coefficients). To achieve this in near-real time, an operational centre requires routine access to NWP forecast fields and a fast simulation capability (Le Borgne et al. 2011). For retrospective processing, NWP re-analysis fields may be used. Either way, a prior estimate for the BT based on simulation is obtained for every satellite pixel. These simulated BTs can then be used in a variety of ways to give improved SST estimates.

If simulated BTs,  $\mathbf{y}_b$  (where subscript  $b$  indicates BTs simulated using prior or ‘background’ information), are used with SST retrieval coefficients, a simulated SST estimate is obtained  $\hat{x}_b = a + \mathbf{a}^T \mathbf{y}_b$ . But the simulation of  $\mathbf{y}_b$  assumes a background SST as input to the RT model,  $x_b$ . The difference  $\hat{x}_b - x_b$  is then an estimate of retrieval bias for the circumstances of the retrieval (i.e., for the circumstances embodied in the NWP information). If this is a good SST bias

estimate, then an SST estimate,  $\hat{x}'$  that improves upon the original estimate,  $\hat{x}'$  can be obtained:

$$\hat{x}' = \hat{x} - (\hat{x}_b - x_b) = x_b + \mathbf{a}^T(\mathbf{y} - \mathbf{y}_b) \quad (15.8)$$

Practical experience has shown that this is indeed a beneficial extension to coefficient based retrieval, reducing geographical biases and the standard deviation of discrepancies in validation (Le Borgne et al. 2011). It requires that simulated and observed BTs have, if necessary, been tuned to have no relative bias on average. Equation 15.8 shows that simulation-based bias correction (central expression) is equivalent to adjusting the background SST in the light of the discrepancy between observed and simulated BTs (rightmost expression).

In the above approach, the coefficients,  $\mathbf{a}$ , are defined as retrieval coefficients that operate on BTs in the usual way. A further alternative is to keep essentially the same equation (adding only an offset coefficient), and then to redefine coefficients specifically for an ‘incremental’ retrieval (Petrenko et al. 2011). This involves regressing differences between background and *in situ* SSTs against differences between matched BT observations and simulated BTs. The relative calibration of sensor and forward model is empirically included within the incremental coefficients in this approach.

Despite their practical successes, none of the above methods (whether purely empirical or including RT) is formally optimal when viewed from the standpoint of inverse theory (Rodgers 2000). Inverse theory gives a coherent framework for analysing SST retrieval as an inverse problem, in terms of a fundamental understanding of how much information is truly present about SST in a given set of BTs. Different ‘optimal estimates’ of SST can, in principle, be defined, that optimize clearly defined aspects of the SSTs obtained. Where the information content of the observations is high for SST, a useful estimator is the maximum likelihood (ML) estimate, which returns the most likely SST given the observations. In an ML retrieval, the background information is used, effectively, as a linearization point for an incremental retrieval with context-specific coefficients (derived dynamically using RT). However, for a traditional split window retrieval using 11 and 12  $\mu\text{m}$  channels, the ML estimate is not always useful, particularly in tropical regions and/or at high satellite zenith angle when the 12  $\mu\text{m}$  channel in particular becomes nearly insensitive to SST in comparison to observational noise. In these circumstances, the BTs fundamentally contain insufficient information on SST to obtain a good retrieval without relying on prior information. (This prior information may be embedded in empirical retrieval coefficients or explicitly represented by NWP profiles – either way, its presence is unavoidable.) Thus, for split window retrieval, an appropriate optimal estimate is the maximum a posteriori (MAP) estimate. A simplified MAP formulation has been shown to be useful for split window retrieval (Merchant et al. 2008). A further benefit of optimal estimation techniques is that they naturally output a goodness-of-fit indicator that gives useful insight into retrieval quality.

For a truly optimal MAP retrieval, several relatively onerous conditions need to be met, including an unbiased RT simulation capability (for both BTs and their partial derivatives) and a thorough understanding of instrumental noise and background error characteristics. In some areas of thermal remote sensing – nadir sounding of trace gases in the atmosphere, perhaps – the inverse problem is sufficiently delicate that a formal optimal approach is virtually obligatory. In the case of SST, strong practical success has been obtained for three decades using more direct, intuitive methods. Nonetheless, renewed interest in driving down SST retrieval uncertainties and in understanding biases has prompted new activity in exploiting RT and in optimal estimation.

### 15.3.3 Evaluating SST Retrievals

The quality of an SST retrieval scheme is typically evaluated in validation by considering ‘error statistics’, usually the mean and standard deviation of discrepancy between the satellite and matched *in situ* SSTs (e.g., Donlon et al. 2009). The mean discrepancy is often interpreted as ‘bias’, but this needs to be done with care. There are real geophysical differences to be expected between satellite and *in situ* measurements (and between different types of *in situ* measurements). No measurements are perfect, and the validation data (*in situ* measurements) can also contribute errors to the discrepancy between satellite and *in situ*. Here, ‘bias’ is avoided in preference to the more descriptive term ‘mean discrepancy’.

Between the mid-1990s and the mid-2000s, drifting buoys that routinely report SST became progressively more numerous (Meldrum et al. 2010). For recent years, it is possible to calculate a statistically sound, geographically resolved mean discrepancy compared to drifting buoys for most of the global oceans (Fig. 15.4). This is a great benefit to development of SST remote sensing. The uncertainty of SST calibration across the ensemble of drifting buoys seems to be about 0.2 K (1  $\sigma$  value; Castro et al. 2012), so in regions of Fig. 15.4 where only a few different drifting buoys have contributed, the mean discrepancy could reflect buoy calibration errors rather than systematic error in satellite SST. In principle, the thermistor technology used in drifting buoys could be calibrated to better than 0.05 K uncertainty (on deployment). New requirements for estimating SST for climate (see later) arguably justify the expense associated with this improvement in the drifting buoy programme. Nonetheless, with the current drifting buoy network, geographical biases in satellite SST can now be inferred (with due care and interpretation) from maps of mean discrepancy covering a long enough time period. Figure 15.4 is based on 20 years of observations (1991 to 2011), with most matches being obtained in the last decade. The satellite SSTs are from a reprocessing for climate of Along Track Scanning Radiometer observations. The mean discrepancy maps have credible structure on length scales of 1,000 km for a large part of the ocean. There is a noticeable variation in bias along the equator seen in Fig. 15.4, particularly with negative biases in the tropical Atlantic. Similar or larger biases in tropical SSTs are

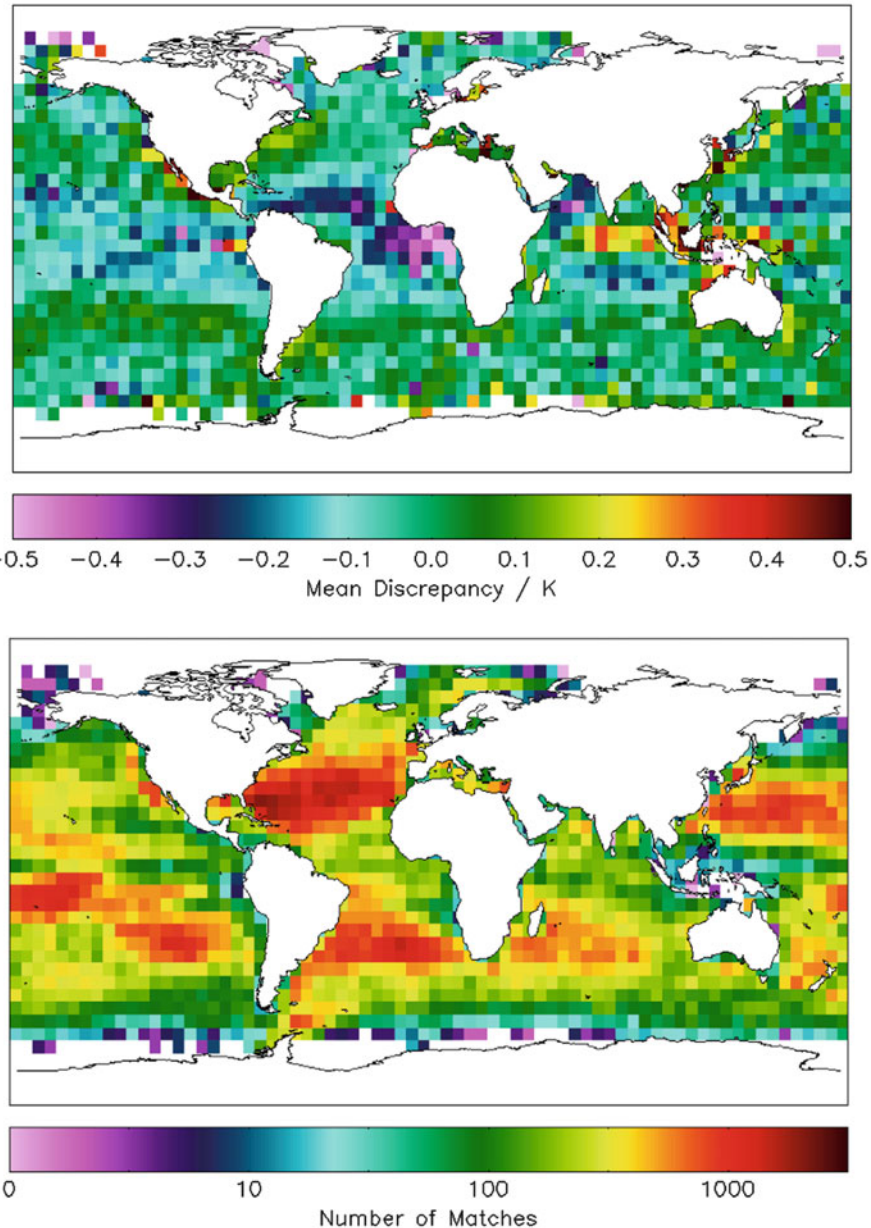


**Fig. 15.4** *Upper panel:* Mean discrepancy map for a single-view split-window SST estimator, adjusted for the SST skin effect and near-surface stratification, relative to drifting buoy SST. This is an estimate of the geographical variation in bias in the SST estimates. The SSTs are for the “nadir two-channel” retrieval for all matches found for a series of three Along Track Scanning Radiometers (ATSRs) between 1991 and 2011. (Note that the ATSRs are dual-view sensors; the geographical variations seen here in the tropics are greatly reduced when taking advantage of dual-view capability.) *Lower panel:* number of ATSR/drifting-buoy matches obtained over two decades. The marked variation in density of matches arises from the combination of drifting buoy deployment patterns and prevalence of cloud cover. Matches are particularly few in the highest latitudes and the tropical warm pool (round Indonesia), where both these factors are unfavourable

a common feature of retrieval of SST by coefficients using the split-window channels in a single view (e.g., Merchant et al. 2009).

The precision of satellite SSTs refers here to the retrieval-error standard deviation. The information available to assess precision includes maps of standard deviation of discrepancy. The values in this measure are an upper limit on precision, since the *in situ* observations errors contribute to the spread of discrepancy. Assuming enough different drifting buoys contribute to a particular calculation of standard deviation of discrepancy, the satellite SST precision can be approximately inferred.

In the context of climate applications of SST, an important quality is stability (e.g., GCOS 2006). Stability is the constancy in time of the SST bias, or, equivalently, the additional uncertainty on any calculated climatic trends arising from (unknown) drift of the calibration of the observing system. The current *in situ* observing system is not well equipped for assessment of stability of satellite SSTs since the SST calibration of drifting buoy and other *in situ* deployments has not been controlled with stability in mind. Long-term deployments of well-calibrated moorings in tropical seas (initially to monitor the El Niño region, and now worldwide; McPhaden et al. 2010) are useful for assessing stability, although geographically limited (Merchant et al. 2012). More recent near-surface (~5 m) measurements from Argo profiling floats (Freeland et al. 2010) may prove a useful global reference for stability as a longer time series accumulates. The ideal for the long-term would be a network of SST reference sites of known, controlled stability, distributed at locations selected to allow assessment of global stability of SST. Research is needed to optimize such a network of reference sites to be effective and cost-effective. At reference site locations, both radiometric and sub-surface measurements of SST should be considered (Minnett and Corlett 2012).

A further parameter to evaluate satellite SST is SST sensitivity (Merchant et al. 2009). SST sensitivity is the fractional response of the retrieved SST to variation in true SST, other factors (such as the atmospheric state) being equal. Ideally, the sensitivity should be  $1 \text{ K K}^{-1}$ , so that a true change in SST causes an identical change in retrieved SST. In general, this is not the case (Fig. 15.5).

SST sensitivity is readily calculated for a coefficient-based retrieval as

$$\frac{\partial \hat{x}}{\partial x} = \mathbf{a}^T \frac{\partial \mathbf{y}}{\partial x} \quad (15.9)$$

where the partial derivatives of BTs are calculated using RT simulation. (Readers familiar with atmospheric sounding will recognize that the averaging kernel is an indispensable tool for interpreting remotely sensed atmospheric profiles. In retrieving SST by optimal estimation, sensitivity is the diagonal term corresponding to SST in the averaging kernel matrix).

Where sensitivity of an SST estimate is much less than  $1 \text{ K K}^{-1}$ , it is expected that the strength of ocean thermal gradients is underestimated (an expectation that requires further validation at the time of writing). Likewise, diurnal variations in SST are attenuated by low-sensitivity estimators (Merchant et al. 2013). Moreover, the SST sensitivity has a deep connection to the information content of the BTs

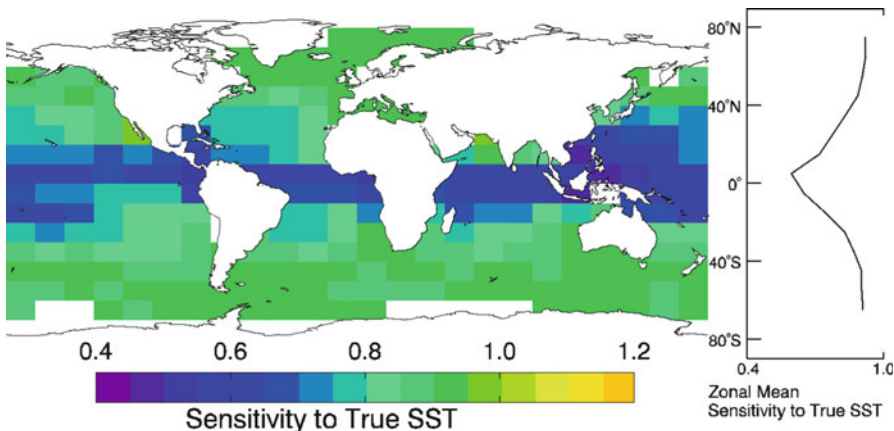


**Fig. 15.5** Change in retrieved SST per unit change in true SST, all other factors being held constant, for a split window SST estimate (non-linear SST retrieval applied to the Advanced Very High Resolution Radiometer on Metop-A (Meteorological Operational Satellite)) (Reproduced from Merchant et al. (2009) with permission)

(Rodgers 2000). SST sensitivity is low when low BT sensitivity to SST reduces the signal-to-noise ratio, in which case the retrieval must depend more heavily on prior SST information. (The prior information may be explicit, as in optimal estimation, or may be implicitly embedded in SST retrieval coefficients.) Thus, the sensitivity can also be interpreted as the fraction of the information in a particular SST estimate that comes from the BTs. Figure 15.5 therefore illustrates the point made previously that typical split-window retrievals rely significantly on prior information in the tropics.

## 15.4 Meanings of ‘Sea Surface Temperature’

It is a general issue in remote sensing that the remotely sensed quantity is not identical to measurements made *in situ* of nominally the same quantity.

In the case of SST, a lot is understood about how different ‘sea surface temperatures’ relate. This understanding is the fruit of research cruises (e.g., Minnett et al. 2011) and profilers (e.g., Ward et al. 2004) that have undertaken intensive multiple observations, and of modelling the near-surface ocean and atmosphere using fundamental physics.

The thermal emission from the sea surface comes from a layer whose characteristic depth varies with wavelength (because the complex refractive index of water varies with wavelength; e.g., Hanafin and Minnett 2005). The radiometric skin depth is  $\sim 10 \mu\text{m}$  at wavelengths around  $12 \mu\text{m}$ , and  $\sim 100 \mu\text{m}$  at wavelengths around

4 µm. As well as this radiometric skin, the ocean surface also has a thermal skin. Heat can be transported through this thermal skin only by molecular heat diffusion, and not via the turbulent motions that are effective in moving heat within the bulk of the fluid. Heat flux is usually from ocean to atmosphere. A temperature gradient must be present within the thermal skin to transport heat via molecular diffusion. For a typical ocean-atmosphere heat flux, the drop in temperature across this thermal skin is of order 0.2 K. The radiometric temperature of the sea surface differs from the thermodynamic temperature of water below the diffusive layer (the ‘sub-skin SST’) both because the sea surface emissivity is less than 1, and because the temperature of the water within the radiometric skin depth is actually different from (usually cooler than) the sub-skin SST.

The sub-skin SST can be very close to the SST measured by drifting buoys (at a depth of order 20 cm), moored buoys (typically of order 1 m depth) or the top observation of conventional Argo profiles (around 5 m). Sub-skin SSTs and *in situ*-depth SSTs are equal when the near-surface is not thermally stratified, reflecting efficient mixing of the near-surface water by wind action. Although near-surface stratification is often small compared to SST uncertainties, it is sometimes considerable (e.g., Clayson and Weitlich 2007). Stratification that causes sub-skin to *in situ*-depth SST differences may be caused by heavy rainfall creating a fresh ‘lens’ of water of a different temperature on the sea surface. However, near-surface stratification has been most clearly observed in satellite SSTs when caused by diurnal warming (e.g., Gentemann et al. 2008).

During the day, sunlight preferentially heats the upper centimetres to metres of the ocean, because most wavelengths of sunlight are absorbed by seawater over such distances. In the absence of wind, this will tend to cause a warm near surface layer – that is, it thermally stratifies the water (Fairall et al. 1996). Under persistently calm conditions (wind speed less than 1 or 2 m s<sup>-1</sup>), this effect can warm the sub-skin SST by 6 or 7 K between sunrise and early afternoon (e.g., Gentemann et al. 2008). Wind action tends to act against stratification, by mixing the heat down, and an increase of wind can fairly rapidly erode diurnal stratification. Under wind speeds of about 6 m s<sup>-1</sup> or more, the peak amplitude of the diurnal cycle in sub-skin SST is no more than a few tenths of kelvin.

In summary:

- The ocean thermal skin effect is generally present, so the skin SST is different (usually cooler) than the sub-skin SST. Measurements by thermal remote sensing are sensitive to this skin SST.
- The difference between sub-skin SST and SST at depths measured by drifting and moored buoys can range from negligible (e.g., night-time, windy conditions) to several degrees (high-insolation, sustained low-wind-speed conditions).

Satellite SSTs obtained using coefficients derived by regression to drifting buoys are sensitive to skin SSTs, but are tuned to remove the mean skin-depth difference present in the matched data set. This ignores the true variability of skin – depth differences, which then becomes part of the error budget for the satellite SST estimate.

Some investigators have restricted the *in situ* observations used for deriving empirical coefficients to situations likely to have negligible stratification. This can be done by specifying that the wind speed around the time of the satellite–*in situ* match must be above a threshold. The satellite SSTs can then be justifiably described as estimates of sub-skin SST on average, since the mean skin – sub-skin difference is tuned out.

Satellite SSTs retrieved using RT methods should return a true skin SST. This has the merit that the estimated quantity is the quantity to which the observations are sensitive. To compare such satellite SSTs to others then requires explicit account to be taken of skin – sub-skin and sub-skin – depth differences. This can be done using physical models (e.g., Kantha and Clayson 1994) driven by heat flux and wind speed over the diurnal cycle (e.g. from NWP) to obtain an adjustment between skin (satellite) and depth (*in situ*) SST (e.g., Embury et al. 2012b). The complication with this approach is that any discrepancy after such an adjustment could arise from model errors as well as observational errors.

The discussion above focusses on geophysical differences in SST with respect to depth. Horizontal variability in SST is also important. *In situ* observations give the SST at a point in space. Satellite SSTs are estimates over an area of typically 1–30 km<sup>2</sup>. Thus, there is point-to-pixel sampling variability in any satellite – *in situ* comparison. Specialist research cruises and a few automated systems make radiometer measurements of SST. Radiometer measurements are attractive to compare with satellite SSTs because both respond to the skin SST, removing ‘vertical’ variability. Point-to-pixel issues remain in such comparisons, however (e.g., Wimmer et al. 2012). For both radiometer and well-calibrated subsurface SST, it seems to be difficult to reduce satellite – *in situ* discrepancies from geophysical variability to less than about 0.1 K (Castro et al. 2010).

## 15.5 The Wider Context for Thermal Remote Sensing of SST

### 15.5.1 Operational SST Production

To support weather forecasting (numerical weather prediction, NWP) and near-real time oceanography, SSTs are produced operationally (Donlon et al. 2010). This means regional-to-global, near-real time, high-availability, continuous generation and distribution of SST products. The requirements on timeliness and availability and the volume of data flow involved mean that operations tend to be undertaken by major agencies that can maintain 24 h/day functions. The ultimate quality of SST products depends as much on the steps relating to calibration of observations and cloud-detection as on the SST retrieval itself.

Users of operational SST are varied. Some require visual interpretation of SST images, perhaps to locate fronts in real time. Such users may prefer ‘level 2’

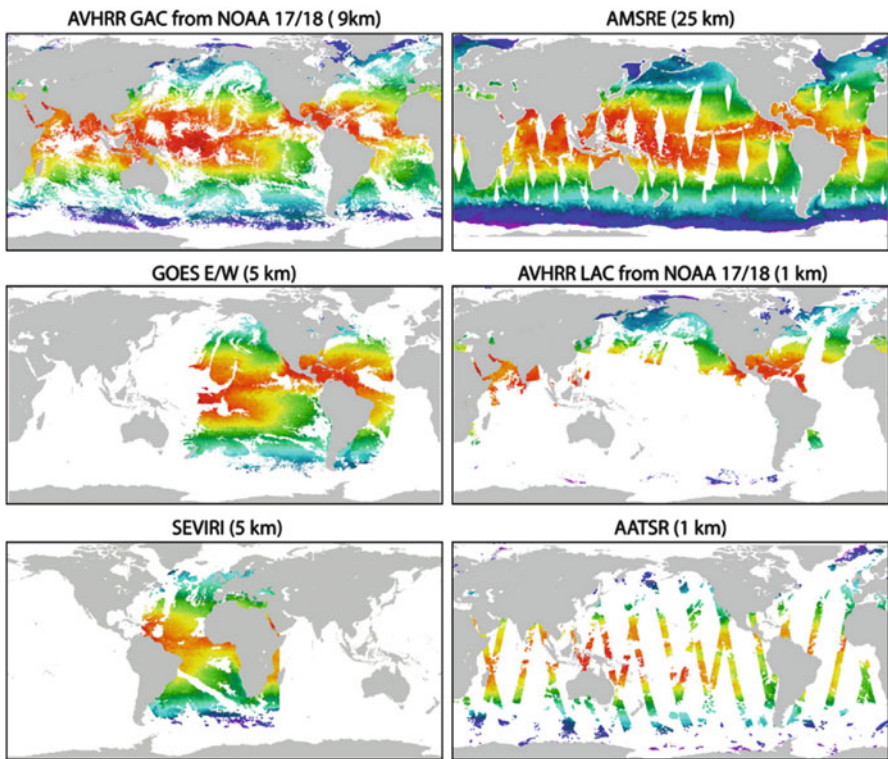


**Fig. 15.6** Typical example of the daily coverage of SST from six different SST data products, at different spatial resolutions, all from the same day (Reproduced from Robinson et al. 2012. With permission)

imagery, where the SSTs are presented on the geographical locations at which they were observed (for the clear-sky areas available). Other users, requiring reduced data volumes and/or more convenient formats, prefer ‘level 3 products’, in which there is some regridding, and averaging or compositing in space and time. A level 3 product might comprise, for example, the daily average on a regular latitude-longitude grid of all the observations within each grid cell taken by a particular sensor.

For many applications, a spatially completed, gridded field is necessary – referred to as an ‘analysis’ or as a ‘level 4 SST product’. To improve the spatial sampling above that observed by a single sensor, blending data from multiple sources is usually performed for level 4 production (e.g., Reynolds et al. 2007; Donlon et al. 2012). This may include *in situ* observations and passive microwave (PMW) SSTs as well as SST from thermal remote sensing. Even so, spatio-temporal gaps will exist, requiring interpolation (gap-filling) – see Fig. 15.6.

There are many approaches to SST analysis (combining data to cope with the different types of data, with different resolutions, gaps, uncertainties and biases).

Irrespective of the method, the process of analysis will tend to create an SST field that, to a greater or lesser degree, has certain limitations. The analysis SST will tend to have poorer resolution of thermal features than the highest resolution data used in the analysis (i.e., thermal gradients and contrasts will tend to be reduced by the analysis process). The results of the analysis are sensitive to the assumptions made about the relative uncertainties of different data sources, and the treatment of bias correction. The SST estimates given in the absence of observations (filling data gaps) are based on assumptions about the correlations of the unobserved SST anomalies to those observed nearby in time and space. Features in gap-filled areas may differ systematically from reality. In general, the SST error statistics across the analysis are far from uniform, although this variation is sometimes neglected in applications. These caveats have to be traded against the practical usefulness of having a spatially complete SST estimate.

Weather and ocean forecasting are major routine applications of near-real time SST products. The atmosphere and ocean interact, exchanging heat, mass (evaporation and rain) and momentum; in maritime climates, air temperature and humidity are partly determined by upwind SST. Surface winds interact with ocean thermal fronts, with the influence of SST changes propagating through the troposphere (Chelton et al. 2001). Meanwhile, cloudiness (via the strength of surface solar heating) and wind affect processes of mixing and stratification in the upper ocean. Numerical simulations for weather forecasting up to several days ahead are, at present, generally performed assuming the most recent level-4 SST analysis as a fixed boundary condition for the bottom of the atmosphere.

### ***15.5.2 SST Production for Climate Services***

Table 15.4 lists some uses of SST products in the realm of climatology and climate services.

The demands on SST accuracy and stability for climate applications are onerous (GCOS 2011). Consistent SST data sets for climate applications have often been provided via reprocessing projects (e.g., Kilpatrick et al. 2001; Merchant et al. 2012). In such a project, an SST record for a particular time period is generated by re-deriving SST from the input satellite (and perhaps *in situ*) data streams in a manner that is consistent, and, hopefully, an improvement over previous products. However, some of the climate-related applications in Table 15.4 are developing into climate services that require an estimate of the thermodynamic state of the ocean that is constantly updated, while simultaneously being of ‘climate quality’ and consistent with a climate data record going back in time. An example is ‘seamless’ prediction of long-range weather, seasonal tendencies and future climate scenarios. This will require systems capable of delivering ‘climate quality’ SST with a relatively short delay from the time of acquisition (perhaps a few days).

**Table 15.4** Established uses of SST in climatology

Use	Purpose(s)	Comments
Quantifying SST/ climate variability and trends	Baseline knowledge of behaviour of atmosphere-ocean system, including geographical patterns of SST variability and corresponding weather anomalies. Assessment of long-term changes, including those associated with human forcing of climate	Of order 100 years of SST required for variability at multi-annual and decadal scale, and for climate trend analyses. In satellite era, this can be addressed with much greater spatiotemporal detail than in pre-satellite era. Satellite SSTs are helpful in establishing modes (spatial patterns) of variability that can be exploited in filling gaps in historical data (“historical reconstruction”)
Detection and attribution of climate changes	Assessment of climatic trends that are ‘stand out’ above climatic variability. Comparison of spatio-temporal progression of SST with expected evolution under different agents forcing change, to attribute which forcings have caused observed trends	Usually requiring historical reconstructions of SST fields over of order 100 years
Boundary condition of atmospheric reanalyses	Atmospheric reanalysis use a numerical weather prediction system retrospectively to infer the best estimate of past weather	Reanalyses to date generally rely on prescribed, spatially complete SST fields. For recent decades these rely heavily on remotely sensed SST. Reanalyses are useful in generating consistent estimates of air-sea fluxes of heat and precipitation, amongst numerous other applications
Boundary condition of climate model runs	Verification that climate models reproduce historical (e.g., twentieth century) climates when driven with best estimate SSTs	SST field is prescribed, while atmosphere and land components evolve in the climate simulation in response. The ability to reproduce the land climate of the 20thC given prescribed SST has been viewed as a basic test for validity of a given climate model
Climate prediction	Forecasts from seasonal to decadal scales of the statistics of future weather	Requires a coupled climate model (one in which ocean is interactive, not prescribed). Relatively slow response time of ocean mixed layer gives some level of predictability for seasonal forecasting. Seasonal forecasting requires that the simulation starts with as realistic as possible an estimate of state of the ocean (accurate ‘initialisation’). On timescales of decades, predictability comes from

(continued)

**Table 15.4** (continued)

Use	Purpose(s)	Comments
Climate-ecological interactions	Research into the responses of plankton, fish and corals to SST variations	dominance of the influence of forcings over internal variability Important in understanding present and future productivity and ecological health of the oceans

### 15.5.3 International Co-operation

There is a well-developed framework of international co-operation in operational remote sensing of SST involving many agencies worldwide. The Group for High Resolution SST (GHRSST) co-ordinates sharing of tasks, including routine inter-comparison of SST products, archiving and product distribution (Donlon et al. 2009). Common standards and data formats have been developed to increase the ease of use of SST from different sources. GHRSST also gives a forum in which the science of SST remote sensing is debated and advanced.

At time of writing, GHRSST has a project office supported by the European Space Agency and is formally linked to the Committee on Earth Observation Satellites (the international forum for co-ordination of civil remote sensing). At the GHRSST web site, see [URL2](#), links to operational and archive products (levels 2, 3 and 4) are available, with routinely updated visualizations of SST products and analyses (Martin et al. 2012; Dash et al. 2012), etc.

### 15.5.4 The SST Sensor Constellation and SST Analysis

Table 15.5 illustrates the constellation of SST relevant sensors. Different classes of sensors/platforms have complementary technical capabilities and roles, with strengths in providing different aspects of the user requirements for remotely sensed SST. For example: geostationary sensors are well suited to resolve sub-daily variability in SST, complementing the higher-resolution less-frequent observations from lower-altitude polar orbiting instruments; dual-view sensors can give higher SST accuracy, but have poorer sampling because a dual-view swath width is unavoidably narrower than that for a traditional single-view imager. (The examples given in Table 15.5 do not include any SST-capable instruments whose products are not included within the GHRSST co-operative framework, although several such instruments are in flight.)

An important complement to the thermal sensing constellation is an SST capability at microwave frequencies (Wentz et al. 2000). Passive microwave (PMW) sensors have some limitations relative to thermal remote sensing using infra-red (IR) wavelengths. First, PMW SSTs have lower spatial resolution. Because the size of footprint of a PMW sensor with a given antenna is inversely related to frequency,

**Table 15.5** Categories of infra-red SST sensors and examples used within the GHRSST framework

Orbit	Channels	View	Role(s) in constellation	Example(s)
Geostationary	Split-window and near-IR (broad channels)	Fixed view of visible Earth disk	High temporal sampling: resolves diurnal cycle; maximizes spatial coverage by tracking gaps in cloud	Spinning Enhanced Visible and Infra-Red Imager (SEVIRI)
Polar	Split-window and near-IR (broad channels)	Single view, across track	Near-global coverage on daily basis including high latitudes (before cloud screening). Main operational meteorological sensors, usually at least two in orbit (morning and afternoon)	Advanced Very High Resolution Radiometer (AVHRR)
Polar	As above plus additional SST relevant channels	Single view, across track	Extended capability relative to AVHRR-like channel set	Moderate-resolution Imager Spectroradiometer (MODIS), near-IR bands centred on 3.95 and 4.05 $\mu\text{m}$
				Visible/Infrared Imager Radiometer Suite (VIIRS)
Polar	Split-window and near-IR (broad channels)	Dual-view, across and along track	High-accuracy SST for climate and/or SST calibration reference. Poorer sampling from narrower swath. Greater robustness to aerosol contamination with dual view	Advanced Along-Track Scanning Radiometer (AATSR) Sea and Land Surface Temperature Radiometer (SLSTR, from c. 2015)

it is difficult to define a single resolution for the multi-frequency PMW retrievals; a reasonable indication is an area of order 2,500  $\text{km}^2$ , which is obviously a much greater than the 1–100  $\text{km}^2$  typical of IR imagers. Second, PMW SSTs are not available or have much increased uncertainty within about 50 km of land and sea-ice, because of sensitivity to the land or ice emission in the side-lobes of the antenna pattern. Third, PMW SSTs to date have to SST uncertainty ( $\sim 0.5$  K), comparable to the less capable IR imagers. A significant contribution in PMW SST uncertainty is the greater sea-state dependence in emissivity. Fourth, problems

with radio frequency interference are degrading PMW SSTs across progressively more of the ocean in European seas and elsewhere.

Nonetheless, PMW SSTs are a very powerful addition to the sensor constellation for SST, because retrievals are available through non-raining clouds. PMW SSTs are particularly beneficial, therefore, in areas and periods of total cloud cover; they may provide the only satellite information about SST near a particular location for days or even weeks, sometimes with important consequences (Wentz et al. 2000).

The full constellation of sensors is beneficial to our ability to estimate the global distribution of SST at a given time – i.e., to the process of creating SST analyses. Synthesis of the different sources of SST information remains a challenge, especially in the face of increasing demands for high spatial resolution (e.g., 1 km globally) and sub-daily temporal resolution (e.g., 3 hourly, capturing the diurnal cycle). Given the sampling limitations of thermal remote sensing (because of clouds) and the resolution limitations of microwave remote sensing (~50 km, one or twice a day per sensor in the open ocean), the degree to which such demands can be met by the present constellation is a topic of ongoing research. (“Meaningfully” here means that the SST variations in the analyses are determined more by real information observed by the SST constellation, than by noise arising from observation uncertainty and the analysis system.) One clear direction for progress is to develop a more complete understanding of the uncertainties of different types of data and the degree of correlation of different components of error in time and space. SST analysis systems properly able to use such improved uncertainty characterization will (i) preserve as much as possible of the true information on SST held in the constellation of sensors, (ii) minimize the introduction of spurious features in the analysed SST, and (iii) deliver realistic estimates of the uncertainty in the analysed SST.

Thermal remote sensing of SST is an integral part of the observation of the ocean, and indeed of the global environment. Space and meteorological agencies are committed to maintaining the capability over the coming decades. This commitment is accompanied by ongoing improvement in our ability to sense the temperature of the ocean surface, bringing many benefits to society.

## References

- Anding D, Kauth R (1970) Estimation of sea surface temperature from space. *Remote Sens Environ* 1(4):217–220. doi:[10.1016/S0034-4257\(70\)80002-5](https://doi.org/10.1016/S0034-4257(70)80002-5)
- Barton IJ (1995) Satellite-derived sea surface temperatures: current status. *J Geophys Res* 100:8777–8790
- Barton IJ (2011) Improving satellite-derived sea surface temperature accuracies using water vapor profile data. *J Atmos Ocean Technol* 28(1):85–93. doi:[10.1175/2010JTECH1502.1](https://doi.org/10.1175/2010JTECH1502.1)
- Castro SL, Wick GA, Minnett PJ, Jessup AT, Emery WJ (2010) The impact of measurement uncertainty and spatial variability on the accuracy of skin and subsurface regression-based sea surface temperature algorithms. *Remote Sens Environ* 114(11):2666–2678. doi:[10.1016/j.rse.2010.06.003](https://doi.org/10.1016/j.rse.2010.06.003)

- Castro SL, Wick GA, Emery WJ (2012) Evaluation of the relative performance of sea surface temperature measurements from different types of drifting and moored buoys using satellite derived reference products. *J Geophys Res* 117:C02029. doi:[10.1029/2011JC007472](https://doi.org/10.1029/2011JC007472)
- Chelton DB, Esbensen SK, Schlaik G et al (2001) Observations of coupling between surface wind stress and sea surface temperature in the eastern tropical Pacific. *J Climate* 14(7):1479–1498. doi:[10.1175/1520-0442\(2001\)014<1479:OOCBSW>2.0.CO;2](https://doi.org/10.1175/1520-0442(2001)014<1479:OOCBSW>2.0.CO;2)
- Clayson CA, Weitlich D (2007) Variability of tropical diurnal sea surface temperature. *J Climate* 20(2):334–352. doi:[10.1175/JCLI3999.1](https://doi.org/10.1175/JCLI3999.1)
- Dash P, Ignatov A, Martin M et al (2012) Group for High Resolution Sea Surface Temperature (GHRSSST) analysis fields inter-comparisons-Part 2: Near real time web-based level 4 SST quality monitor (L4-SQUAM). *Deep Sea Res Part II Top Stud Oceanogr* 77–80(Special Issue):31–43. doi:[10.1016/j.dsrr.2012.04.002](https://doi.org/10.1016/j.dsrr.2012.04.002)
- Deschamps PY, Phulpin T (1980) Atmospheric corrections of infrared measurements of sea surface temperature using 3.7 μm, 11 μm and 12 μm. *Bound Layer Meteorol* 13:131–143
- Donlon CJ, Casey KS et al (2009) The GODAE high resolution sea surface temperature pilot project. *Oceanography* 22(3):34–45
- Donlon C, et al (2010) Successes and challenges for the modern sea surface temperature observing system. In: Hall J, Harrison DE, Stammer D (eds) *Proceedings of OceanObs'09: sustained ocean observations and information for society*, vol 2. Venice, 21–25 Sept 2009, ESA Publication WPP-306, doi: [10.5270/OceanObs09.cwp.24](https://doi.org/10.5270/OceanObs09.cwp.24)
- Donlon CJ, Martin M, Stark J, Roberts-Jones J, Fiedler E, Wimmer W (2012) The Operational Sea Surface Temperature and Sea Ice Analysis (OSTIA) system. *Remote Sens Environ* 116:140–158. doi:[10.1016/j.rse.2010.10.017](https://doi.org/10.1016/j.rse.2010.10.017)
- Embry O, Merchant CJ, Filipiak MJ (2012a) A reprocessing for climate of sea surface temperature from the along-track scanning radiometers: basis in radiative transfer. *Remote Sens Environ* 116:32–46. doi:[10.1016/j.rse.2010.10.016](https://doi.org/10.1016/j.rse.2010.10.016)
- Embry O, Merchant CJ, Corlett GK (2012b) A reprocessing for climate of sea surface temperature from the along-track scanning radiometers: initial validation, accounting for skin and diurnal variability. *Remote Sens Environ* 116:62–78. doi:[10.1016/j.rse.2011.02.028](https://doi.org/10.1016/j.rse.2011.02.028)
- Emery WJ, Yu YY, Wick GA (1994) Correcting infrared satellite estimates of sea surface temperature for atmospheric water vapor attenuation. *J Geophys Res* 99(C3):5219–5236. doi:[10.1029/93JC03215](https://doi.org/10.1029/93JC03215)
- Fairall CW, Bradley EF, Godfrey JS, Wick GA, Edson JB, Young GS (1996) Cool-skin and warm-layer effects on sea surface temperature. *J Geophys Res* 101:1295–1308
- Freeland H, et al (2010) Argo – a decade of progress. In: Hall J, Harrison DE, Stammer D (eds) *Proceedings of OceanObs'09: sustained ocean observations and information for society*, vol 2. Venice, Italy, 21–25 Sept 2009, ESA Publication WPP-306, doi: [10.5270/OceanObs09.cwp.32](https://doi.org/10.5270/OceanObs09.cwp.32)
- GCOS [Global Climate Observing System] (2006) Systematic observation requirements for satellite-based products for climate – supplemental details to the satellite-based component of the GCOS implementation plan. GCOS-107
- GCOS [Global Climate Observing System] (2011) Systematic observation requirements for satellite-based products for climate – supplemental details to the satellite-based component of the GCOS implementation plan for the global observing system for climate in support of the UNFCCC – 2011 update. GCOS-154
- Gentemann CL, Minnett PJ, Le Borgne P, Merchant CJ (2008) Multi-satellite measurements of large diurnal warming events. *Geophys Res Lett* 35(22):L22602. doi:[10.1029/2008GL035730](https://doi.org/10.1029/2008GL035730)
- Hanafin JA, Minnett PJ (2005) Measurements of the infrared emissivity of a wind-roughened sea surface. *Appl Opt* 44(3):398–411. doi:[10.1364/AO.44.000398](https://doi.org/10.1364/AO.44.000398)
- Kantha LH, Clayson CA (1994) An improved mixed-layer model for geophysical applications. *J Geophys Res* 99(C12):25235–25266. doi:[10.1029/94JC02257](https://doi.org/10.1029/94JC02257)
- Kilpatrick KA, Podesta GP, Evans R (2001) Overview of the NOAA/NASA advanced very high resolution radiometer Pathfinder algorithm for sea surface temperature and associated matchup database. *J Geophys Res* 106(C5):9179–9197

- Le Borgne P, Roquet H, Merchant CJ (2011) Estimation of sea surface temperature from the spinning enhanced visible and infra red imager, improved using numerical weather prediction. *Remote Sens Environ* 115:55–66. doi:[10.1016/j.rse.2010.08.004](https://doi.org/10.1016/j.rse.2010.08.004)
- Li X, Pichel W, Maturi E, Clemente-Colon P, Sapper J (2001) Deriving the operational nonlinear multichannel sea surface temperature algorithm coefficients for NOAA-15 AVHRR/3. *Int J Remote Sens* 22(4):699–704
- Martin M, Dash P, Ignatov A et al (2012) Group for High Resolution Sea Surface temperature (GHRSST) analysis fields inter-comparisons. Part 1: A GHRSST multi-product ensemble (GMPE). *Deep Sea Res Part II Top Stud Oceanogr* 77–80:21–30. doi:[10.1016/j.dsr2.2012.04.013](https://doi.org/10.1016/j.dsr2.2012.04.013)
- McClain EP, Pichel WG, Walton CC (1985) Comparative performance of AVHRR-based multi-channel sea surface temperatures. *J Geophys Res* 90:11587–11601
- McMillin LM, Crosby DS (1984) Theory and validation of the multiple window sea surface temperature technique. *J Geophys Res* 89(C3):3655–3661
- McPhaden M, et al (2010) The global tropical moored buoy array. In: Hall J, Harrison DE, Stammer D (eds) *Proceedings of OceanObs'09: sustained ocean observations and information for society*, vol 2. Venice, Italy, 21–25 Sept 2009, ESA Publication WPP-306, doi: [10.5270/OceanObs09.cwp.61](https://doi.org/10.5270/OceanObs09.cwp.61)
- Meldrum D, et al (2010) Data buoy observations: the status quo and anticipated developments over the next decade. In: Hall J, Harrison DE, Stammer D (eds) *Proceedings of OceanObs'09: sustained ocean observations and information for society*, vol 2. Venice, Italy, 21–25 Sept 2009, ESA Publication WPP-306, doi: [10.5270/OceanObs09.cwp.62](https://doi.org/10.5270/OceanObs09.cwp.62)
- Merchant CJ, Harris AR (1999) Toward the elimination of bias in satellite retrievals of sea surface temperature 2. Comparison with in situ measurements. *J Geophys Res* 104(C10):23579–23590. doi:[10.1029/1999JC00106](https://doi.org/10.1029/1999JC00106)
- Merchant CJ, Le Borgne P (2004) Retrieval of sea surface temperature from space, based on modelling of infrared radiative transfer: capabilities and limitations. *J Atmos Ocean Technol* 21(11):1734–1746. doi:[10.1175/JTECH1667.1](https://doi.org/10.1175/JTECH1667.1)
- Merchant CJ, Harris AR, Murray MJ, Zavodny AM (1999) Toward the elimination of bias in satellite retrievals of skin sea surface temperature 1. Theory, modeling and inter-algorithm comparison. *J Geophys Res* 104(C10):23565–23578
- Merchant CJ, Horrocks LA, Eyre JR, O'Carroll AG (2006) Retrievals of sea surface temperature from infrared imagery: origin and form of systematic errors. *Q J R Meteorol Soc* 132 (617):1205–1223. doi:[10.1256/qj.05.143](https://doi.org/10.1256/qj.05.143)
- Merchant CJ, Le Borgne P, Marsouin A, Roquet H (2008) Optimal estimation of sea surface temperature from split-window observations. *Remote Sens Environ* 112(5):2469–2484. doi:[10.1016/j.rse.2007.11.011](https://doi.org/10.1016/j.rse.2007.11.011)
- Merchant CJ, Harris AR, Roquet H, Le Borgne P (2009) Retrieval characteristics of non-linear sea surface temperature from the Advanced Very High Resolution Radiometer. *Geophys Res Lett* 36:L17604. doi:[10.1029/2009GL039843](https://doi.org/10.1029/2009GL039843)
- Merchant CJ, Embury O, Rayner NA, Berry DI, Corlett G, Lean K, Veal KL, Kent EC, Llewellyn-Jones D, Remedios JJ, Saunders R (2012) A twenty-year independent record of sea surface temperature for climate from Along Track Scanning Radiometers. *J Geophys Res.* doi:[10.1029/2012JC008400](https://doi.org/10.1029/2012JC008400)
- Merchant CJ, LeBorgne P, Roquet H, Legendre G (2013) Extended optimal estimation techniques for sea surface temperature from the Spinning Enhanced Visible and Infra-Red Imager (SEVIRI). *Remote Sens Environ* 131:287–297
- Minnett PJ (1990) The regional optimisation of infrared measurements of sea surface temperature from space. *J Geophys Res* 95:13497–13510
- Minnett PJ, Corlett GK (2012) A pathway to generating Climate Data Records of sea-surface temperature from satellite measurements. *Deep-Sea Res II* 77–80:44–51. doi:[10.1016/j.dsr2.2012.04.003](https://doi.org/10.1016/j.dsr2.2012.04.003)

- Minnett PJ, Smith M, Ward B (2011) Measurements of the oceanic thermal skin effect. Deep Sea Res Part II Top Stud Oceanogr 58(6):861–868. doi:[10.1016/j.dsr2.2010.10.024](https://doi.org/10.1016/j.dsr2.2010.10.024)
- Munk WH (1950) On the wind-driven ocean circulation. J Meteorol 7(2):79–93
- Petrenko B, Ignatov A, Shabanov N, Kihai Y (2011) Development and evaluation of SST algorithms for GOES-R ABI using MSG SEVIRI as a proxy. Remote Sens Environ 115(12):3647–3658. doi:[10.1016/j.rse.2011.09.003](https://doi.org/10.1016/j.rse.2011.09.003)
- Pichel W, Maturi E, Clemente-Colón P, Sapper J (2001) Deriving the operational nonlinear multichannel sea surface temperature algorithm coefficients for NOAA-15 AVHRR/3. Int J Remote Sens 22(4):699–704. doi:[10.1080/01431160010013793](https://doi.org/10.1080/01431160010013793)
- Reynolds RW, Smith TM, Liu C, Chelton DB et al (2007) Daily high-resolution-blended analyses for sea surface temperature. J Climate 20(22):5473–5496. doi:[10.1175/2007JCLI1824.1](https://doi.org/10.1175/2007JCLI1824.1)
- Robinson IS (2004) Measuring the oceans from space: the principles and methods of satellite oceanography. Praxis Publishing Ltd., Chichester. ISBN 3-540-42647-7
- Robinson IS, Piollé JF, Le Borgne P, Poulter D, Donlon C, Olivier A (2012) Widening the application of AATSR SST data to operational tasks through the Medspiration Service. Remote Sens Environ 116:126–139. doi:[10.1016/j.rse.2012.01.019](https://doi.org/10.1016/j.rse.2012.01.019)
- Rodgers CD (2000) Inverse methods for atmospheric sounding: theory and practice. World Scientific Publishing Co Ltd., Singapore. ISBN 081-02-2740-X
- Rothman LS (2010) The evolution and impact of the HITRAN molecular spectroscopic database. J Quant Spectrosc Radiat Transf 111(11):1565–1567. doi:[10.1016/j.jqsrt.2010.01.027](https://doi.org/10.1016/j.jqsrt.2010.01.027)
- Walton CC, Pichel WG, Sapper JF, May DA (1998) The development and operational application of nonlinear algorithms for the measurement of sea surface temperatures with the NOAA polar-orbiting environmental satellites. J Geophys Res 103:C12. doi:[10.1029/98JC02370](https://doi.org/10.1029/98JC02370)
- Ward B, Wanninkhof R, Minnett PJ, Head MJ (2004) SkinDeEP: a profiling instrument for upper-decameter sea surface measurements. J Atmos Ocean Technol 21(2):207–222. doi:[10.1175/1520-0426\(2004\)021<0207:SAPIFU>2.0.CO;2](https://doi.org/10.1175/1520-0426(2004)021<0207:SAPIFU>2.0.CO;2)
- Wentz F, Gentemann C, Smith D et al (2000) Satellite measurements of sea surface temperature through clouds. Science 288(5467):847–850. doi:[10.1126/science.288.5467.847](https://doi.org/10.1126/science.288.5467.847)
- Wimmer W, Robinson IS, Donlon CJ (2012) Long-term validation of AATSR SST data products using shipborne radiometry in the Bay of Biscay and English channel. Remote Sens Environ 116:17–31. doi:[10.1016/j.rse.2011.03.022](https://doi.org/10.1016/j.rse.2011.03.022)
- URL1: <http://www.atsr.rl.ac.uk/images/sample/atsr-2>
- URL2: [www.ghsst.org](http://www.ghsst.org)

# Chapter 16

## Soil Moisture from Thermal Infrared Satellite Data: Synergies with Microwave Data

Claudia Kuenzer, Ursula Gessner, and Wolfgang Wagner

**Abstract** Soil moisture is an important geophysical parameter and information on soil moisture is needed by many scientific disciplines in the context of climate modeling, hydrologic modeling, flood and drought forecasting, or in the context of geo-health applications. Changes in soil moisture can be the driver for changes in vegetation cover and might directly impact land use and agricultural yield.

A lot of approaches to derive soil moisture from remotely sensed spaceborne earth observation data exist. Most of them are based on the utilization of radar data, such as scatterometer data derived from instruments onboard the ERS satellite (ERS-Scat) or the Advanced Scatterometer onboard of the METOP satellite (METOP-Ascat). Such data comes at resolutions of 50 and 25 km respectively and has the large advantage that it can be acquired independent of solar illumination and cloud cover. Furthermore, several scientists have used higher resolution synthetic aperture radar (SAR) data for soil moisture estimation. It is less well-known that thermal infrared satellite data is also suitable to retrieve soil moisture information. As thermal data usually is available at a higher resolution (1 km and better) it is an attractive alternative to radar data. This chapter presents approaches of soil moisture retrieval from thermal data, and discusses advantages and shortcoming of soil moisture extraction based on this data type. Benefits on a synergistic operational soil moisture product based on both thermal and radar data are discussed.

---

C. Kuenzer (✉) • U. Gessner  
German Remote Sensing Data Center (DFD), Earth Observation Center (EOC),  
German Aerospace Center (DLR), Oberpfaffenhofen, Germany  
e-mail: [Claudia.kuenzer@dlr.de](mailto:Claudia.kuenzer@dlr.de)

W. Wagner  
Department of Geodesy and Geoinformation,  
Vienna University of Technology, Vienna, Austria

## 16.1 Introduction

Soil moisture has a considerable impact on a number of land surface processes such as surface energy fluxes, vegetation productivity and runoff (Legates et al. 2011). Time series data sets of soil moisture are particularly useful for the prediction and monitoring of droughts, agricultural yields and evaporation. Furthermore, soil moisture data has the potential to contribute to early warning of floods, as highly saturated soil moisture conditions in a watershed can lead to increased runoff and subsequent flooding (Brocca et al. 2009, 2012). There are several methods for the in-situ measurement of soil moisture (e.g., time-domain-reflectance TDR, gravimetric methods) which are typically labour intensive and limited to the assessment of small areas. To make in-situ soil moisture data more readily available the International Soil Moisture Network (ISMN) has recently been established (Dorigo et al. 2011). The ISMN is developing quickly, already containing data from more than three dozen networks worldwide ([URL1](#)). Yet, most of the land surface is still poorly covered, which is why satellite methods for spatially complete assessment are required. Fortunately, a large variety of methods for the retrieval of soil moisture from satellite data have been developed in the past decade. In contrast to in-situ measurements, these approaches show potential for an operational, spatially and temporally consistent derivation of soil moisture for large areas. Most of the current satellite-based soil moisture products rely on microwave data but an increasing number of studies have proven the potential of thermal infrared remote sensing data for soil moisture retrieval.

After a short overview of the current status of microwave-based soil moisture products, this paper gives a comprehensive review of the state of the art in soil moisture retrieval from thermal data. In addition, recent synergistic studies incorporating both microwave and thermal infrared data are presented. Summarizing the complementary strengths and weaknesses of thermal and microwave data with respect to thematic content, spatial resolution, temporal sampling, accuracy and data availability, we conclude that the synergistic use of both remote sensing data types into combined soil moisture products is highly promising for operational, large-area applications.

## 16.2 Soil Moisture Retrieval from Microwave Data

The majority of approaches for the retrieval of soil moisture from satellite data rely on microwave sensors (Engman and Chauhan 1995; Wagner et al. 2007), encompassing microwave radiometers and scatterometers for regional to global applications and Synthetic Aperture Radars (SARs) for local scale applications. The first satellite dedicated to monitoring soil moisture over land is the Soil

Moisture and Ocean Salinity (SMOS) mission of the European Space Agency (ESA), which was launched in November 2009 (Kerr et al. 2010). It is a passive radiometer operated at a wavelength of about 21 cm (L-band). At this wavelength, the sensitivity of the brightness temperature measurements acquired by microwave radiometers is enhanced compared to brightness temperature measurements carried out at shorter wavelengths in the range from about 3 to 6 cm. Nevertheless, measurements at these wavelengths are readily available from operational instruments such as the Advanced Microwave Scanning Radiometer – Earth Observing System (AMSR-E) and are accordingly widely used for soil moisture retrieval (Paloscia et al. 2006; Mladenova et al. 2011; Parinussa et al. 2011).

Another sensor suited to soil moisture monitoring is the Advanced Scatterometer (ASCAT), which is an active microwave sensor operating at a wavelength of 5.7 cm (C-band). ASCAT is being flown on-board a series of three Meteorological Operational Satellite (METOP) satellites operated by the European Organization for the Exploitation of Meteorological Satellites (EUMETSAT), with the first satellite (METOP-A) launched in October 2006 and the second (METOP-B) in September 2012. Both satellites are currently operated in parallel, acquiring global backscatter measurements at a spatial resolution of 25 km, which is comparable to the resolution offered by microwave radiometers. Since December 2008 ASCAT soil moisture data are available in near-real-time through EUMETSAT (EUMETSAT 2013; Wagner et al. 2012), see Fig. 16.1 for an illustration of the daily global coverage achieved by METOP-A and METOP-B.

A major advantage of microwave instruments such as SMOS, AMSR-E and ASCAT is their near-global coverage and their ability to sense the land surface independent of cloud cover and daytime. Thus, they guarantee frequent temporal coverage. Also, both sensors provide a rather direct measure of soil moisture content due to the pronounced dependency of microwave emission and backscatter on soil dielectric properties, and hence on soil moisture. However, their spatial resolution is only in the order of tens of kilometres (25–50 km), which is a severe limitation on the usability of these data in many applications. This limitation will be partly overcome by the Soil Moisture Active Passive (SMAP) mission that will acquire L-band brightness temperature data at 30 km and L-band backscatter measurements at about 3 km (Entekhabi et al. 2010), opening up the possibility to create soil moisture products with a spatial resolution as fine as 3 km. Synthetic Aperture Radars (SARs) would in principle be able to provide soil moisture data at even finer scales but algorithmic problems stemming from the complexity of modelling backscatter measurements at fine spatial scale and the limited temporal availability of the data still limit their usefulness in application (Kornelsen and Coulibaly 2012). With the upcoming Sentinel-1 SAR satellites the latter constraint will be overcome, but much research and development work is still needed to establish robust retrieval algorithms embedded in operational processing frameworks (Hornacek et al. 2012).

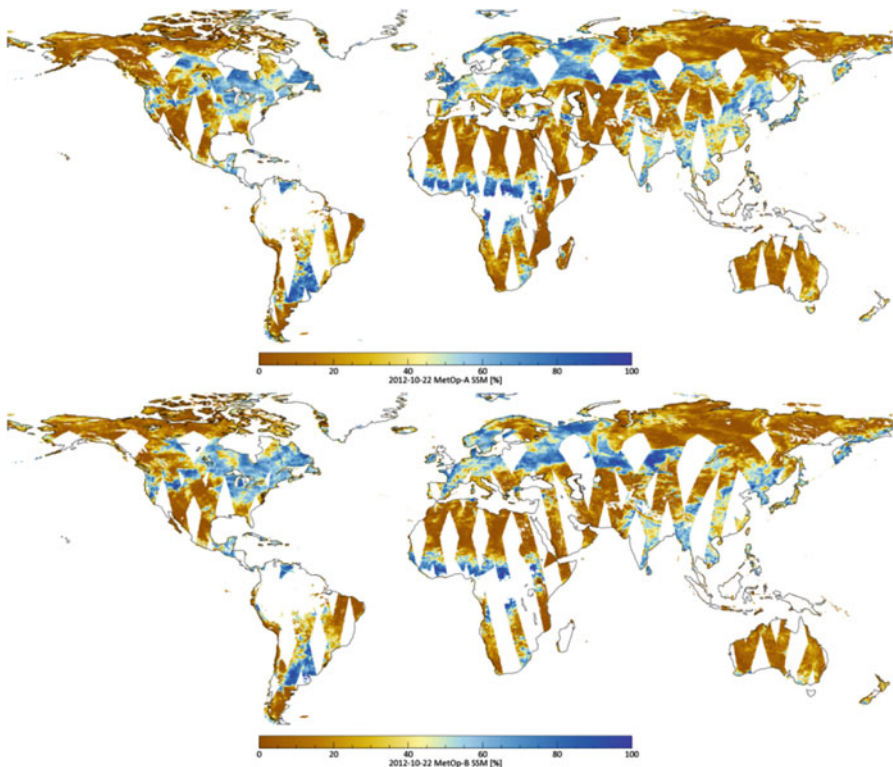


**Fig. 16.1** Global ASCAT soil moisture images from METOP-A (top) and METOP-B (bottom) for 22 October 2012. METOP-B was on that day still in the commissioning phase, yet as the high agreement of both images demonstrates, both ASCAT instruments work extremely well, providing much improved spatio-temporal coverage with a single instrument. The ASCAT soil moisture data were processed by EUMETSAT, whereas the images were produced by TU Wien. It should be considered here that the METOP-B data displayed is Cal/Val data

### 16.3 Thermal Parameters as a Key for Soil Moisture Derivation

An increasing number of studies rely on thermal infrared remote sensing data to derive soil moisture. However, a widely applicable direct link between temperature data and soil moisture does not exist (Jackson et al. 1997). Also soil moisture does not directly enter the energy balance equation of the land surface. However, the water content of a soil strongly influences the evapotranspiration term of the equation as well as the specific heat capacity and emissivity in the same. The thermal expression of a soil is thus altered depending on its moisture content, and thermal physical parameters can support the indirect retrieval of information on soil moisture conditions. Many authors have followed this direction of thermal infrared (TIR) based soil moisture estimation utilising a large variety of data from sensors

such as HCMM (Heat Capacity Mapping Mission), TIROS-N (Television and InfraRed Observation Satellite), NOAA-AVHRR (National Oceanic and Atmospheric Administration – Advanced Very High Resolution Radiometer), GOES (Geostationary Operational Environmental Satellite), Meteosat (Meteorological Satellite), MODIS (Moderate Resolution Imaging Spectroradiometer), and Landsat, amongst others (Carlson 1981, 1986; Price 1983, Carlson et al. 1984, 1994; Jones et al. 1998; McNider et al. 1994; Portmann et al. 2003; Gillies and Carlson 1995; Rosema et al. 2001; Shih and Jordan 1993; van den Hurk 2001; Verstraeten et al. 2006; Wetzel and Woodward 1987). Approaches range from the application of simple indices to the assimilation of TIR data in soil-vegetation-atmosphere transfer (SVAT) models.

### 16.3.1 The Triangle Approach

Empirical relationships between the thermal infrared emissivity of bare soils and surface soil moisture could be established in laboratory experiments and locally restricted studies (e.g., Mira et al. 2010; Sanchez et al. 2011; Hulley et al. 2010). However, for vegetated land surfaces, plant cover considerably influences this relationship. Price (1990) has demonstrated a unique relationship between fractional vegetation cover, soil moisture, and soil temperature, which results in a triangular or trapezoidal shaped scatterplot of surface temperatures and the remotely sensed NDVI (Normalized Difference Vegetation Index). This empirically derived relationship was later verified by SVAT models (Gillies et al. 1997). Following this triangle concept, soil moisture was estimated e.g., by Carlson et al. (1994), Chauhan et al. (2003) and Wang et al. (2007) using NDVI and Land Surface Temperature (LST) from remote sensing in combination with field measurements of soil moisture. Building on the triangle approach, Sandholt et al. (2002) developed the temperature-vegetation dryness index (TVDI)

$$TVDI = \frac{T_s - T_{s_{min}}}{a + b * NDVI - T_{s_{min}}} \quad (16.1)$$

where  $T_{s_{min}}$  is the minimum surface temperature of an area representing the full range from wet to dry and bare to densely vegetated conditions.  $T_s$  is the actual surface temperature at a given pixel. NDVI is the observed NDVI. The coefficients  $a$  and  $b$  define the dry edge in the triangle, modelled as a linear fit ( $T_{s_{max}} = a + b * NDVI$ ), where  $T_{s_{max}}$  is the maximum observed surface temperature for a given NDVI. TVDI was used for soil moisture retrieval in semi-arid regions of Senegal (Sandholt et al. 2002) and in a sub-humid study area in India (Patel et al. 2008). Comparisons with in-situ and modeled soil moisture support the applicability of the TVDI approach for large areas, particularly when vegetation cover is sparse.

### ***16.3.2 Integration of Thermal Data into Land Surface Models***

Other TIR-based approaches for deriving soil moisture integrate thermal infrared data in land surface or SVAT models (e.g., Coudert and Ottlé 2007; Crow et al. 2008; Gillies and Carlson 1995; Portmann et al. 2003). Such models are often highly complex and need a large number of input variables to yield sufficient results. Some approaches use variables derived from thermal remote sensing as direct input for the models. In other studies, boundary conditions or parameters are adjusted to match observed variables. Hence, the obtained results strongly depend on the choice of the model, the chosen input parameters, and the accuracy of the latter. However, large scale or even globally applicable approaches with high temporal resolution offering operational readiness have only been implemented in rare cases.

McNider et al. (1994) developed a technique to integrate satellite-derived skin temperature in atmospheric models by matching the modeled rate of temperature change to the satellite observations. Jones et al. (1997) have extended this technique by additionally integrating a prognostic soil model to adequately consider the relative heating rates of bare soil and vegetation components. Another example is the work of Portmann et al. (2003), who modified the TESSEL (Tiled ECMWF (European Centre for Medium-Range Weather Forecasts) Scheme for Surface Exchanges over Land model) and adjusted model soil moisture so that a modeled surface temperature rise matched observed in-situ temperature increases. The surface energy balance model ALEXI (Atmosphere-Land Exchange Inversion, Anderson et al. 1997, 2007; Mecikalski et al. 1999) combines a TIR-based two-source model with an atmospheric boundary layer model. Remotely sensed radiometric temperatures are partitioned into soil and vegetation temperatures, and subsequently soil and canopy energy budgets are balanced separately. Hain and Mecikalski (2009) applied the ALEXI model for Oklahoma using hourly GOES thermal infrared data and derived the available water in the soil profile.

### ***16.3.3 Thermal Inertia and Apparent Thermal Inertia Approaches***

Of great potential for TIR based soil moisture retrieval is the concept of thermal inertia of an object,  $I$  ( $\text{J m}^{-2} \text{s}^{-0.5} \text{K}^{-1}$ ), which is defined as the resistance of an object to its heating for 1 K, depending on three parameters. Firstly, the energy needed to raise the temperature of a material for 1 K (heat capacity  $c$ ) per mass unit of the substance ( $m$ ), secondly the density of a material,  $\rho$  – the main determining factor – and thirdly the thermal conductivity,  $K$ , of an object. Hence,  $P = \sqrt{c \cdot K \cdot \rho}$ . Variations of  $I$  affect the diurnal temperature difference  $\Delta T$ , defined as the difference between the maximum and minimum temperature occurring during a diurnal solar cycle (Kahle et al. 1976). Low thermal inertias indicate low resistance to

temperature changes, resulting in a high  $\Delta T$ . The opposite applies for materials with a high thermal inertia, e.g., water. Hence,  $\Delta T$  decreases with increasing soil moisture. As already stated in Chap. 1, remote sensing does not allow for the direct derivation of  $I$  ( $c$ ,  $\rho$  and  $K$  can only be measured in-situ), but the concept still allows exploitation of the impact of soil moisture ( $\theta$ ) on  $T$  and  $\Delta T$ .  $\Delta T$  is calculated by subtracting the minimum nighttime temperature from the maximum daytime temperature for corresponding ground resolution cells.

Already in the 1970s, Price (1977), Idso et al. (1975), and Schmugge et al. (1978) analysed the potential of  $\Delta T$  for soil moisture retrieval. Building on these studies, several techniques were developed for modeling the thermal inertia of soils and deriving soil moisture that include  $\Delta T$  from remote sensing data (Cai et al. 2007; Matushima et al. 2012; Minacapilli et al. 2009; Sobrino and El Kharraz 1999; Xue and Cracknell 1995).

As an approximation to the actual thermal inertia, the so called Apparent Thermal Inertia (ATI) is defined as  $ATI = (1 - A)/\Delta T$ . As stated in Chap. 1,  $A$  is the albedo of the pixel in the visible band (VIS). This helps to compensate for the fact that dark materials with low albedo absorb more sunlight than light materials with a high albedo. ATI cannot compensate for relief induced variations in  $\Delta T$ . In an area of uniform material, shadowed areas have a lower radiant temperature during the day and hence a lower  $\Delta T$  than the same material exposed on a sunlit slope. Here, topographic data and solar elevation and azimuth information can be employed to overcome relief induced variation of  $\Delta T$ . Depending on the resolution of the data sets and the scale of an envisaged product this might not play a crucial role though. An advantage of ATI when compared to the actual thermal inertia is that it can be derived directly from VIS and TIR remote sensing imagery. Numerous studies followed this approach and found high potential for soil moisture estimation based on ATI.

Tramutoli et al. (2000) assessed the potential of ATI derived from AVHRR to describe the spatial and temporal variability of soil moisture. They compared ATI based soil moisture estimates for a river basin in Italy with precipitation data and assessed the robustness and sensitivity of the approach by spatial variability analyses. The authors conclude that AVHRR-based ATI provides useful information on soil moisture, e.g., for the calibration of hydrological models.

The concept of ATI was furthermore employed for European forests by Verstraeten et al. (2006) using Meteosat data. Since ATI represents the temporal and spatial variability of soil and canopy moisture, the highest and lowest ATI values in an ATI time series for a specific pixel can represent the residual and saturated soil moisture. Verstraeten et al. (2006) thus derive a change detection based soil moisture saturation index (SMSI) according to the quotient  $SMSI(t) = (ATI(t) - ATI_{min})/(ATI_{max} - ATI_{min})$ , which is modified further to retrieve soil moisture content (SMC) based on the European soil database (JRC-INRA 1999). Additionally, they employ a filtering approach developed by Wagner et al. (1999) which estimates the status of soil profile moisture content based on time series of the surface soil moisture content. Correlation coefficients between TIR-based SMC results and EUROFLUX site in-situ data as well as ERS (European Remote-Sensing Satellite)

scatterometer derived SWI (Soil Water Index) are satisfactory. Verstraeten et al. (2006) discuss that the errors retrieved from their TIR based approach are in the same order of magnitude as those reported for microwave derived soil moisture products. The approach of Verstraeten et al. (2006) was adopted by Veroustraete et al. (2012) to infer soil moisture from MODIS data for a semi-arid region in China. In this study, soil texture parameters were derived from a detailed regional soil map which allowed for defining spatially explicit residual and saturated soil moisture values. Comparisons of the ATI-based SMC with in-situ measurements showed good applicability of the approach in semi-arid regions.

Van Doninck et al. (2011) present an approach to derive ATI from daily Terra and Aqua MODIS data where  $\Delta T$  is estimated based on a sinusoidal approximation of the LST measurements that are available for a specific day. ATI is not transformed to soil moisture, but the temporal profiles of ATI show good agreement with AMSR-E (Advanced Microwave Scanning Radiometer – Earth Observing System) derived soil moisture, particularly for arid and semi-arid areas. In more densely vegetated areas, Van Doninck et al. (2011) noticed a rather poor performance of ATI, which is in contrast to Verstraeten et al. (2006), who successfully delineated soil moisture over forests using their ATI-based approach and Meteosat data. Van Doninck et al. (2011) assume that reasons for this contradiction could be the stronger cloud contamination of MODIS data when compared to the more frequent Meteosat observations.

Another promising study on the potential of ATI for soil moisture derivation was conducted by Minacapilli et al. (2012). In laboratory experiments the authors could delineate surface soil moisture based on ATI with an acceptable accuracy and found good agreement between TI- and ATI-based approaches. Scheidt et al. (2010) found ATI inferred from ASTER (Advanced Spaceborne Thermal Emission and Reflection) useful for estimating the soil moisture and aeolian erosion potential of dune fields. Notarnicola et al. (2012) derived soil moisture for three test sites in Europe from daily MODIS data using an ATI approach. Comparisons with in-situ measurements showed generally good agreement, but the authors mention considerable problems in mountainous regions and in situations of high cloud coverage. The synergistic use of MODIS and Meteosat-SEVIRI data is suggested as a promising way to reduce cloud-related problems.

### **16.3.4 Approaches Involving High Resolution TIR Data**

Several other approaches based on relatively high resolution data, e.g., Landsat multispectral and thermal imagery, exist (Shih and Jordan 1993). However, since we consider these approaches unsuitable because of insufficient spatial or temporal coverage we do not discuss them further. Nevertheless, it should be kept in mind that TIR approaches can be pursued with any sensor data offering diurnal coverage. For locally intended case studies and hydrologists working on specific catchments such data might be sufficient.

### 16.3.5 Comparative Studies of Microwave and TIR Based Approaches

The positive results from TIR-based approaches are also supported by the results of Naeimi et al. (2006). They compared four satellite soil moisture time series data sets derived with four different approaches from three different sensors. Correlation coefficients between the TDR probe in-situ data and ERS Scatterometer-derived soil moisture, two AMSR-E-derived soil moisture products and the Meteosat-derived TIR based soil moisture index presented by Rosema et al. (2001) range from 0.64 for the ERS Scatterometer-derived product to 0.83 for an AMSR-E product developed by Vrije University Amsterdam. The Meteosat product yields a satisfactory  $r^2$  of 0.65, while no correlation was found comparing the in-situ data with an AMSR-E product derived by NASA-NSIDC (NASA – National Snow and Ice Data Center). This supports the hypothesis that the soil moisture retrieval algorithm is as important as the sensor providing the data.

A high potential of TIR-based soil moisture retrieval is also confirmed by the comparative study of Hain et al. (2011). Here, AMSR-E-derived soil moisture and soil moisture inferred from the TIR-based ALEXI model were compared with soil moisture estimates of the Noah Land Surface Model (Noah-LSM) that served as a reference. The spatial correspondence between ALEXI and Noah-LSM was found to be better than between AMSR-E and Noah-LSM. With respect to the temporal variations of soil moisture, the microwave-based data agreed better in sparsely vegetated areas, while the TIR-based ALEXI model performed better in moderate to densely vegetated areas.

## 16.4 Synergy of Microwave and Thermal Data for Soil Moisture Retrieval

During the last decade, several approaches emerged that synergistically use thermal and microwave remote sensing data for generating soil moisture products.

Chauhan et al. (2003) combine soil moisture inferred from microwave SSM/I data with soil moisture information derived from VNIR (Visible and Near-Infrared) and TIR AVHRR data using the triangle approach. The high resolution (1 km) information of AVHRR is used to disaggregate the coarser (25 km) microwave-based soil moisture. Good agreement between high and low resolution soil moisture was found with RMSE (Root Mean Square Error) around 5 %. A series of studies by Merlin et al. (2008, 2009, 2010) investigate in detail the potential of disaggregating coarse resolution microwave-retrieved soil moisture products using higher resolution VNIR/TIR data. SMOS (Soil Moisture and Ocean Salinity satellite) surface soil moisture at a spatial resolution of 40 km was simulated from 1 km Polarimetric L-band Multibeam Radiometer (PLMR) data for a 40 km  $\times$  60 km study site. In their first study (Merlin et al. 2008), the authors derived soil evaporative efficiency

from MODIS VNIR/TIR data as a proxy for soil moisture using a triangle approach. Four downscaling algorithms were tested that consider linear and nonlinear relationships and different spatial resolutions of soil moisture data sets between 10 m and 40 km. The best RMSE between downscaled and 1 km microwave-derived soil moisture range between 1.4 and 1.8 % v./v. In a similar setting, Merlin et al. (2009) used 100 m VNIR/TIR ASTER data in addition to MODIS for disaggregating the simulated SMOS surface soil moisture information. The optimal downscaling resolution was found to be four to five times the spatial resolution of the TIR sensor, i.e., 4 km for MODIS and 500 m for ASTER data. RMSE for the soil moisture product disaggregated to 500 m was 0.062 vol./vol. with a bias of  $-0.045$  vol./vol. Again based on MODIS and simulated SMOS data, Merlin et al. (2010) tested a number of disaggregation methods that differ with regard to the formulation of fractional vegetation cover, with respect to the model applied to derive soil evaporative efficiency from MODIS, and with respect to the considered downscaling relationships. The best results with RMSE of 0.012 vol./vol. could be derived when including combined Aqua and Terra MODIS data. Li et al. (2010) tested the value of simultaneously assimilating microwave-based surface soil moisture and TIR-based root zone soil moisture into a soil water balance model. Using synthetic data, the analyses approved that thermal-based estimates of root-zone soil moisture should improve hydrologic modeling studies for applications that require information on vertically-integrated soil moisture, particularly for clay- and silt-rich soils. An application of the assimilation approach using tower-based thermal infrared temperature observations and in-situ surface soil moisture measurements showed that only slight improvements of root zone soil moisture estimations could be related to the assimilation of thermal data (increase of  $r^2$  by 0.03). The authors assume that a reason could be the sandy soils of the study site, which allows for the extrapolation of surface soil moisture observations beyond the root zone with high confidence by vertical coupling without requiring thermal-based root zone soil moisture information. Li et al. (2010) note that further studies including a broader range of study sites are necessary to confirm their results. Notarnicola et al. (2013) combined ATI-based soil moisture inferred from MODIS data with the NASA AMSR-E soil moisture product. The incorporation of microwave data seems promising for regional applications; it could reduce noise and improve the daily cycle sampling of the frequently cloud affected VNIR/TIR data. In a validation study of the AMSR-E soil moisture product with in-situ measurements, Choi and Hur (2012) disaggregated the microwave-based soil moisture using soil moisture derived from 1 km MODIS data using a triangle approach. This workflow allowed for reducing the spatial mismatch between microwave-based data and in-situ measurements. The disaggregated soil moisture showed clearly improved spatial and temporal patterns and better error statistics when compared to the original AMSR-E data. Choi and Hur (2012) see high potential of the disaggregation approach for improving the spatial distribution of the AMSR-E product and similar future soil moisture data sets.

## 16.5 Conclusions and Outlook

Soil moisture retrieval approaches based on thermal infrared remote sensing have been developed and refined in numerous studies during the last decades. However, there are some general shortcomings of TIR-based soil moisture retrieval. Firstly, surface information cannot be inferred during cloud cover conditions, an option, which is unique to microwave frequencies below 10 GHz. Secondly, soil moisture can only be retrieved indirectly by analyzing its effect on surface temperature and other surface variables. Furthermore, some authors (Jackson et al. 1997; Mira et al. 2010) discuss that TIR based soil moisture retrieval works for rather dry conditions only. This is due to the fact that land surface temperature (LST) is controlled by evaporation as long as the soil is relatively wet. Only as it dries is it controlled by thermal inertia. In addition, the importance of the inertia effect decreases as vegetation cover increases because of radiation shielding effects and increased evapotranspiration from leaves. However, other authors (e.g., Hain and Mecikalski 2009; Hain et al. 2011) emphasize the advantage of TIR-based approaches to estimate root zone soil moisture over vegetated areas by detecting vegetation stress.

As a last point, the effect of wind on the surface temperature should be mentioned. While, in principle, the physical mechanisms are well understood, in practice it is difficult to account for wind due to the lack of wind observations.

Nevertheless, advantages of thermal data for the retrieval of soil moisture are at hand. Diurnal thermal data is available on a daily basis from Meteosat at 5 km, from Meteosat Second Generation's (MSG) Spinning Enhanced Visible and Infrared Imager (SEVIRI) instrument at 3 km, from NOAA-AVHRR at 1.1 km and from MODIS at 1 km, all nadir resolution. Soil moisture products derived, for example, via diurnal thermal inertia approaches could thus convince with much higher spatial detail than for example, the daily available 25 km ASCAT products. The thermal approach can be especially beneficial in areas of low cloud cover. Weekly products interpolated for cloud gaps could deliver additional data for mid-latitude regions. The LST of a pixel is mainly dependent on the object's albedo, its thermal inertia and outer conditions such as relief and wind. The roughness component, which influences microwave derived products, is negligible in the 8–14  $\mu\text{m}$  part of the spectrum. Provided that the albedo component can be corrected through visible bands as incorporated in the ATI approach, in even terrain the thermal signal is then mainly governed by the material's composition itself. For natural environments the LST is then mainly a function of material (surface) moisture.

Besides technical and scientific arguments it is also important that users – who are generally not remote sensing experts – comprehend the information content of a product. In this respect, a disadvantage of microwave technologies is that a good physical understanding is in general necessary to understand the benefits and shortcomings of microwave products. On the other hand, thermal imagery is more widely accepted, since temperature images can be interpreted more easily. Therefore, a soil moisture product derived from a thermal data set might be more readily accepted by the geoscience community. Also, data from NOAA-AVHRR,

**Table 16.1** Advantages and disadvantages of microwave and thermal infrared remote sensing data for the retrieval of soil moisture

	Microwave data	Thermal infrared data
Spatial resolution	–	+
Temporal resolution	+	+
Perturbation by clouds	No	Yes
Perturbation by relief	Strong	Weaker
Easy to understand → user acceptance	–	+
Retrieval for wet conditions	+	–
Retrieval for dry conditions	+	+
Retrieval of root zone soil moisture under dense vegetation	–	+

METEOSAT, MSG or MODIS is more widely employed and users might be less skeptical about products derived therefrom.

From a user perspective, there are strong arguments for working towards an operational synergistic product that integrates the complementary advantages of thermal and microwave data (Table 16.1). The most important aspect is the capability of such a synergistic product to bridge and connect the two scales existing in soil moisture remote sensing – the local scale dominated by vegetation, topography and soil influences, and the global scale, where atmospheric forcing causes large scale soil moisture patterns (Entin et al. 2000). This connection widens the user group from globally or country-wide operating users to users interested in the regional scale. Especially in highly complex terrain, TIR data has an advantage over actively sensed scatterometer data, which are strongly influenced in their backscattering signal by difficult terrain (Parajka et al. 2006).

Further refinements can be expected for the modeling of the infiltration process and thus the derivation of profile soil moisture content. Here accuracy is thought to improve when integrating thermal data, since moisture and temperature diffusion in the profile are related (Entekhabi et al. 1994). Thus, research is needed to fuse profile soil moisture estimation approaches as presented from the microwave and the thermal domain.

In brief, the benefits of a synergistic, operational soil moisture product based on TIR and microwave data might be as follows:

- Higher spatial and temporal resolution, increase in detail
- Bridging the gap between the local and global scale
- Offering cross validation and comparison options for time series and neighbour disciplines
- Modelling of  $\theta$  and  $T_s$  over the soil profile can be improved
- Acceptance by (new) user community expected

Hence, we propose to further investigate the possibilities of merging radar-based and thermal products. Especially ATI based products seem very appealing with respect to their simplicity.

## References

- Anderson MC, Norman JM, Diak GR, Kustas WP, Mecikalski JR (1997) A two-source time-integrated model for estimating surface fluxes using thermal infrared remote sensing. *Remote Sens Environ* 60(2):195–216
- Anderson MC, Norman JM, Mecikalski JR, Otkin JA, Kustas WP (2007) A climatological study of evapotranspiration and moisture stress across the continental United States based on thermal remote sensing: 1. Model formulation. *J Geophys Res* 112(D10)
- Brocca L, Melone F, Moramarco T, Morbidelli R (2009) Antecedent wetness conditions based on ERS scatterometer data. *J Hydrol* 364:73–87
- Brocca L, Moramarco T, Melone F, Wagner W, Hasenauer S, Hahn S (2012) Assimilation of surface- and root-zone ASCAT soil moisture products into rainfall runoff modeling. *IEEE Trans Geosci Remote Sens* 50(7):2542–2555
- Cai G, Xue Y, Hu Y, Wang Y, Guo J, Luo Y, Wu C, Zhong S, Qi S (2007) Soil moisture retrieval from MODIS data in Northern China Plain using thermal inertia model. *Int J Remote Sens* 28(16):3567–3581
- Carlson TN, Dodd JK, Benjamin SG, Cooper JN (1981) Satellite estimation of the surface energy balance, moisture availability and thermal inertia. *J Appl Meteorol* 20:67–87
- Carlson TN (1986) Regional-scale estimates of surface moisture availability and thermal inertia using remote thermal measurements. *Remote Sens Rev* 1:197–247
- Carlson TN, Gillies RR, Perry EM (1994) A method to make use of thermal infrared temperature and NDVI measurements to infer surface soil water content and fractional vegetation cover. *Remote Sens Rev* 9(1–2):161–173
- Carlson TN, Rose FG, Perry EM (1984) Regional-scale estimates of surface moisture availability from GOES infrared satellite measurements. *Agron J* 76:972–979
- Chauhan NS, Miller S, Ardanuy P (2003) Spaceborne soil moisture estimation at high resolution: a microwave-optical/IR synergistic approach. *Int J Remote Sens* 24(22):4599–4622
- Choi M, Hur Y (2012) A microwave-optical/infrared disaggregation for improving spatial representation of soil moisture using AMSR-E and MODIS products. *Remote Sens Environ* 124:259–269
- Coudert B, Ottlé C (2007) An improved SVAT model calibration strategy based on the optimisation of surface temperature temporal dynamics. *Geophys Res Lett* 34(4):L04402
- Crow WT, Kustas WP, Prueger JH (2008) Monitoring root-zone soil moisture through the assimilation of a thermal remote sensing-based soil moisture proxy into a water balance model. *Remote Sens Environ* 112(4):1268–1281
- Dorigo WA, Wagner W, Hohensinn R, Hahn S, Paulik C, Xaver A, Gruber A, Drusch M, Mecklenburg S, van Oevelen P, Robock A, Jackson T (2011) The international soil moisture network: a data hosting facility for global in situ soil moisture measurements. *Hydrol Earth Syst Sci* 15(6):1675–1698
- Engman ET, Chauhan N (1995) Status of microwave soil moisture measurements with remote sensing. *Remote Sens Environ* 51:189–198
- Entekhabi D, Nakamura H, Njoku EG (1994) Solving the inverse problem for soil moisture and temperature profiles by sequential assimilation of multifrequency remotely sensed observations. *IEEE Trans Geosci Remote Sens* 32(2):438–448
- Entekhabi D, Njoku EG, O'Neill PE, Kellogg KH, Crow WT, Edelstein WN, Entin JK, Goodman SD, Jackson TJ, Johnson J, Kimball J, Piepmeyer JR, Koster R, Martin N, McDonald KC, Moghaddam M, Moran S, Reichle R, Shi JC, Spencer MW, Thurman SW, Tsang L, Van Zyl J (2010) The Soil Moisture Active Passive (SMAP) mission. *Proc IEEE* 98(5):704–716
- Entin JK, Robock A, Vinnikov KY, Hollinger SE, Liu S, Namkhai A (2000) Temporal and spatial scales of observed soil moisture variations in the extratropics. *J Geophys Res* 105:11865–11877
- EUMETSAT (2013) Product Navigator. <http://www.eumetsat.int/Home/Main/DataProducts/ProductNavigator/index.htm>
- Gillies RR, Carlson TN (1995) Thermal remote sensing of surface soil water content with partial vegetation cover for incorporation into climate models. *J Appl Meteorol* 34:745–756

- Gillies RR, Carlson TN, Cui J, Kustas WP, Humes KS (1997) A verification of the ‘triangle’ method for obtaining surface soil water content and energy fluxes from remote measurements of the Normalized Difference Vegetation Index (NDVI) and surface radiant temperature. *Int J Remote Sens* 18(15):3145–3166
- Hain CR, Crow WT, Mecikalski JR, Anderson MC, Holmes T (2011) An intercomparison of available soil moisture estimates from thermal infrared and passive microwave remote sensing and land surface modeling. *J Geophys Res* 116(D15):D15107
- Hain CR, Mecikalski JR (2009) Retrieval of an available water-based soil moisture proxy from thermal infrared remote sensing. Part I: Methodology and validation. *J Hydrometeorol* 10:665–683
- Hornacek M, Wagner W, Sabel D, Truong HL, Snoeij P, Hahmann T, Diedrich E, Doubková M (2012) Potential for high resolution systematic global surface soil moisture retrieval via change detection using Sentinel-1. *IEEE J Sel Top App Earth Obs Remote Sens* 5(4):1303–1311
- Hulley GC, Hook SJ, Baldridge AM (2010) Investigating the effects of soil moisture on thermal infrared land surface temperature and emissivity using satellite retrievals and laboratory measurements. *Remote Sens Environ* 114(7):1480–1493
- Idso SB, Schmugge TJ, Jackson RD, Reginato RJ (1975) The utility of surface temperature measurements for the remote sensing of surface water soil status. *J Geophys Res* 80:3044–3049
- Jackson TJ, O'Neill PE, Swift CT (1997) Passive microwave observation of diurnal surface soil moisture. *IEEE Trans Geosci Remote Sens* 35:1210–1222
- Jones AS, Guch IC, Vonder Haar TH (1997) Data assimilation of satellite-derived heating rates as proxy surface wetness data into a regional atmospheric mesoscale model. *Mon Weather Rev* 126(3):634–645
- Jones AS, Guch IC, Vonder Haar TH (1998) Data assimilation of satellite-derived heating rates as proxy surface wetness data into a regional atmospheric mesoscale model, Part II: a case study. *Mon Weather Rev* 126:646–667
- JRC-INRA (1999) The European soil database version 1. Ispra, Italy, JRC. [http://eusoils.jrc.ec.europa.eu/ESDB\\_Archive/ESDB/](http://eusoils.jrc.ec.europa.eu/ESDB_Archive/ESDB/). Last accessed 09 Apr 2013
- Kahle AB, Gillespie AR, Goetz AFH (1976) Thermal inertia imaging: a new geological mapping tool. *Geophys Res Lett* 3:26–28
- Kerr Y, Waldteufel P, Wigneron JP, Delwart S, Cabot F, Boutin J, Escorihuela MJ, Font J, Reul N, Gruhier C, Juglea SE, Drinkwater MR, Hahne A, Martin-Neira M, Mecklenburg S (2010) The SMOS mission: new tool for monitoring key elements of the global water cycle. *Proc IEEE* 98(5):666–687
- Kornelsen KC, Coulibaly P (2012) Advances in soil moisture retrieval from synthetic aperture radar and hydrological applications. *J Hydrol* 476:460–489
- Legates DR, Mahmood R, Levina DF, DeLiberty TL, Quiring SM, Houser C, Nelson FE (2011) Soil moisture: a central and unifying theme in physical geography. *Prog Phys Geogr* 35(1):65–86
- Li F, Crow WT, Kustas WP (2010) Towards the estimation root-zone soil moisture via the simultaneous assimilation of thermal and microwave soil moisture retrievals. *Adv Water Resour* 33(2):201–214
- Matushima D, Kimura R, Shinoda M (2012) Soil moisture estimation using thermal inertia: potential and sensitivity to data conditions. *J Hydrometeorol* 13:638–648
- McNider RT, Song AJ, Casey DM, Wetzel PJ, Crosson WL, Rabin RM (1994) Toward a dynamic-thermodynamic assimilation of satellite surface temperature in numerical atmospheric models. *Mon Weather Rev* 122:2784–2803
- Mecikalski JR, Diak GR, Anderson MC, Norman JM (1999) Estimating fluxes on continental scales using remotely sensed data in an atmospheric–land exchange model. *J Appl Meteorol* 38:1352–1369
- Merlin O, Al Bitar A, Walker JP, Kerr Y (2009) A sequential model for disaggregating near-surface soil moisture observations using multi-resolution thermal sensors. *Remote Sens Environ* 113(10):2275–2284

- Merlin O, Al Bitar A, Walker JP, Kerr Y (2010) An improved algorithm for disaggregating microwave-derived soil moisture based on red, near-infrared and thermal-infrared data. *Remote Sens Environ* 114(10):2305–2316
- Merlin O, Walker JP, Chehbouni A, Kerr Y (2008) Towards deterministic downscaling of SMOS soil moisture using MODIS derived soil evaporative efficiency. *Remote Sens Environ* 112(10):3935–3946
- Minacapilli M, Cammalleri C, Ciraolo G, D'Asaro F, Iovino M, Maltese A (2012) Thermal inertia modeling for soil surface water content estimation: a laboratory experiment. *Soil Sci Soc Am J* 76:92–100
- Minacapilli M, Iovino M, Blanda F (2009) High resolution remote estimation of soil surface water content by a thermal inertia approach. *J Hydrol* 379(3–4):229–238
- Mira M, Valor E, Caselles V, Rubio E, Coll C, Galve JM, Niclos R, Sanchez JM, Boluda R (2010) Soil moisture effect on thermal infrared (8–13- $\mu$ m) emissivity. *IEEE Trans Geosci Remote Sens* 48(5):2251–2260
- Mladenova I, Lakshmi V, Jackson TJ, Walker JP, Merlin O, de Jeu RAM (2011) Validation of AMSR-E soil moisture using L-band airborne radiometer data from National Airborne Field Experiment 2006. *Remote Sens Environ* 115(8):2096–2103
- Naeimi V, Wagner W, Scipal K, de Jeu R, Martínez-Fernández J (2006) Soil moisture from operational meteorological satellites. *Hydrogeol J* 15(1):121–131
- Notarnicola C, Caporaso L, Di Giuseppe F, Temimi M, Ventura B, Zebisch M (2012) Inferring soil moisture variability in the Mediterrean Sea area using infrared and passive microwave observations. *Can J Remote Sens* 38(1):46–59
- Notarnicola C, Lewinska KE, Temimi M, Zebisch M (2013) Application of the apparent thermal inertia concept for soil moisture estimation in agricultural areas. In: Kuenzer C, Dech S (eds) *Thermal infrared remote sensing*. Springer, Dordrecht, pp XXX–XXX
- Paloscia S, Macelloni G, Santi E (2006) Soil moisture estimates from AMSR-E brightness temperatures by using a dual-frequency algorithm. *IEEE Trans Geosci Remote Sens* 44 (11):3135–3144
- Parajka J, Naeimi V, Blöschl G, Wagner W, Merz R, Scipal K (2006) Assimilating scatterometer soil moisture data into conceptual hydrologic models at the regional scale. *Hydrol Earth Syst Sci* 10:353–368
- Parinussa RM, Meesters A, Liu YY, Dorigo W, Wagner W, de Jeu RAM (2011) Error estimates for near-real-time satellite soil moisture as derived from the land parameter retrieval model. *IEEE Geosci Remote Sens Lett* 8(4):779–783
- Patel NR, Anapashsha R, Kumar S, Saha SK, Dadhwal VK (2008) Assessing potential of MODIS derived temperature/vegetation condition index (TVDI) to infer soil moisture status. *Int J Remote Sens* 30(1):23–39
- Portmann F, Wagner W, Scipal K (2003) Evaluation of early morning heating rate derived soil moisture in Southern Europe. In: The 2003 EUMETSAT meteorological satellite conference, Weimar, 29 Sept–3 Oct 2003
- Price JC (1977) Thermal inertia mapping: a new view of the Earth. *J Geophys Res* 82 (18):2582–2590
- Price JC (1990) Using spatial context in satellite data to infer regional scale evapotranspiration. *IEEE Trans Geosci Remote Sens* 28(5):940–948
- Price JC (1983) Estimating surface temperatures from satellite thermal infrared data—a simple formulation for the atmospheric effect. *Remote Sens Environ* 13(4):353–361
- Rosema A, Verhees L, van Putten E, Gielen H, Lack T, Wood J, Lane A, Fannon J, Estrela T, Dimas M, de Bruin H, Moena A, Meijninger W (2001) European energy and water balance monitoring system. Final report of 4th framework programme of the European Commission Contract Nr. ENV4-CT97-0478, EARS Remote Sensing Consultants, Delft, The Netherlands, pp 147

- Sanchez JM, French AN, Mira M, Hunsaker DJ, Thorp KR, Valor E, Caselles V (2011) Thermal infrared emissivity dependence on soil moisture in field conditions. *IEEE Trans Geosci Remote Sens* 49(11):4652–4659
- Sandholt I, Rasmussen K, Andersen J (2002) A simple interpretation of the surface temperature/vegetation index space for assessment of surface moisture status. *Remote Sens Environ* 79 (2–3):213–224
- Scheidt S, Ramsey M, Lancaster N (2010) Determining soil moisture and sediment availability at White Sands Dune Field, New Mexico, from apparent thermal inertia data. *J Geophys Res* 115 (F2):F02019
- Schmugge T, Blanchard B, Anderson A, Wang J (1978) Soil moisture sensing with aircraft observations of the diurnal range of surface temperature. *Water Resour Bull* 14:169–178
- Shih SF, Jordan JD (1993) Use of Landsat thermal-IR data and GIS in soil moisture assessment. *J Irrig Drain Eng* 119(5):868–879
- Sobrino JA, El Kharraz MH (1999) Combining afternoon and morning NOAA satellites for thermal inertia estimation 1. Algorithm and its testing with Hydrologic Atmospheric Pilot Experiment-Sahel data. *J Geophys Res* 104(D8):9445–9453
- Tramutoli V, Claps P, Marella M (2000) Hydrological implications of remotely sensed thermal inertia. *Proceedings of remote sensing and hydrology symposium, Santa Fe, IAHS Publication* 267:207–211
- Van den Hurk B (2001) Energy balance based surface flux estimation from satellite data, and its application for surface soil moisture estimation. *Meteorol Atmos Phys* 76:43–52
- Van Doninck J, Peters J, De Baets B, De Clercq EM, Ducheyne E, Verhoest NEC (2011) The potential of multitemporal Aqua and Terra MODIS apparent thermal inertia as a soil moisture indicator. *Int J Appl Earth Obs Geoinfo* 13(6):934–941
- Veroustraete F, Li Q, Verstraeten WW, Chen X, Bao A, Dong Q, Liu T, Willems P (2012) Soil moisture content retrieval based on apparent thermal inertia for Xinjiang province in China. *Int J Remote Sens* 33(12):3870–3885
- Verstraeten WW, Veroustraete F, van der Sande CJ, Grootaers I, Feyen J (2006) Soil moisture retrieval using thermal inertia, determined with visible and thermal spaceborne data, validated for European forests. *Remote Sens Environ* 101(3):299–314
- Wagner W, Lemoine G, Rott H (1999) A method for estimating soil moisture from ERS scatterometer and soil data. *Remote Sens Environ* 70:191–207
- Wagner W, Blöschl G, Pampaloni P, Calvet JC, Bizzarri B, Wigneron JP, Kerr Y (2007) Operational readiness of microwave remote sensing of soil moisture for hydrologic applications. *Nord Hydrol* 38(1):1–20
- Wagner W, Hahn S, Kidd R et al (2012) The ASCAT soil moisture product: specifications, validation results, and emerging applications. *Meteorol Z* (submitted)
- Wang L, Qu JJ, Zhang S, Hao X, Dasgupta S (2007) Soil moisture estimation using MODIS and ground measurements in eastern China. *Int J Remote Sens* 28(6):1413–1418
- Wetzel PJ, Woodward RH (1987) Soil moisture estimation using GOES-VISSLR infrared data: a case study with a simple statistical method. *J Clim Appl Meteor* 26:107–117
- Xue Y, Cracknell AP (1995) Advanced thermal inertia modelling. *Int J Remote Sens* 16 (3):431–446
- URL1: <http://www.ipf.tuwien.ac.at/insitu/>

# Chapter 17

## Application of the Apparent Thermal Inertia Concept for Soil Moisture Estimation in Agricultural Areas

Claudia Notarnicola, Katarzyna Ewa Lewińska, Marouane Temimi, and Marc Zebisch

**Abstract** The objective of this study is to infer information on Soil Moisture Content (SMC) in agricultural areas using daily gradient of brightness temperature and albedo from MODIS AQUA, based on the so-called apparent thermal inertia (ATI) approach. The developed algorithm has been validated over two different test sites in Italy, Emilia Romagna and South Tyrol regions, and one test site in France, the Pyrenees region, where ground truth measurements were available. For the Emilia Romagna and the Pyrenees test sites, the obtained ATI values were well correlated with SMC values. For the South Tyrol test site, due to large heterogeneity in the mountain landscape, the correlation between ATI and SMC was relatively weak. Cloud coverage which reduces the number of available observations and the vegetation cover which decreases the sensitivity of ATI to SMC were the main limitations in all analyzed test sites. This study showed that a combination of data with a frequent revisit time and polar orbiting sensors can alleviate the impact of cloud coverage on the retrieval. In fact, a comparison between ATI derived from MSG (Meteosat Second Generation) SEVIRI (Spinning Enhanced Visible and Infrared Imager) and MODIS indicated a good correlation between the two estimates thus demonstrating the potential of a possible synergy between the two sensors.

### 17.1 Theoretical Background

Information on the spatial and temporal variability of soil moisture is of great importance in hydrological applications, such as like flood prediction in case of extreme rainfall events, watershed management during dry periods, irrigation

---

C. Notarnicola (✉) • K.E. Lewińska • M. Zebisch  
European Academy of Bozen/Bolzano (EURAC), Bolzano, Italy  
e-mail: [claudia.notarnicola@eurac.edu](mailto:claudia.notarnicola@eurac.edu)

M. Temimi  
NOAA-CREST, The City College, The City University of New York, New York, NY, USA

scheduling, precision farming, and earth sciences, like climate change analysis and meteorology.

Techniques and methods to retrieve soil moisture have been largely based on the use of passive and active microwave instruments because of their sensitivity to liquid water in the upper few centimeters of the soil. Active microwave (MW) sensors, such as SAR (Synthetic Aperture Radar), have demonstrated capability to detect soil moisture under a variety of topographic and vegetation conditions from watershed to field scale (Moran et al. 2000). Another main characteristic of the microwave sensors is the independence from meteorological conditions. SAR as an active microwave sensor can provide information on a small scale and at remarkably high spatial resolution (from 100 m to less than 1 m). The revisiting time of SAR sensors can reach 10 days (e.g. TerraSAR-X and RADARSAT2 using their capability to steer the antenna and point to the same area with different viewing angles). However, for some daily operational applications, this revisiting time cannot be adequate. On the other hand, active microwave sensors like ASCAT (Advanced Scatterometer) onboard METOP (Meteorological Operational Satellite), and the ERS (European Remote-Sensing Satellite) Scatterometer or passive microwave sensors like AMSR-E (Advanced Microwave Scanning Radiometer – Earth Observing System) can provide daily and reliable information on soil moisture. However, their spatial resolution is still relatively coarse ranging from 10 to 25 km (Wagner et al. 1999; Njoku et al. 2003).

As an alternative, the exploitation of optical and infrared sensors such as METEOSAT (Meteorological satellite) and AVHRR (Advanced Very High Resolution Radiometer) (Xue and Cracknell 1995) which were mainly designed for atmospheric operational monitoring to infer land surface parameters has increased in recent years. Despite their reduced sensitivity to the SMC when compared to microwave instruments, optical and infrared sensors offer the potential of providing daily information on the soil moisture status. Their main limitation, however, is the cloud presence which reduces notably the number of images to be used. One of the methods proposed for detecting soil moisture with infrared data is based on the thermal inertia (TI) concept. As it was initially proposed by Price (1977), the TI-based concept exploits information on thermal conductivity, bulk density and specific heat capacity of the target. However, the application of this method is not straightforward as the knowledge of the physical properties of the target is required. So, the apparent thermal inertia (ATI) was proposed to make the determination of TI easier using the diurnal gradient of surface thermal responses (physical temperature) and thus can be derived directly from multi-spectral remotely sensed imagery (Xue and Cracknell 1995). The relationship between SMC and ATI has been investigated in numerous previous studies for both bare soil and vegetated areas. Xue and Cracknell (1995) applied the ATI approach to AVHRR data to determine land surface thermal inertia. Cai et al. (2007) used MODIS (Moderate Resolution Imaging Spectroradiometer) images over the northern Chinese Plain and obtained a mean difference between measured and estimated soil moisture values of 4.3 % over bare and sparsely vegetated fields. To infer reliable SMC estimates derived from ATI, the temperature difference should be larger than 10°C.

Verstaeten et al. (2006) applied this method to METEOSAT (Meteorological Satellite) data to monitor soil moisture in forested areas. Due to the negative effect of vegetation particularly dense forest on soil moisture retrieval, the evaluation of the derived SMC against EUROFLUX data led to a RMSE (root mean square error) ranging from 0.01 to 0.08 m<sup>3</sup>/m<sup>3</sup>. The main limitation of geostationary satellites, such as METEOSAT, lies in their coarse spatial resolution (around 3–4 km at mid latitudinal areas such as Italy and France). For this reason, focus has been placed more on the exploitation of polar orbiting sensors such as MODIS and AVHRR which provide thermal infrared data at 1 km resolution (Minacapilli et al. 2009; Scheidt et al. 2010; Van doninck et al. 2011). Schiedt et al. (2010) applied the ATI approach to ASTER (Advanced Spaceborne Thermal Emission and Reflection Radiometer) and MODIS images in order to determine soil moisture values and to provide a predictive tool for wind erosion in arid environments. Van Doninck et al. (2011) studied the use of MODIS day and night acquisitions to determine the full temperature cycle to be used later in the ATI calculation.

The main limitation of the ATI-based approach is certainly cloud coverage which can reduce the number of useful acquisitions up to 50 % (Notarnicola et al. 2012). The use of multiple sensors can mitigate this limitation. Possible data fusion approaches can include different optical sensors like MODIS and SEVIRI which was adopted for meteorological studies of cloud properties (Deneke et al. 2007) and land surface temperature comparison (Atitar et al. 2008; Zakšek and Schroedter-Homscheidt 2009). Merging data from MODIS and SEVIRI for ATI determination is possible because of their similar spectral bands (for the albedo and brightness temperature calculation). In addition, the temporal frequency of SEVIRI (images every 15 min) can be highly useful to solve the problem of cloud coverage.

This chapter has two main objectives:

- Testing the applicability of MODIS derived ATI for SMC retrieval in three different locations (two flat agricultural areas and one mountain locations covering diverse ecosystems from wild vegetation to lowlands under mainly agricultural land use). In all three cases time series of around 1 year of data were exploited in order to provide the confidence level of accuracy.
- Testing a possible merge of data from optical sunsynchronous and geostationary sensors to overcome the problem of cloud obstruction. The consistency of ATI values from MODIS and SEVIRI was analyzed to ensure that both products can be used in synergistic way.

## 17.2 Test Site Description

The selection of the test sites and the timeframe of the study were mainly motivated by the availability of long time series of SMC ground measurements. Another crucial factor was related to availability of daily MODIS images due to cloud coverage and their derived products that are used to determine ATI. As a result three test sites were selected:

- **Emilia Romagna region** test site located at around 44°39'N-11°37'E with an acquisition period of SMC ground measurements from June 2008 to June 2009;

- **South Tyrol region** test site located at around 46°37'N-11°24'E with an acquisition period of SMC ground measurements from January to December 2010;
- **Pyrenees region** (belonging partly to the Midi-Pyrénées and partly to the Languedoc-Roussillon regions in France) test site located at around 44°44'N-1°54'E with an acquisition period of SMC ground measurements from January to December 2007.

The Emilia Romagna test site is located within the flatlands of the Italian Po Valley, which is mostly covered by farmlands. Vegetation is therefore a mixture of crops, vineyards, orchards, rice fields, and meadows. Five measurement spots, one pre-existent located in an intensive meteorological base of San Pietro Capofiume, and four newly created stations equipped with soil moisture ground sensors were used in the study. Observations are recorded on an hourly basis by a Time-Domain Reflectometer (TDR) which measures SMC and temperature profiles at eight unevenly spaced levels below the ground between 10 and 100 cm. In this study, 10 cm depth measurements were considered.

The South Tyrol (Northern Italy) test site is located in a completely different environment dominated by mountainous landscape. The study area chosen for the experimental analysis is the Mazia Valley which is a small side valley in the north-western part of South Tyrol region. It covers an area of around 100 km<sup>2</sup> ranging from 920 m a.s.l. (Sluderno) to 3,738 m a.s.l. (Palla Bianca). Despite the relatively small dimension, the Mazia Valley is representative of geomorphologic and topographic conditions in Alpine regions. The area is constantly monitored by 16 meteorological stations distributed along the valley in specific locations which were selected according to elevation, slope, aspect, soil type, and land cover conditions. These stations measure SMC at 10 and 20 cm and other meteorological variables such as air temperature and humidity, precipitation, wind speed and direction, and solar radiation. Excluding forests, the most diffuse land cover/use types are meadow and pasture which present quite heterogeneous characteristics in term of vegetation, spatial distribution, and human usage.

The third test site that is part of SMOSMANIA (Soil Moisture Observing System – Meteorological Automatic Network Integrated Application) (Calvet et al. 2007; Albergel et al. 2008) activities is dedicated to the validation of Soil Moisture and Ocean Salinity (SMOS) products. The ground measurement stations are located in the Pyrenees region (France) in relatively flat areas. The vegetation cover at those sites consists of natural fallow cut once or twice a year. Four soil moisture probes, ThetaProbe ML2X of Delta-T Devices, were horizontally installed per station at depths of 5, 10, 20 and 30 cm (Albergel et al. 2008). In this study 5 cm depth measurements were considered. These soil moisture data have been retrieved from the “International Soil Moisture Network” (Dorigo et al. 2010).

In all test sites, in situ observations of SMC were carried out at 1 h interval. Daily values are an arithmetic average of the observation collected during the entire day.

## 17.3 Satellite Data Sets

As MODIS images, MODIS AQUA level 1B MYD02 at-sensor reflectances and MODIS AQUA level 2 MYD09 at-surface reflectances and the MYD35 cloud cover product were obtained from the LAADS (Level 1 Atmosphere Archive and Distribution System) ([URL1](#)) and National Snow and Ice Data Center ([URL2](#)) web sites. MODIS AQUA images were selected instead of MODIS TERRA due to the acquisition time (early afternoon and soon after midnight) over the three test sites. The overpass time of MODIS AQUA, around 1:30 AM/PM grants that temperatures observation is occurring close to the daily minima and maxima. Acquisitions from AQUA lead therefore to a better estimate of the temperature diurnal gradient which is considered a key factor for the determination of the apparent thermal inertia. This aspect is important in order to capture the whole diurnal cycle of temperature. This issue is addressed in this chapter where daily maxima and minima temperature are compared to satellite acquisition time.

## 17.4 Methodology: Theory and Practical Implementation

### 17.4.1 Theoretical Description of Thermal Inertia

Thermal inertia (TI) is a physical parameter that indicates the capability of a material to conduct or to store heat and is an indicator of the material resistance to changes in temperature. In other words, it expresses bodies' capability to store heat during the day and re-irradiate it during the night and is defined as:

$$TI = \sqrt{\rho K c} \left( \text{J m}^{-2} \text{K}^{-1} \text{s}^{-1/2} \right) \quad (17.1)$$

where  $\rho$  is the material density ( $\text{kg m}^{-3}$ ),  $K$  is the thermal conductivity ( $\text{W m}^{-1} \text{K}^{-1}$ ) and  $c$  the specific heat capacity ( $\text{J kg}^{-1} \text{K}^{-1}$ ). Water bodies have a higher TI than dry soils and rocks and then exhibit a lower diurnal temperature fluctuation. When soil water content increases, TI increases proportionally, thereby reducing the diurnal temperature fluctuation.

A theoretical expression for the thermal inertia as a function of soil moisture was proposed by Ma and Xue ([1990](#)) and written as:

$$TI = \left\{ \left( 2.1 ds^{[1.2 - 0.02(ds/d)w]} e^{[-0.007(wds/d - 20)^2]} \right) + ds^{[0.8 + 0.02(ds/d)w]} \right\} \times \\ (0.2w/d)ds^2 / 0.001\sqrt{100} \quad (17.2)$$

where  $ds$  is the soil density,  $d$  is the water density and  $w$  is the percentage of soil moisture. With the knowledge of these parameters, for example from ground measurements, an estimate of TI can be derived. Considering this expression, a unique relationship between soil moisture and TI values is defined. In this work, the TI values as described in Eq. (17.2) are compared to corresponding ATI values estimated from remotely sensed data in order to verify the consistency between the two variables and detect the variability under different vegetation conditions.

### **17.4.2 *Proposed Methodology for ATI***

As mentioned in the introduction, ATI is considered as a surrogate (apparent) value for the actual thermal inertia and is obtained from spectral measurements of the surface albedo A and the diurnal temperature range  $\Delta T$  with the following simple formulation:

$$ATI = \frac{(1 - A)}{\Delta T} \quad (17.3)$$

The proposed method for ATI calculation which is based on MODIS AQUA images is adapted from the one proposed by Cai et al. (2007). In order to calculate the ATI maps, from the MODIS images (MYD02, MYD09, and MYD35 products), the processing steps are:

- First step: Data re-projection. In this first phase, the images are reprojected to the same georeference system by using ENVI add-on re-projection module MODIS toolkit. MODIS AQUA 1B, MYD02, data sets are in swath geometry and then are re-projected to UTM WGS 84. MODIS AQUA 2B MYD09 images are in ISIN projection and are also transformed into UTM WGS 84 in order to have all the images in the same georeference system.
- Second step: Data calibration and calculation of physical variables. The MYD02 images band 31 (11  $\mu\text{m}$ ), day and night acquisitions are transformed from DN to radiance and then to brightness temperature (BT) values by using the inverse Planck law. Being level-2 data, the MYD09 images are already set in at-surface reflectances as these products also include atmospheric corrections of reflectance and thermal data. The albedo (A) is calculated through the expression proposed by Liang (2000) by using the atmospherically corrected resampled to 1 km images of bands 1, 2, 3, 4, 5, and 7 available in MYD09 product. In the last step the BT and albedo bands are stacked together.
- Third step: Cloud screen. A cloud mask is applied to the image to reduce the influence of cloud cover. The MYD35 products are considered in this phase.
- Fourth step: ATI calculation from BT day and night and Albedo bands by using Eq. (17.3).

As auxiliary information, land-use and MODIS derived NDVI maps were used for the masking of agricultural areas and for the distinction of areas with different levels of vegetation densities.

## 17.5 Comparison of ATI and SMC Ground Measurements Over the Selected Test Sites

### 17.5.1 *Emilia Romagna Test Site*

In the Emilia Romagna test site, the ATI values derived from 57 cloud-free MODIS images acquired from June 2008 to June 2009 were compared with corresponding SMC measurements. This temporal analysis was performed in order to understand the ATI behavior under different SMC, vegetation and meteorological conditions throughout the seasons.

Two further processing steps were considered to reduce the noise observed in the ATI time series. Based on the experience and values found in the literature (Tramutoli et al. 2001; Cai et al. 2007), the ATI values outside the range  $0\text{--}0.15 \text{ K}^{-1}$  were considered as invalid values. These outliers may be caused by persistent clouds which were not included in the cloud mask. A moving window averaging filter (MWA) was applied to further reduce the noise present in the data.

In Fig. 17.1, ATI values with and without the MWA filter are compared with SMC in situ measurements. The ATI values exhibit two clusters: one for low values of NDVI (below 0.4) and another for higher values of NDVI (higher than 0.4). From this graph, we can deduce that the presence of vegetation reduces ATI dynamics mainly due to the different thermal properties of vegetation. ATI variability is the highest in bare or sparsely vegetated soils (Cai et al. 2007).

One main difficulty with this kind of comparisons is that soil moisture observations are local point measurements while ATI values are estimated on a pixel basis. In this case, the spatial average is not representative of the point observations because of the mismatch between observation scales. For this reason the median value has been assumed to be a reasonable estimator (Tramutoli et al. 2001).

The determination coefficients which were determined to assess the agreement between SMC values and ATI values, when the MWA filter is not applied to the data, are indicated in Table 17.1. All the determination coefficients are significant with 95 % confidence level. In this case, the application of the filter does not seem to introduce any significant improvement.

ATI values were also compared to TI values determined using Eq. (17.2). In the formulation of TI, the SMC data derived from ground measurements were considered as input, the same used in the comparison with ATI values in Fig. 17.2. The used soil density values which vary between  $2.5$  and  $3 \text{ g/cm}^3$  are in agreement with values recommended in the literature (Cai et al. 2007; Scheidt et al. 2010). The determination coefficients between ATI (filtered) and TI values were  $R^2 = 0.30$

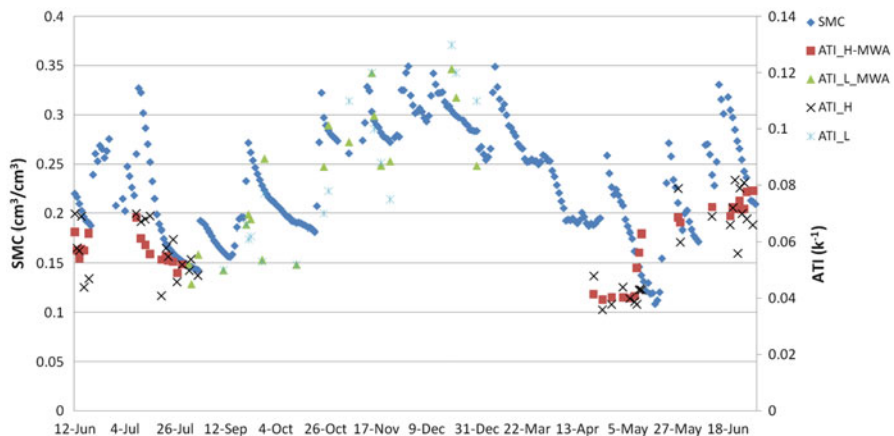


**Fig. 17.1** Comparison of the temporal trend among SMC ( $\text{cm}^3/\text{cm}^3$ ), ATI originally calculated and ATI filtered (MWA) for the Emilia Romagna test site.  $H$  stands for High NDVI values ( $>0.4$ ) and  $L$  stand for Low NDVI values ( $<0.4$ )

**Table 17.1** Comparison between ATI and measured soil moisture values (SMC) over 1 year period (57 observations/days) for Emilia Romagna test site

	No filter	MWA filter
NDVI < 0.4	0.58	0.59
NDVI > 0.4	0.45	0.45

The values represent the determination coefficients between ATI values and SMC with and without the filter applications

and 0.77 for vegetated areas and for bare soils, respectively. The vegetation effect reduces the sensitivity of ATI to soil moisture which is similar to the effect determined by lower values of soil density. For this reason two exponential trends of ATI with soil moisture were introduced and compared with the exponential trend of TI values.

To qualitatively evaluate the spatial distribution of soil moisture values derived using the ATI-based approach, examples of ATI maps and the corresponding soil moisture classes illustrated in Fig. 17.3 were compared. Based on ATI values, only four main classes of soil moisture were identified:

- low SMC values for ATI lower than  $0.05 \text{ K}^{-1}$ ;
- medium SMC values for  $0.05 \text{ K}^{-1} < \text{ATI} < 0.07 \text{ K}^{-1}$
- medium-high SMC values for  $0.07 \text{ K}^{-1} < \text{ATI} < 0.085 \text{ K}^{-1}$
- high SMC values for ATI higher than  $0.085 \text{ K}^{-1}$ .

The spatial distribution of soil moisture inferred from ATI values seems to be reasonable and in line with land surface conditions and topographic features.

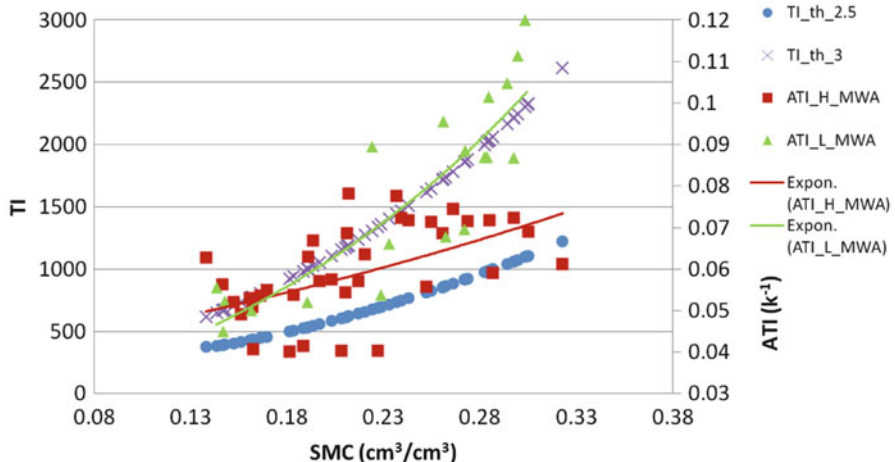


**Fig. 17.2** Comparison between TI and ATI filtered (MWA) for the Emilia Romagna test site. *H* stands for High NDVI values ( $>0.4$ ) and *L* stand for Low NDVI values ( $<0.4$ )

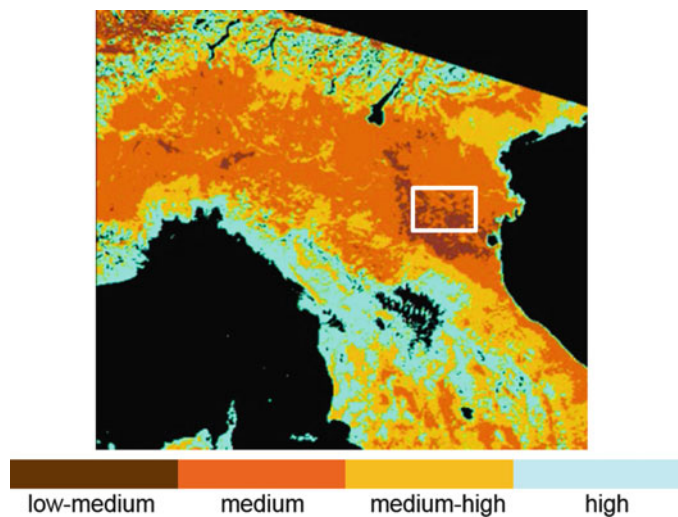


**Fig. 17.3** SMC derived classes for the Emilia Romagna test site on 3rd March 2008. The *white rectangle* indicates the locations of ground measurements stations

Figure 17.3 shows soil moisture classes obtained for the area of North Italy (Emilia Romagna test site is situated in the central part of the area). Higher soil moisture values are obtained in the northern and the southern parts (Alps and Apennines) of the image, close to the mountainous areas while the lowest are found in the Po valley that in summer season can experience also long dry periods.

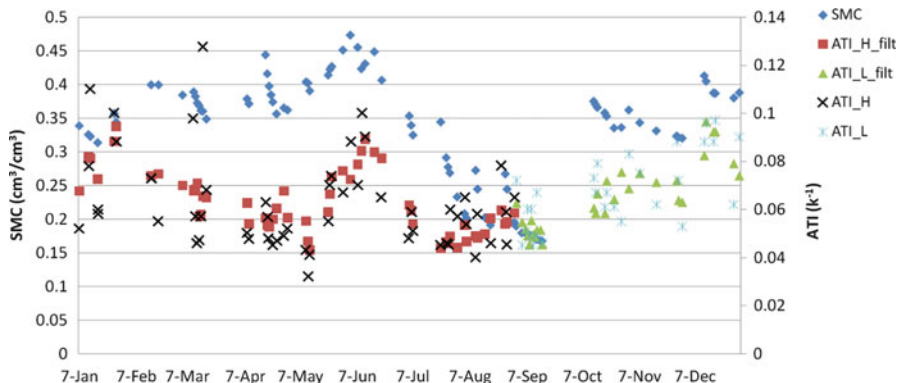


**Fig. 17.4** Comparison of the temporal trend among SMC ( $\text{cm}^3/\text{cm}^3$ ), ATI originally calculated and ATI filtered (MWA) over the Pyrenees test site.  $H$  stands for High NDVI values ( $>0.4$ ) and  $L$  stand for Low NDVI values ( $<0.4$ )

**Table 17.2** Temporal comparison between ATI and measured soil moisture values (SMC) over 1 year period (87 days) for Pyrenees test site

	No filter	MWA filter
NDVI < 0.4	0.61	0.68
NDVI > 0.4	0.23	0.24

The values represent the determination coefficients between ATI values and SMC in the different cases considered

### 17.5.2 Pyrenees Test Site

In the Pyrenees test site, ATI values were derived and compared to SMC in situ measurements for 87 cloud free days in 2007. In Fig. 17.4, the comparison between ATI and SMC values for the French test site is shown and in Table 17.2 the determination coefficients for the filtered and non-filtered data are reported. Also, in this case, the obtained values were separated into two main classes according to their NDVI value. The two obtained clusters were similar to those found using values from the Emilia Romagna test site.

Eliminating the outliers through the application of the MWA has improved the determination coefficients only in the case of bare or sparsely vegetated soils ( $\text{NDVI} < 0.4$ ). For  $\text{NDVI} > 0.4$  no relevant change is found. All the determination coefficients are significant with 95 % confidence level. In case of  $\text{NDVI} > 0.4$  the confidence level was 90 %. The comparison of ATI to TI values (Fig. 17.5) as calculated from expression (17.3) lead to determination coefficients of  $R^2 = 0.42$  for vegetated areas and 0.83 for bare soils and show a pattern similar to that found in the Emilia Romagna test site.

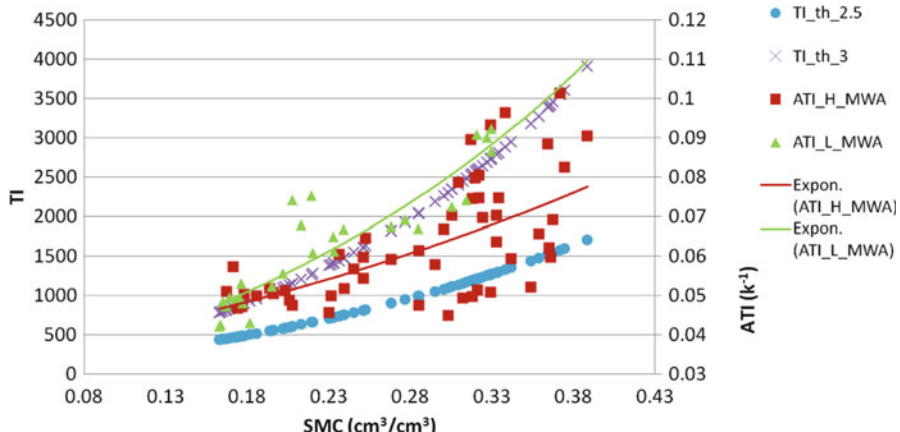


**Fig. 17.5** Comparison between TI and ATI filtered (MWA) for the Pyrenees test site. *H* stands for High NDVI values ( $>0.4$ ) and *L* stand for Low NDVI values ( $<0.4$ )

### 17.5.3 South Tyrol Test Site

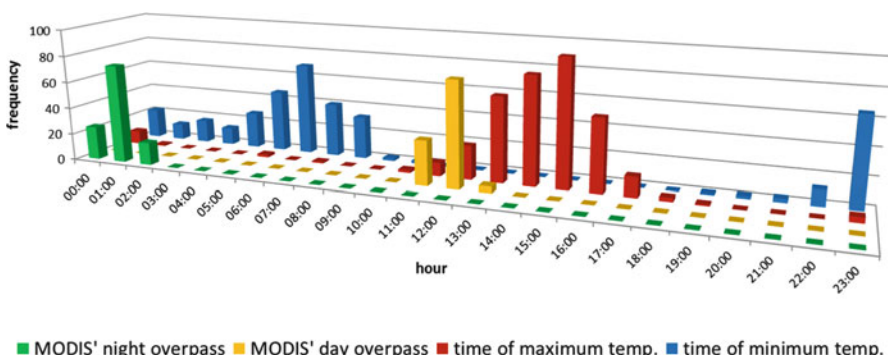
For the South Tyrol test site, ATI values derived for 116 days of the year 2010 were compared with SMC ground measurements. Among the selected test sites, South Tyrol can be considered as a particular case. Results did not show strong relationship between the two considered variables. SMC variability was not in agreement with MODIS derived ATI values which show a significant amount of noise. The noise in ATI values is persistent and can be observed at different NDVI intervals and vegetation densities. The weak agreement between ATI values and SMC can be attributed to several factors. First, the coarse resolution of MODIS-based ATI estimates, 1 km, is not appropriate for an accurate monitoring of soil moisture, particularly in complex mountainous areas such as South Tyrol. It is difficult to capture within one pixel homogeneous areas with the same land cover, exposition and elevation parameters. Since the change in any of these parameters should affect ATI values, then it is impossible to link ATI values on the pixel basis to point measurements. Second, dry climate conditions in South Tyrol and the scarcity of precipitation lead to – especially in agricultural areas – frequent irrigation practices. Obviously, this additional volume of water, artificially introduced, strongly affected the ATI values and their agreement with in situ observation of SMC. Moreover, the amount of ground truth data used for the validation is limited considering the complexity of the study site. Meteorological stations, used for SMC measurements, are located mainly in the valleys' floor, leaving higher placed areas with an information gap.

## 17.6 Analysis of the Temperature Cycle and Its Relationship with Satellite Acquisition Time

The brightness temperature measurements should be acquired when the air temperature reaches its local maxima and minima in order to estimate the proper SMC values. However, the overpass time of MODIS/AQUA i.e. 1:30 AM/PM, may not coincide with the diurnal extremes of surface temperature.

In order to understand this problem and shed more light on ATI monitoring, AQUA overpass time over South Tyrol was compared to time of the minimum and maximum temperature recorded at the selected meteorological station located in the Mazia Valley. The analysis was done using daily ground measurements data recorded in 2010 and MODIS acquisition time for day and night brightness temperature recorded for all available 116 days. Results presented in Fig. 17.6 showed a weak agreement between MODIS/AQUA overpass time and actual time of diurnal extreme temperatures occurrence. Satellite overpass takes place usually around 1:30 a.m. (descending overpass) for night, and 1:30 p.m. (ascending overpass) for day acquisition. Reported temperature measurements are not in phase with extreme diurnal temperatures. The lowest daily temperatures were recorded usually during the early morning (from 5 to 7 a.m.), while the highest temperatures were observed in early afternoon (from 1 until 4 p.m.).

A similar investigation was done for the Emilia Romagna test site. Also, in this case, obtained results confirmed discrepancies between AQUA overpass time and the occurrence of the minimum temperature. For the majority of days diurnal minimum temperature was recorded in the early morning. This pattern is obviously a result of natural heat radiation processes, connected directly with daily sun cycle. The proven lack of synchronicity between recorded MODIS brightness temperature images, and real minimum and maximum temperature might result in the inaccuracy of ATI measurements. In order to take into account this inaccuracy, Van Doninck et al. (2011) suggested modeling extreme diurnal temperatures using sinusoidal approximation fitted to available MODIS temperature measurements.



■ MODIS' night overpass ■ MODIS' day overpass ■ time of maximum temp. ■ time of minimum temp.

**Fig. 17.6** Comparison between timing (local time) of day and night MODIS/Aqua overpasses with actual time of minimum and maximum temperature occurrence during the day (On the bases on meteorological measurements acquired for all 365 days of the year 2010, and 116 pairs of day and night brightness temperature satellite images)

## 17.7 Synergy with MSG-SEVIRI

Although MODIS Aqua satellite images belong to the most suitable visible (VIS) and TIR data for the ATI monitoring at the moment, they are very vulnerable to cloud cover and atmospheric contamination, which obviously limits the number of potential observations.

One of the considered solutions to overcome this limitation and thus increase the number of available ATI observations is the synergy between MODIS images (or any other moderate resolution satellite data suitable for ATI calculation) and data acquired with higher temporal frequency. Currently, the only possible options are sensors on board of geostationary, meteorological satellites such as METEOSAT, NOAA or Kalpana-1. Although the resolution of images from these radiometers is rather coarse (from one up to few kilometers) data are registered with a sub-hour frequency. For the area of Europe and Africa SEVIRI (onboard on MSG – METEOSAT Second Generation) data provide probably the best opportunity for synergy with MODIS images. SEVIRI acquires data in 12 bands (4 VIS/NIR and 8 IR) at 3 km of resolution. For ATI monitoring the availability of VIS (0.3–0.4  $\mu\text{m}$ ) and IR bands (10.8 and 12.0  $\mu\text{m}$ ) are especially crucial. A SEVIRI repetition time of 15 min considerably increases chances for cloud free observations for the area corresponding to the test site.

The study was carried out for a lowland area of around 4,230  $\text{km}^2$  located in Emilia Romagna (Italy) using pairs of MODIS-SEVIRI data registered during seven chosen days of 2009. Data were selected in order to limit the time difference between acquisition of corresponding MODIS and SEVIRI images to not more than 5 min. ATI values were calculated for MODIS images using the approach presented in the previous section and for SEVIRI images using land surface temperature (LST) (Freitas et al. 2010) and albedo (LSA SAT 2010). Mutual similarities in mean and standard deviation of ATI values were reported for all considered pairs of datasets. Correlation performed between corresponding MODIS and SEVIRI derived ATI images indicated good accordance between data, especially for images acquired during clear-sky conditions (Table 17.3).

During the analysis, geometric limitations of SEVIRI scanner for sensing highlands and mountainous regions were found and confirmed. Moreover, the importance of cloud detection in both images was highlighted and defined as essential for accurate data fusion of the two sensors.

**Table 17.3** Basic correlation statistics obtained for ATI ( $\text{K}^{-1}$ ) values derived for corresponding cloud free MODIS-BT and SEVIRI-LST datasets

Date	Number of pixels	Regression	t-value of regression	Constant (offset)	$R^2$
27 July	364	1.230*	28.157	0.011	0.687*
2 August	423	1.019*	28.193	0.016	0.654*
1 September	423	1.798*	43.907	-0.008	0.821*
13 October	425	1.478*	37.225	-0.013	0.767*

\*Sig = 0.000

Despite considerable differences in data characteristics, general comparison between MODIS and SEVIRI for ATI monitoring was found very promising thus deserving further investigation.

## 17.8 Conclusions

The Apparent Thermal Inertia (ATI) concept has been tested for soil moisture content (SMC) evaluation in agricultural areas. ATI estimates derived from MODIS Aqua images were applied to three test sites. In all three cases ATI values were compared with SMC values derived from in-situ sensors. This analysis provides a fair assessment of what can be extracted from thermal images in terms of soil moisture information. While quantitative values of SMC are far from being achievable due to the high variability of ATI values and the noise arising from the interference with vegetation, information on the soil status are still clearly extractable with an acceptable level of accuracy. By considering all the diverse sources of errors which affect the ATI estimates, it was still possible to determine 3–4 levels of soil moisture which in many applications can still suffice for an effective territory monitoring on a daily basis. The main drawback of the use of MODIS data remains the strong effect of vegetation and cloud presence. Vegetation determines a lower sensitivity of ATI values to soil moisture changes in all the analyzed cases. These behaviors are evident when comparing both with SMC values and TI theoretical values.

A separate case can be considered at the South Tyrol test site. In this case, vegetation, geomorphology, landscape and the occurrence of minimum and maximum temperature not in coincidence with satellite overpasses make the SMC monitoring through ATI values very difficult.

To reduce the impact of cloud coverage, MODIS capabilities could be complemented with the use of geostationary satellite data such as SEVIRI, which, with a temporal resolution of 15 min, can provide good cloud free acquisitions soon after or just before the MODIS images. In this context, a comparison between MODIS and SEVIRI ATI products was performed for the Emilia Romagna test site. The analysis indicates a good agreement and the possibility to identify a clear calibration relationship between the two sensors.

Some final considerations are needed regarding the ATI products in relationship to the daily SMC operational products from sensors as ERS-Scatterometer and METOP (Wagner et al. 1999; Bartalis et al. 2007). These data were already tested and proved their suitability for many applications. In the last years also ASAR ENVISAT (Advanced Synthetic Aperture Radar, Environmental Satellite) Global Monitoring images (Wagner et al. 2008) were used to provide SMC maps at 1 km resolution. With respect to these SMC products, SMC derived from ATI approach can be used as a complementary source of information for two main reasons. First, the resolution of SMC from ERS-Scatterometer and METOP (10–25 km) is not adequate for local and regional applications. In this case the resolution of 1 km of

SMC maps from ATI can be exploited to take into account the heterogeneity of the area. In this case the high resolution active microwave sensors will be the most suitable to investigate small scale phenomena. However, the time frequency which can reach up to 10 days with most recent sensors (TERRASAR-X, COSMO-SkyMed (Constellation of small Satellites for the Mediterranean basin Observation)) and the upcoming Sentinel 1 cannot be suitable for applications requesting daily information on SMC. Second, as the ATI is derived from bands available on most of the optical sensors such as MODIS and AVHRR and on new launched sensors such as Suomi NPP (Suomi National Polar-orbiting Partnership) the SMC information can be provided on a more continuous basis filling also the temporal gaps due to sensor failure as the one which affected ENVISAT in 2012.

**Acknowledgements** The authors would like to thank Ing. Giacomo Bertoldi from EURAC-Institute for Alpine Environment for providing SMC data over the South Tyrol region, and Dr. Francesca Digiuseppi from ARPA-Emilia Romagna for providing SMC data over the Emilia Romagna region.

## References

- Albergel C, Rüdiger C, Pellarin T, Calvet JC, Fritz F, Froissard F, Suquia D, Petitpa A, Piguet B, Martin E (2008) From near-surface to root-zone soil moisture using an exponential filter: an assessment of the method based on insitu observations and model simulations. *Hydrol Earth Syst Sci* 12:1323–1337
- Atitar M, Sobrino JA, Soria G, Wigneron JP, Jiménez- Muñoz JC, Julien Y, Ruescas AB (2008) Land surface temperature retrieved from SEVIRI/MSG2 data: algorithm and validation. Presentation: EUMETSAT – AMS meteorological satellite conference, EUMETSAT, Darmstadt, 8–12 Sept 2008
- Bartalis Z, Wagner W, Naeimi V, Hasenauer S, Scipal K, Bonekamp H, Figa J, Anderson C (2007) Initial soil moisture retrievals from the METOP-A Advanced Scatterometer (ASCAT). *Geophys Res Lett* 34, L20401. doi:[10.1029/2007GL031088](https://doi.org/10.1029/2007GL031088)
- Cai G, Xue Y, Hu Y, Wang Y, Guo J, Luo Y, Wu C, Zhong S, Qi S (2007) Soil moisture retrieval from MODIS data in Northern China Plain using thermal inertia model. *Int J Remote Sens* 28 (16):3567–3581
- Calvet J-C, Fritz N, Froissard F, Suquia D, Petitpa A, Piguet B (2007) In situ soil moisture observations for the CAL/VAL of SMOS: the SMOSMANIA network. In: International geoscience and remote sensing symposium, IGARSS-international geoscience and remote sensing symposium, Barcelona. doi:[10.1109/IGARSS.2007.4423019](https://doi.org/10.1109/IGARSS.2007.4423019)
- Deneke HM, Roebeling RA, Wolters ELA, Feijt A (2007) Intercomparison of cloud property retrievals from MSG-SEVIRI and MODI. Presentation: EUMETSAT – AMS meteorological satellite conference, EUMETSAT, Amsterdam, 24–28 Sept 2007
- Dorigo W, Hahn S, Hohensinn R, Paulik C, Wagner W, Drusch M, van Oevelen P (2010) The international soil moisture network-a data hosting facility for in situ soil moisture measurements in support of SMOS cal/val, *Geophysical research abstract*, vol 12, EGU2010-12063
- Freitas SC, Trigo IF, Bioucas-Dias JM, Götsche FM (2010) Quantifying the uncertainty of land surface temperature retrievals from SEVIRI/Meteosat. *IEEE Trans Geosci Remote Sens* 48 (1):523–534

- Liang S (2000) Narrow to broadband conversions of land surface albedo I algorithm. *Remote Sens Environ* 76:213–238
- LSA SAF (2010) The EUMETSAT Satellite Application Facility on Land Surface Analysis (LSA SAF), product user manual land surface albedo, SAF/LAND/MF/PUM\_AL/1.5 Issue 1.5, 19 Mar 2010
- Ma AN, Xue Y (1990) A study of remote sensing information model of soil moisture. In: Proceedings of the 11th Asian conference on remote sensing I. 15–21 Nov, International Academic Publishers, Beijing, pp P-11-1–P-11-5
- Minacapilli M, Iovino M, Blanda F (2009) High resolution remote estimation of soil surface water content by a thermal inertia approach. *J Hydrol* 379:229–238
- Moran MS, Hymer DC, Qi J, Sano EE (2000) Soil moisture evaluation using multi-temporal Synthetic Aperture Radar (SAR) in semiarid rangeland. *Agric Forest Meteorol* 105:69–80
- Njoku EG, Jackson TJ, Lakshmi V, Chan TK, Nghiem SV (2003) Soil moisture retrieval from AMSR-E. *IEEE Trans Geosci Remote Sens* 41(2):215–229
- Notarnicola C, Caporaso L, Di Giuseppe F, Temimi M, Ventura B, Zebisch M (2012) Inferring soil moisture variability in the Mediterranean Sea area using infrared and passive microwave observations. *Can J Remote Sens* 38(1):46–59
- Price JC (1977) Thermal inertia mapping: a new view of the Earth. *J Geophys Res* 82:2582–2590
- Scheidt S, Ramsey M, Lancaster N (2010) Determining soil moisture and sediment availability at White Sands Dune Field, NM from apparent thermal inertia. *J Geophys Res Earth Surf* 115: F02019. doi:[10.1029/2009JF001378](https://doi.org/10.1029/2009JF001378)
- Tramutoli V, Claps P, Marella M (2001) Hydrological implications of remotely sensed thermal inertia. In: Owe M et al (eds) *Remote sensing and hydrology 2000*, IAHS publication no. 267. IAHS Press, Wallingford, pp 207–211
- Van doninck J, Peters J, De Baets B, De Clercq EM, Ducheyne E, Verhoest NEC (2011) The potential of multitemporal Aqua and Terra MODIS apparent thermal inertia as a soil moisture indicator. *Int J Appl Earth Obs Geoinf* 13(6):934–941
- Verstaeten WW, Veroustraete F, van der Sande CJ, Grootaers I, Feyen J (2006) Soil moisture retrieval using thermal inertia, determined with visible and thermal spaceborne data, validated for European forest. *Remote Sens Environ* 101:299–314
- Wagner W, Lemoine G, Borgeaud M, Rott H (1999) A method for estimating soil moisture from ERS scatterometer and soil data. *Remote Sens Environ* 70:191–207
- Wagner W, Pathe C, Doubkova M, Sabel D, Bartsch A, Hasenauer S, Blöschl G, Scipal K, Martínez-Fernández J, Löw A (2008) Temporal stability of soil moisture and radar backscatter observed by the Advanced Synthetic Aperture Radar (ASAR). *Sensors* 8:1174–1197
- Xue Y, Cracknell AP (1995) Advanced thermal inertia modeling. *Int J Remote Sens* 16:431–446
- Zakšek K, Schroedter-Homscheidt M (2009) Parameterization of air temperature in high temporal and spatial resolution from a combination of the SEVIRI and MODIS instruments. *ISPRS J Photogramm Remote Sens* 64:414–421
- URL1: <http://ladsweb.nascom.nasa.gov>
- URL2: [http://nsidc.org/data/modis/order\\_data.html](http://nsidc.org/data/modis/order_data.html)

# Chapter 18

## Thermal Remote Sensing of Active Vegetation Fires and Biomass Burning Events

Martin J. Wooster, Gareth Roberts, Alistair M.S. Smith, Joshua Johnston,  
Patrick Freeborn, Stefania Amici, and Andrew T. Hudak

**Abstract** Thermal remote sensing is widely used in the detection, study, and management of biomass burning occurring in open vegetation fires. Such fires may be planned for land management purposes, may occur as a result of a malicious or accidental ignition by humans, or may result from lightning or other natural phenomena. Under suitable conditions, fires may spread rapidly and extensively, affecting the land cover properties of large areas, and releasing a wide variety of gases and particulates directly into Earth's troposphere. On average, around 3.4 % of the Earth's terrestrially vegetated area burns annually in this way. Vegetation fires inevitably involve high temperatures, so thermal remote sensing is well suited to its identification and study. Here we review the theoretical basis of the key approaches used to (1) detect actively burning fires; (2) characterize sub-pixel fires; and (3) estimate fuel consumption and smoke emissions. We describe the types of

---

M.J. Wooster (✉) • P. Freeborn

Department of Geography, King's College London (KCL), Strand, London, UK  
e-mail: [Martin.wooster@kcl.ac.uk](mailto:Martin.wooster@kcl.ac.uk)

G. Roberts

Geography and Environment, University of Southampton, Southampton, UK

A.M.S. Smith

Department of Forest Resources, College of Natural Resources, University of Idaho, Moscow, ID, USA

J. Johnston

Department of Geography, King's College London (KCL), Strand, London, UK

Canadian Forest Service, Natural Resources Canada, Great Lakes Forestry Centre, Sault Ste. Marie, ON, Canada

S. Amici

Istituto Nazionale di Geofisica e Vulcanologia (INGV), Rome, Italy

A.T. Hudak

US Forest Service Rocky Mountain Research Station, Moscow Forestry Sciences Laboratory, Moscow, ID, USA

airborne and spaceborne systems that deliver data for use with these active fire thermal remote sensing methods, and provide some examples of how operational fire management and fire research have both benefited from the resulting information. We commence with a brief review of the significance and magnitude of biomass burning, both within the ‘whole Earth’ system and in more regional situations, aiming to highlight why thermal remote sensing has become so important to the study and management of open vegetation burning.

## 18.1 Significance of Global Biomass Burning

Biomass burning is a key process shaping the Earth system, affecting the terrestrial biosphere and atmosphere through the combustion of vegetation and organic soils, and transferring the vast bulk of their chemical constituents directly into the troposphere. Seiler and Crutzen (1980) are often credited with providing amongst the earliest scientific insights into the large scale significance of biomass burning. However, in fact in the late nineteenth century von Danckelman (1884) already drew attention to its magnitude and potential consequence (Brönnimann et al. 2009).

Detailed information on the many ways in which biomass burning impacts Earth’s land and atmospheric properties are included in reviews such as Jacobson et al. (2000), Lavorel et al. (2007), Bowman et al. (2009), and Akagi et al. (2011). In the context of this chapter, it is sufficient that the reader appreciates the huge areas and very significant mass of vegetation and organic soil globally affected, in order to comprehend the need for large-scale fire assessment and monitoring via thermal remote sensing methods.

Amongst the most recent burned area estimates are those of Giglio et al. (2010), who used datasets derived from (mainly optical) satellite remote sensing to estimate that between 1997 and 2008 global vegetation fires cumulatively burned 44.5 million km<sup>2</sup>, equivalent to the combined area of North and South America, or ~40 % of Earth’s total terrestrially vegetated area. Some of this burning is planned and under human control; other areas are ignited and left to spread largely unhampered by man; still others are ignited accidentally or by natural phenomena (primarily lightning). Much of the 44.5 million km<sup>2</sup> burned includes re-burning in the savannah ecosystems of Africa, South America, and Australia. Here, a combination of large areas of highly combustible grassy fuels, annually reoccurring ‘fire seasons’, a ready supply of human ignition sources, and rapid post-fire vegetation recovery, combine to support mean fire return intervals that can be as short as 1–3 years. Indeed, such burning is in part responsible for maintaining the structure and function of savannah ecosystems, which in total constitute ~20 % of Earth’s land surface area (Bond and van Wilgen 1996).

The maps of Giglio et al. (2010) indicate that, on average, ~3.4 % of the Earth’s terrestrially vegetated area burns annually, with resulting large scale effects on surface properties and land cover, landscape heterogeneity, and ecology (e.g. Turner et al. 1994; De Bano et al. 1998; Wallace 2004; Bond and Keeley 2005;

Pausas and Keeley 2009). Clearly, the importance of a wide-scale disturbance phenomena like biomass burning is highly significant within the Earth system. This includes impacts from large-scale slash-and-burn practices and severe forest fires, particularly in disturbed areas, that contribute significantly to tropical deforestation and forest degradation (Bond et al. 2005; Cochrane 2003; Wooster et al. 2012).

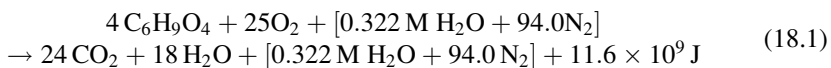
In addition to altering land surface dynamics, vegetation fires greatly affect Earth's atmospheric composition. They release an amount of carbon to the atmosphere equivalent to perhaps around one quarter, possibly more, of global annual industrial emissions (van der Werf et al. 2010); mostly in the form of CO<sub>2</sub>. Furthermore, van der Werf et al. (2009) demonstrate that deforestation and tropical peatland fire emissions (which unlike savannah emissions are not rapidly re-sequestered) equate to the equivalent of perhaps 15 ± 5 % of industrial CO<sub>2</sub> emissions. In addition to CO<sub>2</sub>, biomass burning releases a vast range of other trace gas and particulate species involved in important atmospheric processes (e.g. Andreae and Merlet 2001; Crutzen and Andreae 1990; Kaufman et al. 2002). Studies such as Page et al. (2002), van der Werf et al. (2004) and Wooster et al. (2012) indicate that land clearance activities, coupled with periods of extreme 'fire weather' such as El Niño related drought, can result in massive increases in the number and size of regional vegetation fires, which sometimes have globally detectable effects on atmospheric composition through the release of these compounds (e.g. Simmonds et al. 2005). At the local to regional scale, the potential loss of property and lives during large fire events, and the impacts on national fire management budgets, can be considerable (Lynch 2004), and fires may result in major smoke and haze events that can greatly impact air quality and human health (Kunii et al. 2002; Naeher et al. 2007).

Since vegetation fires occur over wide areas, are sporadic and rapidly changing in nature, are international in scope, and often occur in isolated regions, remote sensing has become a key tool in their identification and study. Thermal remote sensing is used widely to map fire extents, examine fire regimes, characterize fire impacts, and estimate and characterize the chemical composition of fire emissions (e.g. McMillan et al. 2003; Coheur et al. 2009; Wooster et al. 2011). The focus of this chapter is primarily to explore the background and techniques related to the thermal remote sensing of the actively burning fires themselves. Hence, we review the theory to both fire detection and fire characterization from airborne and spaceborne platforms, and their use in support of both research and operational applications.

## 18.2 Thermal Remote Sensing of Vegetation Combustion

Vegetation combustion is a complex process that involves simultaneous coupled heat and mass transfer, with the chemical reactions and fluid flows made more complex by the nature and non-uniformity of 'natural' fuels (Jenkins et al. 1998). Vegetation combustion involves significant energy releases, including as radiant energy, and hence is able to be targeted using thermal remote sensing methods.

Biomass consists mainly of cellulose, hemi-cellulose, and lignin produced through the process of photosynthesis, along with water, small amounts of nitrogen, sulphur, and some inorganic compounds that remain as ash after a fire (Jenkins et al. 1998). The polymeric organic compounds that comprise plant material can be generally described by the chemical formula C<sub>6</sub>H<sub>9</sub>O<sub>4</sub> (Byram 1959), and the nature of the chemical reaction involved in the complete air-based combustion of vegetation fuel of moisture content M% by dry weight can be represented by:



See Byram (1959) and Ward (2001) for a complete description of Eq. (18.1), where the moisture in the fuel and nitrogen in the air are shown as bracketed quantities since they do not take part in the combustion reaction. The same equation also describes decomposition, a much slower form of oxidation; both combustion and decomposition are essentially the reverse of photosynthesis. By dry weight, vegetation fuels are approximately 50 % carbon, 44 % oxygen and 5 % hydrogen (Ward 2001), and when burned completely approximately half the dry mass is converted to CO<sub>2</sub> and half to water in the manner described in Eq. (18.1). The ‘heat of combustion’ released by this energetic reaction equates to ~20.1 MJ per kilogram of dry fuel burned, and varies by less than 10 % between the woody and herbaceous fuel types occurring in most forests and savannahs (Stocks et al. 1997; Trollope 2002). Some of the released energy is used as the latent heat of vaporisation for the water contained in the fuel and formed by the reaction, so the actual ‘heat yield’ (or ‘low heat of combustion’) from vegetation fires burning under natural conditions is somewhat lowered (Byram 1959; Pyne 1984). Mean values are often ~18 MJ kg<sup>-1</sup> of dry fuel burned (e.g. Cheney and Sullivan 2008), and depend on factors such as the exact fuel moisture content and combustion completeness (Byram 1959; Alexander 1982; Dietenberger 2002). Incomplete combustion results in the production of significant amounts of additional compounds beyond carbon dioxide and water vapor, including carbon monoxide, hydrocarbons, and black carbon particles (each of which are some of the major constituents of ‘smoke’). The proportion of a fire’s heat yield released as radiation varies with fire characteristics and is still a subject of active research (e.g. Freeborn et al. 2008). Byram (1959) estimated around 10–20 % of a fire’s energy is radiated away from the combustion zone in the form of electromagnetic radiation of different wavelengths, which is then available to be measured by remote sensing devices. Figure 18.1 shows some example data of a forest fire targeted by an airborne imaging spectrometer acquisition that collected multispectral visible (VIS), near infrared (NIR) and shortwave infrared (SWIR) imagery and spectra.

In Fig. 18.1, the majority of the visible (VIS) wavelength radiation measured at point A in the inset is actually emitted radiation from the burning fuel, and its strong increase with increasing wavelength can be seen in Fig. 18.1c when compared to point B. At point B, the measurement of the fires emitted VIS wavelength radiation is strongly hindered by the overlying smoke. Our eyes ‘see’ only this VIS wavelength radiation emitted by such burning vegetation; but more of the energy is

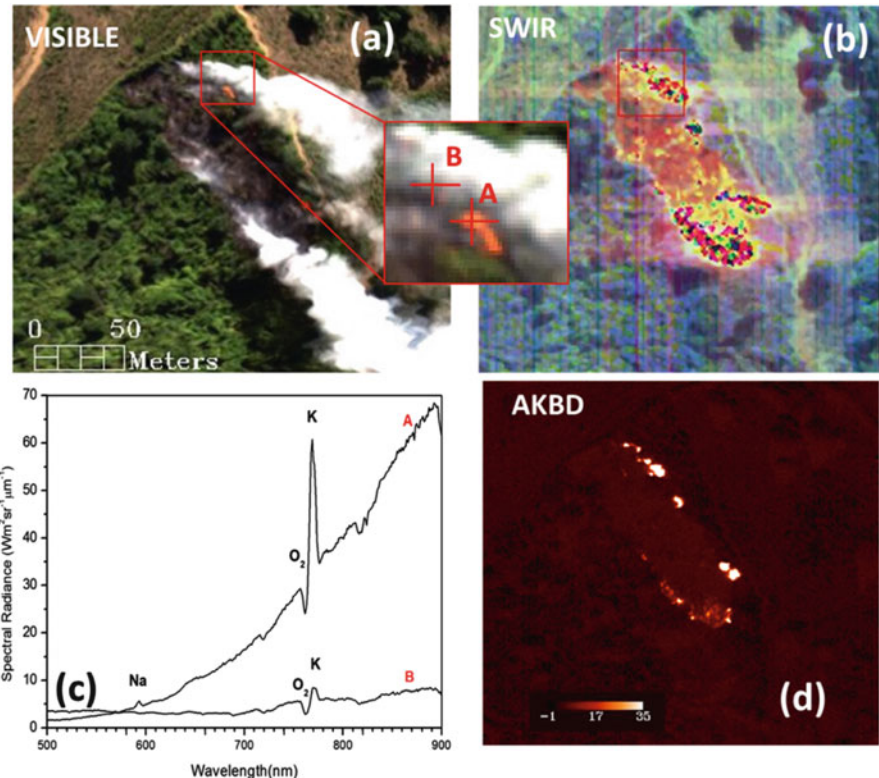


**Fig. 18.1** Forest fire remote sensing data from the HYPER-SIM.GA airborne spectrometer imagery described in Amici et al. (2011). (a) True colour composite along with a magnification better highlighting an area of emitted visible wavelength radiation resulting from flaming combustion. (b) False color composite of the same area derived using shortwave infrared wavebands, illustrating the ability to penetrate the smoke at these wavelengths and highlight both actively burning and already burned areas. (c) Spectra of location A (flaming fire; relatively smoke-free) and B (smoke-covered fire) identified in the magnified inset of (a). (d) The ‘Advanced Potassium Band Difference (AKBD)’ metric of Amici et al. (2011) which uses NIR spectral measurements inside and outside of the potassium absorption line region noted in (c) to identify flaming areas. The image is shown at the same scale and covering the same areas as (a). The location of flaming areas, even those burning underneath smoke, are clearly discernible using this simple multispectral technique

actually emitted at longer infrared (IR) wavelengths. The majority of this emitted energy is ‘blackbody’ type radiation emitted in accordance with Planck’s radiation law, and flames have very high emissivity’s at flame depths greater than a few meters and so are strong IR sources (e.g. Águeda et al. 2010; Pastor et al. 2002). The spectra of point A included in Fig. 18.1c demonstrates the characteristic shape of a Planck curve, though the curve is clearly peaking at an IR wavelength somewhat beyond the maximum wavelength shown in the plot. As Fig. 18.1b shows, the smoke also becomes increasingly transparent at such longer (IR) wavelengths, and the sensors SWIR wavebands easily identify both areas of emitted SWIR radiation from the burning fuel and the change in reflected solar SWIR radiation resulting from areas of already burned vegetation, even through the smoke.

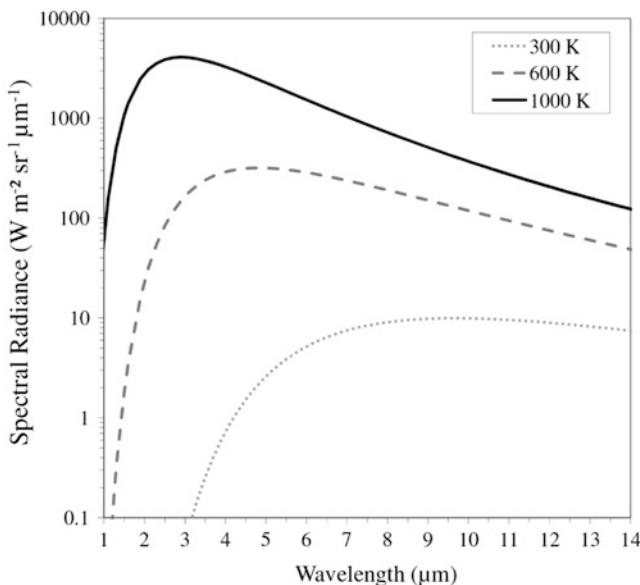


**Fig. 18.2** Modeled thermal emission from a 1000, 600, and 300 K object, representing a flame, a smoldering fire, and the ambient background respectively. Calculations were made using Planck's Law assuming blackbody behavior. The shift of the peak wavelength of thermal emission as the emitted temperature increases is described by Wien's Displacement Law. Note the logarithmic scale of the y-axis, and so the large increase in thermally emitted spectral radiance at all wavelengths as temperature increases from ambient to flaming conditions. Also note that increases in the middle infrared (MIR) spectral region (3–5  $\mu\text{m}$  atmospheric window) are of a much greater magnitude than those in the long-wave infrared (LWIR) spectral region (8–14  $\mu\text{m}$  atmospheric window)

Superimposed on the Planckian thermal emission shown in Fig. 18.1c is near infrared (NIR) line emission from thermally excited trace elements within the burning vegetation, in this case potassium (K)  $\sim$ 0.76–0.77  $\mu\text{m}$ , and sodium (Na) at 0.59  $\mu\text{m}$  (Amici et al. 2011). This signature can also be used to identify specific areas of flaming activity through smoke (Fig. 18.1d), since the production of this line emission requires the high temperatures specific to flaming rather than smoldering combustion. Additional band radiation is also superimposed on the Planckian thermal signatures, due to the H<sub>2</sub>O, CO<sub>2</sub> and other hot gases produced during combustion. This occurs within particular absorption and emission spectral regions, sometimes at wavelengths outside of the main ‘atmospheric window’ regions normally used to image the Earth. See Boulet et al. (2011) for a detailed discussion of such gaseous thermal emission and absorption features. Some active fire remote sensing applications make use of these types of line emission and gaseous band emission features, but most rely on the detection of Planckian thermal emission signatures, most commonly in the middle IR atmospheric window (MIR; 3–5  $\mu\text{m}$ ) where fire IR emissions generally peak and where solar radiation signal is lower than in the SWIR (Fig. 18.2). Observations in the longwave IR atmospheric window (LWIR; 8–14  $\mu\text{m}$ ) are also commonly used to enhance fire detection

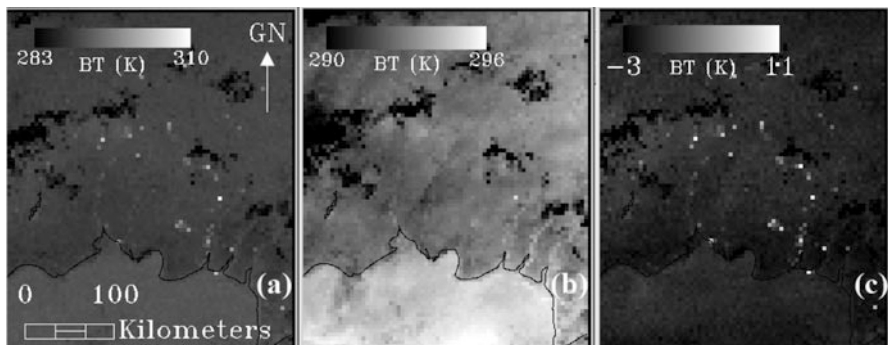


**Fig. 18.3** Nighttime thermal imagery subset collected by the AVHRR sensor over southern Borneo on 24th August 1991 (coastline vector in *black*). Land clearance fires, large scale forest and peatland degradation and an El Niño related drought conspired at this time to allow large scale fires to develop across the region. AVHRR collects data in both the (a) MIR [3.6–3.9  $\mu\text{m}$  waveband] and (b) LWIR atmospheric windows [in this case the 10.3–11.3  $\mu\text{m}$  waveband]. Clearly at the 1.1 km nadir spatial resolution of AVHRR, the fires are not filling pixels, but rather are highly subpixel events as modeled in Fig. 18.4. The original spectral radiance measures, of the type simulated in Fig. 18.4, have here been converted to brightness temperature measures via the inverse Planck function, and a linear contrast stretch applied for display purposes. The fires affect the MIR pixel integrated brightness temperatures much more than the LWIR brightness temperatures. The image subset shown in (c), calculated as the difference between the MIR and LWIR brightness temperatures, therefore highlights fire affected pixels particularly well

methods, and can be made through the full depth of Earth's atmosphere, even through significant smoke (Fig. 18.3).

Of course, in contrast to the passive solar reflectance observations that are typically used to detect burn ‘scars’, the thermal radiation emitted by fires must (by necessity) be measured whilst combustion is actually occurring. Hence, the technique is often referred to as ‘active fire’ remote sensing. Taking 600 and 1000 K as representative temperatures of smoldering and flaming combustion, respectively (Kaufman et al. 1998a; Sullivan et al. 2003; Dennison et al. 2006), Fig. 18.2 indicates that in comparison to the radiant energy emitted from the ambient temperature background ( $\sim 300$  K), (i) the rate of thermal radiant energy release from a vegetation fire is much greater, and (ii) the peak thermal radiant energy release is at much shorter wavelengths. These two physical principles, which stem directly from Planck's Law and Wien's Displacement Law, serve as the basis for the thermal remote sensing of active fires.

The fact that actively burning fires emit IR so strongly, particularly at MIR wavelengths as demonstrated in Figs. 18.2 and 18.3, means that their identification, even from Earth orbit, can be based on relatively simple detection algorithms (see Sect. 18.3). It also means that (i) the output of such detection algorithms (such as ‘hotspot’ counts and fire location maps) can be rapidly delivered to users, and (ii) fires that cover only a very small fraction of the pixel area can in theory still be detected since they can significantly increase the MIR ‘pixel integrated’ signal (Fig. 18.3; Robinson 1991; Giglio and Justice 2003). Figure 18.4 demonstrates this

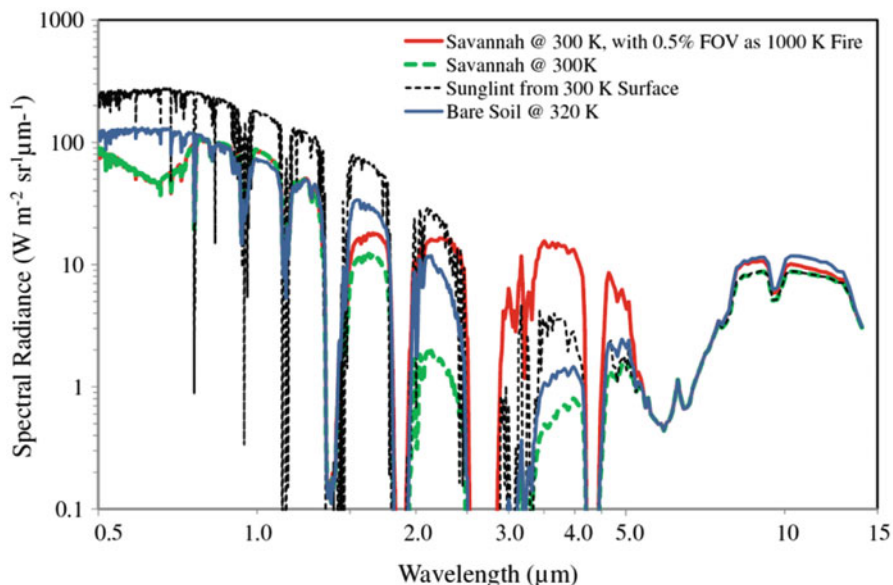


**Fig. 18.4** Top-of-atmosphere spectral radiance simulated at four different target pixels (note logarithmic x and y axes) using the MODTRAN 5 radiative transfer code. Shown are simulations for a savannah surface at 300 K; the same surface but with a 1000 K fire covering 0.5 % of the ground field-of-view (FOV), specularly reflected sunglint from a 300 K surface; and solar-heated (320 K) bare soil. The pixel containing the sub-pixel fire shows a signal highly elevated in the MIR (3–5  $\mu\text{m}$ ) spectral region compared to all other targets, equivalent to a brightness temperature of around 400 K (See Wooster et al. 2012 for more detail)

principle further by simulating the spectral signature of a series of different ground targets observed from Earth orbit using the MODTRAN-5 (MODerate resolution atmospheric TRANsmision) radiative transfer code, assuming a US 1976 Standard atmosphere and rural aerosol. Whilst the savannah pixel containing a 0.5 % coverage of a 1000 K fire shows a slightly elevated signal in the LWIR (8–14  $\mu\text{m}$ ) compared to the non-fire savannah, it actually shows a lower signal than the 320 K solar heated bare soil. The fire pixel is, however, very well separated from all the ambient pixels in the MIR (3–5  $\mu\text{m}$ ), where it has a spectral radiance signal  $\sim 20\times$  higher than the non-fire savannah pixel. However, as also illustrated, sun glints can also generate high spectral radiances in the MIR, and relatively lower spectral radiances in the LWIR, so can potentially be confused with pixels containing sub-pixel sized fires. However, sunglint pixels can be discriminated from active fire pixels using measurements in the VIS-to-NIR spectral region (0.4–1.2  $\mu\text{m}$ ), since highly sub-pixel fires emit insignificantly here (see Fig. 18.4).

The informative, rapid and directly useable capability to detect even very highly sub-pixel sized areas of burning vegetation has led to the widespread utilisation of active fire remote sensing over the last few decades, including from spaceborne platforms and at scales ranging from local and regional (e.g. Figs. 18.1 and 18.3) to

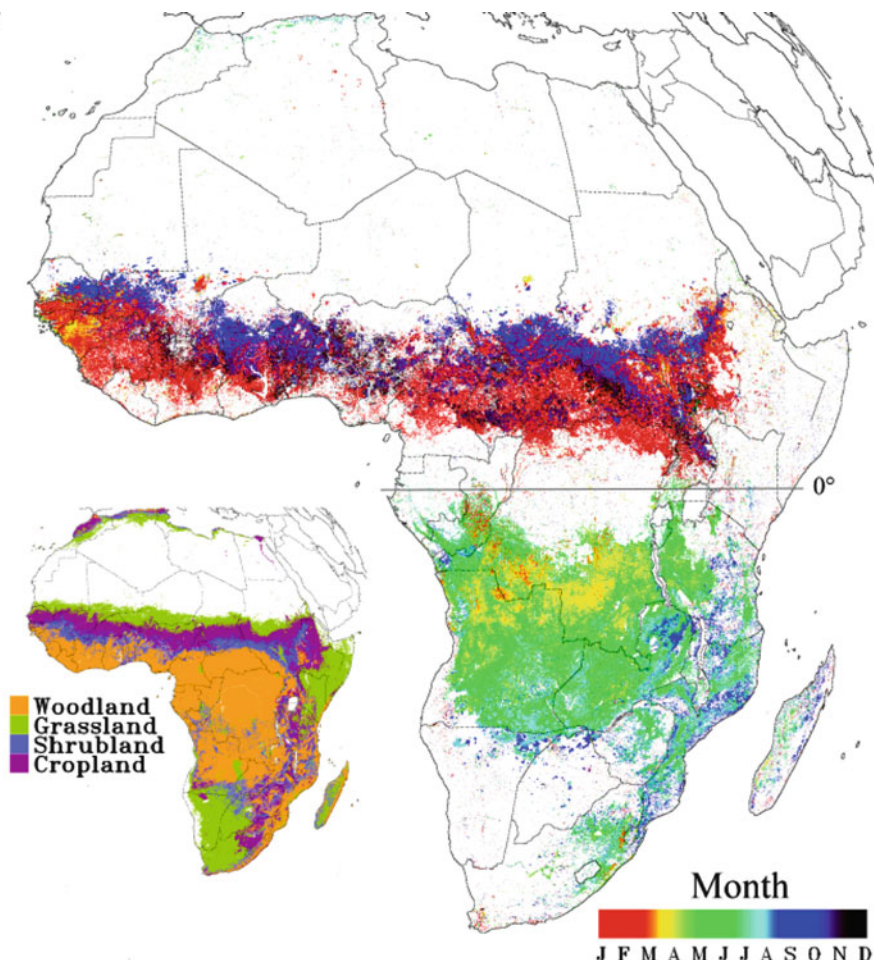


**Fig. 18.5** Active fire detections made across Africa in 12 months (February 2004 to January 2005) using data from the geostationary Meteosat SEVIRI instrument. Detections are coloured by day of detection to define the different fire seasons north and south of the equator. Multiple fires in the same grid cell are given the date of the last detected fire event. Fire detections were made using the algorithm of Roberts and Wooster (2008), an adaptation of which is used to generate the near real-time Meteosat FRP (fire radiative power) Pixel products available from the EUMETSAT Land Satellite Application Facility ([URL2](#)). Inset shows African land cover aggregated into four broad classes, as derived from the Global Land Cover 2000 dataset (Mayaux et al. 2004) (Figure adapted from Roberts et al. 2009)

continental and global (e.g. Figs. 18.5 and 18.6). As just one example, the Fire Information for Resource Management System archives and distributes MODIS (Moderate Resolution Imaging Spectroradiometer) Active Fire detections and associated fire maps in near real time to many worldwide users ([URL1](#); Davies et al. 2009). Furthermore, thermal remote sensing techniques can move beyond fire

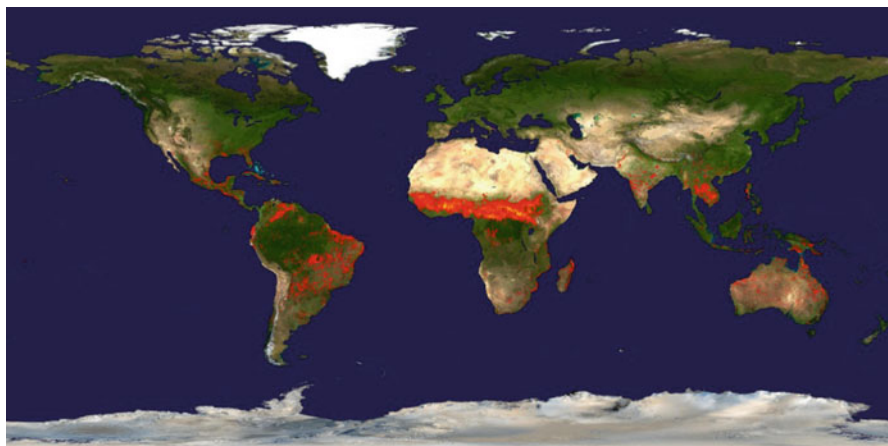


**Fig. 18.6** Global active fire map based on the accumulated locations of fires detected by the MODIS instrument on board the Terra and Aqua satellites. Detections were made over a 10-day period (16–25 December 2012) using the algorithm of Giglio et al. (2003). Each red/yellow dot indicates a location where MODIS detected at least one fire during the compositing period. Colour ranges from red (low fire count) to yellow (high fire count). Fire map created by Jacques Descloitres. Fire detection algorithm developed by Louis Giglio. *Blue Marble* background image created by Reto Stokli. The latest near-real time image maps can be obtained via the NASA LANCE (Land and Atmosphere Near-real-time Capability for Earth Observing) system ([URL3](#)) and links therein, whilst regularly updated global active fire location data is available from MODIS via the FIRMS (Fire Information for Resource Management System) ([URL1](#))

detection to offer more quantitative descriptions of fire's radiant energy release (Kaufman et al. 1998a; Wooster et al. 2003). Equation (18.1) indicates that the radiant energy released by a fire relates linearly to the amount of material combusted, and the amount of gas and aerosol emissions ('smoke') produced, pointing the way to the estimation of these quantities via measurement of fire-emitted electromagnetic radiation (Kaufman et al. 1998a; Wooster et al. 2005; Freeborn et al. 2008; Ichoku and Kaufman 2005; Kaiser et al. 2012; see Sect. 18.7).

Though very detailed observations of fires can be made through smoke, meteorological cloud cover remains a problem. Fortunately, the 'fire season' of most fire-affected regions generally follows dominant climatic patterns, and times of peak fire usually coincide with dryer periods with lower cloud cover (Fig. 18.5).

Furthermore, in many ecosystems the majority of the area burned in wildfires, and thus the majority of the smoke emitted, occurs in the largest few percent of fire events. Therefore, many thermal remote sensing applications need not aim to detect every single fire, but can rather focus on the more significant, larger and/or longer-lived events, which are generally the easiest to detect (Schroeder et al. 2008a). Figure 18.6 illustrates the global fire situation for a 10 day period based on data from the polar-orbiting MODIS sensors.

## 18.3 Methods of Active Fire Detection from Space

### 18.3.1 Algorithm Basics

Flaming fires emit very significantly in the shortwave infrared (SWIR) atmospheric window (1.6–2.5  $\mu\text{m}$ ; Figs. 18.1 and 18.2). However, as already stated, strong daytime solar reflections at these wavelengths, and the fact that many more fires burn by day than by night (Fig. 18.7), has steered the development of active fire detection towards use of the middle infrared (MIR) atmospheric window (3–5  $\mu\text{m}$ ). Here, levels of solar reflected radiation are lower than in the SWIR, while thermal energy emission rates from fires are very much higher than from the ambient temperature background, such that pixels containing even highly sub-pixel active fires often show up clearly in MIR imagery (Figs. 18.3 and 18.4). As a result, cooler, smoldering fires that might be almost impossible to detect in the SWIR region can still be quite clear in the MIR, and flaming fires generally show up extremely well. Many works have outlined the basis by which such ‘fire pixels’ can be automatically discriminated (e.g. Robinson 1991). Since at MIR wavelengths the spectral radiance ( $\text{W m}^{-2} \text{sr}^{-1} \mu\text{m}^{-1}$ ) emitted from flaming vegetation can be up to four orders of magnitude higher than from the surrounding ambient background (Fig. 18.2), areas of combustion occupying even a very small fraction of the pixel area (e.g. 0.1–1.0 %) can result in significant increases in the pixel-integrated signal (see example in Fig. 18.4). Detection of these types of elevated MIR channel signals is therefore the basis of most active fire detection algorithms (Robinson 1991), and a review can be found in Li et al. (2002).

By day, solar-heating of bare ground and/or specularly reflected sunlight can increase MIR channel signals in non-fire pixels, potentially resulting in false positives if fire pixel detection is based on thresholding of the MIR channel pixel signals alone (Zhukov et al. 2006). Therefore, in addition to simple MIR channel signal thresholding, a series of additional spectral and/or spatial tests are generally employed to best discriminate ‘true’ fire from false alarms. Rather than identifying fires based on the pixel-integrated spectral radiances, such as are modeled in Fig. 18.4, most active fire detection algorithms in fact work on brightness temperature (BT) measures, which are easily calculated from the spectral radiances using the inverse Planck function (Wooster et al. 1995). Areas of solar heated vegetation, bare soil, and rock tend to exhibit quite similar brightness temperatures in the MIR and LWIR atmospheric windows (i.e.  $\text{BT}_{\text{MIR}} \cong \text{BT}_{\text{LWIR}}$ ), but pixels containing sub-pixel sized actively burning fires can be discriminated these since the latter typically show  $\text{BT}_{\text{MIR}} \gg \text{BT}_{\text{LWIR}}$  as was demonstrated in Fig. 18.3. Therefore, thresholds based on the brightness temperature difference measured between the MIR and LWIR channels is a common feature of active fire remote sensing algorithms. Although such elevated BT differences can also occur in pixels affected by sunglint (either from clouds or water bodies), it is possible to exclude such pixels since they typically show increased signals in the visible wavelength region, while active fire pixels usually do not (Fig. 18.4). Based on these basic principles,

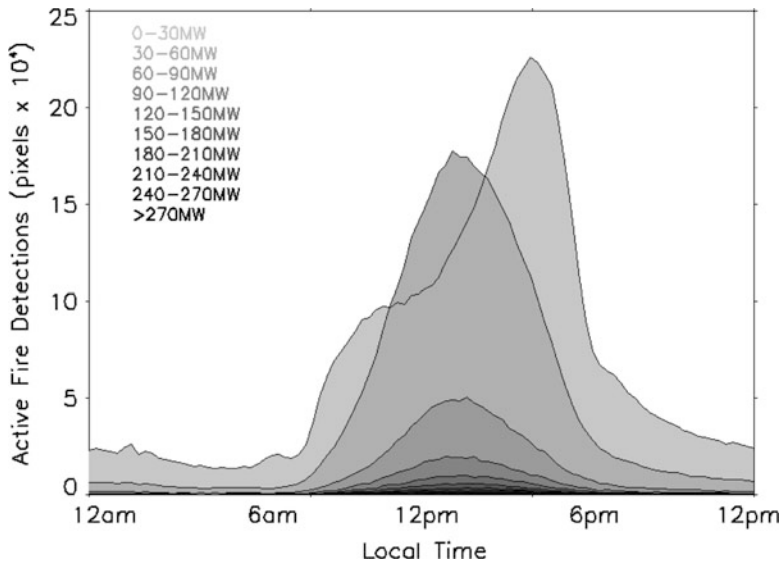


**Fig. 18.7** The diurnal fire cycle in northern hemisphere Africa, based on the number of active fire detections made using data from the geostationary Meteosat SEVIRI imaging radiometer, examples of which were shown in Fig. 18.5. The fire pixel detection statistics are here shown binned into fire radiative power (FRP) bins covering 30 MW intervals (shown in various grey shades). FRP is a measure of the rate of release of thermal radiative energy by all fires burning within the pixel (see Sect. 18.6 of main text). Numbers of fire pixels decrease as FRP increases, which is also demonstrated in the frequency-density plots shown later in Fig. 18.14. Fire pixels at all FRP magnitudes are maximal in the early to late afternoon, which is the peak of the diurnal fire cycle in most fire affected regions

multispectral active fire detection algorithms enable the identification of even highly sub-pixel actively burning fires, while mostly avoiding false alarms (e.g. Giglio et al. 2003; Zhukov et al. 2006; Roberts and Wooster 2008).

Early active fire detection algorithms were designed for data collected in a particular geographic region and/or season, often relying on subjectively fixed detection thresholds (e.g. Flannigan and Vonder Haar 1986). Most were intended for use with data from polar orbiting satellite instruments such as the Advanced Very High Resolution Radiometer (AVHRR), which has a spatial resolution of 1.1 km at nadir or lower if the sub-sampled GAC version of the data are used (e.g. Wooster and Strub 2002). For example, Baum and Trepte (1999) classed AVHRR pixels as containing actively burning fires if they passed the following four simple tests:

$$BT_{MIR} > 314 \text{ K} \quad (18.2)$$

$$BT_{MIR} - BT_{LWIR} > 10 \text{ K} \quad (18.3)$$

$$BT_{LWIR(\text{clear sky})} - BT_{LWIR} < 6 \text{ K} \quad (18.4)$$

$$BT_{LWIR} < 310 \text{ K} \quad (18.5)$$

Fixed-threshold approaches such as this can work well for individual scenes or time periods, but often provide poor performance during multi-regional and/or multi-seasonal analyses, and are not really appropriate for use in studies where the sensor used may change over time. In such cases, issues such as spatio-temporal changes in the ambient background thermal conditions make the use of fixed thresholds problematic (Giglio et al. 1999). This realization led to the development of so-called ‘contextual’ active fire detection approaches (Justice et al. 1996; Flasse and Ceccato 1996; Kaufman et al. 1998a). These approaches generally have two pathways by which pixels containing actively burning fires can be identified. The first ‘fixed threshold’ pathway may use a single algorithm stage, and is designed to detect pixels unambiguously containing large and/or intensely burning fires. The stage generally consists of thresholding tests akin to those in Eqs. (18.2), (18.3), (18.4), and (18.5), with fixed thresholds set sufficiently high such that in theory only pixels certain to contain fires pass the tests. The second ‘contextual’ pathway typically consists of two or more stages, whereby potential fire pixels (PFPs) are first identified using a fixed threshold approach based on relatively low thresholds (thus selecting many non-fire pixels as well as true fires), and then testing each PFP against the statistical properties of its immediately surrounding ‘ambient background’ pixels in order to confirm whether or not it is a ‘true’ fire pixel. The entire algorithm, incorporating the ‘two pathway’ approach, is generally termed a ‘contextual active fire detection algorithm’.

Most current methods for identifying actively burning fires include some form of contextual approach, including the algorithms used to generate the Geostationary Operational Environmental Satellite (GEOS) Advanced Biomass Burning Algorithm (ABBA) fire products (Prins and Menzel 1992), the MODIS Active Fire and Thermal Anomaly products (Giglio et al. 2003), the BIRD Hotspot Recognition Sensor (HSRS) fire products (Zhukov et al. 2006) and the Meteosat SEVIRI fire products (Roberts and Wooster 2008). Variants of the approach exist in each algorithm, for example the algorithms developed for use with BIRD HSRS and Sentinel-3 Sea and Land Surface Temperature Radiometer (SLSTR) data first divide each scene into a set of sub-scene windows, from which obvious non-fire pixels are masked out. A set of ‘background statistics’ calculated from these non-fire pixels are then used to test whether the remaining pixels within the window are likely to contain active fires (Zhukov et al. 2006; Wooster et al. 2012).

Table 18.1 lists the main polar orbiting Earth Observation sensors currently used for active fire detection, including their basic spectral, spatial, and temporal specifications, and some suggestions for references where further information can be obtained. While the Defense Meteorological Satellite Program (DMSP) Operational Linescan System (OLS) does not have a dedicated MIR or LWIR spectral band for active fire detection, the low-light visible wavelength imaging capability of this sensor has long been used for active fire detection (Elvidge et al. 1996). Apart from the DMSP OLS, and the Terra Advanced Spaceborne Thermal

**Table 18.1** Specifications of currently operating polar-orbiting systems commonly used for active fire detection and study

Satellite(s) sensor	Repeat cycle/equator crossing with satellite number	Coverage global	Spatial resolution	Example reference(s)	Example product(s)
NOAA POES AVHRR	~4 × per day, local crossing times vary with satellite number	2,400 km swath, global	1.1 km at nadir	Li et al. (2000), Stroppiana et al. (2000)	Global AVHRR Active Fires (1992–93) EC JRC (bioval.jrc.ec.europa.eu)
Terra & Aqua MODIS	10:30/22:30 hrs and 01:30/13:30 hrs local time	2,340 km swath, global	1 km at nadir	Kaufman et al. (1998a), Giglio et al. (2003)	MODIS Active Fires (2000–current); NASA (reverb.echo.nasa.gov)
ERS & ENVISAT (A)ATSR	~4 overpasses/month at equator to ~12 at ±70°N/S (night)	512 km swath, global	1 km at nadir	Mota et al. (2006), Giriraj et al. (2010)	(A)ATSR World Fire Atlas (1996–current) ESA (earth.esa.int)
DMSP OLS	09:54/21:54 and 06:04/18:04 local time (night)	3,000 km swath, global	0.56 km, “smoothed” to 2.7 km	Elvidge et al. (1996)	No regular, web-based accessible global product known
Terra ASTER	Limited to a prioritized acquisition schedule	60 km swath, limited schedule	30 m	Giglio et al. (2008)	No global product
TRMM VIRS	Twice/day every other day at equator, and twice/day at temperate latitudes	720 km swath, ±40° of the equator	2.1 km at nadir	Giglio et al. (2000), Giglio (2007)	TRMM VIRS Monthly Fire Product NASA (1998–2005) (disc.sci.gsfc. nasa.gov)

Emission and Reflection Radiometer (ASTER) sensor, whose active fire detection capability is based on analysis of 30 m spatial resolution SWIR data, all other sensors listed primarily employ MIR and LWIR measurements in the active fire detection process. Furthermore, in addition to these polar orbiting instruments, there exists a strong capability to detect fires from geostationary sensors, with improved temporal resolution compared to polar-orbiting systems. Examples here include fire products created from the GOES East and West imagers (Prins and Menzel (1992, 1998, [URL4](#)), Xu et al. (2011; [URL5](#)) and from Meteosat Second Generation (MSG) (Roberts and Wooster 2008; [URL2](#)). Examples of data from the latter were shown in Fig. 18.5.

### **18.3.2 Further Active Fire Detection Algorithm Adaptations**

In addition to the multispectral tests discussed above, several additional processing methods can be used to potentially improve active fire detection accuracy, and/or increase processing speed. For example, the aforementioned Sentinel-3 SLSTR algorithm uses the ‘spatial filter’ edge detection test first introduced for use with geostationary Earth observation imagery by Roberts and Wooster (2008) and then by Xu et al. (2011). The aim is to enable use of very liberal thresholds during Stage 1 of the contextual detection pathway, maximising the ability to detect small or weakly burning fires, whilst minimizing the number of non-fire PFPs passed to the ‘contextual’ Stage 2 due to these being relatively computationally demanding (and thus time-consuming). In order to reduce errors of omission and commission, the unique high frequency, fixed viewing geometry afforded by geostationary platforms enables further inclusion of multi-temporal tests that make use of imagery taken at different times of day. Figures 18.5 and 18.7 show examples of the broad spatial coverage, high temporal resolution data that can be gathered from use of geostationary fire detection methods, in this case applied to Meteosat SEVIRI (Roberts et al. 2009). The Advanced Biomass Burning Algorithm (ABBA) developed for use with the GOES imager (Prins and Menzel 1992) makes use of high temporal information to filter out active fire pixels detected only once at the same pixel location in any 12 h period, assuming most of these to be false alarms (Prins et al. 1998). An alternative multi-temporal approach, also developed for GOES and described by Xu et al. (2011), does not filter out such ‘single pixel detects’, but instead separates fires from false alarms by exploiting fluctuations in a pixel’s MIR radiometric signal as a new fire ignites, intensifies, and ultimately extinguishes or propagates into a neighboring pixel.

Since meteorological clouds are generally quite opaque at IR wavelengths, and very thick smoke plumes can also be difficult to sense through, the utility of any active fire detection strategy can be thwarted under such conditions. Therefore, in an active fire remote sensing product, a pixel may be denoted as a ‘non-fire pixel’ due to the presence of cloud cover, rather than as the result of active fire detection testing. For this reason, a number of satellite-based active fire products also include

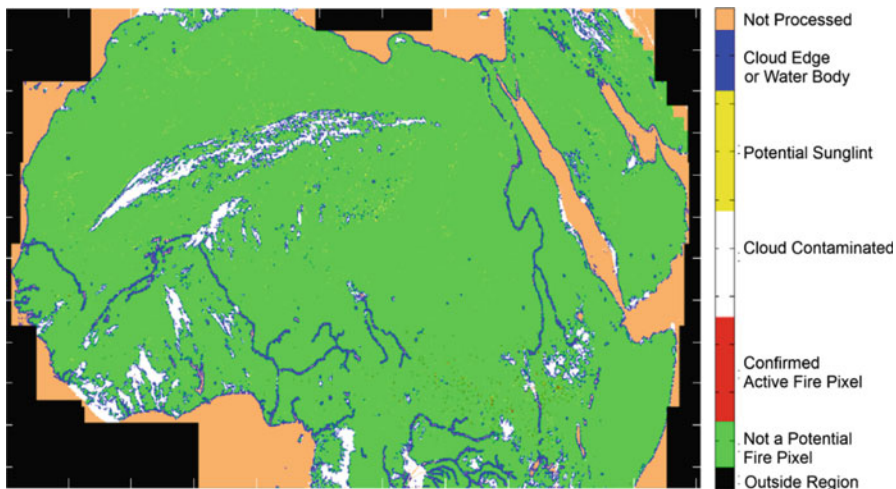


**Fig. 18.8** Fire mask for North Africa down to the equator, created from Meteosat SEVIRI imagery. The mask delineates pixels which are processed by the active fire detection algorithm, and which are not (due for example to cloud cover, or to their being classified as water bodies). Other information includes which pixels are potentially contaminated by sun glint, and which are confirmed active fires. This mask forms the ‘Quality Flag’ component of the ‘FRP Pixel product’ obtainable in near real-time from the EUMETSAT Land Satellite Application Facility ([URL2](#))

cloudiness metrics for each pixel, sometimes alongside other information such as a land/water classification and a mask of areas identified as sun glint. The MODIS Active Fire and Thermal Anomaly (MOD14/MYD14) products listed in Table 18.1 include this type of information (Giglio et al. 2003), as do the Meteosat SEVIRI FRP-PIXEL products available from the EUMETSAT (European Organisation for the Exploitation of Meteorological Satellites) Land Satellite Application Facility ([URL2](#)). An example of the latter is shown in Fig. 18.8, and some studies use this type of information to normalize active fire pixel counts for the proportion of the land surface actually viewed, for example to better compare active fire statistics across space and time (e.g. Di Bella et al. 2006) or to estimate total fire activity from the viewable fraction (e.g. Kaiser et al. 2012).

## 18.4 Airborne Active Fire Detection

Whilst the active fire detection capability from the low Earth orbit systems listed in Table 18.1 offers a high degree of utility and data richness, and the geostationary systems can offer an additional coarser spatial resolution but much higher temporal resolution view, satellite-based systems are still restricted in what they can provide to help analyze the type of fine scale, rapid variations in fire behavior associated with variable topography, fuel properties, and weather. Furthermore, the real or

**Table 18.2** Example specifications of some of the key airborne IR sensors commonly used for active fire detection and study

Sensor	Bands	Spectral coverage	IFOV	FOV
AVIRIS	224	VIS-NIR-SWIR	1 mrad	34°
Phoenix	2	MIR-LWIR		120°
ABAS	3	NIR-MIR-LWIR	0.3 mrad 0.7 mrad	80° 19°
AIRDAS	4	VIS-SWIR MIR-LWIR	2.6 mrad	108°
AMS	12	VIS-NIR-SWIR MIR-LWIR	1.3 or 2.5 mrad	43° or 86°
FireMapper	2	LWIR	1 mrad	35°
MASTER	50	VIS-SWIR MIR-LWIR	2.5 mrad	86°
MAS (now enhanced MAS)	50	VIS-SWIR MIR-LWIR	2.5 mrad	86°

perceived delays involved in the obtaining of satellite active fire products are often cited by field personnel involved in fire management as reasons against incorporating such products into operational and strategic fire management plans (Trigg and Roy 2007). This is despite the actually quite rapid delivery of EO products such as those supported by, for example, FIRMS ([URL1](#); Davies et al. 2009), GOES ABBA ([URL4](#)), and the EUMETSAT Land Satellite Application Facility ([URL2](#)). Nevertheless, the fact that airborne systems can operate near continuously as needed (albeit at a logistical and financial cost), and can quite easily provide meter or even sub-meter spatial resolution imagery, at repetition frequencies as high as every few minutes or even better, means they are highly capable of supporting fire management operations. Table 18.2 details some of the commonly used airborne remote sensing systems related to active fire observations, and although issues of geo-referencing and calibration typically become more significant hurdles than with satellite data products, there are airborne systems that can directly deliver quantitatively useful datasets rapidly to users on the ground. Airborne thermal remote sensing therefore provides a very useful tool with regard to active fires, and its exploitation has followed two main paths. Firstly an ‘operational’ agenda for direct use in fire suppression and post-fire rehabilitation operations, and secondly a research agenda related in some cases to future satellite instrument or algorithm development.

#### 18.4.1 Operational Airborne Thermal Fire Mapping

Thermal imaging systems have had a long and widespread use in patrol aircraft, aiding spotters looking for new forest fires. Many airborne IR systems are also used

as decision support tools. Though costly to acquire and deploy operationally, the use of IR imaging in this way can help minimize ineffective fire suppression strategies. This is particularly the case during prolonged responses to large or contentious wildfires (often termed ‘project fires’, ‘siege campaigns’, or in the United States as ‘Type 1’ fires), where the Incident Commander is responsible not only for effecting fire suppression, but also for defending human, economic and cultural values. This task can require a great deal of information to affect successfully, including on both current and forecast fire behavior. Such ‘project fires’ often take place in situations involving severe fire behavior and significant risk to human, economic and/or cultural values, resulting in suppression costs often exceeding US \$1 million per day.

During a large fire event, the suppression tactics employed depend strongly on knowledge of a fire’s current behavior. However, thick smoke columns, heterogeneous fuel structures, and dense canopy cover often conspire to make assessment of the fire situation difficult with the human eye, even from an airborne vantage point. Tasks such as differentiating the intensity of surface fuel combustion within a single fire perimeter, or locating spot fires outside of the perimeter, can become very difficult. In such cases, the enhanced view of the fire provided by airborne thermal imaging, which as mentioned above can penetrate smoke, and to some extent also vegetation cover, allows for a much better assessment of current fire behavior (see example in Fig. 19.9). This capability helps Incident Commanders evaluate the success of ongoing suppression efforts, allowing them to make better informed tactical decisions regarding the distribution of manpower and other resources. The ability to provide clearer views of the fire situation than can be gained with unaided eyesight or optical wavelength imaging is also the operational driver for the installation of thermal imagers onboard fixed wing tanker aircraft. This allows pilots to acquire suitable targets for water or flame retardant drops, even through smoke columns. In the later stages of fire suppression, ground personnel are also sometimes equipped with handheld thermal imagers, particularly to help locate areas of smoldering combustion below layers of ash, and thus ensure that more thorough suppression is conducted and new fires cannot start from still smoldering areas of fuel.

Much of the early development work regarding the thermal imaging of fires from aircraft was conducted by the United States Forest Service (USFS). USFS projects like FIRESCAN had been using thermal sensors for ‘wildland’ fire detection, monitoring and decision support since the early 1960s (Warren and Celarier 1991; Lentile et al. 2006). According to Warren (1992), the focus was on airborne systems even in the early days, with little or no use made of the type of ‘fixed area’ thermal scanners used in several European countries at the time. Such tower mounted systems usually included both a thermal and optical imaging capability, which were exploited by an operator to perform scans of all or part of the full 360° view around the installation. Thermal imaging from aircraft allowed larger areas to be rapidly surveyed, and early USFS studies were based on IR line scanners, often modified militarily equipment operating in both the longwave IR (8–14 µm using a HgGe detector) and middle IR (3–5 µm using an InSb detector) spectral regions. These systems were considered to deliver data with acceptable accuracy at the time,

could image in excess of  $2,500 \text{ km}^2 \text{ h}^{-1}$ , and were able to detect very small fires. Particularly so when the dual waveband systems were used, due to the aforementioned increased hotspot sensitivity and algorithm performance when exploiting MIR data (Sect. 18.3; Hirsch and Madden 1969; Warren and Celarier 1991). When ‘handheld’ ‘Forward Looking Infrared’ (FLIR) thermal imaging systems first became commercially available in the late 1970s and 1980s, they also became part of the airborne fire detection arsenal. The small size of FLIR systems, and (unlike line scanners) their lack of a requirement for aircraft forward motion to build a 2D image, meant they were particularly well suited to deployment on helicopters, which due to their ability to hover, takeoff and land in small spaces, and carry a variety of payloads, are widely used in fire management and suppression operations (Warren and Celarier 1991). The helicopter-mounted FLIR imagers often provided much more detail than line scanning systems, albeit generally over smaller areas, and due to their high spatial resolution it was not particularly necessary to have a system that operated at MIR wavelengths since in many cases pixels were completely filled by fire.

From 1985, the US Forest Service ‘Fire Mouse Trap’ (Flying Infrared Enhanced Maneuverable Operational User Simple Electronic Tactical Reconnaissance and Patrol) system attempted to exploit FLIR technology alongside LORAN navigation to deliver a semi-near real time forest fire mapping capability from helicopters and small fixed wing aircraft (Dipert and Warren 1988; Warren and Celarier 1991). Around the same time, the United States National Aeronautics and Space Administration’s Jet Propulsion Laboratory (NASA-JPL) developed an airborne fire mapping program called the Fire Logistics Airborne Mapping Equipment (FLAME) project. The FLAME instrument was a dual-band (MIR and LWIR) IR-scanner system, apparently able to detect  $1 \text{ m}^2$  fires from 3.5 km altitude (Nichols et al. 1989). The subsequent ‘Firefly’ system exploited same two wavelengths, and became the first digital fire detection and monitoring system used by the United States National Interagency Fire Center, with data processed onboard aircraft and transmitted by way of satellite to the Incident Command Post (Warren and Celarier 1991; USFS 2012). FLAME was further upgraded in 1998 and repackaged as the Phoenix system, which also provided digital imagery output. More recently, the US Wildfire Airborne Sensor Program (WASP) has been developed using three commercially available FLIR-style cameras operating at 1.3, 3.25, and  $8.6 \mu\text{m}$  (Li et al. 2002). In Canada, systems such as the Airborne Wildfire Intelligence System (AWIS) and the ITRES TABI-1800 (Thermal Broadband Imager) provide similar support to operational fire management (Fig. 18.9).

In addition to its role in fire management and response, an important additional remit for airborne thermal remote sensing in relation to fire has been to assist national agencies and aerospace organizations in the testing of new instrument types, the evaluation of new algorithms, and the calibration of satellite-based sensors. Instruments often more capable than those typically deployed on fires on an operational basis are often used for these applications. Examples are the Airborne Visible/Infrared Imaging Spectrometer (AVIRIS) measuring from 0.4 to  $2.5 \mu\text{m}$  in 224 contiguous spectral bands, the FireMapper IR imaging radiometer (Riggan and Tissell 2009), and the MODIS Airborne Simulator (MAS) (Green 1996; Hook et al. 2001). MAS for example is a scanning imaging spectro-radiometer which measures

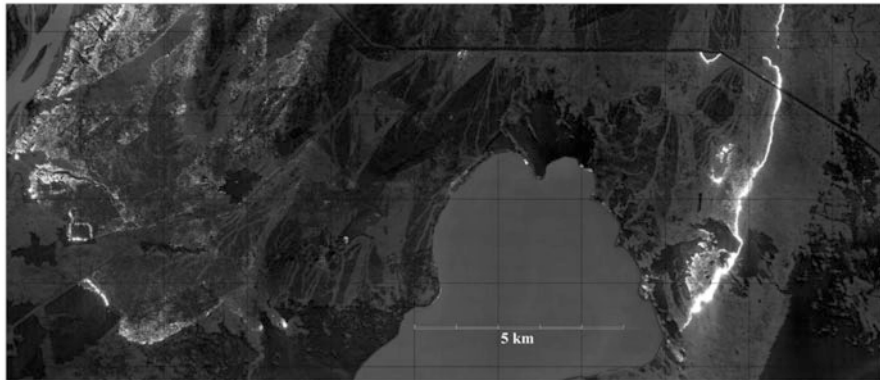


**Fig. 18.9** Geocoded thermal imagery produced during a Alberta Environment and Sustainable Resource Development (*ESRD*) response to a 2011 Northern Alberta wildfire, where active fire fronts and residual hot-spots are evident as white pixels. The image was acquired using the ITRES Thermal Airborne Broadband Imager (TAB1-1800), which has 1800 across-track pixels and provides MIR data to produce ortho-mosaic thermal maps in the 3.7–4.8  $\mu\text{m}$  wavelength range ([URL5](#)). Vector data products of active fire fronts, hot-spots, and fire perimeters can be extracted from the imagery and used along with the thermal map to support fire suppression activities. The high temperature sensitivity of the TAB1-1800 (NEdT < 30mK) allows for discrimination of subtle thermal details in addition to the highly radiant fire pixels (Image courtesy of Alberta ESRD). Image courtesy of ITRES ([URL6](#))

reflected solar and emitted thermal radiation in 50 narrowband channels between 0.55 and 14.2  $\mu\text{m}$ . At nadir it delivers 50 m spatial resolution data from the NASA ER-2 aircraft flying at 20 km altitude. An evolution of MAS is the MASTER MODIS/ASTER airborne simulator, developed firstly to support ASTER data validation and secondly as a back-up instrument for MAS (Hook et al. 2001). MAS was deployed during the Southern African Regional Science Initiative (SAFARI-2000), which conducted prescribed burns coincident with overpasses of the then recently launched EOS (Earth Observing System) Terra satellite, in part to help validate the MODIS active fire detection algorithms (Swap et al. 2002).

#### 18.4.2 Unmanned Aerial Vehicles

There are limitations to the use of airborne thermal imaging in wildfire activities, often related to the high operational costs involved, and to the risks to aircraft and crews when flying in potentially dangerous low visibility/high turbulence situations close to fires and/or smoke columns. To try to overcome some of these issues, Unmanned Aerial Vehicles (UAVs) equipped with thermal imaging capabilities can be exploited. In the mid-2000s, the Altair-FIRE project (First Response Experiment) was amongst the first efforts aimed at demonstrating the utility of integrating UAV capabilities, advanced thermal imaging, cost-effective telemetry and (semi-) automated image geo-rectification systems (Ambrosia et al. 1994; Wegener et al.

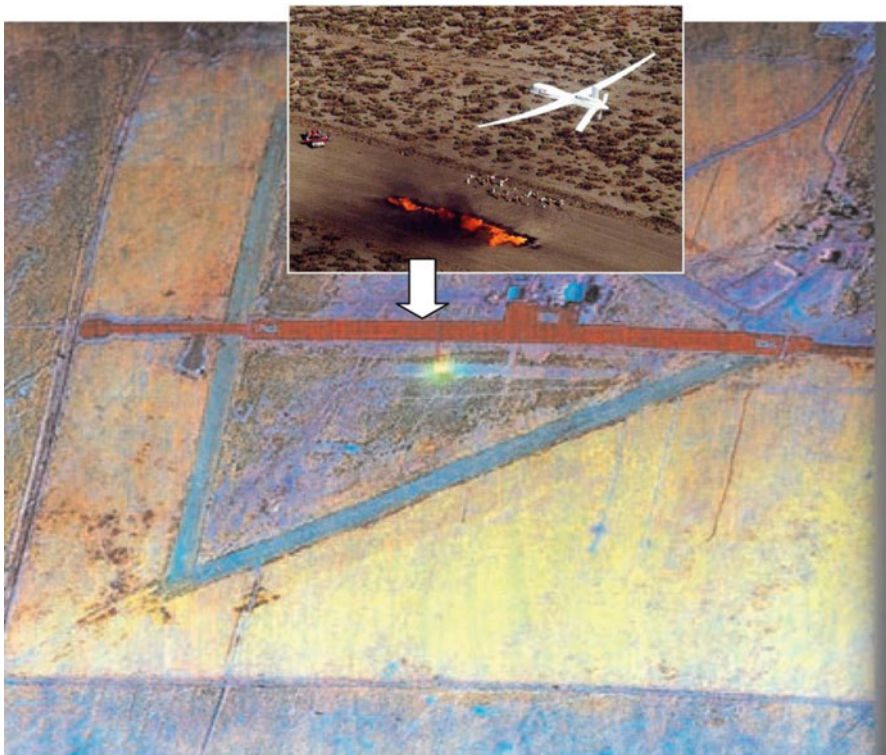


**Fig. 18.10** The FiRE demonstration controlled burn conducted at El Mirage, California on 6th September 2001 (Lat  $34^{\circ} 37.4'$ , Lon  $-117^{\circ} 36.2$ ). The infrared colour composite collected by the ALTUS II in flight at  $\sim 945$  m altitude highlights the highly radiant location of the fire, with a photographic view of the scene taken from a higher altitude aircraft shown in the *inset*

2002; Ambrosia et al. 2003). Mounted on an Altair platform, a modified version of the military ‘*Predator*’ UAV, the payload consisted of a multispectral imager having a visible-to-thermal imaging capability (Fig. 18.10). In parallel, studies such as Merino et al. (2006) have tested the capability of much lower cost civilian UAVs and small micro-bolometer based LWIR cameras for the detection, monitoring, and measurement of forest fire targets.

## 18.5 Thermal Imagery Contributions to Burned Area Mapping

While the focus of the spaceborne and airborne thermal remote sensing methods discussed thus far has been on the detection of actively burning fires, such measurement capabilities also have some relevance to the identification and mapping of burned areas. This has often been simply through use of active fire detections to

gauge the ultimate size of the fire-affected area, generally via some form of empirical relationship linking the number of active fire detections to the size of the area burned (e.g. Giglio et al. 2005). Since fire behaviour varies greatly between environments, such associations require careful testing and calibration. Reported slopes of the linear relationships linking the two metrics ranged in the global study of Giglio et al. (2005) between  $0.29 \text{ km}^2$  of burned area per active fire pixel in southern-hemisphere South America, to  $6.6 \text{ km}^2$  of burned area per active fire pixel in Central Asia. Once such relationships are established for the areas of interest, the types of long term active fire detection record available from MODIS, TRMM VIRS (Tropical Rainfall Measuring Mission, Visible and Infrared Scanner) and (A) ATSR ((Advanced) Along Track Scanning Radiometer) can be used to estimate burned area trends, provided of course that the active fire products are appropriately inter-calibrated for differences in sensor spatial resolution (and thus minimum active fire size), satellite overpass time, and image repetition frequency.

Until the recent version 3 of the widely-used Global Fire Emissions Database (GFED; Van der Werf et al. 2010), this ‘hotspot counting’ approach to burned area estimation based on active fire detections (Giglio et al. 2006) actually provided the vast majority of the burned area estimates used within GFED, proving its utility at a time when global burned area datasets based on spectral reflectance measurements were still largely at the development and testing stage. The most commonly used wavelengths for burned area mapping reside within the near-infrared ( $\sim 0.8\text{--}1.2 \mu\text{m}$ ) and shortwave infrared ( $\sim 1.6\text{--}2.2 \mu\text{m}$ ) spectral regions, where changes in vegetation cover and of the proportion of bare soil and charred surfaces have significant impact on reflectances. Burning of less than half of the pixel can be detected by such methods (Pereira et al. 1997; Smith et al. 2007), which while far less sensitive than active fire detection methods is still a very useable change detection threshold. The types of surface spectral reflectance change seen on burning are also often accompanied by changes in the emitted spectral radiance, and thus in the apparent brightness temperature (Fig. 18.11; Trigg and Flasse 2000; Smith et al. 2007). Such thermal changes result, for example, from the albedo decreases that come from the presence of charred surfaces, to the increased cover of exposed soils, from evapotranspiration decreases due to stress or loss of live vegetation, and from the presence of still smouldering or glowing combustion (Eva and Lambin 1998; Smith and Wooster 2005). LWIR observations are therefore sometimes used to attempt performance enhancement of burned area mapping algorithms. When mapping fire affected areas in Central Africa from ERS-1 satellites Along Track Scanning Radiometer (ATSR), Eva and Lambin (1998) noted that upon burning many pixels exhibited a sharp fall in SWIR spectral reflectance, and a simultaneous increase in LWIR brightness temperature. This was exploited to map burn scars across the Central African Republic, and without the inclusion of the LWIR data to expand the information beyond the single ATSR solar reflected ( $1.6 \mu\text{m}$ ) waveband it is likely that classification accuracies would have been reduced. Despite this success however, most approaches attempting to incorporate both emitted and reflected spectral radiance data in a single ‘burned area mapping’ index have shown mixed results (e.g. Holden et al. 2005; Smith et al. 2007), and widespread adoption of the approach has not occurred. This is in part because the temperature

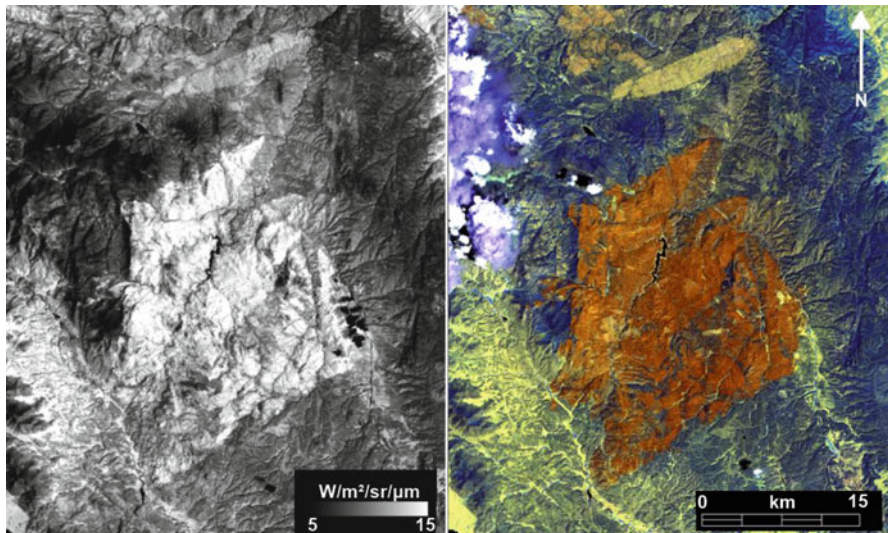


**Fig. 18.11** 2002 Landsat ETM+ imagery of the 559 km<sup>2</sup> Hayman Fire (Colorado, USA; Lat 39° 10.0', Lon –105° 15.0'). At right is a false color composite (RGB = ETM+ bands 7, 5, 4), where exposed soil and charred surfaces appear as a *reddish colour*, and areas of unburned vegetation appear *blue*. The *right image* depicts the low-gain ETM+ band 6 LWIR spectral radiance data of the same area in a *greyscale* rendition. This indicates the burned area to have generally higher spectral radiances (warmer). However, careful interpretation of such thermal data is necessary, since areas of exposed soil (*scene bottom left*) and forest clear cuts (*scene top*) also show signs of being warmer than the vegetated areas

of post-fire surfaces is controlled not only by land cover characteristics, but also by processes unrelated to vegetation fires (e.g. other landcover properties, solar insolation and cloudiness variations; see Fig. 18.11). Also, VIS-SWIR wavelength data are often available from spaceborne sensors at a much higher spatial resolution than are the accompanying thermal imagery (e.g. MODIS' 250 m/500 m optical bands, compared to the matching 1 km thermal bands; and Landsat 7 ETM's 30 m optical bands compared to the 60 m LWIR band), making the merging of the thermal and optical wavelength imagery a less attractive prospect.

Another avenue of investigation aiming to exploit thermal measurements in burned area mapping applications has been to separate the daytime MIR spectral radiance signal into its separate solar reflected and thermally emitted contributions. This aims to exploit the perceived strong sensitivity of the reflected component to changes in certain surface characteristics, including vegetation moisture (Boyd and Petitcolin 2004). Petitcolin and Vermote (2002) detail one way to attempt this separation, based on careful atmospheric correction and the use of the Temperature Independent Spectral Indices of Emissivity (TISIE) defined by Becker and Li (1990). The resulting MIR spectral reflectance measures can, for example, be used in place of VIS wavelength data in various types of vegetation index (Kaufman and Remer 1994; Barbosa et al. 1999), and under certain conditions

this has been shown to add value when attempting to discriminate burned and unburned pixels (Libonati et al. 2009).

In terms of approaches to exploiting thermal band data in burned area (BA) mapping algorithms, probably the most successful has been the inclusion of active fire detections into burned area data processing chains. Specifically, the locations of detected active fire pixels (made using the types thermally-based algorithms covered in Sect. 18.3) can very usefully act as ‘seed locations’ for optical waveband change detection methods aimed at identifying newly burned areas from optical wavelength data. Among the earliest examples is the Hotspot And NDVI Differencing Synergy (HANDS) algorithm, used to map burned areas across the Canadian boreal forest (Fraser et al. 2000). More recently, Giglio et al. (2009) utilised the technique to produce a global, multi-year burned area product from the 10+ year MODIS data record, a product which is now used as the primary burned area dataset within version 3 of the Global Fire Emissions Database (GFED; Van der Werf et al. 2010).

## 18.6 Fire Characterization

In addition detecting active fire pixels and contributing to the mapping of post-fire burned area, thermal IR remote sensing has a strong part to play in the characterisation of fire properties, for example the temperature and area covered by the active fire, and its rate of radiative energy emission.

### 18.6.1 *Fire Radiative Power and Fire Radiative Energy*

The complete combustion of a fixed amount of biomass releases an approximately fixed amount of thermal energy (the so-called fuel heat yield discussed in Sect. 18.2 and defined by e.g. Byram 1959 and Pyne 1984). Assuming the fraction released as radiant energy does not vary too much, then remotely sensed measurements of emitted IR radiation hold strong potential to be used to ‘back calculate’ the amount of fuel that was burned to produce that energy (Kaufman et al. 1998a; Wooster et al. 2005).

Initial attempts to use thermal remote sensing to quantify total energy emission from open vegetation fires were largely based on airborne imaging of fire spread rates. For example, Budd et al. (1997) used airborne IR data to map fire perimeters at 6–7 min intervals over a series of experimental bushfires in Australian Eucalypt. By inserting the derived rate of spread and pre-burn fuel load into the formula for Byram’s (1959) fireline intensity, it was estimated that peak head fire intensity for most fires (averaged over 6 min) exceeded 1000 kW per meter of the fire front ( $\text{kW m}^{-1}$ ), and ranged as high as 3,280  $\text{kW m}^{-1}$ . Assuming a fuel heat yield of around 18  $\text{MJ kg}^{-1}$  discussed in Sect. 18.2, these figures equate to fuel consumption rates exceeding 3  $\text{kg min}^{-1}$  per meter of fireline length. At a similar time, Kaufman

et al. (1998a) proposed estimating the rate of radiant energy release from burning vegetation fires more directly, via direct quantitative analysis of the thermally radiant signals themselves. MODIS Airborne Simulator (MAS) was used, and the target was Brazilian cerrado fires, with the ‘radiative energy release rate’ metric defined by Kaufman et al. (1998a) (now usually termed ‘fire radiative power’, FRP) calculated via an empirical relation based on MIR brightness temperature ( $BT_{MIR}$ ) measurements (Eq. 18.6). This equation has subsequently been used to generate the FRP information stored within the MODIS Active Fire Products (Giglio 2010):

$$FRP = 4.34 \cdot 10^{-19} A_{sampler} \sum (BT_{MIR}^8 - BT_{MIR,bg}^8) \quad (18.6)$$

where  $BT_{MIR}$  and  $BT_{MIR,bg}$  are the MIR brightness temperature (K) of the fire pixel and surrounding ambient temperature background pixels respectively, and  $A_{sampler}$  is the MODIS ground pixel area ( $\text{km}^2$ ). Note that pixel area did not appear in the original formulation of Kaufman et al. (1998a), so earlier versions of the MODIS Active Fire Products (Collection 4 and previous) delivered FRP data in units of  $\text{W m}^{-2}$  for any pixel location in the swath. However, the most recent version of the MODIS Active Fire Products (Collection 5 onwards) accounts for the change in pixel area across the MODIS swath, and so provides FRP data directly in MW per pixel (Giglio 2010).

Equation (18.6) was derived specifically for the spectral and spatial characteristics of MODIS, and the coefficients were optimized for the retrieval of FRP from fire pixels with a maximum  $BT_{MIR}$  of  $\sim 450\text{--}500$  K (which represents the approximate saturation temperature of the MODIS’  $3.95\text{ }\mu\text{m}$  ‘fire’ channel [band 21]). When applied to much higher spatial resolution imagery, where fire often fills a greater pixel proportion and  $BT_{MIR}$  values can be much higher than for MODIS, the coefficients in Eq. (18.6) are no longer appropriate. In part to counteract this, Wooster et al. (2003, 2005) derived an alternative approach to estimating FRP, approximating the Planck function with a simple power law and using this to linearly relate FRP to the fire’s emitted MIR spectral radiance (Wooster et al. 2003):

$$FRP = \frac{A_{sampler} \cdot \sigma \cdot \epsilon}{a \cdot \epsilon_{MIR}} (L_{MIR} - L_{MIR,bg}) \quad (18.7)$$

where  $\sigma$  is the Stefan-Boltzmann constant ( $5.67 \times 10^{-8} \text{ J s}^{-1} \text{ m}^{-2} \text{ K}^{-4}$ ) and  $\epsilon$  and  $\epsilon_{MIR}$  are the broadband and MIR spectral emissivities respectively (which cancel if the fire can be considered a greybody or blackbody, which is the commonly assumed case).  $L_{MIR}$  is the MIR spectral radiance of the fire pixel,  $L_{MIR,bg}$  is the MIR spectral radiance of the ambient background (both in units  $\text{W m}^{-2} \text{ sr}^{-1} \mu\text{m}^{-1}$ ), and a [ $\text{W m}^{-2} \text{ sr}^{-1} \mu\text{m}^{-1} \text{ K}^{-4}$ ] is dependent upon the sensor spectral response (see Wooster et al. (2005) for a full derivation).

Using multiple overpasses of fires by MAS in the Brazilian cerrado, Kaufman et al. (1998a) successfully related the detected FRP at each timestep to the rate of increase of burned area. The coefficient of determination ( $r^2$ ) between the time

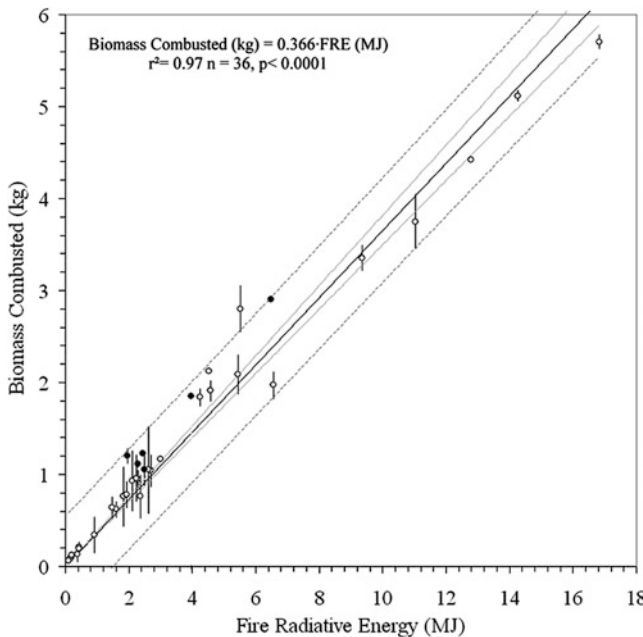


**Fig. 18.12** Linear relationship between fuel consumption and Fire Radiative Energy (FRE, J). FRE is the temporal integral of the fires radiative power output (FRP, MW) over the fires lifetime. Open circles represent herbaceous fuel, and closed circles are woody fuel. Results taken from laboratory scale fire experiment detailed in Wooster et al. (2005). The ‘combustion factor’ C relating these two measures is calculated as  $0.366 \text{ (kg MJ}^{-1}\text{)}$

integrated FRP and the change in burn scar size over the same period was 0.94, significantly stronger than the  $r^2 = 0.74$  relationship between the number of active fire pixels integrated over the same period and the change in burn scar size. This improvement helps indicate the additional value of quantitative thermal analyses of active fire pixels, and specifically the FRP metric, beyond simple counting of numbers of ‘hotspot’ pixels. The assertion of Kaufman et al. (1998a) that FRP could be directly related to fuel consumption and smoke production was later experimentally tested by Wooster et al. (2005) and Freeborn et al. (2008) under laboratory conditions. Handheld thermal imaging cameras were used to collect MIR data at a sample rate of one frame per second, and estimates of FRP derived using Eq. (18.7) were temporally integrated over the lifetime of each fire to calculate Fire Radiative Energy (FRE, MJ). The FRE was found to be very well related to the fuel biomass burned, and the slope of the linear best fit relationship between FRE and fuel burned was termed the ‘combustion factor’ C ( $\text{kg MJ}^{-1}$ ) (Fig. 18.12).

Whilst integrating time-series measurements of FRP to yield FRE is tractable at higher imaging frequencies (e.g. the 1 Hz or better available with ground-based thermal imaging systems, or the few minutes available from repeated aircraft overpasses), retrieving FRE from sequential satellite images can become problematic since assumptions must be made about the temporal trajectory of fire behavior

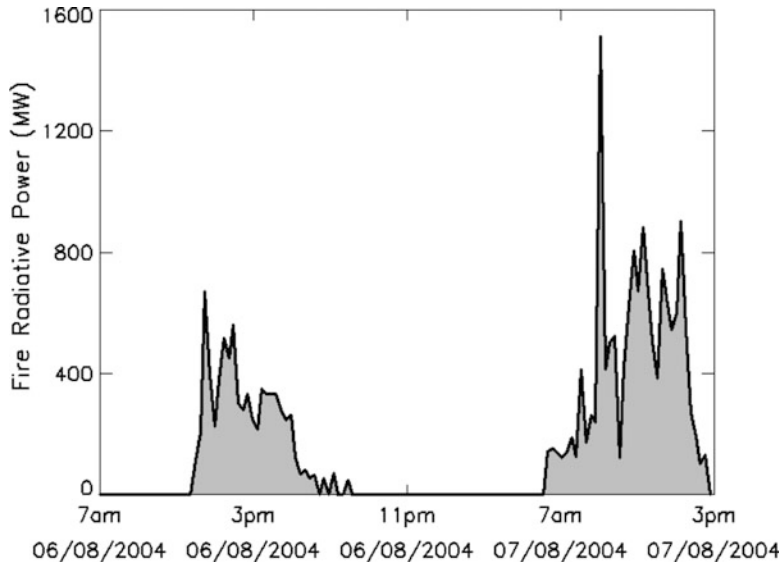


**Fig. 18.13** Time-series of fire radiative power (FRP) observations made using the geostationary Meteosat SEVIRI instrument over a single fire that burned on 6–7 August 2004 in an area of grassland in northern Botswana ( $26.12^{\circ}$  E,  $18.28^{\circ}$  S). SEVIRI FRP observations are available every 15 min, and for this fire there was minimal cloud cover to obstruct the surface from view during the entire measurement period. All detected active fire pixels at each imaging slot had their FRP calculated using Eq. (18.7), and the total FRP for that time slot calculated via summation of the individual per-pixel values. The typically strong fire diurnal cycle results in this case with the fire falling below SEVIRI’s active fire pixel detection threshold at night, only to be re-detected the next day. The total FRE for the fire is calculated from temporal integration of the individual FRP records for the fire made at each 15 min time-slot, and equates to  $12 \times 10^6$  MJ. Using these data in Eq. (18.10) and applying the ‘combustion factor’ ( $C$ , kg MJ $^{-1}$ ) from Fig. 18.12, this FRE equates to  $\sim 4,400$  ton of dry biomass. The SEVIRI FRP product is operationally available from the EUMETSAT Land Satellite Application Facility ([URL2](#))

based on often prolonged, uneven, and temporally undersampled observation times (Freeborn et al. 2009). Hence, geostationary satellites become attractive since they offer the highest sampling rates available from Earth orbit and are thus able to take data semi-continuously across the full diurnal cycle (Fig. 18.7).

### 18.6.2 Fire Diurnal Cycle and Geostationary FRP Observations

Geostationary active fire observations can provide unprecedented temporal detail from high Earth orbit (Fig. 18.13). Such data show vegetation fires undergoing characteristic changes in size and/or intensity that are reflected in the FRP time-series. These variations often correlate with the metrological diurnal cycle of relative humidity, air temperature and wind, leading to the typical fire diurnal cycle seen in Fig. 18.7. More detailed analysis of FRP data returned from analysis

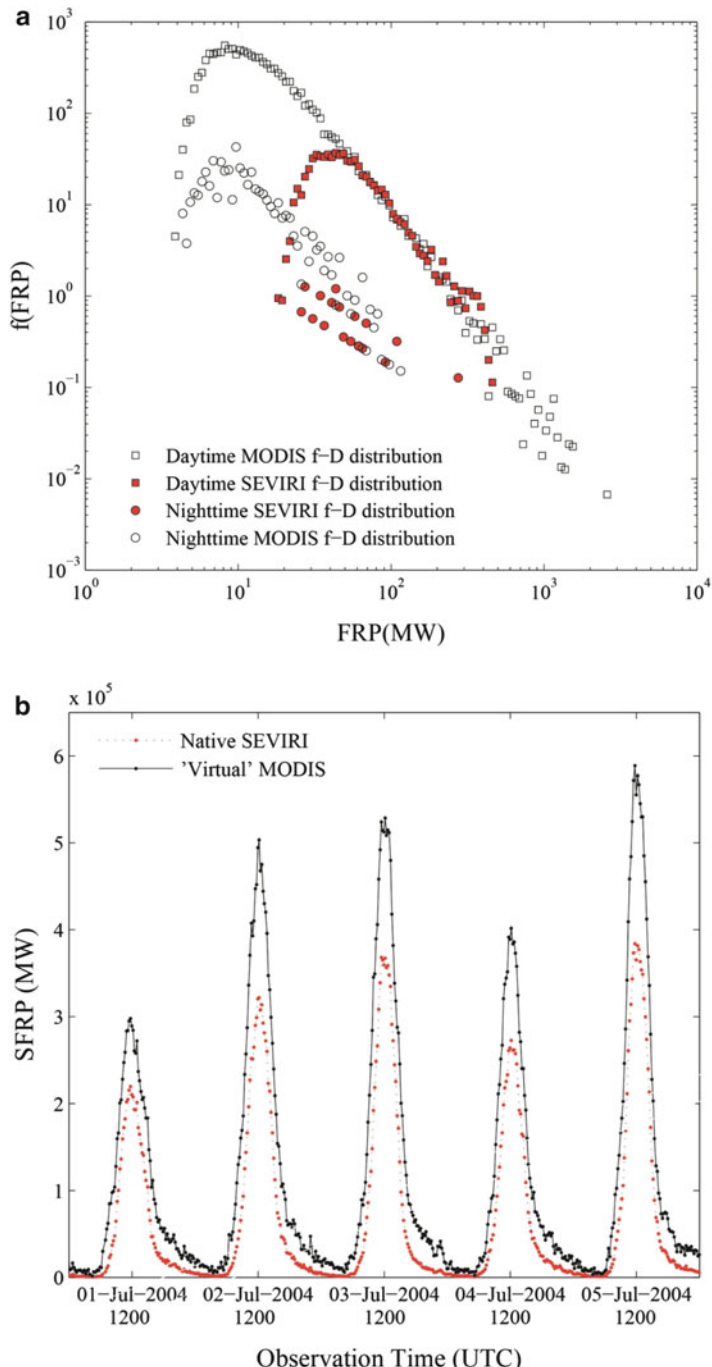


**Fig. 18.14** (a) Fire radiative power (FRP) data of Africa, collected by the polar orbiting MODIS and geostationary SEVIRI instruments. (a) Day and night frequency density distributions of FRP for collocated fire pixels detected at the same time by SEVIRI and MODIS. Both sensors record

of Meteosat SEVIRI imagery by Roberts et al. (2009) illustrated the somewhat skewed distribution of the African fire diurnal cycle. The highest FRP fire pixels appear to occur most frequently at the peak of the diurnal fire cycle, ~14:00 hrs local time, and progression in fire activity throughout the afternoon and into the evening is characterized by a greater proportion of lower FRP fire pixels.

However, the larger pixels sizes typically available from geostationary orbit do offer some limitations, and when polar orbiting and geostationary systems view a fire affected area at the same time, the latter typically fail to detect a greater proportion of the true fire activity (Freeborn et al. 2009). Since lower FRP fires are generally more frequent than high FRP fires (Fig. 18.14a), the omission of the lowest FRP fire pixels may result in a somewhat altered apparent fire diurnal cycle, and a spatio-temporal bias in both the FRP and FRE records. To attempt to account for such biases, Freeborn et al. (2009) combined spatially and temporally concurrent geostationary (Meteosat SEVIRI) and polar orbiting (Aqua and Terra MODIS) observations, to estimate the FRP that would be derived from a MODIS-like sensor operating at the temporal resolution of SEVIRI. Figure 18.14b indicates that this ‘virtual MODIS’ FRP record lies consistently above that of the native SEVIRI sensor, reflecting the fact that, when viewing the same area at the same time, MODIS-type instruments generally detect a more complete record of regional fire activity than do geostationary sensors. However, in reality polar orbiters only provide such data at best a few times per day at most locations.

An alternative approach to bias correction was taken by Roberts et al. (2011), who attempted to blend geostationary FRP data with the types of burned area information commonly derived from optical remote sensing (Fig. 18.15).

The aim was again to adjust the measurement record for the presence of non-detected active fires, which remained undetected either due to their low size and FRP, or because of near continuous cloud cover while they were burning. Figure 18.15 displays the results of this ‘blending’ approach, indicating that this methodology provides fuel consumption estimates across Africa closer to those presented in version 3 of the GFED database than are the estimates derived from the geostationary FRE record alone. A related integrating approach based on MODIS-derived FRP and burned area data had been previously explored by Boschetti and

---

**Fig. 18.14** (continued) fewer fire pixels at night due to the strong fire diurnal cycle (see Figs. 18.7 and 18.13), and distributions suffer from left-hand truncation due to the inability to identify a substantial proportion of the (very frequent) smaller and/or less intensely burning fires. This truncation appears at a higher FRP threshold for SEVIRI since the SEVIRI ground pixel area is  $\sim 10 \times$  that of MODIS at nadir, and the FRP detection limit is directly related to pixel area. Note the distributions also suffer from (more limited) right-hand truncation due to sensor saturation over some of the largest/highest intensity fires. (b) Fire radiative power (FRP) data of Africa, collected by the polar orbiting MODIS and geostationary SEVIRI instruments. (b) Direct comparison between summed FRP actually measured by SEVIRI for a  $5^\circ$  grid cell over Africa every 15-min, and the higher values which would be measured by MODIS over the same area if it could operate at the same temporal resolution as SEVIRI (Adapted from Freeborn et al. 2009)

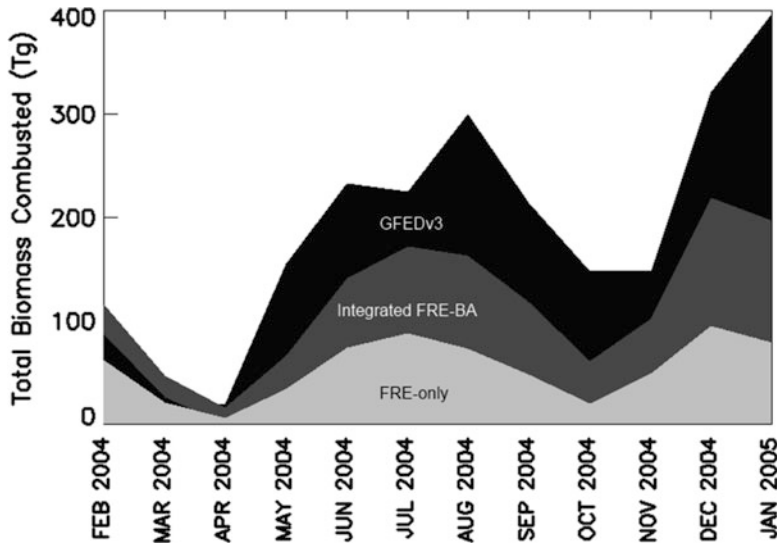


**Fig. 18.15** Monthly total biomass consumption in fires across the African continent, calculated from three different methods. The ‘FRE-only’ approach uses the SEVIRI FRP product (Roberts and Wooster 2008) to calculate the total Fire Radiative Energy released by fires across the continent, in a manner akin to that shown in Fig. 18.13 for a single fire. This FRE total is then converted into an estimate of fuel consumption using Eq. (18.10) and the ‘combustion factor’ ( $C$ ,  $\text{kg MJ}^{-1}$ ) derived in Fig. 18.12. The ‘Integrated FRE-BA’ approach combines the SEVIRI-derived FRE estimates with burned area maps from the MODIS sensor, in order to attempt to adjust the FRE-only estimate for the non-detection of some fire events, due for example to their being low-FRP events or burning under cloud cover (Roberts et al. 2011). The ‘GFEDv3’ approach is based on the MODIS burned area maps alone (no FRE data) combined via a version of Eq. (18.9) with estimates of fuel load ( $\beta$ ,  $\text{g m}^{-2}$ ), derived from the CASA ecosystem production model, and combustion completeness ( $\gamma$ , unitless) derived from e.g. soil moisture estimates (van der Werf et al. 2010). Integrating the burned area maps with the FRE observations results in a fuel consumption estimate closer to that of GFED version 3

Roy (2009), in this case attempting to limit the impact of the lower temporal resolution sampling provided by MODIS rather than the lower spatial resolution sampling provided from geostationary orbit.

### 18.6.3 Sub-pixel Fire Characteristics

In addition to the estimation of fire radiative power and energy, the primary additional active fire characteristic directly derivable from spaceborne and airborne thermal remote sensing is the ‘fire effective’ temperature and (sub-pixel) active fire area (Dozier 1981; Robinson 1991; Giglio and Kendall 2001). Note that ‘area’ in this sense does not refer to the size of the burn scar, but rather the instantaneous area undergoing (flaming and/or smoldering) combustion at the time of thermal image

acquisition. Of course, a single temperature and active fire area cannot precisely match the multi-thermal component structure of an actual vegetation fire, so these metrics instead can be viewed as representing the temperature and size of a perfect IR emitter that would provide the same spectral signal as observed from the active fire itself. Nevertheless, despite being an oversimplification of the actual fire situation, such data may be useful in a variety of wildfire measurement and/or modeling scenarios (Zhukov et al. 2006; Dennison et al. 2006; Freitas et al. 2007; Eckmann et al. 2008; Reid et al. 2009).

The primary approach taken to derive the ‘fire effective’ temperature and (sub-pixel) area is the bi-spectral (or ‘dual band’) method of Dozier (1981), originally developed to support sub-pixel hotspot detection (Robinson 1991). The technique is based upon measurements of infrared spectral radiance made at two (or sometimes more) well-separated wavelengths, most often with regard to active fires in the MIR and LWIR spectral regions. The same method is also commonly used for analysis of volcanic IR spectral radiance data, though SWIR wavebands are more commonly used in the volcanological case (e.g. Rothery et al. 1988; Francis and Rothery 2000; Ramsey and Harris 2012).

Robinson (1991), Giglio and Kendall (2001), Wooster et al. (2003) and Zhukov et al. (2006) provide great detail on the theory of the bi-spectral method applied to vegetation fire analysis. Assuming blackbody fire behavior, and given the spectral radiance ( $L_\lambda$ ) measured at a detected fire pixel in waveband  $\lambda$ , along with a radiance estimate for the non-fire fraction of the fire pixel ( $L_{\lambda, bg}$ ) obtained from surrounding non-fire pixels, the following equation can be formulated for two different wavebands and thus solved to provide an estimate of the fire’s effective temperature ( $T_f$ ) and sub-pixel areal proportion ( $p_f$ ):

$$L_\lambda = p_f \tau_\lambda B(\lambda, T_f) + (1 - p_f)L_{\lambda, bg} + p_f L_\lambda^{\uparrow atm} \quad (18.8)$$

Where  $B(\lambda, T)$  is the Planck function ( $\text{W m}^{-2} \text{ sr}^{-1} \mu\text{m}^{-1}$ ) for waveband  $\lambda$  and temperature  $T$ , and  $\tau_\lambda$  and  $L_\lambda^{\uparrow atm}$  are respectively the atmospheric transmissivity and upwelling atmospheric radiance in that spectral band. The last term will always be small compared to one of the first two terms, and can thus be neglected, enabling the ‘fire effective’ temperature ( $T_f$ ) and proportion ( $P_f$ ) to be retrieved using versions of Eq. (18.8) operating in two different wavebands.

Giglio and Kendall (2001) and Giglio and Justice (2003) provide great detail on the bi-spectral approach, including on limitations related to uncertainties in the ambient background signal at LWIR wavelengths, where the fire signal is typically very much weaker (see Figs. 18.2, 18.3, and 18.4). Additional problems potentially arise from imprecise co-registration between the two spectral channels used, and/or large differences in their point spread function (Langas 1995). Shephard and Kennelly (2003) modeled the potentially large magnitude of these geometric errors, but Zhukov et al. (2006) suggest they can be largely mitigated against by applying the bi-spectral technique to the average spectral radiances measured at hotspot clusters, rather than at individual fire pixels. Many researchers continue to use the

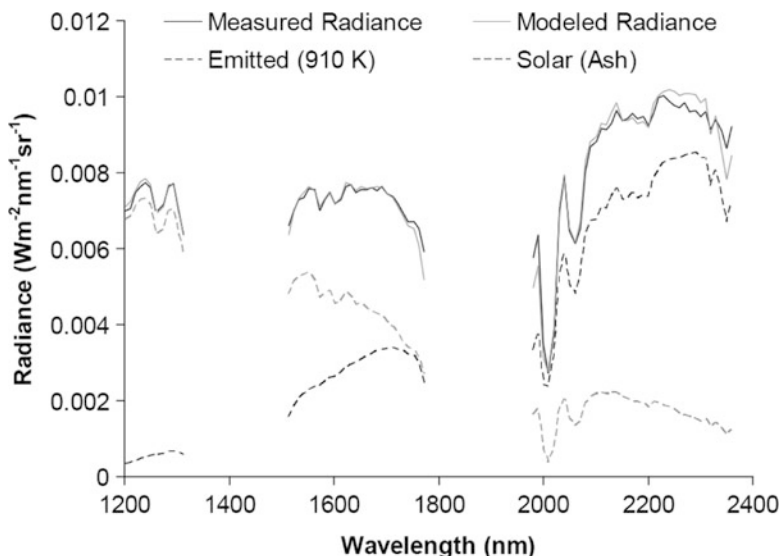


**Fig. 18.16** Spectral fits between the measured spectral radiance recorded at an active fire pixel by the airborne AVIRIS instrument, and the modeled best-fit spectrum (calculated as a function of emitted and solar reflected spectral signals). Minimisation of the residuals between the measured and best-fit modeled spectrum allows fire characteristics (e.g. ‘fire effective’ temperature and sub-pixel size) controlling the emitted radiance component of the measured spectrum to be retrieved (Figure adapted from Dennison et al. 2006)

bi-spectral approach (e.g. Qian and Kong 2012), and the fire effective temperature output from the method may hold some relevance when attempting to discriminate different combustion zones or combustion effects, for example areas of predominantly flaming or smoldering activity or different levels of soil heating (Zhukov et al. 2006; Hanley and Fenner 1998). Similarly, the fire effective area has been used within models of smoke plume injection height (Freitas et al. 2007) and to estimate the fraction of pixels that are releasing smoke into the atmosphere (Reid et al. 2009). Of course,  $T_f$  and  $p_f$  can also be used together to estimate FRP via the Stefan Boltzman Law (e.g. Wooster et al. 2003).

Alternative approaches to the estimation of subpixel fire effective temperature and area also exist, including those related to the work of Green (1996) and others who used the shape and magnitude of the spectra recorded at active fire pixels by the AVIRIS imaging spectrometer to deduce active fire properties. Dennison et al. (2006) built on this approach to ‘unmix’ AVIRIS active fire pixel signals into a combination of subpixel (endmember) features (Fig. 18.16). This ‘multiple endmember spectral mixture analysis’ (MESMA) method was later adapted for use with imagery from alternative IR imaging sensors, such as MODIS (Eckmann et al. 2008) and the HYPER-SIM.GA (Galileo Avionica Multisensor Hyperspectral System) imager whose active fire spectral were shown in Fig. 18.1 (Amici et al. 2011).

## 18.7 Carbon, Trace Gas and Aerosol Emissions Calculations

Once information on the location and thermal characteristics of actively burning fires have been obtained from the types of remote sensing approaches detailed in the preceding sections, a variety of downstream information can be calculated, for example the rate of spread, (radiative) fireline intensity, and head fire or backfire classification, based on various spatio-temporal analyses of the active fire detection and FRP records (e.g. Smith and Wooster 2005). But perhaps the most significant application is related to estimation of pyrogenic carbon, trace gas and aerosol emissions (e.g. Riggan et al. 2004; Roberts et al. 2009; Kaiser et al. 2012).

Conventional calculations aimed at estimating the mass ( $M_x$ ) of a particular chemical species  $x$  released in a smoke plume are generally based on a multiplication of the amount of biomass burned (kg) by an emissions factor ( $EF_x$ , g kg<sup>-1</sup>). Tables of  $EF_x$  for different environments and for dozens of different chemical species present in biomass burning plumes are available in papers such as Andreae and Merlet (2001) and Akagi et al. (2011), so the primary task is to reliably estimate  $M_x$ . The approach of Seiler and Crutzen (1980), which in fact was very similar to the original calculations made by von Danckelman (1884), was to determine the amount of biomass burned via the multiplication of burned area ( $A$ , m<sup>2</sup>), fuel load per unit area ( $\beta$ , g m<sup>-2</sup>), and the fraction of the available fuel that burns ( $\gamma$ , on a 0–1.0 scale):

$$M_x = A \times \beta \times \gamma \times EF_x \quad (18.9)$$

As satellite-derived burned area estimates have been refined through use of increased spatial resolution datasets and improved burned area detection algorithms (see Sect. 18.5), attention has turned toward uncertainties in the pre-burn fuel load and combustion completeness, which possibly exceed 100 % in some circumstances (Reid et al. 2009; Knorr et al. 2012). To help tackle this limitation, independent estimates of total fuel consumption are often welcomed, at the very least for comparison to those derived via the approach. Results such as those shown in Fig. 18.12 indicate that fire radiative energy (FRE) should be linearly related to the mass of fuel consumed in a fire (Wooster et al. 2005; Freeborn et al. 2007), and use of an FRE measure and a simple ‘combustion factor’  $C$  (kg MJ<sup>-1</sup>) therefore allows Eq. (18.9) to be replaced by:

$$M_x = FRE \times C \times EF_x \quad (18.10)$$

The FRP time series for a single African fire was shown in Fig. 18.13, and in this case the FRE and equivalent biomass consumption was estimated as  $12 \times 10^6$  MJ and ~4,400 ton respectively. Roberts et al. (2009) include comparisons between a set of such FRE-derived fuel consumption estimates and those derived from burned area measures and pre-fire fuel loads, indicating a reasonably linear relationship

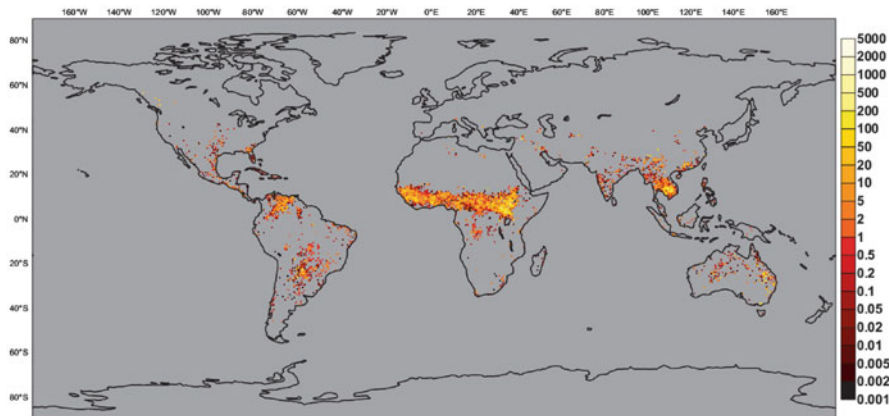


**Fig. 18.17** Example global active fire FRP data record for 19 January 2013, produced by the prototype GMES Atmospheric Service currently being developed by the Monitoring Atmospheric Composition and Climate (MACC II) project ([URL8](#)). The widespread nature of biomass burning activity is easily seen in this global view. The data represent the daily average of the Fire Radiative Power (FRP) observations made from all active fires detected on this day in 125 km grid cells and expressed in units of FRP divided by grid-cell area [ $\text{mW}/\text{m}^2$ ] (max. value  $0.49 \text{ W}/\text{m}^2$ ). Since the rate of release of thermal radiation by a fire is believed to be related to the rate at which fuel is being consumed and thus smoke produced (see e.g. Fig. 18.12), these data are used for the global estimation of open vegetation fire trace gas and particulate emissions, which are then passed onto the other MACC services for incorporation as model source terms. Publicly available data are at present mostly derived from FRP observations made by the MODIS instruments, and future increases in temporal resolution beyond daily averages are planned via use of geostationary FRP products. Products and examples of severe atmospheric perturbation by fire emissions can be found at [URL9](#) and the reader is referred to Kaiser et al. (2012) for further details

between the two approaches. The fire radiative power approach to estimating emissions of carbon, trace gases and aerosols has now reached semi-operational status in the prototype Global Monitoring of Environment and Security (GMES) Atmospheric Service ([URL8](#)), currently planned to become operational around 2014. Figure 18.17 shows a map of global ‘fire radiative power areal density’ ( $\text{mW m}^{-2}$ ) produced by the Global Fire Assimilation System (GFAS) of the GMES Atmospheric Service. The GFAS system uses spaceborne FRP observations to map the daily global release of 40 gas-phase and aerosol trace species present within biomass burning smoke, based on an adaptation of Eq. (18.10) (Kaiser et al. 2012). The system presently assimilates only MODIS FRP observations, and spatially varying adjustments to the ‘combustion factor’  $C$  have been calculated for different land cover types via a comparison between the FRP-derived metrics calculated by GFAS and version 3 of the GFED database. The resulting emissions fields are fed into a variety of regional and global atmospheric chemistry transport models, supporting near-real time decision making and policy development, including for air quality applications (see [URL9](#) for examples).

## 18.8 Summary, Conclusions and Some Recommendations

This chapter has demonstrated the basic principles and developments in the thermal remote sensing of active fires, and has reviewed some of the ways in which the resultant datasets have contributed to both (i) a research agenda, aimed for example at better quantification of the amount and variability of worldwide biomass burning, studying its behavior and effects on both the land and atmosphere, and (ii) an operational agenda related to both fire management and fire suppression, and to the monitoring (and sometimes forecasting) of the effects of biomass burning events on the land surface, atmospheric composition, air quality and climate. The prototype GMES Atmospheric Service ([URL8](#)) is just one example of how active fire satellite thermal remote sensing now directly supports real-time operational monitoring and management of biomass burning impacts in this way, another being the FLAMBE (Fire Locating and Modeling of Burning Emissions) system described in Reid et al. ([2009](#)). The active fire information available in real-time from systems such as FIRMS ([URL1](#)) and the EUMETSAT Land Satellite Applications Facility ([URL2](#)) also support other, sometimes unexpected, applications. For example, whilst the use of active fire detections in the planning of vegetation management strategies to aid future fire severity reductions might perhaps be foreseen, their use by the South African power company Eskom in avoiding damage from fire-induced “flashover” events in power distribution systems seems far from obvious (Davies et al. [2009](#)).

The 2000s have seen a strong degree of growth in the use of thermal remote sensing to study vegetation fires and biomass burning events. According to an analysis using Google Scholar, prior to 1998 there were fewer than 100 journal articles including the words “active fire” published annually, but that number has grown in a strong linear trend ( $r^2 = 0.97$ ,  $n = 14$ ) to  $\sim 600$  year $^{-1}$  currently. This growth has most likely been driven both by the availability of new datasets, including most importantly from the highly successful NASA Earth Observing System (EOS) and the accompanying publically available data records (Kaufman et al. [1998b](#)), and by the increasing realization that even relatively spatially limited fire events such as the 1997–1998 fires on Borneo and Sumatra can significantly affect the environment at regional (e.g. Mott et al. [2005](#)) and global scales (Page et al. [2002](#); Simmonds et al. [2005](#)).

Further developments in sensor technologies and observing systems will be one of the key drivers of future active fire remote sensing. Spaceborne systems such as the proposed Hyperspectral Infrared Imager (HyspIRI; [URL10](#)) offer more thermal bands with improved performance with regard to active fire observations than are available currently from systems such as Landsat ETM+ (Enhanced Thematic Mapper Plus) and ASTER. The next generation of imagers onboard the operational GOES and Meteosat satellites will also provide significant benefits for active fire observation. Planning for each of these includes one or more ‘low gain’ thermal bands, somewhat akin to the current MODIS Band 21 ‘fire channel’ (Kaufman et al. [1998b](#)), which should allow unsaturated thermal observations of even very large and/or intensely burning fires. The forthcoming Sentinel-3 SLSTR (Sea and Land Surface Temperature Radiometer) instrument, which follows on from the long-standing (A) ATSR series, also offers a similar capability (Wooster et al. [2012](#)).

Being a rapidly changing, somewhat transient phenomena, validation of active fire observations is in some ways more difficult than for longer-lived occurrences such as burn scars. Validation of the MODIS active fire detection products was greatly aided by the presence of the higher spatial resolution ASTER thermal sensor onboard the same Terra platform, albeit with ASTER's spatial coverage limited to coverage of the central region of the MODIS swath (Morisette et al. 2005; Schroeder et al. 2008a, b). Validation remains an important research focus, not only in terms of active fire detections, but also in terms of the outputs from fire characterization algorithms. The efficacy of metrics such as 'fire effective' temperature and area' deduced via the Dozier (1981) or similar sub-pixel analysis techniques (Sect. 18.6) has received relatively little scrutiny compared to active fire detection accuracy, in part because of their difficulty of validation and because they are in any case only approximations to the true heterogeneous reality existing within fires. This situation is rather similar to that of satellite volcanology, where strategies using very high spatial resolution handled (FLIR) observations have been employed to at least validate some of the assumptions made when using such sub-pixel analysis methods (e.g. Wright and Flynn 2003). Coordinated under flights of satellites with manned aircraft or UAVs carrying more sophisticated thermal sensors is another avenue for cross-comparison, similar to that conducted during SAFARI-2000 shortly after MODIS launch (Swap et al. 2002). This should be repeated for different environments now that data processing chains are more mature.

In addition to validating the algorithms themselves, another key requirement is gaining confidence in the parameters used to quantify fuel consumption and biomass burning emissions. For example, increasing use of fire radiative power and energy approaches requires that the combustion factor ( $C$ , kg MJ<sup>-1</sup>; Sect. 18.6) be verified beyond the limited range of fuels and small fires investigated so far (e.g. Wooster et al. 2005; Freeborn et al. 2008), and the impacts of attenuation by smoke, the ambient atmosphere and vegetation canopies (particularly for surface fires) should gain increased consideration (Kaiser et al. 2012). The optimization of emissions factors ( $EF_x$ ; see Sect. 18.7) used in deriving chemical emissions estimates from measures of fuel consumption will also continue, driven by required improvements in plume chemistry and transport modelling (e.g. Van Leeuwen and van der Werf 2011). Estimates of fuel moisture, fuel load, fire severity, FRP, and perhaps metrics resulting from other existing or as yet undeveloped fire characterization methods may all have a part to play in such optimization.

The outputs from emissions monitoring and modelling systems (e.g. the GMES Atmospheric Service and FLAMBE) should be continuously evaluated against more direct atmospheric constituent observations (e.g. from satellite, aircraft, tall tower or lidar-based systems; Kaiser et al. 2012), and research into methods to adjust for the limited temporal sampling provided by polar orbiting systems, and/or the non-detection of smaller/lower FRP fires, needs to be continued (Vermote et al. 2009; Ellicott et al. 2009; Boschetti and Roy 2009; Freeborn et al. 2009, 2010; Roberts et al. 2011). Here, the development of 'fire-targeted' satellite remote sensing missions, such as TET-1 (Technology Experiment Carrier 1) and BIROS (Berlin InfraRed Optical System) (Roemer and Halle 2010) can very likely contribute, telling us the frequency distribution of different fire types (Zhukov et al. 2006).

Current BIRD HSRS data suggest that fires having  $\text{FRP} < 10 \text{ MW}$  are by far the most common, but are often missed by MODIS class sensors. These data also suggest that such fires are responsible for only a few percent of globally observed total FRP (Zhukov et al. 2006), so the impact of these omissions could be limited. However, the same records indicate that fires with FRP below 100 MW are also responsible for only ~7 % of the global FRP record, which seems incompatible with indications of a roughly two-fold difference between the amount of FRP detected by MODIS and by geostationary systems during long duration, simultaneous sampling periods (Roberts and Wooster 1998; Freeborn et al. 2009). The fact that the BIRD mission preferentially targeted large fire events is one possible cause of these discrepancies, and missions like TET-1, BIROS and future higher resolution thermal imagers such as HyspIRI should ideally be used to evaluate the true situation.

Beyond the above suggestions, further objectives come from the ‘Global Observation of Forest Cover and Land Cover Dynamics’ (GOFC-GOLD) initiative ([URL11](#)), which in addition to a focus on data availability, quality and validity is stimulating the development of a ‘geostationary active fire network’ to provide almost continuous coverage of fire at lower latitudes, albeit currently with the low-spatial resolution bias associated with geostationary observations. GOFC-GOLD is also highlighting the need for continued production of long-term datasets for better climate-relevant records, against which potential changes in fire regimes may be tested (e.g. Krawchuk et al. 2009). The MODIS data record demonstrates a very strong start in this area, as does the ATSR World Fire Atlas that contains a global record of active fire detections back to 1995 made using a simple nighttime fixed thresholding approach (Mota et al. 2006). It is possible that exploitation of the long-term AVHRR data record, at least for some areas and ‘extreme fire’ periods warrants further attention (e.g. Cahoon et al. 1994; Stroppiana et al. 2000), particularly after adjusting for differing levels of cloud cover and satellite overpass times (e.g. Wooster et al. 2012).

At the time of writing, the active fire product from the new Visible/Infrared Imager Radiometer Suite (VIIRS) sensor, building on the MODIS experience and flying onboard the NPOESS (National Polar-orbiting Operational Environmental Satellite System) Preparatory Project Suomi satellite, is undergoing testing and calibration ([URL7](#)). The VIIRS sensor, along with the ESA Sentinel-3 SLSTR and future ‘fire-capable’ geostationary imagers, are planned to provide operational active fire datasets for the next two decades. This should stimulate the development of new algorithms and analysis methods, which will likely influence the next generation of spaceborne and airborne sensors for Earth system monitoring, along with their exploitation in continued active fire research and fire management operations.

**Acknowledgements** The authors would like to thank everyone who provided figures for use in the chapter, the funding agencies who supported the work covered here, and the reviewers for their supportive and useful comments. Martin Wooster was partly supported by the NERC National Centre for Earth Observation (UK) and the European Union’s Seventh Framework Programme (FP7/2007–2013) under Grant Agreement no. 283576 (MACC-II project). Alistair Smith is partly supported by NASA under award number NNX11AO24G and the National Science Foundation under award EPS-0814387.

## References

- Águeda A, Pastor E, Perez Y, Planas E (2010) Experimental study of the emissivity of flames resulting from the combustion of forest fuels. *Int J Therm Sci* 49(3):543–554
- Akagi SK, Yokelson RJ, Wiedinmyer C, Alvarado MJ, Reid JS, Karl T, Crounse JD, Wennberg PO (2011) Emission factors for open and domestic biomass burning for use in atmospheric models. *Atmos Chem Phys* 11(9):4039–4072
- Alexander ME (1982) Calculating and interpreting forest fire intensities. *Can J Bot* 60(4):349–357
- Ambrosia VG, Brass JA, Allen JB, Hildum EA, Higgins RG (1994) AIRDAS, development of a unique four channelscanner for natural disaster assessment. In: Proceedings of the first international airborne remote sensing conference, Strasbourg, 11–15 Sept 1994, pp 129–141
- Ambrosia VG, Wegener SS, Sullivan DV, Buechel SW, Dunagan SE, Brass JA, Stoneburner J, Schoenung SM (2003) Demonstrating UAV-acquired real-time thermal data over fires. *Photogramm Eng Remote Sens* 69(4):391–402
- Amici S, Wooster MJ, Piscini A (2011) Multi-resolution spectral analysis of wildfire potassium emission signatures using laboratory, airborne and spaceborne remote sensing. *Remote Sens Environ* 115(8):1811–1823
- Andreae MO, Merlet P (2001) Emission of trace gases and aerosols from biomass burning. *Glob Biogeochem Cycle* 15(4):955–966. doi:[10.1029/2000GB001382](https://doi.org/10.1029/2000GB001382)
- Barbosa PM, Grégoire J-M, Pereira JMC (1999) An algorithm for extracting burned areas from time series of AVHRR GAC data applied at a continental scale. *Remote Sens Environ* 69(3):253–263. doi:[10.1016/S0034-4257\(99\)00026-7](https://doi.org/10.1016/S0034-4257(99)00026-7)
- Baum BA, Trepte Q (1999) A grouped threshold approach for scene identification in AVHRR imagery. *J Atmos Ocean Technol* 16(6):793–800
- Becker F, Li Z (1990) Temperature independent spectral indices in thermal infrared bands. *Remote Sens Environ* 32(1):17–33
- Bond WJ, Keeley JE (2005) Fire as a global ‘herbivore’: the ecology and evolution of flammable ecosystems. *Trends Ecol Evol* 20(7):387–394. doi:[10.1016/j.tree.2005.04.025](https://doi.org/10.1016/j.tree.2005.04.025)
- Bond WJ, van Wilgen BW (1996) Fire and plants. Chapman & Hall, New York
- Bond WJ, Woodward FI, Midgley GF (2005) The global distribution of ecosystems in a world without fire. *New Phytol* 165(2):525–538. doi:[10.1111/j.1469-8137.2004.01252.x](https://doi.org/10.1111/j.1469-8137.2004.01252.x)
- Boschetti L, Roy DP (2009) Strategies for the fusion of satellite fire radiative power with burned area data for fire radiative energy derivation. *J Geophys Res* 114:D20302. doi:[10.1029/2008JD011645](https://doi.org/10.1029/2008JD011645)
- Boulet P, Parent G, Acem Z, Collin A, Séro-Guillaume O (2011) On the emission of radiation by flames and corresponding absorption by vegetation in forest fires. *Fire Saf J* 46(1–2):21–26
- Bowman DMJS, Balch JK, Artaxo P, Bond WJ, Carlson JM, Cochrane MA, D’Antonio CM, DeFries RS, Doyle JC, Harrison SP, Johnston FH, Keeley JE, Krawchuk MA, Kull CA, Marston JB, Moritz MA, Prentice IC, Roos CI, Scott AC, Swetnam TW, van der Werf GR, Pyne SJ (2009) Fire in the earth system. *Science* 324(5926):481–484. doi:[10.1126/science.1163886](https://doi.org/10.1126/science.1163886)
- Boyd DS, Petitcolin F (2004) Remote sensing of the terrestrial environment using middle infrared radiation (3.0–5.0  $\mu\text{m}$ ). *Int J Remote Sens* 25(17):3343–3368. doi:[10.1080/01431160310001654356](https://doi.org/10.1080/01431160310001654356)
- Brönnimann S, Volken E, Lehmann K, Wooster MJ (2009) Biomass burning aerosols and climate – a 19th century perspective. *Meteorol Z* 18:349–353
- Budd GM, Brotherhood JR, Hendrie AL, Jeffery SE, Beasley FA, Costin BP, Zhien W, Baker MM, Cheney NP, Dawson MP (1997) Project Aquarius 4. Experimental bushfires, suppression procedures, and measurements. *Int J Wildland Fire* 7(2):99–104. doi:[10.1071/WF9970099](https://doi.org/10.1071/WF9970099)
- Byram M (1959) Combustion of forest fuels. In: Davis KP (ed) Forest fire: control and use. McGraw-Hill, New York, pp 61–89
- Cahoon DR, Stocks BJ, Levine JS, Cofer WR, Pierson JM (1994) Satellite analysis of the severe 1987 forest fires in northern China and southeastern Siberia. *J Geophys Res* 99(D9):18627–18638
- Cheney P, Sullivan A (2008) Grassfires: fuel, weather and fire behaviour. CSIRO Publishing, Melbourne, 150 p
- Cochrane MA (2003) Fire science for rainforests. *Nature* 421:913–919. doi:[10.1038/nature01437](https://doi.org/10.1038/nature01437)

- Coheur PF, Clarisse L, Turquety S, Hurtmans D, Clerbaux C (2009) IASI measurements of reactive trace species in biomass burning plumes. *Atmos Chem Phys* 9:5655–5667
- Crutzen PJ, Andreae MO (1990) Biomass burning in the tropics: impact on atmospheric chemistry and biogeochemical cycles. *Science* 250:1669–1678
- Davies DK, Ilavajhala S, Wong MM, Justice CO (2009) Fire information for resource management system: archiving and distributing MODIS active fire data. *IEEE Trans Geosci Remote Sens* 47(1):72–79
- De Bano LF, Neary DG, Ffolliott PF (1998) Fire's effects on ecosystems. Wiley, Chichester
- Dennison PE, Charoensiri K, Roberts DA, Peterson SH, Green RO (2006) Wildfire temperature and land cover modeling using hyperspectral data. *Remote Sens Environ* 100:212–222. doi:[10.1016/j.rse.2005.10.007](https://doi.org/10.1016/j.rse.2005.10.007)
- Di Bella CM, Jobbág EG, Paruelo JM, Pinnock S (2006) Continental fire density patterns in South America. *Glob Ecol Biogeogr* 15:192–199. doi:[10.1111/j.1466-822x.2006.00225.x](https://doi.org/10.1111/j.1466-822x.2006.00225.x)
- Dietenberger M (2002) Update for combustion properties of wood components. *Fire Mater* 26(6):255–267
- Dipert D, Warren JR (1988) Mapping fires with the FIRE MOUSE TRAP. *Fire Manag Note US Dep Agric* 49(2):28–30
- Dozier J (1981) A method for satellite identification of surface temperature fields of subpixel resolution. *Remote Sens Environ* 11:221–229
- Eckmann TC, Roberts DA, Still CJ (2008) Using multiple endmember spectral mixture analysis to retrieve subpixel fire properties from MODIS. *Remote Sens Environ* 112(10):3773–3783
- Ellicott E, Vermote E, Giglio L, Roberts G (2009) Estimating biomass consumed from fire using MODIS FRE. *Geophys Res Lett* 36(13):1–5
- Elvidge CD, Kroehl HW, Kihn EA, Baugh KE, Davis ER, Hao WM (1996) Algorithm for retrieval of fire pixels from DMSP operational linescan system data. In: Levine JS (ed) *Biomass burning and global change*, vol 1, Remote sensing, modeling and inventory development, and biomass burning in Africa. MIT Press, Cambridge, MA, pp 73–85
- Eva H, Lambin EF (1998) Burnt area mapping in Central Africa using ATSR data. *Int J Remote Sens* 19(18):3473–3497. doi:[10.1080/014311698213768](https://doi.org/10.1080/014311698213768)
- Flannigan MD, Vonder Haar TH (1986) Forest fire monitoring using NOAA satellite AVHRR. *Can J For Res* 16:975–982
- Flasse SP, Ceccato P (1996) A contextual algorithm for advanced very high resolution radiometer (AVHRR fire detection). *Int J Remote Sens* 17(2):419–424. doi:[10.1080/01431169608949018](https://doi.org/10.1080/01431169608949018)
- Francis P, Rothery DA (2000) Remote sensing of active volcanoes. *Annu Rev Earth Planet Sci* 28:81–106
- Fraser RH, Li Z, Cihlar J (2000) Hotspot and NDVI differencing synergy (HANDS): a new technique for burned area mapping over boreal forest. *Remote Sens Environ* 74:362–376. doi:[10.1016/S0034-4257\(00\)00078-X](https://doi.org/10.1016/S0034-4257(00)00078-X)
- Freeborn P, Wooster MJ, Hao WM, Ryan CA, Nordgren BL, Baker SP, Ichoku C (2008) Relationships between energy release, fuel mass loss, and trace gas and aerosol emissions during laboratory biomass fires. *J Geophys Res* 113:D01301. doi:[10.1029/2007JD008679](https://doi.org/10.1029/2007JD008679)
- Freeborn PH, Wooster MJ, Roberts G, Malamud BD, Xu W (2009) Development of a virtual active fire product for Africa through a synthesis of geostationary and polar orbiting satellite data. *Remote Sens Environ* 113(8):1700–1711
- Freeborn PH, Wooster MJ, Roberts G (2010) Addressing the spatiotemporal sampling design of MODIS to provide estimates of the fire radiative energy emitted from Africa. *Remote Sens Environ* 115(2):45–489
- Freitas SR, Longo KM, Chatfield R, Latham D, Silva Dias MAF, Andreae MO, Prins E, Santos JC, Gielow R, Carvalho JA Jr (2007) Including the sub-grid scale plume rise of vegetation fires in low resolution atmospheric transport models. *Atmos Chem Phys* 7:3385–3398
- Giglio L (2007) Characterization of the tropical diurnal fire cycle using VIRS and MODIS observations. *Remote Sens Environ* 108(4):407–421. doi:[10.1016/j.rse.2006.11.018](https://doi.org/10.1016/j.rse.2006.11.018)
- Giglio L (2010) MODIS collection 5 active fire product user's guide, version 2.4. Department of Geography, University of Maryland

- Giglio L, Justice CO (2003) Effect of wavelength selection on characterization of fire size and temperature. *Int J Remote Sens* 24(17):3515–3520
- Giglio L, Kendall JD (2001) Application of the Dozier retrieval to wildfire characterization: a sensitivity analysis. *Remote Sens Environ* 77:34–49
- Giglio L, Kendall JD, Justice CO (1999) Evaluation of global fire detection algorithms using simulated AVHRR infrared data. *Int J Remote Sens* 20(10):1947–1985. doi:[10.1080/014311699212290](https://doi.org/10.1080/014311699212290)
- Giglio L, Kendall JD, Tucker CJ (2000) Remote sensing of fires with the TRMM VIRS. *Int J Remote Sens* 21(1):203–207
- Giglio L, Descloitres J, Justice CO, Kaufman YJ (2003) An enhanced contextual fire detection algorithm for MODIS. *Remote Sens Environ* 87:273–282. doi:[10.1016/S0034-4257\(03\)00184-6](https://doi.org/10.1016/S0034-4257(03)00184-6)
- Giglio L, van der Werf GR, Randerson JT, Collatz GJ, Kasibhatla P (2006) Global estimation of burned area using MODIS active fire observations. *Atmos Chem Phys* 6:957–974
- Giglio L, Randerson JT, van der Werf GR, Kasibhatla PS, Collatz GJ, Morton DC, DeFries RS (2010) Assessing variability and long-term trends in burned area by merging multiple satellite fire products. *Biogeosciences* 7:1171–1186
- Giglio L, Loboda T, Roy DP, Quayle B, Justice CO (2009) An active-fire based burned area mapping algorithm for the MODIS sensor. *Remote Sens Environ* 113(2):408–420
- Giriraj A, Babar S, Jentsch A, Sudhakar S, Murthy M (2010) Tracking fires in India using Advanced Along Track Scanning Radiometer (AATSR) data. *Remote Sens* 2:591–610
- Green RO (1996) Estimation of biomass fire temperature and areal extent from calibrated AVIRIS spectra. Summ Sixth Annu JPL Airborne Earth Sci Workshop JPL Publ 96(4):105–113
- Hanley ME, Fenner M (1998) Pre-germination temperature and the survivorship and onward growth of Mediterranean fire-following plant species. *Acta Oecol* 19:181–187
- Hirsch SN, Madden FH (1969) Airborne infrared line scanners for forest fire surveillance. In: 14th SPIE Annual technical symposium proceedings, vol 2, pp 51–57
- Holden Z, Smith AMS, Morgan P, Rollins MG, Gessler PE (2005) Evaluation of novel thermally enhanced spectral indices for mapping fire perimeters and comparisons with fire atlas data. *Int J Remote Sens* 26(21):4801–4808
- Hook SJ, Myers JJ, Thome KJ, Fitzgerald M, Kahle AB (2001) The (MASTER) – a new instrument for earth science studies. *Remote Sens Environ* 76(1):93–102
- Ichoku C, Kaufman YJ (2005) A method to derive smoke emission rates from MODIS fire radiative energy measurements. *IEEE Trans Geosci Remote Sens* 43(11):2636–2649. doi:[10.1109/TGRS.2005.857328](https://doi.org/10.1109/TGRS.2005.857328)
- Jacobson MC, Hansson H-C, Noone KJ, Charlson RJ (2000) Organic atmospheric aerosols: review and state of the science. *Rev Geophys* 38(2):267–294
- Jenkins BM, Baxter LL, Miles TR Jr, Miles TR (1998) Combustion properties of biomass. *Fuel Proc Technol* 54:17–46
- Justice CO, Kendall JD, Dowty PR, Scholes RJ (1996) Satellite remote sensing of fires during the SAFARI campaign using NOAA AVHRR data. *J Geophys Res* 101:23851–23863
- Kaiser JW, Heil A, Andreae MO, Benedetti A, Chubarova N, Jones L, Morcrette J-J, Razinger M, Schultz MG, Suttie M, van der Werf GR (2012) Biomass burning emissions estimated with a global fire assimilation system based on observed fire radiative power. *Biogeosciences* 9:527–554. doi:[10.5194/bg-9-527-2012](https://doi.org/10.5194/bg-9-527-2012)
- Kaufman YJ, Remer LA (1994) Detection of forests using MID-IR reflectance – an application for aerosol studies. *IEEE Trans Geosci Remote Sens* 32(3):672–683
- Kaufman Y, Justice C, Flynn L, Kendall J, Prins E, Giglio L, Ward D, Menzel W, Setzer A (1998a) Potential global fire monitoring from EOS-MODIS. *J Geophys Res* 103(D24):32215–32238
- Kaufman Y, Kleidmann RG, King MD (1998b) SCAR-B fires in the tropics: properties and remote sensing from EOS-MODIS. *J Geophys Res* 103(D24):31955–31968
- Kaufman YJ, Tanre D, Boucher O (2002) A satellite view of aerosols in the climate system. *Nature* 419(6903):215–223

- Knorr W, Lehsten V, Arneth A (2012) Determinants and predictability of global wildfire emissions. *Atmos Chem Phys Discuss* 12:4243–4278. doi:[10.5194/acpd-12-4243-2012](https://doi.org/10.5194/acpd-12-4243-2012)
- Krawchuk MA, Moritz MA, Parisien M-A, Van Dorn J, Hayhoe K (2009) Global pyrogeography: the current and future distribution of wildfire. *PLoS One* 4(4):e5102. doi:[10.1371/journal.pone.0005102](https://doi.org/10.1371/journal.pone.0005102)
- Kunii O, Kanagawa S, Yajima I, Hisamatsu Y, Yamamura S, Amagai T, Ismail ITS (2002) The 1997 haze disaster in Indonesia: its air quality and health effects. *Arch Environ Health* 57(1):16–22
- Langaas S (1995) A critical review of sub-resolution fire detection techniques and principles using thermal satellite data. University of Oslo, Oslo
- Lavorel S, Flannigan MD, Lambin EF, Scholes MC (2007) Vulnerability of land systems to fire: interactions among humans, climate, the atmosphere, and ecosystems. *Mitig Adapt Strat Glob Chang* 12(1):33–53. doi:[10.1007/s11027-006-9046-5](https://doi.org/10.1007/s11027-006-9046-5)
- Lentile LB, Holden ZA, Smith AMS, Falkowski MJ, Hudak AT, Morgan P, Lewis SA, Gessler PE, Benson NC (2006) Remote sensing techniques to assess active fire characteristics and post-fire effects. *Int J Wildland Fire* 15(3):319–345. doi:[10.1071/WF05097](https://doi.org/10.1071/WF05097)
- Li Z, Kaufman YJ, Ichoku C, Fraser R, Trishchenko A, Giglio L, Jin J (2002) A review of AVHRR-based active fire detection algorithms: principles, limitations, and recommendations. In: Ahern FJ, Goldammer JG, Justice CO (eds) *Global and regional vegetation fire monitoring from space: planning and coordinated international effort*. SPB Academic Pub, The Hague, pp 199–225
- Libonati R, Pereira JMC, Setzer AW, de Faria Peres L (2009) Retrieval of middle-infrared reflectance using remote sensing data: the tropical point of view. In: *Simpósio Brasileiro de Sensoriamento Remoto*, 14 (SBSR) 2009, pp 5917–5924
- Lynch DL (2004) What do forest fires really cost? *J For* 102(6):42–49
- Mayaux P, Bartholomé E, Fritz S, Belward A (2004) A new land-cover map of Africa for the year 2000. *J Biogeogr* 31(6):861–877
- McMillan WW, McCourt WM, Revercomb HE, Knuteson RO, Christian TG, Doddridge BG, Hobbs PV et al (2003) Tropospheric carbon monoxide measurements from the scanning high-resolution interferometer sounder on 7 September 2000 in southern Africa during SAFARI 2000. *J Geophys Res* 108(D13):8492. doi:[10.1029/2002JD002335](https://doi.org/10.1029/2002JD002335)
- Merino L, Caballero F, Martínez-de Dios JR, Ferruz J, Ollero A (2006) A cooperative perception system for multiple UAVs: application to automatic detection of forest fires. *J Field Robot* 23(3–4):165–184
- Morisette JT, Giglio L, Csizsar I, Justice CO (2005) Validation of the MODIS active fire product over Southern Africa with ASTER data. *Int J Remote Sens* 26(19):4239–4264
- Mota BW, Pereira JMC, Oom D, Vasconcelos MJP, Schultz M (2006) Screening the ESA ATSR-2 World Fire Atlas (1997–2002). *Atmos Chem Phys* 6:1409–1424. doi:[10.5194/acp-6-1409-2006](https://doi.org/10.5194/acp-6-1409-2006)
- Mott JA, Mannino DM, Alverson CJ, Kiyu A, Hashim J, Lee T, Falter K, Redd SC (2005) Cardiorespiratory hospitalizations associated with smoke exposure during the 1997 Southeast Asian forest fires. *Int J Hyg Environ Health* 208(1):75–85
- Naeher LP, Brauer M, Lipsett M, Zelikoff JT, Simpson CD, Koenig JQ, Smith KR (2007) Woodsmoke health effects: a review. *Inhal Toxicol* 19(1):67–106
- Nichols JD, Parks GS, Voss JM, Mortensen RA, Logan TL (1989) Designing an infrared system to map and detect wildland fires. In: 1989 Orlando symposium. International Society for Optics and Photonics, pp 7–14
- Page SE, Siegert F, Rieley JO, Boehm HDV, Jaya A, Limin S (2002) The amount of carbon released from peat and forest fires in Indonesia during 1997. *Nature* 420:61–65. doi:[10.1038/nature01131](https://doi.org/10.1038/nature01131)
- Pastor E, Rigueiro A, Zárate L, Giménez A, Arnaldos J, Planas E (2002) Experimental methodology for characterizing flame emissivity of small scale forest fires using infrared thermography techniques. *Forest fire research & wildland fire safety*. Millpress, Rotterdam
- Pausas JG, Keeley JE (2009) A burning story: the role of fire in the history of life. *Bioscience* 59(7):593–601. doi:[10.1525/bio.2009.59.7.10](https://doi.org/10.1525/bio.2009.59.7.10)

- Pereira JMC, Chuvieco E, Beudoin A, Desbois N (1997) Remote sensing of burned areas: a review. In: Chuvieco E (ed) A review of remote sensing methods for the study of large wildland fires. Departamento de Geografía, Universidad de Alcalá, Alcalá de Henares, pp 127–184
- Petitcolini F, Vermote E (2002) Land surface reflectance, emissivity and temperature from MODIS middle and thermal infrared data. *Remote Sens Environ* 83(1):112–134
- Prins EM, Menzel WP (1992) Geostationary satellite detection of biomass burning in South America. *Int J Remote Sens* 13:2783–2799. doi:[10.1080/01431169208904081](https://doi.org/10.1080/01431169208904081)
- Prins EM, Feltz JM, Menzel WP, Ward DE (1998) An overview of GOES-8 diurnal fire and smoke results for SCAR-B and 1995 fire season in South America. *J Geophys Res Atmos* (1984–2012) 103(D24):31821–31835
- Pyne SJ (1984) Introduction to wildland fire: fire management in the United States. Wiley, New York
- Qian YG, Kong SX (2012) A method to retrieve subpixel fire temperature and fire area using MODIS data. *Int J Remote Sens* 33:5009–5025
- Ramsey MS, Harris AJL (2012) How will thermal remote sensing of volcanic surface activity evolve over the next decade. *J Volcanol Geoth Res* 249:217–233. doi:[10.1016/j.jvolgeores.2012.05.011](https://doi.org/10.1016/j.jvolgeores.2012.05.011)
- Reid JS, Hyer EJ, Prins EM, Westphal DL, Zhang J, Wang J, Christopher SA, Curtis CA, Schmidt CC, Eleuterio DP, Richardson KA, Hoffman JP (2009) Global monitoring and forecasting of biomass-burning smoke: description of and lessons from the Fire Locating and Modeling of Burning Emissions (FLAMBE) program. *IEEE J Sel Top Appl Earth Obs Remote Sens* 2 (3):144–162. doi:[10.1109/JSTARS.2009.2027443](https://doi.org/10.1109/JSTARS.2009.2027443)
- Riggan PJ, Tissell RG (2009) Airborne remote sensing of wildland fires. In: Bytnerowicz A, Arbaugh M, Andersen C, Riebau A (eds) Wildland fires and air pollution, vol 8, Developments in environmental science. Elsevier, Amsterdam, pp 139–168
- Riggan PJ, Tissell RG, Lockwood RN, Brass JA, Pereira JAR, Miranda HS, Miranda AC, Campos T, Higgins RG (2004) Remote measurement of energy and carbon flux from wildfires in Brazil. *Ecol Appl* 14(3):855–872
- Roberts G, Wooster MJ (2008) Fire detection and fire characterization over Africa using Meteosat SEVIRI. *IEEE Trans Geosci Remote Sens* 46:1200–1218. doi:[10.1109/TGRS.2008.915751](https://doi.org/10.1109/TGRS.2008.915751)
- Roberts G, Wooster MJ, Lagoudakis E (2009) Annual and diurnal African biomass burning temporal dynamics. *Biogeosciences* 6:849–866. doi:[10.5194/bg-6-849-2009](https://doi.org/10.5194/bg-6-849-2009)
- Roberts G, Wooster MJ, Freeborn P, Xu W (2011) Integration of geostationary FRP and polar-orbiter burned area datasets for an enhanced biomass burning inventory. *Remote Sens Environ* 115:2047–2061. doi:[10.1016/j.rse.2011.04.006](https://doi.org/10.1016/j.rse.2011.04.006)
- Robinson JM (1991) Fire from space: global fire evaluation using infrared remote sensing. *Int J Remote Sens* 12(1):3–24. doi:[10.1080/01431169108929628](https://doi.org/10.1080/01431169108929628)
- Roemer S, Halle W (2010) TET-1 and BIROS a semi-operational fire recognition constellation, UN/Austria/ESA symposium on small satellite programs for sustainable development: payloads for small satellite programs, Graz, 21–24 Sept 2010
- Rothery DA, Francis PW, Wood CA (1988) Volcano monitoring using short wavelength infrared data from satellites. *J Geophys Res* 93:7993–8008
- Schroeder W, Prins E, Giglio L, Csizsar I, Schmidt C, Morisette J, Morton D (2008a) Validation of GOES and MODIS active fire detection products using ASTER and ETM+ data. *Remote Sens Environ* 112(5):2711–2726. doi:[10.1016/j.rse.2008.01.005](https://doi.org/10.1016/j.rse.2008.01.005)
- Schroeder W, Csizsar I, Morisette J (2008b) Quantifying the impact of cloud obscuration on remote sensing of active fires in the Brazilian Amazon. *Remote Sens Environ* 112(2):456–470. doi:[10.1016/j.rse.2007.05.004](https://doi.org/10.1016/j.rse.2007.05.004)
- Seiler W, Crutzen PJ (1980) Estimates of gross and net fluxes of carbon between the biosphere and the atmosphere from biomass burning. *Clim Chang* 2:207–247
- Shephard MW, Kennelly EJ (2003) Effect of band-to-band coregistration on fire property retrievals. *IEEE Trans Geosci Remote Sens* 41(11):2648–2661. doi:[10.1109/TGRS.2003.814912](https://doi.org/10.1109/TGRS.2003.814912)
- Simmonds PG, Manning AJ, Derwent RG, Ciais P, Ramonet M, Kazan V, Ryall D (2005) A burning question. Can recent growth rate anomalies in the greenhouse gases be attributed to large-scale biomass burning events? *Atmos Environ* 39(14):2513–2517. doi:[10.1016/j.atmosenv.2005.02.018](https://doi.org/10.1016/j.atmosenv.2005.02.018)

- Smith AMS, Wooster MJ (2005) Remote classification of head and backfire types from MODIS fire radiative power observations. *Int J Wildland Fire* 14:249–254. doi:[10.1071/WF05012](https://doi.org/10.1071/WF05012)
- Smith AMS, Drake N, Wooster MJ, Hudak A, Holden ZA, Gibbons CJ (2007) Production of Landsat ETM reference imagery of burned areas within Southern African savannahs: comparison of methods and application to MODIS. *Int J Remote Sens* 28:2753–2775
- Stroppiana D, Pinnock S, Gregoire J-M (2000) The global fire product: daily fire occurrence from April 1992 to December 1993 derived from NOAA AVHRR data. *Int J Remote Sens* 21 (6–7):1279–1288
- Stocks BJ, Van Wilgen BW, Trollope WSW (1997) Fire behaviour and the dynamics of convection columns in African savannas. In: Van Wilgen BW, Andreae MO, Goldammer GJ, Lindesay JA (eds) *Fire in southern African Savannas: ecological and atmospheric perspectives*. Wits University Press, Johannesburg, pp 47–55
- Sullivan AL, Ellis PF, Knight IK (2003) A review of radiant heat flux models used in bushfire applications. *Int J Wildland Fire* 12(1):101–110. doi:[10.1071/WF02052](https://doi.org/10.1071/WF02052)
- Swap RJ, Annegarn HJ, Suttles JT, Haywood J, Helmlinger MC, Hely C, Hobbs PV, Holben BN, Ji J, King MD, Landmann T, Maenhaut W, Otter L, Pak B, Piketh SJ, Platnick S, Privette J, Roy D, Thompson AM, Ward D, Yokelson R (2002) The Southern African regional science initiative (SAFARI 2000): overview of the dry season field campaign. *S Afr J Sci* 98:125–130
- Trigg S, Flasse S (2000) Characterizing the spectral-temporal response of burned savannah using in situ spectroradiometry and infrared thermometry. *Int J Remote Sens* 21(16):3161–3168. doi:[10.1080/01431160050145045](https://doi.org/10.1080/01431160050145045)
- Trigg SN, Roy DP (2007) A focus group study of factors that promote and constrain the use of satellite derived fire products by resource managers in southern Africa. *J Environ Manage* 82:95–110
- Trollope WSW (2002) Fire behaviour a key factor in the fire ecology of African grasslands and savannas. In: Viegas DX (ed) *Forest fire research and wildland fire safety: proceedings of IV international conference on forest fire research/2002 wildland fire safety summit*, Coimbra. Millpress, Rotterdam, pp 1–17
- Turner MG, Hargrove WW, Gardner RH, Romme WH (1994) Effects of fire on landscape heterogeneity in Yellowstone National Park, Wyoming. *J Veg Sci* 5(5):731–742
- van der Werf GR, Randerson JT, Collatz GJ, Giglio L, Kasibhatla PS, Arellano AF Jr, Olsen SC, Kasischke ES (2004) Continental-scale partitioning of fire emissions during the 1997 to 2001 El Niño/La Niña period. *Science* 303(5654):73–76. doi:[10.1126/science.1090753](https://doi.org/10.1126/science.1090753)
- van der Werf GR, Morton DC, DeFries RS, Olivier JGJ, Kasibhatla PS, Jackson RB, Collatz GJ, Randerson JT (2009) CO<sub>2</sub> emissions from forest loss. *Nat Geosci* 2:737–738. doi:[10.1038/ngeo671](https://doi.org/10.1038/ngeo671)
- van der Werf GR, Randerson JT, Giglio L, Collatz GJ, Mu M, Kasibhatla PS, Morton DC, DeFries RS, Jin Y, van Leeuwen TT (2010) Global fire emissions and the contribution of deforestation, savanna, forest, agricultural, and peat fires (1997–2009). *Atmos Chem Phys* 10:11707–11735. doi:[10.5194/acp-10-11707-2010](https://doi.org/10.5194/acp-10-11707-2010)
- Van Leeuwen TT, van der Werf GR (2011) Spatial and temporal variability in the ratio of trace gases emitted from biomass burning. *Atmos Chem Phys* 11:3611–3629
- Vermote E, Ellicott E, Dubovik O, Lapyonok T, Chin M, Giglio L, Roberts GJ (2009) An approach to estimate global biomass burning emissions of organic and black carbon from MODIS fire radiative power. *J Geophys Res* 114:D18205
- von Danckelman A (1884) Die Bewölkungsverhältnisse des südwestlichen Afrikas. *Meteorol Z* 1:301–311
- Wallace LL (2004) After the fires: the ecology of change in Yellowstone National Park. Yale University Press, New Haven
- Ward D (2001) Combustion chemistry and smoke. In: Johnson EA, Miyanishi K (eds) *Forest fires: behavior and ecological effects*. Academic Press, San Diego, pp 55–77
- Warren JR (1992) Advanced fire sensing and locating systems, remote sensing and natural resource management: proceedings of the fourth forest service remote sensing applications conference, 6–11 Apr, Orlando, FL, pp 212–220

- Warren JR, Celarier DN (1991) A salute to infrared systems in fire detection and mapping. *Fire Manag Note US Dep Agric* 52(3):3–18
- Wegener SS, Ambrosia VG, Stoneburner J, Sullivan DV, Brass JA, Buechel SW, Higgins RG, Hildum EA, Schoenung SM (2002) Demonstrating acquisition of real-time thermal data over fires utilizing UAVs. In: Proceedings of AIAA's 1st technical conference and workshop on unmanned aerospace vehicles, systems, technologies, and operations, vol AIAA-2002-3406, Portsmouth, VA, 20–23 May 2002
- Wooster MJ, Strub N (2002) Borneo fires: quantitative analysis using global area coverage (GAC) satellite data. *Glob Biogeochem Cycle* 16(1):9. doi:[10.1029/2000GB001357](https://doi.org/10.1029/2000GB001357)
- Wooster MJ, Richards T, Kidwell KB (1995) NOAA 11 AVHRR/2 – thermal channel calibration update. *Int J Remote Sens* 16(2):359–363. doi:[10.1080/01431169508954401](https://doi.org/10.1080/01431169508954401)
- Wooster MJ, Zhukov B, Oertel D (2003) Fire radiative energy for quantitative study of biomass burning: derivation from the BIRD experimental satellite and comparison to MODIS fire products. *Remote Sens Environ* 86:83–107
- Wooster MJ, Roberts G, Perry GLW, Kaufman YJ (2005) Retrieval of biomass combustion rates and totals from fire radiative power observations: FRP derivation and calibration relationships between biomass consumption and fire radiative energy release. *J Geophys Res* 110:D24311. doi:[10.1029/2005JD006318](https://doi.org/10.1029/2005JD006318)
- Wooster MJ, Freeborn PH, Archibald S, Oppenheimer C, Roberts GJ, Smith TEL, Govender N, Burton M, Palumbo I (2011) Field determination of biomass burning emission ratios and factors via open-path FTIR spectroscopy and fire radiative power assessment: headfire, backfire and residual smouldering combustion in African savannahs. *Atmos Chem Phys* 11:11591–11615
- Wooster MJ, Perry GLW, Zoumas A (2012) Fire, drought and El Niño relationships on Borneo (Southeast Asia) in the pre-MODIS era (1980–2000). *Biogeosciences* 9:317–340. doi:[10.5194/bg-9-317-2012](https://doi.org/10.5194/bg-9-317-2012)
- Wright R, Flynn LP (2003) On the retrieval of lava-flow surface temperatures from infrared satellite data. *Geology* 31(10):893–896
- Xu W, Wooster MJ, Roberts G, Freeborn PH (2011) New GOES imager algorithms for cloud and active fire detection and fire radiative power assessment across North, South and Central America. *Remote Sens Environ* 114:1876–1895
- Zhukov B, Lorenz E, Oertel D, Wooster MJ, Roberts G (2006) Spaceborne detection and characterization of fires during the bi-spectral infrared detection (BIRD) experimental small satellite mission (2001–2004). *Remote Sens Environ* 100(1):29–51. doi:[10.1016/j.rse.2005.09.019](https://doi.org/10.1016/j.rse.2005.09.019)
- URL1: <http://earthdata.nasa.gov/firms>
- URL2: <http://landsaf.meteo.pt/>
- URL3: <http://lance.nasa.gov>
- URL4: <http://cimss.ssec.wisc.edu/goes>
- URL5: <http://wildfire.geog.kcl.ac.uk/wordpress>
- URL6: <http://www.itres.com>
- URL7: <http://viiirsfire.geog.umd.edu>
- URL8: <http://www.gmes-atmosphere.eu/>
- URL9: <http://www.gmes-atmosphere.eu/fire>
- URL10: <http://hyspiri.jpl.nasa.gov/>
- URL11: <http://gofc-fire.umd.edu/objectives/index.php>

# Chapter 19

## Analysis of Lava Flow Effusion Rate Using High Spatial Resolution Infrared Data

Valerio Lombardo and Maria Fabrizia Buongiorno

**Abstract** Remote sensing thermal data of active lava flows allow for the evaluation of instantaneous effusion rates. This is made possible by simple formulae relating the lava effusion rate to the power energy radiated per unit time from the surface to the flow. The most questionable assumption is probably the constancy of the surface temperature. Due to the assumptions of the model, this formula implies that heat flux, surface temperature and lava temperature varies as a function of the flow thickness. These relationships, never verified or validated before, have been used by several authors as a proof of the weakness of the model. Herein, MIVIS (Multi-spectral Infrared and Visible Imaging Spectrometer) high spatial resolution (5–10 m) thermal data acquired during Etna’s 2001 eruption were used to investigate down-flow heat-flux variations in the lava flow emitted from a vent located at 2,100 m a.s.l. A high correlation between the down-flow heat-flux and the lava flow thickness (measured from a pre-existing digital elevation model) was found. According to this relationship, observed changes in the surface temperature would be the expected consequence of differences in the down-flow lava flow thickness due to topographic variations.

### 19.1 Introduction

Remotely sensed data can be used to estimate heat and mass fluxes of active lava flows. The movement of lava flows is a complex subject that has provoked debate regarding the mechanisms that control the areal extent and physical character of the flow (e.g. Pieri and Baloga 1986; Lipman and Banks 1987; Oppenheimer 1991; Oppenheimer et al. 1993a, b, c; Harris et al. 1997a, b, 1998, 1999; Lombardo et al. 2004, 2006, 2009; Lombardo and Buongiorno 2006). The effusion rate, defined as

---

V. Lombardo (✉) • M.F. Buongiorno  
Istituto Nazionale di Geofisica e Vulcanologia (INGV), Rome, Italy  
e-mail: [Valerio.lombardo@ingv.it](mailto:Valerio.lombardo@ingv.it)

either an instantaneous or time-averaged volume flux feeding a lava flow from a vent, is a major consideration in evaluating flow dynamics and the potential threat posed by a lava flow. Higher effusion rates produce channel-fed flows that are longer, more rapidly moving, voluminous, and extensive than flows with low effusion rates (Walker 1973; Wadge 1977; Pieri and Baloga 1986). Flows with high effusion rates thus have far greater potential to inflict damage on distant communities with less advance warning. Measuring effusion rates is therefore of great interest. Field methods for their determinations are usually based on estimates of lava channel dimensions and lava flow velocity (e.g. Lipman and Banks 1987; Barberi and Villari 1994). However, errors due to uncertainties in channel dimension, especially depth, are a major problem. Although not particularly useful for monitoring purposes, accurate post-eruption measurements of total flow field volumes provide reliable estimates of average effusion rates if the eruption duration is known (e.g. Calvari et al. 1994).

Determining effusion rates for lava flows from space is an important but challenging task. The evaluation of lava effusion rates builds on a formula originally proposed by Pieri and Baloga (1986) which relates the flow rate to the planimetric area of a flow. If the flow rate is assumed to coincide with the effusion rate, the formula states that the effusion rate is proportional to the heat radiated per unit time by the surface of the flow. The formula of Pieri and Baloga (1986) was lately adapted to extract effusion rates from satellite thermal data by Harris et al. (1997a, b, 1998, 2000, 2005) by including: the thermal contributions of convection in the air and crystallization of lava and the contribution of heat conduction to the ground. Although the formulae by Pieri and Baloga (1986) and Harris et al. (1997b) yield reasonable results, Dragoni and Tallarico (2009) demonstrated how the current use of the formula is often not consistent with the model itself. In this study, starting from model assumptions and drawbacks, we show how our experimental measurements match the theoretical basis of the Pieri and Baloga formula (1986).

## 19.2 From Heat to Mass Flux: History of a Model

The energy produced by an active lava flow is lost to the environment through a combination of conduction, convection, and radiation. The formula originally proposed by Pieri and Baloga (1986) can be obtained from a simple model representing a lava flow cooling by radiation only. Following this approach effusion rate ( $E_r$ ) can be estimated from the heat flux for a moving flow ( $Q$ ) from:

$$E_r = \frac{Q}{\rho c_p \Delta T} \quad (19.1)$$

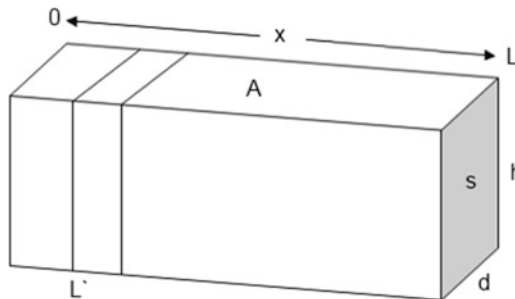


**Fig. 19.1** ADD Summary and sketch of the model assumptions proposed by Pieri and Baloga (1986). The lava flow is an unbounded fluid layer with uniform thickness  $h$ , length  $L$ , and width  $d$  flowing on a sloping plane. The temperature  $T$  of lava depends only on  $x$ :  $T(0)$  is the eruptive temperature and  $T(L)$  is the temperature at the lava front. The model can be applied to small portion of the overall volume (length  $L'$ ) to estimate the effusion rate as a function of the local decrement in  $T$

where  $\rho$  is lava density,  $c_p$  is lava specific heat capacity,  $\Delta T$  is the difference between temperatures of fluid lava at the vent  $T_e$  and at the front  $T(L)$ ,  $L$  being the flow length (Fig. 19.1).

In this model,  $Q$  is calculated using only the radiant contribution  $Q_{rad}$ :

$$Q_{rad} = \varepsilon \sigma A T_s^4 \quad (19.2)$$

In which  $\varepsilon$  is the emissivity,  $\sigma$  is the Stefan-Boltzmann constant and  $A$  is the flow area.

There are several assumptions underlying this model (Fig. 19.1):

1. The lava flow is an unbounded fluid layer with uniform thickness  $h$ , flowing on a sloping plane.
2. The flow is in a steady state both mechanically and thermally.
3. The fluid motion is unidirectional (occurring in the  $x$  direction).
4. The velocity  $v$  is uniform and constant (in particular the variation with  $z$  is neglected).
5. The heat loss takes place exclusively by radiation at the upper surface of the flow  $z = h$ .
6. The surface temperature  $T_s$  is constant.
7. The ambient temperature is negligible with respect to  $T_s$ .
8. The temperature  $T$  of lava depends only on  $x$ :  $T(x)$  must be intended as the average temperature over the flow thickness.
9. Viscous dissipation and heat produced by crystallization are negligible.
10. The heat flux  $q$  within the lava flow depends linearly on  $z$ .
11. The lava is incompressible and its  $\rho$ ,  $c_p$  and thermal emissivity  $\varepsilon$  are constant.

Harris et al. (1997b) introduced the thermal contributions of convection in the air and crystallization of lava. Harris et al. (2005) also included the heat loss by

conduction. These formulae are based on the same model as Pieri and Baloga's (1986) formula.

The thermal contributions of convection ( $Q_{conv}$ ) is calculated using the free convection case given by Harris et al. (1997b, 1998). This reduces to:

$$Q_{conv} = h_c [T_s - T_{air}] \quad (19.3)$$

in which  $h_c$  is the convective heat transfer coefficient and  $T_{air}$  is the ambient air temperature.

The heat conducted through the base of the flow is given by (Harris et al. 1997b):

$$Q_{cond} = Ak\delta T/\delta h \quad (19.4)$$

where  $k$  is the lava thermal conductivity and  $\delta T$  is the temperature difference across a flow of thickness  $\delta h$ .

Therefore, the total heat loss  $Q$  in Eq. (19.1) can be described by a simple model for a subaerial channel-fed flow

$$Q = Q_{rad} + Q_{conv} + Q_{cond}. \quad (19.5)$$

And Eq. (19.1) becomes:

$$E_r = \frac{Q}{\rho [c_p \Delta T + \phi C_L]} \quad (19.6)$$

where  $\phi$  is mass fraction of crystals grown in cooling through  $\Delta T$  and  $C_L$  is the latent heat of crystallization. Because Eq. (19.1) is time-independent, which is a consequence of the steady-state assumption, the same value of the effusion rate should be obtained independently of the time when the measurement of  $Q$  is performed. If we assume that the effusion rate is constant, as longer as the area of the flow increases, increments in  $Q$  (Eq. 19.2) are balanced by a linear increments in the temperature difference  $\Delta T$  with  $L$  (Dragoni and Tallarico 2009). Therefore a constant value of  $E_r$  is obtained from Eq. (19.1) at different times. Similarly, at a given time,  $E_r$  has a constant value over the entire flow length considering that  $\Delta T$  is a function of  $x$  ( $0 < x < L$ ) and can assume values in the range  $0 < \Delta T < T_e - T_s$ .

Dragoni and Tallarico (2009) infer that the most questionable assumption in the model is probably the constancy of the surface temperature  $T_s$ . On the one hand, several field (Pinkerton et al. 2002) and remote sensing measurements (Lombardo et al. 2009) confirmed that  $T_s$  is not uniform in actual flows. On the other hand, the simple relationship between  $E_r$  and  $Q$  can be obtained only assuming that  $T_s$  does not vary within the flow. Dragoni and Tallarico (2009) showed that Pieri and Baloga's (1986) formula can work only if the surface temperature decreases rapidly enough (at least exponentially) with the distance from the vent. This condition would ensure that  $Q$  is independent of  $L$ . Herein, starting from the assumptions of this model, we use high spatial thermal data to investigate the implication of thermal flux distribution within active lava flows.

### 19.3 The 2001 Etna Eruption and MIVIS Airborne Campaign

The July–August 2001 eruption of Mount Etna was characterized by both effusive and explosive activity. A detailed chronology of the events that comprised this eruption is given by Calvari and Pinkerton (2004), Behncke and Neri (2003) and Coltelli et al. (2007). We here focus on the lava flow erupted from the lower-most fissure on the southern flank. This vent was located between 2,100 and 2,150 m and was termed Lower Fissure System 1 (LFS1) by Coltelli et al. (2007). The channel-fed lava flow field fed by this fissure was continuously active for 23 days from 18 July to 9 August, and was described and mapped by Behncke and Neri (2003) and Coltelli et al. (2007). The lava flow field reached a maximum length of 6.4 km, extending down to an elevation of 1,040 m. The toe of the flow evolves from channel-contained to dispersed. LIDAR (Light Detection And Ranging) measurements (Favalli et al. 2010), supported by field mapping, show that the flow front comprised eight lobes each 10–20 m high. The flow front appears to have advanced not as a single unit, but as a series of lobes moving forward one lobe at a time. Primary lobes were centered on the channel axis and marginal lobes were off-axis. The lobes advanced as breakouts of low-yield-strength lava from the flow core of the stalled flow front. Marginal lobes were abandoned and contributed to marginal levees flanking the transitional channel. Maximum time-averaged discharge rate (TADR), obtained on the basis of daily mapping, was  $\sim 31 \text{ m}^3/\text{s}$  (Coltelli et al. 2007). This measurement was made on 22 July; TADRs of 24 and  $18 \text{ m}^3/\text{s}$  were obtained on 20 and 26 July (Coltelli et al. 2007). At this time, the maximum lava flow length was attained. Following 27 July, effusive activity began to wane. The TADR fell to  $\sim 5 \text{ m}^3/\text{s}$  by 2 August and the flow front progressively retreated up-channel as the effusion waned (Coltelli et al. 2007; Behncke and Neri 2003). The final volume for the LFS1 flow field was  $21.4 \pm 0.37 \times 10^6 \text{ m}^3$  (Coltelli et al. 2007), which gives a mean output rate over the 23 days of activity of  $\sim 11 \text{ m}^3/\text{s}$ .

An airborne survey carrying a multi-spectral infrared and visible imaging spectrometer (MIVIS) was carried out on 29th July 2001, with the primary objective of obtaining high-spatial-resolution image data to aid in tracking the 2,100-m-vent flow that was moving towards *Nicolosi* (Fig. 19.2).

MIVIS is an airborne sensor flown on a CASA-212 aircraft recording in 102 wavebands between 0.4 and 12  $\mu\text{m}$ . These are split between the very near infrared (VNIR), short wave infrared (SWIR) and thermal infrared (TIR), with 80 wavebands in the 0.4–2.5  $\mu\text{m}$  range and 22 in the 8–12  $\mu\text{m}$  range. The MIVIS flight altitude on 29th July was of 6,400 m a.s.l. giving a ground pixel resolution in the range 6–12 m, depending on the surface elevation. We thus calculate pixel resolution on a pixel-by-pixel basis using the pixel instantaneous field of view (IFOV) and the difference between MIVIS flight altitude (6,400 m) and topographic elevation obtained for each pixel (derived from a 10 m digital terrain model to which the MIVIS image was fitted). The high spatial resolutions of unsaturated infrared MIVIS data allow for detailed mapping of the lava flow surface

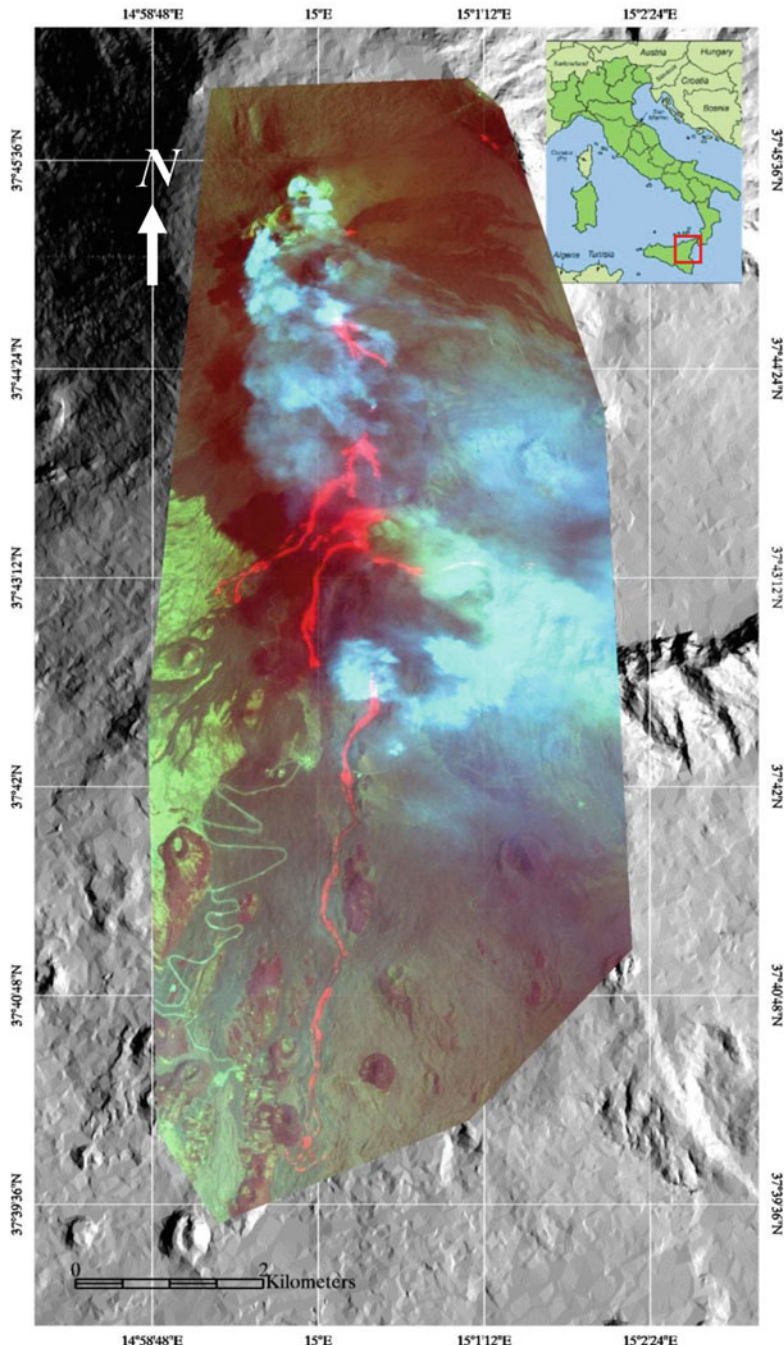


**Fig. 19.2** Shaded relief and coregistered composed MIVIS image (RGB = 2.20, 1.52, 0.68  $\mu\text{m}$ ) acquired on 29th July 2001

temperature and thermal flux distribution (Lombardo et al. 2006, 2009). TIR data were corrected for atmospheric effects using the atmospheric radiative transfer model MODTRAN (MODerate resolution atmospheric TRANsmision) (Kneizys et al. 1983).

## 19.4 Surface Temperature and Radiative Heat Flux

In order to assess the importance of radiative cooling for the lava flow, it is crucial to examine the different heat flux contributions from vent to lava front. The map of surface temperature derived from MIVIS thermal band is shown in Fig. 19.3.

Significant variations of the surface temperature occur within the flow, ranging from about 313 to over 700 K with a mean value of 386 K. Therefore, the assumption of  $T_s$  as constant is not realistic as stated from the formula of Pieri and Baloga. Figure 19.4 shows the down flow  $T_s$  temperature profile obtained for the lava channel fed by the 2,100 m vent.

The trend displays a spatial variation in thermal structure consistent with rapid near-vent surface cooling, a dominant zone of cooler, stable temperatures, and an increase in temperature towards the flow front. This trend is consistent with that proposed by Lipman and Banks (1987) and Harris et al. (2007) for channel-fed Etnean flows, where the proximal channel represents the hottest zone of high heat losses, but the majority of the flow is well-insulated as the surface cools and reduces heat loss. We thus divided the flow into three thermally distinguishable zones: proximal, medial-distal, and toe. The proximal zone is characterized by relatively high  $T_s$  which rapidly decrease from a temperature of 750 to about 500 K after flowing 0.4 km. Five saturated pixels (Fig. 19.4) mark the main outbreak zone along the 2,100 vent fracture. The medial zone is defined by decrement in  $T_s$  showing a weak down-flow decline. The medial trend is interrupted by a sudden increment in the temperature profile at about 3.0 km from the lava vent (Fig. 19.3). This event is followed by a rapid decrement in  $T_s$  and again by another progressive stabilization of the decrement rate. We can recognize three further similar events at 3.9, 4.8 and 5.8 km respectively (Fig. 19.3). Finally, temperature variations at the toe of the flow reflect the complexity of the lava structure emplacing in an “alluvial fan” fashion (Fig. 19.3). Surface temperature suddenly falls down to a minimum of 320 K beyond the stalled front of the lava flow.

Figure 19.3b shows the map of radiative heat flux calculated from Eq. (19.2). While the maximum radiative heat flux in the image is 997 kW, the mean and minimum values are 139 and 60 kW, respectively. Highest values ( $>950$  kW) occur at the vent location and throughout the channelized sections of the flow where  $Q_{rad}$  is 400–700 kW. In order to investigate variations in radiative heat flux, cross-flow profiles from vent to front have been analyzed for location given in Fig. 19.3b. On the basis of our heat flux observations and following the classification of Lipman and Banks (1987), we can divide the flow into four distinct zones: the channel-contained zone, the transitional channel zone, the dispersed zone, and the lava front

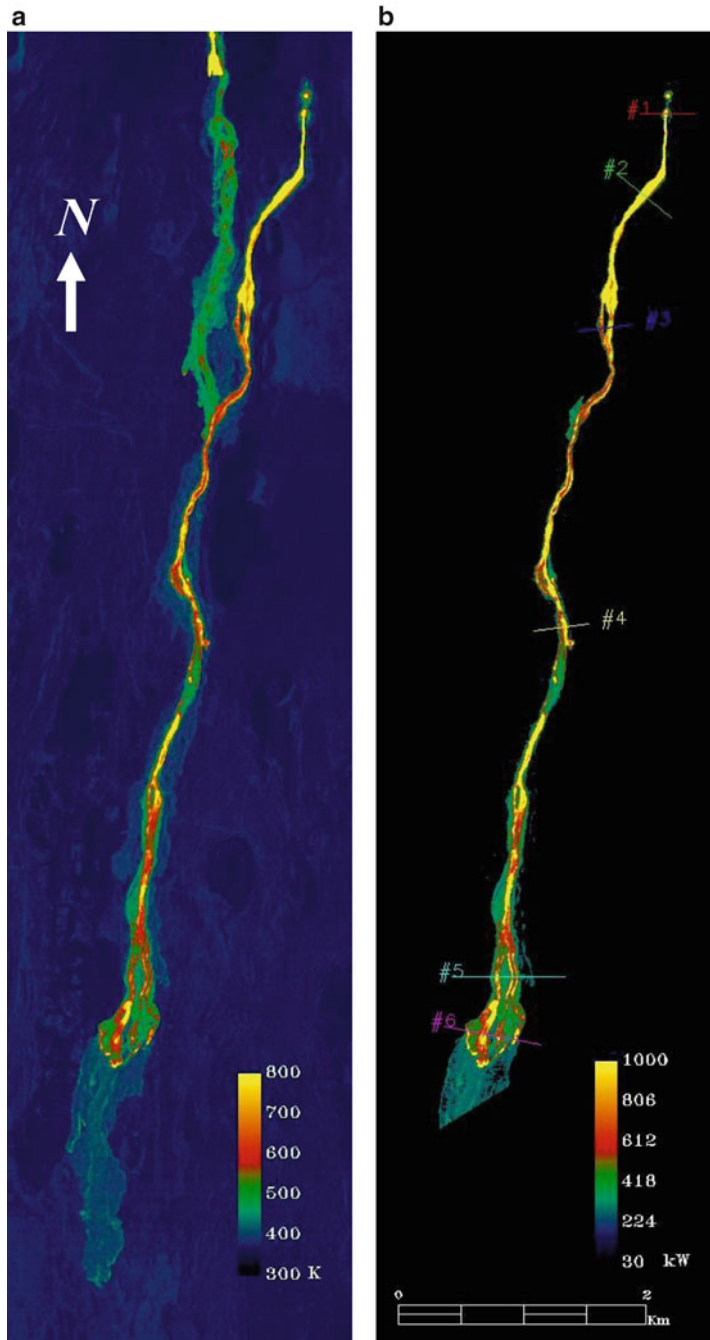


**Fig. 19.3** Surface temperature (a) and radiative heat flux (b) spatial distribution derived from the 29th July 2001 MIVIS data for the 2,100 m lava flow field with locations of profiles given in Fig. 19.5

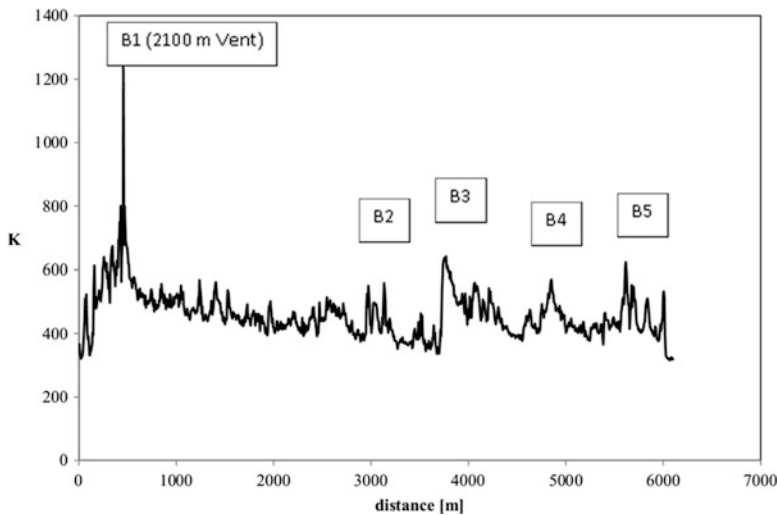


**Fig. 19.4** Down flow profile of calculated surface temperature with locations of temperature peaks ( $B_1, \dots, B_6$ ). Highest temperatures (1,240 K) occur at the vent location ( $B_1$ )

(Favalli et al. 2010). Channel-contained zones are concentrated in a well-defined, stable, central channel, bounded by broad zones of stationary lava which form the levees (Lipman and Banks 1987). Examination of the cross-flow variation for channel-contained zones reveals an abrupt reduction in heat loss when we move from the middle of the active channel to the margin zones (Fig. 19.5, profile 1 and 2).

Mean heat-fluxes for the channelized and margin zones are 550 and 40 kW respectively. The transitional channel is marked by a distinct channel bounded by blocky or clinkery lava which form marginal zones of stagnant lava (Lipman and Banks 1987). Zones of stagnant lava may include abandoned channel (profile 3) or evolve into levees needed to create a self-formed channel (profile 4). The dispersed zone is the section of flow across which movement is widespread, and the main channel splits into two or more branches. Different branches are marked by distinct peaks in the radiative heat loss profile 5 (Fig. 19.5d). Finally, the flow front of 2,100 m lava flow comprises eight discrete lobes, each 30–80 m across and 10–15 m height, with a maximum thickness of 20 m (Favalli et al. 2010). Lobes are separated from one another by a shallow valley of rubbly ‘a’ā clinker material (Favalli et al. 2010). Figure 19.5e shows flux values of 250–300 and 80–120 kW for lobes and clinker material respectively.

Analysis of cross-flow temperature profile for channel-contained zones shows a Gaussian trend to fit our experimental data (Fig. 19.6a). Therefore, we use a Gaussian interpolation to predict temperatures for saturated data (Fig. 19.6b). A maximum surface temperature of 1,240 K was obtained at the flow vent.

In the case of 2,100 lava flow, there is an evident correlation between the zones proposed by Lipman and Banks (1987) and the three thermal zones we identified on the basis of our downflow thermal measurements. In the proximal zone, the heat

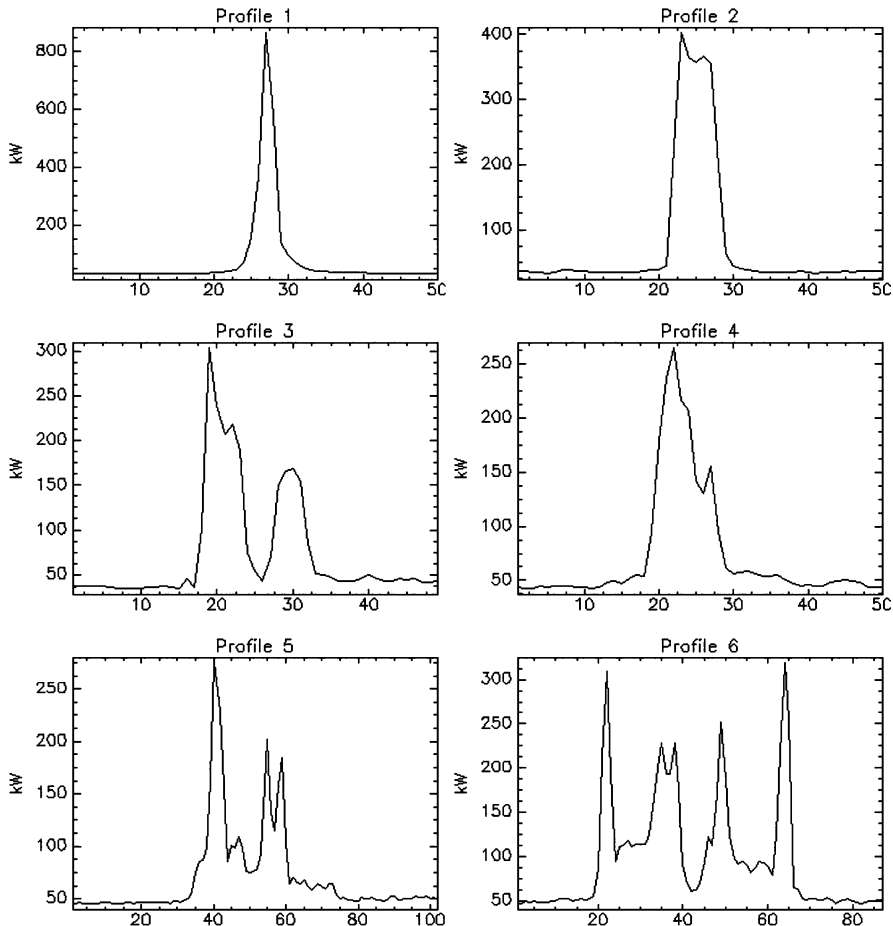


**Fig. 19.5** Cross-flow heat flux profiles for locations given on Fig. 19.3b. The heat flux profile varies from a single finely tuned peak (e.g. *profile 1* and 2) to multiple broad peaks (e.g. *profile 5* and 6) as the flow evolves from channel-contained to dispersed

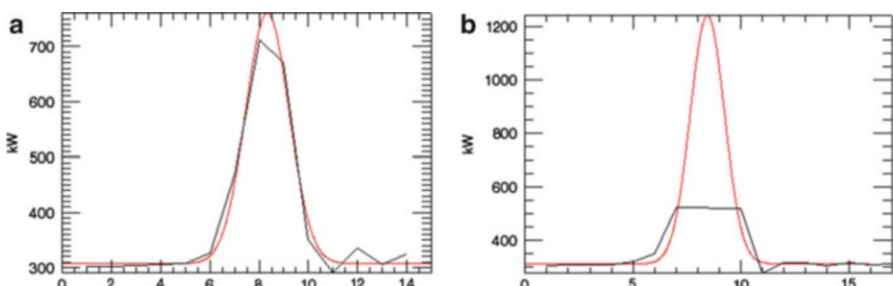


**Fig. 19.6** Gaussian interpolation of heat flux cross-flow unsaturated (a) and saturated (b) data. Interpolation of saturated data gives a maximum heat flux of about 1,200 kW

flux profile (Fig. 19.5, profile 1 and 2) shows a well defined channel and lateral levees. The distal segment of Etna's 2001 lava flow showed an excellent transition from stable channel-contained flow to dispersed flow. The lava toe includes a wider dispersed zone and the lava front characterized by many discrete lobes.

## 19.5 Heat Flux and Topography

The radiative heat flux map (Fig. 19.3b) reveals alternation of decreasing and increasing trends when moving from vent to lava front. Starting from the underlying relationship between effusion rate and heat flux (Eq. 19.1), we investigate the effects of topography on heat flux variations. In Fig. 19.7, the heat flux map overlays a digital elevation model (DEM) to create a 3D composite view of the 2,100 m lava flow area. A qualitative analysis of Fig. 19.7 suggests that major variations in  $Q_{rad}$  occur with variations in slope profile. Figure 19.7a shows the elevation drops from the 2,100 m vent down to the lava toe at about 1,100 m.  $Q_{rad}$  is displayed as a color map which varies from yellow (eruptive temperatures) to blue (ambient temperatures). Smooth color gradients from yellow, to red, to green indicate decrements in  $Q_{rad}$  with a slightly constant down-flow decline.

Decreasing trends are interrupted by abrupt increases which are marked by color changes from green to yellow. Five major peak-increments have been identified (including the highest  $Q_{rad}$  value at the vent) corresponding to the temperature maxima analyzed in the down-flow  $T_s$  profile of Fig. 19.4.  $Q_{rad}$  peak locations along the lava flow are shown in Fig. 19.7b.

Comparison between elevation and heat flux profile (Fig. 19.8) indicates that peak-increments in  $Q_{rad}$  occur where significant changes in the terrain slope angle occur. Down-flow topographic profile consist of facets of constant slope separated by local dips and scarps (Fig. 19.8).

On the one hand, all peak values (with the exception of B3) are located in proximity of topographic scarps. On the other hand, post-peak decreasing trends are usually associated with constant-slope facet. Correlation between slope and heat flux measurements is also evident at a larger-scale. Minor peaks that appear within  $Q_{rad}$  decreasing events (e.g. b<sub>1</sub>, b<sub>2</sub>, and b<sub>3</sub>) still correspond to small scarps in the topographic profile.

Our DEM analysis shows significant down-flow variations in terms of geometry of the lava channel. Variations in surface morphology produce changes in depth and width of the cross-sectional area ( $S$ ) of the lava flow. Since  $Er$  can be expressed as the product of the flow velocity ( $v$ ) and  $S$ , we use DEM and MIVIS data to investigate the influence of changes in  $S$  on  $Q_{rad}$ . Radiative heat flux has been estimated for each cross-section profile ( $Q'$ ) of the flow.  $Q'$  represents the area under the  $Q_{rad}$  profile curve (e.g. profiles shown in Fig. 19.5). The same profiles have been used to calculate the cross-sectional area of the flow from vertical height measurements on DEM data (Fig. 19.9).

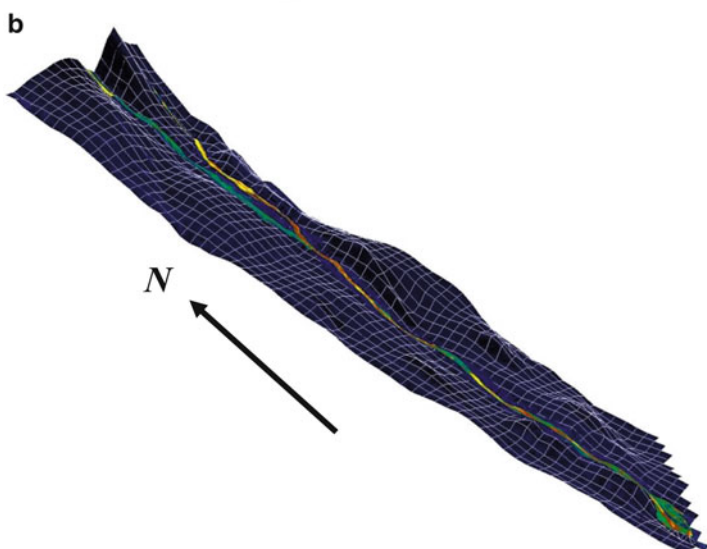
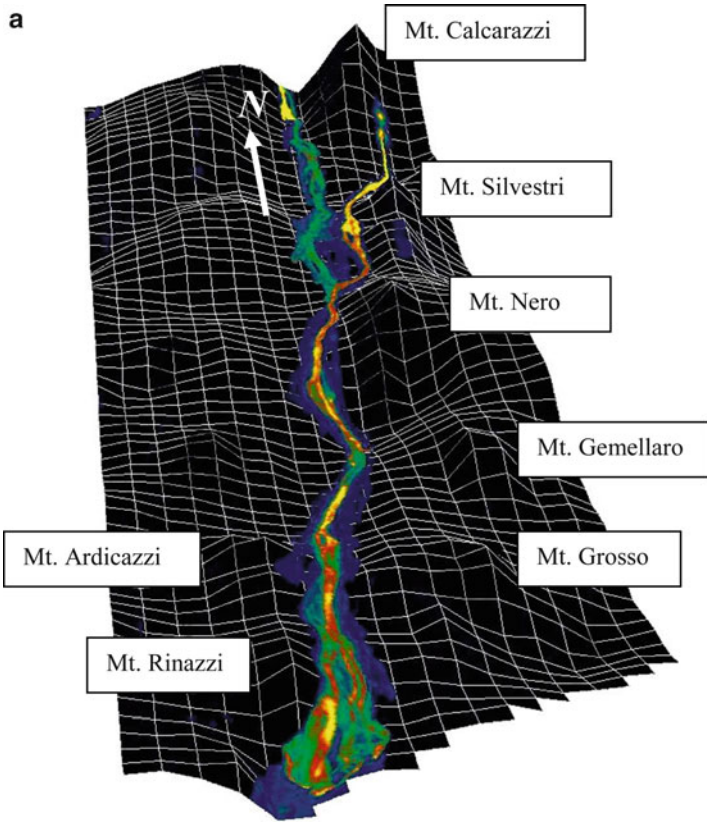


**Fig. 19.7** (a) 3D view of the radiative heat flux distribution derived from MIVIS data for the 2,100 m lava flow with locations of main topographic reliefs (a) and locations of temperature peaks given in Fig. 19.7b. (b) 3D view of the radiative heat flux distribution derived from MIVIS data for the 2,100 m lava flow with locations of temperature peaks

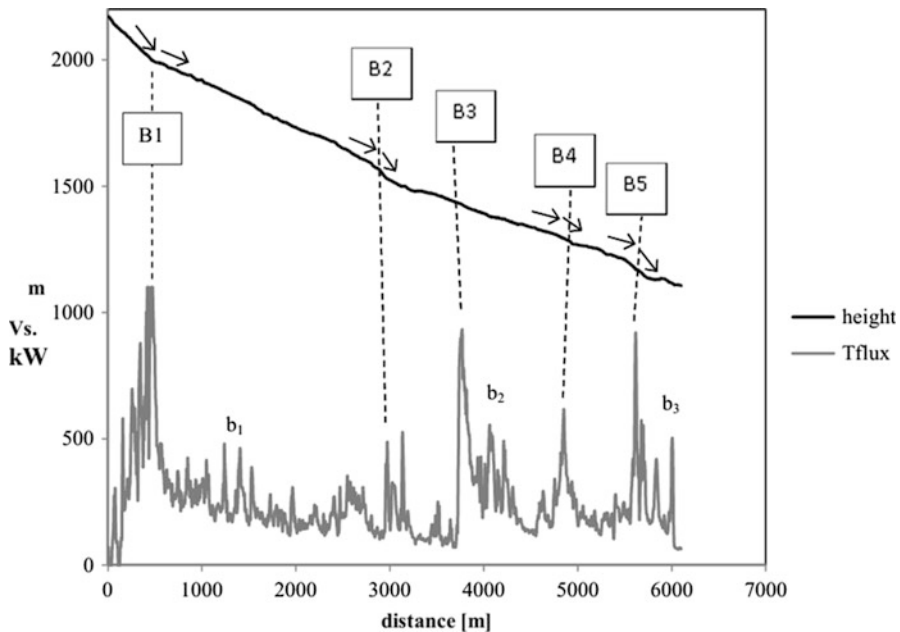


**Fig. 19.8** Comparison between slope and radiative heat flux down flow profiles. Major peaks in the heat flux profile ( $B_1, \dots, B_6$ ) occur in correspondence with main slope variations. Also minor peaks appear to be related to significant topographic changes ( $b_1, \dots, b_3$ )

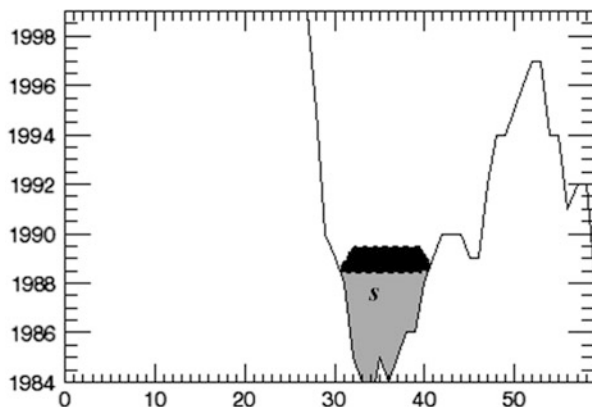


**Fig. 19.9** Example of cross-flow sectional area derived from digital elevation data. The cross-flow sectional area has been calculated from difference between the maximum height and every elevation value below the flow planimetry

Our analysis demonstrates that, at least for the medial zone, flow depth variations are larger than variations in width. Therefore, changes in lava flow thickness mainly account for variations in  $S$ . An average lava thickness ( $H_m$ ) has been calculated for every cross-section profile.

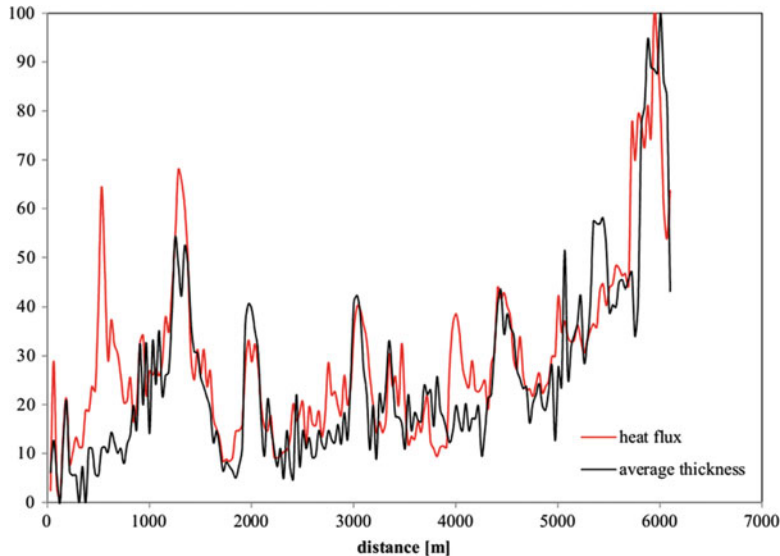


**Fig. 19.10** Comparison between normalized heat flux and lava thickness profiles shows a high correlation. Heat flux varies with lava flow thickness that is triggered by topographic changes as stated by the Pieri and Baloga formula

When we compare the down-flow  $H_m$  with  $Q'$ , a good agreement simply emerges from the inspection of the two trends (Fig. 19.10).

$Q'$  and  $H_m$  are normalized to allow for easy comparison of the different measurement units. A cross correlation value of 0.82 is obtained indicating a reliable match between the two trends. When comparing  $Q'$  vs.  $H_m$ , it is important to note that measurements were derived from completely different datasets:  $Q'$  from remote sensing radiance data and  $H_m$  from digital elevation data. Plots in Fig. 19.10 clearly show that surface temperature, radiative heat flux, and effusion rate estimate depend on the lava flow thickness, which is triggered by preexistent topography.

## 19.6 Discussion

Starting from Eq. (19.1), the law of conservation of mass implies that a constant  $E_r$  is maintained at every cross-sectional area of the flow. Therefore, if  $\Delta T'$  is the temperature drop of the lava flowing across  $S$ , under the assumptions of Pieri and Baloga model (1986), the ratio of  $Q'$  to  $\Delta T'$  should be a constant throughout the flow.

If we assume a  $\Delta T$  of 200 °C (difference between eruptive temperature at the vent and solidus temperature at the front for Etna basalts) and a linear decrement of  $T$  with  $x$ , the lava temperature drop per unit length becomes  $\Delta T/L$ . Due to MIVIS

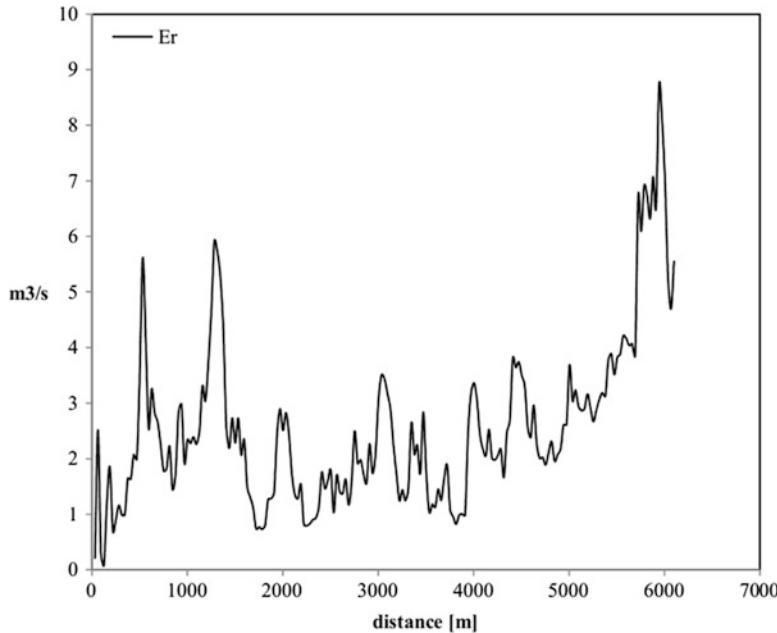


**Fig. 19.11** Apparent variations in derived down flow effusion rates. These variations are not real but caused by the assumption that lava flow has a uniform thickness  $h$ , flowing on an inclined plane with constant slope

spatial resolution,  $\Delta T'$  is equal to  $px \Delta T/L$ , where  $px$  is the MIVIS pixel size. Effusion rate derived at every cross-section of the flow is given by:

$$E'_r = \frac{Q'}{\rho c_p \Delta T'} \quad (19.7)$$

Figure 19.11 shows the down-flow profile of derived  $E'_r$  for the 2,100 m lava flow.  $E'_r$  is spanning a wide range from 0.1 to more than 9  $m^3/s$  along the flow, that is far from being considered as a constant. Why did the model fail to yield the predicted mass-flux constancy?

Relationship between  $Q'$  and  $H_m$  provides a key to understanding the apparent changes in down-flow derived  $E_r$ . Let us suppose that a lava flow is flowing with a constant effusion rate  $E_r$ , through two different cross-sectional area  $S_1$  and  $S_2$ . After the same time interval  $\Delta t$ , the volumes passed through  $S_1$  and  $S_2$  are the same, but the ratio between velocities is:

$$v_1/v_2 = S_2/S_1 \quad (19.8)$$

According to the model, the ratio between radiative heat fluxes is then

$$Q_1/Q_2 = S_2/S_1 \quad (19.9)$$

However, if the cross-sectional areas have the same width, Eq. (19.9) also implies

$$Q_1/Q_2 = h_2/h_1 \quad (19.10)$$

Which is exactly what we observe in our experimental data: the heat flux measured for a thick flow is greater than that measured for a thin flow.

From Eq. (19.8) we can derive that the distance  $L$  travelled by the flow through the two sectional areas over a time  $\Delta t$  is

$$L_1/L_2 = S_2/S_1 \quad (19.11)$$

Under the assumptions of the model of Pieri and Baloga (1986), the temperature difference  $\Delta T$  is proportional to the distance  $L$ . Then

$$\Delta T_1/\Delta T_2 = h_1/h_2 \quad (19.12)$$

Which means that also the lava temperature varies with the flow thickness. This explains for the apparent changes in downflow  $E'_r$  (Fig. 19.11) obtained by assuming a constant lava decrement with  $x$ . Thus, we can infer that surface temperature variations in actual flows are the expected consequence of the Pieri and Baloga (1986) model assumptions.

Our results suggest that topography affects heat flux changes at different scales. On the one hand, the average slope angle appears to control the rate of decrement of heat flux. The overall trend show a very rapid decrement from the vent followed by a smoothly graded decrease over constant slope trajectories. Because surface temperature rapidly decreases with the distance from the vent (Fig. 19.4), we can infer that heat-flux can be considered independent from the flow length. The overall trend is interrupted by abrupt increases in  $Q_{rad}$ . These peaks are mainly associated with significant slope changes such as dips and topographic scarps. On the other hand, small variations in topographic height cause changes in lava flow thickness. Therefore heat flux varies according to Eq. (19.10) as predicted by the model of Pieri and Baloga (1986).

## 19.7 Conclusions

The formula originally proposed by Pieri and Baloga (1986), relates the effusion rate to the heat flux radiated by the flow surface. Due to the assumptions of the model, this formula also implies that heat flux, surface temperature and lava

temperature varies as a function of the flow thickness. These relationships have been recognized as a weakness of the model by several authors. Our study demonstrated that such relationships do exist and that the Pieri and Baloga model (1986) accurately predicts the lava flow emplacement mechanisms. These results were achieved thanks to the effectiveness of high spatial resolution thermal data acquired by MIVIS sensor during the 2001 Etna eruption. MIVIS thermal data allowed for detailed mapping and analysis of the 2,100 m a.s.l lava flow. Integrated results from digital elevation model (DEM) and MIVIS data indicate that topography affects down-flow derived temperature, heat flux, and effusion rate estimates. As a future work, we plan to extend our analysis to include different eruptive styles (e.g. pahoehoe lava flows) and different thermal infrared datasets.

## References

- Barberi F, Villari L (1994) Volcano monitoring and civil protection problems during the 1991–1993 Etna eruption. *Acta Vulcanol* 4:157–166
- Behncke B, Neri M (2003) The July–August 2001 eruption of Mt. Etna (Sicily). *Bull Volcanol* 65:461–476
- Calvari S, Pinkerton H (2004) Birth, growth and morphologic evolution of the “Laghetto” cinder cone during the 2001 Etna eruption. *J Volcanol Geotherm Res* 132:225–239. doi:[10.1016/S0377-0273\(03\)00347-0](https://doi.org/10.1016/S0377-0273(03)00347-0)
- Calvari S, Coltellini M, Neri M, Pompilio M, Scribano V (1994) The 1991–1993 Etna eruption: chronology and geological observations. *Acta Vulcanol* 4:1–14
- Coltellini M, Proietti C, Branca S, Marsella M, Andronico D, Lodato L (2007) Lava flow mapping: the case of 2001 flank eruption of Etna. *J Geophys Res* 112:F02029. doi:[10.1029/2006JF000598](https://doi.org/10.1029/2006JF000598)
- Dragoni M, Tallarico A (2009) Assumptions in the evaluation of effusion rates from heat radiation. *Geophys Res Lett* 36:L08302. doi:[10.1029/2009GL037411](https://doi.org/10.1029/2009GL037411)
- Favalli M, Harris AJL, Fornaciai A, Pareschi MT, Mazzarini F (2010) The distal segment of Etna’s 2001 basaltic lava flow. *Bull Volcanol* 72:119–127. doi:[10.1007/s00445-009-0300-z](https://doi.org/10.1007/s00445-009-0300-z)
- Harris AJL, Butterworth AL, Carlton RW, Downey I, Miller P, Navarro P, Rothery DA (1997a) Low cost volcano surveillance from space: case studies from Etna, Krafla, Cerro Negro, Fogo, Lascar and Erebus. *Bull Volcanol* 59:49–64
- Harris AJL, Blake S, Rothery DA, Stevens NF (1997b) A chronology of the 1991 to 1993 Mount Etna eruption using advanced very high resolution radiometer data: implications for real-time thermal volcano monitoring. *J Geophys Res* 102:7985–8003
- Harris AJL, Flynn LP, Keszthelyi L, Mouginis-Mark PJ, Rowland SK, Resing JA (1998) Calculation of lava effusion rates from Landsat TM data. *Bull Vulcanol* 60:52–71
- Harris AJL, Flynn LP, Rothery DA, Oppenheimer C, Sherman SB (1999) Mass flux measurements at active lava lakes: implications for magma recycling. *J Geophys Res* 104(B4):7117–7136
- Harris AJL, Murray JB, Aries SE, Davies MA, Flynn LP, Wooster MJ, Wright R, Rothery DA (2000) Effusion rate trends at Etna and Krafla and their implications for eruptive mechanisms. *J Vulcanol Geotherm Res* 102:237–269
- Harris AJL, Bailey J, Calvari S, Dehn J (2005) Heat loss measured at a lava channel and its implications for down-channel cooling and rheology. *GSA special paper* 396, pp 125–146
- Harris AJL, Favalli M, Mazzarini F, Pareschi MT (2007) Best-fit results application of a thermo-rheological model for channelized lava flow to high-spatial resolution morphological data. *Geophys Res Lett* 34:L01301. doi:[10.1029/2006GL028126,2007](https://doi.org/10.1029/2006GL028126,2007)

- Kneizys FX, Shettle EP, Gallery WO, Chetwynd Jr JH, Abreu LW, Selby JEA, Clugh SA, Fenn RW (1983) Atmospheric transmittance/radiance: computer code LOWTRAN 6. Environ Res Pap 846. Air Force Geophys Lab Hanscom AFB, MA
- Lipman PW, Banks NG (1987) Aa flow dynamics, Mauna Loa 1984. USGS professional paper 1350, pp 1527–1567
- Lombardo V, Buongiorno MF (2006) Lava flow thermal analysis using three infrared bands of remote sensing imagery: a study case from Mt.Etna 2001 eruption. *Remote Sens Environ* 101(2):141–149
- Lombardo V, Buongiorno MF, Merucci L, Pieri DC (2004) Differences in Landsat TM derived lava flow thermal structure during summit and flank eruption at Mount Etna. *J Volcanol Geotherm Res* 134(1–2):15–34
- Lombardo V, Buongiorno MF, Amici S (2006) Characterization of volcanic thermal anomalies by means of sub-pixel temperature distribution analysis. *Bull Volcanol* 68(07–08):641–651
- Lombardo V, Harris AJL, Calvari S, Buongiorno MF (2009) Spatial variations in lava flow field thermal structure and effusion rate derived from very high spatial resolution hyperspectral (MIVIS) data. *J Geophys Res* 114:B02208. doi:[10.1029/2008JB005648](https://doi.org/10.1029/2008JB005648)
- Oppenheimer C (1991) Lava flow cooling estimated from Landsat Thematic Mapper infrared data: the Lonquimay eruption (Chile, 1989). *J Geophys Res* 96:21865–21878
- Oppenheimer C, Francis PW, Rothery DA, Carlton RWT, Glaze L (1993a) Infrared image analysis of volcanic thermal features: Láscar Volcano, Chile, 1984–1992. *J Geophys Res* 98:4269–4286
- Oppenheimer C, Rothery DA, Pieri DC, Abrams MJ, Carrere V (1993b) Analysis of Airborne Visible/Infrared Imaging Spectrometer (AVIRIS) data of volcanic hot spots. *Int J Remote Sens* 14(16):2919–2934
- Oppenheimer C, Rothery DA, Francis PW (1993c) Thermal distribution at fumarole fields: implications for infrared remote sensing of active volcanoes. *J Volcanol Geotherm Res* 55:97–115
- Pieri DC, Baloga S (1986) Eruption rate, area and length relationships for some Hawaiian lava flows. *J Volcanol Geotherm Res* 30(29):45
- Pinkerton H, James M, Jones A (2002) Surface temperature measurements of active lava flows on Kilauea volcano, Hawai'i. *J Volcanol Geotherm Res* 113:159–176
- Wadge G (1977) The storage and release of magma on Mount Etna. *J Volcanol Geotherm Res* 2:361–384
- Walker GPL (1973) Lengths of lava flows. *Philos Trans R Soc Lond A274:107–118*

# Chapter 20

## Thermal Analysis of Volcanoes Based on 10 Years of ASTER Data on Mt. Etna

Maria Fabrizia Buongiorno, David Pieri, and Malvina Silvestri

**Abstract** The EOS-1 Terra ASTER (Advanced Spaceborne Thermal Emission and Reflection Radiometer) has acquired about 200 images (100 of them sufficiently cloud-free to be used) over Mt. Etna since 1999. This chapter shows the results from the analysis of 10 years Mt Etna activity using thermal infrared (TIR) high spatial resolution data by a semi-automatic procedure that extracts radiance values of the summit area with the goal of detecting variation related to eruptive events. Night time data showed a good correlation with the main eruptive events that occurred both in the summit and in the flank areas. A comparison of the variance of maximum ASTER TIR radiance with variance of the maximum AVHRR TIR radiance (Advanced Very High Resolution Radiometer) for the same area confirms good correlation in terms of trend and values between the two data sets. Finally this study emphasizes the importance of high spatial resolution TIR data during background monitoring to detect changes in the thermal emission that may be related to an impending eruption and the need to further improve the spatial resolution in the TIR channels to better separate the thermal active areas in volcanic systems.

### 20.1 Introduction to Current Challenges in Volcano Observation

Using remote sensing techniques to understand the world's volcanoes is a focus of the world's major scientific agencies and space-faring countries (Solomon et al. 2003; USNRC decadal survey 2007). Such emphasis on volcanoes reflects the fact

---

M.F. Buongiorno (✉) • M. Silvestri  
Istituto Nazionale di Geofisica e Vulcanologia (INGV), Rome, Italy  
e-mail: [Fabrizia.buongiorno@ingv.it](mailto:Fabrizia.buongiorno@ingv.it)

D. Pieri  
Jet Propulsion Laboratory, California Institute of Technology, Pasadena, CA, USA

that 500 million people live under the direct threat of volcanic eruptions or their associated environmental effects along with the pursuit of basic earth system scientific information. Warning signs of eruptions, however, are inconsistent and prediction time windows are imprecise and inaccurate. Eruption prediction is a chancy idiosyncratic affair, as volcanoes often manifest waxing and/or waning pre-eruption emission, geodetic, and seismic behavior that is unsystematic. Thus, fundamental to increased prediction accuracy and precision are good and frequent assessments of the time-series behavior of relevant precursor geophysical, geochemical, and geological phenomena, especially when volcanoes become restless.

Signaling the onset of an eruption requires observing the thermal flux of a restless volcano as an important source of information of both persistent low-level thermal activity due to seasonal/diurnal geo-hydrothermal variations, and about rarer anomalous precursor thermal activity (e.g., Pieri and Abrams 2005). To detect such behavior it is important to have knowledge of the thermal activity datum related to a particular volcano in addition to the observation and characterization of its thermal anomaly.

In the past several years there has been progress in using daily 1 km/pixel observations of the Moderate Resolution Imaging Spectroradiometer (MODIS) data. For such data, automated thermal thresholding algorithms are used to detect global thermal anomalies (Wright et al. 2004) and measure volcanic plume and SO<sub>2</sub> gas emissions (Realmuto et al. 1994). Although volcanic thermal features are usually much smaller than a MODIS pixel, these data are capable of showing some sub-pixel thermal anomalies, but typically miss many small subtle thermal anomalies. The Advanced Spaceborne Thermal Emission and Reflection Radiometer (ASTER; Yamaguchi et al. 1998) with multispectral Visible/Near InfraRed (VNIR), Short Wave InfraRed (SWIR) and Thermal InfraRed (TIR) data measured at higher spatial resolution (15, 30 and 90 m, respectively), detects even very small thermal anomalies that are missed by MODIS (Vaughan and Hook 2006). ASTER can point off nadir to view selected targets, such as erupting volcanoes, every few days, thus supplementing the nominal 16 day nadir repeat cycle (Pieri and Abrams 2004).

Here we report on the utilization of ASTER's thermal infrared (TIR) remote sensing capabilities and the Jet Propulsion Laboratory (JPL) ASTER Volcano Archive (AVA) as tools to systematically analyze the spatial and temporal relationships (positively correlated, uncorrelated, and/or negatively correlated) of volcanogenic thermal anomalies and eruptions at Mt. Etna on the Italian island of Sicily. We have examined approximately 200 day and night ASTER images of Mt. Etna with respect to:

1. seasonally biased thermal emission baseline behavior;
2. the form and magnitude of time-dependent thermal emission variability;
3. the limits of spatio-temporal detection of pre-eruption temporal changes in thermal emission in the context of eruption precursor behavior.

Our goal has been to create and analyze a catalog of data by examining the magnitude, frequency, and distribution of Mt. Etna's summit crater thermal signatures at the highest available spatial resolution (90 m/pixel) to exploit one of the largest thermal remote sensing time series of Mt. Etna ever compiled. Further, we demonstrate the value of high spatial resolution TIR time-series data for monitoring significant volcanogenic hazards and risks, especially in the area of thermal precursor activity detection.

Important specific questions inherent in the thermal monitoring of volcanoes are:

- (a) Can eruption precursor phenomena be reliably detected by optical remote sensing techniques?
- (b) What are the spatial, temporal, and spectral intensity relations and detection limits as defined by statistical analyses at high accuracy (e.g., snow vs. cloud mapping for DEM (Digital Elevation Model) creation; low temperature precursor detection; hydrothermal alteration detection);
- (c) How do measurements of relevant time-variable precursors relate among themselves and to overall eruption processes?
- (d) How do such measurements relate to the magnitude, character, and timing of consequent eruptions?
- (e) Are there regional inter-volcano trends in precursor and eruptive phenomena?
- (f) Finally, do the points above relate to the style of volcanism, and can we identify areas where improvement is needed with respect to instrument design or observation strategies?

Systematic global cataloging of volcanic thermal anomalies as measured from high spatial resolution spaceborne sensors is still in its infancy. As the topic matures, it will help to understand the relationships between precursor phenomena and eruptions in the context of global volcanism, as well as in developing a comprehensive observational strategy for spaceborne global monitoring of volcanoes. Moreover, deviations in thermal flux (especially when correlated with gas emissions and surface deformation) may be precursors of changes in the activity state of a volcano, and a subsequent eruption. Nevertheless, eruption forecasting requires both knowledge of the thermal flux data of a given volcanic center and the past relationship between deviations and eruption onset to recognize and rationalize significant change. Ultimately emerging methodologies should and will be refined for applications by the volcanological community to further benefit from presently held and future data sets for active and potentially-active volcanoes.

In particular, such insights and databases will be of use for researchers studying volcanoes that threaten population centers (e.g., Mt. Etna, Mt. Rainier, Mt. Hood, Mt. St. Helens, Vesuvius; the African Rift volcanoes) or air routes (e.g., volcanoes of the Pacific Northwest (Cascades); Indonesian-Philippine archipelagos), especially where volcanoes are not routinely monitored due to the combination of remote location and few resources. Eruption and hazard forecasting for such sites is complicated when there is no sustained local volcanological infrastructure, and when anecdotal reports of volcanic activity conflict. High spatial resolution satellite monitoring

(e.g., ASTER, EO-1) can validate eruption reports, especially where little systematic data exist beyond satellite measurements (Vaughan et al. 2007).

## 20.2 Theoretical Background of Volcano Monitoring

There is and has been a long and evolving heritage of the spaceborne monitoring of volcanoes. Thermal anomalies associated with volcanic activity with low-resolution weather satellite images were first recognized in the 1960s and 1970s (Gawarecki et al. 1965; Simkin and Kreuger 1977), and subsequent monitoring and analyses progressed from low resolution hot spot detection to more precise and accurate temperature measurements using higher spatial resolution SWIR and TIR data (Lombardo et al. 2006; Ramsey and Dehn 2004). Time-series analyses followed along with techniques for modeling the heterogeneous structure of sub-pixel temperature components (Dozier 1981; Francis and Rothery 1987; Rothery et al. 1988; Crisp and Baloga 1990; Pieri et al. 1990; Oppenheimer 1993; Oppenheimer et al. 1993a, b; Flynn et al. 1994, 2001; Oppenheimer and Francis 1997; Oppenheimer and Yirgu 2002; Wooster and Rothery 1997, 2000; Harris et al. 1997, 1999; Wright et al. 1999, 2000; Lombardo and Buongiorno 2003, 2006; Wright and Flynn 2003; Kaneko and Wooster 2005; Pieri and Abrams 2005; Vaughan et al. 2005, 2007; Vaughan and Hook 2006; Harris and Ripepe 2007).

Currently, for prompt response and hazard mitigation, long time series based on low spatial resolution images (e.g., 250–1,000 m/pixel) with high revisit time are used, as MODIS (Flynn et al. 2002; Wright et al. 2004; Dean et al. 2004; Harris and Ripepe 2007), AVHRR (Harris et al. 1997), GOES (Geostationary Operational Environmental Satellite) (Harris et al. 2001; Pergola et al. 2004), MSG (Meteosat Second Generation) and other weather satellites (Gouhier et al. 2012).

Far fewer studies have utilized higher spatial resolution data (such as ASTER [15 m panchromatic, 30 m multispectral VIS-SWIR, 90 m TIR] or Landsat [30 m multispectral VIS-SWIR, 120 m (MSS, TM) or 60 m (ETM + (Enhanced Thematic Mapper Plus)) TIR]) to obtain more spatially detailed time-series of thermal measurements over volcanoes (Pieri and Buongiorno 1995; Pieri and Abrams 2005; Vaughan and Hook 2006; Ramsey and Dehn 2004). This is because of less frequent observation opportunities of higher spatial resolution ASTER data for a particular volcano due to its smaller swath width and less frequent revisit as compared to the weather satellites. Therefore, an increased probability of obscuration by cloud cover exists. However, since the launch of ASTER in December 1999, 140,000+ images of volcanoes have been acquired worldwide with a number of volcanoes seen frequently enough with ASTER at acceptable cloud coverage. Thus, useful times series data analyses can be undertaken. For instance, one such analysis (Pieri and Abrams 2005) detected winter-time summit crater meltwater in advance of an early spring eruption by the sub-arctic Chikurachki Volcano in the Kurile Islands. ASTER data are currently the only orbital remote sensing data set which allow the detection of low temperature thermal anomalies smaller than the resolution limit of the coarser spatial resolution, MODIS data.

## 20.3 Mt. Etna Volcano

### 20.3.1 Geological Background

Mt Etna is a large basaltic composite volcano near the eastern coast of Sicily. It is located in a complex geodynamic environment characterized by the collision of the African and Eurasian continental lithospheric plates (Fig. 20.1a). The geological history of Mt. Etna is subdivided into four main periods (Branca et al. 2004) starting with early submarine activity dated about 500,000 years back to the mid-Pleistocene, to a stratovolcano phase that began about 60,000 years before present, when the eruptive activity further shifted toward the northwest.

Mt Etna is Europe's largest volcano, rising 3,320 m above sea level and with a volume of  $>350 \text{ km}^3$ , and one of the most active volcanoes on Earth (in the sense of eruptive deposit volumes "production" and eruption frequency, Fig. 20.1b). It has frequent periods of intermittent to persistent activity in the summit area and major eruptions from new vents on its flanks every 1–20 years. The main feature of Etnean activity is voluminous lava emission with occasionally strong explosive activity that occurs in its current configuration of four summit craters. Some of the eruptions from its flanks also show high degrees of explosivity, such as those in 1669, 1879, and 2002–2003 (as reported in [URL 1](#) and [URL 2](#)). Mt. Etna lies near the eastern (Ionian) coast of Sicily and occupies a surface area of around 1,200  $\text{km}^2$  with a perimeter exceeding 135 km. Its summit height varies frequently as a function of eruptive activity or due to minor collapse events at the summit craters. Growth of the summit was concentrated at the Northeast Crater, a feature that was formed in 1911 with nearly constant activity at the crater since the mid-1950s which has led to the growth of a large cone around it. Activity at the Northeast Crater became rather infrequent since the mid-1980s and since then the height of its cone decreased to 3,330 m asl (as measured in 2007). The Southeast Crater which was formed in 1971 has the youngest cone of the four summit craters, and underwent a period of dramatic growth between 1998 and 2001. Within the last 2 years, that growth has continued causing instability of the aggrading growing cone and there have been frequent lava fountains and lava flow eruptions.

Mt. Etna is unique for a number of reasons. First, it has the longest record of historical eruptions among all volcanoes on Earth (Simkin and Siebert 1994; Branca and Del Carlo 2004). Its first historically documented eruption occurred at about 3500 BP, and the total number of documented Mt. Etna eruptions is 209 (18 among them questionable) through late 1993 (Simkin and Siebert 1994). In addition to these aforementioned eruptions, relatively recently spectacular and vigorous summit eruptions have occurred in 1995–2001, flank eruptions in 2001, 2002–2003, 2004–2005, and 2008–2009, plus a period of intermittent summit activity during the period 2006–2011. Over to the last four centuries Mt. Etna has shown a rapid increase of activity also in terms of magma erupted (Fig. 20.1b).

Most magma ascends to the surface through the central conduit system of Etna, which leads to the frequent summit activity. Unless magma ascent is very rapid,

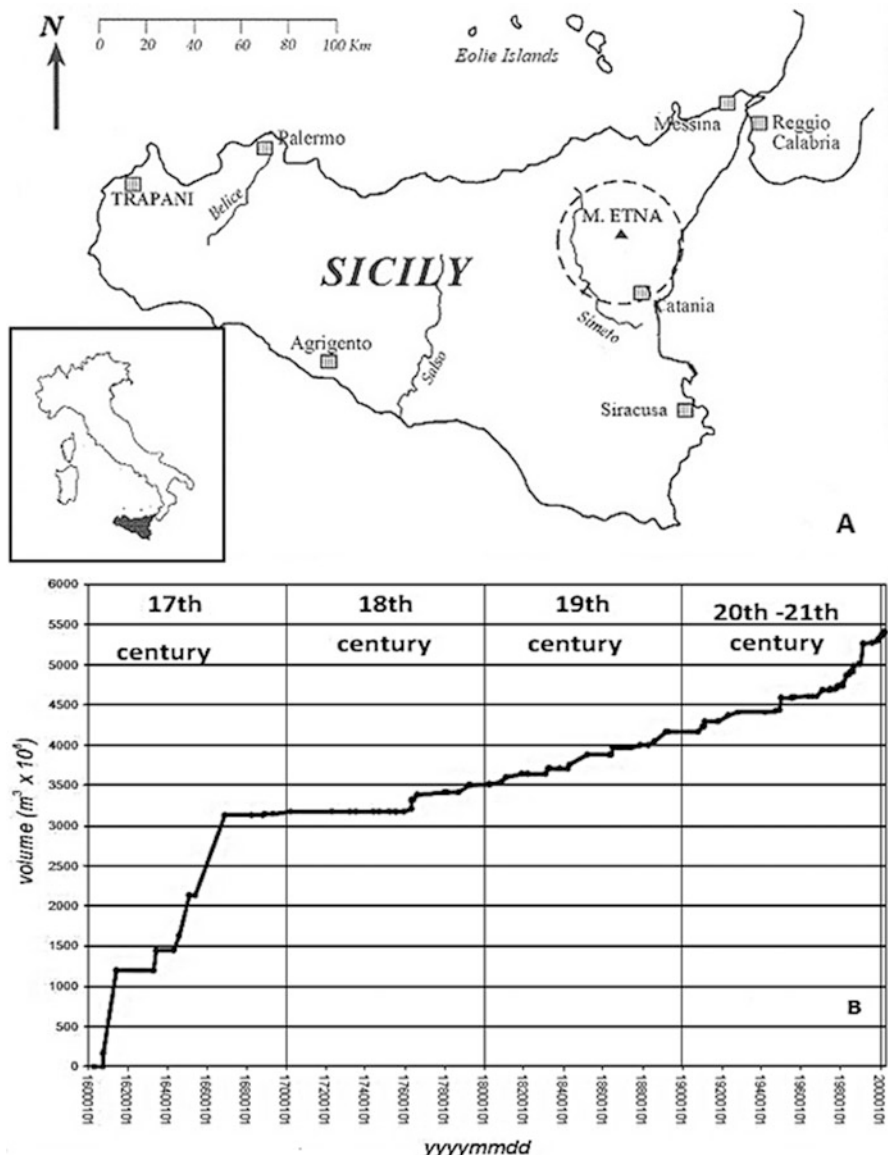


**Fig. 20.1** (a) Mt. Etna geographic location; (b) a plot showing the increase of erupted magma volume starting from the end of the eighteenth century and a further increase between the end of the twentieth and the beginning of twenty-first century (Courtesy of Behncke et al. 2005; Neri et al. 2011). Note also the most recent increased rate of magma eruption

much gas is lost from the magma during its ascent to the surface, and significant volumes of relatively gas-poor magma are stored in the shallow plumbing system of the volcano (Fig. 20.2). During many flank eruptions of Etna, such gas-poor magma exits laterally from the central conduits, resulting in relatively weak or almost no

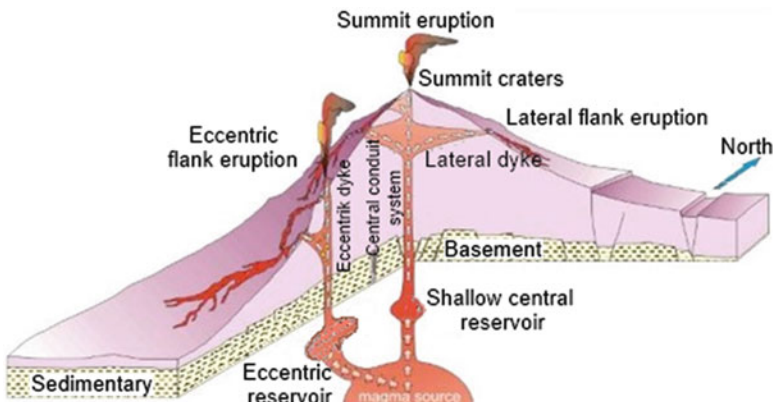


**Fig. 20.2** Hypothetical and simplified scheme of the magmatic plumbing system of Etna, illustrating magma transport feeding summit activity and the two different types (lateral vs. eccentric) flank eruptions (Courtesy of Behncke and Neri 2003, edited)

explosive activity but copious lava outflow. Most flank eruptions during the twentieth century were of this type; they are commonly called “lateral” flank eruptions. Typically such eruptions are accompanied by the cessation of summit activity and some collapse at the summit craters, as the central conduit system is drained of magma.

### 20.3.2 Study Area

Our analysis was focused on the Mt. Etna summit area in order to monitor and detect changes in the thermal emission during both quiescent and eruptive periods (e.g., selected Area of Interest [AOI, rectangle] in inset a of Fig. 20.3). A second area, called “Piano delle Concrazze” (inset b of Fig. 20.3) was also selected as a reference background since it is characterized by mineralogically homogeneous terrain composed of fine tephra and ash deposits.

## 20.4 Available Data and Data Processing

### 20.4.1 ASTER Thermal Infrared Data Set Acquired Between Year 2000 and 2010

ASTER is one of the five sensors systems on-board the Terra platform launched in December 1999 as part of the NASA Earth Observing System (EOS). ASTER was built by a consortium of the Japanese government, industry, and research groups.

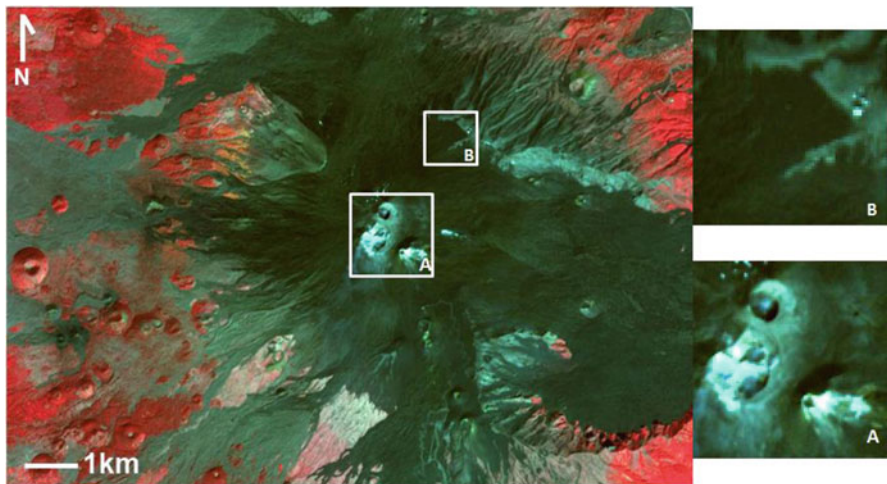


**Fig. 20.3** Aster image acquired on 2009, 7th October . Summit craters area and Piano delle Concazze reference area shown on ASTER RGB composite from VIS channels. (a) Selected Area of Interest [AOI, rectangle]: upper left corner =  $37^{\circ}44'25.98''$  lat  $14^{\circ}59'10.97''$  lon; lower right corner =  $37^{\circ}45'43''$  lat  $15^{\circ}0'27''$  lon; maximum elevation = 3,330 mASL; 550 pixels in area; (b) AOU center =  $37^{\circ}45'53.64''$  lat  $14^{\circ}1'9.84''$  lon, elevation = 2,800 mASL, approximately 5 pixels in area

Currently, it is the only known available sensor acquiring images at high spatial resolution in TIR channels (Table 20.1).

Since the launch of the EOS-1 Terra Satellite, images have been acquired over the 10 year period between 2000 and 2010 for Mt Etna area, in Sicily. During this period a number of eruptions have occurred with substantially different intensity and durations. Some occurred at the summit while others occurred on the flanks of Mt. Etna, and several eruptions have manifested as small lava fountains events.

Here we focus on the changes of thermal emission in the summit area of Mt. Etna as analyzed in 200 ASTER images, including 91 daytime and 109 nighttime images. Table 20.2 shows the whole ASTER Mt. Etna data collection reported in terms of number of images per year, broken down with respect to daytime and nighttime acquisitions (e.g. 10:00 AM UTC time and about 21:00 UTC time, respectively).

#### 20.4.2 AVHRR Thermal Infrared Data Set Acquired During the 2006 Eruption

In 2004 INGV established a NOAA-AVHRR (National Oceanic and Atmospheric Administration – Advanced Very High Resolution Radiometer) station, which

**Table 20.1** ASTER instrument characteristics (Yamaguchi et al. 1998)

Instrument	VNIR		SWIR		TIR	
Bands and spectral range ( $\mu\text{m}$ )	1	0.52–0.60	4	1.60–1.70	10	8.125–8.475
	2	0.63–0.69	5	2.145–2.185	11	8.475–8.825
	3N	0.78–0.86	6	2.185–2.225	12	8.925–9.275
			7	2.235–2.285	13	10.25–10.95
			8	2.295–2.365	14	10.95–11.65
			9	2.360–2.430		
Spatial resolution (m)	15		30		90	
Swath width (km)	60		60		60	
Cross track pointing	$\pm 318 \text{ km} (\pm 24^\circ)$		$\pm 116 \text{ km} (\pm 8.55^\circ)$		$\pm 116 \text{ km} (\pm 8.55^\circ)$	
Quantisation (bits)	8		8		12	
Revisit time (days)	16		16		16	

**Table 20.2** ASTER data collection during 10 years, daytime and nighttime images and main eruptive events

Year	n. of ASTER images daytime (about 10:00 UTC)	n. of ASTER images nighttime (about 21:00 UTC)	Start main eruptive events	Stop main eruptive events
2000	4	3		
2001	4	13	17 July	9 August
2002	6	21	26 October	
2003	13	12		23 January
2004	15	7	7 September	
2005	4	10		8 March
2006	8	13	14 July	15 December
2007	15	12	4 September	5 September
			23 November	24 November
2008	9	5	13 May	
2009	4	7		4 July
2010	9	6	–	–

consists of a fully integrated antenna tracking and ground station for receipt of AVHRR satellite imagery.

The AVHRR sensor provides imagery in the visible, near infrared and thermal infrared wavelength bands. The NOAA satellites have a circular, polar, sun-synchronous orbit, with an altitude of 850 km and with a period of about 100 min. A sun-synchronous orbit means that each satellite overpass always occurs at the same point at the same local time. For the NOAA satellite constellation, this allows up to ten overpasses per day, depending on the latitude of the volcano target (Table 20.3).

The AVHRR is a radiation-detection imager that can measure the surface emitted/reflected electromagnetic radiation in different bands ranging through visible, near IR and IR wavelengths.

For this work we focus on the changes of thermal emission in the summit area of Mt. Etna as analyzed in 579 overall AVHRR images nighttime starting from 1st June 2006 to 30th November 2006. The result of this analysis will be compared in the next sessions with results obtained by using ASTER data. The 2006 eruption has been chosen for the high availability of ASTER and AVHRR data.

**Table 20.3** AVHRR instrument characteristics (from NOAA web site, [URL 3](#))

Instrument	VNIR	MIR-SWIR	TIR
Bands and spectral range ( $\mu\text{m}$ )	1      0.580–0.680 2      0.725–1.000	3a     1.580–1.640 3b     3.550–3.930	4      10.3–11.3 5      11.5–12.5
Spatial resolution (km)	1.1	1.1	1.1
Swath width (km)	$\pm 1,447$	1,447	1,447
Revisit time (considering all NOAA constellation)	Daily (about 7 acquisition per day)	Daily (about 7 acquisition per day)	Daily (about 7 acquisition per day)

### 20.4.3 Data Processing: Method

Considering the goal of detecting very small changes in the radiant emission from volcano summit craters, the methodology adopted in this study was based on the analysis of the radiance values measured by the ASTER sensor. We avoided the application of inversion algorithms to calculate the ground temperature, due to its strong dependence on knowledge of the ground emissivity and local atmospheric conditions. The availability of a stable reference background area (“Piano delle Concazze”) very near to the summit crater area permits us to use a statistical approach for a long time series of observations. A goal of this study is to calculate changes in thermal emissions from very well calibrated and geocorrected TIR images to perform a rapid analysis of the thermal behaviour in active volcanic areas where the ground monitoring is not available or insufficient.

The ASTER data product L1B data (i.e., radiance at the sensor) was first separated into daytime and nighttime data, as well as summer and winter acquisitions. The L1B was used because it contains images already resampled to the geometry of the appropriate UTM projection with the WGS84 Datum. In fact the ASTER Level-1B Registered Radiance at the Sensor product contains radiometrically calibrated and geometrically co-registered data for the acquired channels of the three different telescopes of Level-1A data. The Level-1B data set is produced by applying the radiometric calibration and geometric correction coefficients to the Level-1A.

The most suitable data for analyses was extracted based on visual inspection selecting 37 daytime and 65 nighttime cloud free ASTER images. Unfortunately, the relatively infrequent repetition cycle of ASTER’s (i.e., 16 day nadir repeat) and cloud occurrence reduced the number of available ASTER observations for the assessments of volcanologically quiescent and active periods.

For each data set, the maximum radiance, mean radiance and variance were calculated using ASTER’s TIR Band 13 (10.65  $\mu\text{m}$ ) that is not affected by  $\text{SO}_2$  emissions. This channel was utilized because of the high elevation of the site (e.g., over 3,000 m asl, hence low atmospheric column water vapor and atmospheric correction were not required because in thermal region the aerosol type plays a negligible role because of the long wavelength) and high emissivity in the selected

TIR channel ( $\epsilon \sim 0.95$  as measured during field campaigns by means of FTIR (Fourier Transform InfraRed) instrument, model 102F, Fig. 20.4).

All cloud free data have been processed by means of IDL code and ENVI algorithms, implemented in three steps:

- first step: from the original cloud free data format (L1B), the georeferenced images are obtained using ENVI batch command and the radiance at the sensor is automatically produced.
- second step: for each image the selected area has been analyzed extracting maximum, variance and mean according to area reported in the inset a of Fig. 20.3.
- third step (only for AVHRR data processing): for each image, considering the area in the inset a of Fig. 20.3, the pixel containing clouds are rejected. As first approximation, the cloud presence is verified if the brightness temperature is negative (AVHRR channel 4 unit is brightness temperature). Only positive pixels are converted in radiance and used to compute the maximum and the variance.

## 20.5 Results and Discussion

Data analysis was performed to test our capability to detect the starting phase of an eruptive event using the variation in thermal emissions from thermal active areas (e.g., summit craters or fumaroles fields) as an index. The 10 years of Mt. Etna activity showed a large number of eruptive episodes spanning modalities that included short-lived explosive emissions of lava in fountains, to persistent effusive lava flow events both from summit craters and flank fissures. This high variability volcanic activity modes made it very difficult to consistently detect initial stages of such events using the variation of surface emitted radiance as a criteria. Additionally, the large area of the volcanic structure exhibited a complex overlay of multi-temperature thermal emission sources comprised of previously-erupted-now-cooling materials in close proximity of a new thermal event. To distinguish these different volcanic phases, and understanding of both the spatial and temporal resolutions of satellite sensors plays a very important role. The ASTER's daytime time series data acquired shows high variance in perceived (surface) thermal energy, and the volcanic thermal emission component is not clearly separable from insolation (Fig. 20.5a). In contrast, ASTER's night observations show well defined episodes of increasing thermal emission of summit craters (Fig. 20.5b) because nighttime data generally exhibit a more uniform background temperature that resulted from the low thermal inertia of the porous volcanic surface tephra layer (e.g., intrinsically low Shannon entropy). Thus, we found that the statistical (Gaussian) variance of thermal radiant emissions is able to delineate main eruptive episodes with respect to the maximum geothermally induced radiance, especially for the 2001, 2002, 2006, and 2008 eruptive episodes (Fig. 20.5b). Even if in 2004–2005 an eruption occurred, the variance value is not high enough to delineate the event. For the two 2007 eruption events no ASTER data were available.

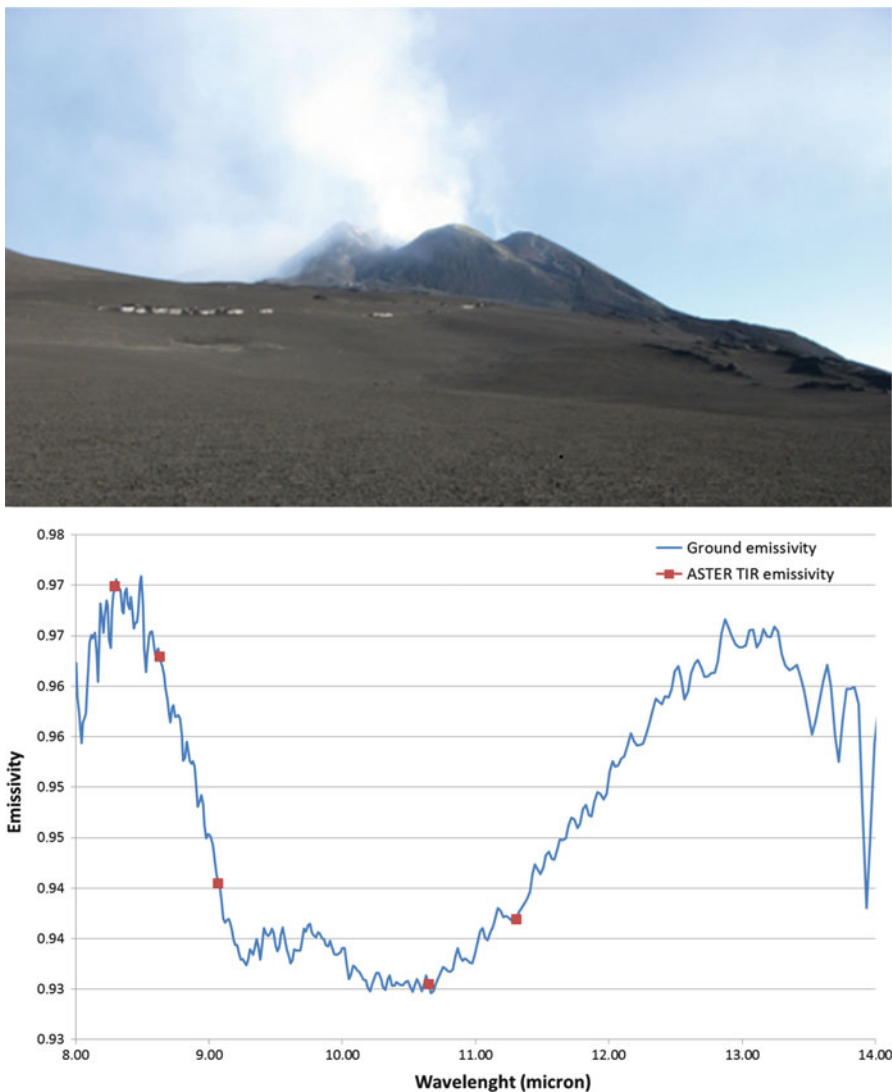


**Fig. 20.4** At the *top* Etna summit craters area are shown; on the *bottom*, summit crater scoria/tephra spectral emissivity measured at this site and spectral signature resampled at ASTER TIR wavelengths. The ground emissivity has been measured during field campaigns (2009, 7th October 2009) by means of FTIR (Fourier Transform InfraRed) instrument, model 102F

Particular focus was directed at the 2006 summit eruption which started in July 2006 and showed many different phases although erupting only manifested with two main lava flows (Fig. 20.6). For this eruption, we analyzed the pre-eruptive phase since four night time ASTER TIR images were available. These data show an

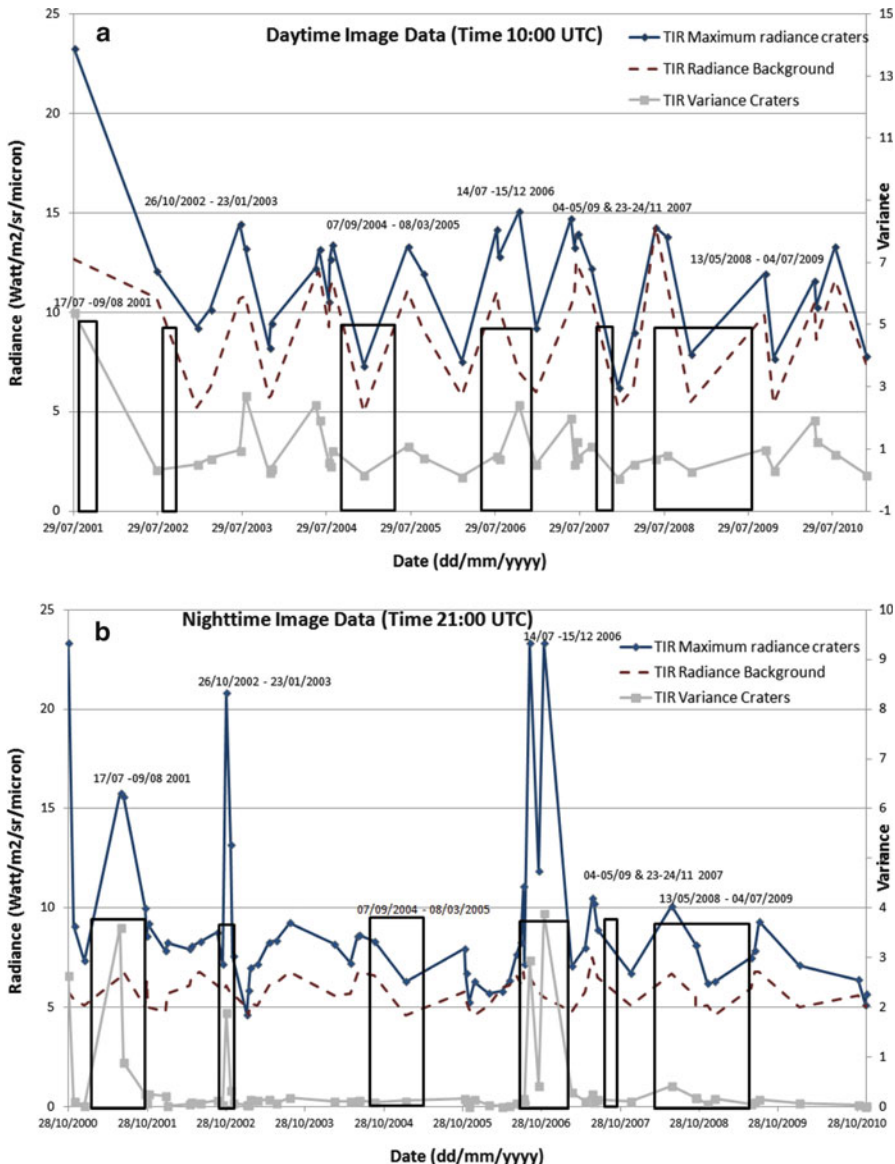


**Fig. 20.5** (a) Maximum summit crater radiances for Mt. Etna, derived from ASTER TIR data, along with the statistical variance of radiance and in the designated background area during daytime. (b) Maximum summit crater radiances for Mt. Etna, derived from ASTER TIR data, along with the statistical variance of radiance and in the designated background area for the nighttime observations, showing the increase of thermal energy emission from the summit areas during the 2001, 2002, 2006 and 2008 eruptions. The *black line* describes for both plots the main eruptive events reported in Table 20.2. For both plots the adimensional variance is reported on the right side of Y axis and the radiance (Watt/m<sup>2</sup>/sr/micron) on the left Y axis, respectively

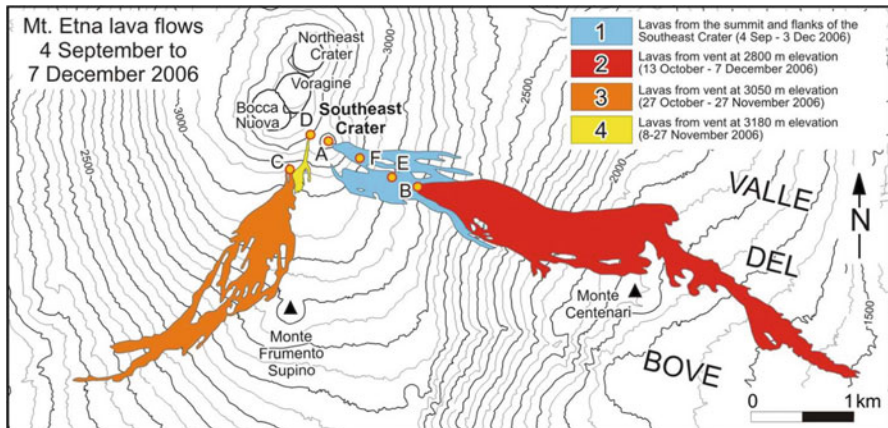


**Fig. 20.6** Map of the 2006 lava flow location and extent (Courtesy of Behnke et al. 2008)

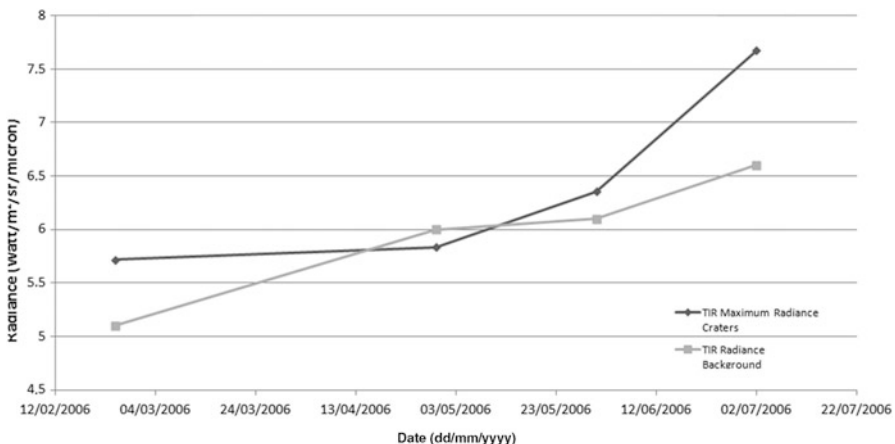


**Fig. 20.7** ASTER maximum radiance emitted from summit craters before the beginning of the July 2006 eruption. The value inversion on April 29th 2006 is due to thin clouds present on summit craters which reduce the radiance values compared with the background

increase in the emitted summit crater radiance starting in May 2006 (Fig. 20.7). In the plot of Fig. 20.7 the presence of an higher value of the background respect to the summit crater area is probably due to the presence of scattered thin clouds over the summit crater area which may absorb part of the emitted radiance toward the sensor for the 29th April 2006 image.

Regrettably, the relatively low frequency of the ASTER data acquisitions (nighttime in particular) did not permit verification of similar pre-eruptive increase in the Mt. Etna summit crater thermal activity for the 2001, 2002 and 2008 eruptions.

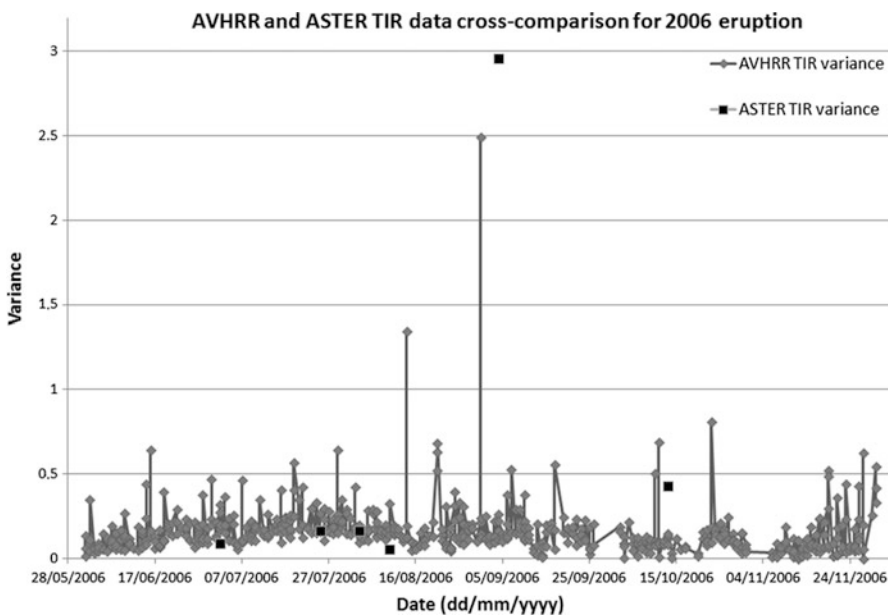


**Fig. 20.8** Cross-comparison of variance values obtained by using AVHRR and ASTER data acquired during the 2006 eruption

Finally, the variance of the maximum ASTER TIR radiance during the 2006 eruption was compared with the variance of the maximum AVHRR TIR radiance for the Mt. Etna summit area. Despite the large difference in spatial resolution difference between the two sensors (ASTER = 90 m/pixel, AVHRR = 1,000 m/pixel) and the dimension of the considered area which in AVHRR case covers all parts of the summit of Mt. Etna, the plot in Fig. 20.8 shows a good correlation in terms of trend and values between the two data sets. ASTER data show a higher variance of maximum radiance values than AVHRR data due to the presence of active lava flows. Clearly, the lower spatial resolution of the AVHRR pixels dilutes and smoothes the contribution of emitting pixels in the variance of the radiant intensity, which is resolved at over two orders of magnitude greater spatial resolution in the ASTER TIR data. Even if this comparison shows that AVHRR sensor provides the frequency necessary to detect the onset of large thermal anomalies, its low spatial resolution allows us to detect only very large or very hot anomalies; similarly the ASTER sensor provides information at an improved spatial scale more suitable for scientific analysis, but less useful for a rapid response monitoring systems (Ramsey and Dehn 2004) because of relatively sparse temporal sampling.

## 20.6 Conclusion

Clearly, the monitoring of thermal features associated with the onset of volcanic eruptions is important for fundamental scientific reasons. Such work has crucial significance for anticipating and mitigating volcanic hazards, not only to people

living in close proximity to volcanic features, but also for those living at long distances from the erupting volcano, but who nevertheless may be affected from related phenomena such as airborne ash hazards.

Recent advances in satellite and airborne remote sensing technologies provide volcanologists with new tools for measuring the thermal emissions of restless volcanoes. In particular, subtle (or not-so-subtle) changes in perceived radiance may be prompt precursors of impending eruptions.

Mt. Etna presents an excellent opportunity for systematic investigation of the potential relationships between changes in thermal radiance and the timing, magnitude, and mode of subsequent eruptive activity because of its current restless state and frequent summit crater activity that is often associated with lava flow extrusions from its summit craters and flanks. In particular, the data record of remote sensing observations provide one of the most comprehensive databases available for volcanoes on Earth. Here especially the Landsat and ASTER earth observation missions are of unprecedented value (e.g., Pieri et al. 1990; Pieri and Buongiorno 1995; Wright et al. 2000; Pieri and Abrams 2004; Lombardo and Buongiorno 2006).

We are now just beginning to mine such data archives and the current insights are preliminary. However, at least a couple of conclusions can be drawn from the results presented here:

1. *For Mt. Etna, the total thermal energy emitted from its summit craters appears to increase before an eruption.* While this may seem intuitive, it is not a guaranteed situation. It is more likely for basaltic volcanoes with fairly open plumbing systems with relatively low viscosity magmas. For volcanoes that are more silicic, and thus have higher viscosity magmas (e.g., Andean volcanoes, such as Lascar), the opposite can be true. This results in the restricted magma ascent in advance of internal pressure build-up and subsequent paroxysmal explosions. This does not seem to be the current pattern at Mt. Etna.
2. *From the remote sensing perspective, an increase in the variance of Mt. Etna summit crater thermal energy output appears to be correlated with the eruption onset.* This tends to be more evident in night time data. However, during an eruption the signal-to-noise ratio (SNR) of summit crater variance to background variance is a factor of five (or more) higher than the SNR of maximum radiance (dependent on measurement of the radiance of single pixel) vs. average background radiance. For data mining applications in newly emerging large time-series data bases this distinction can be significant for automatic eruption detection algorithms.
3. *Volcanic summit crater activity at Mt. Etna is well-characterized at spatial scales of <100 m/pixel and characterized relatively poorly at spatial scales equal to or greater than 1,000 m/pixel for TIR data.* At larger spatial scales, maximum temperatures and variances are diluted and smoothed. In daytime data effects of solar insolation hamper the detection of relevant changes in summit crater radiant emissions, except for very strong precursor activity. This has not

been viewed as a persuasive argument to increase the spatial resolution of new TIR sensors planned for future earth orbital missions in Europe or the United States. However, data and analyses presented here provide concrete evidence of such a monitoring scenario. For volcanoes elsewhere, where observing conditions may not be as optimal (e.g., frequent cloud cover, high humidity, cryo-burdened summits – see Pieri and Abrams 2005) a spatial resolution <100 m/pixel may be critical in detecting thermal precursors.

4. *Frequent temporal sampling is also a crucial component in detecting thermal changes that may precede eruptions, even for very well-posed volcano natural laboratories like Mt. Etna.* Current and recent orbital remote sensing missions in low earth orbit (e.g., ASTER, EO-1, Landsat) have nadir repeat intervals of about 16 days. ASTER with off-nadir pointing can reduce the revisit time up to 3 days but off-nadir view looks are disadvantageous in viewing geometry. Nevertheless, future missions should investigate schemes for increasing temporal sampling at high spatial resolutions (<100 m/pixel) for TIR instruments. Some strategies could include a constellations of satellites (e.g., “cube-sats”) or satellites with much larger instantaneous fields of view. Clearly in the future, such approaches are crucial to improve both our basic knowledge of volcanoes, and our ability to protect property and human life from volcanic hazards.

We also hope that our work will support the development of future multispectral and hyper-spectral airborne (e.g., manned and UAV) and spaceborne imagers by providing a basis for instrument requirements (e.g., spatial and spectral resolution, wavelength range, dynamic range) with respect to volcanogenic thermal anomaly detection as convolved with intrinsic (e.g., flux, intensity, emissivity), and extrinsic (e.g., atmospheric emissions, water vapor, clouds) scene parameters. Such knowledge will also significantly influence the development of data collection strategies (e.g., image swath, repeat time, pointing capability, orbital parameters) to maximize the probability that subtle early low intensity thermal anomalies related to subsequent eruption activity will be effectively detected. We hope that this work will help to guide the development of future airborne (manned/unmanned) and orbital instrumentation for NASA (National Aeronautics and Space Administration), ESA (European Space Agency), ASI (Agenzia Spaziale Italiana), DLR (German Aerospace Center) and others, for prediction and mitigation of volcanic hazards, and in the pursuit of basic knowledge of volcanoes.

**Acknowledgments** The authors would like to thank US and Japanese colleagues of the ASTER Joint Science Team, the NASA Land Processes Distributed Active Archive Center in Sioux Falls, South Dakota (USA) and the Earth Remote Sensing Data Analysis Center (ERSDAC) in Tokyo (Japan) for cooperation in obtaining and analyzing the ASTER data used for this study, as well as the Japanese Ministry of Economy, Trade and Industry (METI) for its support of the ASTER mission. This work was carried out, in part, at the Jet Propulsion Laboratory (JPL) of the California Institute of Technology under contract to the Science Mission Directorate of NASA. Moreover the authors would like to thank Marco Neri and Boris Behncke working at INGV Mt. Etna Observatory who have provided the Mt. Etna eruption history and maps and Massimo Musacchio working at INGV in Rome for many helpful discussions.

## References

- Behncke B, Neri M (2003) The July–August 2001 eruption of Mt. Etna (Sicily). *Bull Volcanol* 65:461–476. doi:[10.1007/s00445-003-0274-1](https://doi.org/10.1007/s00445-003-0274-1)
- Behncke B, Neri M, Nagay A (2005) Lava flow hazard at Mount Etna (Italy): new data from a GIS-based study. In: Manga M, Ventura G (eds) Kinematics and dynamics of lava flows. *Geol Soc Am Spec Pap* 396, pp 187–205. doi:[10.1130/0-8137-2396-5.189](https://doi.org/10.1130/0-8137-2396-5.189)
- Behncke B, Calvari S, Giannamico S, Neri M, Pinkerton H (2008) Pyroclastic density currents resulting from interaction of basaltic magma with hydrothermally altered rock: an example from the 2006 summit eruptions of Mount Etna. Italy *Bull Volcanol* 70:1249–1268. doi:[10.1007/s00445-008-0200-7](https://doi.org/10.1007/s00445-008-0200-7)
- Branca S, Del Carlo P (2004) Eruptions of Mt. Etna during the past 3,200 years: a revised compilation integrating the historical and stratigraphic records. In: Bonaccorso A, Calvari S, Coltellini M, Del Negro C, Falsaperla S (eds) *Etna volcano laboratory*, Geophysical monograph series 143. AGU, Washington, DC, pp 1–28, 369pp
- Branca S, Coltellini M, Grippelli G (2004) Geological evolution of Etna volcano. In: Bonaccorso A, Calvari S, Coltellini M, Del Negro C, Falsaperla S (eds) *Etna volcano laboratory*, Geophysical monograph series 143. AGU, Washington, DC, pp 49–63
- Crisp J, Baloga S (1990) A model for lava flows with two thermal components. *J Geophys Res* 95 (B2):1255–1270
- Dean KG, Dehn J, Papp KR, Smith S, Izbekov P, Peterson R, Kearney C, Steffke A (2004) Integrated satellite observation of the 2001 eruption of Mt. Cleveland, Alaska. *J Volcanol Geotherm Res* 135:51–72
- Dozier J (1981) A method for satellite identification of surface temperature fields of subpixel resolution. *Remote Sens Environ* 11:221–229
- Flynn LP, Mouginis-Mark PJ, Horton KA (1994) Distribution of thermal areas on active lava flow field: Landsat observations of Kilauea, Hawaii, July 1991. *Bull Volcanol* 56:284–296
- Flynn LP, Harris AJL, Wright R (2001) Improved identification of volcanic features using Landsat 7 ETM+. *Remote Sens Environ* 78:180–193
- Flynn LP, Wright R, Garbeil H, Harris AJL, Pilger E (2002) A global thermal alert using MODIS: initial results from 2000–2001. *Adv Environ Monit Model* 1:37–69
- Francis PW, Rothery DA (1987) Using the Landsat thematic mapper to detect and monitor active volcanoes: an example from Lascar Volcano, northern Chile. *Geology* 15:614–617
- Gawarecki SJ, Lyon RJP, Nordberg W (1965) Infrared spectral returns and imagery of the Earth from space and their application to geological problems: scientific experiments for manned orbital flight. *Am Astronaut Soc Sci Technol Ser* 4:13–133
- Gouhier M, Harris A, Calvari S, Labazuy P, Guéhenneux Y, Donnadieu F, Valade S (2012) Lava discharge during Etna's January 2011 fire fountain tracked using MSG-SEVIRI. *Bull Volcanol* 74(4):787
- Harris A, Ripepe M (2007) Temperature and dynamics of degassing at Stromboli. *J Geophys Res* 112, B03205. doi:[10.1029/2006JB004393](https://doi.org/10.1029/2006JB004393)
- Harris AJL, Blake S, Rothery DA, Stevens NF (1997) A chronology of the 1991 to 1993 Etna eruption using AVHRR data: implications for real time thermal volcano monitoring. *J Geophys Res* 102:7985–8003
- Harris AJL, Wright R, Flynn LP (1999) Remote monitoring of Mount Erebus Volcano, Antarctica, using polar orbiters: progress and prospects. *Int J Remote Sens* 20(15–16):3051–3071
- Harris AJL et al (2001) Automated, high temporal resolution, thermal analysis of Kilauea volcano, Hawai'i, using GOES satellite data. *Int J Remote Sens* 22(6):945–967
- Kaneko T, Wooster MJ (2005) Satellite thermal analysis of the 1986 Izu-Oshima lava flows. *J Volcanol Geotherm Res* 148:355–371
- Lombardo V, Buongiorno MF (2003) Temperature distribution analysis of July 2001 Mt. Etna eruption observed by the airborne hyperspectral sensor MIVIS. *Ann Geophys* 46(6)

- Lombardo V, Buongiorno MF (2006) Lava flow thermal analysis using three infrared bands of remote-sensing imagery: a study case from Mount Etna 2001 eruption. *Remote Sens Environ* 101(2):141–149
- Lombardo V, Buongiorno MF, Amici S (2006) Characterization of volcanic thermal anomalies by means of sub-pixel temperature distribution analysis. *Bull Volcanol* 68:641–651
- Neri M, Acocella V, Behncke B, Giannanco S, Mazzarini F, Rust D (2011) Structural analysis of the eruptive fissures at Mount Etna (Italy). *Ann Geophys* 54(5):464–479. doi:[10.4401/ag-5332](https://doi.org/10.4401/ag-5332)
- NRC Committee on Earth Science and Applications from Space (2007) Earth science and applications from space: national imperatives for the next decade and beyond. The National Academies Press of the National Research Council (NRC), Washington, DC, 428pp
- Oppenheimer C (1993) Thermal distributions of hot volcanic surfaces constrained using three infrared bands of remote sensing data. *Geophys Res Lett* 20:431–434
- Oppenheimer C, Francis PW (1997) Remote sensing of heat, lava and fumarole emissions from Efta' Ale Volcano, Ethiopia. *Int J Remote Sens* 18:1661–1692
- Oppenheimer C, Yirgu G (2002) Thermal imaging of an active lava lake: Erta 'Ale volcano, Ethiopia. *Int J Remote Sens* 23:4777–4782
- Oppenheimer C, Francis PW, Rothery DA, Carlton RWT, Glaze LS (1993a) Infrared image analysis of volcanic thermal features: Lascar Volcano, Chile 1984–1992. *J Geophys Res* 98:4269–4286
- Oppenheimer C, Rothery DA, Francis PW (1993b) Thermal distribution at fumarole fields: implications for infrared remote sensing of active volcanoes. *J Volcanol Geotherm Res* 55:97–115
- Pergola N, Tramutoli V, Marchese F (2004) Automated detection of thermal features of active volcanoes by means of Infrared AVHRR records. *Remote Sens Environ* 93:311–327
- Pieri D, Abrams M (2004) ASTER watches the world's volcanoes: a new paradigm for volcanological observations from orbit. *J Volcanol Geotherm Res* 135(1–2):13–28
- Pieri D, Abrams M (2005) ASTER observations of thermal precursors to the April 2003 eruption of Chikurachki Volcano, Kurile Islands, Russia. *Remote Sens Environ* 99:84–94
- Pieri DC, Buongiorno MF (1995) Landsat TM observations of Mt. Etna summit crater radiance increases before the 1991–1993 eruption: implications for ASTER observations. *EOS Trans Am Geophys Union* 1995 Fall Meeting, 76, 46, Nov 7/Supplement, F135
- Pieri D, Glaze LS, Abrams MJ (1990) Thermal radiance observations of an active lava flow during the June 1984 eruption of Mount Etna. *Geology* 18:1018–1022
- Ramsey MS, Dehn J (2004) Spaceborne observations of the 2000 Bezymianny, Kamchatka eruption: the integration of high-resolution ASTER data into near real-time monitoring using AVHRR. *J Volcanol Geotherm Res* 135(1–2):127–146
- Realmuto V, Abrams M, Buongiorno MF, Pieri D (1994) The use of multispectral thermal infrared image data to estimate the sulfur dioxide flux from volcanoes: a case study from Mount Etna, Sicily, July 29, 1986. *J Geophys Res* 99(B1):481–488. doi:[10.1029/93JB02062](https://doi.org/10.1029/93JB02062)
- Rothery DA, Francis PW, Wood CA (1988) Volcano monitoring using short wavelength infrared data from satellites. *J Geophys Res* 93:7993–8008
- Simkin T, Kreuger AF (1977) Skylab 4 observation of volcanoes: Part B – summit eruption of Fernandina Caldera, Galapagos Islands, Ecuador. *Skylab Explores the Earth, NASA Spec Publ 380*, pp 171–172
- Simkin T, Siebert L (1994) Volcanoes of the world: a regional directory, gazetteer, and chronology of volcanism during the last 10,000 years, 2nd edn. Geoscience Press, Tucson, 368pp
- Solomon SC, Baker VR, Bloxham J, Booth J, Donnellan A, Elachi C, Evans D, Rignot E, Burbank D, Chao BF, Chave A, Gillespie A, Herring T, Jeanloz R, LaBrecque J, Minster B, Pitman WC III, Simons M, Turcotte DL, Zoback ML (2003) Plan for living on a restless planet sets NASA's solid earth agenda. *EOS Trans Am Geophys Union* 84(45):485–491
- Vaughan RG, Hook SJ (2006) Using satellite data to characterize the temporal thermal behavior of an active volcano: Mount St. Helens, WA. *Geophys Res Lett* 33, L20303

- Vaughan RG, Hook SJ, Ramsey MS, Realmuto VJ, Schneider DJ (2005) Monitoring eruptive activity at Mount St. Helens with TIR image data. *Geophys Res Lett* 32(19)
- Vaughan RG, Abrams MJ, Hook SJ, Pieri DC (2007) Satellite observations of new volcanic island in Tonga. *EOS* 88(4):37–41
- Wooster MJ, Rothery DA (1997) Thermal monitoring of Lascar Volcano, Chile using infrared data from the along track scanning radiometer, a 1992–1995 time series. *Bull Volcanol* 58:566–579
- Wooster MJ, Rothery DA (2000) A review of volcano surveillance applications using the ATSR instrument series. *Adv Environ Monit Model* 1(1):3–35
- Wright R, Flynn LP (2003) On the retrieval of lava flow surface temperatures from infrared satellite data. *Geology* 31:893–896
- Wright R, Rothery DA, Blake S, Harris AJL, Pieri DC (1999) Simulating the response of the IEOS Terra ASTER sensor to high temperature volcanic targets. *Geophys Res Lett* 26:1773–1776
- Wright R, Rothery DA, Blake S, Pieri DC (2000) Improved remote sensing estimates of lava flow cooling: a case study of the 1991 to 1993 Mount Etna eruption. *J Geophys Res (Solid Earth)* 105:23681–23694
- Wright R, Flynn L, Garbeil H, Harris A, Pilger E (2004) MODVOLC: near-real-time thermal monitoring of global volcanism. *J Volcanol Geotherm Res* 135:29–49
- Yamaguchi Y, Kahle AB, Tsu H, Kawakami T, Pniel M (1998) Overview of advanced spaceborne thermal emission and reflection radiometer (ASTER). *IEEE Trans Geosci Remote Sens* 36:1062–1071
- URL1: <http://www.volcano.si.edu>
- URL2: <http://vulcani.ingv.it/en/etna.html>
- URL3: <http://noaasis.noaa.gov/NOAASIS/ml/avhrr.html>

# Chapter 21

## Thermal Infrared Remote Sensing of Surface and Underground Coal Fires

Claudia Kuenzer, Jianzhong Zhang, Li Jing, Guo Huadong,  
and Stefan Dech

**Abstract** Surface and underground coal fires are burning in numerous countries worldwide. China, India, the USA, Australia, Indonesia, South Africa, and many other countries all report uncontrollably burning coal fires. They ignite through spontaneous combustion of coal, or through lightning, forest fires, fires in garbage dumps, or careless human behaviour. Coal fires lead to the loss of the valuable resource and lead to the emission of green-house gasses as well as toxic gasses. These gasses contribute to climate change and also impact human health. Vegetation above the fires deteriorates. Due to the volume loss underground coal fires also trigger land subsidence and surface bedrock collapses. The surface and underground fires can be detected and monitored by means of remote sensing. Data acquired with handheld thermal cameras, airborne sensors, and also spaceborne sensors have been analyzed by numerous authors. However, exact and simultaneously standardized as well as transferable methods for coal fire detection and monitoring are hard to establish, and research gaps still exist. This chapter presents a broad overview of past and current coal fire work, as well as the challenges which can be addressed based on thermal data of recent and upcoming sensors.

---

C. Kuenzer (✉) • S. Dech

German Remote Sensing Data Center (DFD), Earth Observation Center (EOC),  
German Aerospace Center (DLR), Oberpfaffenhofen, Germany  
e-mail: [Claudia.kuenzer@dlr.de](mailto:Claudia.kuenzer@dlr.de)

J. Zhang  
Beijing ESKY Technology Limited, Beijing, China

L. Jing  
College of Resources Science and Technology, Beijing Normal University, Beijing, China

G. Huadong  
Center for Earth Observation and Digital Earth (CEODE), Beijing, China

## 21.1 Introduction to Coal Fires

Coal fires are fires which occur in accumulations of coal. Coal fires can burn sub-surface in underground coal seams, or can occur as surface coal fires in exposed seams, coal storage piles, or coal waste piles. The oxidation of the carbon contained in the coal with the oxygen of the surrounding air is an exothermal process, during which heat is released. If this heat cannot disperse easily the coal can start to ignite at temperatures as low as 80 °C. This process is termed spontaneous combustion. It occurs in well-aerated coal volumes underground, as well as in surface accumulations. Spontaneous combustion probability is the higher, the lower the rank of the coal, the higher its volatile contents, the more the coal volume is fractured, the larger the coal's inner surface (e.g., through frequent quelling and shrinking due to moisture), and the hotter the general outside temperatures. Mining activities often produce many of the above-mentioned preconditions (e.g., by exposing formerly covered seams to air, fracturing the coal volumes, increasing the inner reactive surface, etc.) (Banerjee 1982, 1985; Banerjee et al. 1972). Anthropogenic activity can also lead to the ignition of coal volumes, such as careless handling of fire (throwing away burning cigarettes in mines, cooking activities, mine gas explosions, power shortages). Coal fires can also be ignited via lightning, nearby forest and peat fires, or burning garbage dumps (Coward 1957).

Kuenzer and Stracher (2011) elaborated that coal fires can be classified into surface versus subsurface coal fires, ancient versus recent coal fires, and natural versus human-induced coal fires, to give only some examples. Furthermore, coal fires can also be ranked according to their burning stage into recently ignited, accelerating, steadily burning, burning out, and extinct coal fires.

The fires occur everywhere around the globe and are a much larger geohazard than the public is aware of. Numerous coal fires rage in coal mining areas of China (Kuenzer 2005) and India (Bhattacharya et al. 1991; Bhattacharya and Reddy 1994), where the problem is most prominent. But also in the USA (Coates et al. 2005), Australia (Ellyett and Fleming 1974), South Africa (Bell et al. 2001; Pone et al. 2007), Venezuela, and eastern Europe coal fires burn uncontrollably. Figure 21.1 below presents a map of fire locations the authors are aware of.

In the USA a burning garbage dump near the small town of Centralia in Pennsylvania led to the ignition of an underground coal seam in 1962. The coal seam started to burn and smoulder underground. This led to volume loss underground, bringing with it dangerous sudden land subsidence and collapse. Toxic fumes started to seep through cracks in the overburden bedrock and into people's houses. After years of unsuccessful coal fire fighting the town of Centralia had to be evacuated. Today, Centralia is an uninhabited 'ghost town' and the coal fire continues to burn (Chaiken et al. 1998; Elick 2001).

Negative impacts of coal fires are countless. They release greenhouse-relevant ( $\text{CO}_2$ ,  $\text{CH}_4$ ) and toxic gases ( $\text{CO}$ ,  $\text{N}_2\text{O}$ ,  $\text{SO}_2$ ,  $\text{NO}_x$ , etc.) which are a threat to climate and human health (Finkelmann 2004), as well as to all biota in the vicinity of the

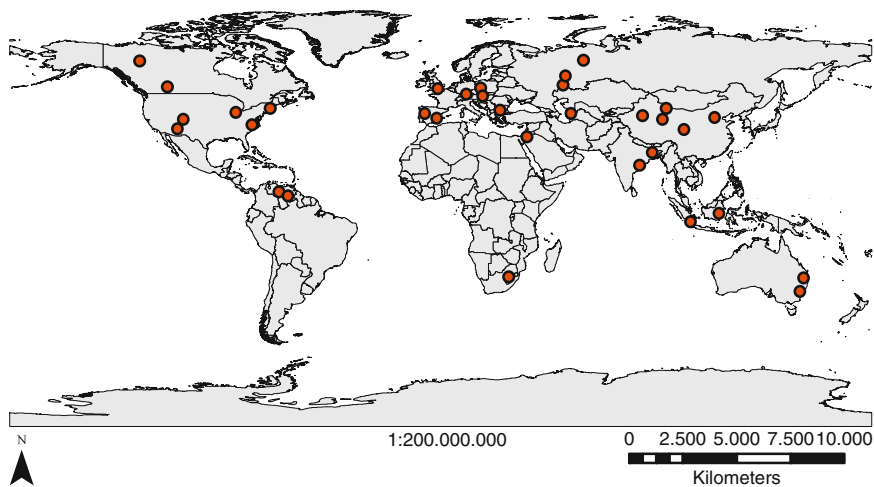


**Fig. 21.1** Coal fires worldwide. The map shows where coal fires have been reported. It was generated based on the best knowledge of the authors and probably underestimates the fire situations, as many coal fire areas are still unknown today

fires. They lead to collapse and fracturing of the land surface due to the volume loss underground, and thus endanger settlement, infrastructure, and general land access. They furthermore lead to the loss of the valuable economic resource coal, as coal that burnt can no longer be sold on the national or international coal market (Kuenzer et al. 2007b) (Fig. 21.2).

Coal fire extinguishing is difficult. Basically, three approaches exist. Firstly, one can deplete the fire of its combustible – the coal itself. This is usually done by digging out burning parts of the coal seam and transporting them to distant areas where the burning coal cannot ignite further coal layers. This is a very dangerous approach, as miners have to excavate glowing coal and load it onto trucks, and injuries are common. However, burning parts of a seam can also be separated from not-yet affected parts of the seam through trenches. In this way burning volumes can also be isolated. A second method is to deplete the fire of oxygen. This is usually done by covering surface or underground fires with loess, sand, or other overburden material in the hope that the filling of cracks, vents, and oxygen supply pathways to the underground will extinguish the fire. In advanced or economically strong mines, colloidal foams (mixtures of water, ash, and oxygen-reducing chemicals) are pressed into the underground via high pressure systems. The third method is to deplete the fire of its energy. This is undertaken via the injection of water. However, it has proven that fire extinguishing is a very complex task, and oftentimes fires flare up again only weeks after they were thought to be extinguished (Fig. 21.3).



**Fig. 21.2** Subsurface coal fires. The release of greenhouse relevant and toxic gasses, land subsidence due to volume loss underground, vegetation deterioration, crystallization of toxic minerals, and the genesis of pyrometamorphic rock are only some of the visible consequences (All photographs taken in Wuda, China, by C. Kuenzer)

## 21.2 An Overview of Coal Fire Remote Sensing

Coal fires are an ideal phenomenon for remote observation and analysis, as access to the fire areas is usually limited for safety reasons. The bedrock surface above subsurface coal fires can easily reach temperatures of 60 °C up to several 100 °C due to long term conduction of underground heat. Hot gasses released from vents, cracks, and fissures in the overlying bedrock have been recorded to even exceed



**Fig. 21.3** Examples of coal fire extinguishing attempts. *Upper left:* on the *upper left* part of the image can be seen former mine entrances, which were improperly sealed with loess and sand. The coal seam below is burning. To rescue other parts of the seam from igniting as well (the part where the people are located), a trench was dug by local miners to separate the burning part of the seam from the not (yet) burning part. The other three photographs show the attempt to pump a mixture of water, coal dust, ash, and special colloids into the underground to fill up cavities and cracks and therefore deplete the fire of oxygen (Photographs taken in Wuda, China, by J. Zhang)

1,000 °C (Kuenzer and Stracher 2011). Furthermore, many coal fire areas are located in remote areas which are already hard to access, irrespective of the fire hazard.

In the infancy years of suitable spaceborne thermal sensors for coal fire mapping and monitoring in the 1970s, thermal assessment of coal fires was still mainly undertaken based on airborne surveys. Especially airborne coal fire monitoring in the USA played a crucial role (Greene et al. 1969; Kim and Chaiken 1993). Even today, numerous fire surveys are still undertaken with thermal cameras and thermal scanners mounted on airplanes or helicopters. Renner (2005), for example, undertook a very detailed survey of over 50 uncontrolled coal fires burning mainly in abandoned mines in the state of Colorado. Here, especially the South Canyon coal fire not far from Glenwood Springs, ignited by a forest fire, has reached fame through numerous publications (Stracher et al. 2007). But also in other countries airborne surveys have been the preferred choice for detailed detection of fire centres and extent, or the monitoring of extinguishing activities, such as undertaken in the Wuda coal mine, China, by the Beijing Remote Sensing Center, BRSC. Airborne

survey has the advantage that it delivers data of very high spatial accuracy in the below-meter range, but it is also very costly. An airborne campaign including renting the airplane, pilot, and scanner, and expenses for gas, flight planning, data analysis, etc. can easily cost several hundred thousand euros or US dollars. Furthermore, airborne data are difficult to analyze, with complex geometry due to the airplane's pitch, roll, and gear during the data acquisition process, as well as relief induced object displacement.

Since the onset of high resolution thermal remote sensing with sensors such as Landsat MSS (Multispectral Scanner) and Landsat TM (Thematic Mapper) (thermal bands at 120 m resolution), coal fire areas have been monitored and analyzed from space (Zhang et al. 2004). Research focussed for many years on the world's large coal fire areas – such as the coal fires burning (up to today) in the Jharia coal field in India (Saraf et al. 1995; Agarwal et al. 2006; Chatterjee 2006; Gangopadhyay 2006), or the coal fires analyzed in depth in the 1980s and the 1990s in Xinjiang, China (Rosema et al. 1999; Cassells 1997; Prakash et al. 1999). From 2000 to today especially the numerous coal fires in the Wuda syncline, Inner Mongolia, China, were investigated (Kuenzer 2005, 2013; Litschke 2005; Litschke et al. 2005), and coal fire research in the USA has also picked up speed again (Stracher and Taylor 2004). Currently, a five volume coal fire atlas, published by Elsevier, is being compiled, of which the first two volumes have already been released. This work of literally over thousands of pages on coal fires is probably the most comprehensive work ever compiled on this subject and addresses all coal fire research disciplines, such as coal fire geology, geomorphology, chemistry, mineralogy (Stracher et al. 2012), geophysics (Wessling et al. 2008), and last but not least also surveying and monitoring techniques based on remote sensing data.

Foci of spaceborne analyses are manifold. Kuenzer (2005) investigated the impact of coal fires on vegetation degradation in the vicinity of the fires and found out that the underground heat in the root zone as well as hot and toxic gasses released by vents and cracks lead to the deterioration of plants. One indicator of underground coal fire activity therefore can be abnormally low vegetation density on the surface.

Coates and Heffern (2000) and Kuenzer (2005) analyzed whether pyrometamorphic rocks – an indicator of coal fires – can be detected in remote sensing data from sensors such as those on Landsat, Aster (Advanced Spaceborne Thermal Emission and Reflection Radiometer), and Quickbird. Pyrometamorphic rocks are rocks which change their colour and texture once they are heated by an adjacent fire. These rocks can have been partially remelted. Usually they have a yellowish, orange to reddish colour and can be well differentiated from the typical background rocks (Zhang 1996).

Chen (1997) tried to detect coal fire related land subsidence based on interferometric synthetic aperture radar data. Several authors found that such approaches are not suitable for coal fire related subsidence analysis, as subsidence in these areas often occurs very suddenly (sudden crack of a sinkhole, very much comparable to subsidence in karst regions) rather than very slowly – like, for example, in very large (non-coal-fire-affected) mining areas or region of groundwater withdrawal. Sudden

subsidence, however, means that the connection of fringes in interferograms is lost, and subsidence thus cannot be quantified.

Yang et al. (2008) focussed on high resolution optical data from sensors such as those on Ikonos or Quickbird to map coal fire induced subsidence and cracks in the overburden bedrock associated with the underground fire front. It is known that the ‘crack fields’ and fissures on the surface of underground fires usually develop orthogonal to the spreading direction of the fire and that cracks and fissures usually act as a precursor to fire movement and can be found in an area also a few meters ahead of the current underground fire front.

Cracknell and Mansor (1992), Kuenzer et al. (2008a, b, c, d), Yang et al. (2005), Zhang (2004), and Hecker et al. (2007) employed time series of thermal daytime and nighttime data to detect coal fire related thermal anomalies with semi-automated and automated methods, and also to derive coal fire related energy release for the extracted burning clusters (Tetzlaff 2004). It was in 2004 that for the first time unknown coal fires were first detected in remote sensing data, and were later found and validated at remote locations in-situ in the field (Kuenzer et al. 2007a). This was a breakthrough in spaceborne remote sensing of coal fires, as before fires were usually analyzed whose location and extent were already known from in-situ observations.

In the past 5 years one focus has been the attempt to utilize remote sensing data to estimate coal fire related greenhouse gas emissions, which might be interesting for post-Kyoto relevant emission trading schemes among countries, such as the Clean Development Mechanism, CDM. However, up to today it was not possible to establish a clear emission baseline for any of the coal fires worldwide that would have led to the trade of emission certificates (van Dijk et al. 2011; IPCC 2006; Ide and Orr 2011; Kuenzer et al. 2007c).

## 21.3 In-Situ Mapping of Coal Fires

### 21.3.1 Coal Fire Characteristics

Surface coal fires occur in open pit coal mines as well as in coal storage and waste piles. They are usually easy to identify, as smoke rising from the burning coal can be observed. Minerals such as sulphur or ammonia condensate near the burning coal are often visible as yellowish or whitish crusts (Fig. 21.4). Sometimes, pyrometamorphic rocks can also form within coal waste piles, where surrounding bedrock (e.g., shale, sandstone, etc.) changes in texture and colour. Surface fires are usually easy to detect in thermal remote sensing data, as the burning coal is not covered by overlying bedrock layers. However, surface coal fires are usually small in size (restricted to the size of a waste or storage pile) and as they are easy to access they are usually extinguished relatively fast (especially in storage piles, which even occur in coal volumes transported on ships). In addition to their thermal signal, these fires can, for



**Fig. 21.4** Measuring underground coal fire related temperatures in-situ with handheld Raytek radiometers (Small image courtesy of Raytek. Photographs: C. Kuenzer (*left*), C. Hecker (*right*))

example, also be indirectly detected. If the first snow falls, the area of surface coal fires usually remains snow-free, as the snow will immediately melt. This phenomenon can be observed in remote sensing data.

Underground coal fires are a more complex phenomenon. Heat from fires in underground seams, abandoned, or even operating mines can be transferred to the bedrock surface via conduction (a process that takes very long, and only yields a weak thermal signal on the surface), or via convection of hot gasses released through vents, cracks, and fissures that form due to the volume loss underground. The gasses released can reach temperature exceeding several hundred degrees Celsius. However, the localities are very small in spatial extent. If a 20 cm long fissure releases 200 °C hot gas, this might only slightly elevate the temperature recorded in a (for example) 60 by 60 m thermal Landsat ETM+ (Enhanced Thematic Mapper Plus) pixel. Thus, the main challenge for the remote sensing based detection of underground fires is the extraction of very subtle thermal anomalies with temperatures only slightly elevated against the background.

### 21.3.2 *Mapping with Radiometers and Handheld Thermal Cameras*

Figure 21.5 depicts coal fire signals as detected with handheld thermal cameras. It can be observed that the thermally anomalous events are relatively confined to the openings in the overburden bedrock. A detailed overview of thermal characteristics of coal fires can be found in Zhang and Kuenzer (2007). These authors present in depth insights on how thermal anomalies behave with growing perpendicular distance to the bedrock opening, how thermal signals behave vertically when

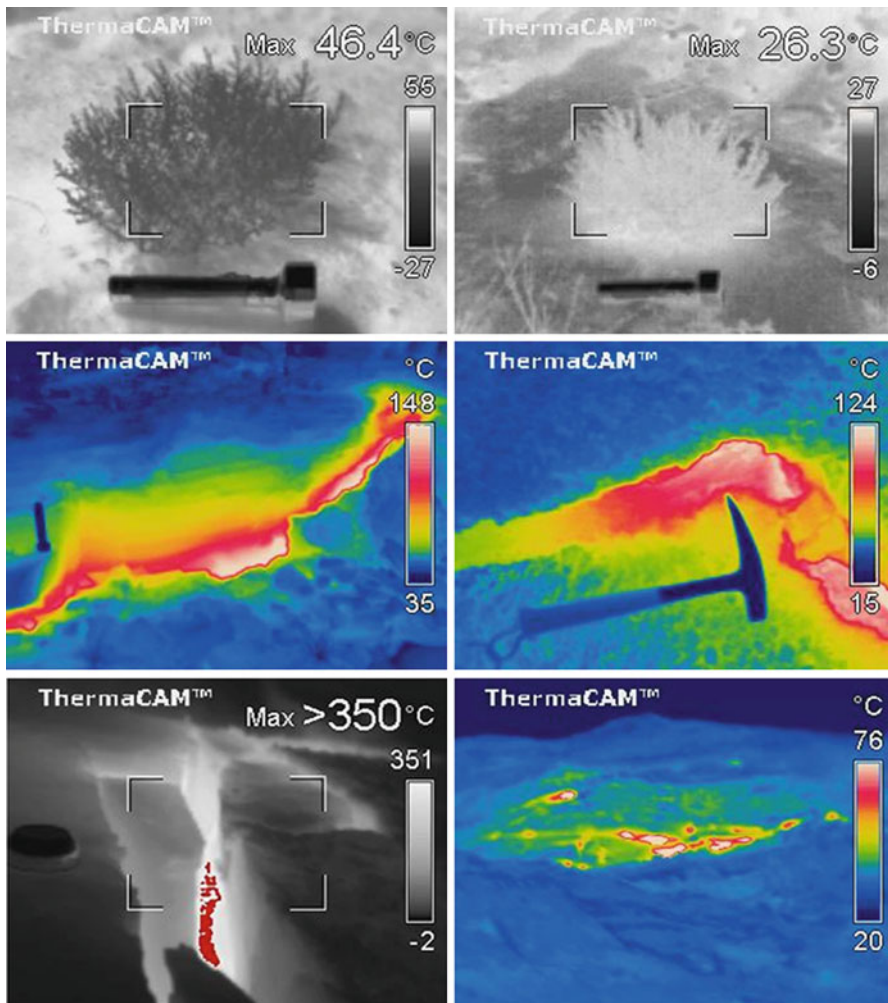


**Fig. 21.5** Coal fires as observed with a handheld thermal camera (FLIR). The *upper* two images show a shrub on a sandstone surface. An aluminium pocket light acts as a scale. The two images visualize the impact of daytime versus nighttime observation. During the daytime (*left*) the shrub (due to its water content) is colder than the surrounding sandstone. The shiny aluminium of the pocket light leads to incorrect temperature readings in the minus-range, due to the extremely low emissivity (see Chap. 1). During nighttime (*upper right*) the shrub is warmer than the surrounding sandstone (high thermal inertia of water in the shrub). Average background temperature of the sandstone is about 40–50 °C during the day, but only around 10–20 °C during the night. The *middle row* depicts images showing cracks in the bedrock surface, where hot gasses reach the surface. Temperatures at the cracks (which are below 1 m in length) reach well above 100 °C. A pocket light and a geology hammer act as a scale. In coal fire areas several such hot anomalies might exist within, e.g., a 60 m × 60 m area (typical Landsat ETM+ pixel); however, the anomalies are usually sub-pixel phenomena. The *lower* two images depict a very hot crack (*left*), where the thermal camera saturates (*red*, temperature far above 350 °C). The *round object* on the *left* is the aluminium lid of a cooking pot (scale). The *lower right* image displays the thermal anomalies of underground coal fires observed in a nighttime landscape

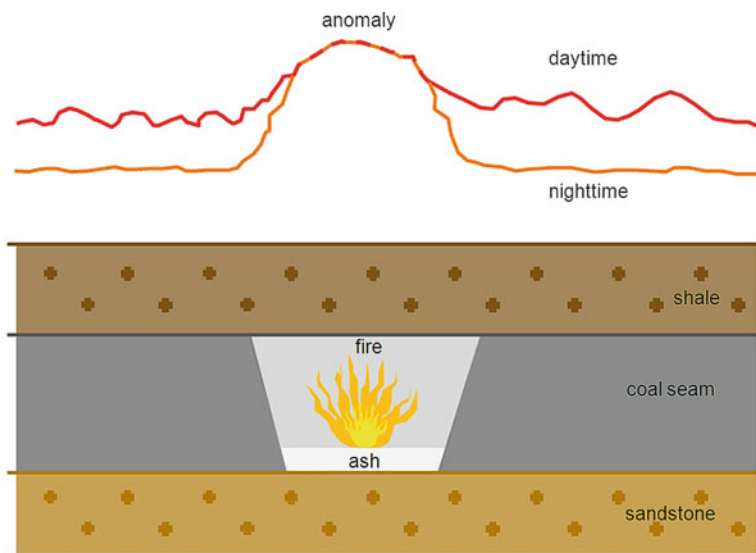


**Fig. 21.6** Underground coal fire induced thermal anomalies during daytime and nighttime; schematic sketch

measured inside a vent, crack, or fissure, and also how the thermal signal of the background is impacted by diurnal temperature variation due to time of day, slope, aspect, and material characteristics. Thermal radiometer readings published by numerous authors confirm that subsurface, fire related thermal signals can range from temperatures only slightly above the background to over 1,000 °C.

Very important is the fact that thermal anomalies have a higher contrast against the background in thermal nighttime data. During the night the bedrock surfaces and objects in the landscape cool off, and a thermal anomaly can be picked up easier than in daytime data. This can also be observed in the sketch shown in Fig. 21.6 below. Figure 21.6 shows that solar illumination impacts the daytime signal of the background surfaces, which is higher and also exhibits a higher variability than during nighttime. Even though the peak anomaly is similar for both recordings, the contrast between the fire related anomaly and the background is stronger in the nighttime data.

The impact of observation time on fire detection and monitoring was assessed in detail in Tetzlaff (2004), Zhang (2004), Zhang et al. (2007), and Zhang and Kuenzer (2007).

Concerning the time of the day, imagery acquired pre-dawn (shortly before sunrise, when the solar effects of the previous day are least accentuated) are best suited for anomaly extraction, but general nighttime data are also suitable and should be favoured over daytime data.

Concerning season, data acquired in the winter (scenes should be snow-free) yield the largest temperature contrast. However, scenes acquired in fall and spring are also suitable, while scenes acquired in summer should be avoided.

The higher the spatial resolution the larger the anomalous area that can be extracted. Landsat-7 ETM+ data outperforms Landsat TM (Thematic Mapper) and MSS (Multispectral Scanner) data, as well as even coarser resolution MODIS (Moderate Resolution Imaging Spectroradiometer) or Envisat AATSR (Advanced Along-Track Scanning Radiometer) data. However, for an in-depth assessment and mapping, airborne thermal scanner data as well as handheld thermal camera data and radiometer recordings deliver the most detailed picture.

## 21.4 Coal Fire Thermal Anomaly Detection in Remote Sensing Data

### 21.4.1 Threshold Techniques for Anomaly Detection

Thermal anomaly detection for coal fire analyses has often been undertaken employing thresholding approaches. With a threshold approach the thermal image analyst usually defines a temperature above which an area is declared ‘anomalous’. However, the shortcomings of such an approach are firstly, that subsurface fire related anomalies which are weaker than the threshold cannot be detected, and secondly that the size of thermally anomalous clusters is very arbitrary. The result of a coal fire mapping will look completely different if, for example, an analyst chooses a threshold at 65 °C or at 70 °C. Therefore, simple threshold approaches have often been criticized as too simplistic for the complexity of the phenomenon (Figs. 21.7 and 21.8).

To overcome the shortcomings associated with simple thresholding, Zhang (2004) developed an algorithm which enables the extraction of subtle regional thermal anomalies. This algorithm enables extraction in one and the same image of, for example, a 55 °C hot pixel within a surrounding of 40 °C hot pixels, as well as a 70° hot pixel in a background of 60 °C hot pixels. This means that pixels of different temperatures can be detected as thermally anomalous. The algorithm is based on a moving window approach, which is explained in the following section.

### 21.4.2 Moving Window Approach for Subtle Anomaly Extraction

As summarized in Kuenzer et al. (2008d), “the algorithm for automated thermal anomaly extraction from the thermal bands of either Landsat 7 ETM+, ASTER or MODIS uses raw satellite data (DN values) or calibrated and corrected thermal data

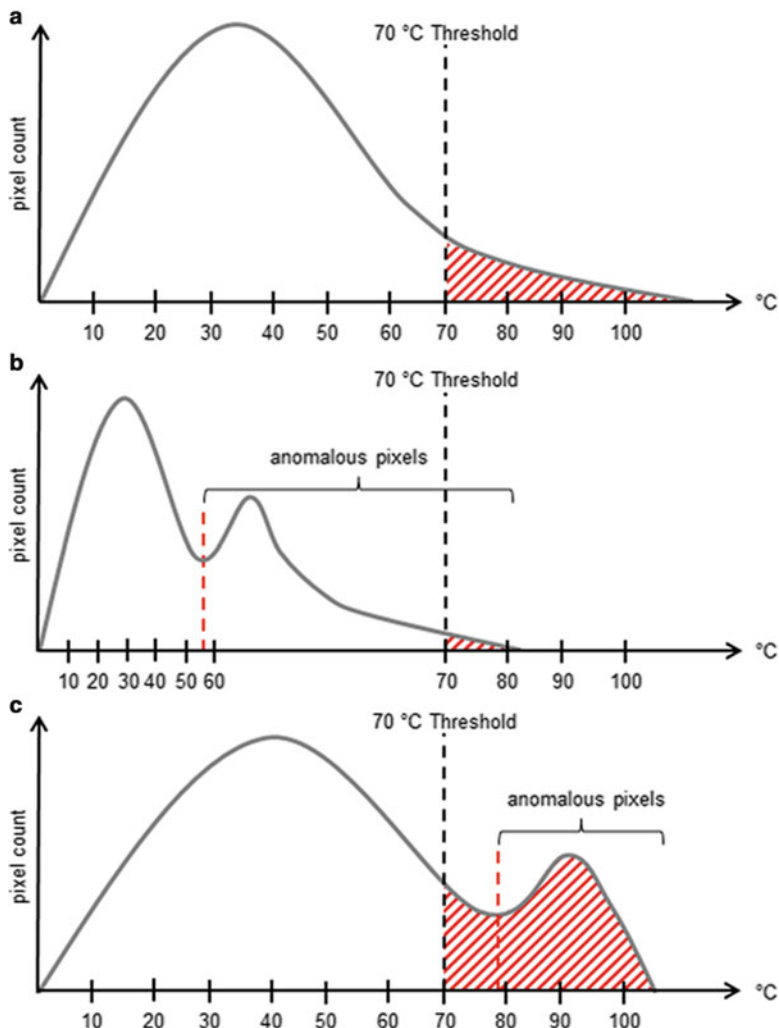


**Fig. 21.7** Principle and shortcomings of simple thresholding approaches. Thresholds yield anomalous images even if they do not exist (*upper*), and might lead to a huge under- (*middle*), or overestimation (*lower* example) of the thermally anomalous area

as input for sub-image statistical analysis. Within a moving window of varying size the histogram for these subsets of the scene are investigated concerning the occurrence of thermally anomalous pixels. Image histogram statistics of coal fires were studied in very great detail and the average statistical “behavior” of coal fires within thermal images was determined. Specific features within the subset histograms (first local minimum after the main maximum) could be defined as thresholds allowing the separation of thermally anomalous pixels from background

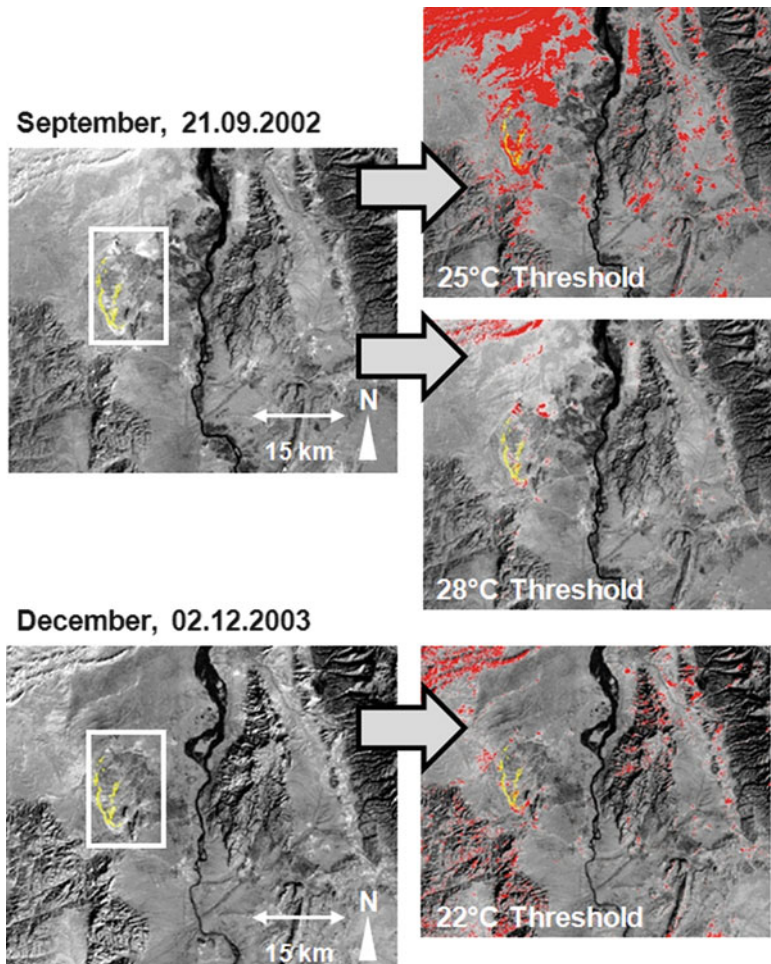


**Fig. 21.8** Disadvantages of simple thresholding in coal fire related analyses. The *upper left* thermal image stems from September 2002. Coal fire related thermal anomalies as mapped *in-situ* during a field campaign are overlain in yellow. We can see that – depending on the choice of the threshold – the number of pixels declared as anomalies varies considerably. When setting the threshold at 25 °C (all pixels above 25 °C declared anomalous) most sunlit slopes (especially sun exposed desert sand dunes, as well as other hills) are extracted as well. At 28 °C only a few anomalies – still including some coal fires – remain. However, in the colder December image already a 22 °C threshold leads to the extraction of some coal fire anomalies, but also here solar effects and sunlit slopes are likewise extracted. There is no overall valid threshold; depending on image acquisition time, thresholds have to be chosen interactively, which is unsatisfying. Large subset: UL: 39°41'54N, 106°20'22E, LR: 39°17'57N, 107°05'03E

pixels. With the concept of a moving window, each pixel within the scene is sampled many ( $>1,000$ ) times. Depending on how often a pixel is regarded as thermally anomalous ( $>70\%$  of cases), it is declared as a thermal anomaly (Zhang 2004). The advantage of this approach is that contrary to an overall threshold

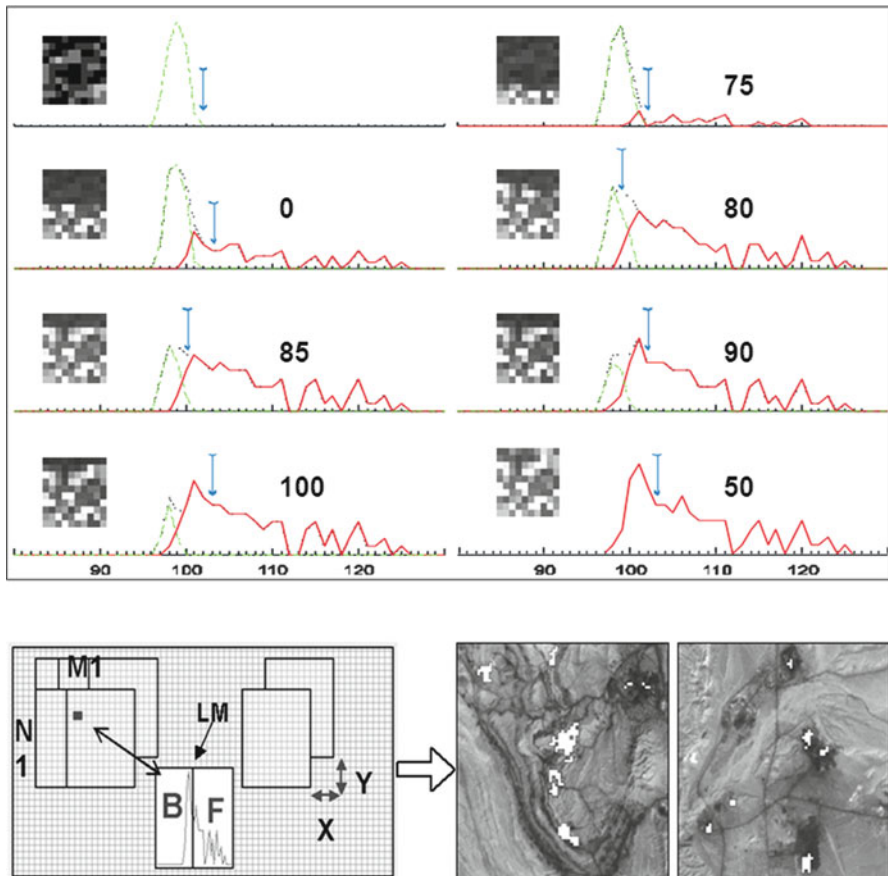


**Fig. 21.9** Method for the extraction of subtle thermal anomalies of differing temperature relative to their background (Zhang 2004; Kuenzer et al. 2008d)

definition regional thermal anomalies will be extracted. This means that – fully depending on the surrounding background – thermal anomalies of completely different temperature can be extracted” (Kuenzer et al. 2008d: 9).

This is also depicted in Fig. 21.9. The temperature band is analyzed within a moving filter of varying window size ( $19 * 19$  up to  $35 * 35$ ). The histogram of this sub-window can contain no thermal anomaly at all, or be gradually filled up to 100 % with a thermal anomaly. Zhang (2004) assumes that every sub-window histogram is made out of the part of the histogram representing the background DNs (temperatures) (in Fig. 21.9, green) and the thermally anomalous part (in Fig. 21.9, red). The first local minimum after the main histogram maximum is defined as the relative threshold to separate the two. This automated method will lead to a loss of thermal anomalies if, e.g., the sub-window is 100 % filled by a thermal anomaly. It will furthermore indicate coal fire or thermal anomalies if no thermally anomalous

area is contained in the image and the high temperature end of the histogram with a Gaussian distribution is extracted. However, since every center pixel is investigated over 1,000 times and has to be declared “thermally anomalous” in at least 70 % of the tests, this last error is kept as low as possible (Kuenzer et al. 2008d).

Furthermore, the thermally anomalous pixels are clustered according to an 8-neighbourhood scheme. Since one pixel is surrounded by eight other pixels, it is checked whether directly adjacent pixels are also anomalous, so that clusters can be formed. These thermally anomalous clusters are numbered and statistically investigated for their minimum, maximum and mean DN, their standard deviation, and their spatial coverage. For example, coal fire areas do not exceed a certain size ( $>1 \text{ km}^2$ ). If the algorithm picks out an anomalous cluster of several square kilometers it is probably a sun illuminated slope. Warm water surfaces can be excluded based on the cluster’s DN or temperature variance. While water surfaces show a very low temperature variance, coal fire clusters show a high variance (Zhang 2004). In this way, the final output image only contains thermal anomalies of small size, which have a reasonable chance of being coal fires.

Nevertheless, automated statistical analysis of thermal anomalies also leads to the extraction of anomalous pixels unrelated to coal fires. These cannot necessarily be distinguished from a coal fire anomaly. Such anomalies can be small, sun illuminated surfaces, thermal anomalies resulting from the heating of houses, industry, the burning of agricultural fields or garbage, limestone burning, or even forest or grassland fires. Demarcated coal fire (risk) areas derived with methods presented in Kuenzer (2005) can serve as a spatial limitation to exclude many of these thermal anomalies not stemming from coal fire influence (Zhang 2004) (Fig. 21.10).

## 21.5 Coal Fire Quantification and Emission Estimation

Coal fire related emission estimation based exclusively on remote sensing data has so far not been successful. However, this is not due to a lack of available ideas or methods, but rather to a lack of suitable thermal data of high spatial and high temporal resolution.

Coal fires release mainly CO<sub>2</sub>, CO, SO<sub>2</sub>, and in some cases also CH<sub>4</sub>. These are the predominant gasses, but others occur as well. Coal fires underground do not burn in a ‘clean’ efficient process, as would be the case in a coal fired furnace for electricity generation. They smoulder under conditions with varying oxygen availability and intruding precipitation-related moisture. However, the relationship between the amount of coal burnt and the greenhouse gasses released can be established, if coal petrology and chemistry is known. In this way a triangle relationship can be established (Fig. 21.11).

If it is known how much coal is burning (or has burnt in a certain amount of time) underground, one can calculate how much greenhouse gas was released. Remote sensing sensors which monitor gas concentrations are however much too coarse in

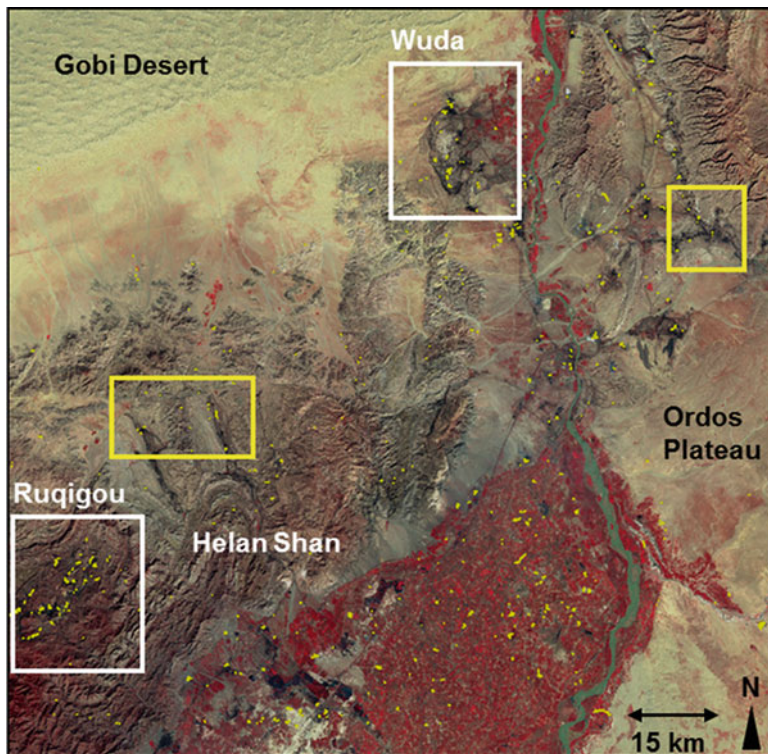


**Fig. 21.10** Result of thermal anomaly extraction using the algorithm presented by Zhang (2004) on Landsat ETM+ nighttime data. Thermal anomalies are presented in yellow. The backdrop is a Landsat ETM+ false colour infrared daytime scene. The two white boxes mark the coal fire regions of Wuda (upper) in Inner Mongolia and of Ruqigou (lower) in Ningxia province. Anomalies within the yellow boxes stem from formerly unknown coal fires in coal waste piles (left, the fires of Hulusitai and Shitanjing) and in surface coal mines (right, east of the Yellow River). Anomalies outside these areas stem from industry, biomass burning, and households

spatial resolution to be of any use for coal fire related research. But additionally, a relationship exists between coal fire related energy release and the amount of coal burning (or burnt) underground. It is therefore possible to observe coal fires and to derive the coal fire related energy release from thermal remote sensing data. From the energy release one can then calculate back to the amount of coal burning.

Tetzlaff (2004) has calculated the energy release from coal fire clusters which were derived by in-situ mapping. Figure 21.12 depicts this based on Landsat ETM + nighttime data for the Wuda coal mining area, China.

However, so far, it has not been possible to really quantify the amount of burnt coal or the amount of greenhouse gases released solely based on earth observation data. Reasons are the following: firstly, coal fire related thermally anomalous clusters cannot be derived with the same precision as is possible with field mapping (see red polygons in Fig. 21.12, left side). Many weaker underground fires cannot

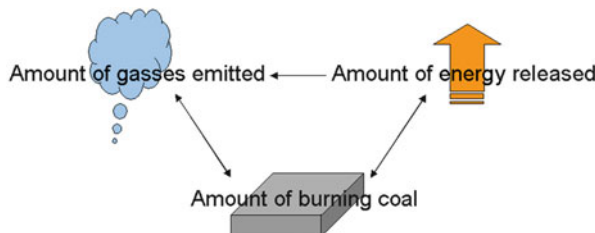


**Fig. 21.11** Triangle relationship between amount of burning (burnt) coal, amount of energy released and amount of gasses emitted (Source: Kuenzer et al. 2007c)

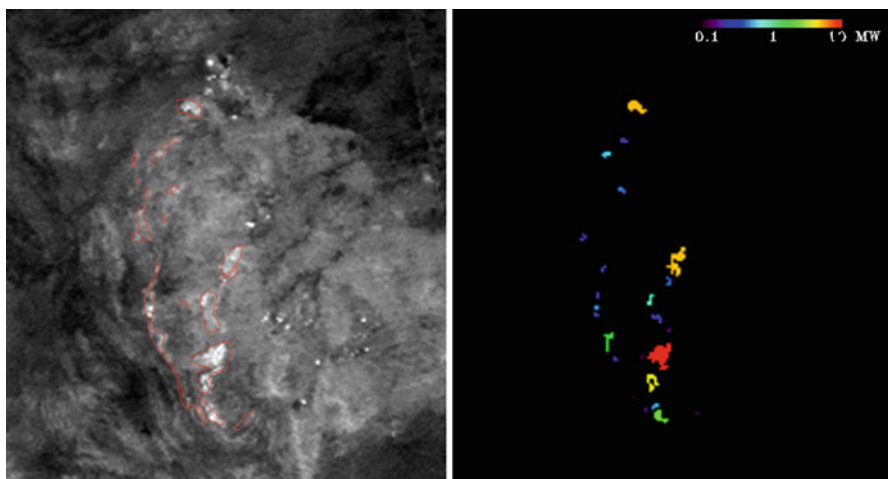


**Fig. 21.12** Coal fire related energy release. *Left:* thermal Landsat-7 ETM+ summer nighttime image from 2002 with red fire outlines overlain on thermal satellite data. *Right:* energy release in MW for the individual coal fires as mapped in situ. Polygons defining an area need to be available so that the algorithm can calculate a fire's energy release. The subset shows  $20 \times 20$  km and represents the Wuda coal mining syncline, UL:  $39^{\circ}36'16''N$ ,  $106^{\circ}30'50''E$ , LR:  $39^{\circ}27'59''N$ ,  $106^{\circ}43'19''E$ , 1,130 m asl. Tetzlaff (2004)

be extracted with thermal data available at a resolution equal to or below 60 m. Furthermore, even if more or less exact coal fire outlines are available from field campaigns, the fire related energy release is hard to determine.

It fluctuates on a daily basis depending on underground processes, precipitation, wind, and changes in the overlying bedrock. Therefore, time series of thermal data would be needed to retrieve representative energy release. Furthermore, coal burning underground might not always lead to surface anomalies. Independent of available data, the calculation of burnt coal amounts based on energy release will always lead to an underestimation of the truly burned coal. Due to all these difficulties and uncertainties, no hard baselines as needed for emission trading protocols can be established.

**Table 21.1** Interrelationships of public, political and economic consequences with regard to low or high estimates of coal fire related greenhouse gas emission

	Low GHG emission number [%]	High GHG emission number [%]
Public attention	Less	More
Research funding money	Less	More
Probability of incorrect estimation	Very low	Very high
Political consequence in investing country	Low economic benefit and probably limited interest in pursuing CDM activities	High economic benefit for single companies, strong interest in pursuing CDM related activities, technology transfer means additional economic benefit
Political consequence in country of emission origin	Probably none. However, country could “proudly” present how harmless the fire problem is	Competition might occur. Country with emissions might be able to choose contractor. Networking
Economic consequence in investing country	Receives fewer (lower) certificates, less extra output “at home” possible	Receives more (higher) certificates, more extra output “at home” possible
Economic consequence in country of emission origin	Need to minimize its own emissions (if capable), less transfer of technology, know-how and ideas from outside the country	Large international projects lead to transfer of technology, know- how, and ideas from outside the country

Source: Kuenzer et al. (2007c)

However, coal fire emission estimation is also very tricky due to political and other biases influencing the numbers that were released in recent years. Table 21.1 suggests that higher greenhouse gas emission numbers might be motivated by authors wanting to generate interest in their own research topic, and even by the desire to obtain higher research funding. Emission estimates furthermore will have an impact on the amount of governmental funding for extinguishing fires. It is thus very hard to find reliable numbers in literature. In our opinion the most transparent article was published by Van Dijk et al. (2011).

## 21.6 Existing Gaps in Coal Fire Research

In the following, challenges for coal fire related remote sensing which are not yet fully solved are indicated.

Most prominent coal fire locations in this world are relatively well known. However, up to now no remote sensing scientists have assessed all these fires based on the same data types, with the same methods, and in a comparable manner. Most scientists have focussed on one specific area, where in-situ validation data was available. However, a global, standardized coal fire monitoring system considering

thermal imagery of the fire areas over a period of several years is urgently needed. Even if fire locations are roughly known it is important to observe the fire's dynamics, to monitor extinguishing activities and their aftermath, and to look for new ignitions in the vicinity of existing fires. The shortcomings here relate to TIR (Thermal infrared) sensor availability and data access over a long period of time.

Furthermore, so far no proper relationships between coal fire related energy release and the amount of coal burnt and greenhouse gasses released could be established. Even though this is a complex endeavour due to a number of unknowns, also here one limiting factor is the lack of frequent data availability at a suitable resolution.

A perfect sensor for coal fire related thermal analyses would be a sensor which contains highly resolved bands in the optical domain (better than 5 m, optimally even 1 m) which allow for mapping coal fire related subsidence, cracks, and even mineralogical features, accompanied by two thermal bands; one in the 3–5  $\mu\text{m}$  domain, and one in the 8–12  $\mu\text{m}$  domain. These thermal bands should allow for a spatial pixel resolution of better than 50 m. The two thermal bands would allow differentiation of the very hottest anomalies from average coal fire induced anomalies. Citizen science – the concept of in situ data collection and publication by non-scientists – could lead to the supply of in-situ gas and temperature measurements via smartphones; currently still a vision, but probably one that is not too far away. Currently, the most important need is for a strong lobby for thermal infrared sensors on board future earth observation platforms.

## 21.7 Conclusions

Thermal remote sensing of coal fires belongs to one of the more complex and challenging tasks in thermal infrared remote sensing. The reason is that coal fires can occur as surface but also – and predominantly – as underground fires. Thermal anomalies on the bedrock surface are very subtle and usually only cover a fraction of a thermal pixel. Unlike very hot lava or forest fires, coal fire heat is either transported via slow conduction processes to the overlying bedrock surface, or via the convection of very hot gasses through vents, cracks, and fissures. The thermal phenomena are usually of subpixel extent, and overall pixels temperatures are only elevated a few degrees against the background. The challenge in coal fire remote sensing therefore lies in the detection of very subtle thermal anomalies. Moving window approaches allowing extraction of relative thresholds based on sub-image histograms are to date the best choice for coal fire related thermal anomaly extraction. However, automatically extracted anomalies can still stem from other heat sources. Therefore, the availability of additional data and indicators (geologic maps indicating coal underground, multispectral data for the extraction of pyrometamorphic rock, patches of degraded vegetation, or a severely cracked bedrock surface) supports thermal coal fire mapping. From 2013 onwards, sensors such as the Landsat ETM+ follow on (Landsat Data Continuity Mission, LDCM)

containing a thermal band will re-activate coal fire researchers to address the still existing challenges. These are the long-term monitoring of coal fire dynamics, the derivation of coal fire related energy release, and last but not least approximating coal fire related greenhouse gas emission.

**Acknowledgements** The authors thank two anonymous reviewers for their valuable comments on the manuscript. Further thanks go all our friends and colleagues who supported our coal fire research in the last years, especially to Sun Yulin, Jia Yaorong, Glenn Stracher, Paul van Dijk, and Wolfgang Wagner.

## References

- Agarwal R, Singh D, Chauhan DS, Singh KP (2006) Detection of coalmine fires in the Jharia coal field using NOAA/AVHRR data. *J Geophys Eng* 3:212–218
- Banerjee SC (1982) A theoretical design to the determination of risk index of spontaneous fires in coal mines. *J Mine Metal Fuel* 30:399–406
- Banerjee SC (1985) Spontaneous combustion of coal and mine fires. A.A. Balkema, Rotterdam, 168pp
- Banerjee SC, Nandy DK, Banerjee DD, Chakravorty RN (1972) Classification of coal with respect to their susceptibility to spontaneous combustion. *Trans Min Metall Inst India* 59(2):15–31
- Bell FG, Bullock SET, Halbich TFJ, Lindsay P (2001) Environmental impacts associated with an abandoned mine in the Witbank Coalfire, South Africa. *Int J Coal Geol* 45:195–216
- Bhattacharya A, Reddy CS (1994) Underground and surface coal mine fire detection in India's Jharia coalfield using airborne thermal infra-red data. *Asian Pac Remote Sens* 7:59–73
- Bhattacharya A, Reddy CS, Mukherjee T (1991) Multi-tier remote sensing data analysis for coal fire mapping in Jharia coalfield of Bihar, India. In: Proceedings, Asian conference on remote sensing, Singapore, 12th, National University of Singapore, pp 22/1–22/6
- Cassells CJS (1997) Thermal modelling of underground coal fires in northern China. PhD thesis, International Institute for Aerospace Survey and Earth Sciences (ITC), Enschede, The Netherlands, ITC dissertation no. 51, 183pp. ISBN 90-6164-234-5
- Chiaken RF, Brennan RJ, Heisey BS, Kim AG, Malenka WT, Schimmel JT (1998) Problems in the control of anthracite mine fires: a case study of the Centralia mine fire. Report of Investigations 8799, U.S. Department of the Interior, Pittsburgh, 68pp
- Chatterjee RS (2006) Coal fire mapping from satellite thermal IR data – a case example in Jharia coalfield, Jharkhand, India. *ISPRS J Photogramm Remote Sens* 60:113–128
- Chen L (1997) Subsidence assessment in the Ruqigou coalfield, Ningxia, China, using a geomorphological approach. MSc thesis, ITC, Enschede, The Netherlands
- Coates DA, Heffern EL (2000) Origin and geomorphology of clinker in the Powder River Basin, Wyoming and Montana. In: Miller R (ed) Coal bed methane and tertiary geology of the Powder River Basin, 50th annual field conference guidebook. Wyoming Geological Association, Casper, pp 211–229
- Coates DA, Heffern EL, Naeser CW, Reiners P (2005) Coal bed fires – a long history of burning and change in the northern Great Plains. In: Proceedings of the international conference on coal fire research, Beijing, China, 29 Nov–01 Dec, pp 98–101
- Coward HF (1957) Research on spontaneous combustion of coal in mines – a review. Safety in Mines Research Establishment Research Report (SMRE), report no. 142, USA, 57pp
- Cracknell AP, Mansor SB (1992) Detection off sub-surface coal fires using Landsat Thematic Mapper data. *Int Arch Photogramm Remote Sens* 29(b7):750–753

- Elick JM (2001) Mapping the coal fire at Centralia, Pa using thermal infrared imagery. *Int J Coal Geol* 87(3, 4):197–203
- Ellyett CD, Fleming AW (1974) Thermal infrared imagery of the Burning Mountain coal fire. *Remote Sens Environ* 3:79–86
- Finkelman RB (2004) Potential health impacts of burning coal beds and waste banks. *Int J Coal Geol* 59:19–24
- Gangopadhyay P (2006) Application of remote sensing to identify coalfires in the Raniganj coalbelt, India. *Int J Appl Earth Obs Geoinform* 8:188–195
- Greene GW, Moxham RM, Harvey AH (1969) Aerial infrared surveys and borehole temperature measurements of coal mine fires in Pennsylvania. In: Proceedings of the sixth international ERIM symposium on remote sensing of environment, 13–16 Oct 1969. University of Michigan, Ann Arbor, pp 517–525
- Hecker C, Kuenzer C, Zhang J (2007) Remote sensing based coal fire detection with low resolution MODIS data. In: Stracher GB (ed) *Geology of coal fires: case studies from around the world*: Geological Society of America, *Reviews in Engineering Geology*, v. XVIII, pp 229–239. doi:[10.1130/2007.4118\(15\)](https://doi.org/10.1130/2007.4118(15))
- Ide ST, Orr FM Jr (2011) Comparison of methods to estimate the rate of CO<sub>2</sub> emissions and coal consumption from a coal fire near Durango, CO. *Int J Coal Geol* 86(1):95–107
- IPCC (2006) 2006 IPCC guidelines for national greenhouse gas inventories. In: Eggleston HS, Buendia L, Miwa K, Ngara T, Tanabe K (eds) Prepared by the National Greenhouse Gas Inventories Programme (NGGIP). IGES, Japan
- Kim AG, Chaiken RF (1993) Fires in abandoned coal mines and waste banks. Bureau of Mines Information Circular 9352 of the United States Department of the Interior, Pittsburgh, 58pp
- Kuenzer C (2005) Demarcating coal fire risk areas based on spectral test sequences and partial unmixing using multi sensor remote sensing data. PhD thesis, Technical University Vienna, Austria, 199pp
- Kuenzer C (2013) Remote and in-situ mapping of coal fires: case studies from China and India. In: Stracher, GB, Sokol EV, Prakash A (eds) *Coal and peat fires: a global perspective*, vol 3: Case studies – coal fires. Elsevier (Accepted for Publication in 2012)
- Kuenzer C, Stracher G (2011) Geomorphology of coal seam fires. *Geomorphology* 138(1):209–222. doi:[10.1016/j.geomorph.2011.09.004](https://doi.org/10.1016/j.geomorph.2011.09.004)
- Kuenzer C, Zhang J, Li J, Voigt S, Mehl H, Wagner W (2007a) Detection of unknown coal fires: synergy of coal fire risk area delineation and improved thermal anomaly extraction. *Int J Remote Sens* 28:4561–4585. doi:[10.1080/01431160701250432](https://doi.org/10.1080/01431160701250432)
- Kuenzer C, Zhang J, Tetzlaff A, Voigt S, van Dijk P, Wagner W, Mehl H (2007b) Uncontrolled coal fires and their environmental impacts: investigating two arid mining environments in north-central China. *Appl Geogr* 27:42–62
- Kuenzer C, Wessling S, Zhang J, Litschke T, Schmidt M, Schulz J, Gielisch H, Wagner W (2007c) Concepts for green house gas emission estimating of underground coal seam fires. *Geophysical Research Abstracts: EGU 2007*, 16–20 Apr 2007, Vienna, (9), p 11716
- Kuenzer C, Hecker C, Zhang J, Wessling S, Wagner W (2008a) The potential of multi-diurnal MODIS thermal bands data for coal fire detection. *Int J Remote Sens* 29:923–944. doi:[10.1080/01431160701352147](https://doi.org/10.1080/01431160701352147)
- Kuenzer C, Bachmann M, Mueller A, Lieckfeld L, Wagner W (2008b) Partial unmixing as a tool for single surface class detection and time series analysis. *Int J Remote Sens* 29(11):3233–3325. doi:[10.1080/01431160701469107](https://doi.org/10.1080/01431160701469107)
- Kuenzer C, Zhang J, Hirner A, Bo Y, Jia Y, Sun Y (2008c) Multitemporal in-situ mapping of the Wuda coal fires from 2000 to 2005 – assessing coal fire dynamics. In: UNESCO Beijing, 2008, *Spontaneous coal seam fires: mitigating a global disaster*. ERSEC ecological book series, vol 4. Tsinghua University Press, Beijing, pp 132–148, 602pp. ISBN: 978-7-302-17140-9
- Kuenzer C, Zhang J, Tetzlaff A, Voigt S, Wagner W (2008d) Automated demarcation, detection and quantification of coal fires in China using remote sensing data. In: UNESCO Beijing, 2008,

- Spontaneous coal seam fires: mitigating a global disaster. ERSEC ecological book series, vol 4. Tsinghua University Press, Beijing, pp 362–380, 602pp. ISBN 978-7-302-17140-9
- Kuenzer C, Zhang J, Sun Y, Jia Y, Dech S (2012) Coal fires revisited: the Wuda coal field in the aftermath of extensive coal fire research and accelerating extinguishing activities. *Int J Coal Geol* 102:75–86. doi:[10.1016/j.coal.2012.07.006](https://doi.org/10.1016/j.coal.2012.07.006)
- Litschke T (2005) Innovative technologies for exploration, extinction and monitoring of coal fires in north China. MSc thesis no. 1239595, University Duisburg-Essen, Institut für Geographie, Abteilung Geologie, 90pp
- Litschke T, Wiegand J, Schloemer S, Gielisch H, Bandelow KF (2005) Detailed mapping of coal fire sites in combination with in situ flux measurements of combustive gases to estimate gas floor balance and fire development. In: Proceedings of the international conference on coal fire research, Beijing, China, pp 161–163
- Pone DN, Hein KA, Stracher GB, Finkelman RB, Annegarn HJ (2007) Potential environmental and health impacts of burning coal in Witbank Coalfield, South Africa. Accepted for ERSEC book series 4 on Coal Fire Research. UNESCO, Beijing
- Prakash A, Gens R, Vekerdy Z (1999) Monitoring coal fires using multi-temporal night-time thermal images in a coalfield in North-west China. *Int J Remote Sens* 20(14):2883–2888
- Renner S (2005) Report on the status of fires at abandoned underground coal mines in Colorado. Unpublished report of the Colorado Division of Mineral and Geology, 41pp
- Rosema A, Guan H, van Genderen JL, Veld H, Vekerdy Z, ten Kate AM, Prakash A, Sharif M (1999) Manual of coal fire detection and monitoring. Report of the project: development and implementation of a coal fire monitoring and fighting system in China. Utrecht, Netherlands Institute of Applied Geosciences, NITG Publications, 245pp. ISBN: 90-6743-640-2
- Saraf AK, Prakash A, Sengupta S, Gupta RP (1995) Landsat TM data for estimating ground temperature and depth of subsurface coal fire in the Jharia coalfield, India. *J Remote Sens* 16(12):2114–2124
- Stracher GB, Taylor PT (2004) Coalfires burning out of control around the world: thermodynamic recipe for environmental catastrophe. *Int J Coal Geol* 59:7–17
- Stracher GB, Lindsley-Griffin N, Griffin JR, Renner S, Schroeder P, Viellenave J, Masalehdani MNN, Kuenzer C (2007) Revisiting the South Cañon Number 1 Coal Mine fire during a geologic excursion from Denver to Glenwood Springs, Colorado. In: Raynolds RG (ed) Roaming the rocky mountains and environs: geological field trips. Geological Society of America field guide, 10. Geological Society of America, Boulder, pp 101–110
- Stracher GB, Kuenzer C, Hecker C, Zhang J, Schroeder PA, McCormack JK (2012) Wuda and Ruqigou coalfield fires of northern China. In: Stracher GB, Prakash A, Sokol EV (eds) Coal and peat fires: a global perspective, vol 2: Photographs and multimedia tours. Elsevier (Accepted for Publication in 2012)
- Tetzlaff A (2004) Coal fire quantification using Aster, ETM and Bird instrument data. PhD thesis, Geosciences, Maximilians-University, Munich, 155pp
- van Dijk P, Zhang J, Jun W, Kuenzer C, Wolff KH (2011) Assessment of the contribution of in-situ combustion of coal to greenhouse gas emission; based on a comparison of Chinese mining information to previous remote sensing estimates. *Int J Coal Geol* 86(1):108–119. doi:[10.1016/j.coal.2011.01.009](https://doi.org/10.1016/j.coal.2011.01.009), Special Issue RS/GIS
- Wessling S, Kuenzer C, Kessels W, Wuttke MW (2008) Numerical modeling for analyzing thermal surface anomalies induced by underground coal fires. *Int J Coal Geol* 74(3–4):175–184. doi:[10.1016/j.coal.2007.12.005](https://doi.org/10.1016/j.coal.2007.12.005)
- Yang B, Chen Y, Li J, Gong A, Kuenzer C, Zhang J (2005) Simple normalization of multi-temporal thermal IR data and applied research on the monitoring of typical coal fires in northern China. In: Proceedings of the geoscience and remote sensing symposium, IGARSS, Seoul, South Korea, pp 5725–5728
- Yang B, Li J, Chen Y, Zhang J, Kuenzer C (2008) Automated detection and extraction of surface cracks from high resolution Quickbird imagery. In: UNESCO Beijing, 2008, Spontaneous coal

- seam fires: mitigating a global disaster. ERSEC ecological book series, vol 4. Tsinghua University Press, Beijing, pp 381–389. ISBN: 978-7-302-17140-9
- Zhang J (1996) SWIR spectra of rocks in areas affected by coal fires, Xinjiang Autonomous Region, P.R. of China. MSc thesis, ITC, Enschede, The Netherlands, 74pp
- Zhang J (2004) Spatial and statistical analysis of thermal satellite imagery for extraction of coal fire related anomalies. PhD thesis, Technical University, Vienna, 161pp
- Zhang J, Kuenzer C (2007) Thermal surface characteristics of coal fires 1: results of insitu measurements. *J Appl Geophys* 63:117–134. doi:[10.1016/j.jappgeo.2007.08.002](https://doi.org/10.1016/j.jappgeo.2007.08.002)
- Zhang J, Wagner W, Prakash A, Mehl H, Voigt S (2004) Detecting coal fire using remote sensing techniques. *Int J Remote Sens* 25(16):3193–3220
- Zhang J, Kuenzer C, Tetzlaff A, Oettl D, Zhukov B, Wagner W (2007) Thermal characteristics of coal fires 2: results of measurements on simulated coal fires. *J Appl Geophys* 63:135–147. doi:[10.1016/j.jappgeo.2007.08.003](https://doi.org/10.1016/j.jappgeo.2007.08.003)

# Chapter 22

## Thermal Infrared Remote Sensing of Geothermal Systems

Christian Haselwimmer and Anupma Prakash

**Abstract** In areas of anomalously high crustal heat flow, geothermal systems transfer heat to the Earth's surface often forming surface expressions such as hot springs, fumaroles, heated ground, and associated mineral deposits. Geothermal systems are increasingly important as sources of renewable energy, or as natural wonders of protected status attracting tourists, and their study is relevant to monitoring deeper magmatic processes. Thermal infrared (TIR) remote sensing provides a unique tool for mapping the surface expressions of geothermal activity as applied to the exploration for new geothermal power resources and long term monitoring studies. In this chapter, we present a review of TIR remote sensing for investigations of geothermal systems. This includes a discussion on the applications of TIR remote sensing to the mapping of surface temperature anomalies associated with geothermal activity, measurements of near-surface heat fluxes associated with these features as input into monitoring and resource assessment, and the mapping of surface mineral indicators of both active and recently active hydrothermal systems.

### 22.1 Introduction

Geothermal systems occur in regions of anomalously high crustal heat flow that may be related to the presence of young igneous bodies or hot rocks located deeper in the crust (Rybáček 1981; DiPippo 2005). This elevated geothermal heat is normally transferred to the surface by the convection of ground waters that forms hydrothermal systems: surface waters circulate to depth where they are heated and rise to the surface via a subterranean ‘plumbing system’ of closely spaced fractures or other zones of permeable rock. If rising hot waters reach the surface then

---

C. Haselwimmer (✉) • A. Prakash  
Geophysical Institute, University of Alaska Fairbanks, Fairbanks, AK, USA  
e-mail: [chha@gi.alaska.edu](mailto:chha@gi.alaska.edu)



**Fig. 22.1** Examples of geothermal surface features; (a) Hot springs and associated surface deposits at Mammoth Hot Springs, Yellowstone National Park, USA (Image source: Brocken Inaglory, 6th July, 2008, Creative Commons Attribution); (b) Geysers in Yellowstone National Park, USA (Image source: Jim Peaco, National Park Service, September 1999); (c) Fumarole at Námafjall, Iceland (Image source: Wolfgang Sauber, 20th July 2009, Creative Commons Attribution); (d) Mud pot at Akan National Park, Japan (Image source: Arama80, 5th March 2012, Creative Commons Attribution)

characteristic geothermal features such as hot springs, fumaroles, geysers, and mud pots may form (Fig. 22.1) (Heasler et al. 2009).

When the heat contained within fluid filling fractures and permeable rocks is sufficiently accessible, this energy can be exploited for power generation or direct use (geothermal energy). Around the world, geothermal energy accounts for approximately 10,700 megawatts-electric (MWe) of power production with estimates of the potential resource ranging from 35 to 2,000 gigawatts-electric (Fridleifsson et al. 2008). In areas of high crustal heat flow geothermal power offers an attractive, reliable, and low-carbon alternative to traditional fossil-fuel based

energy resources. For example, as of 2010, Iceland produces ~26 % of its nation's energy from geothermal sources (Landsvirkjun 2012). The interest in geothermal power has stimulated increasing efforts to undertake exploration and characterization of these resources around the world.

Studying surface geothermal activity and heat loss associated with magmatic-related systems is important for monitoring of subsurface igneous activity. For example, the abundant geothermal features at Yellowstone National Park are the surface expressions of the largest active volcanic system in North America. Surface hydrothermal activity at Yellowstone has changed over time indicating variations in geothermal system activity that may be in-turn related to changes in magmatic activity (Heasler et al. 2009). In addition, the monitoring of geothermal activity has a role to play in efforts to conserve geothermal systems that are of cultural significance or are economically important tourism destinations; with the increasing development of geothermal resources there is potential to negatively impact these sites (Bromley et al. 2010).

Thermal infrared (TIR) remote sensing provides data with synoptic coverage for investigating the surface manifestations of geothermal systems as applied to both geothermal energy exploration and also for more fundamental research and monitoring. TIR remote sensing provides a method for rapid mapping and quantifying surface geothermal features in support of exploration and assessment of new resources (Hodder 1970; Mongillo 1994; Allis et al. 1999; Mongillo and Graham 1999; Eneva et al. 2006, 2007; Kratt et al. 2006a, b; Coolbaugh et al. 2007; Rockwell and Hofstra 2008; Kienholz et al. 2009; Littlefield and Calvin 2009, 2010; Scherer et al. 2009; Taranik et al. 2009; Haselwimmer et al. 2011; Reath and Ramsey 2011). In addition, TIR data can be used to monitor these features at developed reservoirs that may provide indications of unsustainable resource extraction (Allis 1980; Bromley et al. 2010) or provide estimates of surface heat loss as input to reservoir models (Bromley et al. 2011). The use of TIR data to map and quantify surface geothermal features also supports long term monitoring of magmatic-related and/or protected systems (Watson et al. 2008; Heasler et al. 2009; Seielstad and Queen 2009).

In this chapter, we describe the use of TIR remote sensing for studying geothermal systems. This includes a discussion on the application of TIR remote sensing to the mapping of surface temperature anomalies associated with geothermal activity, the measurement of near-surface heat fluxes associated with these features as input to monitoring and resource assessments, and mapping of surface mineral indicators of both active and recently active hydrothermal systems.

## 22.2 Surface Manifestations of Geothermal Systems

Geothermal systems display surface manifestations when there is sufficient permeability that enables geothermal waters to rise to, and outflow at the surface (DiPippo 2005). Depending upon the temperature and outflow rate of geothermal

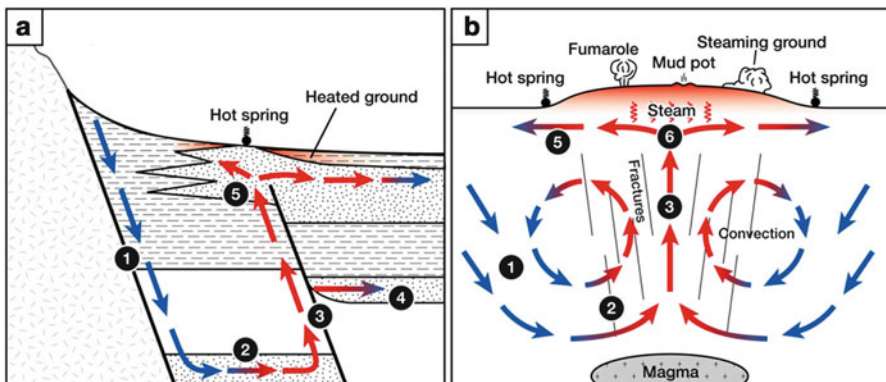


**Fig. 22.2** Schematic diagram of geothermal systems (a) formed by deep circulation of fluids along faults and (b) related to magmatic activity. Arrows indicate direction of flow of meteoric and geothermally-heated waters. Numbers on the figure indicate: 1 zone of recharge of meteoric waters, 2 conductive heating of waters by geothermal source, 3 upflow along fault or fractures, 4 lateral outflow in deep aquifer forming a blind reservoir, 5 outflow in shallow aquifer with associated surface manifestations, 6 boiling of geothermal waters in the subsurface (Source: this work)

fluids, discrete surface features can include hot springs, seeps, fumaroles, geysers, mud-pots, and steam-heated pools. More widespread areas of heated or steaming ground occur due to conductive heat loss above outflow zones containing geothermal fluids and as a result of the direct convective heating from steam or hot water (Rybáček 1981; DiPippo 2005) (Fig. 22.2). The temperatures of geothermal fluids show a considerable range: low-temperature systems ( $<90\text{ }^{\circ}\text{C}$ ) are referred to as spring-dominated as outflow occurs via hot springs or seeps. Systems with intermediate ( $90\text{--}150\text{ }^{\circ}\text{C}$ ) and high ( $150\text{--}240\text{ }^{\circ}\text{C}$ ) temperature fluids are vapor-dominated as these fluids boil in the subsurface, due to lowering hydrostatic pressure, producing steam or water/steam dominated surface features such as fumaroles, geysers, and steaming ground (Rybáček 1981) (Fig. 22.2).

Subsurface geothermal fluids will dissolve minerals in the rocks along the fluid circulation paths that they travel. This can lead to the development of new alteration minerals, such as clays, zeolites, and calcite and the removal of minerals as the dissolved load in geothermal fluids (Glassley 2010). Mineral alteration in geothermal systems reflects the temperature and chemistry of geothermal waters, as well as the composition of the surrounding bedrock. As geothermal waters cool and move away from the heat source, the dissolved mineral load will start to precipitate. In some cases, surface discharge of these fluids forms mineral deposits as the waters cool and the dissolved load precipitates that include: (1) siliceous sinters encompassing various forms of silica deposited by high-temperature fluids ( $>175\text{ }^{\circ}\text{C}$ ); (2) travertine, which is mainly calcium carbonate deposited by lower temperature geothermal fluids; (3) borates, sulfates, and chlorides (Glassley 2010).

Many geothermal systems do not display active surface expressions and are termed 'blind' systems. These may occur when geothermal fluids cool before they

reach the surface or are unable to reach the surface due to lateral flow in deeper aquifers or the presence of impermeable capping layers (Fig. 22.2). Considerable effort has focused on the exploration for blind geothermal resources. Coolbaugh and Shevenell (2004), for example, estimate that these undiscovered geothermal resources in the State of Nevada significantly exceeds the known resources.

### 22.3 Mapping Geothermal Surface Temperature Anomalies

TIR remote sensing data can be used to map and quantify temperature anomalies associated with surface geothermal features such as hot springs, geysers, fumaroles, and heated ground. This approach has been used as a cost-effective tool for geothermal exploration over large areas enabling subsequent selection of targets for further exploration using ground-based surveys (Hodder 1970; Lee 1978; Mongillo 1994; Haselwimmer et al. 2011). In addition, TIR remote sensing has been applied to the cataloguing and long-term monitoring of thermal features associated with developed and protected geothermal systems (Mongillo 1994; Seielstad and Queen 2009).

Much of the published research on the use of TIR remote sensing for mapping surface temperature anomalies has focused on the use of airborne thermal imagery acquired with broadband (Hodder 1970; Lee 1978; Haselwimmer et al. 2011) or multispectral instruments (Mongillo 1994; Seielstad and Queen 2009). High resolution airborne thermal data (i.e. <5 m pixels) enables detailed mapping of surface geothermal features that may be small in size or display limited temperature contrast with surrounding non-geothermal surfaces.

Hodder (1970) acquired pre-dawn broadband thermal imagery (in the 8–14  $\mu\text{m}$  wavelength region) in the region of Long Valley and the Salton Sea, California, USA to map surface geothermal anomalies. Simple visual analysis and application of thresholds to the thermal data provided the basis for identification of hot waters at springs and heated ground overlying faults providing potential indicators of geothermal upwelling zones. Lee (1978) also exploited pre-dawn airborne thermal imagery to map geothermal features in the Black Rock Desert area of Nevada, USA. The thermal data provided an effective method for inventorying known geothermal features and mapping many previously unreported hot springs and related fractures.

Mongillo (1994) utilized a GEOSCAN MkII aerial scanner to acquire 3 m spatial resolution, multispectral TIR data (six bands in the 8.4–11.6  $\mu\text{m}$  wavelength region) during 1992 and 1993 for a 100  $\text{km}^2$  area covering the Waimangu-Waiotapu geothermal region with the aim of mapping and monitoring surface geothermal features. The acquired thermal data was empirically calibrated using in-situ measurements of non-geothermal water bodies and the resultant surface temperature data was visually interpreted. The results enabled mapping of all the known and

many previously unidentified geothermal features including hot springs, hot ground, and thermal seeps into lakes. The results clearly outlined that geothermal features at the Waiotapu field occur along lineations providing strong evidence for a fault controlled upflow/outflow of geothermal fluids. Comparison of the results from different years indicates that a large hot spring appeared in the Waimangu geothermal field between the two survey dates, which demonstrates the potential of TIR data for monitoring temporal changes in geothermal surface features.

Seielstad and Queen (2009) used airborne multispectral midwave- (MWIR: 3.6–5.1  $\mu\text{m}$ ) and longwave-infrared (8.1–12.4  $\mu\text{m}$ ) data acquired with an ADS SpectraView and US Fish and Wildlife Service (USFWS) ‘Firemapper’ system respectively to map and monitor thermal features in the Norris Geyser Basin, Yellowstone National Park. The ~1–3 m spatial resolution data acquired during daytime and nighttime surveys in 2005 and 2006 were calibrated to surface kinetic temperature values with an empirical correction using in-situ temperature measurements. The TIR data enabled detailed mapping of surface geothermal phenomena in the Norris Geyser Basin including discrete features such as hot springs and geysers as well as ‘background’ areas of sinter and heated ground. Seielstad and Queen (2009) used the data to broadly delineate the geographic boundaries of the Norris Geyser Basin that was previously poorly defined. In addition, more detailed mapping of a series of sub-basins within the Norris Geyser Basin was also undertaken. For the 2005 data, snow fall prior to the survey facilitated the mapping of geothermal ground that was snow free in contrast to the surrounding snow covered non-geothermal areas.

Haselwimmer et al. (2011) acquired ~1 m spatial resolution airborne thermal imagery using a broadband FLIR (Forward Looking Infrared) systems A320 camera (operating in the 7.5–13  $\mu\text{m}$  wavelength region) during fall and winter-time surveys over Pilgrim Hot Springs located near Nome in Western Alaska. The TIR data was calibrated to surface temperature values using a combination of MODTRAN (MODerate resolution atmospheric TRANsmission) and an empirical adjustment with in-situ temperature measurements. Georeferencing of the data was undertaken using the GPS positions of low-emissivity thermal blankets that provided distinctive ‘cold’ targets in the TIR imagery. The mosaicked and calibrated data enabled the detailed mapping of known and previously unmapped geothermal features including hot springs and pools, thermally anomalous ground (Fig. 22.3), and ice free-areas on the nearby Pilgrim River that indicated geothermal outflow at a distance from the known spring’s site. In particular, this data provided very detailed information on the location and temperature of hot springs and sources of more diffuse geothermal outflow that were not obvious from field investigations. Mapping these features indicated two broad swaths of generally high temperature and low temperature springs that suggested the presence of an elongated zone of permeability, possibly related to an N-S oriented fault. The 2011 TIR data, acquired during Alaskan winter-time conditions, was effective for mapping areas of heated ground that appeared as areas of anomalous snow-melt. These areas did not display anomalous surface temperatures in the fall 2010 survey, due to the presence of vegetation cover or the effects of solar heating.

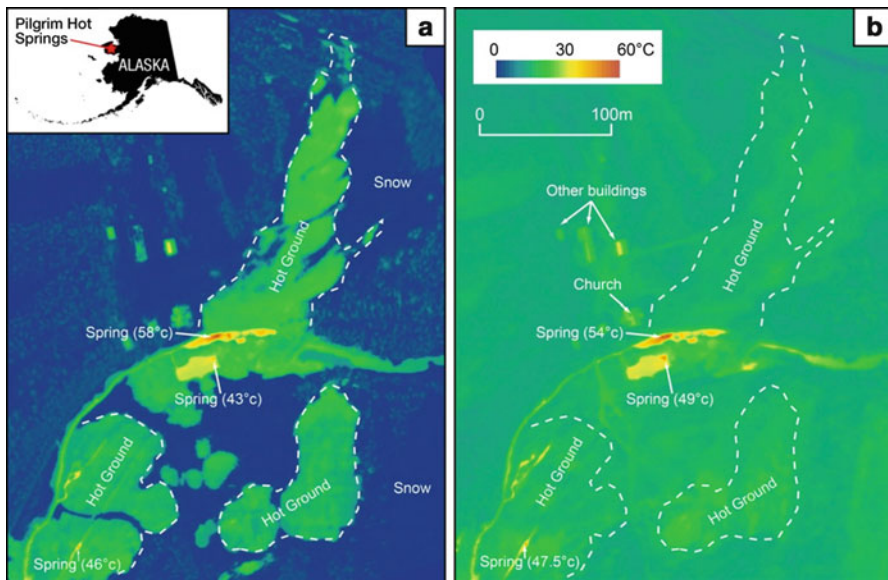


**Fig. 22.3** Calibrated surface temperature data for part of Pilgrim Hot Springs acquired during winter 2011 (a) and fall 2010 (b) airborne surveys using a FLIR thermal camera. This data highlights the location of hot springs, hot pools and areas of heated ground as manifested in areas of anomalous snow melt in the winter 2011 data (From Haselwimmer et al. 2011)

Although coarse spatial resolution satellite thermal sensors (60–90 m pixels), such as Landsat or ASTER, have limited potential for detailed mapping of discrete geothermal features a number of studies have exploited these datasets for broader scale detection of geothermal anomalies (Coolbaugh et al. 2007; Eneva et al. 2007; Eneva and Coolbaugh 2009; Kienholz et al. 2009). These studies have commonly applied data processing techniques to enhance and detect what may be subtle surface temperature anomalies. At the resolution of satellite TIR data, pixels corresponding to geothermal areas normally record a mixture of emitted radiance from geothermal sources as well as from background non-geothermal surfaces. This acts to reduce the measured temperature of pixels corresponding to geothermal sources. When this is compounded by other environmental factors such as land surface type, topography, albedo, and thermal inertia then it can be difficult to locate geothermal anomalies with confidence.

Kienholz et al. (2009) used multi-temporal Landsat thermal data to map geothermal anomalies on the Island of Akutan located on Alaska's Aleutian Arc. Twelve summertime cloud-free scenes were selected from the Landsat archive corresponding to acquisitions over Akutan Island between 1985 and 2008. The Landsat thermal bands were calibrated to surface kinetic temperature and an image stacking procedure was used to highlight persistent surface temperature anomalies and subdue background transient temperature effects associated with local scene specific conditions. As some persistent temperature effects remained after stacking,

the results were further classified based upon elevation, slope, vegetation type and geology. This processing strategy mapped the locations of the known fumarole field and thermal springs and also revealed three new distinct regions of surface thermal anomalies providing targets for field investigations.

A number of studies have used ASTER (Advanced Spaceborne Thermal Emission and Reflection Radiometer) data to detect surface geothermal anomalies by minimizing the temperature variations caused by diurnal solar heating effects (Coolbaugh et al. 2007; Eneva et al. 2007; Eneva and Coolbaugh 2009). Factors such as albedo, topographic slope/aspect, emissivity, and thermal inertia affect the temperature changes of Earth surfaces over the 24-h temperature cycle (Taranik et al. 2009). These variations potentially mask subtle temperature anomalies related to subsurface geothermal heating in TIR data. An example of this is the main sinter terrace at Steamboat Springs, Nevada, USA, where pre-dawn TIR images do not detect a thermal anomaly in spite of their being numerous fumaroles present at the site (Taranik et al. 2009). This is explained by the high albedo of the sinter that reflects much of the sun's energy during the day, and its low thermal inertia, which causes it to cool off rapidly at night.

In a study of Brady's Hot Springs, Nevada, USA, Coolbaugh et al. (2007) processed a day/night pair of ASTER scenes (acquired on the same date) to minimize the effects of diurnal heating. Using the ASTER Level 2 on-demand surface kinetic temperature product (AST08), Coolbaugh et al. (2007) applied corrections for albedo, topographic slope, and thermal inertia based upon a simplified heat energy model describing net surface radiation flux. Surface temperature variations related to differences in albedo were corrected using the ASTER visible and infrared bands and a Digital Elevation Model (DEM) was used to correct for the effects of topographic slope and aspect. The impact of thermal inertia on surface temperature was corrected using mean surface temperatures for the diurnal cycle derived by adjusting the average of the ASTER day/night pair using field measurements of ground surface temperatures made over the same 24-h period (Coolbaugh et al. 2007). The resultant processed image (Fig. 22.4) shows that background variations in temperature were reduced by 30–50 % whilst the intensity values of geothermal anomalies were retained. This made it easier to distinguish geothermal activity from false thermal anomalies associated with variations in topography, rock/soil types, and non-thermal springs (Coolbaugh et al. 2007).

Eneva et al. (2006) applied a simplified version of the method used by Coolbaugh et al. (2007) to map thermal anomalies in the Coso geothermal field, California, USA, also using a daytime/nighttime pair of ASTER images. In this study, the correction for thermal inertia effects was simplified due to the lack of field measurements of surface temperatures over the 24 h cycle. In spite of this, the processed ASTER data was effective in enhancing some thermal anomalies and suppressing false positives.

Whilst the method of Coolbaugh et al. (2007) is effective at enhancing geothermal anomalies and suppressing many non-geothermal effects, there are several limitations of this approach. The method uses a simplified surface energy balance model that does not account for sensible and latent heat losses. The assumption of radiation being the main control on heat loss is valid for dry non-vegetated ground,

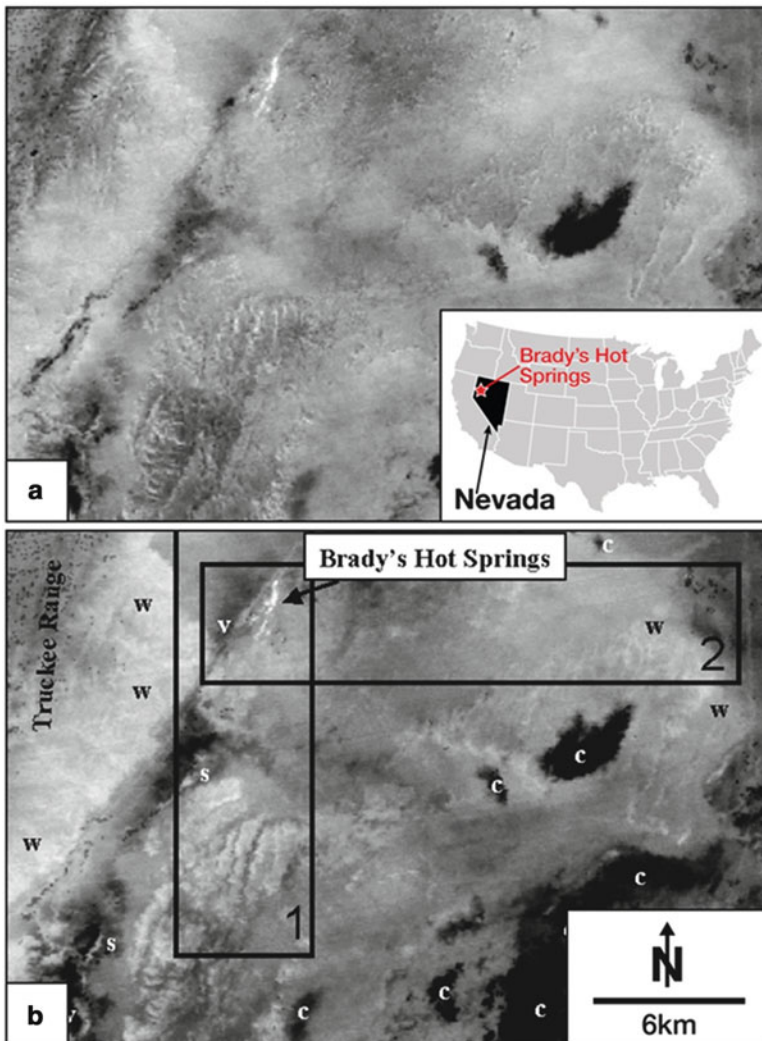


**Fig. 22.4** ASTER day-night image for the Brady's Hot Springs area processed to minimize variations in temperature related to albedo, topographic slope/aspect, and thermal inertia (a) and unprocessed ASTER nighttime surface kinetic temperature (AST08) image (b). Around 34–53 % of temperature variation in (b) has been removed in (a) as evidenced from the variances in temperature of the areas encompassed in boxes 1 and 2. This processing has resulted in the Fumaroles at Brady's Hot Springs being more readily discernible. Abbreviations: c clouds, s ground water springs, v vegetation, W 'warm' ground (Adapted from Coolbaugh et al. 2007)

such as is commonly encountered in the Great Basin of the Western US, but will not hold for areas of moist ground or vegetation where heat loss will be dominated by evaporation and transpiration (Coolbaugh et al. 2007). Eneva and Coolbaugh (2009) describe how elevation and temperature inversions may effect ASTER surface temperature values and that these factors should ideally be taken into account when processing thermal images to enhance geothermal anomalies.

## 22.4 Quantifying Geothermal Heat Fluxes

Hot springs, fumaroles, mud-pots, and steaming or heated ground are the surface expressions of conductive and convective heat loss from geothermal systems. As described in the previous section, TIR remote sensing provides a means to map the spatial distribution, extent, and temperature of these features that can in turn be used to estimate the conductive and convective heat loss near the surface. The measurement of this surface heat loss (aka. the near surface Geothermal Heat Flux – GHF) is important for long-term monitoring of geothermal systems (Heasler et al. 2009), can be used to assess the resource potential of undeveloped geothermal reservoirs (Wisian et al. 2001), and also be applied to monitoring and modeling of developed resources (Allis 1980).

Although TIR remote sensing has been widely used to monitor heat loss from volcanoes (e.g. Pieri and Abrams 2004; Carter et al. 2008), it has been applied less in the monitoring of geothermal or hydrothermal systems. Much of this work has focused on Yellowstone National Park. Airborne thermal surveys of the Norris Geyser basin acquired between 2002 and 2006 have been used to map surface geothermal activity and monitor the associated GHF (Seielstad and Queen 2009) (Fig. 22.5). Seielstad and Queen (2009) estimated a lower bounds for the GHF by calculating emitted radiation from the calibrated surface temperature values (derived from the airborne thermal imagery) using the Stefan-Boltzmann equation:

$$M = \sigma T^4 \quad (22.1)$$

where  $M$  is emitted radiation in units of  $\text{W m}^{-2}$ ,  $\sigma$  is the Stefan-Boltzmann constant ( $5.667 \times 10^{-8}$ ), and  $T$  is the surface radiant temperature in Kelvin. For geothermal features the emitted radiation from surfaces at background temperatures was subtracted to leave just the emitted radiation related to the geothermal activity. Rather than using a single value for the background flux, the flux was calculated for each land cover type. For example, the background flux of vegetation outside the geothermal areas was used to correct flux values of vegetated patches within elevated temperature areas. Using this approach Seielstad and Queen (2009) estimated the GHF for Norris Geyser Basin from 2002, 2005, and 2006 airborne thermal data to be 136, 137, and 114 megawatts of thermal energy ( $\text{MW}_{\text{th}}$ ), respectively. Given the uncertainty in background flux, combined with noise from calibration and emissivity separation, Seielstad and Queen (2009) concluded that there was no detectable change in the GHF over this period. Seielstad and Queen (2009) also highlighted that from a synoptic perspective most of the geothermal heat loss did not occur from discrete high temperature features, such as hot springs or fumaroles, but from the more spatially extensive areas of ‘background’ thermally anomalous ground.

Watson et al. (2008) mapped a lower bound for the surface GHF for Yellowstone National Park using Landsat 7 ETM+ (Enhanced Thematic Mapper Plus) data by calculating a residual terrestrial emittance anomaly (TEA) for snow free areas using

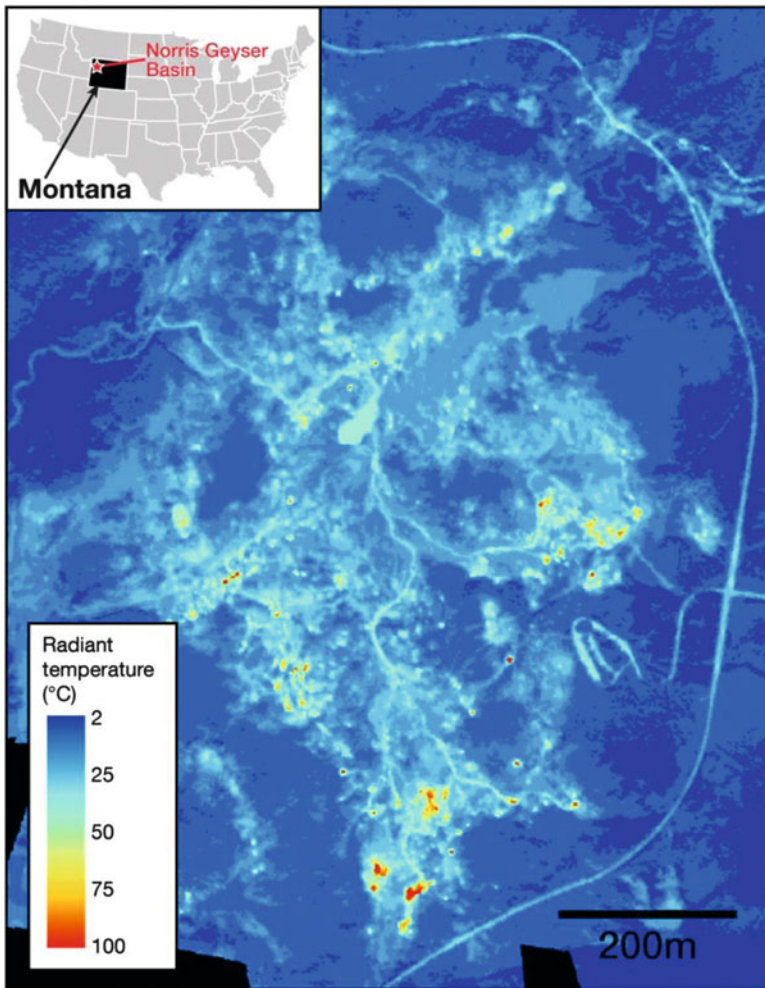


**Fig. 22.5** Radiant temperature values (in °C) for Norris Geyser Basin, Yellowstone National Park, USA, acquired on October 06, 2005 between 1 and 3 pm using ADS SpectraView system (From Seielstad and Queen 2009)

a surface energy balance model. In this model, terrestrial emittance ( $M_{terr}$ ) represents one component in a system of fluxes at the surface that balances heat losses against heat gains:

$$M_{terr} + H_S + H_L + H_Q = GHF + S - R + M_{down} - M_{refl} + H_p + \Delta \quad (22.2)$$

where  $S$  and  $R$  are incident and reflected total solar radiation,  $H_S$  and  $H_L$  are sensible and latent heat exchange with the atmosphere,  $H_p$  and  $H_Q$  are advected heat flux in precipitation and runoff, and  $\Delta$  accounts for change in storage in the subsurface.

Based upon a simplified version of this surface energy balance equation Watson et al. (2008) calculated the TEA as the residuals of a multiple linear regression model linking surface heat losses to the surface temperature and non-geothermal heat gains to elevation and absorbed solar radiation. The latter was derived from a simple model of solar irradiation of hilly terrain, and surface albedo estimated from summation of the non-thermal bands of the ETM+ data (Watson et al. 2008). Using this approach, Watson et al. (2008) mapped the TEA with values ranging from 0 up to  $94 \text{ W m}^{-2}$  throughout Yellowstone National Park that clearly discriminated geothermal from non-geothermal areas. The TEA results were validated against values of GHF calculated from the inversion of a snowpack model. Comparison of TEA and GHF values showed good agreement although the TEA was consistently lower and therefore provided a lower bound on GHF for the Yellowstone geothermal system (Watson et al. 2008).

Vaughan et al. (2011) analyzed ASTER and MODIS (Moderate Resolution Imaging Spectroradiometer) thermal data for Yellowstone National Park acquired in the 2000–2010 period with the aim of monitoring surface geothermal activity by calculating the radiant component of heat loss for geothermal areas. This study aimed to identify normal background thermal changes so that significant or abnormal changes related to geothermal activity could be recognized. Frequent but low resolution (1 km) MODIS data were analyzed and a method for subtracting the seasonal variation in background thermal flux was developed. Analysis of the MODIS data using this method indicated that all of the thermal areas were stable during the 2000–2010 period. Vaughan et al. (2011) used higher spatial resolution but less frequently acquired ASTER thermal data to calculate radiant GHF for the whole of Yellowstone National Park that resulted in an estimate of  $\sim 2 \text{ GW}_{\text{th}}$  (gigawatts thermal energy), which is somewhat lower than the value of 4–6  $\text{GW}_{\text{th}}$  calculated from geochemical methods.

A number of studies have applied airborne TIR remote sensing to estimate geothermal heat flow in support of the assessment of new geothermal prospects and monitoring of existing developed resources (Allis et al. 1999; Mongillo and Graham 1999; Bromley et al. 2011; Haselwimmer and Prakash 2011). Allis et al. (1999) analyzed pre-dawn airborne thermal imagery over the Dixie Valley (Nevada, USA) and Wairakei (New Zealand) developed geothermal fields with the aim of mapping the near-surface conductive component of GHF. Using in-situ shallow temperature measurements and a fixed value of soil thermal conductivity ( $\sim 0.5 \text{ W/m}^{\circ}\text{C}$ ), Allis et al. (1999) established an empirical relationship between surface conductive heat flow and thermal infrared surface temperature values for areas of heated ground. Although this approach provided a simple method of converting TIR imagery into surface heat flow maps, Allis et al. (1999) point out a number of significant limitations and uncertainties with this approach: (1) the ‘ambient’ temperature of non-geothermal ground must be in the range 15–20 °C; (2) the surface soil temperature for geothermally heated ground must be less than 90 °C so that steam does not affect TIR-derived temperature values; (3) the effects of solar heating, emissivity or rainfall should be minimized. Mongillo and

Graham (1999) applied the same empirical approach to estimate conductive heat flow using airborne thermal data acquired over part of the Taupo geothermal area in New Zealand. Moreover, they mapped anomalous geothermal features with temperatures  $>2$  °C above background and estimated a conductive heat flow of  $\sim 2.5$  MW<sub>th</sub> that was supporting these features.

Bromley et al. (2011) used airborne thermal imagery to estimate the heat flux associated with steaming ground at the Wairakei-Tauhara geothermal system in New Zealand. Three different approaches were applied to the airborne thermal data to calculate the heat flux associated with steam-heated ground:

1. For thermally anomalous ground, areas of steam heating were delineated (based upon a dip in expected surface temperature related to the presence of steam) and surface temperature values for these areas were used to derive boiling point depths that then formed the basis of heat flux estimates using an empirical relationship.
2. For areas of steam-heating, the heat flux was directly calculated using an empirical relationship between heat flux and the temperature difference between steam-heated ground and ambient atmosphere.
3. For areas of steam-heated ground, the thermal flux was calculated directly from the surface temperature data by accounting for radiative, convective and conductive heat fluxes from anomalously hot ground to the air.

Bromley et al. (2011) produced consistent values for heat flux associated with steam heated ground of 35.6, 33.4, and 32.4 MW<sub>th</sub> respectively for the three different methods. When these measurements were coupled with heat flux estimates from springs, seeps, and craters a total heat flux of  $\sim 86$  MW<sub>th</sub> was calculated for the Wairakei-Tauhara area.

Haselwimmer and Prakash (2011) used airborne thermal imagery acquired over Pilgrim Hot Springs during two surveys to quantify the convective heat flux and corresponding outflow rate of surface geothermal fluids as input into the resource assessment of this undeveloped system. The convective geothermal heat flux associated with surface geothermal fluids (i.e. hot springs, hot pools) was estimated from calibrated TIR surface temperature data for areas of hot water by accounting for radiative, evaporative, and sensible heat losses as well as heat gains from the geothermal source, incoming solar and atmospheric TIR radiation. Using this approach, the total convective heat flux supporting geothermal fluid outflow was conservatively estimated at  $\sim 3.65$  MW<sub>th</sub>, which corresponded to a flow rate of  $\sim 195$  gallons per minute (GPM), assuming a fixed hot spring temperature of 81 °C. This value for the hot spring heat flux was higher than previous estimates of  $\sim 2$  MW<sub>th</sub> of energy that was derived from in-situ measurements of the flow rate of the hot springs. Given the difficulty in determining the flow rate of diffuse hot springs/seeps and the lack of well confined outflow at Pilgrim Hot Springs, Haselwimmer and Prakash (2011) suggest that the airborne thermal imagery provides a more realistic estimate of the total hot spring heat flux and flow rate.

## 22.5 Mapping Geothermal Indicator Minerals

Surface minerals commonly deposited or produced from geothermal waters or hydrothermal alteration have spectral absorption features in the visible to thermal infrared wavelength regions related to electronic and molecular vibrations. These spectral absorption features provide the basis for mapping of these materials using multispectral and hyperspectral remote sensing that can map both active and blind geothermal systems (Kratt et al. 2006a, b).

Numerous studies have exploited the visible/near-infrared to shortwave infrared (VNIR/SWIR) wavelength region for mapping hot spring deposits and related bedrock alteration products using multispectral (Kruse 2002; Hellman and Ramsey 2004; Kratt et al. 2006a, b) and hyperspectral (Hellman and Ramsey 2004; Nash et al. 2004; Kratt et al. 2006a, b; Littlefield and Calvin 2010) remote sensing. In the 0.4–2.5  $\mu\text{m}$  wavelength region, mineral spectral absorption features record the interaction of light with cations (Fe, Mg, Al), and anions (OH,  $\text{H}_2\text{O}$ ,  $\text{CO}_3$ ) in mineral structures (Hunt 1977). Minerals displaying diagnostic absorption features that occur in and typify hydrothermal alteration systems include hydroxyl bearing clays, sulfates, carbonates, and sinters (Huntington 1996).

In the TIR wavelength region, mineral groups including silicates, carbonates, sulfates, phosphates, and hydroxides display diagnostic spectral absorption features (reststrahlen features) that appear as emissivity minima, which are related to fundamental molecular vibrations within different anion groups such as  $\text{CO}_3$ ,  $\text{SO}_4$ ,  $\text{PO}_4$ , and  $\text{SiO}_4$ . Further, the stretching and bending modes of major cations (e.g. Mg, Fe, Ca, Na) provide the basis for detailed discrimination of mineral species and excellent identification of specific silicate and carbonate minerals (Christensen et al. 2000). At TIR wavelengths the spectral emission properties of mixed materials can be considered to represent the linear combination of the constituents spectra weighted by their areal proportion (Hapke 1993). This provides the basis for quantitative estimation of the modal compositions of mixed thermal emission spectra based upon approaches such as linear spectral deconvolution (Ramsey and Christensen 1998). Typical minerals deposited by hot springs or associated with hydrothermal alteration display unique spectral emission features in the thermal infrared (Fig. 22.6). Although many minerals of importance for geothermal exploration do display distinctive absorption features in the VNIR/SWIR region, emission data provides capabilities in particular for discrimination of silicate and carbonate minerals. The synergistic use of VNIR/SWIR and TIR spectral data provides the greatest potential for unambiguous mapping of specific mineral occurrences in support of geothermal exploration (Riley et al. 2008).

Most research on the application of thermal emission data for mapping geothermal indicator minerals has focused on the use of the airborne SEBASS (the Spatially Enhanced Broadband Array Spectrograph System) and MASTER (MODIS-ASTER Airborne Simulator) instruments particularly for study sites located in the Great Basin of the Western United States. SEBASS is an airborne pushbroom hyperspectral imaging spectrometer designed by the Aerospace Corporation that acquires

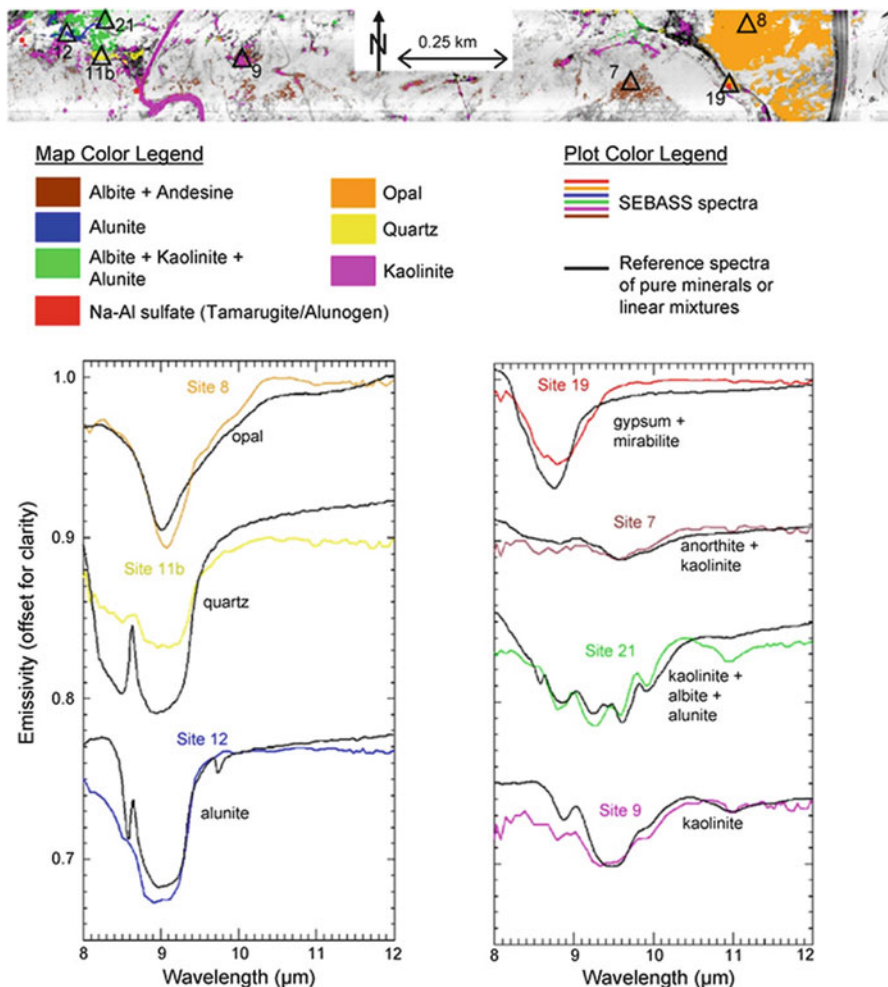


**Fig. 22.6** Top: results of mineral mapping using SEBASS data for Steamboat Springs – mapped minerals are shown in the different colors overlaid onto a gray-scale emissivity image. Bottom: SEBASS spectra (colored lines) for the field localities indicated by triangles on the mineral map shown next to pure and mixed mineral library spectra (black lines) (From Vaughan et al. 2005)

256 channels of data, 128 in the 2.5–5.2 and 128 in the 7.5–13.5  $\mu\text{m}$  wavelength regions (Hackwell et al. 1996). The MASTER system was designed by the NASA Ames Research Center and the Jet Propulsion Laboratory to simulate the MODIS and ASTER instruments on board the NASA Terra satellite (Hook et al. 2001). MASTER acquires multispectral TIR imagery using 15 and 10 bands covering the 3.1–5.2, and 7.8–12.9  $\mu\text{m}$  wavelength regions, respectively.

Vaughan et al. (2005) have made the most significant contribution to the geothermal remote sensing literature in their study of the Steamboat Springs active

geothermal system in Nevada, USA. This study used high spatial resolution MASTER (5 m) and SEBASS (2 m) thermal emission data acquired on airborne surveys over Steamboat Springs during September 1999. The at-sensor long-wave infrared radiance data for the two instruments were atmospherically corrected using the MODTRAN radiative transfer model (Berk et al. 1989) and the ISAC (In Scene Atmospheric Compensation) (Johnson 1998; Vaughan et al. 2003) algorithm, respectively, followed by temperature-emissivity separation using the TeS, (Gillespie et al. 1998) and emissivity-normalization (Kealy and Gabell 1990) methods. Mineral mapping using SEBASS and MASTER thermal emission data were undertaken using the commonly applied ‘hour-glass’ processing workflow (Kruse et al. 2003) that couples procedures for image data reduction (Minimum Noise Fraction transformation), end-member extraction (Pixel Purity Index), and spectral classification (Spectral Angle Mapper/Matched Filter). The mineralogy of mapped end-member classes were interpreted with reference to the spectra of pure minerals from the ASTER (Baldridge et al. 2009) and Arizona State University (ASU) (Christensen et al. 2000) spectral libraries. For the SEBASS results, linear mixtures of pure mineral library spectra were calculated to approximate the SEBASS end-member spectra and identify the presence of the dominant mixed components. The results of mineral mapping with MASTER data enabled broad discrimination of silica- and sulfate-rich ground (mapped as quartz, alunite, or opal) representing active geothermal areas and clay-rich ground (mapped as kaolinite or montmorillonite) corresponding to areas of hydrothermal alteration. The spectral resolution of the SEBASS data enabled more detailed discrimination of pure minerals and assemblages including opal, quartz, alunite, albite, andesine, kaolinite, and a Na-Al sulfate. These mineral maps provided the basis for mapping of:

1. Opaline sinter formed by recent geyser activity.
2. Chalcedonic sinter (quartz) formed by older geyser activity.
3. Na-Al sulfates formed around active fumaroles.
4. Rocks that have undergone steam heated acid-sulfate alteration.

Vaughan et al. (2005) found that the SEBASS thermal emission data provided the unique capability for discrimination of opaline sinter, which is a primary indicator mineral characteristic of active or recently-active geothermal systems.

More recently, Reath and Ramsey (2011) analyzed SEBASS data acquired during airborne surveys in 2009 and 2010 over the Salton Sea active geothermal field in California, USA. Linear spectral deconvolution (Ramsey and Christensen 1998) was applied to the 128 long-wave infrared channels to map surface mineral assemblages associated with geothermally active areas. Mapped minerals included anhydrite, gypsum, and an unidentified sulfate mineral. Mapping results for the latter indicated variations in abundance and extent between the two data acquisitions suggesting this mineral is of a transitory nature having been formed due to surface and ground water activity. Scherer et al. (2009) integrated SEBASS with the airborne VNIR/SWIR ProspectTIR sensor to acquire full spectrum wavelength hyperspectral data in 600 channels across the VNIR/SWIR, mid-wave, and

long-wave (thermal) infrared regions for the purposes of mineral mapping. The use of this combined system provided complimentary spectral information to map a variety of minerals associated with active and recently active hydrothermal systems.

Littlefield and Calvin (2009) used MASTER data for geothermal exploration in the region of Buffalo Valley, Nevada, USA. Mineral mapping using the MASTER thermal bands discriminated silica- and clay-rich surface materials. The MASTER VNIR/SWIR bands mapped carbonate and green vegetation. Overall, the results were inconclusive in terms of identifying specific geothermal indicator minerals. Littlefield and Calvin (2009) attribute this to either the absence of these surface minerals or to the low spectral resolution of MASTER data that was unable to uniquely identify geothermal minerals.

Although ASTER TIR data (bands 10–14) have been used to map surface temperature anomalies associated with geothermal systems (Coolbaugh et al. 2007) and for broader lithological mapping (Ninomiya et al. 2005) this has not been used extensively in the mapping of specific geothermal indicator minerals. This reflects the low spatial (90 m) and spectral resolution of this instrument that has limited potential for mapping small exposures of minerals produced by hydrothermal activity (Kruse 2002; Littlefield and Calvin 2009). ASTER thermal data does have potential to contribute regional-scale information that could be used to generate exploration targets or provide context for higher spatial resolution airborne surveys. For example, Rockwell and Hofstra (2008) investigated the potential of ASTER thermal emission data to contribute to geological mapping and resource exploration studies across northern Nevada. This work analyzed a regional mosaic of ASTER thermal emission data to map quartz and carbonate minerals. For a number of localities these mineral maps corresponded to siliceous and travertine deposits associated with active hot springs.

## 22.6 Conclusions

TIR remote sensing provides a unique tool for qualitative and quantitative investigations of surface geothermal activity that can be applied to the exploration for new geothermal power resources and the study and monitoring of geothermal systems. Airborne broadband TIR data enable detailed mapping of discrete surface geothermal features such as hot springs and fumaroles as well as more extensive areas of thermally anomalous ground. This supports geothermal power exploration by providing a means to locate unidentified resources as well as enabling detailed mapping of known systems that can contribute to targeting and planning of field work (e.g. using maps of hot spring locations to guide water sampling). Airborne and spaceborne TIR data supports long-term monitoring of geothermal systems by providing a rapid and repeatable method of inventorying surface geothermal features. In addition, methods for relating the temperatures of surface geothermal

phenomena to estimates of near-surface heat loss provide important inputs to the monitoring of geothermal activity and as applied to geothermal resource assessment and modeling. The application of these methods to high resolution airborne TIR data provides estimates of conductive or convective heat loss supporting specific surface geothermal features. This information can provide system-wide estimates of near-surface heat loss, when integrated over the larger geothermal area. Time series of these data may indicate changes in geothermal activity related to deeper-seated magmatic unrest, hydrological changes, or caused by unsustainable production of developed geothermal reservoirs. The increasing availability of low-cost broadband and multispectral TIR imaging systems, Unmanned Aerial Systems (UAS), and advanced image processing software (particularly for automated image registration and mosaicking) will reduce the costs of acquiring high spatial resolution airborne TIR imagery over large areas. This will support the use of airborne TIR imaging as a routine tool for exploration and monitoring of geothermal systems.

Although the spatial resolution of satellite TIR data is too coarse to investigate specific geothermal features at this time it has an important role to play in geothermal exploration and monitoring. Approaches to enhancing geothermal anomalies in TIR data have potential to facilitate the mapping of undiscovered resources, including blind systems, over large areas and at low-cost. The repeat coverage of satellite TIR sensors also provides a crucial capability for long-term monitoring studies and augments airborne surveys by providing rapid, basin-wide estimates of geothermal heat loss in a consistent and repeatable manner. Exploration and monitoring of geothermal systems will be supported by current and future satellite TIR imaging instruments. In particular, the enhanced spatial and temporal resolution of the proposed NASA HyspIRI (Hyperspectral Infrared Imager) instrument has the potential to enhance monitoring capabilities.

Airborne hyperspectral thermal emission data, whilst currently not routinely used for mapping of surface mineral deposits or alteration products for geothermal exploration, has potential in the future to support these activities in synergy with hyperspectral VNIR/SWIR data. Hyperspectral TIR emission data provides improved capabilities over data from the VNIR/SWIR region for quantitative mapping of silicates and carbonates that may be associated with surface hydrothermal activity. This has the potential to improve the mapping of blind geothermal systems based upon the recognition of old hot spring deposits. The application of hyperspectral TIR emission data for these purposes will be supported by the further development of instrumentation by both government and commercial organizations.

**Acknowledgements** Research by the authors at Pilgrim Hot Springs, Alaska was supported by a Department of Energy Geothermal Technologies Programme (CID: DE-EE0002846; PI: Gwen Holdmann) and the Alaska Energy Authority Renewable Energy Fund Round III. We thank the anonymous reviewers for their thorough evaluation and constructive recommendations for improving this manuscript.

## References

- Allis RG (1980) Changes in heat flow associated with exploitation of Wairakei geothermal field, New Zealand. *N Z J Geol Geophys* 24:1–19
- Allis RG, Nash GD et al (1999) Conversion of thermal infrared surveys to heat flow: Comparisons from Dixie Valley, Nevada, and Wairakei, New Zealand. *Geotherm Resour Counc Trans* 23:499–504
- Baldridge AM, Hook SJ et al (2009) The ASTER spectral library version 2.0. *Remote Sens Environ* 113(4):711–715
- Berk A, Bernstein LS et al (1989) MODTRAN: a moderate resolution model for LOWTRAN7. GL-TR-89-0122. Air Force Geophysics Lab, Bedford
- Bromley CJ, van Manen SM et al (2010) Monitoring surface geothermal features using time series of aerial and ground-based photographs. American Geophysical Union, Fall Meeting 2010, abstract #IN33B-1308, San Francisco
- Bromley CJ, van Manen SM et al (2011) Heat flux from steaming ground: reducing uncertainties. In: Thirty-sixth workshop on geothermal reservoir engineering. Stanford University, Stanford
- Carter AJ, Girina O et al (2008) ASTER and field observations of the 24 December 2006 eruption of Bezymianny Volcano, Russia. *Remote Sens Environ* 112(5):2569–2577
- Christensen PR, Bandfield JL et al (2000) A thermal emission spectral library of rock-forming minerals. *J Geophys Res* 105(E4):9735–9739
- Coolbaugh MF, Shevenell LA (2004) A method for estimating undiscovered geothermal resources in Nevada and The Great Basin. *Geotherm Resour Counc Trans* 28:13–18
- Coolbaugh MF, Kratt C et al (2007) Detection of geothermal anomalies using Advanced Spaceborne Thermal Emission and Reflection Radiometer (ASTER) thermal infrared images at Bradys Hot Springs, Nevada, USA. *Remote Sens Environ* 106(3):350–359
- DiPippo R (2005) Geothermal power plants: principles, applications and case studies. Elsevier, Kidlington, Oxford, UK
- Eneva M, Coolbaugh M (2009) Importance of elevation and temperature inversions for the interpretation of thermal infrared satellite images used in geothermal exploration. *Geotherm Resour Counc Trans* 33
- Eneva M, Coolbaugh M et al (2006) Application of satellite thermal infrared imagery to geothermal exploration in East Central California. *Geotherm Resour Counc Trans* 30
- Eneva M, Coolbaugh MF et al (2007) In search for thermal anomalies in the coso geothermal field (California) using remote sensing and field data. In: Thirty-second workshop on geothermal reservoir engineering. Stanford University, Stanford
- Fridleifsson IB, Bertani R et al (2008) The possible role and contribution of geothermal energy to the mitigation of climate change. IPCC scoping meeting on renewable energy sources, Luebeck, Germany
- Gillespie A, Rokugawa S et al (1998) A temperature and emissivity separation algorithm for Advanced Spaceborne Thermal Emission and Reflection Radiometer (ASTER) images. *IEEE Trans Geosci Remote Sens* 36(4):1113–1126
- Glassley WE (2010) Geothermal energy: renewable energy and the environment. CRC Press, Boca Raton
- Hackwell JA, Warren DW et al (1996) LWIR/MWIR imaging hyperspectral sensor for airborne and ground-based remote sensing. SPIE, Bellingham
- Hapke B (1993) Theory of reflectance and emittance spectroscopy. Cambridge University Press, Cambridge
- Haselwimmer CE, Prakash A (2011) Use of airborne thermal imaging to quantify heat flux and flow rate of surface geothermal fluids at Pilgrim Hot Springs, Alaska. AGU Fall Meeting 2011, San Francisco
- Haselwimmer CE, Prakash A et al (2011) Geothermal exploration at Pilgrim Hot Springs, Alaska using airborne thermal infrared remote sensing. Geothermal Resource Council annual meeting 2011, San Diego

- Heasler H, Jaworowski C et al (2009) Geothermal systems and monitoring hydrothermal features. In: Young R, Norby L (eds) Geological monitoring. Geological Society of America, Boulder
- Hellman MJ, Ramsey MS (2004) Analysis of hot springs and associated deposits in Yellowstone National Park using ASTER and AVIRIS remote sensing. *J Volcanol Geotherm Res* 135 (1–2):195–219
- Hodder DT (1970) Application of remote sensing to geothermal prospecting. *Geothermics* 1:368–380
- Hook SJ, Myers JJ et al (2001) The MODIS/ASTER airborne simulator (MASTER) – a new instrument for earth science studies. *Remote Sens Environ* 76(1):93–102
- Hunt GR (1977) Spectral signatures of particulate minerals in the visible and near infrared. *Geophysics* 42(3):501–513
- Huntington JF (1996) The role of remote sensing in finding hydrothermal mineral deposits on Earth. In: Evolution of hydrothermal ecosystems on Earth (and Mars?), Ciba foundation symposium 202. Wiley, Chichester, pp 214–235
- Johnson BR (1998) In scene atmospheric compensation: application to SEBASS data collected at the ARM site. Part 1. Aerospace corporation technical report, ATR-99 (8407)-1
- Kealy PS, Gabell AR (1990) Estimation of emissivity and temperature using alpha coefficients. In: Proceedings of the second TIMS workshop. JPL Publ., vol. 90–95, Jet Propulsion Laboratory, Pasadena, CA, pp 11–15
- Kienholz C, Prakash A et al (2009) Geothermal exploration in Akutan, Alaska, using multitemporal thermal infrared images. American Geophysical Union, Fall Meeting 2009, abstract #H53F-1009, San Francisco
- Kratt C, Calvin W et al (2006a) Geothermal exploration with HyMap hyperspectral data at Brady–Desert Peak, Nevada. *Remote Sens Environ* 104(3):313–324
- Kratt C, Coolbaugh MF et al (2006b) Remote detection of quaternary borate deposits with ASTER satellite imagery as a geothermal exploration tool. *Geotherm Resour Coun Trans* 30
- Kruse FA (2002) Combined SWIR and LWIR mineral mapping using MASTER/ASTER. In Geoscience and remote sensing symposium, 2002. IGARSS'02. 2002 IEEE international, vol. 4. IEEE, pp 2267–2269
- Kruse FA, Boardman JW et al (2003) Comparison of airborne hyperspectral data and EO-1 Hyperion for mineral mapping. *IEEE Trans Geosci Remote Sens* 41(6):1388–1400
- Landsvirkjun (2012) Hydro and geothermal stations. Retrieved 21 Nov 2012, from <http://www.landsvirkjun.com/Company/PowerStations/>
- Lee K (1978) Analysis of thermal infrared imagery of the Black Rock Desert geothermal area. *Q Colo Sch Mines (United States)* 73(3):31–43
- Littlefield E, Calvin W (2009) Remote sensing for geothermal exploration over Buffalo Valley, NV. *Geotherm Resour Coun Trans* 33:495–499
- Littlefield E, Calvin W (2010) Geothermal exploration using AVIRIS remote sensing data over Fish Lake Valley. *Geotherm Resour Coun Trans* 34:599–603
- Mongillo M (1994) Aerial thermal infrared mapping of the Waimangu-Waiotapu geothermal region, New Zealand. *Geothermics* 23(5/6):511–526
- Mongillo MA, Graham DJ (1999) Quantitative evaluation of airborne video TIR survey imagery. In: Proceedings of the 21st NZ geothermal workshop, University of Auckland, pp 151–156
- Nash GD, Johnson GW et al (2004) Hyperspectral detection of geothermal system-related soil mineralogy anomalies in Dixie Valley, Nevada: a tool for exploration. *Geothermics* 33(6):695–711
- Ninomiya Y, Fu B et al (2005) Detecting lithology with Advanced Spaceborne Thermal Emission and Reflection Radiometer (ASTER) multispectral thermal infrared “radiance-at-sensor” data. *Remote Sens Environ* 99(1–2):127–139
- Pieri D, Abrams M (2004) ASTER watches the world’s volcanoes: a new paradigm for volcanological observations from orbit. *J Volcanol Geotherm Res* 135(1–2):13–28
- Ramsey MS, Christensen PR (1998) Mineral abundance determination: quantitative deconvolution of thermal emission spectra. *J Geophys Res* 103(B1):577–596

- Reath KA, Ramsey MS (2011) Hyperspectral thermal infrared analysis of the Salton Sea, CA geothermal field. AGU Fall Meeting 2011, San Francisco
- Riley DN, Peppin WA et al (2008) Joint airborne collection of hyperspectral systems: mineral mapping in cuprite in VNIR-SWIR and MWIR-LWIR with 613 spectral channels. Annual general meeting of the Geological Remote Sensing Group 2008, London
- Rockwell BW, Hofstra AH (2008) Identification of quartz and carbonate minerals across northern Nevada using ASTER thermal infrared emissivity data – implications for geologic mapping and mineral resource investigations in well-studied and frontier areas. *Geosphere* 4(1):218–246
- Rybach L (1981) Geothermal systems, conductive heat flow, geothermal anomalies. In: Muffler LJP, Rybach L (eds) *Geothermal systems: principles and case histories*. Wiley, Chichester
- Scherer GJ, Riley DN et al (2009) Geothermal exploration with visible through long wave infrared imaging spectrometers. *Clean Technology* 2009, Houston
- Seielstad C, Queen L (2009) Thermal remote monitoring of the Norris Geyser Basin, Yellowstone National Park. Final report for the National Park Service Cooperative Ecosystem Studies Unit, Agreement no. H1200040001, 38pp
- Taranik JV, Coolbaugh MF et al (2009) An overview of thermal infrared remote sensing with applications to geothermal and mineral exploration in the Great Basin, Western United States. In: Bedell R, Crosta A, Grunsky E (eds) *Remote sensing and spectral geology, Reviews in economic geology* 16. Society of Economic Geologists Inc, Littleton
- Vaughan RG, Calvin WM et al (2003) SEBASS hyperspectral thermal infrared data: surface emissivity measurement and mineral mapping. *Remote Sens Environ* 85(1):48–63
- Vaughan RG, Hook SJ et al (2005) Surface mineral mapping at Steamboat Springs, Nevada, USA, with multi-wavelength thermal infrared images. *Remote Sens Environ* 99(1–2):140–158
- Vaughan RG, Keszthelyi LP et al (2011) Measuring and monitoring heat flow and hydrothermal changes in the Yellowstone Geothermal System using ASTER and MODIS thermal infrared data. AGU Fall Meeting 2011, San Francisco
- Watson FGR, Lockwood RE et al (2008) Development and comparison of Landsat radiometric and snowpack model inversion techniques for estimating geothermal heat flux. *Remote Sens Environ* 112(2):471–481
- Wisian KW, Blackwell DD et al (2001) Correlation of surface heat loss and total energy production for geothermal systems. *Geotherm Resour Counc Trans* 25

# Chapter 23

## Analysis of Surface Thermal Patterns in Relation to Urban Structure Types: A Case Study for the City of Munich

Wieke Heldens, Hannes Taubenböck, Thomas Esch, Uta Heiden,  
and Michael Wurm

**Abstract** Scientists have reached to a large extent agreement on climate warming for the coming decades. This will especially have immense impact on cities which show in general a significantly higher temperature compared to rural surroundings, e.g. due to high percentage of impervious surfaces. This study shows capabilities of airborne and spaceborne thermal remotely sensed data to derive and analyze land surface temperatures (LST). Dependencies of LST to urban structure types (UST) with respect to their location within the city are analyzed. Results prove distinct correlations between LST and vegetation fraction as well as percentage of impervious surfaces. Beyond this, different USTs prove influences on LST. Last but not least, a general decrease of LST with increasing distance to the city center is confirmed for the city of Munich. However, the USTs superimpose this trend and have a significant influence on the local LST.

### 23.1 Introduction

Land surface temperature is an important parameter for urban climate studies. It influences the air temperature in the lower layer of the urban atmosphere, plays an important role in the energy balance, supports the analysis of the internal climate of buildings and indirectly affects the human comfort in cities (Voogt and Oke 2003). Thermal remote sensing can be used to map urban surface temperature patterns and the surface urban heat island (SUHI) (Weng 2009). The SUHI indicates the often higher surface temperatures of urbanized areas in comparison with the surrounding rural area. Intra-city differences in surface temperature occur due to differing surface material types, urban morphology or vegetation fraction. This phenomenon

---

W. Heldens • H. Taubenböck (✉) • T. Esch • U. Heiden • M. Wurm  
German Remote Sensing Data Center (DFD), Earth Observation Center (EOC),  
German Aerospace Center (DLR), Oberpfaffenhofen, Germany  
e-mail: [wieke.heldens@dlr.de](mailto:wieke.heldens@dlr.de)

has been studied frequently, for example for the cities of Beijing (China) (Cai et al. 2011), Toronto (Canada) (Rinner and Hussain 2011), Seoul (Korea) (Bhang and Park 2009), Debrecen (Hungary) (Bottyán et al. 2005) or Athens (Greece) (Stathopoulou and Cartalis 2009). It should be noted, that the surface temperature – and thus the surface urban heat island – differs from the air temperature and the according urban heat island (UHI) (Roth et al. 1989; Voogt and Oke 2003). For example, where the SUHI reaches its highest intensity during the day, the UHI intensity reaches its maximum during the night. Among others, the air temperature within the urban canopy is also influenced by convection and therefore differs from the surface temperature (Voogt and Oke 2003).

For urban planners it is important to know the location of local heat islands as well as the causes so they can mitigate the negative effects. Areas with similar climatic conditions require similar planning measurements (Fehrenbach et al. 2001; Houet and Pigeon 2011). This chapter focuses on the surface temperature patterns and not on air temperature because it is made use of thermal remote sensing. If the urban morphology shows systematic correlations to LST, urban planning options for reducing the effect of SUHI can be identified. For this analysis, the concept of urban structure types (UST) is used. This is a common means to group urban areas with similar characteristics (Pauleit 1998) which require consequently similar planning measures.

In this chapter, we show how the analysis of thermal patterns can be carried out based on the framework of urban structure types using the example of the city of Munich (Germany). First, the concept of urban structure types is introduced. Second, the thermal patterns of the city of Munich are addressed as they are recorded by both, an airborne and a satellite-based sensor. Third, the mapping of urban structure parameters, with which the urban structure types can be identified and differentiated, is presented. Fourth, different methods that relate surface temperature to urban structure types and their spatial characteristics are discussed. We combine these approaches to suit the analysis within the framework of USTs and finally discuss the advantages and limitations of such an approach for urban planning purposes.

## 23.2 Urban Structure Types

Urban structure type (UST) mapping is a commonly used tool in many German cities to support urban planning. This approach delineates the urban system into distinct configurations of built-up areas, impervious open spaces, urban green spaces and infrastructure (Heiden et al. 2012). The principle of UST was introduced in the 1990s in Germany and since has been applied to a wide range of German cities (Pauleit 1998; Sukkopp and Wittig 1998; Wickop et al. 1998) and adapted by other countries as well (Tang 2007). USTs are characterized by a number of features describing their physical properties (e.g. surface materials, building density or floor space index),

their environmental characteristics (e.g. climate, hydrology) and functional properties (e.g. land use) (Pauleit and Duhme 2000; Wurm et al. 2010).

The city of Munich is selected as study area. In this city, a large range of urban structure types (UST) are present. In an UST map provided by the municipality of Munich, 41 structure types are distinguished, including both urban and agricultural types (Fischer 2002). The structure types are assigned on the basis of building blocks (the smallest area surrounded by public streets). The city consists of more than 7,000 building blocks.

Here we focus on a selection of eight urban structure types: block development (I), perimeter block development (II), regular block development (III), row house development (IV), detached and semi-detached housing (V), high rise buildings (VI), large multi-storey buildings (VII) and parks and urban green (VIII). Together these eight urban structure types are found in almost 4,500 building blocks in Munich. Table 23.1 shows an exemplary building block of each of the eight urban structure types.

### 23.3 Thermal Patterns of Urban Structure Types

Remotely sensed thermal infrared data are widely used to study LST patterns for urban climate and environment studies (Weng 2009; Tomlinson et al. 2011; Arnfield 2003). Often the UHI effect is studied (e.g. Weng et al. 2011; Stathopoulou and Cartalis 2009; Hart and Sailor 2009; Yuan and Bauer 2007) or the relationship between LST and various biophysical parameters (e.g. Zhang et al. 2009; Weng and Hu 2008; Yue et al. 2007).

For this study, thermal imagery of the Landsat satellite (60 m pixel size) and of the airborne sensor Daedalus (4 m pixel size) was available. The Daedalus data were recorded on 2007-6-25 at 12:05 AM, the Landsat scene 2 months later, on 2007-8-26 at 11:56 AM. The Landsat data covered the whole city of Munich and its surroundings. The Daedalus data consisted of one flight line, covering a part of the city in the northern half of the image and rural area in the southern half. The LST of the Landsat thermal band was calculated with the software package ATCOR (Atmospheric and Topographic Correction for Satellite Imagery) (Richter 2009). With this software a temperature-emissivity-separation (TES) algorithm was applied. Since only one thermal band is available, an emissivity of 0.98 was assumed for all land cover types. The airborne Daedalus image was received as calibrated temperature equivalents, corresponding with at-sensor brightness temperature. To retrieve (near) land surface temperature a correction for the atmospheric water vapour column is required, e.g. with the ATCOR software package. However, an extensive atmospheric correction was not possible due to a lack of meta-data. Therefore, it was assumed that the water vapour column in the Daedalus image is equal over the whole image and an offset based on the difference to the Landsat retrieved surface temperature was applied to adjust the Daedalus

**Table 23.1** Examples of the eight selected urban structure types (ortho-photos with varying scales)

Description	Example	Description	Example
I Block development		V Detached and semi-detached housing	
II Perimeter block development		VI High rise buildings	
III Regular block development		VII Large multi-storey buildings	
IV Row house development		VIII Parks and urban green	

temperature to the land surface temperature of Landsat. All surface temperatures are converted to degree Celsius.

By comparing the mean surface temperature of the city – defined by the municipal boundaries – to the mean surface temperature of the rest of the image, the SUHI intensity can be determined. For the Landsat data, a SUHI intensity of 2.8 °C was found. The municipality covered 5 % of the Landsat image. The dominant land cover in the rest of the image is agricultural land, followed by forests and smaller settlements. Using the Daedalus data, a SUHI intensity of 5.3 °C was determined. The municipality covers 33 % of the Daedalus image. The remaining part of the image consists mainly of forest, followed by urban area and agricultural land. The difference in the intensity of the SUHI between the two

sensors can be explained among others by the acquisition date. At the end of the summer when the Landsat image was recorded, many fields are harvested. The resulting bare soil causes a much higher surface temperature for the rural area, whereas the surface temperature in the city is similar. This matches results published by Imhoff et al. (2010). They analyzed the SUHI intensity for many cities in the USA, categorised after different biomes. In biomes with higher amounts of standing biomass, such as temperate broadleaf and mixed forests higher SUHI intensities were found than in biomes with mainly grassland. Although the difference thus can be explained, the difference in SUHI intensity measured from the two sensors also shows the large dependency of this measure on the time of the year, the sensor field of view and the ratio of urban and rural area within the image.

The LST maps of the municipality of Munich derived from both sensors are shown in Fig. 23.1. The LST in the city centre is the highest and decreases towards the border of the city. The dark blue patches are the cooler, large parks, such as the Nymphenburger Park (A) and the flood plains of the river Isar (B). Patches of high LST outside the city centre are mainly industrial areas (e.g. C). Also along the main rail road tracks there is a higher LST (D, E). The high resolution data of the Daedalus sensor shows similar patterns. A closer look shows that different LST of buildings, vegetation and roads can be separated in the Daedalus data, whereas in the Landsat map only the cooler park can be recognised. Sobrino et al. (2012) studied the impact of spatial resolution by resizing airborne thermal imagery in the city of Madrid. They found that small thermal structures, such as streets or gardens can be detected at spatial resolutions up to 50 m. With coarser resolutions, these patterns become mixed and from 500 m onward the heterogeneity between neighbourhoods is lost. At a spatial resolution of 1 km thermal structures within different districts cannot be recognised anymore.

Figure 23.2 shows the variation of LST within each of the eight USTs for the two sensors. The 25 % of the pixels with lower LST than the median are indicated by the blue range, the 25 % of the pixels with higher LST than the median are indicated in red. Thus, the blue and red ranges together cover the values of 50 % of the pixels belonging to a certain UST. The figure shows that the general pattern of the LST between the UST and the two remote sensing sources are quite similar. However the variation within the Daedalus data is much larger than in the Landsat data. This is due to the influence of the spatial resolution. The Landsat data not only covers a larger area with one pixel – meaning each pixel provides a more averaged temperature, but also fewer pixels contribute to the USTs.

The differences between the eight USTs are most clear in the height of the median LST. Block development and large multi-storey buildings have the highest LST. In the Landsat data even all pixels belonging to these USTs have values higher than the mean of the whole image (all UST, dotted line). The UST with the lowest temperatures is ‘parks and urban green’, of which almost 90 % of the pixels have temperature values below the image mean. The temperature ranges of regular block developments and row house development are similar to each other. The LST of detached and semi detached housing is comparable to these two USTs as well, but

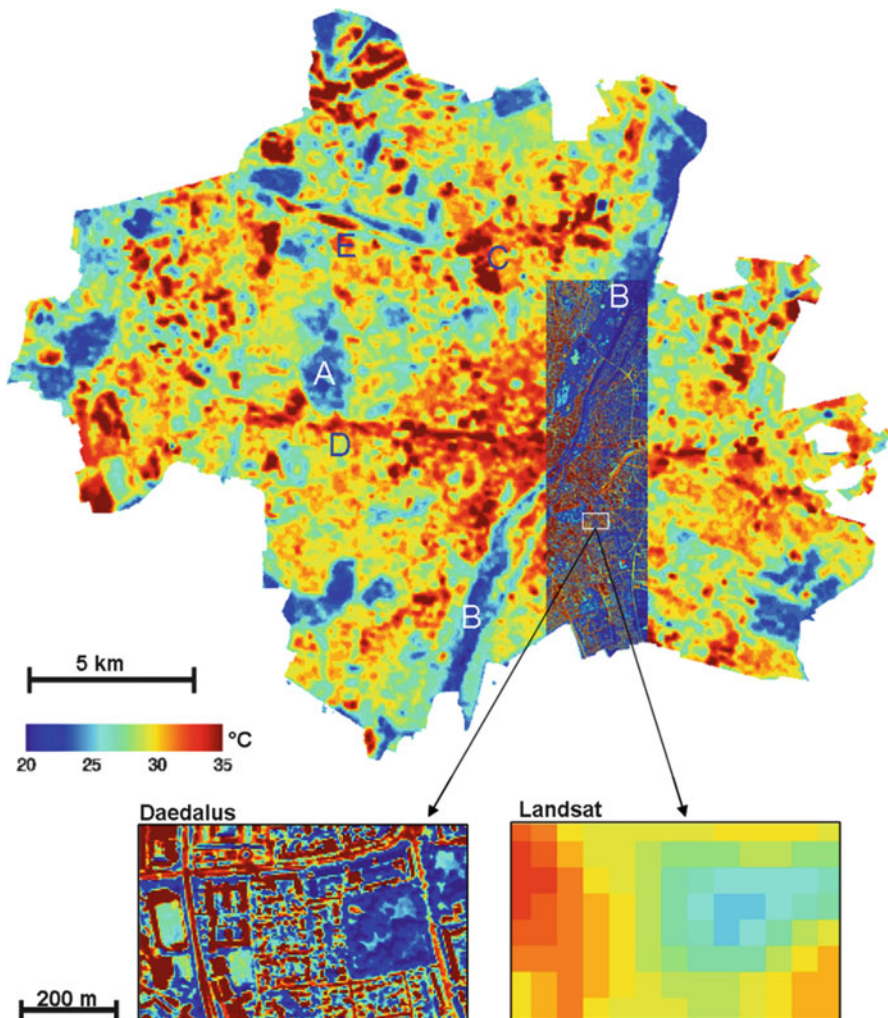


**Fig. 23.1** Surface temperature of the city of Munich as measured by Landsat (60 m pixel size) and Daedalus (5 m pixel size)

with slightly lower values. In Daedalus data, the 25 % of the pixels with an LST below median cover a smaller range than the 25 % above the median.

In general we observe that those UST showing significantly different physical parameters also showed significant differences in LST. However, the empirical estimation of the temperature is not possible just based on the USTs

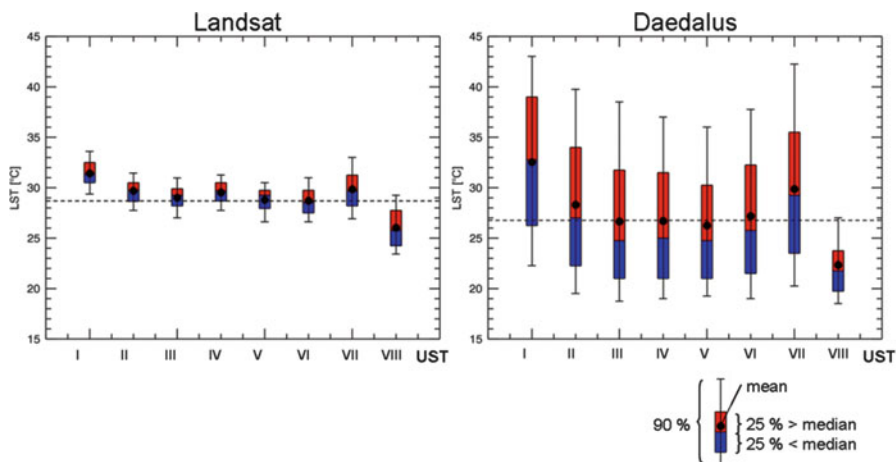


**Fig. 23.2** Variation of LST within different USTs. The *dotted line* indicates the mean LST of the whole study area (Landsat: 28.8 °C, Daedalus: 27.0 °C). *I* block development, *II* perimeter block development, *III* regular block development, *IV* row house development, *V* detached and semi-detached housing, *VI* high rise buildings, *VII* large multi-storey buildings and *VIII* parks and urban green

## 23.4 Spatial Characteristics of Urban Structure Types

Urban areas can be described with remote sensing data by a range of parameters (Heldens et al. 2011). In addition to land cover, common examples are building density (Orenstein et al. 2011; Zha et al. 2003; Bochow et al. 2009), impervious surfaces (Weng 2012) or vegetation fraction (Chen et al. 2006; Stefanov and Netzband 2005), describing the spatial characteristics of urban areas. Further parameters include e.g. floor space index, construction volume (Taubenböck et al. 2010; Wurm et al. 2011), building alignment, morphological homogeneity (Taubenböck and Kraff 2013) or dominating materials (Heldens 2010). Approaches such as texture analysis or spatial metrics are also used to describe urban structure (Herold et al. 2003; Pesaresi et al. 2008). To characterise the urban structure types in Munich within the scope of urban climate, the parameters building density, percentage impervious surface (imperviousness), vegetation fraction, surface material and sky view factor are selected. These parameters are important factors contributing to the LST in urban environments (Weng 2009).

The surface cover material, building density, impervious surfaces and vegetation fraction are derived from airborne hyperspectral data, supported by height data. Other relevant information is the sky view factor. It is calculated based on a DEM derived from stereo photogrammetry and described below.

Hyperspectral data used here were recorded in June 2007 by the HyMap sensor with 125 spectral bands and a spatial resolution of 4 m (Cocks et al. 1998). Before use, the HyMap data were atmospherically corrected with the ATCOR software (Richter 2009) and geometrically corrected with ORTHO (Müller et al. 2005).

The surface material map is derived from the HyMap data using a linear spectral unmixing algorithm developed especially for urban applications by the GFZ German Research Centre for Geosciences (Roessner et al. 2011; Heiden et al. 2012). With this unmixing approach, up to 40 urban surface materials can be identified at sub-pixel level. They include various roof materials, materials of impervious, partially pervious and pervious non-built surfaces and three vegetation types (grass, coniferous and deciduous trees). The result is an abundance map for each material, with the coverage percentage for each pixel. In order to express the characteristics of a building block, the abundance maps of the materials are aggregated. To calculate the imperviousness, building density and vegetation fraction, the abundances of the materials for each pixel are also aggregated per building block. The building density is defined as the average abundance of all roof materials. The imperviousness is defined as the average abundance of all roof materials, all non-built impervious surfaces (e.g. asphalt roads) and 0.5 times the abundance of partially impervious surfaces (e.g. cobblestone pavements). The average abundance of all vegetation types defines the vegetation fraction per building block. The results of these three indicators are expressed in percentage per building block (the detailed methodology is described in Heiden et al. (2012) and Heldens (2010)).

The sky view factor (SVF) is frequently used in urban climate studies (Eliasson et al. 2006; Rigo and Parlow 2007). The SVF has been defined by Watson and Johnson (1987) as “the ratio of radiation received by a planar surface from the sky to that received from the entire hemispheric radiating environment”. Thus expressing the amount of radiation that can maximally reach or leave the surface, the SVF plays a role in the heating of the surface during the day and its cooling during the night. This way, SVF is an important variable in understanding both the surface and air urban heat island.

For this study, SVF was calculated based on a DEM (Digital Elevation Model) recorded with the HRSC (High Resolution Stereo Camera) (Scholten et al. 2003) in 2004. The DEM contained both buildings and vegetation. A ray tracing program implemented in ATCOR was used to calculate the SVF which is scaled from 0 to 100 % (Richter 2009). The resulting SVF calculated for the top of canopy, providing values for either the ground surface or the top of any present objects (e.g. building roofs and tree crowns).

The results of the analysis of urban surface characteristics are shown in the Figs. 23.3 and 23.4. Figure 23.3 shows the average material abundance for the eight urban structure types. The most common roofing material is roofing tiles. The abundance of green roofs is overestimated because of classification errors, caused by buildings covered by tree crowns and the general spectral confusion between vegetation on roofs and vegetation on the ground. In the urban structure types with larger buildings (VI: high rise buildings, VII: halls and storage buildings, but also I: dense block developments), roofing materials commonly found on flat roofs, such as concrete, metal and bitumen are more common. The non built surfaces in all urban structure types are mainly covered by vegetation (both trees and lawns), but also asphalt and concrete contribute to up to 10 % of the area. Hereby it should be

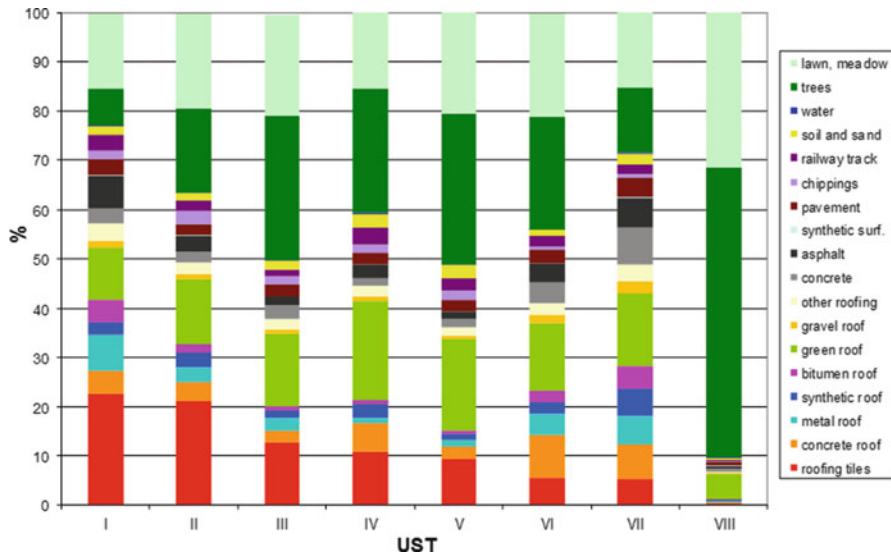


**Fig. 23.3** Mean material abundances in the different UST. Type I represents block development, II perimeter block development, III regular block development, IV row house development, V detached and semi-detached housing, VI high rise buildings, VII large multi-storey buildings and VIII parks and urban green

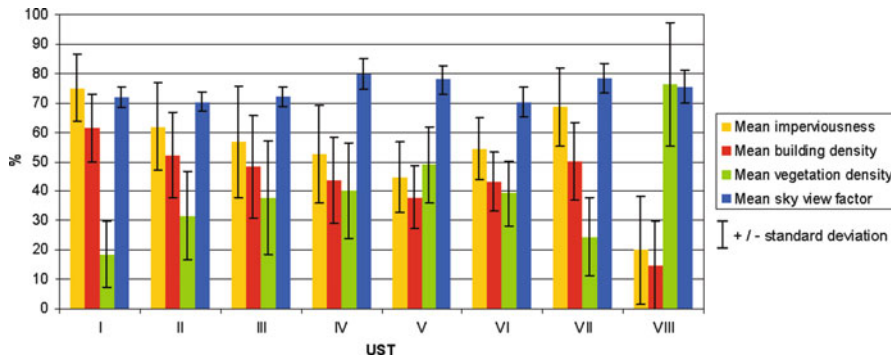


**Fig. 23.4** Mean spatial characteristics for different urban structure types. Type I shows block development, II perimeter block development, III regular block development, IV row house development, V detached and semi-detached housing, VI high rise buildings, VII large multi-storey buildings and VIII parks and urban green

noted, that by the definition of the building blocks the roads separating the building blocks have been excluded from the analysis.

Figure 23.4 shows the mean and standard deviation of four spatial indicators for the selected urban structure types. Each of the USTs has a typical combination of the four indicators. The mean sky view factor for most USTs is around 70 %. Higher

sky view factors are reached for row houses, detached and semi-detached housing, halls and storage buildings and parks. These are all structure types with either relatively low building density (IV, V, VIII) or few large buildings and little trees (VII). The largest percentage of impervious surface is found in block development, followed by large multi-storey buildings. The vegetation fraction in the residential USTs ranges from 18 to 49 %. Of course the vegetation fraction in the parks and urban green (76 %) is very high.

## 23.5 Relating Thermal Patterns to Urban Structure Types

To analyse the relationship of thermal patterns and urban structure types and their spatial characteristics, a regression analysis at building block level was carried out. For each building block the mean abundance of surface cover materials and the spatial indicators as presented in the previous section were used as independent variables. The building blocks belonging to the different urban structure types have been analyzed separately. A multiple linear regression was applied, using IDL (Interactive Data Language) regression routines (ITT 2010). As dependent variable the mean LST for each building block is used. As a result, for each urban structure type a regression equation consisting of a constant and coefficients for each variable were retrieved, as well as the multiple linear correlation coefficient and the linear correlation coefficients for each variable. To improve the comparability among USTs, the coefficients of the regression equation are normalised to percentage. Additionally, scatter plots of the LST against each of the spatial variables have been produced, in which the different urban structure types are indicated. A selection of these plots is shown in Fig. 23.5.

The results of the regression analysis of the surface materials and the LST show high multiple correlation coefficients ranging from 0.59 (dense block development) to 0.70 (halls and storage buildings) for the LST derived from Landsat. For the Daedalus derived LST the multiple correlation coefficients are even higher: they range from 0.69 (parks and urban green) to 0.89 (high rise buildings). For most USTs the coefficients of the different materials are within the same range, around 8 %. Materials with a slightly higher coefficient are the different types of vegetation (in high rise buildings, halls and storage buildings and parks), roofing tiles (in dense block development and row house development), metal roofing materials (dense block development), synthetic roofing materials (perimeter block development) and asphalt (regular block development). Among the Landsat derived regression coefficients the variation is larger and also the mean value of the coefficients is lower (around 4 %). Higher contributions are from vegetation (multiple types), vegetated roof, other roofing materials, roofing tiles, roofing bitumen. They contribute with 10–29 % to the equation. Except for the vegetation types (including green roofs) all materials have a positive correlation to LST. Figure 23.5a, b show the correlation between LST and roofing tiles and LST and asphalt. The correlation coefficients of roofing tiles to LST are not very high (0.2 for most of the USTs).

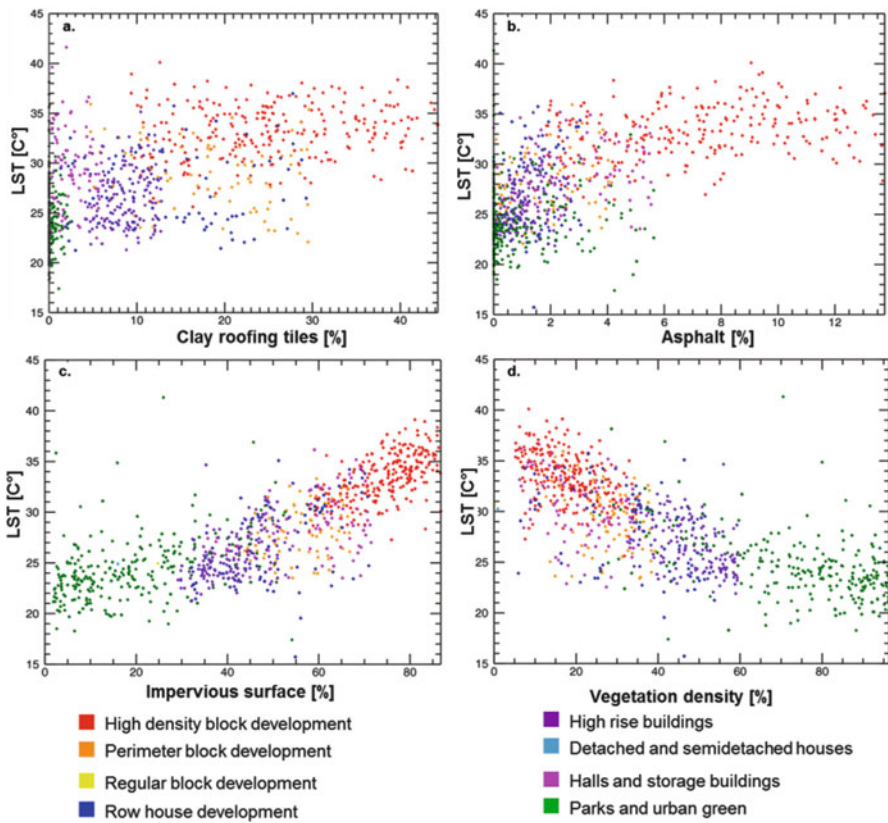


**Fig. 23.5** Scatter plots of mean LST (Daedalus data) and mean abundance of selected surface materials and indicators per building block

For asphalt they are slightly higher, ranging from 0.23 to 0.49. Whereas the different USTs have each a clear position on the scale of asphalt and roofing tile abundances, USTs of the same type cover a broad range of LST values. This is especially true for halls and storage buildings, perimeter block development and row house development.

The regression analysis of the indicators shows similar results. The multiple correlation coefficients range from 0.55 to 0.74 in the Daedalus data and from 0.49 to 0.64 within Landsat data. The USTs with the highest multiple correlation coefficients are perimeter block development (0.74) and high rise buildings (0.73) in Daedalus data and with Landsat data parks and urban green (0.64), detached and semi detached housing and regular block developments (both 0.63). The coefficients of the different indicators in the regression equation vary largely. For most USTs, either vegetation fraction or imperviousness has the highest coefficient (up to 55 % for vegetation fraction and up to 48 % for imperviousness), suggesting a large influence of these indicators on the LST. In the Landsat data additionally

building density and sky view factor have large coefficients with contributions of up to 27 % to the multiple regression equation. In Daedalus data fully sealed surfaces determine the LST distinctively with contributions up to 39 %. These results suggest that, in order to reduce LST, for all USTs it would be advantageous to reduce imperviousness, building density and/or the amount of fully sealed surfaces or increase the vegetation fraction (negative correlation). Changes in the amount of partially sealed surfaces, soil or water will have less effect, according to this analysis. The importance of vegetation fraction and imperviousness is also illustrated by the fact that these indicators have also the highest linear correlation coefficients (0.43–0.64 for vegetation fraction and 0.40–0.64 for imperviousness), where the higher coefficients are reached with the Daedalus data. Figure 23.5c, d show the correlation of imperviousness and vegetation fraction for the different USTs in a scatter plot. The plots are almost inverse to each other. At lowest and highest percentages of impervious surface, all building blocks with the UST parks and dense block development are located. The other USTs are somewhat mixed at medium LST and impervious surface percentages. The same is the case in the scatterplot of vegetation density (Fig. 23.5d). However, here dense block development is mixed with perimeter block development, and halls and storage buildings which have also very low vegetation fraction in many building blocks. Bechtel (2011) found similar patterns in Hamburg while assessing mean height, the normalised difference vegetation index (NDVI), and the dominant land use in comparison to the mean annual surface temperature and the yearly amplitude of the surface temperature for seven urban and non urban structure types. Houet and Pigeon (2011) found significant differences in climate between different urban structure types (urban climate zones) in Toulouse. Making use of the differences in spatial characteristics, Stewart and Oke (2012) defined a classification scheme in order to support urban temperature observations e.g. in the context of urban heat island analysis. These ‘local climate zones’ resemble urban structure types.

The previous analyses show the relationship of the urban structure types to LST by means of the surface cover parameters. However, also the location of the building block within the city might play a role in the LST of urban structure types. The SUHI in Munich has the highest temperatures in the centre of the city and the intensity decreases towards the border of the city. Therefore, the spatial organization of urban structure types and LST within the city is analyzed. The results are presented in Fig. 23.6. As representative centre of the city, the Marienplatz was selected. Its location is indicated by the crossing of the transects in the map of Munich in Fig. 23.6. The four transects (from west to centre, centre to east, north to centre and centre to south) provide a means to analyze the LST from the urban centre to the urban periphery. Beyond this, the analysis can be carried out with respect to the particular urban structure types that occur along the transects. The eight USTs are displayed in colour in Fig. 23.6 with their respective location. The figure shows that dense block development is mainly found in the centre of the city, followed by a ring of regular block development and on the outer ring detached and semi-detached housing. Parks and halls and storage buildings are spread

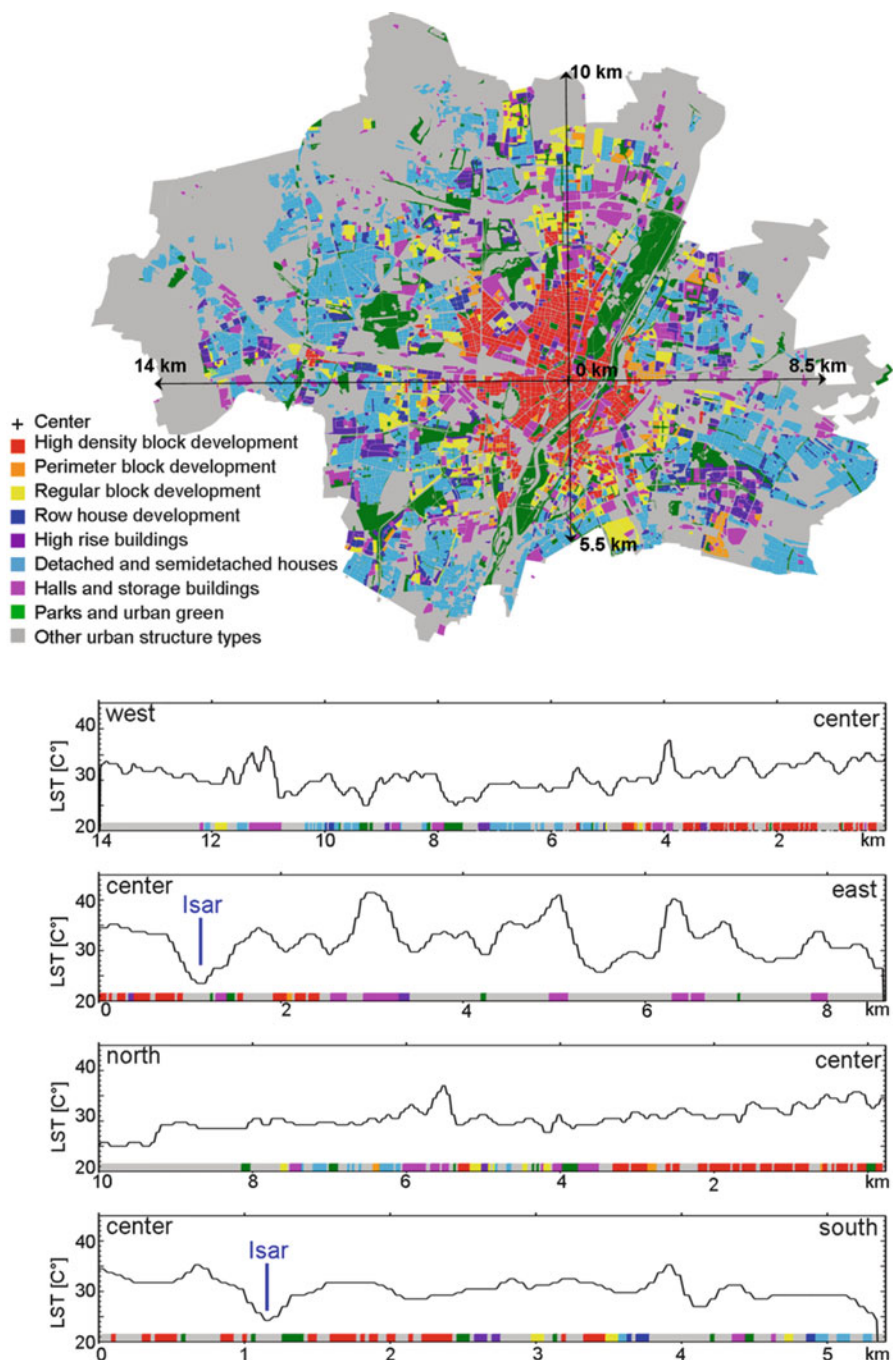


**Fig. 23.6** LST profiles over the USTs in Munich along the transects (black lines) indicated in the map. The colour bars in the LST figures correspond to the colours of the urban structure types in the map

irregularly over the entire city. This is also true for regular block development, row house development and high rise buildings, but their amount is not as large.

For the analysis LST profiles are derived from the Landsat data along the transects. The four profiles are shown in the lower part of Fig. 23.6. The colours below each profile indicate the spatially associated urban structure types. All profiles generally show an increasing LST towards the city centre. In the eastern and southern profile the influence of the river Isar is clearly visible by a dip in the LST of 5° (south) and 10° (east). Other dips in LST in the eastern profile at 5.5 and 7 km have to be contributed to agricultural fields. Peaks are visible at almost all locations where halls and storage buildings occur, but they vary largely in height with a maximum difference to the surrounding of up to 10°. Dips of LST can be found at the location of most of the parks. They are up to 5° cooler than their surroundings. The peaks and dips are more pronounced in the east – west profiles than in the north – south profiles.

It is interesting to note that the transect north of the centre shows the lowest variance and a generally consistent increase in LST. This is due to the characteristics of the transect which is not interrupted by parks or any other open spaces. The only significant peak is measured at the halls and storage buildings of an industrial site. In comparison, the three other transects show a higher variance due to a frequent change of open spaces and built environment as well as a higher spatial alternation of USTs. Thus it becomes obvious that in Munich LST decreases with distance to the city centre. However, the influence of USTs on the LST superimposes this trend and determines the local LST.

## 23.6 Discussion and Conclusion

In the previous sections results on the mapping and characterisation of urban structure types and LST using two thermal sensors at different spatial resolutions have been presented. The higher spatial resolution of the airborne sensor is advantageous for this analysis. It allows the mapping of small scale variations in thermal patterns and the resulting correlation of LST and spatial indicators and surface materials is stronger for the different building blocks and USTs. These findings correspond with extensive studies on spatial scale for urban thermal pattern mapping by Sobrino et al. (2012). Nevertheless, the Landsat data provide some useful insights in the variation of LST within the city. Because of the larger pixel size, it is no problem to cover the entire urban area of 25 by 15 km.

The regression analysis showed that vegetation fraction and impervious surfaces are main determining factors for the LST. This is in agreement with the results of many other studies (e.g. Jenerette et al. 2007; Mostovoy et al. 2008; Zhang et al. 2009; Weng et al. 2004, 2011; Xiao et al. 2007). These results are confirmed by Figs. 23.2 and 23.4 as well. Dense block development has the highest imperviousness and the lowest vegetation density of all USTs (Fig. 23.4). At the

same time, this UST shows the highest LSTs (Fig. 23.3). The profiles in Fig. 23.6 show also an increase of LST with an increase of dense block development. However, one should notice that the occurrence of dense block development increases towards the city centre. The UST with the second highest LST, halls and storage buildings, have similar values for vegetation fraction and imperviousness but are more evenly spread over the city. In many instances, their high percentage of impervious surfaces and low vegetation fraction result in an LST higher than their surroundings. But this UST is characterised by a high variation both within the building blocks (Fig. 23.2) and among the building blocks of this UST (Fig. 23.5). It might be the case that the location of the building blocks within the city also plays a role in this. For the analysis, administrative borders of the building blocks (public streets) were used; local (weather) characteristics were not considered. To gain more insight on the influence of the location within the city on the LST in building blocks and the variation among building blocks of the same types, profiles of more cities should be analyzed.

Although the different USTs show characteristic values for SVF, this parameter seems not to be very dominant in determining LST. However, studies on SVF and street geometry emphasise on the importance of these parameters for the energy balance and wind flow (Hoyano et al. 1999; Rigo and Parlow 2007; Offerle et al. 2007; Eliasson et al. 2006).

In the literature, often research is done on the influence of land use on LST and strong relationships were found (Chen et al. 2006; Hart and Sailor 2009; Hu and Jia 2010). Although land use was not investigated in this study, urban structure types are closely related to land use. The definition of the USTs is based on physical characteristics, but the building blocks belonging to one type often show similar land use. This is an advantage for the use of USTs as framework for LST analysis in urban areas.

Surface temperature is only a part of the urban climate. Remote sensing maps surface temperature at different heights (street, roof, tree tops), of which many are not very relevant for inhabitants. Thus, the LST measured by remote sensing explains only a small part of the urban climate. Nevertheless, analyses such as carried out here can provide insight on materials and spatial characteristics that can mitigate or intensify unwanted climatic effect, because the surface properties also influence the energy balance. The relation of USTs to the energy balance, air temperature, wind and other climate parameters is important for urban planning practice (Pauleit and Duhme 2000). Quah and Roth (2012) analyzed the contribution of different urban structures and land uses on the energy balance in which the anthropogenic heat produced by the different land uses plays an important role. Since USTs in Germany are closely related to land use, they might provide a means to estimate the anthropogenic heat production in a generalised way. Future research should therefore further combine the knowledge on the various climatic aspects and their interaction with urban morphology and surface cover within the framework of urban structure types.

**Acknowledgements** The authors wish to thank Rolf Städter (DLR) for pre-processing the Daedalus data and Rolf Annecke of the Referat für Gesundheit und Umwelt (Department of Health and Environment) of the Municipality of Munich for providing the urban structure type classification of Munich. The HRSC height data was kindly provided by DLR Berlin. Part of this research was carried out with funding of the German Ministry of Education and Research (BMBF) in the context of the project “REFINA Flächenbarometer” (funding no. 0330737A). The comments of the reviewers greatly helped to improve the manuscript.

## References

- Arnfield AJ (2003) Two decades of urban climate research: a review of turbulence, exchanges of energy and water, and the urban heat island. *Int J Climatol* 23:1–26
- Bechtel B (2011) Multisensoral remote sensing for the microclimatic characterisation and classification of urban structures. *Photogrammetrie Fernerkundung Geoinformation* 2011(5):325–338
- Bhang KJ, Park SS (2009) Evaluation of the surface temperature variation with surface settings on the urban heat island in Seoul, Korea, using Landsat-7 ETM+ and SPOT. *IEEE Geosci Remote Sens Lett* 6:708–712
- Bochow M, Taubenböck H, Segl K, Kaufmann H (2010) An automated and adaptable approach for characterizing and partitioning cities into urban structure types. In: 2010 IEEE international geoscience and remote sensing symposium proceedings. IEEE, Honolulu, Hawaii, pp 1796–1799
- Bottyán Z, Kircsi A, Szegedi S, Unger J (2005) The relationship between built-up areas and the spatial development of the mean maximum urban heat island in Debrecen, Hungary. *Int J Climatol* 25:405–418
- Cai G, Du M, Xue Y (2011) Monitoring of urban heat island effect in Beijing combining ASTER and TM data. *Int J Remote Sens* 32:1213–1232
- Chen XL, Zhao HM, Li PX, Yin ZY (2006) Remote sensing image-based analysis of the relationship between urban heat island and land use/cover changes. *Remote Sens Environ* 104:133–146
- Cocks T, Jenssen R, Stewart A, Wilson I, Shields T (1998) The HyMap airborne hyperspectral sensor: the system, calibration and performance. In: Proceedings of the 1st EARSeL workshop on imaging spectroscopy, Zurich, Switzerland
- Eliasson I, Offerle B, Grimmond C, Lindqvist S (2006) Wind fields and turbulence statistics in an urban street canyon. *Atmos Environ* 40:1–16
- Fehrenbach U, Scherer D, Parlow E (2001) Automated classification of planning objectives for the consideration of climate and air quality in urban and regional planning for the example of the region of Basel/Switzerland. *Atmos Environ* 35:5605–5615
- Fischer HS (2002) Flächencharakterisierung der im Rahmen der Stadtbiotopkartierung erfassten Struktureinheiten Ifanos Landschaftsökologie, im Auftrag der Landeshauptstadt München
- Hart M, Sailor D (2009) Quantifying the influence of land-use and surface characteristics on spatial variability in the urban heat island. *Theor Appl Climatol* 95:397–406
- Heiden U, Heldens W, Roessner S, Segl K, Esch T, Mueller A (2012) Urban structure type characterization using hyperspectral remote sensing and height information. *Landsc Urban Plan* 105(4):361–375. doi:[10.1016/j.landurbplan.2012.01.001](https://doi.org/10.1016/j.landurbplan.2012.01.001)
- Heldens W (2010) Use of airborne hyperspectral data and height information to support urban micro climate characterisation. Phd thesis, Bayerischen Julius-Maximilians Universität Würzburg, Germany
- Heldens W, Heiden U, Esch T, Stein E, Müller A (2011) Can the future EnMAP mission contribute to urban applications? A literature survey. *Remote Sens* 3:1817–1846
- Herold M, Liu X, Clarke KC (2003) Spatial metrics and image texture for mapping urban land use. *Photogramm Eng Remote Sens* 69:991–1001

- Houet T, Pigeon G (2011) Mapping urban climate zones and quantifying climate behaviors – an application on Toulouse urban area (France). *Environ Pollut* 159:2180–2192
- Hoyano A, Iino A, Ono M, Tanighchi S (1999) Analysis of the influence of urban form and materials on sensible heat flux – a case study of Japan's largest housing development 'Tama New Town'. *Atmos Environ* 33:3931–3939
- Hu Y, Jia G (2010) Influence of land use change on urban heat island derived from multi-sensor data. *Int J Climatol* 30:1382–1395
- Imhoff ML, Zhang P, Wolfe RE, Bounoua L (2010) Remote sensing of the urban heat island effect across biomes in the continental USA. *Remote Sens Environ* 114:504–513
- ITT Visual Information Solutions (2010) IDL 8.0 and ENVI 4.8 users' guide. ITT VIS, Boulder, CO, USA
- Jenerette GD, Harlan SL, Brazel A, Jones N, Larsen L, Stefanov WL (2007) Regional relationships between surface temperature, vegetation, and human settlement in a rapidly urbanizing ecosystem. *Landsc Ecol* 22:353–365
- Mostovoy GV, Anantharaj V, King RL, Filippova MG (2008) Interpretation of the relationship between skin temperature and vegetation fraction: effect of subpixel soil temperature variability. *Int J Remote Sens* 29:2819–2831
- Müller R, Holzwarth S, Habermeyer M, Müller A (2005) Ortho image production within an automatic processing chain for the hyperspectral airborne scanner ARES. In: Proceedings of the EARSeL workshop 3D-remote sensing, Porto, Portugal
- Offerle B, Eliasson I, Grimmond C, Holmer B (2007) Surface heating in relation to air temperature, wind and turbulence in an urban street canyon. *Bound Layer Meteorol* 122:273–292
- Orenstein DE, Bradley BA, Albert J, Mustard JF, Hamburg SP (2011) How much is built? Quantifying and interpreting patterns of built space from different data sources. *Int J Remote Sens* 32:2621–2644
- Pauleit S (1998) Das Umweltwirkgefüge städtischer Siedlungsstrukturen: Darstellung des städtischen Ökosystem durch eine Strukturtypenkartierung zur Bestimmung von Umweltqualitätszielen für die Stadtplanung. Dissertation, Technische Universität München
- Pauleit S, Duhme F (2000) Assessing the environmental performance of land cover types for urban planning. *Landsc Urban Plan* 52:1–20
- Pesaresi M, Gerhardinger A, Kayitakire F (2008) A robust built-up area presence index by anisotropic rotation-invariant textural measure. *IEEE J Sel Top Appl Earth Observ Remote Sens* 1:180–192
- Quah AK, Roth M (2012) Diurnal and weekly variation of anthropogenic heat emissions in a tropical city, Singapore. *Atmos Environ* 46:92–103
- Richter R (2009) Atcor 4 user guide. DLR – German Aerospace Centre, Remote Sensing Data Centre, Oberpfaffenhofen
- Rigo G, Parlow E (2007) Modelling the ground heat flux of an urban area using remote sensing data. *Theor Appl Climatol* 90:185–199
- Rinner C, Hussain M (2011) Toronto's urban heat island—exploring the relationship between land use and surface temperature. *Remote Sens* 3:1251–1265
- Roessner S, Segl K, Bochow M, Heiden U, Heldens W, Kaufmann H (2011) Potential of hyperspectral remote sensing for analyzing the urban environment. In: Yang X (ed) *Urban remote sensing: monitoring, synthesis and modeling in the urban environment*. Wiley-Blackwell, Chichester
- Roth M, Oke TR, Emery WJ (1989) Satellite-derived urban heat islands from three coastal cities and the utilization of such data in urban climatology. *Int J Remote Sens* 10:1699–1720
- Scholten F, Gwinner K, Tauch R, Boulgakova O (2003) HRSC-AX - high-resolution orthoimages and digital surface models for urban regions. In: Proceedings of the 2nd GRSS/ISPRS joint workshop on remote sensing and data fusion over urban areas (URBAN 2003), Berlin, Germany, pp 225–229
- Sobrino J, Oltra-Carrió R, Sòria G, Bianchi R, Paganini M (2012) Impact of spatial resolution and satellite overpass time on evaluation of the surface urban heat island effects. *Remote Sensing of Environment*. *Remote Sens Urban Environ* 117:50–56

- Stathopoulou M, Cartalis C (2009) Downscaling AVHRR land surface temperatures for improved surface urban heat island intensity estimation. *Remote Sens Environ* 113:2592–2605
- Stefanov WL, Netzbard M (2005) Assessment of ASTER land cover and MODIS NDVI data at multiple scales for ecological characterization of an urban center. *Remote Sens Environ* 99:31–43
- Stewart ID, Oke T (2012) ‘Local climate zones’ for urban temperature studies. *Bull Am Meteorol Soc* 93:1879–1900
- Sukkop H, Wittig R (eds) (1998) *Stadtökologie. Ein Fachbuch für Studium und Praxis*, 2nd edn. Gustav Fischer, Stuttgart
- Tang Y (2007) An integrated GIS-spatial analysis of Atlanta’s urban structure and urban space. PhD thesis, University of Georgia, USA. <http://athenaeum.libs.uga.edu/handle/10724/10039>. Accessed on 5 Mar 2012
- Taubenböck H, Heldens W, Heiden U, Wurm M (2010) Physische Indikatoren für die Stadtplanung. In: Taubenböck H, Dech S (eds) *Fernerkundung im urbanen Raum. Wissenschaftliche Buchgesellschaft*, Darmstadt, pp 86–93
- Taubenböck H, Kraft N (2013) The physical face of slums – a structural comparison of slums in Mumbai, India based on remotely sensed data. *J Built Environ*. doi:[10.1007/s10901-013-9333-x](https://doi.org/10.1007/s10901-013-9333-x)
- Tomlinson CJ, Chapman L, Thorne JE, Baker C (2011) Remote sensing land surface temperature for meteorology and climatology: a review. *Meteorol Appl* 18:296–306
- Voogt JA, Oke TR (2003) Thermal remote sensing of urban climates. *Remote Sens Environ* 86:370–384
- Watson ID, Johnson GT (1987) Graphical estimation of sky view-factors in urban environments. *J Climatol* 7:193–197
- Weng Q (2009) Thermal infrared remote sensing for urban climate and environmental studies: Methods, applications, and trends. *ISPRS J Photogramm Remote Sens* 64:335–344
- Weng Q (2012) Remote sensing of impervious surfaces in the urban areas: Requirements, methods, and trends. *Remote Sens Environ* 117:34–49
- Weng QH, Hu XF (2008) Medium spatial resolution satellite imagery for estimating and mapping urban impervious surfaces using LSMA and ANN. *IEEE Trans Geosci Remote Sens* 46:2397–2406
- Weng Q, Lu D, Schubring J (2004) Estimation of land surface temperature-vegetation abundance relationship for urban heat island studies. *Remote Sens Environ* 89:467–483
- Weng Q, Rajasekar U, Hu X (2011) Modeling urban heat islands and their relationship with impervious surface and vegetation abundance by using ASTER images. *IEEE Trans Geosci Remote Sens* 49:4080–4089
- Wickop E, Böhm P, Eitner K, Breuste J (1998) Qualitätszielkonzept für Stadtstrukturtypen am Beispiel der Stadt Leipzig, UFZ technical report 14
- Wurm M, Taubenböck H, Dech S (2010) Quantification of urban structures on building block level utilizing multisensoral remote sensing data. SPIE Europe, Toulouse, p 13
- Wurm M, Taubenböck H, Schardt M, Esch T, Dech S (2011) Object-based image information fusion using multisensor earth observation data over urban areas. *Int J Image Data Fusion* 2 (2):121–147
- Xiao R, Ouyang Z, Zheng H, Li W, Schienke EW, Wang X (2007) Spatial pattern of impervious surfaces and their impacts on land surface temperature in Beijing, China. *J Environ Sci* 19:250–256
- Yuan F, Bauer ME (2007) Comparison of impervious surface area and normalized difference vegetation index as indicators of surface urban heat island effects in Landsat imagery. *Remote Sens Environ* 106:375–386
- Yue W, Xu J, Tan W, Xu L (2007) The relationship between land surface temperature and NDVI with remote sensing: application to Shanghai Landsat 7 ETM+ data. *Int J Remote Sens* 28:3205–3226

- Zha Y, Gao J, Ni S (2003) Use of normalized difference built-up index in automatically mapping urban areas from TM imagery. *Int J Remote Sens* 24:583–594
- Zhang Y, Odeh IO, Han C (2009) Bi-temporal characterization of land surface temperature in relation to impervious surface area, NDVI and NDBI, using a sub-pixel image analysis. *Int J Appl Earth Observ Geoinform* 11:256–264

# Chapter 24

## Mineral Mapping with Airborne Hyperspectral Thermal Infrared Remote Sensing at Cuprite, Nevada, USA

Dean N. Riley and Christoph A. Hecker

**Abstract** This is a case example of mineral mapping of unaltered and altered rocks at the Cuprite mining district, southwestern Nevada using the Spatially Enhanced Broadband Array Spectrograph System (SEBASS), a thermal infrared hyperspectral sensor that collects radiance measurements in the mid-wave infrared and thermal infrared portions of the electromagnetic spectrum. Cuprite, Nevada has been a test bed for a variety of multispectral and hyperspectral sensors that have predominantly covered the visible through short-wave infrared portion of the electromagnetic spectrum. In 2008, 20 SEBASS flight lines were collected at an average altitude of 4,735 m yielding an average 3.35 m ground sample distance (GSD).

Rock forming and alteration minerals found in this mining district have reststrahlen features (emission minima due to fast changes in refractive index with wavelength) in the thermal infrared portion of the electromagnetic spectrum (7.5–13.5  $\mu\text{m}$ ). Mineral mapping with hyperspectral thermal infrared data provides unique and complementary information to visible-shortwave (0.4–2.5  $\mu\text{m}$ ) hyperspectral data. Mineral maps were produced using a spectral feature fitting algorithm with publicly available mineral spectral libraries containing signatures.

These mineral maps were compared to the geological and alteration maps along with mineral maps generated by previous studies of visible-shortwave infrared hyperspectral sensors to assess some of the difference in mineral mapping with a hyperspectral thermal infrared sensor. This study shows that hyperspectral thermal infrared data can spectrally map rock forming minerals associated with unaltered rocks and alteration minerals associated with different phases of alteration in altered rocks at Cuprite, Nevada.

---

D.N. Riley (✉)

The Aerospace Corporation, Chantilly, VA, USA

SpecTIR, LLC, Fairfax, VA, USA

e-mail: [DnRiley@spectir.com](mailto:DnRiley@spectir.com)

C.A. Hecker

Faculty of Geo-Information Science and Earth Observation (ITC),  
University of Twente, Enschede, The Netherlands

## 24.1 Introduction

Thermal spectroscopy of rocks and minerals has been of interest to the geological community and in its infancy was assisted by Kennecott Mining, and NASA (Lyon et al. 1959; Lyon and Burns 1963). The Air Force Research Lab and the USGS continued to support the early work of Lyon, Hunt, Salisbury, Vincent and others (Lyon and Burns 1963; Lyon 1965; Hunt 1970; Hunt and Salisbury 1974, 1976; Vincent et al. 1975) and show that the silicate and carbonate minerals have reflectance features from 8.0 to 14.0 microns ( $\mu\text{m}$ ). These minerals are the primary rock forming minerals for almost every type of igneous, sedimentary, and metamorphic rock. Since this early work, these researchers and their students developed many of the techniques originally used in the multispectral remote sensing community. Work in the Long-wave Infrared (LWIR) did not stop after this early work.

NASA and the USGS conducted numerous field studies in the late 1970s and 1980s to develop and characterize multispectral airborne sensors (TIMS (Thermal Infrared Multispectral Scanner), GER-D (Kahle et al. 1980; Kahle 1987)). Continuation of the work led to the development of DAIS 7915, NASA's MASTER (MODIS-ASTER Airborne Simulator) airborne instrument and others (Hook et al. 2001; Mauger 2003; Müller et al. 2005). MASTER has 25 bands in the Midwave Infrared (MWIR, 3.0–5.5  $\mu\text{m}$ ) and LWIR in addition to 25 bands in the VNIR-SWIR (visible to short-wave infrared). Airborne LWIR (long-wave infrared) hyperspectral sensors were first built in the 1990s that included the MIRACO<sub>2</sub>LAS (midinfrared airborne CO<sub>2</sub> laser system), SEBASS, AHI (Airborne Hyperspectral Imager), and ARGUS sensors (Whitbourn et al. 1990; Hackwell et al. 1996; Lucey et al. 1998; Cudahy et al. 1999). MIRACO<sub>2</sub>LAS and ARGUS are line profiling instruments; whereas, SEBASS and AHI are airborne imaging instruments. ITRES of Canada (Pignatti et al. 2011) has started to sell and fly its 32 channel LWIR imager (TASI, Thermal Airborne Spectrographic Imager) and Specim of Finland (Holma et al. 2009, 2011) has begun production of its 84 channel LWIR imager (OWL). Moreover, The Aerospace Corporation (Aerospace) has built and flown new sensor designs, a 32-channel LWIR imager, MAGI (Mineral and Gas Identifier) (Hall et al. 2008), and a 128-channel LWIR imager, MAKO (Hall et al. 2011), using Dyson spectrometers, and NASA Jet Propulsion Laboratory (JPL) just recently flew HyTES (Hyperspectral Thermal Emission Spectrometer) in late 2012 (Hook 2012, personal communication). There has been a continued maturation of LWIR instruments from research and development prototypes towards production and this will increase the amount of TIR data that is available for exploitation.

Cuprite Hills of Nevada, USA has been imaged with a variety of airborne and spaceborne multispectral and hyperspectral instruments (ATM (Technology Microwave Sounder), AIS (Airborne Imaging Spectrometer), TIMS, Geoscan, AVIRIS (Airborne Visible/Infrared Imaging Spectrometer), AISA (Airborne Hyperspectral Imaging Systems), CASI (Compact Airborne Spectral Imager), HYDICE (Hyperspectral Digital Imagery Collection Experiment), MASTER, Landsat, Hyperion, ASTER (Advanced Spaceborne Thermal Emission and Reflection

**Table 24.1** Flight log of SEBASS collection over Cuprite, Nevada

Session	Target X time (GMT)	Target name	Platform HAE (m) WGS84	Frames	IFOV (mrad)
080614_122714	12:32:12	CPRT4m_02	4738.88	3,500	1,100
080614_123753	12:42:19	CPRT4m_01	4717.83	3,500	1,100
080614_124749	12:52:42	CPRT4m_03	4725.82	3,500	1,100
080614_125914	13:03:02	CPRT4m_04	4749.33	3,500	1,100
080614_130855	13:13:31	CPRT4m_05	4717.25	3,500	1,100
080614_131925	13:23:56	CPRT4m_06	4732.5	3,500	1,100
080614_132934	13:34:21	CPRT4m_07	4732.18	3,500	1,100
080614_134040	13:44:53	CPRT4m_08	4740.28	3,500	1,100
080614_135032	13:55:14	CPRT4m_09	4731.83	3,500	1,100
080614_140047	14:05:12	CPRT4m_10	4753.42	3,500	1,100
080614_141108	14:15:26	CPRT4m_11	4746.1	3,500	1,100
080614_142046	14:25:41	CPRT4m_12	4731.78	3,500	1,100
080614_143111	14:35:36	CPRT4m_13	4731.21	3,500	1,100
080614_144104	14:45:30	CPRT4m_14	4730.06	3,500	1,100
080614_145038	14:55:16	CPRT4m_15	4721.26	3,500	1,100
080614_150031	15:05:12	CPRT4m_16	4733.35	3,500	1,100
080614_151028	15:14:40	CPRT4m_17	4732.91	3,500	1,100
080614_152001	15:24:27	CPRT4m_18	4753.63	3,500	1,100
080614_153016	15:34:33	CPRT4m_19	4743.58	3,500	1,100
080614_153943	15:44:08	CPRT4m_20	4747.14	3,500	1,100

Radiometer), and SEBASS) (Abrams et al. 1977; Ashley and Abrams 1980; Kahle and Goetz 1983; Kruse and Taranik 1989; Swayze et al. 1992; Mumon et al. 1996; Clark et al. 2003; Rowan et al. 2003; Allibone et al. 2004; Benavides et al. 2008a, b; Hecker 2012). The focus of this chapter is a case study demonstrating mineral mapping of rock forming and alteration minerals using airborne emittance spectroscopy over a site that has been consistently tested with visible to short-wave infrared (VNIR-SWIR) hyperspectral airborne and spaceborne sensors. Results from this study can be compared with the results from lower spectral resolution systems and lower signal to noise airborne sensors such as Aerospace's Mineral and Gas Identifier (MAGI), NASA JPL's MODIS/ASTER Airborne Simulator (MASTER), ITRES's TASI, or Specim's OWL sensors or current spaceborne sensors such as the Advanced Spaceborne Reflection and Emission Radiometer (ASTER) or NASA's proposed HYSPRI sensor. Twenty SEBASS flight lines were flown and radiance data was recorded from 3.0 to 5.5  $\mu\text{m}$  and 7.7 to 13.5  $\mu\text{m}$  on June 14th, 2008 with a 3.35 meter (m) spatial resolution (Table 24.1).

## 24.2 Geologic Setting

In the southwestern part of the Great Basin in the United States south of the town of Goldfield, Nevada are the Cuprite Hills. These hills have limited vegetation cover and range from 1,400 to 1,700 m above sea level. Topographic relief in the western

part of the hills is controlled by a north trending ridge and circular hills in the eastern part of the hills. This area has moderately easy access as U.S. Highway 95 runs through the area (Ashley and Abrams 1980) (Fig. 24.1).

In the Cuprite Hills, the oldest rocks are found in the western section and are Cambrian in age. These are the Harkless, Mule Spring, and Emigrant Formations. The Harkless Formation ( $\text{Ch}$ ) is the oldest sequence in the area and is composed of siltstone, quartizitic siltstone, and orthoquartzite sandstone. Minerals present in these rocks are commonly chlorite, muscovite, biotite, and quartz. This is overlain by the Mule Spring Formation ( $\text{Cms}$ ) which is a thin-bedded limestone that is finely crystalline. The primary mineral present in this formation is calcite. Overlying the Mule Spring Formation is the Emigrant Formation ( $\text{Ce}$ ) which has limited outcrops and consists primarily of limestone and chert (Albers and Stewart 1972; Ashley and Abrams 1980) (Fig. 24.1).

Unconformably overlaying the Cambrian rocks are a series of Tertiary volcanic and sedimentary lithologies. The oldest Tertiary rocks are a rhyolite ( $\text{Ts}$ ) that is observed in the eastern and western sections of the area and a quartz latite tuff, which is found in the western section. Minerals present are sanidine, quartz, plagioclase, and biotite. Plagioclase is absent in the quartz latite dike and biotite is limited. In the eastern section, there are exposures of porphyritic plagioclase olivine basalt that overlie the rhyolitic rocks ( $\text{Ts}$ ). The minerals in this basalt ( $\text{Tb1}$ ) are olivine and calcic-rich plagioclase. The basalt is overlain by the Stonewall Flat Tuff ( $\text{TsF}$ ) that consists of devitrified sodic rhyolitic ash-flow tuffs and some quartz latite dikes. Minerals present in this formation are sanidine, quartz, plagioclase and biotite. Whereas, the quartz latite dike in this formation has quartz, sanidine, and biotite phenocrysts. Lastly, the Pediment basalt ( $\text{Tb2}$ ), in the western section, is a olivine-rich basalt and is the youngest of the Tertiary rocks with olivine and plagioclase as the primary minerals (Ashley and Abrams 1980) (Fig. 24.1).

The youngest rocks in the area are, Quaternary sand and gravel deposits ( $\text{Qal}$ ) and Quaternary playa that overlay the Tertiary age rocks unconformably (Ashley and Abrams 1980) (Fig. 24.1).

### 24.2.1 Hydrothermal Alteration

Silicic, Opaline, and Argillic hydrothermal alteration were mapped in the area using traditional geological alteration mapping methods (Fig. 24.2). Silicic alteration is most prevalent in the eastern section of the area, but the areal extent is less than present in the western section. Hydrothermal quartz is the dominant mineral with minor kaolinite, alunite, and calcite (Ashley and Abrams 1980).

The most prevalent alteration is opalization. Opal, alunite, and kaolinite are the dominant minerals associated with this alteration. To a lesser degree, dickite, pyrophyllite, calcite, buddingtonite, muscovite, montmorillonite, and jarosite are observed in these rocks (Ashley and Abrams 1980; Swayze et al. 1992; Swayze 1997) (Fig. 24.2).

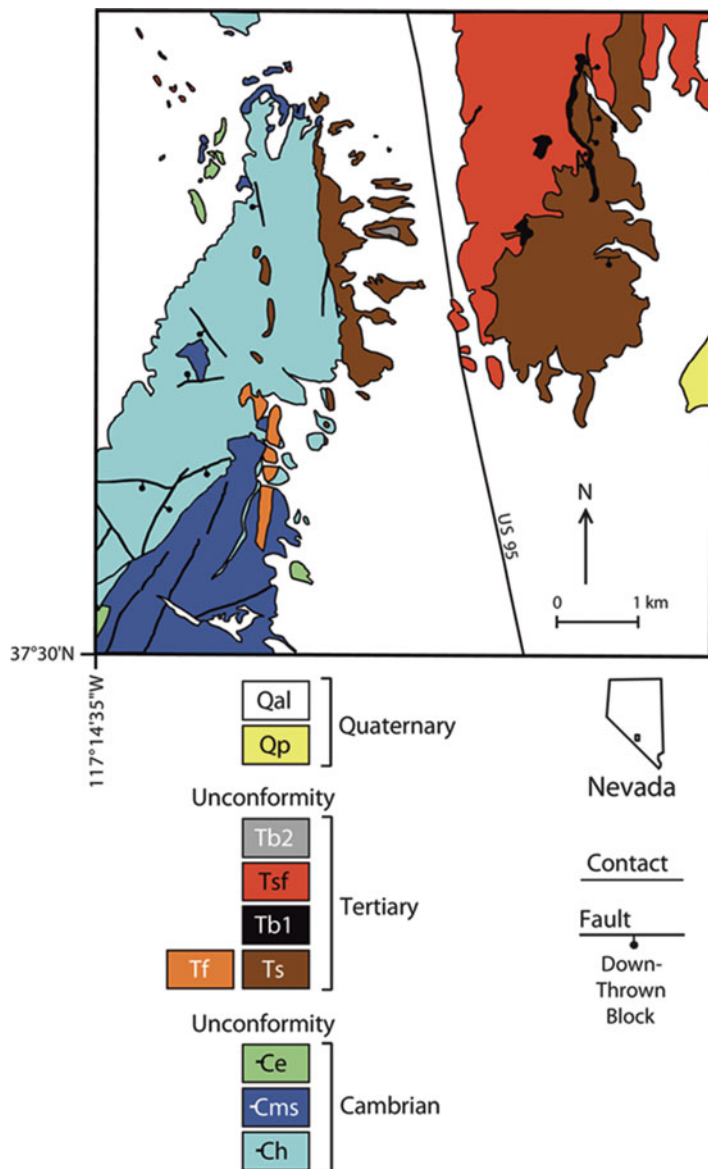


**Fig. 24.1** Generalized geologic map of Cuprite mining district, Nevada (Rowan et al. 2003). *Qal* sand, gravel, and boulders, *Qp* playa deposits, *Tb2* olivine basalt, *Tsf* sodic ash-flow tuff, *Tb1* porphyritic olivine basalt, *Ts* crystal-rich rhyolite and latite tuff, conglomerate, and sandstone, *Tf* quartz latitic felsites,  $\ominus e$  limestone and chert,  $\ominus ms$  limestone and lower limey siltstone,  $\ominus h$  phyllitic siltstone and minor sandy limestone (Modified from Ashley and Abrams 1980; Swayze 1997); inset map shows location of area in western Nevada

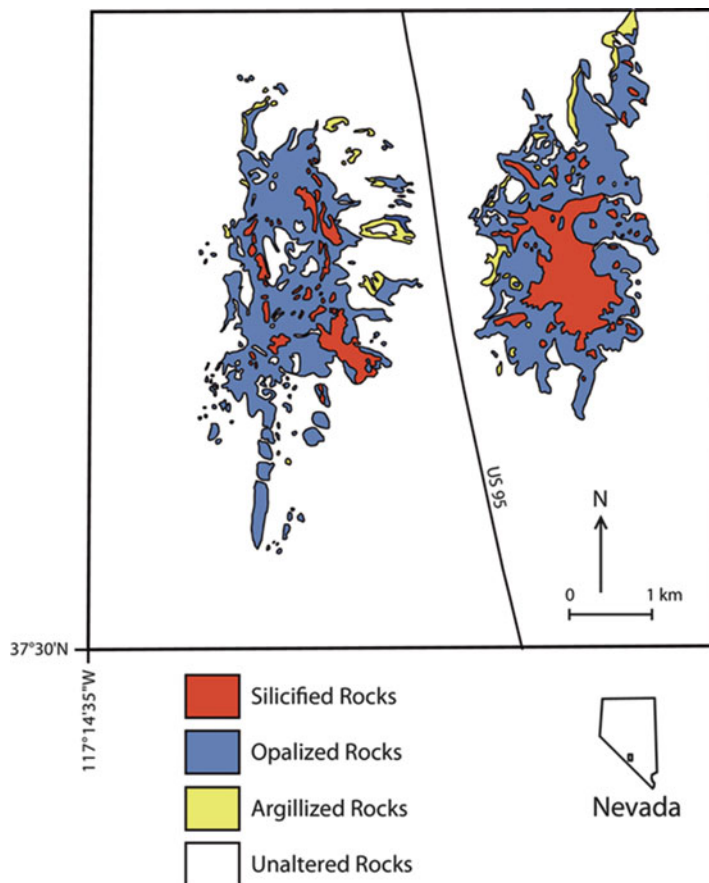


**Fig. 24.2** Generalized map showing the distribution of three hydrothermally altered rock units: (1) red, silicified; (2) blue, opalized; and (3) yellow, argillized (Rowan et al. 2003) (Modified from Ashley and Abrams 1980)

Argillic alteration is the least intense and prevalent alteration style in the district. Recognition of this alteration is observed by plagioclase altering to kaolinite, bleaching of biotite, and volcanic glass altering to opal, montmorillonite, and kaolinite with quartz and sanidine remaining unaltered (Ashley and Abrams 1980) (Fig. 24.2).

### 24.3 Emittance of Minerals at Cuprite

Rock forming minerals have spectral features in the Thermal Infrared (TIR) region of the electromagnetic spectrum (5–25  $\mu\text{m}$ ). Fundamental vibrational frequencies of silicates, carbonates, sulfates, and phosphates show spectral features

in the 8–14  $\mu\text{m}$  portion. Mineral identification is feasible because the spectral features (reststrahlen bands, i.e., emission minima due to fast changes in refractive index with wavelength) are diagnostic and display variations in wavelength position due to cation substitution (Salisbury et al. 1991; Hapke 1993).

Rocks and minerals have been measured in the laboratory using TIR spectroscopy and are used for mapping and identification of surface materials (Lyon et al. 1959; Lyon 1965; Farmer 1974; Salisbury et al. 1991; Christensen et al. 2000). Spectral libraries are readily available for mapping with airborne and spaceborne multispectral and hyperspectral data that contain spectra from 5 to 45  $\mu\text{m}$ . The United States Geological Survey (USGS), NASA's Jet Propulsion Laboratory (JPL), Johns Hopkins University (JHU), Arizona State University (ASU) all have developed spectral libraries and are available online. NASA's ASTER spectral library is available online and is a compilation of the JPL's, JHU's, and the USGS's spectral libraries (Clark et al. 2007).

1. ASU spectral library ([URL1](#))
2. ASTER spectral library ([URL2](#))
3. USGS spectral library ([URL3](#))

TIR spectra measured in hemispherical reflectance can be used to calculate emissivity using Kirchhoff's law. Emissivity ( $\epsilon$ ) is related to hemispherical reflectance ( $\rho$ ) with the following equation (Salisbury et al. 1994).

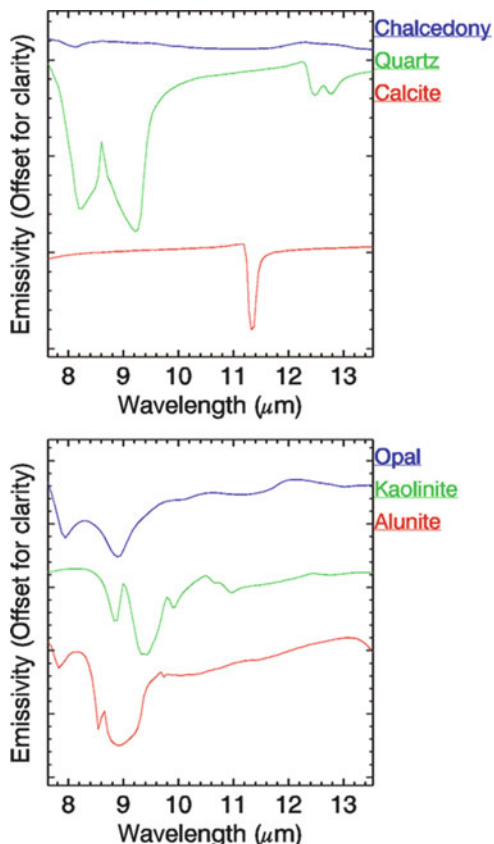
This allows the use of rock and mineral spectral libraries collected in hemispherical reflectance to be used for spectral mapping of TIR data that has been converted to emissivity.

Mineral groups that have been mapped using multispectral TIR remote sensing data include silicates, carbonates, sulfates, phosphate, and clays (Kahle and Rowan 1980; Kahle and Goetz 1983; Gillespie et al. 1984; Kahle et al. 1988; Sabine et al. 1994; Crowley and Hook 1996; Hook et al. 1999; Rowan and Mars 2003). The use of hyperspectral TIR data for mineral mapping has received considerably less attention; however, silicates, carbonates, sulfates, and clays have been mapped (Cudahy et al. 2000; Hewson et al. 2000; Calvin et al. 2001; Vaughan et al. 2003, 2005; Vaughan and Calvin 2005; Riley et al. 2007, 2008; Aslett et al. 2008). In previous hyperspectral TIR studies a single flight line was flown over interesting geological features. This study involves mineral mapping of unaltered and altered rocks at Cuprite, across several parallel flightlines.

### 24.3.1 Unaltered Rocks

The Harkless Formation is made up of chlorite, muscovite, biotite, and quartz (Ashley and Abrams 1980). Chlorite has three reststrahlen bands in the 8–12  $\mu\text{m}$  region, a deep one at 9.75  $\mu\text{m}$  and two shallower features at 9.35 and 10.4  $\mu\text{m}$ . Muscovite has reststrahlen features at 9.25 and 9.4  $\mu\text{m}$ . The reststrahlen features of biotite are 9.2 and 9.8  $\mu\text{m}$ . Quartz has two doublet reststrahlen features, one centered at 8.65  $\mu\text{m}$  with minima at 8.5 and 8.9  $\mu\text{m}$  and the other at 12.6  $\mu\text{m}$  with

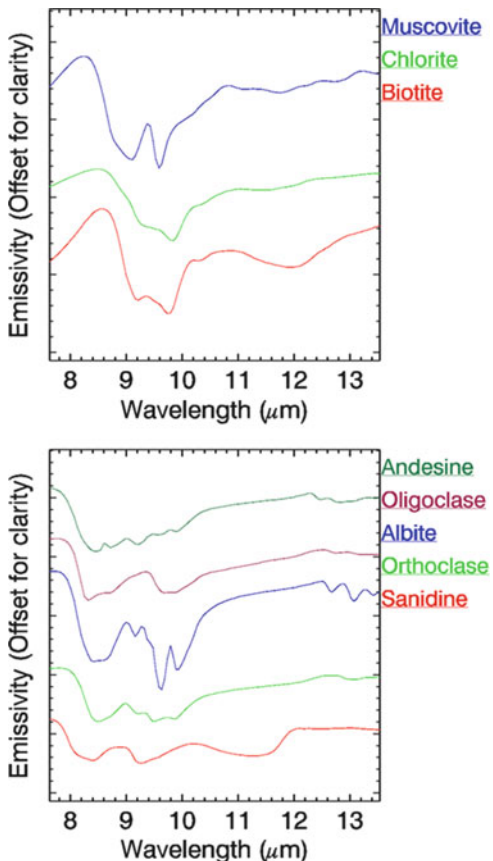
**Fig. 24.3** *Upper plot:* Thermal spectral signatures of chalcedony (blue, upper), quartz (green, middle), calcite (red, lower). *Lower plot:* Thermal spectral signatures of opal (blue, upper), kaolinite (green, middle), alunite (red, lower)



minima at 12.5 and 12.8  $\mu\text{m}$ . Whereas, the Mule Spring Formation is limestone and its primary mineral is calcite which has a reststrahlen feature at 11.3  $\mu\text{m}$  (Figs. 24.3 and 24.4).

Rhyolite (Ts) is composed of quartz, sanidine, plagioclase, and biotite phenocrysts. The quartz latite tuff (Tf) consists of predominantly quartz and alkali-feldspar (sanidine) with scarce biotite phenocrysts. The Stonewall Flat Tuff (Tsf) is composed of devitrified sodic rhyolite ash-flow tuffs and a quartz latite dike. These rocks have sanidine phenocrysts with quartz and sodic feldspar groundmass (Ashley and Abrams 1980). Plagioclase in silicic volcanic rocks is commonly albite, oligoclase or even andesine. Reststrahlen bands for sanidine are at 8.65 and 9.5  $\mu\text{m}$  and biotite has bands at 9.2 and 9.8  $\mu\text{m}$ . Albite has multiple reststrahlen features at 8.7, 9.2, 9.6, and 9.9  $\mu\text{m}$ . Oligoclase has reststrahlen bands at 8.7 and 9.9  $\mu\text{m}$  and andesine has bands at 8.8 and 9.9  $\mu\text{m}$ . As the calcic content of plagioclase increases from albite to andesine there is a shift to longer wavelength from 8.7 to 9.0  $\mu\text{m}$  reststrahlen band. The reststrahlen bands for plagioclase shift from anorthite to albite (Cudahy et al. 2000) (Figs. 24.3 and 24.4).

**Fig. 24.4** *Upper plot:* Thermal spectral signatures of muscovite (blue, upper), chlorite (green, middle), biotite (red, lower). *Lower plot:* Thermal spectral signatures of andesine (dark green, upper), Oligoclase (dark red, upper-middle), albite (blue, middle), orthoclase (green, lower-middle), sanidine (red, lower)



### 24.3.2 Altered Rocks

Silicic alteration is more prevalent in eastern section of area, but the areal extent is less in the western section. Hydrothermal quartz is the dominant mineral with minor kaolinite, alunite, and calcite (Ashley and Abrams 1980). Hydrothermal quartz has a doublet of reststrahlen features with a peak in between centered at 8.65  $\mu\text{m}$  and the features at 8.5 and 8.9  $\mu\text{m}$ . Kaolinite has multiple reststrahlen features at 8.9, 9.6, 9.9, and 11.0  $\mu\text{m}$  with the features at 9.6 and 11.0 being the most significant. Alunite has an asymmetric doublet with a peak at 8.7  $\mu\text{m}$  and the features at 8.4 and 9.0  $\mu\text{m}$  (Figs. 24.3 and 24.4). An asymmetric doublet that is slightly different than pure quartz has been noted (Vaughan et al. 2003). Moreover, chalcedony has an asymmetric doublet that is similar to the quartz-alunite combined signature. As noted by (Vaughan et al. 2003), these spectral similarities make separating quartz, alunite, quartz-alunite, chalcedony, and opal in the TIR difficult (Figs. 24.3 and 24.4), but feasible.

Opalized alteration is the most prevalent alteration present. Opal, alunite, and kaolinite are the dominant minerals associated with this alteration. Dickite, pyrophyllite, calcite, buddingtonite, muscovite, montmorillonite, and jarosite can be observed in these rocks as well (Ashley and Abrams 1980; Swayze et al. 1992; Swayze 1997). Opal has a single reststrahlen feature at 8.8  $\mu\text{m}$ . Alunite has reststrahlen bands at 8.4 and 9.0  $\mu\text{m}$  with a peak in between at 8.7  $\mu\text{m}$ . Kaolinite's multiple reststrahlen bands are at 8.9, 9.6, 9.9, and 11.0  $\mu\text{m}$  (Figs. 24.3 and 24.4). Calcite has a reststrahlen band at 11.3  $\mu\text{m}$  and muscovite has features at 9.25 and 9.4  $\mu\text{m}$ . The reststrahlen features of dickite, pyrophyllite, buddingtonite, montmorillonite, and jarosite will not be discussed as these minerals will not be mapped for brevity (Figs. 24.3 and 24.4).

The areal extent of argillic alteration in the district is the least intense and prevalent. This alteration is recognized by plagioclase altering to kaolinite, bleaching of biotite, and volcanic glass altering to opal, montmorillonite, and kaolinite. Quartz and sanidine are unaltered (Figs. 24.3 and 24.4).

## 24.4 SEBASS Analysis

### 24.4.1 Data Collection and Calibration

Spatially Enhanced Broadband Array Spectrograph System (SEBASS) measures reflected and emitted radiation with 128 channels from 2.5 to 5.3  $\mu\text{m}$  and measures emitted radiation with 128 channels from 7.6 to 13.5  $\mu\text{m}$  of the electromagnetic spectrum. This instrument operates as a pushbroom sensor with 128 pixels in the cross-track direction and has a 7.8° FOV and 1.1-mrad IFOV per pixel. A flight altitude of approximately 3,000 m above ground level (AGL) producing a 3.35-m resolution was flown for this study. When flown with greater area coverage, the signal-to-noise (SNR) ratio has been tested greater than 2,000:1 (Hackwell et al. 1996).

Under clear sky conditions, SEBASS data were collected over Cuprite, Nevada in June, 2008. Following the steps outlined by Hackwell et al. (1996), these data were calibrated to at-sensor radiance. Especially important was the use of cold and hot blackbodies at the beginning and end of each flight line for in flight calibration. These data were preprocessed for striping prior to atmospheric compensation and masking of bad pixels (Dykstra and Segal 1985). At surface radiance data were produced using an In Scene Atmospheric Correction (ISAC) algorithm (Young et al. 2002). These data were converted to apparent emissivity and temperature using a Emissivity Normalization Method (ENM) for the temperature emissivity separation (TeS) (Gillespie 1986; Kealy and Hook 1993). The emissivity data were smoothed using a Savitzky-Golay filter prior to spectral mapping (Savitzky and Golay 1964; Tsai and Philpot 1998; King et al. 1999; Ruffin and King 1999). Lastly, these LWIR data were subset from 8.0 to 12.0  $\mu\text{m}$  prior to spectral feature

absorption mapping because most of minerals at Cuprite have absorption features constrained to this region.

#### 24.4.2 Image Analysis

Figure 24.5 shows a false color composite image and a decorrelation image of SEBASS's channels at 11.09, 9.60, and 9.02  $\mu\text{m}$  displayed as red, green, and blue (Gillespie et al. 1986). Vaughan et al. (2003) noted that quartz dominated regions should appear yellow, clay-rich areas are magenta, quartz-sulfate mixtures are a green, and quartz-feldspar-clay mixtures are orange-brown in color. At Cuprite using similar wavelengths, the Harkless Formation appears as red which primarily composed of chlorite, muscovite, biotite, and quartz. Whereas, the Mule Spring Formation appear as blue (calcite-rich) and the Stonewall Flat Formation appears as blue with a lot of orange-brown (quartz- and feldspar-rich). The alteration centers appear as green with yellow and they are dominated with quartz-alunite mixtures; while, the orange-brown areas are quartz, feldspar, and clay rich.

#### 24.4.3 Spectral Feature Processing

Spectral mapping of the minerals was conducted using spectral feature fitting in ENVI with a spectral library constrained to the probable minerals at Cuprite which is similar to the methods developed by (Clark and Roush 1984; Swayze 1997; Clark et al. 2003). ENVI's spectral feature fitting routine produces a scaled image and a root mean square (RMS) image for each spectral signature mapped using a least squares routine and a "fit image" can be generated by dividing the scaled image with the rms image. A threshold of two standard deviations was applied to the fit image.

Alunite is spectrally mapped in the western section moderately well when compared to VNIR-SWIR spectral mapping of Clark et al. (2003). Spatially there is less alunite mapped in eastern alteration location. In both cases, alunite is spectrally mapped as a bulls-eye pattern around the silicified alteration. The alluvium is mapping some alunite which is probably from the weathering of the rocks.

Spectral mapping of chlorite is predominantly in the Harkless Formation ( $\text{Eh}$ ), western section of Fig. 24.7. Chlorite is seen in the alluvium as well and is most likely from the weathering of the Harkless Formation. The Stonewall Flat Tuff (Tsf) also has some chlorite spectrally mapping on it. The weathering of biotite to chlorite is most likely the result of this spectral mapping.

In the eastern alteration center, the spectral mapping of quartz is coherent and overlies the silicified alteration described by Ashley and Abrams (1980). Quartz also maps well the smaller silicified alteration observed in the western alteration

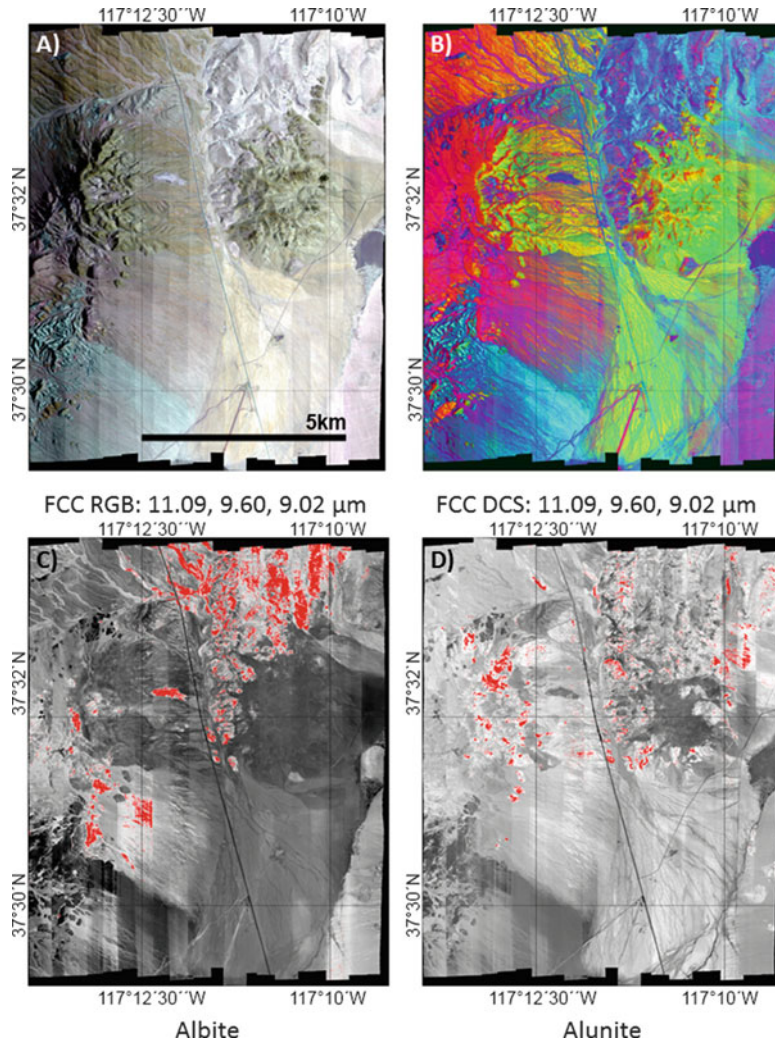


**Fig. 24.5** *Upper left:* Mosaicked false color composite (FCC) image at R: 11.09, G: 9.60, and B: 9.02  $\mu\text{m}$ . *Upper right:* Mosaicked decorrelation stretch false color composite (FCC-DCS) image at R: 11.09, G: 9.60, and B: 9.02  $\mu\text{m}$ . *Lower left:* Mosaicked albite gray scale image from least squares material matching algorithm overlain with threshold at 2 standard deviations. *Lower right:* Mosaicked alunite gray scale image from least squares material matching algorithm overlain with threshold at 2 standard deviations

center. The rhyolitic tuffs and quartz latite is spectrally mapped well in the northwestern section (Fig. 24.8).

Calcite is spectrally mapped in the southwestern portion of the figure and correlates well with the Mule Spring Formation. Calcite is also mapped spectrally in smaller outcrops in the northwest and in the southeast. U.S Highway 95 is also

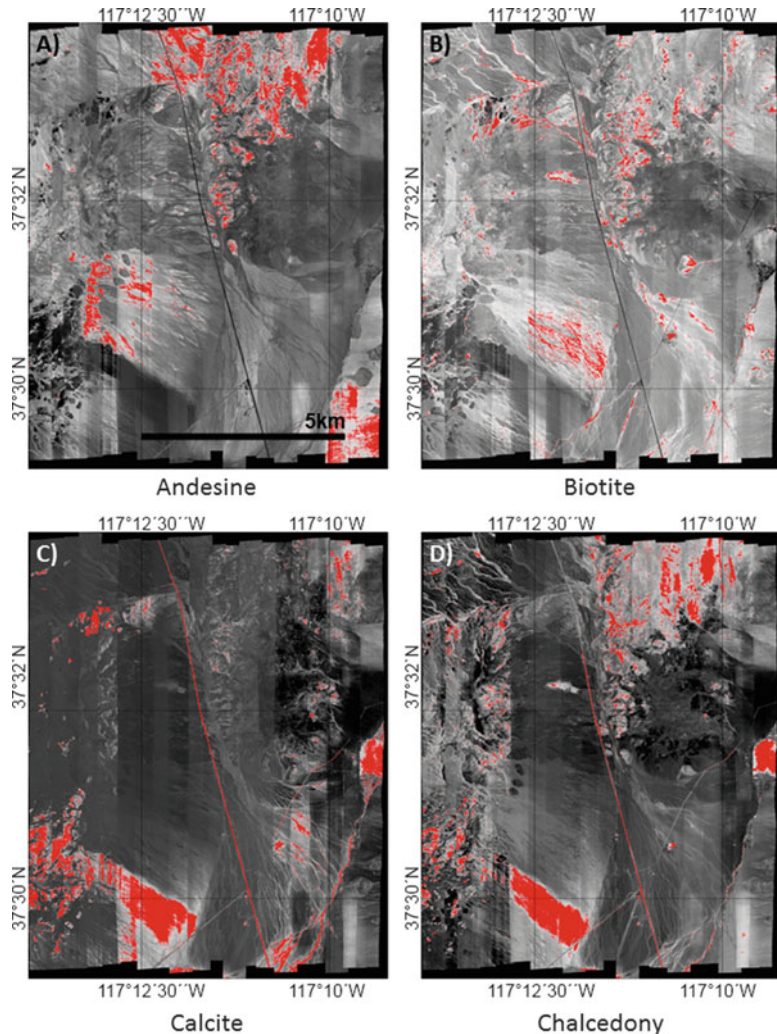


**Fig. 24.6** *Upper left:* Mosaicked andesine gray scale image from least squares material matching algorithm overlain with threshold at 2 standard deviations. *Upper right:* Mosaicked biotite gray scale image from least squares material matching algorithm overlain with threshold at 2 standard deviations. *Lower left:* Mosaicked calcite gray scale image from least squares material matching algorithm overlain with threshold at 2 standard deviations. *Lower right:* Mosaicked chalcedony gray scale image from least squares material matching algorithm overlain with threshold at 2 standard deviations

mapped with calcite which is not surprising since asphalt commonly has calcite in it (Fig. 24.6).

Chalcedony is spectrally mapped in the western alteration center overlying the silicified alteration zone. It is also mapped in the Stonewall Flat Tuff (Tsf) and over

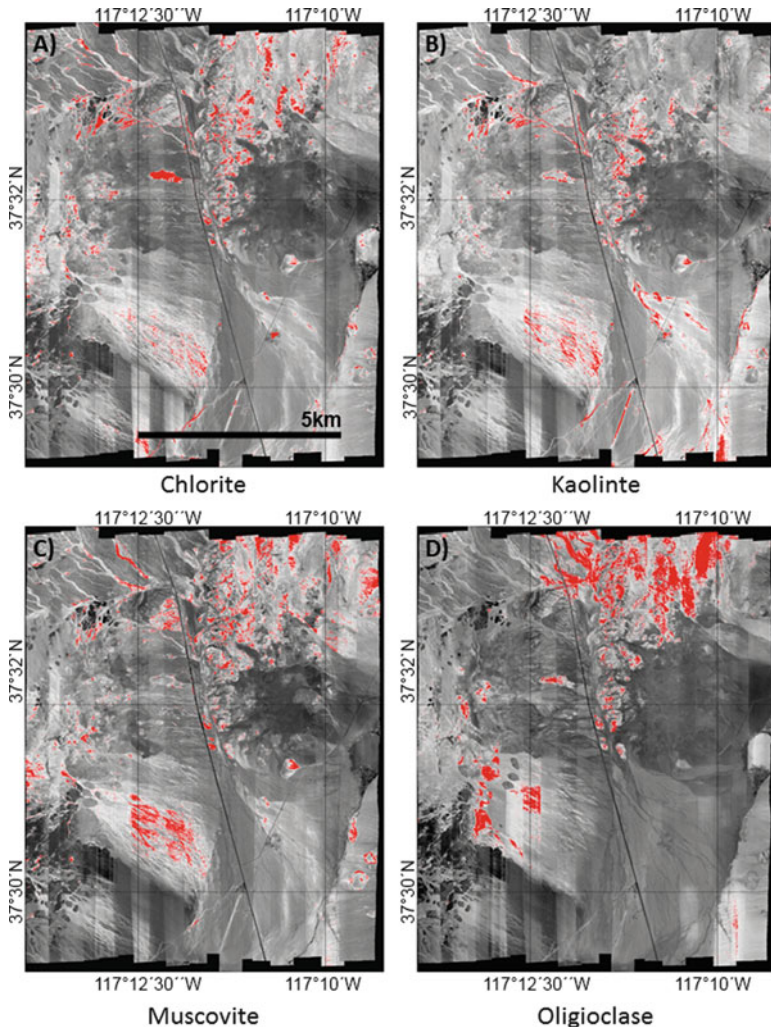


**Fig. 24.7** *Upper left:* Mosaicked chlorite gray scale image from least squares material matching algorithm overlain with threshold at 2 standard deviations. *Upper right:* Mosaicked kaolinite gray scale image from least squares material matching algorithm overlain with threshold at 2 standard deviations. *Lower left:* Mosaicked muscovite gray scale image from least squares material matching algorithm overlain with threshold at 2 standard deviations. *Lower right:* Mosaicked oligoclase gray scale image from least squares material matching algorithm overlain with threshold at 2 standard deviations

parts of the Mule Spring Formation (Gms). The spatial coherency of chalcedony is less than quartz spectral mapping over the silicified alteration center (Fig. 24.6).

Spectral mapping of muscovite occurs over the Harkless Formation in the western alteration area and in some of the argillic alteration area in the east alteration center (Fig. 24.7). This mapping in the eastern area is mainly located between the eastern alteration area and the Stonewall Flat Tuff (Tsf).

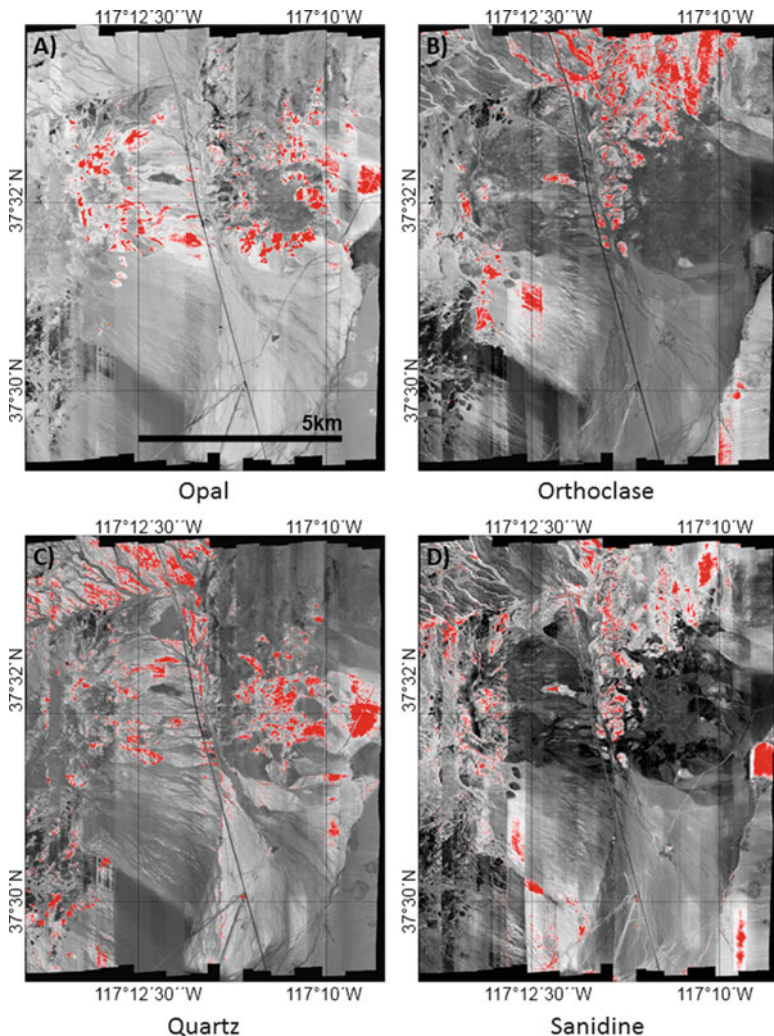


**Fig. 24.8** *Upper left:* Mosaicked opal gray scale image from least squares material matching algorithm overlain with threshold at 2 standard deviations. *Upper right:* Mosaicked orthoclase gray scale image from least squares material matching algorithm overlain with threshold at 2 standard deviations. *Lower left:* Mosaicked quartz gray scale image from least squares material matching algorithm overlain with threshold at 2 standard deviations. *Lower right:* Mosaicked sanidine gray scale image from least squares material matching algorithm overlain with threshold at 2 standard deviations

Kaolinite spectrally maps mostly in the western alteration area and along the west and north of the eastern alteration area. Kaolinite is also found in the alluvium as well and maps around the Pediment basalt (Tb2) coherently (Fig. 24.7).

Opal is found from spectral mapping in the western alteration area and outside of the silicified alteration in the eastern alteration area. Opal is spectrally mapped in

the Stonewall Flat Tuff (Tsf) which is the result of weathering and devitrification of the rhyolites and quartz latite (Fig. 24.8).

Coherent patterns of alunite, calcite, chalcedony, chlorite, kaolinite, muscovite, opal, quartz, sanidine were mapped using a least-squares based spectral feature fitting algorithm applied to SEBASS apparent emissivity data. Rock forming minerals associated with unaltered rocks were mapped correlating with the Harkless, Mule Spring, and Stonewall Flat Tuff Formations. Alteration minerals associated with argillic, opalized, and silicified alteration were mapped and correlate with alteration map produced by (Ashley and Abrams 1980).

Mineral mapping of chlorite correlates with the Harkless formation. Some muscovite and quartz spectrally maps with the Harkless Formation as well. Calcite spectrally maps predominantly within the Mule Spring Formation in the southwest section of the district.

Argillic alteration is limited, but kaolinite and muscovite both map outside of the opalized alteration in the eastern and western alteration centers.

Opalized alteration is predominantly in the eastern alteration center and is spectral mapped using an opal signature. Alunite was detected in the opalized alteration areas as well, while Chalcedony does not significantly overlap with opal.

Silicified alteration (represented by quartz spectral map) is dominantly detected in the eastern alteration center. Chalcedony maps in the silicified alteration as well, but this is more likely the result of minor alunite being present than chalcedony being present. This is similar to what was seen with other quartz-alunite rocks having a similar spectral signature to chalcedony (Vaughan et al. 2003). Separating different types of siliceous minerals is feasible even though the minerals have similar spectral shapes and absorption features.

## 24.5 Summary and Conclusions

Thermal infrared hyperspectral remote sensing at Cuprite, Nevada shows Stonewall Flat Tuff, rhyolite, and quartz-latite tuff can be spectrally mapped. This is in addition to the Harkless and Mule Spring Formations being spectrally mapped as well. The eastern and western alteration centers with their silicic, opaline, and argillic alteration are also mapped spectrally. These results indicate that rock forming and alteration minerals can be mapped with similar and complementary results to visible to short-wave infrared hyperspectral mineral mapping. Differentiating chlorite and calcite in the thermal infrared is much easier in the thermal infrared than in the short-wave infrared since the absorption features of these minerals do not overlap this portion of the electromagnetic spectrum. Moreover, mineral mapping techniques developed for the visible to short-wave infrared hyperspectral sensors are applicable in the thermal infrared once the data has been converted to emissivity.

**Acknowledgements** This work was funded by The Aerospace Corporation through internal research and development money to Dean Riley while he was at Aerospace. The authors would also like to thank the anonymous reviewers who helped improve this chapter.

## References

- Abrams MJ, Ashley RP, Rowan LC, Goetz AFH, Kahle AB (1977) Mapping of hydrothermal alteration in the Cuprite mining district, Nevada, using aircraft scanner images for the spectral region 0.46 to 2.36  $\mu\text{m}$ . *Geology* 5(12):713–718
- Albers JP, Stewart JH (1972) Geology and mineral deposits of Esmeralda County, Nevada. Nev Bur Mines Geol Bull 78:80
- Allibone A, Hayden P, Cameron G, Duku F (2004) Paleoproterozoic gold deposits hosted by albite- and carbonate-altered tonalite in the Chirano District, Ghana, West Africa. *Econ Geol* 99:479–497
- Ashley RP, Abrams MJ (1980) Alteration mapping using multispectral images – Cuprite mining district, Esmeralda County, Nevada. Open-File Report, United States Geological Survey, 17p, 14 plates, (some col.), maps; 28 cm
- Aslett Z, Taranik JV, Riley DN (2008) Mapping rock-forming minerals at daylight pass, Death Valley National Park, California, using SEBASS thermal-infrared hyperspectral image data. In: Geoscience and remote sensing symposium, 2008. IGARSS 2008. IEEE International, Boston
- Benavides J, Kyser TK, Clark AH, Stanley C, Oates C (2008a) Application of molar element ratio analysis of lag talus composite samples to the exploration for iron oxide–copper–gold mineralization: Mantoverde area, northern Chile. *Geochem Explor Environ Anal* 8(3–4):369–380
- Benavides J, Kyser TK, Clark AH, Stanley C, Oates C (2008b) Exploration guidelines for copper-rich iron oxide–copper–gold deposits in the Mantoverde area, northern Chile: the integration of host-rock molar element ratios and oxygen isotope compositions. *Geochem Explor Environ Anal* 8(3–4):343–367
- Calvin WM, Vaughan RG, Taranik JV, Smailbegovic A (2001) Mapping natural and human influenced acid sulfate weathering near Reno, NV using the SEBASS hyperspectral instrument. In: Geoscience and remote sensing symposium, 2001. IGARSS '01. IEEE 2001 International. Sidney NSW, Australia
- Christensen PR, Bandfield JL, Hamilton VE, Howard DA, Lane MD, Piatek JL, Ruff SW, Stefanov WL (2000) A thermal emission spectral library of rock-forming minerals. *J Geophys Res* 105(E4):9735–9739
- Clark RN, Roush TL (1984) Reflectance spectroscopy' quantitative analysis techniques for remote sensing applications. *J Geophys Res* 89(B7):6329–6340
- Clark RN, Swayze GA, Livo KE, Kokaly RF, Sutley SJ, Dalton JB, McDougal RR, Gent CA (2003) Imaging spectroscopy: Earth and planetary remote sensing with the USGS Tetracorder and expert systems. *J Geophys Res* 108(E12):5131
- Clark RN, Swayze GA, Wise R, Livo KE, Hoefen TM, Kokaly RF, Sutley SJ (2007) USGS digital spectral library splib06a, Digital data series 231. U.S. Geological Survey, Denver
- Crowley JK, Hook SJ (1996) Mapping playa evaporite minerals and associated sediments in Death Valley, CA, with multispectral thermal infrared images. *J Geophys Res* 101(B1):643–660
- Cudahy TJ, Whitbourn LB, Connor PM, Mason P, Phillips RN (1999) Mapping surface mineralogy and scattering behavior using backscattered reflectance from a hyperspectral midinfrared airborne CO<sub>2</sub> laser system (MIRACO2LAS). *IEEE Trans Geosci Remote Sens* 37(4):2019–2034
- Cudahy TJ, Okada K, Yamato Y, Maekawa M, Hackwell JA, Huntington JF (2000) Mapping skarn and porphyry alteration mineralogy at Yerington, Nevada, using airborne hyperspectral TIR

- SEBASS data. CSIRO Exploration and Mining report 734R. CSIRO Exploration and Mining, Underwood Avenue, Floreat Park, WA, Australia, p 78
- Dykstra JD, Segal DB (1985) Analysis of AIS data of the recluse oil field, Recluse, Wyoming. In: Proceedings AIS workshop. NASA Jet Propulsion Laboratory, Pasadena, CA
- Farmer VC (1974) The infrared spectra of minerals. Mineralogical Society, London
- Gillespie AR (1986) Lithologic mapping of silicate rocks using TIMS. The TIMS data users' workshop. NASA Jet Propulsion Laboratory, Pasadena
- Gillespie AR, Kahle AB, Palluconi FD (1984) Mapping alluvial fans in Death Valley, CA using multispectral thermal infrared images. *Geophys Res Lett* 11:1153–1156
- Gillespie AR, Kahle AB, Walker RE (1986) Color enhancement of highly correlated images. I. Decorrelation and HSI contrast stretches. *Remote Sens Environ* 20(3):209–235
- Hackwell JA, Warren DW, Bongiovi RP, Hansel SJ, Hayhurst TL, Mabry DJ, Sivjee MG, Skinner JW (1996) LWIR/MWIR imaging hyperspectral sensor for airborne and ground-based remote sensing. SPIE, Denver
- Hall JL, Hackwell JA, Tratt DM, Warren DW, Young SJ (2008) Space-based mineral and gas identification using a high-performance thermal infrared imaging spectrometer. SPIE, San Diego
- Hall JL, Boucher RH, Gutierrez DJ, Hansel SJ, Kasper BP, Keim ER, Moreno NM, Polak ML, Sivjee MG, Tratt DM, Warren DW (2011) First flights of a new airborne thermal infrared imaging spectrometer with high area coverage. SPIE, Orlando
- Hapke B (1993) Combined theory of reflectance and emittance spectroscopy. In: Pieters CM, Englert PAJ (eds) Topics in remote sensing 4-remote geochemical analysis: elemental and mineralogical composition. Cambridge University Press, Cambridge, pp 31–42
- Hecker CA (2012) Mapping feldspars from above - a thermal infrared and partial least squares-based approach. Doctorate of Philosophy dissertation, University of Twente, Enschede
- Hewson RD, Hausknecht P, Cudahy TJ, Huntington JF, Mason P, Hackwell JA, Nikitas J, Okada K (2000) An appraisal of the hyperspectral thermal-infrared SEBASS data recorded from Oatman, Arizona and a comparison of their unmixed results with AVIRIS. Exploration and Mining report 668 F. CSIRO Exploration and Mining, Wembley, Western Australia, p 38
- Holma H, Hyvarinen T, Lehtomaa J, Karjalainen H, Jaskari R (2009) Advanced pushbroom hyperspectral LWIR imagers. SPIE, Orlando
- Holma H, Mattila AJ, Hyvarinen T, Weatherbee O (2011) Advances in hyperspectral LWIR pushbroom imagers. SPIE, Orlando
- Hook SJ, Abbott EA, Grove C, Kahle AB, Palluconi FD (1999) Use of multispectral thermal infrared data in geological studies. In: Rencz AN (ed) Remote sensing for the earth sciences. Wiley, New York, p 3
- Hook SJ, Myers JJ, Thome KJ, Fitzgerald M, Kahle AB (2001) The MODIS/ASTER airborne simulator (MASTER) – a new instrument for earth science studies. *Remote Sens Environ* 76 (1):93–102
- Hunt GR (1970) Visible and near-infrared spectra of minerals and rocks: I. Silicate minerals. *Mod Geol* 1:283–300
- Hunt GR, Salisbury JW (1974) Mid-infrared spectral behavior of igneous rocks. Environmental research paper. U.S. Air Force Cambridge Research Laboratory, Cambridge
- Hunt GR, Salisbury JW (1976) Mid-infrared spectral behavior of metamorphic rocks. Environmental research paper. U.S. Air Force Cambridge Research Laboratory, Cambridge
- Kahle AB (1987) Surface emittance, temperature, and thermal inertia derived from Thermal Infrared Multispectral Scanner (TIMS) data for Death Valley, California. *Geophysics* 52 (7):858–874
- Kahle AB, Goetz AFH (1983) Mineralogic information from a new airborne thermal infrared multispectral scanner. *Science* 222:24–27
- Kahle AB, Rowan LC (1980) Evaluation of multispectral middle infrared aircraft images for lithologic mapping in the East Tintic Mountains, Utah. *Geology* 8:234–239

- Kahle AB, Madura DP, Soha JM (1980) Middle infrared multispectral aircraft scanner data: analysis for geological applications. *Appl Opt* 19(14):2279–2290
- Kahle AB, Gillespie AR, Abbott EA, Abrams MJ, Walker RE, Hoover G, Lockwood JP (1988) Relative dating of Hawaiian lava flows using multispectral thermal infrared images: a new tool for geologic mapping of young volcanic terrains. *J Geophys Res* 93:15239–15251
- Kealy PS, Hook SJ (1993) Separating temperature and emissivity in thermal infrared multispectral scanner data: implications for recovering land surface temperatures. *IEEE Trans Geosci Remote Sens* 31(6):1155–1164
- King RL, Ruffin C, LaMastus FE, Shaw DR (1999) The analysis of hyperspectral data using Savitzky-Golay filtering-practical issues. 2. In: Geoscience and remote sensing symposium, 1999. IGARSS '99 Proceedings. IEEE 1999 International. Hamburg, Germany
- Kruse FA, Taranik DL (1989) Mapping hydrothermally altered rocks with the airborne imaging spectrometer (AIS) and the airborne visible/infrared imaging spectrometer. In: Geoscience and remote sensing symposium, 1989. IGARSS'89. 12th Canadian symposium on remote sensing, 1989 International. Vancouver, Canada
- Lucey PG, Williams TJ, Mignard M, Julian J, Kobubun D, Allen G, Hampton D, Schaff W, Schlangen MJ, Winter EM, Kendall WB, Stocker AD, Horton KA, Bowman AP (1998) AHI: an airborne long-wave infrared hyperspectral imager. *SPIE*, San Diego
- Lyon RJP (1965) Analysis of rocks by spectral infrared emission (8 to 25 microns). *Econ Geol* 60 (4):715–736
- Lyon RJP, Burns EA (1963) Analysis of rocks and minerals by reflected infrared radiation. *Econ Geol* 58(2):274–284
- Lyon RJP, Tuddenham WM, Thompson CS (1959) Quantitative mineralogy in 30 minutes. *Econ Geol* 54(6):1047–1055
- Mauger A (2003) Comparison of various remote sensing and spectral radiometer instruments. *MESA J* 29:26–29
- Müller A, Richter R, Habermeyer M, Dech S, Segl K, Kaufmann H (2005) Spectroradiometric requirements for the reflective module of the airborne spectrometer ARES. *IEEE Geosci Remote Sens Lett* 2(3):329–332
- Mumin AH, Fleet ME, Longstaffe FJ (1996) Evolution of hydrothermal fluids in the Ashanti gold belt, Ghana; stable isotope geochemistry of carbonates, graphite, and quartz. *Econ Geol* 91:135–148
- Pignatti S, Lapenna V, Palombo A, Pascucci S, Pergola N, Cuomo V (2011) An advanced tool of the CNR IMAA EO facilities: overview of the TASI-600 hyperspectral thermal spectrometer. In: 3rd workshop on hyperspectral image and signal processing: evolution in remote sensing (WHISPERS), Lisbon, 6–9 June 2011. Lisbon, Portugal. doi:[10.1109/WHISPERS.2011.6080890](https://doi.org/10.1109/WHISPERS.2011.6080890)
- Riley DN, Cudahy TJ, Hewson RD, Jansing D, Hackwell JA (2007) SEBASS imaging for copper porphyry and skarn deposits, Yerington, NV. In: Proceedings of exploration 07: fifth decennial international conference on mineral exploration, Toronto, Canada
- Riley DN, Mars JC, Cudahy TJ, Hewson RD (2008) Mineral mapping for copper porphyry exploration using multispectral satellite and hyperspectral airborne sensors. In: Spencer JE, Titley SR (eds) Ores and orogenesis: circum-pacific tectonics, geologic evolution, and ore deposits, Arizona Geological Society Digest 22. Arizona Geological Society, Tuscon, pp 111–125
- Rowan LC, Mars JC (2003) Lithologic mapping in the Mountain Pass, California area using Advanced Spaceborne Thermal Emission and Reflection Radiometer (ASTER) data. *Remote Sens Environ* 84(3):350–366
- Rowan LC, Hook SJ, Abrams MJ, Mars JC (2003) Mapping hydrothermally altered rocks at Cuprite, Nevada, using the Advanced Spaceborne Thermal Emission and Reflection Radiometer (ASTER), a new satellite-imaging system. *Econ Geol* 98(5):1019–1027
- Ruffin C, King RL (1999) The analysis of hyperspectral data using Savitzky-Golay filtering-theoretical basis. 1, Geoscience and remote sensing symposium, 1999. IGARSS '99

- proceedings. IEEE 1999 international, Hamburg, Germany vol 2, pp 756–758, 28 Jun–02 Jul 1999. doi:[10.1109/IGARSS.1999.774430](https://doi.org/10.1109/IGARSS.1999.774430)
- Sabine C, Realmuto VJ, Taranik JV (1994) Quantitative estimation of granitoid composition from Thermal Infrared Multispectral Scanner (TIMS) data, Desolation Wilderness, northern Sierra Nevada, California. *J Geophys Res* 99:4261–4271
- Salisbury JW, Walter LS, Vergo N, D'Aria DM (1991) Infrared (2.1–25 mm) spectra of minerals. Johns Hopkins University Press, Baltimore
- Salisbury JW, Wald AE, D'Aria DM (1994) Thermal infrared remote sensing of Kirchhoff's Law: 1. Laboratory measurements. *J Geophys Res* 99(B6):11897–11911
- Savitzky A, Golay MJE (1964) Smoothing and differentiation of data by simplified least squares procedures. *Anal Chem* 36(8):1627–1639
- Swayze GA (1997) The hydrothermal and structural history of the Cuprite mining district, southwestern Nevada: an integrated geological and geophysical approach. PhD, University of Colorado, Boulder
- Swayze GA, Clark RN, Kruse FA, Sutley SJ (1992) Ground-truthing AVIRIS mineral mapping at Cuprite, Nevada. In: Summaries of the third annual JPL airborne geoscience workshop. R. O. Green. JPL Publication 92–14. Jet Propulsion Laboratory, Pasadena, California, pp 47–49
- Tsai F, Philpot W (1998) Derivative analysis of hyperspectral data. *Remote Sens Environ* 66 (1):41–51
- Vaughan RG, Calvin WM (2005) Mapping weathering and alteration minerals in the Comstock and Geiger Grade areas using visible to thermal infrared airborne remote sensing data. In: Rhoden HN, Steininger RC, Vikre PG (eds) Geological Society of Nevada symposium. Geological Society of Nevada, Reno, pp 1–20
- Vaughan RG, Calvin WM, Taranik JV (2003) SEBASS hyperspectral thermal infrared data: surface emissivity measurement and mineral mapping. *Remote Sens Environ* 85(1):48–63
- Vaughan RG, Hook SJ, Calvin WM, Taranik JV (2005) Surface mineral mapping at Steamboat Springs, Nevada, USA, with multi-wavelength thermal infrared images. *Remote Sens Environ* 99(1–2):140–158
- Vincent RK, Rowan LC, Gillespie RE, Knapp C (1975) Thermal-infrared spectra and chemical analyses of twenty-six igneous rock samples. *Remote Sens Environ* 4:199–209
- Whitbourn LB, Phillips R, James G, O'Brien MT, Waterworth MD (1990) An airborne multiline CO<sub>2</sub> laser system for remote sensing of minerals. *J Mod Opt* 37(11):1865–1872
- Young SJ, Johnson BR, Hackwell JA (2002) An in-scene method for atmospheric compensation of thermal hyperspectral data. *J Geophys Res* 107(D24):4774
- URL1: <http://tes.asu.edu/speclib/index.html>
- URL2: <http://speclib.jpl.nasa.gov>
- URL3: <http://speclab.cr.usgs.gov>

# **Chapter 25**

## **Validation of Thermal Infrared (TIR) Emissivity Spectra Using Pseudo-invariant Sand Dune Sites**

**Glynn Hulley and Alice Baldridge**

**Abstract** Land surface temperature and emissivity (LST&E) are important variables used in surface energy balance models, monitoring land-cover land-use changes, and in surface composition mapping. For most retrieval algorithms that generate LST&E products from spaceborne thermal infrared data, accurate retrieval of the LST depends on an accurate estimate of the spectral emissivity in the TIR region between 8 and 12  $\mu\text{m}$ . This is because both determine the amount of thermal radiance that gets emitted to the atmosphere from the Earth's surface. Consequently, validation of emissivity products from sensors such as MODIS and AIRS is a critical aspect for better quantifying uncertainties in the long-term LST record, and to help better constrain surface energy balance modeling. Two methods of validating the emissivity currently exist; an in situ method that utilizes TIR instruments such as radiometers employed in the field, and a laboratory-based method that uses a high spectral resolution spectrometer to measure field collected samples in a controlled environment. This chapter will discuss the methodology for validating emissivity products over pseudo-invariant sand dune sites using the lab-based method.

### **25.1 Introduction**

Accurate knowledge of the land surface emissivity in the Thermal Infrared (TIR: 8–12  $\mu\text{m}$ ) domain of the electromagnetic spectrum is essential to derive accurate Land Surface Temperatures (LSTs) from spaceborne TIR measurements such as the

---

G. Hulley (✉)

Jet Propulsion Laboratory, California Institute of Technology, National Aeronautics and Space Administration (NASA), Pasadena, CA, USA  
e-mail: [Glynn.Hulley@jpl.nasa.gov](mailto:Glynn.Hulley@jpl.nasa.gov)

A. Baldridge

Planetary Science Institute, Tucson, AZ, USA

Atmospheric Infrared Sounder (AIRS) (Susskind et al. 2003), the Moderate-Resolution Imaging Spectrometer (MODIS) (Wan 2008) and the Advanced Spaceborne Thermal Emission and Reflection Radiometer (ASTER) (Gillespie et al. 1998; Hulley et al. 2008). LST and emissivity are both key parameters used in monitoring land surface dynamics, climate modeling, and surface-boundary layer interactions. The emissivity in particular is an important constraint for balancing the Earth's surface radiation budget. For example recent sensitivity tests based on the NCAR (National Center for Atmospheric Research) Community Land Model (Bonan et al. 2002) indicate that an emissivity error of 0.1 (10 %) in desert regions will result in current climate models having errors of almost  $7 \text{ Wm}^{-2}$  in their upward longwave radiation estimates (Jin and Liang 2006; Zhou et al. 2003). This represents a much larger term than the surface radiative forcing due to an increase in greenhouse gases ( $\sim 2\text{--}3 \text{ Wm}^{-2}$ ), and makes accurate knowledge of the surface emissivity a key component for climate change studies.

The standard ASTER LST product, AST08, has been validated primarily over vegetated and water surfaces (Coll et al. 2005; Hook et al. 2007; Tonooka and Palluconi 2005), while the emissivity product, AST05, has been validated primarily over bare surfaces (Hulley et al. 2009a; Sabol et al. 2009; Schmugge et al. 2003; Schmugge and Ogawa 2006). Currently, the most comprehensive emissivity validation of the ASTER product encompassing a wide variety of different minerals was performed in validating the North American ASTER Land Emissivity Surface Database (NAALSED) v2.0 emissivity product (Hulley et al. 2009a). NAALSED was validated over arid/semi-arid regions using a set of large pseudo-invariant sand dune sites in the southwestern USA. The emissivity of sand samples collected at each of the dunes sites was measured in the laboratory using a Nicolet 520 FT-IR spectrometer and convolved with the appropriate ASTER system response functions. The average difference in emissivity with the lab measurements was found to be 1.6 % for all wavelengths (Hulley et al. 2009a). Other sensors such as AIRS and MODIS are more difficult to validate because of their coarse spatial resolution at 1 km or more. For example, due to the coarse resolution of the AIRS emissivity product ( $\sim 50 \text{ km}$ ), two large sand seas in southern Africa – the Namib Desert in Namibia, and the Kalahari desert in Botswana, were used to validate the AIRS v5 emissivity product using lab-measured sand samples collected from both sites (Hulley et al. 2009b). Different versions of the MODIS MOD11B1 emissivity product were also validated in the same manner at the Namib site (Hulley and Hook 2009a), while a new MODIS TES (MODTES) product, which uses the same retrieval algorithm as ASTER, was validated at Kelso dunes and the Algodones dunes in southern California using the lab-based method (Hulley and Hook 2011).

Validation of emissivity data from space ideally requires a site that is homogeneous in emissivity at the scale of the imagery, allowing several image pixels to be validated over the target site (Hulley et al. 2009a). Pseudo-invariant bare ground sites such as playas, salt flats, and claypans are generally the preferred targets for the long-term validation and calibration of visible, shortwave, and thermal infrared data (Bannari et al. 2005; Teillet et al. 1998). More recently Hulley and Hook (2009a) found that large, homogeneous sand dune fields are particularly useful for

the validation of TIR emissivity spectra due to their consistent and homogeneous mineralogy and physical properties over long time periods. One big advantage that sand dunes have over playas is that after rain events water gets rapidly infiltrated into the ground, whereas playas store water for much longer periods. Furthermore, drying of the sand surface does not lead to cracks and fissures, which typically occurs at any site with a large clay component such as playas and silt pans. It has been shown that surface roughness and cracks could artificially raise the emissivity due to cavity radiation effects (Mushkin and Gillespie 2005).

Using sand samples collected at specific sites, the mineralogy and composition of the sand can be accurately determined in the laboratory using reflectance and x-ray diffraction (XRD) measurements. Ideally the dune sites should be spatially uniform and any temporal variability of the surface due to changes in soil moisture and vegetation cover should be minimal since these changes have the effect of increasing the emissivity for all wavelengths.

The ten U.S. sand dune sites that have been proposed for the long term validation of TIR include: Great Sands National Park, Colorado; White Sands National Monument, New Mexico; Kelso Dunes, California; Algodones Dunes, California; Stovepipe Wells Dunes, California; Coral Pink Sand Dunes, Utah; Little Sahara Dunes, Utah; Killpecker Dunes, Wyoming; Moses Lake Basalt Dunes, Washington, and Sand Mountain, Utah. Of these sites, a super-set of the best sites in terms of size, homogeneity, and long term stability will be discussed in this chapter. These are the Algodones dunes, White Sands, Kelso Dunes, Great Sands, and Little Sahara.

## 25.2 Sand Dune Fieldwork

### 25.2.1 *Sampling Methods*

Sand samples at each of the ten sand dune sites were collected during five separate field campaigns from July–September 2008 (Hulley et al. 2009a). The samples were collected in dry conditions, i.e. no soil moisture from dew or recent rainfall. Google maps were used to locate the most homogeneous areas of the dune sites with minimal vegetation cover. Samples were collected randomly in these regions at intervals of approximately 100 m over an area roughly equivalent to 100 ASTER pixels (1 km × 1 km). At a few sites, samples were collected along transects across the dune site. Sampling areas included the crests, troughs, windward and leeward slopes of the dunes, including interdune areas. Approximately one tablespoon of sand was collected per sample, and the location recorded by GPS. Samples were collected by scooping the upper most few millimeters of the surface of the dunes which most closely represents what the satellite instrument observes in the TIR.

### 25.2.2 Laboratory Measurements

The reflectivity of each sand sample was measured from 2.5 to 15  $\mu\text{m}$  using a Nicolet 520 FT-IR spectrometer equipped with a Labsphere integrating sphere (Baldridge et al. 2009), and then converted to emissivity using Kirchhoff's law,  $\epsilon = 1 - r$ . The measurement consists of 1,000 scans at 4  $\text{cm}^{-1}$  spectral resolution acquired over a 10 min/sample and then average together (Baldridge et al. 2009). The uncertainty associated with the Nicolet FT-IR emissivities is 0.002 (0.2 %) (Korb et al. 1999). In order to remove background radiation, a spectrum is first acquired using a diffuse gold plate and then subtracted from the measurement. The corresponding emissivity for any particular sensor can then be found by convolving the lab spectrum with the appropriate sensor's system response function.

Figure 25.1 shows an example of lab emissivity measurements using the Nicolet that have been convolved to the spectral response functions of ASTER TIR bands 10–14. The solid line shows the mean lab spectra of 12 sand samples collected at the Kelso Dunes in southern California at full resolution. Errorbars on the convolved lab spectra (crosses) show the standard deviation of the different samples measured. Emissivity variations are typically greatest in the quartz Reststrahlen band which falls roughly between 8.3 and 9.6  $\mu\text{m}$ . Figure 25.2 shows mean lab emissivity spectra for the ten sand dune sites where sand samples were collected. This selection of dune sites was chosen because they encompass the full range of expected surface emissivities for bare surfaces in the TIR region. For example,

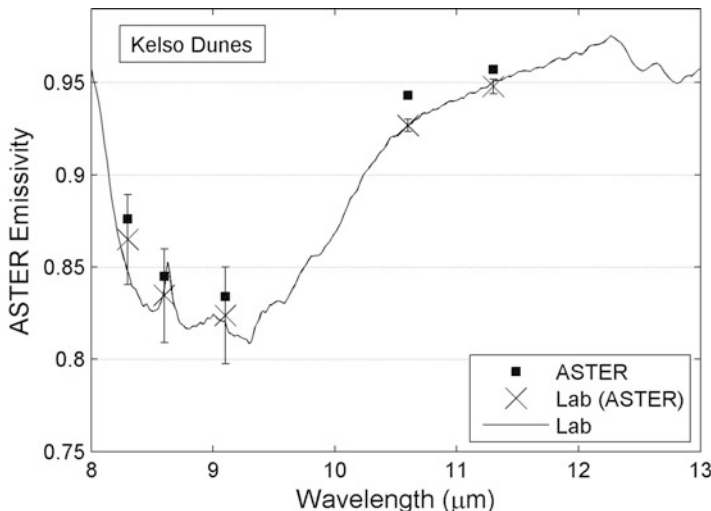


**Fig. 25.1** Emissivity spectra comparisons between ASTER (solid squares), lab measurements convolved to ASTER bandwidths (crosses), and the measured full resolution laboratory spectra (solid line) for the Kelso Dunes in southern California. Errorbars show standard deviation of the lab measured sand samples

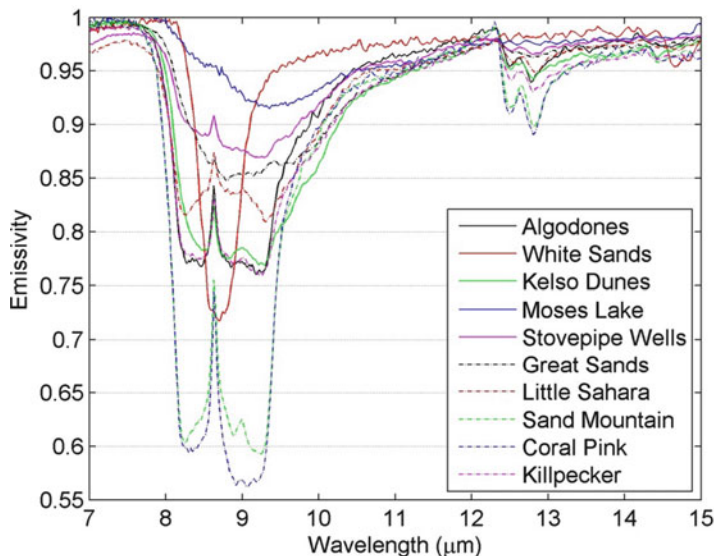


**Fig. 25.2** Mean emissivity spectra measured by the Nicolet 520 FT-IR spectrometer of sand samples collected from ten sand dunes sites in the southwestern USA

emissivities in the quartz band range from as low as 0.55 (Coral Pink) all the way up to 0.95 (Moses Lake).

X-Ray Diffraction (XRD) measurements were made for each sample at Arizona State University using the Rigaku D/Max-IIB. Samples were powdered and mounted on glass slides and scanned over the full  $2\theta$  range at a scan rate of 2 s per step at intervals of  $0.020^\circ$ . XRD peak lists were compared against the full International Catalog of Diffraction Data (ICDD) powder database for bulk mineral analysis. Each sample was also sorted and sieved. Table 25.1 shows the bulk mineralogy for each sand dune site in terms of their major and minor constituents as determined from the XRD measurements.

### 25.3 Sand Dune Sites

The following sections will describe the four super-set of sand dune sites in terms of locality, sand source and mineralogy. Each dune site section includes a figure (Figs. 25.3, 25.4, 25.5, 25.6, and 25.7) that shows an ASTER visible image of the dune site showing sampling areas, and emissivity spectra comparisons between the lab measured samples and the ASTER standard AST05 emissivity product.

**Table 25.1** Grain size and bulk mineralogy for ten sand dune sites determined from X-Ray Diffraction (XRD) measurements

Dune site	Grain size	Mineralogy (XRD)	
		Major	Minor
Algodones 32.95 N, 115.07 W	Medium to coarse	Quartz	–
Coral Pink 37.04 N, 112.72 W	Medium	Quartz	–
Great Sands 37.77 N, 105.54 W	Medium to coarse	Quartz	Potassium feldspar
Kelso 34.91 N, 115.73 W	Medium	Quartz	Potassium feldspar, magnetite
Killpecker 41.98 N, 109.10 W	Medium	Quartz	Plagioclase feldspar, epidote, magnetite
Little Sahara 39.7 N, 112.39 W	Fine	Quartz	Plagioclase feldspar, pyroxene carbonate, magnetite
Stovepipe Wells 36.62 N, 117.11 W	Medium	Quartz	Plagioclase feldspar, potassium feldspar
Moses Lake 47.05 N, 119.31 W	Fine	Quartz	Albite
White Sands 32.89 N, 106.33 W	Fine	Gypsum	–

### 25.3.1 The Algodones Dunes

The Algodones Dunes are located along the eastern portion of the Salton Trough near El Centro in the southeastern portion of California. The dunes are approximately 72 km long by 10 km wide, with dunes up to 80 m high and have very little vegetation cover. The prevailing northerly and westerly winds in the area cause the dunes to trend along a northwest-southeast axis (Norris and Norris 1961). The Imperial Valley and the Coachella Valley form the elongated, enclosed Cahuilla Basin, which was cut off from the Gulf of California by the formation of the Colorado River. Longshore currents moved large volumes of sand from the Whitewater River system at the north end of the lake. The shoreline gradually swings from south to southeast. Wind from the northwest moves sand parallel to the beach. The main source of sand, therefore, is deposits from the eastern beaches of Lake Cahuilla, which are composed primarily of quartz and feldspar (McCoy 1987).

### 25.3.2 White Sands National Monument

White Sands National Monument, located in the Tularosa Basin in south-central New Mexico, form the largest gypsum dune field in the world. The dune fields are a

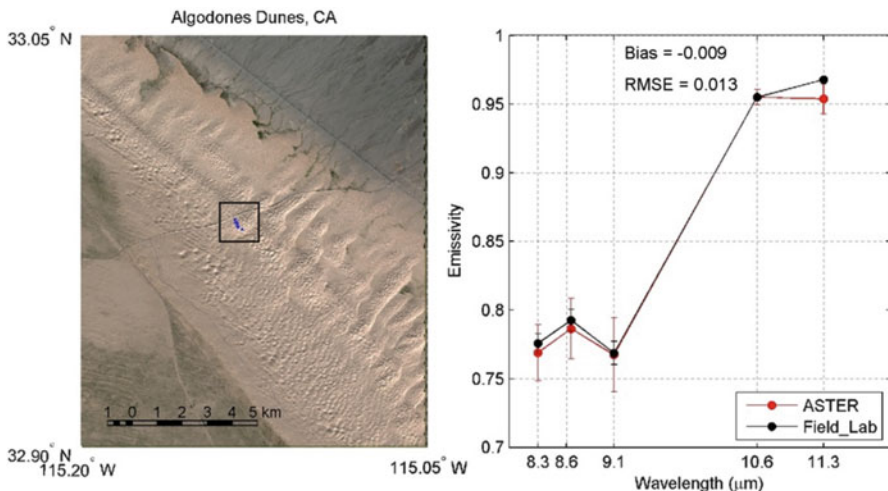


**Fig. 25.3** Visible ASTER image (left) showing locality of dune site and sampling locations (blue dots within box) for the Algodones dunes, California and emissivity spectra comparisons (right) between lab measurements of sand samples collected during 2008 and a mean ASTER emissivity standard product from 2000 to 2009

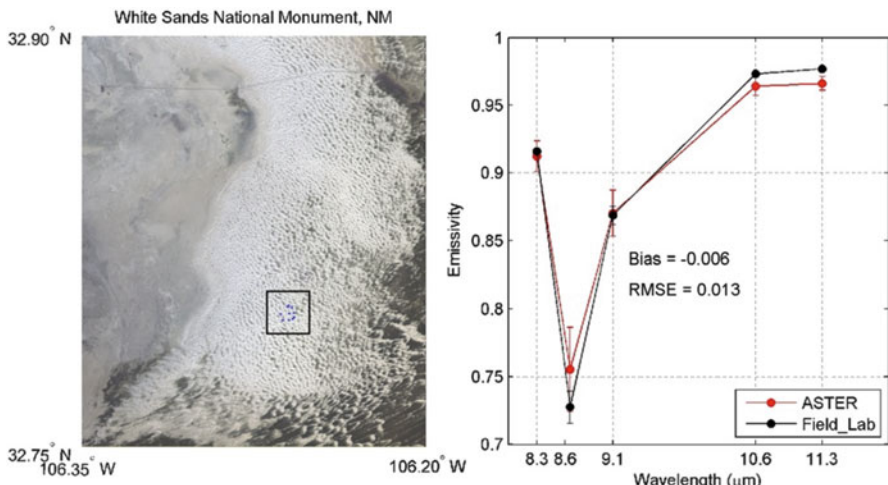


**Fig. 25.4** Same as Fig. 25.3 except results are for White Sands National Monument, New Mexico

maximum of 10 m high and cover an area of approximately  $704 \text{ km}^2$ , with the active dunes moving up to 10 m a year in the northeasterly direction. The dunes are bordered on the southwest by ephemeral Lake Lucero, on the west by the Sand Andres Mountains and on the east by the Sacramento Mountains. The dune sand originates from ablation and transport of Lake Lucero evaporitic gypsum deposits by southwesterly winds (McKee 1966).

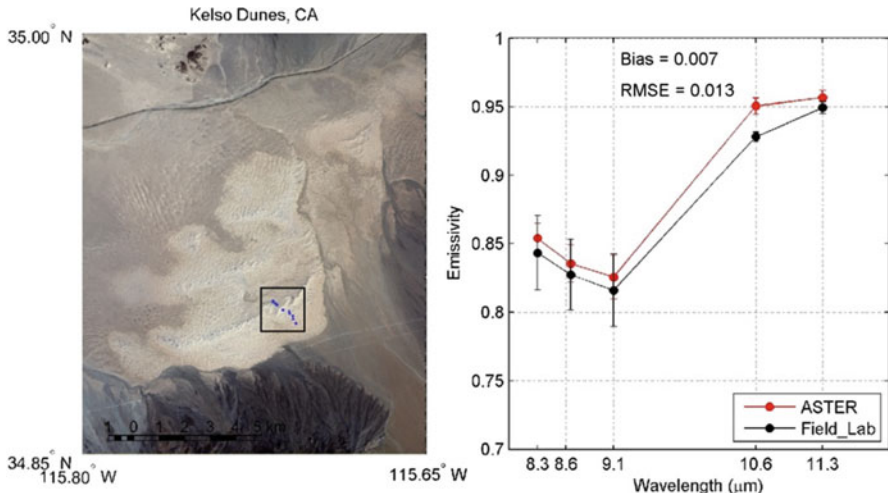


**Fig. 25.5** Same as Fig. 25.4 except results are for Kelso Dunes, California

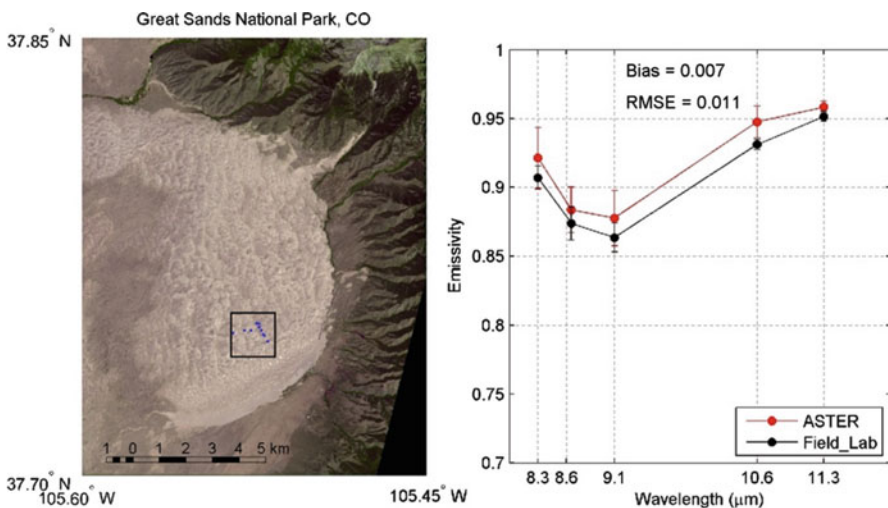


**Fig. 25.6** Same as Fig. 25.5 except results are for Great Sands National Park, Colorado

### 25.3.3 Kelso Dunes

The Kelso Dunes are located in the Mojave Desert National Preserve southeast of Baker, CA. Sand from the Mojave River alluvial apron is driven approximately 56 km by predominantly westerly winds, piling up at the base of the Granite and Providence mountains, which flank the south and southeast sides of the dune field. The dune field covers an area of 115 km<sup>2</sup> and contains dunes that rise up to 195 m

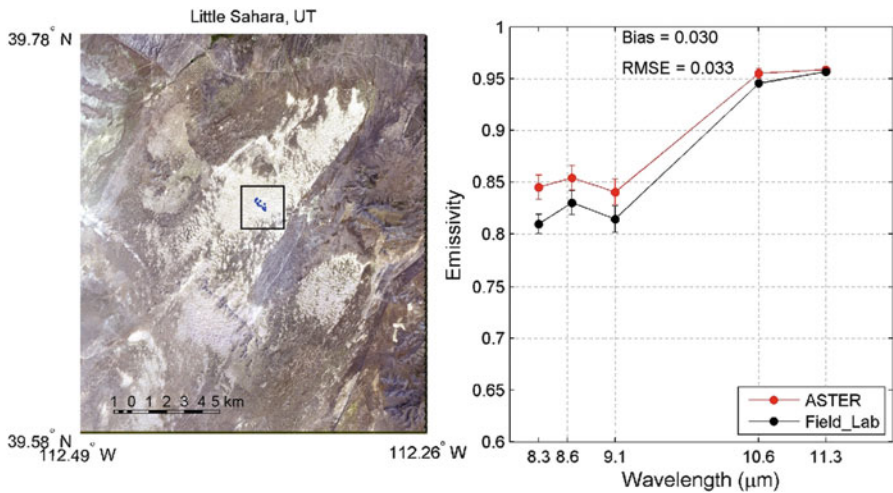


**Fig. 25.7** Same as Fig. 25.6 except results are for Little Sahara, Utah

above the terrain. Large portions of the dunes have sparse vegetation cover that stabilizes areas of previously drifting sand. The dunes are composed predominately of quartz and feldspar eroded from granites of San Bernardino Mountains to the south but also contain a large proportion of lithic fragments (Edgett and Lancaster 1993).

### 25.3.4 Great Sands National Park

Southwesterly prevailing winds have deposited sand in the San Luis Valley of southern Colorado and have deposited the greatest mass of sand near the western flank of the Sangre de Cristo Mountains. This area is preserved as the Great Sand Dunes National Monument, covering approximately  $104 \text{ km}^2$  and containing the tallest dunes in North America. The tallest dune rises 230 m from the floor of the San Luis Valley to an altitude of 2,600 m above sea level. The dunes are composed of up to 70 % volcanic rock fragments derived from the surface of the Santa Fe and Alamosa formations along with more recent fluvial and lacustrine deposits carried from the San Juan Mountains by the Rio Grande (Johnson 1967).

### 25.3.5 Little Sahara Dunes National Recreation Area

The Little Sahara sand dunes are the largest dune field in Utah at  $563 \text{ km}^2$ . The dune field is located 10 km north of Lynndyl and 40 km northeast of Delta, UT. The dune field is made up of primarily northwest trending active traverse dunes that average

about 10 m high, but climb to 200 m tall at the Sand Hills. One of the largest Lake Bonneville depositional features preserved is the Provo Shoreline related delta of the Sevier River. Regression of the lake from the Provo shoreline exposed the deltaic deposits, which were subsequently reworked into the aeolian dunes (Sack 1987). While the sand consists primarily of quartz grains, with minor amounts of feldspar, biotite, calcite from these deltaic deposits, they also contain lithic fragments, garnet and magnetite derived from the basaltic ash of the Pahvant Butte south of Delta, UT.

## 25.4 Discussion and Summary

Sand dune sites have been proposed as validation targets for validating high to medium spatial resolution emissivity products from spaceborne and aircraft sensors due to their pseudo-invariant characteristics over long time periods (Hulley et al. 2009a). Factors that could potentially result in temporal and spatial surface changes include seasonal vegetation phenology, aeolian processes such as wind erosion, deposition and transport, and daily variations in surface soil moisture from precipitation, dew, and snowmelt. Field observations by Hulley et al. (2009a) during the summer of 2008 showed the major portion of the dune sites to be bare, with the exception of Kelso and Little Sahara, which contained sparse desert grasses and reeds on the outer perimeter of the dune field and in some interdunal areas. As a result, care was taken not to include any ASTER pixels bordering on perimeter areas of the dunes in the validation results. Rainfall events, which would increase the surface soil moisture over the sand would result in a significant increase in TIR emissivity at the dune sites, especially in the 8–10  $\mu\text{m}$  range (Hulley et al. 2010; Mira et al. 2007). However, careful analysis using a combination of Advanced Microwave Scanning Radiometer – EOS (AMSR-E) soil moisture data and Tropical Rainfall Measuring Mission (TRMM) rainfall data showed no precipitation events close to the ASTER observations used for the validation. Furthermore, the majority of dune validation sites are in windy regions, at high altitude with low humidity <40 % (except for Algodones), and in semi-arid regions with high mean annual temperatures. These factors would limit lifetime of soil moisture in the first few micrometers of the surface skin layer as measured in the TIR. Using controlled lab measurements, Hulley et al. (2010) showed that almost all soil moisture in the top layer of two different types of sand were evaporated within the first hour of being exposed to morning sunlight resulting in emissivity decreasing back to the equilibrium ‘dry state’. This is in contrast to clays and silt pans that hold water for much longer periods due to their high clay content.

Figures 25.3, 25.4, 25.5, 25.6, and 25.7 show validation results of ASTER emissivity spectra from the North American ASTER Land Surface Emissivity Database (NAALSED) v2.0 (Hulley and Hook 2009b) with laboratory measurements of sand samples collected at each site. Errorbars show spatial standard deviations of the lab-measured sand samples and spatio-temporal variations of the ASTER observations

for each site. ASTER visible images of each dune site are included showing dune coloration, surrounding topography and sampling locations (blue dots). The results show that ASTER matches closely the shape and magnitude of the lab emissivity at the majority of dune sites. ASTER emissivity differences with the lab results were on average <1.6 % for all wavelengths. For Kelso, Great Sands, and Little Sahara ASTER typically had emissivities a few tenths of a percent higher than the lab measurements, and this is most likely due to either limitations in the TES calibration curve to capture the full spectral contrast, or atmospheric correction effects.

## 25.5 Conclusions

Sand dune sites have been shown to be excellent targets for validating emissivity data from TIR sensors. This is due to the pseudo-invariant characteristics with respect to temporal and spatial surface changes and their consistent composition over long time periods. It is expected that TIR data from future missions such as the Hyperspectral Infrared Imager (HyspIRI) spaceborne sensor and the Hyperspectral Thermal Emission Spectrometer (HyTES) aircraft sensor will use sand dune targets as their primary validation targets. New field campaigns will be scheduled to collect a new set of sand samples in order to assess any temporal changes in composition at each site.

## References

- Baldridge AM, Hook SJ, Grove CI, Rivera G (2009) The ASTER spectral library version 2.0. *Remote Sens Environ* 114:711–715
- Bannari A, Omari K, Teillet RA, Fedosejevs G (2005) Potential of Getis statistics to characterize the radiometric uniformity and stability of test sites used for the calibration of earth observation sensors. *IEEE Trans Geosci Remote Sens* 43:2918–2926
- Bonan GB, Oleson KW, Vertenstein M, Levis S, Zeng XB, Dai YJ, Dickinson RE, Yang ZL (2002) The land surface climatology of the community land model coupled to the NCAR community climate model. *J Clim* 15:3123–3149
- Coll C, Sánchez JM, Caselles V, Valor E, Niclòs R, Galve JM (2005) Validation of ASTER derived surface temperatures and emissivities with ground measurements. *Geophys Res Abstr* 7:06440
- Edgett KS, Lancaster N (1993) Volcanoclastic aeolian dunes: terrestrial examples and applications to martian sands. *J Arid Environ* 25:271–297
- Gillespie A, Rokugawa S, Matsunaga T, Cothern JS, Hook S, Kahle AB (1998) A temperature and emissivity separation algorithm for Advanced Spaceborne Thermal Emission and Reflection Radiometer (ASTER) images. *IEEE Trans Geosci Remote Sens* 36:1113–1126
- Hook SJ, Vaughan RG, Tonooka H, Schladow SG (2007) Absolute radiometric in-flight validation of mid infrared and thermal infrared data from ASTER and MODIS on the Terra spacecraft using the Lake Tahoe, CA/NV, USA, automated validation site. *IEEE Trans Geosci Remote Sens* 45:1798–1807

- Hulley GC, Hook SJ (2009a) Intercomparison of versions 4, 4.1 and 5 of the MODIS land surface temperature and emissivity products and validation with laboratory measurements of sand samples from the Namib Desert, Namibia. *Remote Sens Environ* 113:1313–1318
- Hulley GC, Hook SJ (2009b) The North American ASTER Land Surface Emissivity Database (NAALSED) version 2.0. *Remote Sens Environ* 113:1967–1975
- Hulley GC, Hook SJ (2011) Generating consistent land surface temperature and emissivity products between ASTER and MODIS data for earth science research. *IEEE Trans Geosci Remote Sens* 49:1304–1315
- Hulley GC, Hook SJ, Baldridge AM (2008) ASTER land surface emissivity database of California and Nevada. *Geophys Res Lett* 35:L13401. doi:[10.1029/2008gl034507](https://doi.org/10.1029/2008gl034507)
- Hulley GC, Hook SJ, Baldridge AM (2009a) Validation of the North American ASTER Land Surface Emissivity Database (NAALSED) version 2.0 using pseudo-invariant sand dune sites. *Remote Sens Environ* 113:2224–2233
- Hulley GC, Hook SJ, Manning E, Lee SY, Fetzer EJ (2009b) Validation of the Atmospheric Infrared Sounder (AIRS) version 5 (v5) land surface emissivity product over the Namib and Kalahari Deserts. *J Geophys Res Atmos* 114, D19104
- Hulley GC, Hook SJ, Baldridge AM (2010) Investigating the effects of soil moisture on thermal infrared land surface temperature and emissivity using satellite retrievals and laboratory measurements. *Remote Sens Environ* 114:1480–1493
- Jin ML, Liang SL (2006) An improved land surface emissivity parameter for land surface models using global remote sensing observations. *J Clim* 19:2867–2881
- Johnson RB (1967) The great sand dunes of southern Colorado. U.S. Geological Survey, Denver, pp C177–C183
- Korb AR, Salisbury JW, D'Aria DM (1999) Thermal-infrared remote sensing and Kirchhoff's law 2. Field measurements. *J Geophys Res Solid Earth* 104:15339–15350
- McCoy WD (1987) Quaternary aminostratigraphy of the Bonneville Basin, western United States. *Geol Soc Am Bull* 98:99–112
- McKee ED (1966) Structures of dunes at White Sands National Monument, New Mexico (and a comparison with structures of dunes from other selected areas). *Sedimentology* 7:1–69
- Mira M, Valor E, Boluda R, Caselles V, Coll C (2007) Influence of soil water content on the thermal infrared emissivity of bare soils: implication for land surface temperature determination. *J Geophys Res Earth Surf* 112, F04003
- Mushkin A, Gillespie AR (2005) Estimating sub-pixel surface roughness using remotely sensed stereoscopic data. *Remote Sens Environ* 99:75–83
- Norris RM, Norris KS (1961) Algodones dunes of Southeastern CA. *Geol Soc Am Bull* 72:605–620
- Sabol DE, Gillespie AR, Abbott E, Yamada G (2009) Field validation of the ASTER temperature-emissivity separation algorithm. *Remote Sens Environ* 113:2328–2344
- Sack DI (1987) Geomorphology of the Lynndyl Dunes, west-central Utah. *Utah Geol Assoc Publ* 16:291–299
- Schmugge T, Ogawa K (2006) Validation of emissivity estimates from ASTER and MODIS data. In: Proceedings of 2006 international geoscience and remote sensing symposium, Toulouse, pp 260–262
- Schmugge T, Ogawa K, Jacob F, French A, Hsu A, Ritchie JC (2003) Validation of emissivity estimates from ASTER data. In: Proceedings of 2003 international geoscience and remote sensing symposium, Toulouse, pp 1873–1875
- Susskind J, Barnet CD, Blaisdell JM (2003) Retrieval of atmospheric and surface parameters from AIRS/AMSU/HSB data in the presence of clouds. *IEEE Trans Geosci Remote Sens* 41:390–409
- Teillet PM, Fedosejevs G, Gautier RP, Schowengerdt RA (1998) Uniformity characterization of land test sites used for radiometric calibration of earth observation sensors. In: Proceedings of the 20th Canadian symposium remote sensing, Calgary, AB, Canada, pp 1–4

- Tonooka H, Palluconi FD (2005) Validation of ASTER/TIR standard atmospheric correction using water surfaces. *IEEE Trans Geosci Remote Sens* 43:2769–2777
- Wan ZM (2008) New refinements and validation of the MODIS land-surface temperature/emissivity products. *Remote Sens Environ* 112:59–74
- Zhou L, Dickinson RE, Tian Y, Jin M, Ogawa K, Yu H, Schmugge T (2003) A sensitivity study of climate and energy balance simulations with use of satellite-derived emissivity data over Northern Africa and the Arabian Peninsula. *J Geophys Res Atmos* 108:4795

# Index

## A

Absolute temperature, 5  
Absolute zero, 1  
Acquisition strategy, 126  
Acquisition time, 20, 222  
Advanced Along-Track Scanning Radiometer (AATSR), 136, 254  
Advanced Biomass Burning Algorithm (ABBA), 359  
Advanced Microwave Scanning Radiometer-Earth Observing System (AMSR-E), 317  
Advanced scatterometer, 315  
Advanced Spaceborne Reflection and Emission Radiometer, 44  
Advanced Spaceborne Thermal Emission & Reflection Radiometer (ASTER), 136, 253  
Advanced Synthetic Aperture Radar (ASAR), 344  
Advanced Very High Resolution Radiometer/3 (AVHRR/3), 142  
Advanced Very High Resolution Radiometer (AVHRR), 136, 254  
Aerosol(s), 291, 379–380  
Aerospace’s Mineral and Gas Identifier (MAGI ), 44  
Agriculture modeling, 145  
Airborne, 349  
Airborne Hyperspectral Imager (AHI), 496  
Airborne Hyperspectral Imaging Systems (AISA), 496  
Airborne Hyperspectral Scanner (AHS ), 277  
Airborne Imaging Spectrometer (AIS), 496  
Airborne survey, 395  
Airborne thermal imagery, 457

Airborne Visible/Infrared Imaging Spectrometer (AVIRIS), 96, 496  
Air temperature, 262  
AISA OWL, 44  
Albedo, 18  
ALEXI model, 320  
Along Track Scanning Radiometer, 299  
Alteration, 498  
Alteration maps, 495  
Ambient temperature background, 357  
Annual temperature curve, 20  
Annual variability, 20  
Anomalies, 278  
Anomalous precursor thermal activity, 410  
Anomaly detection, 439  
Anthropogenic forcing, 267  
Anti-saturation mechanism, 156  
Apparent brightness temperature, 181  
Apparent thermal inertia (ATI), 17, 320–322  
AQUA platform, 142  
Aquatic environments, 120  
ARGUS, 496  
Array nonuniformity, 104  
Artefacts, 22  
ASTER Volcano Archive (AVA), 410  
ATI time series, 337  
Atmosphere-Land Exchange Inversion (ALEXI), 320  
Atmospheric contamination, 273  
Atmospheric correction, 14, 253  
Atmospheric correction (ATCOR), 269, 477  
Atmospheric disturbances, 17  
Atmospheric Infrared Sounder (AIRS), 516  
Atmospheric windows, 4–5, 154  
At-sensor radiance, 15  
AVHRR LST, 217  
AVIRIS imaging spectrometer, 378

**B**

Background flux, 462  
 Barometric height sensor, 74  
 Berlin InfraRed Optical System (BIROS), 149–175  
*Bi-conical reflectance*, 58  
 Bidirectional reflectance distribution function (BRDF), 18  
 Biomass Burning, 347–383  
 Bi-spectral approach, 377  
 Bi-spectral infrared detection (BIRD), 119, 136, 149–175, 269  
 Bi-spectral method, 166  
 8-bit, 12  
 12-bit, 12  
 Black body(ies), 8, 289  
 Blackbody fit, 52  
 Blackbody radiance at the ground surface, 15  
 Blackbody radiation, 5  
 Blimp, 70  
 Bolometers, 30  
 Brightness temperature (BT), 78, 289  
 Building density, 486  
 Building façade, 38  
 Building models, 36  
 Buoy, 301  
 Burned area, 368  
 Burning garbage dumps, 430  
 Burn scars, 368  
 Burnt area, 145

**C**

Calibration functions, 14  
 Calibration lamps, 178  
 Calibration procedures, 163  
 Calibration results, 27  
 Calibration systems, 178  
 Camera calibration, 40  
 Carbon dioxide, 350  
 Carbon monoxide, 350  
 Carnegie Airborne Observatory (CAO), 96  
 CASA-212 aircraft, 395  
 CBER-4, 141  
 CBERS-3, 136, 141  
 CBERS-2b, 141  
 CBERS-4b, 141  
 Centralia, 430  
 Cerrado fires, 371  
 CH<sub>4</sub>, 430  
 Change detection, 276  
 Chemical constituents, 45  
 China-Brazil Earth Resources Satellite (CBERS), 137, 141  
 Cities, 476

Classification accuracies, 368

Classification scheme, 486  
 Climate change, 267  
 Climate of buildings, 475  
 Climate services, 306–308  
 Climatology and evaporation, 145  
 Close-range applications, 27  
 Cloud contamination, 270–274  
 Cloud cover, 412  
 Cloud's and Earth's Radiant Energy System (CERES), 136  
 CO<sub>2</sub>, 349  
 Coal and peat fire detection, 145  
 Coal fire emission estimation, 446  
 Coal fires, 429  
 Collimator optics, 164  
 Compact Airborne Spectral Imager (CASI), 496  
 Compilation of application studies, 143  
 Conductive transport, 84  
 Constellation, 308  
 Contamination, 182  
 Contrast, 438  
 Convective heat flux, 465  
 Cooler, 93  
 Cooling, 394  
 Cooling engines, 160  
 Core Services, 198  
 Cross-section, 403  
 Cross-track Infrared Sounder (CrIS), 136  
 Crustal heat flow geothermal power, 454  
 Cryocooler, 187  
 Cryocooler electronics (CCE), 184  
 Cryogenic temperatures, 93

**D**

Daedalus, 477  
 Daily amplitude, 270  
 Dark current, 104  
 Decadal Survey, 120  
 Decentring distortion, 27  
 Detector, 11  
 Detector saturation, 12, 137  
 Diffuse reflectance spectra, 60  
 Digital elevation model (DEM), 407  
 Digital number (DN), 14  
 Directional-hemispherical reflectance (DHR), 46  
 Disturbance phenomena, 349  
 Diurnal cycle, 303  
 Diurnal fluctuation, 221  
 Diurnal temperature curves, 17  
 Diurnal temperature difference ΔT, 320  
 Diurnal temperature fluctuation, 335

- Diurnal temperature range, 336  
Diurnal thermal characteristics, 17  
3D modelling, 27  
Dozier, 237  
Dozier's model, 152  
Drought, 349  
Dynamic ranges, 11  
Dyson design, 98
- E**  
Early warning system, 156  
Earth Science Technology Office (ESTO), 128  
Earth Watch Programme, 198  
Ecosystem function, 121  
Effusion rates, 391  
Electromagnetic spectrum, 515  
El Niño, 301  
Emission baseline, 410  
Emission estimation, 443  
Emission signatures, 352  
Emissivities of metals, 9  
Emissivity, 254  
    correction, 15  
    effects, 15  
    error, 15  
    minima, 466  
    spectra, 262  
Emitted radiance, 14  
Empirical Mode Decomposition (EMD), 275  
Energy balance, 489  
Enhanced thematic mapper (ETM), 136  
Enhanced thematic mapper plus (ETM+), 269  
ENVI, 505  
Environmental Satellite (ENVISAT), 344  
Epidemiology, 201–202  
ERS satellite (ERS-Scat), 315  
Eruption forecasting, 411  
Eruptive temperature, 404  
European Organization for the Exploitation of Meteorological Satellites (EUMETSAT), 317  
European Space Agency (ESA), 198, 425  
ExoScan 4100, 60  
Exothermal process, 430  
Experimental measurements, 392  
Experiments, 31  
Exposure, 17  
External cooling system, 30  
Extinguishing, 431  
Extinguishing activities, 447
- F**  
False alarms, 159  
Fast Fourier Transform (FFT), 272  
Fast-Track, 198  
Feldspar, 502  
Fire characterization, 349  
Fire detection, 349  
    algorithms, 357  
    systems, 268  
Fire emissions, 349  
Fire experiment, 372  
Fire extents, 349  
Fire-fighting management, 150  
Fire impacts, 349  
Fire Information for Resource Management System (FIRMS), 355, 363  
Fire Locating and Modeling of Burning Emissions (FLAMBE), 382  
Fire Logistics Airborne Mapping Equipment (FLAME), 365  
Fire monitoring, 199  
Fire parameters, 155  
Fire Radiative Energy (FRE), 372  
Fire Radiative Power (FRP), 379  
Fire Recognition System (FIRES) study, 149  
Fire Recognition with Bi spectral Infra-Red Detector (FIREBIRD), 172  
Fire regimes, 349  
Fires, 347  
FIRESCAN, 364  
Fire weather, 349  
Fixed-wing, 70  
Flags, 242  
Flames, 351  
Flare up, 431  
Flight control, 77  
Flight lines, 495  
FLIR B200, 34  
FLIR InfraCAM, 34  
Focal length, 32  
Focal plane array (FPA), 97, 99  
Focal plane electronics (FPE), 190  
Forest degradation, 349  
Forest fire detection, 145  
Forward looking infrared (FLIR), 365  
Fourier-transform infrared (FTIR)  
    spectrometer, 53  
Fuegosit, 197–211  
Fuegosit Synthesis Study (FSS), 197  
Fuel consumption, 347  
Fuel moisture, 350  
Fumarole, 454  
Fumaroles fields, 419

**G**

Gain selection, 11  
 Gangopadhyay, P., 145  
 Gas flares, 22  
 Geometric distortions, 14  
 Geoscan, 496  
 Geostationary Operational Environmental Satellite (GOES), 319  
 Geostationary sensors, 361  
 Geothermal activity, 453  
 Geothermal features, 455  
 Geothermal fluids, 456  
 Geothermal Heat Flux (GHF), 462  
 Geothermal heat loss, 470  
 Geothermally induced radiance, 419  
 Geothermal reservoirs, 470  
 Geothermal systems, 453–470  
 Geothermal waters, 456, 466  
 German Aerospace Center (DLR), 119, 150, 425  
 Germanium, 27  
 Geysers, 454  
 Global Fire Assimilation System (GFAS), 380  
 Global Fire Emissions Database (GFED), 368  
 Global Fire Monitoring Center (GFMC), 150  
 Global Inventory Modeling and Mapping Studies (GIMMS), 275  
 Global Monitoring for Environment and Security (GMES), 198, 380  
 Globar source, 48  
 GMES Service Elements, 198  
 Goddard Space Flight Center (GSFC), 95  
 Google Scholar, 381  
 GPS, 73  
 Grassland fires, 443  
 Graybody, 258  
 Green-house gasses, 429  
 Gridded field, 305  
 Ground-based, 1  
 Ground control points, 14  
 Ground to sensor atmospheric transmittance, 15  
 Group for High Resolution SST (GHRSSST), 308  
 GTOPO30, 262

**H**

Handheld radiometer, 19  
 Handheld thermal cameras, 436  
 Harmonic Analysis of NDVI Time Series (HANTS), 272  
 Hazard mitigation, 412  
 Hazards, 200–201  
 24 h cycle, 20

**H**

Health, 200–201  
 Heat buffering objects, 162  
 Heat Capacity Mapping Mission (HCMM), 319  
 Heat flux, 303  
 Helicopter, 70  
 Hemispherical reflectance, 501  
 High-gain modes, 12  
 High-gain options, 12  
 High Resolution Infrared Radiation Sounder (HIRS), 137  
 High temperature events (HTE), 166, 198  
 High-temperature fluids, 456  
 Histogram statistics, 440  
 HJ-1B satellite, 141  
 Homogeneity filter, 220  
 Hot gas, 436  
 Hotspot Recognition Sensor (HSRS), 359  
 Hot springs, 454  
 Human health, 121  
 Hydrothermal alteration, 466  
 Hydrothermal quartz, 498  
 Hydrothermal system, 462  
 Hyperspectral, 466  
 HYperspectral Digital Imagery Collection Experiment (HYDICE), 496  
 Hyperspectral Infrared Imager (HypIRI), 44, 64, 117–129, 381  
 Hyperspectral Thermal Emission Spectrometer (HyTES), 44, 93–114  
 Hyperspectral visible-near infrared-shortwave infrared (VSWIR) imaging spectrometer, 94  
 HypIRI-TIR instrument, 94

**I**

Ideal radiator, 5  
 Ignite, 430  
 Illumination source, 12  
 Image Assessment System (IAS), 181  
 Imaging, 350  
 Imaging Infrared Radiometer (IIR), 136  
 Imaging sensors, 29  
 Imperviousness, 486  
 Improved Multispectral Visible and Infra-red Scan Radiometer (IVISSR), 137  
 Incomplete combustion, 350  
 Infrared Atmospheric Sounding Interferometer (IASI), 137  
 Infrared Medium Resolution Camera (IRSCAM), 136  
 InfraRed MultiSpectral Sensor (IRMSS), 136  
 Infrared payload, 161

- InfraTec VarioCAM, 34  
*insitu*, 296  
Instantaneous field of view (IFOV), 95  
Instrument calibration, 296  
Intelligent payload module (IPM), 95, 126  
Intercalibrated, 23  
Inter-comparison, 242–246  
Internal baffling, 100  
Intra-annual temperature development, 20–21  
IPCC, 279  
Iterative Interpolation for Data Reconstruction (IDR), 273
- J**  
Jet Propulsion Laboratory (JPL), 53, 95, 410
- K**  
Kalpana-1, 343  
Kelvin, 1  
Keystone distortion, 98  
Kinetic temperature, 9  
Kirchhoff's law, 501
- L**  
Lab emissivity, 518  
Laboratory, 43–64, 372  
Lambertian effects, 262  
Land cover-dependence, 244  
Landsat 8, 183–191  
Landsat Data Continuity Mission (LDCM), 137, 139, 177  
Landsat ETM+, 381  
Landsat 7 ETM+ data, 8  
Landsat MSS, 269  
Landscape heterogeneity, 348  
Land subsidence, 434  
Land surface composition, 121  
Land surface dynamic, 349  
Land surface temperature (LST), 215, 253  
    profiles, 488  
    retrieval, 144  
Latent heat, 350  
Launch site, 193  
Lava density, 393  
Lava flow, 391–407  
    Lava flow velocity, 392  
    Lava specific heat capacity, 393  
    Lava temperature, 406–407  
Least squares material matching, 507  
Lenses, 27
- Light Detection And Ranging (LIDAR), 395  
Lightning, 429  
Limestone burning, 443  
Linear constraint, 297  
Line scanners, 365  
Liquid helium, 106  
Liquid nitrogen, 11  
Lithologies, 498  
Long Term Acquisition Plan (LTAP), 137  
Long Term Data Record (LTDR), 275  
Long-wave infrared (LWIR), 44  
Low earth orbit, 94  
Low-gain options, 12  
Lunar views, 124
- M**  
Magma, 424  
MAKO, 44, 496  
Man-made materials, 62  
Mann-Kendall framework, 278  
Mapping, 368  
Market prices, 33  
Mars Odyssey spacecraft, 119  
Material properties, 17  
Maximum likelihood (ML), 298  
Maximum radiative heat flux, 397  
Maximum surface temperature, 319  
Mean absolute differences (MADs), 242  
Measurement cycle, 57  
Mechanical cryocoolers, 106  
Mechanical scanning mirrors, 162  
Medium Resolution Spectral Imager (MERSI), 136  
Meteosat Second Generation (MSG), 331  
Meteosat Second Generation–Spinning Enhanced Visible and InfraRed Imager (MSG-SEVIRI), 136  
METOP-A, 317  
METOP-B, 317  
METOP satellite (METOP-Ascat), 315  
Micro-bolometer, 367  
MicroSatellite for Thermal InfraRed Ground Surface Imaging (MISTIGRI), 211  
Microscanning technique, 30  
MIDAC, 56  
Mid-wave infrared (MWIR), 44  
Mineral and Gas Identifier (MAGI), 496  
Mineral Mapping, 495–510  
Minerals, 60, 498  
MIRACO<sub>2</sub>LAS, 496  
Mixed emissivities, 15  
Mixed pixel, 15

- 8–14  $\mu\text{m}$ , 14  
 MobileIR M4, 78  
 MOD10, 258  
 MOD44, 258  
 Model validation and assimilation, 16  
 Moderate resolution atmospheric Transmission (MODTRAN), 254  
 Moderate Resolution Imaging Spectroradiometer (MODIS), 136, 253, 410  
 MODIS AQUA, 331  
 MODIS-ASTER Airborne Simulator (MASTER ), 44, 466, 496  
 MODIS LST, 216  
 MODIS TERRA, 335  
 MODTRAN-5 radiative transfer code, 354  
 Moisture content, 45  
 Mount Etna, 395  
 Moving window, 439–443  
 Mt Etna, 413  
 Mud-pots, 462  
 Multi-diurnal thermal mapping, 14  
 Multispectral data classification, 16  
 Multispectral Infrared Visible Imaging Spectrometer (MIVIS), 120, 395  
 Multispectral scanning imager-radiometer (MSU-GS), 136  
 Multispectral scanning imager-radiometer (MSU-MR), 136  
 Multispectral Visible and Infra-red Scan Radiometer (MVISR), 137  
 MYD02, 335  
 MYD09, 335
- N**  
 National Aeronautics and Space Administration (NASA), 95, 183, 253, 356  
 National Buoy Data Center, 182  
 National Oceanic and Atmospheric Administration—Advanced Very High Resolution Radiometer (NOAA-AVHRR), 275  
 National Polar-orbiting Operational Environmental Satellite System (NPOESS), 383  
 Near infrared (NIR), 350  
 Near-surface heat fluxes, 453  
 Near-surface water, 303  
 Negative temperature, 21  
 Negative temperature values, 138  
 NERC-FSF, 57
- New Infrared Sensor Technology (NIRST), 136  
 Nicolet FT-IR emissivities, 518  
 Nighttime data, 438  
 Nighttime scenes, 228  
 Normalized Difference Vegetation Index (NDVI), 258  
 North American ASTER Land Surface Database (NAALSED), 516
- O**  
 Ocean, 303  
 Octocopter, 74  
 On-board blackbody, 122  
 On-board cavity blackbody, 178  
 Opaque, 9  
 Orbital drift, 270  
 Ordinary least squares (OLS) regression, 278  
 Oscillating mirror motion, 22  
 Overflight, 22  
 Overpass time, 342
- P**  
 Pan-sharpening, 37–40  
 Path-leng, 234  
 Path radiance, 259  
 Peat fires, 430  
 Perfect IR emitter, 377  
 Persistent surface temperature anomalies, 459  
 Phases of alteration, 495  
 Photogrammetric analyses, 78  
 Physical principles, 24  
 Pixel-integrated signal, 357  
 Planck's law, 5  
 Planck's radiation law, 351  
 Plumes, 379  
 Point spread function, 377  
 Polarimetric L-band Multibeam Radiometer (PLMR), 323  
 Post-eruption, 392  
 Precursor phenomena, 411  
 Pre-dawn, 14, 457  
 Pre-dawn airborne thermal imagery, 464  
 Pre-launch, 181  
 Pre-launch performance, 191–193  
 Principal distance, 27  
 Principal point, 27  
 Pseudo-Invariant, 515–525  
 Pushbroom sensor, 504  
 Pushbroom sensor operation, 183  
 Pyro-electric detectors, 30  
 Pyrometamorphic rocks, 434

**Q**

Quantum detectors, 30  
Quantum Well Earth Science Testbed (QWEST), 94, 96  
Quantum well infrared photodetector (QWIP) arrays, 187

**R**

Radial distortion, 27  
Radiance temperature, 1  
Radiant exitance, 21  
Radiant flux, 7  
Radiative energy emission, 370  
Radiative transfer, 253, 291  
Radiometric accuracy, 192  
Rapid mapping, 455, 456  
Raw spectrum, 50  
Reference channel method, 51  
Reference field, 30  
Reference material, 47  
Research gaps, 429  
Reststrahlen bands, 501  
Retrieval coefficients, 296  
Retrieval-error, 301  
Rock forming minerals, 495  
Roof surface, 38  
Root Mean Square Error (RMSE), 324

**S**

SAFARI-2000, 382  
Sampling methods, 517  
Satellite overpass, 342  
Saturation, 12  
Saturation levels, 122  
Savannah ecosystem, 348  
Savitzky-Golay filter, 504  
Scan mirror, 11, 125  
Scene-by-scene calibration, 182  
Sealed surfaces, 486  
Season, 17, 439  
Sea surface emissivity, 291  
Sea surface reflectivity, 291  
Sea surface temperature (SST), 287–310  
Sea surface temperature retrieval, 144, 292–302  
Seeps, 456  
Sensor calibration, 19  
Sentinel 3 satellite, 133  
Sentinel-3 SLSTR, 381  
SEVIRI FRP-PIXEL, 362  
SEVIRI LST1, 247–249

SEVIRI LST2, 247–249  
Shear, 27  
Shortwave infrared (SWIR), 350  
Signal, 289  
Signal-to-noise ratio, 104  
Simulations, 295  
Slash-and-burn, 349  
Smoke emissions, 347  
Smoldering, 378  
Snow-free, 436  
Soil moisture, 315  
Soil Moisture Active Passive (SMAP) mission, 317  
Soil Moisture and Ocean Salinity (SMOS), 317  
Soil Moisture Content (SMC), 338  
Soil moisture saturation index (SMSI), 321  
Soil temperature, 21  
Soil-vegetation atmosphere transfer (SVAT) models, 319  
Solar elevation, 321  
Solar heating, 14, 458  
Solar radiance, 291  
Solar Zenithal Angle (SZA), 274  
Solid state sensors, 27  
Solidus temperature, 404  
Spaceborne, 349  
Spaceborne thermal sensors, 433  
Spatially Enhanced Broadband Array Spectrograph System (SEBASS ), 466  
Spatial resolution, 267  
Spatio-temporal detection, 410  
Spatio-temporal sampling, 296  
Spectral calibration, 110  
Spectral emission features, 466  
Spectral emittance, 9  
Spectral libraries, 501  
Spectral library, 501  
Spectral response(s), 171, 237  
Spectral sensitivity, 289  
Spectral smoothness, 52  
Spectrometer, 350  
Spectroscopy, 43–64  
Sphere sample port, 62  
Spinning Enhanced Visible and Infrared Imager (SEVIRI), 233–250, 331  
Split-window, 254  
Spontaneous combustion, 430  
Stability, 301  
Steam heating, 465  
Steaming ground, 456  
Stefan-Boltzmann constant, 7, 371  
Stefan-Boltzmann law, 6  
Sub-pixel, 155, 354

- Subpixel extent, 447  
 Subpixel fires, 347  
 Sub-skin SST, 303  
 Subsurface, 430  
 Subsurface geothermal fluids, 456  
 Subtle anomaly extraction, 439–443  
 Subtle thermal anomalies, 436  
 Sub-window, 442  
 Sun-sensor-object geometries, 19  
 Sun-synchronous, 126  
 Surface anomalies, 445  
 Surface coal fires, 430  
 Surface cover material, 481  
 Surface emissivity, 15  
 Surface temperature, 15  
     patterns, 476  
     rise, 320  
 Surface urban heat island (SUHI), 475  
 Surveillance, 202–203  
 Synchronicity, 342  
 Synthetic aperture radar (SAR), 315
- T**  
 $\Delta T$ , 17  
 Target points, 32  
 Technologie Entwicklungsträger (TET), 136, 149–175  
 Technologie Entwicklungsträger 1 (TET-1), 383  
 Technology Microwave Sounder (ATM), 496  
 Telescope, 100  
 Television and InfraRed Observation Satellite (TIROS-N), 319  
 Temperature change, 320  
 Temperature data loggers, 23  
 Temperature differences, 169  
 Temperature-emissivity separation (TES), 254, 477  
 Temperature error, 15  
 Temperature-independent spectral indices (TISI), 239  
 Temperature Independent Spectral Indices of Emissivity (TISIE), 369  
 Temperature profile, 399  
 Temperature variability, 21  
 Temperature variations, 397  
 Temperature vegetation dryness index (TVDI), 319  
 TERRA, 279  
 TERRA platform, 142  
 TERRASAR-X, 332  
 TES algorithm, 254  
 Test fields, 27  
 Testo 880–3, 34  
 Thematic mapper (TM), 136, 269  
 Theoretical background, 1–24  
 Thermal absorption, 14  
 Thermal Airborne Spectrographic Imager (TASI), 44  
 Thermal anisotropy, 270  
 Thermal anomalies, 435  
 Thermal anomaly detection, 268  
 Thermal array sensors, 30  
 Thermal band detector array, 179  
 Thermal band vicarious calibration, 181  
 Thermal camera, 4  
 Thermal conductivity, 320  
 Thermal downwelling flux on the ground, 15  
 Thermal dynamics, 3  
 Thermal Emission Imaging System (THEMIS), 119  
 Thermal flux distribution, 394  
 Thermal gradients, 106  
 Thermal inertia, 17, 320–322  
 Thermal infrared (TIR), 253, 318, 322  
     analyses, 21  
     detectors, 11  
     domain, 1, 4–5  
     hyperspectral sensor, 495  
     spectra, 501  
     spectroscopy, 44  
 Thermal Infrared Explorer (TIREX), 211  
 Thermal Infrared Instrument, 93  
 Thermal Infrared Multispectral Scanner (TIMS), 95, 496  
 Thermal infrared sensor (TIRS), 136  
 Thermally anomalous, 443  
 Thermal path radiance, 15  
 Thermal remote sensing community, 148  
 Thermal signal, 5, 436  
 Thermal skin effect, 303  
 Thermal spectroscopy, 496  
 Thermal water pollution, 1  
 Thermistors, 178  
 Thermodynamic temperature, 303  
 Thermographic cameras, 27–41  
 Threshold Techniques, 439  
 Tier 2 Decadal Survey missions, 93  
 Time-averaged discharge rate (TADR), 395  
 Time-domain reflectance (TDR), 316  
 Time series, 267–281  
 Time series analysis, 269  
 TIRS telescope, 186  
 Topography, 362  
 Total column water vapour (TCWV), 292

- Toxic gasses, 429  
Trace gas, 379–380  
Trend analyses, 278–281  
Triangle approach, 319  
Tropical Rainfall Measuring Mission (TRMM), 368, 524
- U**  
UAV-borne thermal imaging, 88  
Underground Coal Fires, 429–448  
United States Forest Service (USFS), 364  
Unmanned Aerial Vehicles (UAVs), 366–367  
Urban areas, 481  
Urban climatology, 145  
Urban environments, 481  
Urban heat island (UHI), 476  
Urbanization, 97  
Urban structure types (UST), 475–489  
US Geologic Survey (USGS), 54
- V**  
Vacuum chamber, 106  
Validating emissivity, 525  
Validation, 271, 515–525  
Vaporisation, 350  
Vegetation combustion, 349  
Vegetation fires, 347–383  
Vegetation fraction, 486  
Vegetation indices, 257  
Vegetation types, 484  
Vents, 87

- Very High Resolution Radiometer (VHRR), 137  
Vicarious, 192  
Visible (VIS), 350  
Visible and Infrared Scanner (VIIRS), 368  
Visible domain, 7  
Visible/Infrared Imager Radiometer Suite (VIIRS), 136  
Volcanic system, 455  
Volcanic thermal anomalies, 411  
Volcanoes, 97, 409–425  
Volume scattering, 61
- W**  
Water management, 199–200  
Water vapor scaling (WVS), 253  
Wavelengths, 292  
Weather forecasting, 304  
Wien, 1  
Wien's displacement law, 353  
Wildfire(s), 97, 151, 377  
Wind flow, 489  
Window, 290  
Wind smear, 22  
Wind speed, 23  
Wind streak, 22  
World Meteorological Organization (WMO), 268
- X**  
X-Ray Diffraction (XRD), 519